UC Berkeley

UC Berkeley Electronic Theses and Dissertations

Title

Structural Behavior of Bent Cap Beams in As-built and Retrofitted Reinforced Concrete Box-Girder Bridges

Permalink

https://escholarship.org/uc/item/1f02v32f

Author

Moustafa, Mohamed Aly Abdel-Razik

Publication Date

2014

Peer reviewed|Thesis/dissertation

Structural Behavior of Bent Cap Beams in As-built and Retrofitted Reinforced Concrete Box-Girder Bridges

By

Mohamed Aly Abdel-Razik Moustafa

A dissertation submitted in partial satisfaction of the

requirements for the degree of

Doctor of Philosophy

in

Engineering – Civil and Environmental Engineering

in the

Graduate Division

of the

University of California, Berkeley

Committee in charge

Professor Khalid M. Mosalam, Chair
Professor Stephen A. Mahin
Professor Allan Sly

Fall 2014

Structural Behavior of Bent Cap Beams in As-built and Retrofitted Reinforced Concrete Box-Girder Bridges

© Copyright 2014

By

Mohamed Aly Abdel-Razik Moustafa

ABSTRACT

Structural Behavior of Bent Cap Beams in As-built and Retrofitted Reinforced Concrete Box-Girder Bridges

By

Mohamed Aly Abdel-Razik Moustafa

Doctor of Philosophy in Engineering – Civil and Environmental Engineering

University of California, Berkeley

Professor Khalid M. Mosalam, Chair

Research on resilient infrastructure systems is expanding. As we experience more infrastructure deterioration in the US, numerous efforts are ongoing for building the nation's new infrastructure and maintaining the existing one. Bridges are key components of infrastructure that are vulnerable to earthquakes and are undergoing retrofit or complete replacement. Thus, optimized seismic design of new bridges and informed retrofit decisions are indispensable. A specific design issue that is concerned with the structural response of bent cap beams in as-built and retrofitted box-girder bridges under gravity and seismic loads is tackled in this dissertation. The lack of proper account of box-girder slabs contribution to the integral bent cap can lead to an uneconomical seismic design of new bridges or unfavorable mode of failure in retrofitting existing ones. A combined experimental and computational research was undertaken in this study to investigate the structural behavior and seismic response of bent cap beams in as-built and retrofitted reinforced concrete box-girder bridges under the combined effect of vertical and lateral loading. In particular, the contribution of the box-girder slabs to the stiffness and strength of the integral bent caps was evaluated for optimized design and enhanced capacity estimation. The computational part of the study consisted of two phases: pre-test and post-test analyses. The experimental program involved testing two 1/4-scale column-bent cap beam-box girder subassembly using quasi-static and Hybrid Simulation (HS) testing methods. The test specimens were adopted from a typical California bridge that is modified from the Caltrans Academy Bridge, and were designed in light of the most recent AASHTO and Caltrans provisions.

The pre-test analysis phase of the computational research utilized one-, two-, and three-dimensional finite element models to carry out different linear and nonlinear static and time history analyses for both of the full prototype bridge and the test specimen. The pre-test analysis successfully verified the expected subassembly behavior and provided beneficial input for the experimental program. The first stage of the experimental program involved quasi-static cyclic loading tests of the first specimen in as-built and repaired conditions. Bidirectional cyclic loading tests in both transverse and longitudinal directions were conducted under constant gravity load.

A rapid repair scheme was adopted for the tested specimen using a Carbon Fiber Reinforced Polymer (CFRP) column jacket. A similar quasi-static cyclic test to the as-built specimen was carried out for the repaired specimen for comparison purposes and to verify the essentially elastic status of the bent cap beam. The second stage of the experimental study embraced the HS testing technique for providing the lateral earthquake loading to the test specimens. A new practical approach that utilized readily available laboratory data acquisition systems as a middleware for feasible HS communication was achieved as part of this study. The proper communication among the HS components and the verification of the HS system were first performed using tests conducted on standalone hydraulic actuators. A full specimen HS trial test was conducted using the previously tested repaired specimen to validate the whole HS system. The last phase in the experimental program involved retrofitting the column of the second specimen using CFRP jacketing before any testing to increase the demands on the bent cap beam for further investigation into its inelastic range of structural response. The retrofitted second specimen was then tested using multi-degree of freedom HS under constant gravity load using several scales of unidirectional and bidirectional near-fault ground motions.

The post-test analysis was the final stage of this study. The results from the as-built first specimen cyclic tests were used to calibrate the most detailed three-dimensional finite element model, which was previously developed as part of the pre-test analysis stage. The calibrated model was used to explore the effect of reducing the bent cap reinforcement on the overall system behavior and to investigate the box-girder contribution at higher levels of bent cap seismic demand. Based on the computational and experimental results obtained in this study, the effective slab width for integral bent caps was revisited. The study concluded that the slab reinforcement within an effective width, especially in tension, should be included for accurate bent cap capacity estimation. The study was finalized with an illustrative design example to investigate the design implications of the revised effective slab width and bent cap capacity estimation on the optimization of the bent cap design for a full-scale bridge.

To my special ones spanning three generations,

My caring parents, Aly and Manal…

My beloved wife, Maryam …

My wonderful kids, Malek and Farida …

ACKNOWLEDGMENTS

i

TABLE OF CONTENTS

LIST OF FIGURES

x

xiii

xviii

xxiii

LIST OF TABLES

1   Introduction

1.1   GENERAL

Bridges are key components of the infrastructure systems that facilitate the traffic flow on all types of highways. There are several types of bridges that vary by the material used in their construction, namely, steel, reinforced concrete (RC), prestressed concrete (PC), or composite bridges. Moreover, bridge types vary by the load-carrying structural system, e.g. box-girder bridges, truss bridges, cable stayed bridges ... etc. In California, RC and PC box-girder bridges are the most common types of bridge systems. Two examples of box-girder bridges in California are the iconic San Diego-Coronado bridge, Figure 1.1, and the overcrossing bridge shown in Figure 1.2. Vertical dead loads and live traffic loads are the main types of daily loading that a typical bridge experiences. On the other hand, lateral loads are less frequent in case of bridges. However, lateral loading that result from extreme events, such as earthquakes, can be catastrophic. Major earthquakes in the past, such as the 1971 San Fernando, CA, the 1989 Loma Prieta, CA, the 1994 Northridge, CA, the 1995 Kobe, Japan, and the 1999 Chi-Chi, Taiwan, events have demonstrated how vulnerable bridges can be to seismic loads. An example of one of the several bridge failures and damages reported after the 1994 Northridge earthquake is shown in Figure 1.3. It is crucial to understand the seismic response of bridge structures and improve their performance during seismic events. Considerable research efforts were undertaken over the past decades to better understand the structural behavior, improve the seismic performance, and optimize the design of bridges. An optimized design for the different components of bridges is beneficial, not only for economic reasons, but also for an enhanced performance.

Figure 1.1 San Diego- Coronado box-girder bridge, California (Photo: Brett Shoaf, Artistic Visuals)

Figure 1.2 Typical California box-girder bridge: W80-E50 Connector Overcrossing, Yolo County, California (courtesy of Mark Yashinsky, Caltrans)

Figure 1.3 Damaged portion of the Golden State Freeway, part of CA Interstate-5, at Gavin Canyon after 1994 Northridge earthquake (courtesy of FEMA Photo Library)

A central concept that is associated with seismic bridge design is the capacity design approach. Many research studies were cultivated to improve the capacity design principles for bridges, especially after the Northridge earthquake. One of the world leading authorities that sponsored and promoted many of those studies is the California Department of Transportation (Caltrans). Their bridge seismic design provisions are published in a special document; Caltrans Seismic Design Criteria (SDC) that is being regularly updated. Recently, the Caltrans SDC was heavily utilized by the American Association of State Highway and Transportation Officials (AASHTO) to produce the national AASHTO Guide Specifications for LRFD Seismic Bridge Design whose 1st edition was published in 2009. The essence of the capacity design approach adopted by either the latest Caltrans SDC (2013) or AASHTO Guide Specifications for LRFD Seismic Bridge Design (2011) is to direct all the damage during extreme events into the bridge columns that are designed to be ductile to prevent overall brittle modes of failures and collapse. The desired column design and ductility can be defined by a Performance-Based Earthquake Engineering (PBEE) framework but still has to satisfy the minimum requirements of Caltrans SDC or AASHTO LRFD seismic design. Designated as capacity-protected members, the bridge superstructure, joints, or bent cap beams are designed, on the other hand, to remain elastic when the column reaches its over-strength capacity. The very specific issue of how the accuracy of the capacity estimation of the integral bent cap beams in RC box-girder bridges can be enhanced as a critical part of the capacity design approach for bridges is the core of the study presented in this report. The main goal of this study is to investigate how the contributions of the box-girder soffit and deck slabs to the stiffness and strength of the bent cap beams can be accurately estimated for the purpose of cap beam capacity calculations.

The motivation of this study and the mechanics of the sought framework are inspired by extensive similar research studies that were carried out for buildings. Unlike bridges, the common practice in capacity seismic design in buildings is the weak beam-strong column (WBSC) approach, where yielding and plastic hinging are desired in the beams rather than the columns. That is because columns are the main gravity load carrying elements especially at elevated axial load levels as in the lower stories of tall buildings. Accordingly, columns in buildings are required to stay elastic to avoid excessive deformations and possible progressive collapse due to formation of soft story mechanisms. The essence of the WBSC, as suggested by ACI-318 (2008) for example, is to ensure that the capacity of the columns at a beam-column joint is at least 1.2 times the capacity of the beams connected at the same joint. Therefore, the capacity of the beam needs to be accurately estimated if the WBSC to be adopted. Otherwise, unexpected failure or undesired mechanism can occur if the column is designed using an underestimated beam capacity.

Since moment frames in buildings are monolithically integrated with the floor systems and slabs, the slab contribution can strengthen and stiffen the beams. The contribution of the slab is accounted for in design by using a flanged section (T-beams are the most popular) where the flange width is the chosen effective width (b_{eff}) according to codes and standards. Based on the loading and the location of the flanged section along the beam, the flange can be in the compression side of the beam (positive or sagging moment location) or it can be in tension (negative or hogging moments) at the top of the supports or at a cantilever supported end for example. Typically, the provisions of building codes are used to account for the effective width in the flanged section only in the compression side. However, in the last decade, new provisions were amended in the building codes to consider the slab contribution and slab transverse reinforcement in an equivalent effective width in the tension side as well. Again this is to make

3

sure the WBSC condition is satisfied if this is the desired mechanism. More details are provided in the background chapter that follows.

The same concept of the flanged effective width in compression and tension for building frames can be utilized in bridges but from a different perspective. As previously mentioned, the desired recent bridge seismic capacity design practice is to concentrate all the damage in the column while the beams remain elastic, i.e. weak column-strong beam (WCSB) approach. Plastic hinges in the cap beams in bridges are undesirable due to limited access to the beam region within the box-girder and uneconomical post-earthquake inspection and repair compared to the plastic hinging of the column. Also, bridge columns do not experience the elevated axial load levels as in the case of tall buildings. Therefore, the Caltrans SDC and AASHTO LRFD seismic design, as noted before, promote the WCSB capacity design framework. Accordingly, the superstructure, i.e. the bridge deck including the bent cap beam, is capacity protected by imposing the 1.2 times capacity check. In cast-in-place RC box-girder with integral bent caps, the contribution of the box-girder slabs results in a flanged bent cap beam section. Currently, the Caltrans SDC (2013) and AASHTO LRFD seismic design (2011) suggest an effective width of 12 times the soffit or deck slab thickness in tension or compression sides for the cap beam capacity check. However, the slab reinforcement is not considered in the capacity check. Evaluating the 12 times the slab thickness effective width along with the validity of considering the box girder slab reinforcement in the process of the bent cap beam design and capacity check are the main outcome of this study.

Because of the nature of earthquakes, it is required to assess the structural dynamic behavior to account for the seismic effects. Several dynamic analysis techniques are available and utilized frequently in quantifying the seismic demands. Nevertheless, predicting the inelastic structural dynamic performance during a severe earthquake is a challenging task. On the other hand, experimental methods are more reliable to determine the structural performance and to validate analytical and computational models. Therefore, this study considered both experimental and computational methods to design a comprehensive mixed framework for evaluating the structural behavior of bent cap beams in RC box-girder bridges. A formal statement of the research problem, more details about the experimental and computational Finite Element (FE) analysis frameworks, and the organization of this dissertation are presented in the next sections..

1.2   PROBLEM STATEMENT AND OBJECTIVES

In this section we explicitly state what was informally mentioned in the previous section. In that regard, the undertaken study attempted to answer the following question: how should accurate estimation of the stiffness and capacity of a bent cap be assessed considering the contributions of the deck and soffit slabs framing into the bent cap in RC box-girder bridge systems under the combined effect of vertical and lateral loading? Alternatively, the problem statement can be stated as: what is the accurate estimate of the effective flange width of the bent cap beam due to the box-girder slabs contributions? Three research objectives further clarify the general problem statement and these can be listed as follows:

1. To investigate the behavior of bridge column-superstructure systems in light of the most recent AASHTO and Caltrans SDC provisions.

2. To investigate the system, particularly the integral cap beam, in different scenarios of as-built, repaired, and retrofitted bridge columns, i.e. to study whether strengthening bridge columns might migrate the mode of failure to the bridge superstructure because of possible amplified demands, i.e. lesser influence of the notion of the capacity protected members.

3. To determine what are the possible design implications and code recommendations, if any, dictated by accurate estimate of cap beam effective flange width and capacity calculation.

A mix of computational and experimental methods is utilized in this study to investigate the previously defined problem in the context of the defined research objectives. More details about the research methodology with focus on the pursued computational and experimental programs are discussed next.

Meanwhile, in light of the defined problem statement and objectives, the following four main contributions garland the study:

1. Revisiting the effective width considered for bent cap beam design to account for the contributions from the box-girder soffit and deck slabs to its stiffness and strength.

2. Investigating the effectiveness of Carbon Fiber Reinforced Polymer (CFRP) repair and retrofit techniques mainly for altering the column structural behavior and evaluating the resulting subassembly performance.

3. Developing and successfully conducting Multi-Degree Of Freedom (MDOF) Hybrid Simulation (HS) as part of the conducted experimental program.

4. Calibrating a detailed FE model for the tested specimens and conducting a parametric study that complements the experimental observations for developing design recommendations of bent cap beams.

1.3   EXPERIMENTAL FRAMEWORK

The undertaken experimental program is the core of this research study as it was expected to provide conclusive observations about the contribution of box-girder slabs to the bent cap beam behavior and to serve as the underlying foundation for the computational model calibration and extended parametric study. The initially envisioned experimental program comprised two identical 1/4-scale subassembly specimens to be tested using two different lateral loading schemes. A quasi-static test that uses cyclic lateral loading was the first chosen loading scheme. HS method for testing using an online computational model subjected to selected earthquake excitation and interacting with the physically tested specimen was the second lateral loading scheme. However, the experimental program was modified in light of the results from the first specimen quasi-static test to finally conclude with 4 different tests. A similar test setup was used for all tests which involved testing the 1/4-scale subassembly in an inverted position, i.e. the box-girder is closer to the strong floor of the laboratory while the column pointing upward. Such setup was chosen for practical reasons and for its feasibility to easily apply the combined gravity and the lateral loads at the column tip in its inverted position. A brief discussion of each of the 4 conducted tests is presented next.

5

The first test in the four-test series, comprising the full experimental program, was a quasi-static test for the first specimen tested in as-built configuration under combined constant gravity load and bidirectional cyclic lateral loading. Two different levels of gravity load were used such that the first level corresponded to only the dead load while the second level considered additional loads due to live loads and the vertical component of the earthquake excitations. The bidirectional cyclic loading was applied independently in one direction at a time, i.e. a group of cycles was applied in the column-bent cap plane (transverse direction) then followed by a similar group of cycles in the box-girder longitudinal direction. The observed mode of failure was the desired Caltrans SDC WCSB which motivated the expansion of the experimental program.

Before proceeding with further testing, a repair decision was made to be pursued for the first tested specimen along with a retrofit decision for the second untested specimen. The retrofit aimed at strengthening the column using CFRP to amplify the moment demand on the cap beam for further bent cap capacity evaluation and exploring different modes of failure, if any. While the second specimen was planned to be tested using HS testing technique, the first tested specimen was repaired to be reused for HS system development and trials before the final test proceeds. However, a similar quasi-static test was also conducted first on the repaired specimen to compare with the as-built test for an evaluation of a rapid repair technique that uses CFRP. Thus, the sequence of the 4 tests evolved as follows: (1) first as-built specimen tested quasi-statically; (2) first repaired specimen and retested quasi-statically; (3) first repaired specimen used in HS development and test trials; and (4) second retrofitted specimen and tested in a HS setting.

As mentioned, the second test in the four-test sequence was a similar quasi-static test to the first test but applied to the first specimen after its CFRP repair. A constant gravity load that corresponds only to the second higher level used in the first test along with bidirectional cyclic lateral loading were used for the second test. Similar group of cycles as used in the first test were reapplied to the repaired specimen in the second test. However, the test was intentionally stopped earlier than the corresponding first test to make sure the repaired specimen still has some remaining force capacity for the sake of the third test.

The third test also utilized the first specimen that was repaired. The main objective of this test was only providing a real HS test trials to verify the development of the HS system that was established particularly for this research study but meant to be generic for future experimentation. Several test runs that used the Northridge earthquake ground motions recorded at the Sylmar and Rinaldi stations were applied with and without the effect of gravity load. Although the gravity load has been part of the original test plan, the trials that did not involve the gravity load were only intended to check the stability of the developed HS system.

The fourth and final test in the experimental program was the HS testing of the second specimen that was already retrofitted before any testing. The HS tests involved several runs that included uni- and bi-directional loading, different scales for the lateral excitations, and three different levels for the gravity load. Moreover, a new testing scheme was proposed and applied in few HS runs to account for the P-delta effect that incorporated not only the gravity load, but also the vertical component of the earthquake. This final test had several objectives as follows:

1. Evaluating the bent cap beam behavior and quantifying the effective slab width at higher moment demands than the design level.

2. Investigating the effectiveness of the CFRP retrofit technique.

3. Exploring the consequences of a column retrofit or its over-design on the mode of failure of the bridge system under seismic loading.

4. Developing a generic and robust HS testing technique that utilizes readily available data acquisition and control systems and combining them with a generic computational framework for a convenient and feasible HS system.

1.4   COMPUTATIONAL FRAMEWORK

The computational framework adopted in this study complemented the experimental program for arriving at comprehensive design implications and conclusions. This framework comprises two broad phases: I) the pre-test analysis phase and II) the post-test analysis phase. All the computational work conducted in this study was based on the FE Analysis (FEA) method. Several FEA software packages were utilized throughout this study in the pre- and post-test analysis phases. These are OpenSees (2000), SAP2000 (2012), and DIANA (2014). In addition, several analysis types were conducted, namely linear analysis under service dead and live loads, nonlinear pushover analysis, and nonlinear time history analysis.

The pre-test analysis primarily provided answers and cleared several issues that were associated with the experimental work. Thus, several linear and nonlinear one-, two-, and three-dimensional (1D, 2D, and 3D) models were utilized in this study to conduct the pre-test analysis before the experimental test specimens were built or the test setup was assembled. Three different types of models were used in the pre-test analysis. The first type used 1D elements for modeling either the full prototype bridge or the test subassembly specimen. The Open System for Earthquake Engineering Simulation (OpenSees) was used for analyzing the 1D models. The second type used 2D plane stress elements mainly for box-girder modeling. The commercial analysis package SAP2000 (Structural Analysis Program 2000) was used for analyzing the 2D models. The most sophisticated level of modeling is the 3D solid element model. The general purpose FEA package DIANA (DIsplacement ANAlyzer) was used for creating and linearly and nonlinearly analyzing the 3D models. The pre-test analysis phase had the following four main objectives where each of the 1D, 2D, and 3D models and the corresponding FEA fulfilled one or more of these objectives:

1. Verify expected subassembly behavior with respect to the mode of failure, and column and bent cap beam structural behavior.

2. Finalize the loading protocol especially for HS tests by ground motion selection and scaling.

3. Estimate the expected lateral forces during cyclic and HS tests for setup design and checks.

4. Inform the decision making on the proper locations and distribution of the instrumentation where maximum and informative straining actions are expected.

The post-test analysis used some of the pre-test analysis models to calibrate them against the experimental results and to carry out further analysis and a parametric study that complements the experimental work. The main focus of the post-test analysis is the 3D DIANA

7

solid model for its accuracy and extended capabilities. The main steps involved in the post-test analysis framework of this study are the model calibration and a parametric study at the tested subassembly level. However, extensions to a full bridge model and parametric study are possible for future work. The model calibration intended to reproduce the experimental results from the 3D DIANA model by focusing on the RC constitutive model parameters. The calibrated model was subsequently utilized to investigate different bent cap beam reinforcement designs for its optimized and economic design.

1.5   ORGANIZATION OF THE DISSERTATION

The dissertation consists of ten chapters and six appendices. Chapter 1 presents a general introduction of the problem statement, methodology, and main objectives of the undertaken study. Chapter 2 provides the necessary background related to the effective width of flanged beams in buildings and bridges. Moreover, the major previous studies that focused on evaluating the effective width and others that investigated bridge subassemblies and systems are reviewed and summarized in Chapter 2. The development of the experimental program, which is the core of the presented study, is the essence of Chapter 3. This chapter covers the prototype bridge geometry, subassembly specimen geometry and design, construction of the test specimens, material properties, test setup and loading protocol, and instrumentation used during the experimental program. Chapter 4 briefly summarizes all the pre-test analyses carried out before embarking on the experimental program. The presented pre-test analysis phase includes models and analyses for both the full prototype bridge and the subassembly specimens.

The experimental tests and discussions comprise the major part of this report and presented in Chapters 5 through 8. Chapter 5 discusses all the experimental observations and results obtained from the quasi-static cyclic testing of the first specimen as it was originally built. A large part of the discussion is dedicated to the bent cap beam behavior and its effective slab width. The repair carried out for the first specimen and a discussion of the repaired specimen quasi-static cyclic loading tests are presented in Chapter 6. All the details about the HS background, system components, and verification are then presented in Chapter 7. This chapter presents the HS trial tests that were conducted on the repaired first specimen as well. Chapter 8 is another major chapter in this report as it discusses the HS tests on the retrofitted second specimen with focus on the bent cap beam behavior and effective slab width.

The second phase of the computational framework, which is the post-test analysis, is discussed in Chapter 9. The design implications based on the outcome of this study is investigated for a full scale bridge bent cap and discussed in Chapter 9 as well. A brief summary and the main conclusions and future work based on this study are presented in Chapter 10. Several appendices are included at the end of the report for the completeness of the presented work. These appendices provide the additional details of specimen design, structural drawings, construction of the specimens, procedure of test setup construction, list of the used instrumentations, and the calibration of the strut load cells used in the tests.

2 Background

The study presented in this report is concerned with the structural behavior of box-girder bridge subassembly. The main focus is on the effective slab width of the integral cap beam which renders the contribution of the box-girder slabs to the cap beam stiffness and strength. This chapter provides important and relevant background associated with the flanged beam effective width in design codes and literature. Three main sections comprise the chapter. The first section presents the concept of the effective width and its importance as dictated by design philosophies. The design philosophy can differ from buildings to bridges. Thus, a brief synopsis of building and bridge design along with code provisions for flanged beam effective width in both buildings and bridges are also presented in the first section. The second and third sections are dedicated to literature review. The relevant previous studies that focused on evaluating the effective width of flanged RC beams, mainly in buildings, are reviewed in the second section. The third section concludes the chapter with a review of major studies that focused on testing bridge systems or subassemblies.

2.1 EFFECTIVE WIDTH

The concept of the effective width in flanged RC beams is a key notion associated with this study. Its importance can vary from preventing collapse in buildings to possible reinforcement optimization in bridges. Therefore, different provisions for the effective width exist in building codes and bridge design standards. More details are discussed in the following subsections.

2.1.1 Concept of Effective Flange Width

Two notions that are tied to flanged sections should be recognized: the behavior of the flange and the effective portion of the flange considered in design, which is designated as effective flange width and commonly abbreviated as effective width. For RC beams cast monolithically with a flange, the flange increases the beam stiffness and strength. This flange can be a floor slab in a building or a soffit or deck slab in a box-girder bridge for example. Traditionally, the flange was assumed to be effective only in compression, but a flange also can act as a tension element (Pantazopoulou et al., 1988). Whether the flange acts in tension or compression depends on the loading and location of the cross-section. In a typical floor system comprising continuous beams with monolithic floor slab framing between columns, some sections will have negative and others will have positive bending moments as Sections A-A and B-B in Figure 2.1, respectively. Different loading will result in a different bending moment distribution, which might change the flange in a given section from being in compression to be in tension or vice versa. In some cases the beam can have flanges from both sides. For example, the integral monolithic bent cap beams

9

in box-girder bridges are double-flanged (I-shape) where one flange will be in tension while the other side in compression or vice versa.

Several illustrations are available in RC mechanics and design handbooks to better understand the behavior of flange and how it relates to shear lag. The example presented here in Figure 2.2, taken after Moehle (2014), shows a cantilever flanged beam that is loaded so that the flange is in tension. Under this loading, elongation of the flexural tension region of the beam web is transferred to the flange along interface *ad*, including shear stress along that interface (Figure 2.2d). Equilibrium of forces in the direction of the beam span is achieved through tensile stresses acting on face *ab* of the flange. Moment equilibrium about point *a* requires tensile stresses along interface *ad*, which in turn requires shear stress along *ab*. Shear stresses acting within the flange panel *abcd* cause cracks to bend away from the fixed edge (Figure 2.2c). Shear distortion, shown shaded in Figure 2.2d, relieves the tensile stresses with increasing distance along lines *ab* and *ad*, such that at sufficient distance the tensile stress drops essentially to zero. This action is what is known as shear lag. Note that equilibrium requires flange tension in both the longitudinal and transverse directions. Therefore, both longitudinal and transverse reinforcement are required in the flange. Several research studies focused only on understanding the shear lag phenomenon and the different factors that affect it, especially in box-girder bridges, such as Jovanovic (1998) and Luo et al. (2002). However, the study presented here and literature reviewed in the following section focus only on the effective width and no further discussion of shear lag is presented for brevity.
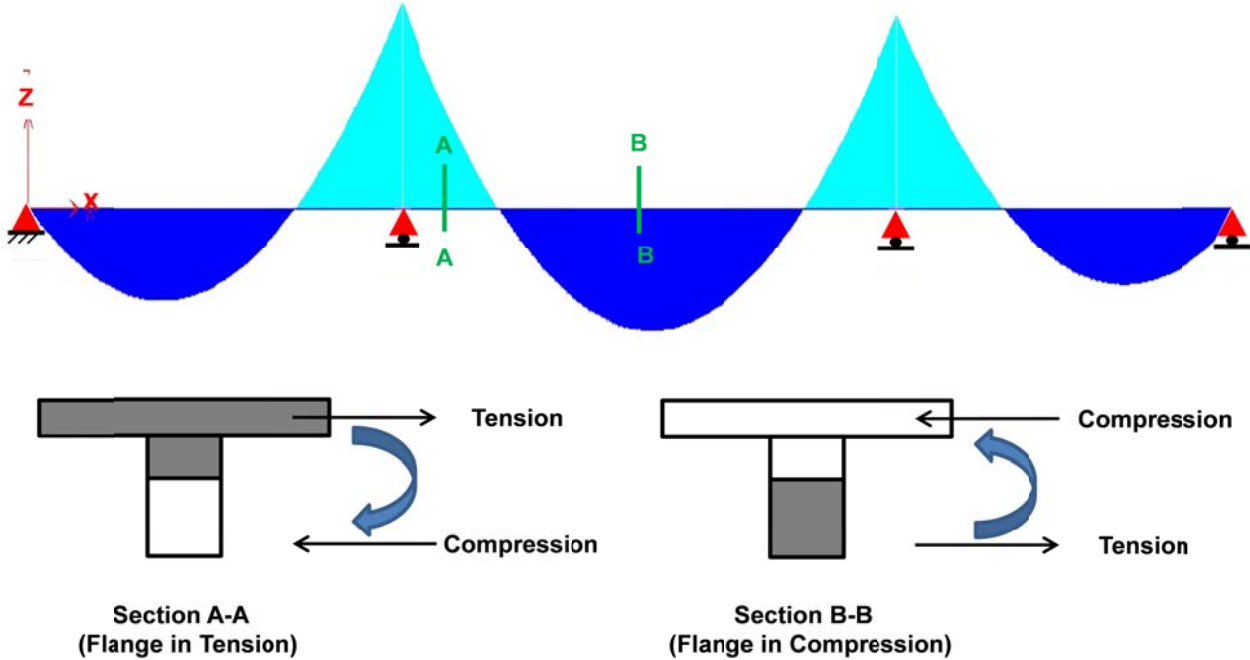
Figure 2.1 Typical bending moment diagram in continuous beam with section flange in tension or compression identified

10
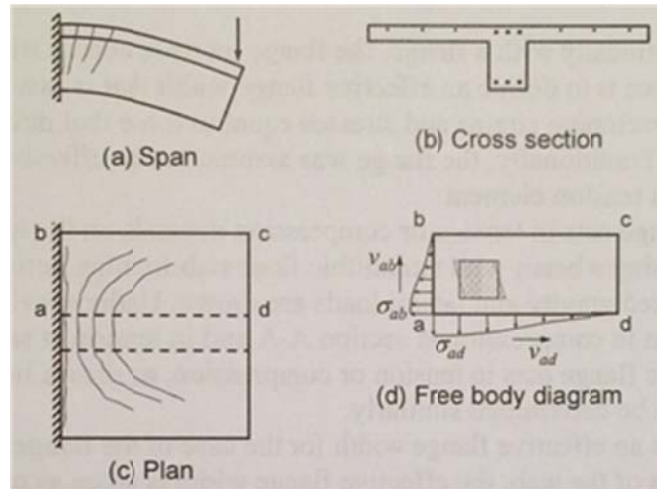
Figure 2.2 Deformations and stresses in a beam flange loaded in tension (Moehle, 2014)

The behavior of the flange was briefly highlighted in the previous paragraphs and the concept of the effective flange width is presented here. Common design practice is to define an effective flange width that is assumed to act monolithically with the beam. The choice of the effective width is typically based on an equivalent region of the slab where strains and stresses are assumed to be equal to those develop in the beam. The actual strain and stress distribution along both lateral sides of the beam would resemble a flat bell-shape where the largest values are developed in the beam and start decaying away from the beam. Figure 2.2d shows such distribution from one side of the beam along the edge *ab*. The strain bell-shape distribution is approximated with an equivalent rectangular strain block featuring similar strain in the beam and the adjacent flanges. The width of the equivalent strain block is what is known as the effective width, and commonly referred to as b_{eff}. Figure 2.3 shows schematically the actual strain distribution in the beam and adjacent flange along with equivalent strain block used to define the effective width. This width is very advantageous in design since it provides a simple way of calculating the cross-section neutral axis and estimating the section properties. For simplicity, design codes provide approximate formulas for estimating the effective width typically as a function of the slab thickness or beam span. The definition of the flange width as given by different building codes and bridge design standards is presented in following subsections.
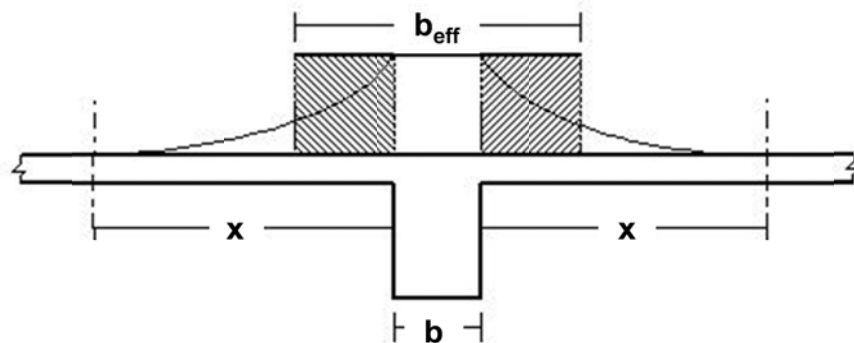
Figure 2.3 Notion of effective flange width

11

2.1.2 Effective Width in Building Codes

The latest provisions related to the effective width of flanged beams in three different buildings codes that are widely used worldwide are presented here. These are the American Concrete Institute Standards: ACI-318 (2011), the European Standards: EN-1992 (2009), and the British Standards: BS-8110 (2008).

2.1.2.1 ACI-318

The ACI-318 is the most popular building design code and is usually used as an underlying reference for various other international building codes. The ACI-318 provides extensive provisions that specify the effective flange width for T-beam (or L-beam) in the compression side. In addition, special provisions that are associated with the capacity seismic design approach (discussed in more details in subsection 2.1.4 of this chapter) exist in the ACI-318. The seismic provisions focus mainly on how the slab reinforcement within a T-beam tension effective width is considered besides special structural flanged-walls design provisions. This subsection provides the general compression side provisions first then the special seismic provisions for beams and walls.

The general provisions for the T-beam effective flange width in compression are given in ACI-318 Section 8.12. These provisions are often recalled for effective flange width in tension, whenever applicable as seen in the seismic provisions, and are summarized as follows:

- In T-beam construction, the flange and web shall be built integrally or otherwise effectively bonded together.

- For beams with slab on both sides (T-beam flanges), the effective width shall not exceed one-quarter of the span length of the beam, and the effective overhanging flange width on each side of the web shall not exceed eight times the slab thickness, and one-half the clear distance to the next web.

- For beams with a slab on one side only, the effective overhanging flange width shall not exceed: one-twelfth the span length of the beam; six times the slab thickness; and one-half the clear distance to the next web.

- Isolated beams, in which the T-shape is used to provide a flange for additional compression area, shall have a flange thickness not less than one-half the width of web and an effective flange width not more than four times the width of web.

- Where primary flexural reinforcement in a slab that is considered as a T-beam flange (excluding joist construction) is parallel to the beam, reinforcement perpendicular to the beam shall be provided in the top of the slab in accordance with the following:

  - Transverse reinforcement shall be designed to carry the factored load on the overhanging slab width assumed to act as cantilever. For isolated beams, the full width of overhanging flange shall be considered. For other T-beams, only the effective overhanging slab width needs to be considered.

  - Transverse reinforcement shall be spaced not farther apart than five times the slab thickness, or 18 inch.

The effective flange width is often recalled for recommended reinforcement distribution to control the cracks. The ACI-318 (2011) provides the following provision for reinforcement distribution in beams and one-way slabs (Section 10.6.6): — Where flanges of T-beam construction are in tension, part of the flexural tension reinforcement shall be distributed over an effective flange width as defined in ACI Section 8.12 (shown above), or a width equal to one-tenth the span, whichever is smaller. If the effective flange width exceeds one-tenth the span, some longitudinal reinforcement shall be provided in the outer portions of the flange.

The special seismic provisions that pertain to the effective flange width for beams and walls are presented. The reference to the tension effective flange width in beams was changed significantly from the ACI-318 2002 version to the 2012 version. In the older 2002 version, Section 21.4.2.2 specifies that the flange effective width for flange under tension should be taken as the smaller of: 25 percent of the beam span; center-to-center spacing of the beams; or sixteen times the slab thickness plus the beam width. In the ACI-318 2008 version, the reference to the tension effective flange width comes in the context of the beam capacity estimation as part of the capacity design approach requirement. The major change from the 2002 is the requirement of considering the tension slab reinforcement within an effective width equals to the one in the compression side only for estimating the overstrength beam capacity. This change was based on research done by Wight and Sozen (1975) and French and Moehle (1991) as mentioned in the commentary R21.6.2. These studies showed that using effective tension flange widths, that complies with what is now the current ACI Section 8.12 provisions for compressive flange width, gave reasonable estimates of girder negative bending strengths of interior connections at interstory displacement levels approaching 2 percent of story height.

In the case of walls, ACI-318 (2011) Section 21.9.5.2 specifies that unless a more detailed analysis is conducted the overhanging effective flange width of flanged sections shall extend from the face of the web a distance equal to the smaller of one-half the distance to an adjacent wall web and 25 percent of the total wall height. The wall provisions are based primarily on data pertaining to the tension flange effective width, but the commentary R21.9.5.2 adds the following: — Where wall sections intersect to form L-, T-, C-, or other cross-sectional shapes, the influence of the flange on the behavior of the wall should be considered by selecting appropriate flange widths. Tests 21.48[1] show that effective flange width increases with increasing drift level and the effectiveness of a flange in compression differs from that for a flange in tension. The value used for the effective compression flange width has little impact on the strength and deformation capacity of the wall; therefore, to simplify design, a single value of effective flange width based on an estimate of the effective tension flange width is used in both tension and compression.

2.1.2.2   EN-1992

EN-1992, also known as Eurocode 2: Design of concrete structures (2009), is the set of European Standards, belonging to Eurocodes, which specify technical rules for the design of concrete, RC and PC structures. The EN 1992 provides the following provisions for the effective flange width for all limit states:

---

[1] 21.48. Wallace, J. W., "Evaluation of UBC-94 Provisions for Seismic Design of RC Structural Walls," E*arthquake Spectra*, V. 12, No. 2, May 1996, pp. 327-348.

- In T beams the effective flange width, over which uniform conditions of stress can be assumed, depends on the web and flange dimensions, the type of loading, the span, the support conditions and the transverse reinforcement. The effective width of flange should be based on the distance l_0 between points of zero moment, which may be obtained as defined in Figure 2.4 below.

- The effective flange width b_{eff} for a T beam or L beam may be derived as given in Equation (2-1) where the parameters $b_{eff,i}$, b_w, and b are defined in Figure 2.5.

$$b_{eff} = \sum b_{eff,i} + b_w \leq b \quad (i = 1,2) \tag{2-1}$$

$$b_{eff,i} = 0.2b_i + 0.1l_o \leq 0.2l_o \tag{2-1}$$

$$b_{eff,i} \leq b_i \tag{2-1}$$
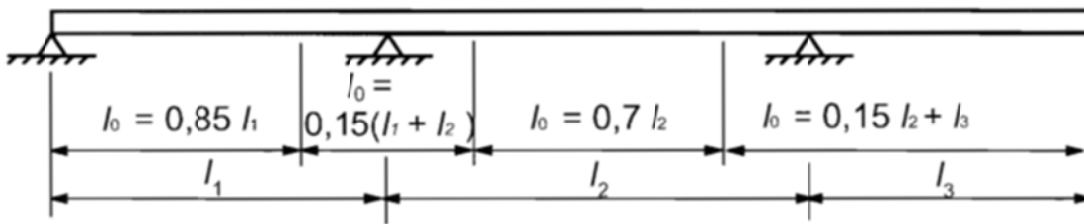
Figure 2.4 Eurocode 2 (EN 1992) definition of l_0 for calculation of effective flange width
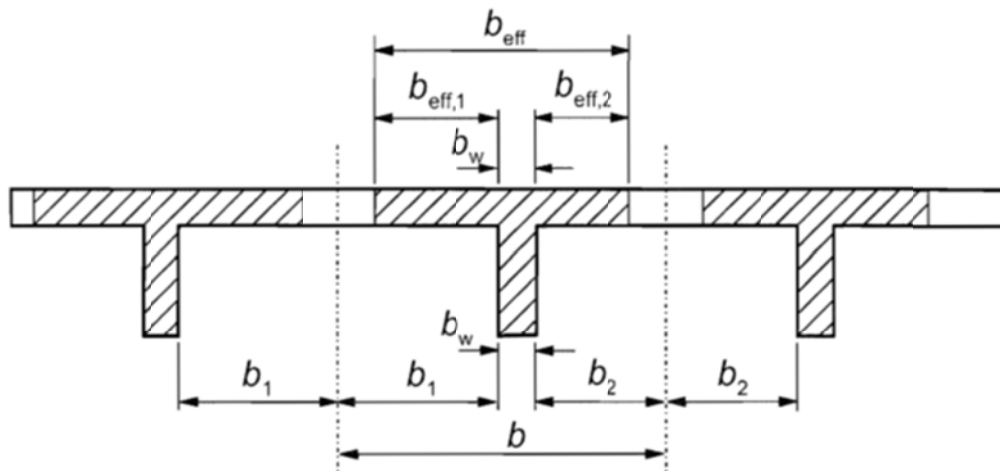
Figure 2.5 Eurocode 2 (EN 1992) effective flange width parameters

2.1.2.3 BS-8110

The British Standards BS-8110 (2008) relates the effective flange width of flanged beams to the beam span only rather than the slab thickness. Its provisions state that in the absence of any more accurate method for the determination of the effective flange width, it should be taken as: the web width + $L_z/5$ or the actual flange width if less in case of T-beams; and the web width + L_z /10 or actual flange width if less in case of L-beams; where L_z is the distance between points of zero moment, and for a continuous beam, may be taken as 0.7 times the effective beam span.

2.1.3 Effective Width in Bridge Codes

The effective width in the bridge design codes and specification often refers to either the distribution under concentrated loads, such as truck wheels, or the effective flange width that result from slab contributions. Only the provisions related to the effective flange width are presented here transverse. Meanwhile, the effective flange width itself can refer to either the slab flanges acting with longitudinal girders and box-girder webs or the effective flanges acting with integral bent cap beams. Here, longitudinal and transverse are with respect to the bridge axis. The integral bent cap effective width is associated usually with lateral, or in particular, seismic loading. On the contrary, the longitudinal girders effective width is associated with both vertical and lateral loading. The AASHTO LRFD Bridge Design Specifications provides provisions only for longitudinal girders. However, special seismic design documents such as the Caltrans SDC or the recently published AASHTO Guide Specifications for LRFD Seismic Bridge Design discuss the integral bent cap beam effective flange width. The AASHTO provisions for longitudinal girders, although is not the focus of this study, are presented for completeness besides the integral bent cap beam seismic design provisions in the following subsections.

2.1.3.1 *AASHTO LRFD Bridge Design Specifications*

The effective flange width of longitudinal superstructure girders or box-girder webs is called at several sections in the AASHTO LRFD Bridge Design Specification 4th Edition (2007). However, Section 4.6.2.6 is the central section where all the main effective flange width provisions are given. The provisions given in clauses 4.6.2.6.1 and 4.6.2.6.3 for general effective width definition and case of cast-in-place multi-cell superstructures are presented here. The reader is referred to clauses 4.6.2.6.2 and 4.6.2.6.4 for additional information regarding effective flange width in cases of segmental concrete box beams and orthotropic composite steel decks.

A relevant part from the AASHTO Section 4.6.2.6 that is worth mentioning is the commentary that defines the effective flange width as follows: "Longitudinal stresses in the flanges are spread across the flange and the composite deck slab by in-plane shear stresses. Therefore, the longitudinal stresses are not uniform. The effective flange width is a reduced width over which the longitudinal stresses are assumed to be uniformly distributed and yet result in the same force as the non-uniform stress distribution would if integrated over the whole width." In addition to the commentary definition, the key provisions that are related to the effective flange width are summarized in Figure 2.6 extracted from AASHTO and the following bullets:

- In the absence of a more refined analysis and/or unless otherwise specified, limits of the width of a concrete slab, taken as effective in composite action for determining resistance for all limit states, shall comply with Section 4.6.2.6 specifications.

- The calculation of deflections should be based on the full flange width.

- The effective span length used in calculating effective flange width may be taken as the actual span for simply supported spans and the distance between points of permanent load inflection for continuous spans, as appropriate for either positive or negative moments.

- The effective width for cast-in-place multi-web cellular superstructures may be taken to be as specified below in the following two bullets, with each web taken to be a beam. It may be

also taken to be the full width of the deck slab if the effects of shear lag in the end zones are investigated.

- For interior beams, the effective flange width may be taken as the least of:

  - One-quarter of the effective span length;

  - 12.0 times the average depth of the slab, plus the greater of web thickness or one-half the width of the top flange of the girder; or

  - The average spacing of adjacent beams.

- For exterior beams, the effective flange width may be taken as one-half the effective width of the adjacent interior beam, plus the least of:

  - One-eighth of the effective span length;

  - 6.0 times the average depth of the slab, plus the greater of one-half the web thickness or one-quarter of the width of the top flange of the basic girder; or

  - The width of the overhang.
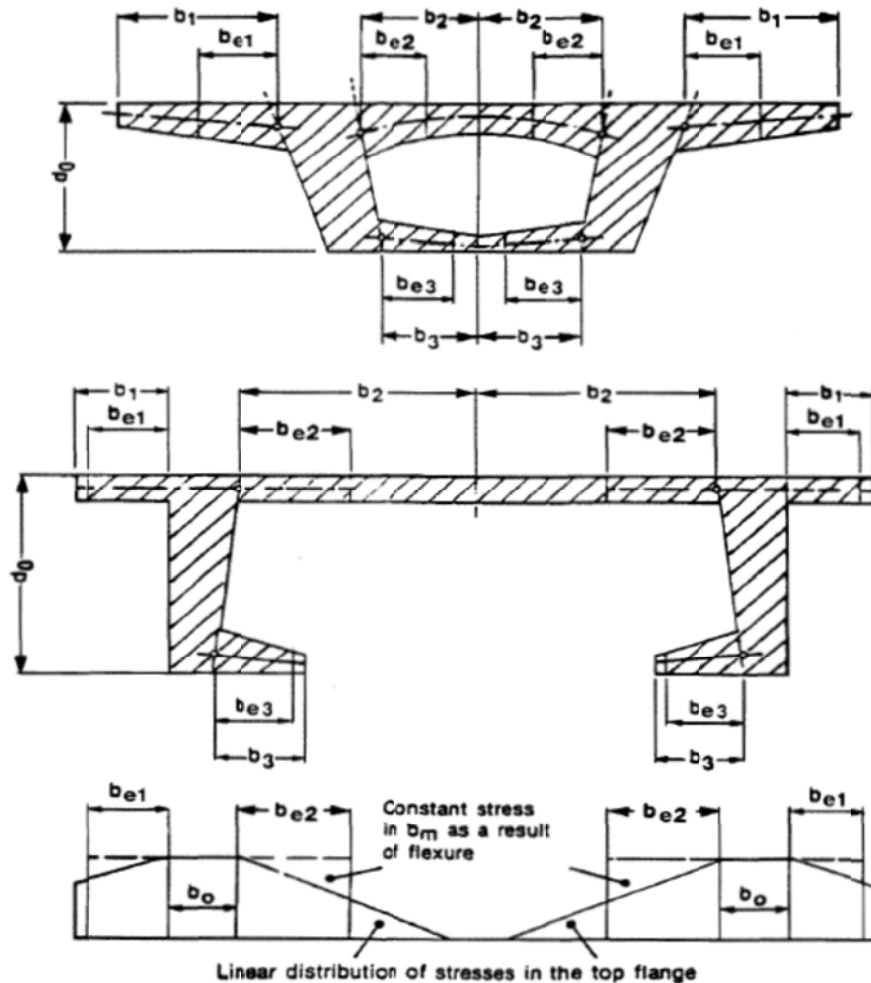
Figure 2.6 AASHTO (2007) Effective flange width in different cases of longitudinal girders and schematic linearized stress distribution along with corresponding effective width

16

Another important section that briefly touches on the effective flange width is section 5.7.3.4 that is concerned with the control of cracking by distribution of reinforcement. In this section, it is required that where flanges of RC T-girders and box girders are in tension at the service limit state, the flexural tension reinforcement shall be distributed over the lesser of the effective flange width, specified in section 4.6.2.6, or a width equal to 1/10 of the average of adjacent spans between bearings. In addition, if the effective flange width exceeds 1/10 the span, additional longitudinal reinforcement, with area not less than 0.4 percent of the excess slab area, shall be provided in the outer portions of the flange as a requirement of crack control.

2.1.3.2   *AASHTO Guide Specifications for LRFD Seismic Bridge Design* (*Caltrans SDC*)

A recent document by AASHTO was first published in 2009 to provide special provisions of bridge seismic design. The document is designated as AASHTO Guide Specifications for LRFD Seismic Bridge Design (2009) and the 2009 version is the 1st edition. These guide specifications differ from the current procedures in the LRFD specifications in the use of displacement-based design procedures instead of the traditional force-based "R-factor" method. The AASHTO seismic design provisions document appears to be inspired by the Caltrans SDC that has been used for more than two decades. It is to be noted that the latest AASHTO seismic guidelines 2nd edition (2011) and Caltrans SDC version 1.7 (2013) are very close. However, the provisions related to the effective flange of bridge superstructure and integral bent caps under seismic loading are identical in both of the AASHTO guide specifications for LRFD seismic design (2011) and Caltrans SDC (2013). A summary of these provisions is presented in the following bullets:

- The effective width of superstructure resisting longitudinal seismic moments, B_{eff} is defined by Equations (2-2) and (2-3).

$$B_{eff} = D_c + 2 \times D_s \quad \text{Box girders \& solid superstructures} \tag{2-2}$$

$$B_{eff} = D_c + D_s \quad \text{Open soffit superstructures} \tag{2-3}$$

  where D_c is the column diameter and D_s is the depth of the superstructure as shown in Figure 2.7. The effective width for open soffit superstructures (e.g. T-Beams & I-Girders) is reduced because they offer less resistance to the torsional rotation of the bent cap.

- The effective superstructure width can be increased for cross-sections away from the bent cap by using a spread from the cap face until the full section becomes effective (see Figure 2.7). On skewed bridges, the effective width shall be projected normal to the girders with one end of the width intersecting the bent face such that one half of the width lies on either side of the column centerline (see Figure 2.7). Additional superstructure width can be considered effective if the designer verifies that the torsional capacity of the cap can distribute the rotational demands beyond the effective width stated in Equations (2-2) and (2-3).

- If the effective width cannot accommodate enough steel to satisfy the overstrength requirements, the following actions may be taken: thicken the soffit and/or deck slabs; increase the resisting section by widening the column; haunch the superstructure; or add additional columns

- Bent caps are considered integral if they terminate at the outside of the exterior girder and respond monolithically with the girder system during dynamic excitation.

- The integral cap width considered effective for resisting flexural demands from plastic hinging in the columns shall be determined by Equation (2-4): (See Figure 2.8)

$$B_{eff} = B_{cap} + (12 \times t) \tag{2-4}$$

where t is thickness of the top or bottom slab. It is to be noted that revisiting the 12-times slab-thickness used in the bent cap beam effective width estimation is one of the main focus of this study.
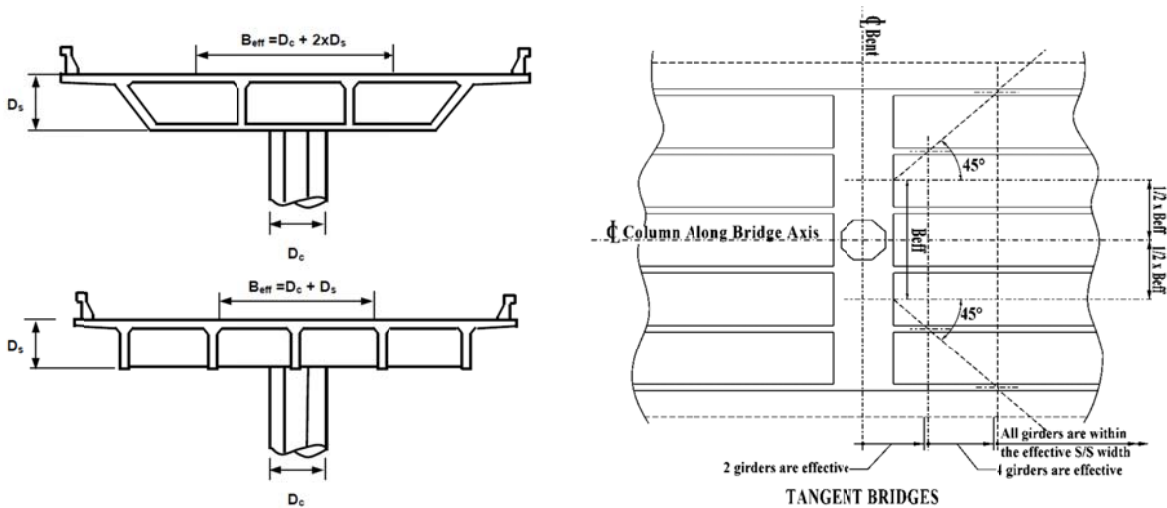
Figure 2.7 Effective width of superstructure girders (left) and its distribution in the plan for one case of unskewed tangent bridges (right) as given by Caltrans SDC (2013)
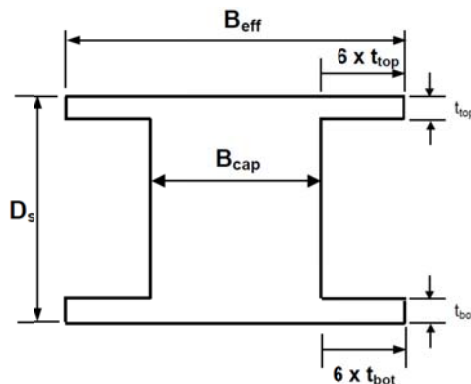
Figure 2.8 Effective width of bent cap beam as given by Caltrans SDC (2013)

2.1.4 Building vs. Bridge Seismic Design Philosophy

It is instructive to denote the importance of the effective flange width in the context of the proper design philosophy. This note is also helpful to present the reasons why the effective width evaluation in buildings has been a more popular research topic than the case of bridges. The

18

simple answer is that the underestimation of the effective width and its contribution to the beams capacity in buildings, and especially moment-resistant frames, can lead to undesired failure mechanisms and fatal collapses. That is because the adopted seismic design philosophy in buildings is the strong-column weak-beam (SCWB). In bridges, it is the other way around where a strong-beam weak-column (SBWC) is desired. Therefore, the underestimation of the slab contribution in bridges might then result in an uneconomic over-designed cap beam, but not a life-threating issue. This study is a first attempt of optimizing the bent cap design by proper accounting of slab contributions. A brief discussion of the SCWB and SBWC capacity design approaches are presented here for a better understanding of the applications of the effective width.

What is capacity design approach? Capacity design is used where it is necessary to control the failure mechanism. The most common application is in seismic design, where a desirable inelastic mechanism under extreme loading is selected, and the structure is then proportioned and designed so that it will be unlikely to fail in other modes. In buildings, the desired mechanism is plastic hinging in beams while columns remain elastic. This is to avoid excessive interstrory drifts which under large axial forces result in soft stories (excessive P-Δ) and eventually a progressive collapse can lead to a complete collapse. Therefore, a SCWB is the desired design philosophy. On the contrary, a desirable mechanism in bridges is plastic hinging in columns while the superstructure remains essentially elastic. The P-Δ effect is not as critical in bridges as in building since most of the bridge systems are equivalent to a one-story frame with low superstructure weight. Meanwhile, plastic hinges are highly undesirable in the superstructure or bent caps due to limited access regions, and in turn, uneconomical post-earthquake inspection and repair. Thus, the SBWC is a more suitable bridge design philosophy.

Whether a SCWB or a SBWC capacity approach is adopted, similar design steps are followed. A summary of a typical capacity design framework that is adopted from Moehle (2014), Caltrans SDC (2013), and ACI-318 (2008) is as follows:

- Select mode of failure that is desired; flexural mode of failure is typically the choice for concrete structures to avoid brittle shear or axial failure modes. In buildings, flexural hinging in beams is desired versus flexural hinging in columns in case of bridges.

- Provide strength for the chosen desired mode using LRFD design methods; the design strength is sought first just to guarantee that no premature inelastic response will occur.

- Detail that mode for ductile response; detail the yield region so that it has appropriate ductility capacity. More details about ductile response are presented in a following paragraph.

- Determine overstrength (often referred to as probable strength) for that mode of failure; overstrength is desired in the capacity design checks as a more realistic actual strength rather than estimated nominal strength. The reasons for overstrength and code requirements to reflect the overstrength is presented in a following paragraph.

- Determine overstrength forces required to cause inelastic response only in the target failure mode.

- Design the remainder of the structure so that either reliable or nominal strength exceeds the resulting internal actions.

As mentioned, ductile response is a characteristic feature of capacity design. The desired members' ductility is typically defined by a performance-based earthquake engineering (PBEE) framework but has to satisfy minimum requirements by design codes. In bridge design, the column and the substructure piers and piles are the chosen ductile members. For example, both of the AASHTO guide specifications for LRFD seismic design (2011) and Caltrans SDC (2013) require displacement ductility for columns in multiple-column bents that should be at least equals to 6, i.e. $\mu_D \geq 6$. Similarly, in buildings design, the ACI-318 specifies certain ductility limits and detailing provisions to achieve ductile beam plastic hinges and ductile joint reinforcement as well.

Another indispensable feature of the capacity design approach is the overstrength estimation. The overstrength at the first place happens because (a) cross-sections may be constructed larger than required; (b) materials usually have overstrength especially concrete where suppliers aims for a higher strength to avoid rejecting their concrete if strength is lower than specified, e.g. the concrete used in the experimental program of this study showed actual strength at test days of slightly higher than 7 ksi when the nominal required strength was only 5 ksi; (c) strain hardening and natural strength gain with time exist; and (d) three-dimensional nature of real structures loading and constraints results in higher strength due to confinement.

In bridges, the Caltrans SDC (2013) SBWC approach requires that the nominal capacity of the superstructure longitudinally and of the bent cap transversely, designated as capacity protected members, must be sufficient to ensure the columns will perform well beyond their elastic limit prior to the superstructure or bent cap reaching their expected nominal strength M_{ne}. Longitudinally, the superstructure capacity shall be greater than the demand distributed to the superstructure on each side of the column by the largest combination of dead load moment, secondary prestress moment, and column earthquake moment. The strength of the superstructure shall not be considered effective on the side of the column adjacent to a hinge seat. Transversely, similar requirements are specified in the bent cap. This approach applies a 20% overstrength magnifier to the plastic moment capacity of the column in order to determine the force demands on essentially elastic members. The set of equations that define the overstrength and guarantees the SBWC in case of superstructure design is given in Equations (2-5) through (2-9) and shown in Figure 2.9.

$$M_o^{col} = 1.2 \times M_p^{col} \tag{2-5}$$

$$M_{ne}^{\sup(R)} \geq \sum M_{dl}^R + M_{p/s}^R + M_{eq}^R \tag{2-6}$$

$$M_{ne}^{\sup(L)} \geq \sum M_{dl}^L + M_{p/s}^L + M_{eq}^L \tag{2-7}$$

$$M_o^{col} = M_{dl}^{col} + M_{p/s}^{col} + M_{eq}^{col} \tag{2-8}$$

$$M_{eq}^R + M_{eq}^L + M_{eq}^{col} + (V_o^{col} \times D_{c.g.}) = 0 \tag{2-9}$$

where:

M_o^{col} = The column's overstrength moment capacity

M_p^{col} = The idealized column's plastic moment capacity

$M_{ne}^{\sup R,L}$ = Expected nominal moment capacity of the adjacent left or right superstructure span

M_{dl} = Dead load plus added dead load moment (unfactored)

20

$M_{p/s}$ = Secondary effective prestress moment (after losses have occurred)

M_{eq}^{col} = The column moment when coupled with any existing dead load and/or secondary prestress moment will equal the column's overstrength moment capacity

$M_{eq}^{R,L}$ = The portion of M_{eq} and $V_o \times D_{c.g.}$ (moment induced by the overstrength shear) distributed to the left or right adjacent superstructure span
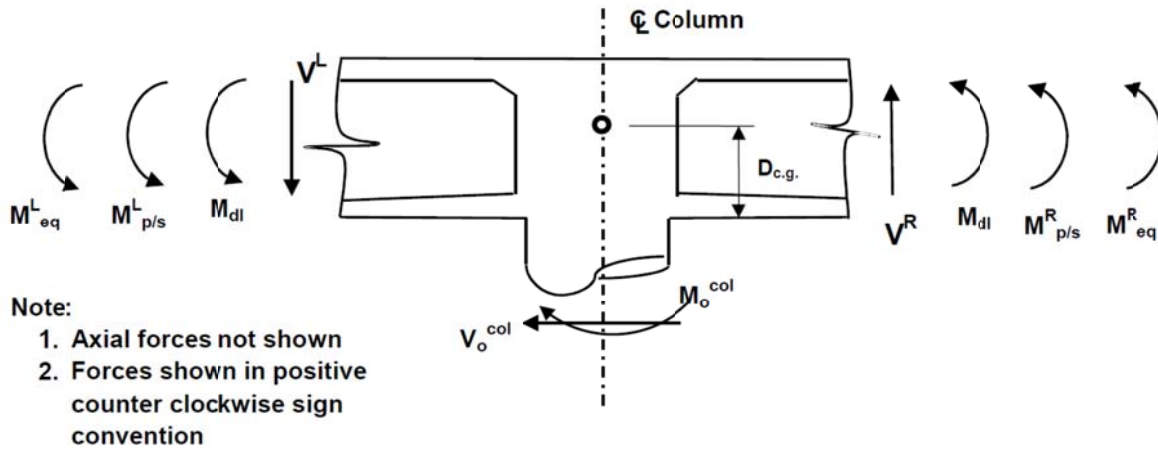
Figure 2.9 Superstructure demand generated by column overstrength moment as given by Caltrans SDC (2013)

In buildings, a similar approach is used but to guarantee the SCWB rather than SBWC. The ACI-318 (2011) provides Equation (2-10) to define the necessary flexural strengths of the columns that are required to remain elastic, i.e. capacity protected members similar to superstructure and bent cap beams in bridges.

$$\sum M_{nc} \geq (6/5)\sum M_{nb} \qquad (2\text{-}10)$$

where:

ΣM_{nc} = sum of nominal flexural strengths of columns framing into the joint, evaluated at the faces of the joint. Column flexural strength shall be calculated for the factored axial force, consistent with the direction of the lateral forces considered, resulting in the lowest flexural strength.

ΣM_{nb} = sum of nominal flexural strengths of the beams framing into the joint, evaluated at the faces of the joint. In T-beam construction, where the slab is in tension under moments at the face of the joint, slab reinforcement within an effective slab width, previously defined in section 2.1.2 in this chapter, shall be assumed to contribute to M_{nb} if the slab reinforcement is developed at the critical section for flexure.

The ACI-318 (2011) consideration of the slab reinforcement in the tension side in T-beam construction for estimating the beam flexural capacity as discussed in previous paragraph is an important motivation for carrying out this study. The history of how this provision evolved over the years to successfully crown couple decades of research is presented as part of the literature review in the next section. In summary, several building failures were observed after major earthquake that were attributed to the underestimation of slab contribution in beam

21

capacity calculation as part of the SCWB design approach (Pantazopoulou and French, 2001). Thus, accurate consideration of the slab contribution to the flanged beams becomes indispensable to achieve a successful SCWB mode of failure under extreme earthquake events. In bridges, while a different mode of failure that sacrifices the column, still the accurate account of box-girder slab contribution to the integral bent cap beam capacity can be very beneficial for a revisited economical design.

2.2 EFFECTIVE SLAB WIDTH LITERATURE REVIEW

The problem of determining the effective flange width of flanged beams has been a classical subject of investigation by many researchers in the past. There are numerous publications on the topic some of which are more than 80 years old (e.g. Metzer 1929; Miller 1929; Chwalla 1936). Earlier attempts of assessing the effective flange width used folded plate theory or its equivalent along with analysis that was based either on stress criterion or deflection consideration. Brendel (1964) used stress criterion in his analysis to determine the effective width, while the analysis done by Fraser and Hall (1973) was based on deflection considerations. A similar strategy was also used by Pecknold (1975) to assess the slab effective width for equivalent frame analysis.

Another classical approach for investigating the effective flange width used the theory of elasticity. The effective width of wide beam flanges investigated by Theodore von Karman, for instance, is discussed in Timoshenko's (1970) "Theory of Elasticity" book. That problem was analyzed by minimum- energy principle using theory of elasticity. Moreover, the nonlinear distribution of flange stresses results from the phenomenon known as shear lag, discussed earlier in the previous section, was another application for the use of the theory of elasticity. Timoshenko and Goodier (1970) studied the effect of shear lag in simple linear elastic systems using the theory of elasticity. Rigorous theory of elasticity investigations of shear lag problems, however, are of theoretical value only and are too complex to use for estimating the effective width in practical engineering problems. In addition, when nonlinearity in material behavior is present, the effective width can no longer be accurately calculated using elastic techniques.

The relatively newer approaches that are based on calibrating empirical analytical models against experimental studies and FE methods were proven to be more successful in developing simplified equations to estimate the effective flange width for design purposes. Thus, a total of 8 different relatively recent studies that focused on the effective flange width are summarized in more details and categorized in three subsections based on the application. The first subsection presents a comprehensive study that focused on effective width in bridge girders (Cheung and Chan, 1978). The second subsection presents 6 studies that used experimental, analytical and computational FE methods for effective width evaluation in framing systems of buildings. These are Pantazopoulou et al., (1988), French and Boroojrdi (1989), French and Moehle (1991), Shahrooz et al. (1992), Pantazopoulou and French (2001), and Küçükarslan (2010). The third subsection deals with an application involving the effective width evaluation is flanged buildings shear walls where the study by Hassan and El-Tawil (2003) is discussed. It is to be noted that a large portion of the available effective width literature focused on the effective load distribution width under a concentrated load rather than the effective width resulting from flange contribution. Those studies were not reviewed here due to their irrelevance.

2.2.1 Effective Width for Bridge Girders

2.2.1.1 CHEUNG AND CHAN (1978)

This study investigated the effective width in concrete and steel-concrete composite beam-slab type and box-girder bridges using the finite strip method. Only the effective width of the bridge longitudinal superstructure girders was considered and nothing related to an integral flanged cap beam in the bridge transverse direction was part of this study. The analytical method used was a variation of the FE method. The results obtained were used to determine the effective width of the compressive flange of the bridge girders. A study of a wide range of bridge models resulted in an empirical relationship for the effective width. The empirical relationship was found to be in good agreement with the design criteria used in the composite road bridge design code of the Federal Republic of Germany back at that time. It was also intended to supplement the effective width specifications in the American and Canadian design codes at that time, which in general were leading to conservative designs.

The older studies that preceded that one in determining the effective flange width of T-beams in the majority of cases investigated specific problems with specific geometric or loading configurations, such as a single T-beam with a flange of infinite width loaded by a concentrated force at mid-span, or multiple T-beams under uniformly distributed loads (Metzer 1929, Chwalla 1936). However, such irregularities as arbitrary girder arrangements, boundary conditions, and loading configurations were proven to be easily handled, to a certain extent, by using the finite strip method (Y. K. Cheung 1969). This was the motivation for Cheung and Chen (1978) to use the finite strip method. ln this method, harmonic functions that mimic the boundary conditions longitudinally were used in conjunction with polynomials for the transverse direction. The stiffness matrix and load vector of the strip were derived in the usual manner of minimization of the total potential energy.

In this study, the finite strip method was applied to the analysis of simply supported concrete and steel-concrete composite beam-slab and box-girder bridges. The results obtained were used to determine the effective width of the compressive flange of the bridge girders. The finite strip selected for this study was derived by combining a plane stress strip with a bending strip, thereby making it suitable for the analysis of folded plate-type structures which are subjected to membrane stresses as well as transverse bending forces. The strip had two nodal lines with four degrees of freedom per nodal line (displacements in the x, y, and z directions and rotation about the nodal line). In the analysis, the girder and deck were divided into a number of strips, thus any combinations of loadings and girder arrangements could be easily accommodated. After solving for the nodal displacements and rotations, the in-plane stresses and bending moments could be calculated at any point of a strip.

The effective compression flange width of a girder was determined by isolating the girder under consideration and required that the summation of the longitudinal in-plane stresses at any cross-section in the isolated girder be zero. The longitudinal bending stresses arising from the local longitudinal bending moment were not included in the calculation since they would be cancelled out in the summation process. The effective width was defined as that portion of the flange over which the maximum compressive stress is assumed to act uniformly to produce a resultant equal to the compression force in the section. The effective width was thus calculated

by dividing the total compression force by the deck thickness times the maximum compressive stress in the flange.

The effective flange widths of box girders were calculated in a similar manner. The study considered the AASHTO HS-25 truck load and extended the results for the AASHTO HS-20 truck load as well since both had identical axle configurations and axle loads that are linearly proportional to each other. The study focused only on the sections experiencing positive bending moment because the common design practice considered the negative moment sections noncomposite where the flange was ignored, and the calculation of effective flange width was therefore not required. The study used the obtained results of all the bridge types studied to conclude the following:

- The variables that had major effects on the effective flange width of bridge girders were girder spacing and span. Within the practical range of bridge member proportions, deck thickness and girder width and depth played a negligible role;

- Up to a span to one-half clear spacing ratio (L/B) of approximately 20, the effective overhanging flange width b_{eff} tended to increase with increasing span and spacing. For L/B ratios greater than 20, b_{eff} becomes more or less equal to the one-half of clear spacing between girders (B);

- The effective flange width of girders was independent of the number of traffic lanes of the bridge;

- Both box-girder bridges and beam-slab type bridges showed an identical trend where the effective width increases with longer span and larger spacing;

- For multi-cell box-girder bridges, the effective flange width of the interior webs was governed by the distance, center to center of webs, whereas the exterior webs follow a trend similar to that of beam-slab type bridges;

- The empirical results were in good agreement with the 1955 composite road bridge design code DIN 1078 of the Federal Republic of Germany. Typical values of the calculated effective widths were also compared to the 1973 AASHTO provisions and the 1974 Canadian Standards Association CSA-S6 values. From the comparisons, it was found that the AASHTO and CSA-S6 values were quite conservative especially for beam-slab type bridges with small L/B ratios. For example, for a L/B ratio of 12, the effective width differences of about 56% for the concrete girder and 100% for the steel girder could result in compressive flexural stress differences of approximately 34% and 48% for the concrete girder and the steel girder, respectively;

- Variation of the effective width along the span was relatively uniform. Using this particular information, the authors attempted to establish an empirical relationship between the effective width, spacing, and span using a least squares curve fitting procedure. A non-dimensional relationship between b_{eff}/B and L/B was derived by fitting the calculated results to a curve described by the polynomial in Equation (2-11).

$$b_{eff} \bigg/ B = \sum_{i=1}^{\infty} A_i (L/B)^i \qquad\qquad (2\text{-}11)$$

where the first four terms were adopted in the polynomial and the constants A_i were determined as follows: $A_1 = 0.21237$, $A_2 = -0.01929$, $A_3 = 0.00078$, and $A_4 = -0.00001$.

- The resulted best-fit empirical curve was applicable to both concrete and steel-concrete composite girders and was in good agreement with the 1955 DIN-1078 values. The best-fit curve was compared against upper and lower bound values obtained by Metzer (1929) and Chwalla (1936) based on the theory of elasticity. It was shown that the fitted curve fell between the limiting curves.

- To apply the empirical design curve to continuous bridges, a number of multi-span continuous beam-slab and box-girder bridges were analyzed. In all cases, it was found that the design curve is applicable if the distance between the points of zero bending moment is adopted as the value L of the span. Therefore, it was recommended that the effective widths of continuous bridge girders be determined from the presented curve, assuming the distance between the points of contraflexure to be the equivalent simple span.

- The design curve developed from a complete folded plate-type analysis, using actual truck loads as was done in this study was claimed to give more realistic values of the effective width of girders. Furthermore, the design curve incorporated two major variables, girder spacing and span, in the evaluation of the effective width while the corresponding AASHTO or CSA specifications provided discontinuous, one variable-dependent (girder spacing, slab thickness, or span) functions that in general led to conservative designs.

2.2.2 Effective Width for Building Framing

Six studies are summarized in this subsection to present how the issue of the slab contribution to flanged beams in buildings has been perceived and evolved over the past two decades. There are many other relevant studies that tackled the same issue such as: Bertero et al. 1984; Durrani and Wight 1982; Ehsani and Wight 1982; and Zerbe and Durrani 1985. However, the chosen more recent studies discussed here built upon those earlier studies and their citation is embedded in the discussion below whenever relevant. This subsection is comprehensive for its relevance to the core objective of this study.

2.2.2.1 Pantazopoulou et al. (1988)

This study was one of the main studies to draw the attention to the importance of considering the effective flange width in tension side as well as compression. The study proposed a simple analytical model to account for the contribution of slabs to the strength and stiffness of beams under negative bending at a beam-column connection in buildings. In the model, the slab was assumed to act as a tensile membrane that reinforces the tension region of the beam. The extent to which the slab contributes to the beam was determined from the geometry of the connection and the mechanical properties of the slab reinforcement. Closed-form expressions were derived for the equivalent width of slab that should be taken into account in the flexural analysis of T- or L-beams.

This study was motivated primarily by the fundamental concept underlying the capacity design philosophy (Park and Pauley 1975) that failure mechanisms in a structure can be

controlled by appropriately combining the member strengths. The study also was beneficial in relating the effective width in the tension side to the SCWB form of the capacity design adopted for frame structures in seismically active regions. Such relation was the cornerstone for later studies that amended ACI 318 to consider the slab reinforcement in the tension side of the flanged beam for capacity calculation (e.g. French and Pantazupoulou 2001).

According to the SCWB method, member strengths are selected so that strength of the structure is limited by beam flexural strength. For the capacity design to be successful, the designer should be able to assess the member strengths under different combinations of loads. Older experiments that preceded Pantazopoulou et al. (1988) study (e.g. Durrani and Wight 1982; and Zerbe and Durrani 1985 among others) have shown that beam strengths cannot be reliably computed if the beams are cast monolithically with slabs. When the beam is flexed such that the slab is in tension, the slab reinforcement acts as additional beam flexural reinforcement in an amount that was not recognized by the design practices back then. Because the beam flexural strength could not be reasonably bounded using available analysis techniques, it was possible then that the beams will be stronger than columns, and the SCWB design will not be realized.

A new approach to gage the effect of the slab on the negative moment resistance of beams was presented in Pantazopoulou et al. (1988). In the approach, the beam web was modeled using conventional flexural theory (Park and Pauley 1975) and the action of the slab was modeled using a simple truss connected to the beam in the tension zone. A closed-form solution was given for the effective slab width to be used in conventional beam analysis. The analytical model was verified by comparison between computed behavior and behavior measured during several previous experiments on beam-slab-column connections. In the model, the slab is assumed to act as a membrane element attached between the longitudinal beam and rigid transverse beams. According to the model, slab strains vary in the transverse direction according to Equation (2-12):

$$\varepsilon_i = \varepsilon_{\max} \sin^2 \alpha \tag{2-12}$$

where ε_i is the longitudinal strain of slab bar b_i at the connection with the transverse beam, and ε_{max} is the strain of the beam longitudinal bars at the column face. This formulation defines a shape function $\sin^2\alpha$ by which slab strains diminish in the transverse direction. The angle α is the acute angle between a link and the transverse beam. The use of the angle α was based on the assumption that the deformation of the slab is distributed along the beam plastic hinge length d in the same pattern as the beam deformation. A schematic representation of the so-called semi-rigid link connection model along with the key parameters used to describe the strain distribution is shown in Figure 2.10. Based on the computed distribution of slab strains, closed form expressions for effective slab widths were derived that were suitable for conventional analysis assuming plane sections remain plane. Six different expressions for the effective width based on several controlling factors that participate in the flexural response of beams: beam depth, steel material properties, the maximum available slab width, and the maximum reinforcement strain. The expressions are not shown here for brevity but the reader is referred to the Pantazopoulou et al. (1988) if more details about the derived effective width formulas are needed.
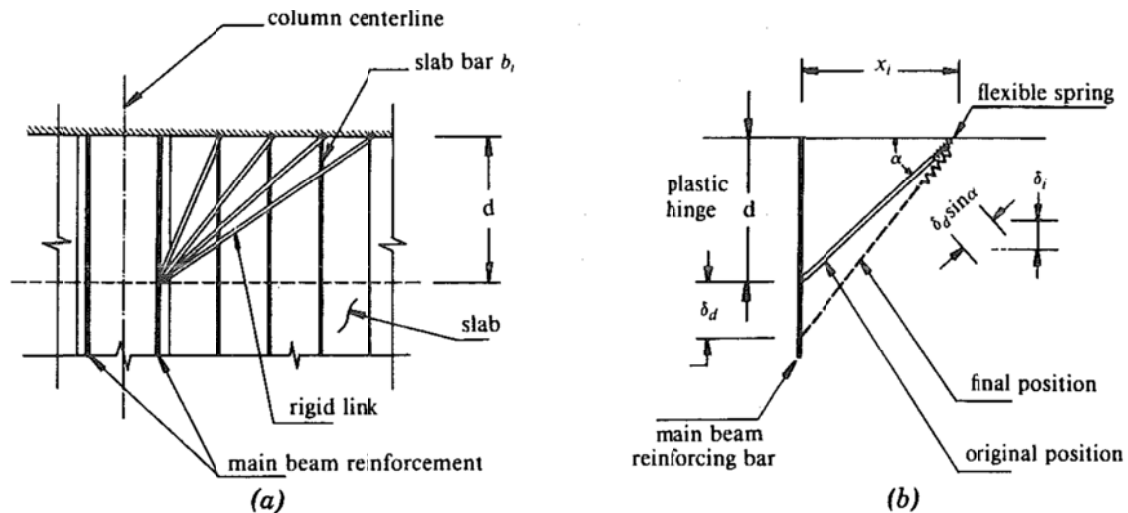
Figure 2.10 Semi-rigid link connection model (after Pantazopoulou et al. 1988) (a) assumed mechanism (b) kinematics of the mechanism

In summary, the behavior computed using the analytical model proposed in Pantazopoulou et al. (1988) was found to correlate well with the measured behavior in previous tests utilized in the study. Consistent with the experimental data, the slab is found to contribute significantly to the negative moment resistance of beams. It is to be noted that the authors in this study roughly expressed the effective slab width on either side of the beam to be on the order of 1.5 times the beam depths for up to yielding, and increased it to approximately 3 times the beam depth for deformations that could be expected during severe earthquake loading. The latter approximate width mentioned exceeded by a significant margin the typical effective width recommended in the ACI-318 Building Code for beams flexed with the slab in compression.

2.2.2.2   *French and Boroojerdi* (*1989*)

This study was motivated by the fact that the effective width of slab to be used for the case of lateral loading was not explicitly addressed in design codes at that time. The authors claimed that inaccurate accounting of slab contribution and effective slab width could lead to a significant underestimation in structural strength and failure mechanisms different from what was anticipated. They provided an evidence to support that claim through a case study for a full-scale test on a seven-story RC structure that was tested at the Building Research Institute in Tsukuba, Japan in 1984. It was found in that test that the measured base shear strength of the structure was approximately 70% more than anticipated (Wolfgram 1984). The difference between the calculated and measured base shear was primarily due to the contribution of the floor slab reinforcement acting as additional tensile reinforcement to the beam. Accordingly, the authors conducted an experimental program where three one-half scale RC beam-column-slab subassemblages were tested at the University of Minnesota Structures Laboratory under cyclic lateral loading. The objective of the tests was to investigate the slab contribution to lateral load resistance as the torsional stiffness of the transverse beam element was varied. The three models were designated as EWl, EW2, and EW3. The transverse beam element was varied in the models from no beam in model EWl to a transverse beam identical to the longitudinal beam in model EW3.

While earthquake loads do not occur in a single direction parallel to the frame line (longitudinal direction), the authors considered the effect of initial damage due to loading in the transverse direction. If the transverse element is damaged from carrying loads in its own direction, it may not be as effective in developing the slab participation in the longitudinal direction. To investigate this effect, models EW2 and EW3 were first tested in the longitudinal direction. The structures were then rotated 90° and subsequently tested in the orthogonal direction. A summary of the conclusions found from this experimental program is as follows:

- The models exhibited a ductile behavior as the structures were taken to interstory drifts exceeding 8%. At the limiting stroke of the actuator, EW3 maintained nearly 90% of its maximum load achieved at 4% interstory drift;

- The effective slab participation was greater for models with increased transverse torsional stiffness. This phenomenon was observed in load-deflection, moment-rotation, and strain distribution measurements. The difference was larger at the beginning of the tests, but became smaller as the deflection amplitude increased. At the maximum measured load, the difference in the flexural strengths among the models was less than 10%. The flexural resistance measured for model EW3 at ultimate was within 18% of the calculated value assuming the full width of slab to be effective as a tension flange to the beam.

- EW1 reached its ultimate load at a much larger interstory drift than EW3 (7.2% versus 4%). This was attributed to the decrease in ultimate curvature associated with increased effective slab participation. The concrete compressive strain was found to control in all slab-in-tension calculations. Consequently, a reduction in ultimate curvature occurs with additional slab reinforcement (increased tensile forces) associated with larger effective slab widths. The different drift levels at ultimate were attributed to a reduced ultimate concrete compressive strain associated with the higher concrete strength of EW3.

- At an interstory drift of 2%, which might be considered a reasonable limiting drift level (Tentative Provisions), the measured flexural strengths of the structures were within 10% of the value calculated using ACI-width assumptions including the ultimate capacity of the remainder of the slab acting independently.

- A reduction in the initial stiffness was observed in the second test of model EW3. This reduction was attributed to the damage caused by initially loading the structure in the transverse direction. This effect became negligible as the structure was displaced beyond the maximum deformation level imposed during the first test.

2.2.2.3 French and Moehle (1991)

This study did not comprise a dedicated experimental or analytical framework. However, it comprehensively reviewed published literature and experimental data and results to draw main conclusions regarding the effective slab width in tension. In structures subjected to lateral loading, slab reinforcement acting as effective tensile reinforcement of the beams has been found to significantly increase the beam flexural strength. The enhanced beam flexural strength has several effects on the structural behavior including a shift in the ratio of strengths between the beams and other members. This may result in a failure mechanism different from that anticipated. The study identified possible variables affecting the slab contribution including the connection type (interior or exterior), lateral deformation level, and lateral load history (uniaxial

or multiaxial). The study summarized general behavior observed during isolated and multiple beam-column- slab connection tests. An approximation was given for estimating the amount of slab reinforcement to be considered as effective tensile reinforcement of the beams. When this study was published, the available U.S. design codes and recommendations did not provide guidance for the effective width of slab to be considered as flexural reinforcement for beams subjected to lateral loading. The provisions of those documents were based largely on test results of subassemblages comprising columns and beams without floor slabs as only little information used to be available on the effect of slab on beam flexural strength. Thus, the comprehensive review by French and Moehle (1991) focused on compiling results of several laboratory experiments of beam-column-slab subassemblages and complete frames subjected to lateral load in addition to reviewing some analytical models of beam-column-slab connections. The conclusions drawn by the authors are summarized as follows:

- The slab action in beam-column-slab systems is a complex phenomenon that depends on a wide range of variables. The main action of the slab identified was its participation as a tensile element that adds to the flexural resistance of the longitudinal beams when the top of the beam is in tension. The slab contribution to the beam resistance depends on several variables including connection type (interior or exterior), transverse beam stiffness, lateral deformation level, and lateral load history (uniaxial or multiaxial). No analytical models that account properly for all pertinent variables were available. However, an attempt to account for as many of these variables as possible was pursued by Shahrooz et al. (1992) as presented next.

- For design, a simple means of accounting for the slab contribution to the beam flexural strength (top of beam in tension) is to assume that all slab reinforcement within a slab effective width acts as beam tension reinforcement. An analysis of the available test data indicated that if the slab effective width was taken equal to the ACI effective width, calculated flexural strength would approximate measured beam resistance for frame lateral drift equal to 2% of height. To account for effects of reinforcement strain hardening in the strength calculation, the effective reinforcement yield stress should be taken not less than 1.25 times the actual yield stress. The actual yield stress may be higher than the nominal value, and this difference should be considered. This particular conclusion made its way to the ACI-318 seismic provisions regarding the capacity check of beams as previously mentioned in subsection 2.1.3.

- In acting with the beam as a tension flange, the slab affected other actions within a beam-column-slab frame. The enhanced beam flexural strength may result in increased beam shear that should be considered in selecting transverse reinforcement. Shifts in beam moment distributions are likely; these should be considered in selecting longitudinal reinforcement details including bar cutoffs. Demands on beam-column connections are also increased. Additional joint shear reinforcement for exterior connections and increased joint sizes for all connections can be rationalized given the increased demand. Finally, the slab contribution should be considered in determining the required column strength to avoid excessive column hinging in frames subject to severe lateral loading.

29

2.2.2.4 Shahrooz et al. (1992)

This study presents an analytical model for the slab contribution and effective slab width taking into account more variables to extend the earlier model proposed by Pantazopoulou et al. (1988). The qualitative model simulating participation of slabs to the behavior of beams was developed by establishing the kinematic relations between beam deformations and the state of strain in the slab. The slab was idealized as a membrane element by using a network of rigid links and flexible springs connecting the slab bars to the supporting beams. Support displacements of the rigid links, such as reinforcement slip, twist, weak axis rotation, and elongation of the transverse beams were considered.

Because of the brittle tensile behavior of concrete, surface elongations (caused by hogging moments) become more important after cracking and are more pronounced at higher levels of lateral displacement. For this reason, slab membrane actions increase with the extent of cracking and, therefore, with increasing lateral story displacement (or lateral drift). Furthermore, because slab participation is a kinematically induced phenomenon, it is likely to be affected by any additional deformation or displacement occurring at the boundaries of the slab. For example, in-plane deflections of the transverse beams reduce the amount of deformation of the slab at a given level of lateral drift; bond slip of the main beam or slab reinforcement at the supports of the slab may cause redistribution of strains over a large transverse distance from the main beam, whereas deformations in the beam-column joint may reduce the deformation demand on the slab-beam assembly at a given level of lateral drift.

An earlier qualitative model has been developed to represent the pattern and distribution of beam deformations in the supported slab. The model, which was derived by using a simple kinematic relation based on a network of rigid links, was proven successful for slabs with relatively rigid supports (Pantazopoulou et al. 1988). However, it was found that the model overestimated slab strains (and, therefore, the extent of slab contribution) in connections with flexible transverse beams and was unable to simulate the strain redistributions under excessive bond slip. To remedy these difficulties, the kinematic relations used in the original study were re-examined in the new model by Shahrooz et al. (1992). In establishing the geometry of deformations, displacement components associated with transverse beam deflections and reinforcement slip were taken into consideration. Correlation with experimental results indicated that the enhanced model had a greater range of applicability, and, as such, it could provide a qualitative measure of the effect of the various connection parameters on the slab contribution. A drawback of the enhanced model (Sharooz et al. 1992) over the original model (Pantazopoulou et al. 1988) was that the proposed formulation could not be simplified into closed-form expressions.

The differences between the enhanced and original model were identified in previous paragraph. The mechanics of the enhanced model are presented here. The model aimed at simulating slab participation to the negative (hogging) flexural behavior of beams. The approach taken was to establish kinematic relations between beam deformations and slab strains. In the model, the slab was assumed to act as a membrane element attached between the longitudinal and transverse beams. This behavior was simulated by a network of rigid links and flexible springs connecting the slab bars to the longitudinal beam. An important improvement over earlier rigid-link models lies in the enhanced compatibility conditions, which account for support displacements such as reinforcement slip due to bond deterioration, and twist, weak axis rotation,

and elongation of the transverse beams (i.e., the assumption of rigid transverse boundaries adopted by the earlier model has been relaxed). Numerical implementation of the model required iterative calculations because of the nonlinear relationships between (1) Axial, flexural, and torsional behavior of the transverse beams and the magnitude and position of the slab forces; (2) the transverse beam stiffness and the load history; (3) bar stress, bond slip, and strain.

Performance of the proposed model was evaluated from correlation studies of previously available experimental data. Generally, computed results compared well with test data from earlier interior and exterior slab-beam-column subassemblies suggesting that the model represented the kinematics of such connections successfully. Whereas the rigid-support assumption of the original rigid-link model restricted its applicability to interior connections with favorable bond conditions, the proposed model appeared not to be subjected to any such limitations. Indeed, by proper modeling of transverse beam flexibility and bond-slip effects, results from experiments of both connection types were successfully estimated by the proposed method. The computed responses were found to be most sensitive to the assumed length of plastic hinge and, to a lesser degree, to the distribution of longitudinal strains within the plastic hinge. In the low deformation range, results appeared to be somewhat sensitive to the assumed value of initial transverse beam stiffness. A longer length of plastic hinge resulted in larger moment capacity and larger strains in slab bars and vice versa. However, available empirical expressions for establishing an approximate length of plastic hinge seem sufficient in practical applications.

2.2.2.5 *Pantazopolou and French (2001)*

The amendments in the ACI 318-99 that affect the estimation of nominal beam flexural capacity in seismic design of frame connections were the motivation for this research. These changes concerned the width of slabs considered effective in beam flexure and represented the culmination of a 15-year long concerted research effort in the U.S., Canada, New Zealand, and Japan aimed at understanding and quantifying slab participation in the lateral load resistance of frames through observed experimental findings. By accounting for slab participation, the Code recognized the diaphragm action of slabs in the seismic response of frames, particularly when the slab is on the tension face of the beam. It is to be noted that until the time of this research published in 2001, it was an established design practice to neglect the presence of the slab in estimating beam stiffness and strength, except when the slab was located in the compression zone of the beam (known as T- beam design). This is exactly the current status for flanged bent cap beams in box-girder bridges, and the main study presented in this report is an attempt to properly recognize the slab contribution in bent cap design. However, the proper recognition of slab contribution in case of bridge beams can lead to an optimized and economical design of bent caps rather than avoiding an undesired mode of failure as in the case of buildings due to the different design philosophy in building (WBSC) and bridges (WCSB) as previously discussed.

Experimental evidence from tests on complete frames and slab-beam-column assemblies illustrated that this practice of neglecting slab contribution in tension resulted in the gross underestimation of beam flexural strength in the assumed plastic hinge regions (at the face of beam- column connections). This neglected source of beam flexural over-strength had significant consequences in the realization of the objectives of the established capacity design framework for RC where beam shear design, joint dimensioning, and column flexure/shear detailing are controlled by the requirement of beam flexural yielding. This study reviewed the practical

implications of the ACI 318-99 amendments in the seismic design and in assessment of the resulting response of RC frame structures. The effects (in terms of demand and capacity) on strength and deformation capacity of the various mechanisms of response, and the hierarchy of failure modes in slab-beam-column connections were identified and discussed.

The study utilized a large amount of data highlighting the mechanism by which the slab participates in the lateral load resisting system of frame structures (Suzuki et al. 1984; Ehsani and Wight 1985; Zerbe and Durrani 1985; Kurose 1987; Durrani and Wight 1987; Pantazopoulou et al. 1988; U.S.-Japan Research 1988; Velez and French 1989; French and Boroojerdi 1989; Qi and Pantazopoulou 1991; Cheung et al. 1991; French and Moehle 1991; Bas 1990; Pantazopoulou and Bas 1994; Alcocer 1998). In light of those previous studies and amendments of ACI 318-99, implications on structural shear capacity, beam shear, bar cutoffs, and joint shear stress input, as well as joint confinement were investigated. The relevant issues were highlighted, quantified, and discussed in the context of practical design as follows: (a) mobilizing slab in lateral frame sway by an equivalent slab width b_{eff}, (b) global effects of slab participation on overall frame response, (c) effects of slab on beam behavior, (d) restraint provided by transverse beams in exterior connections, (e) joint shear in connections with floor slab, and (f) role of continuity reinforcement on slab contribution.

In summary, the study presented a review of proposed code changes with regard to the effect of slab participation and the experimental and analytical evidence that motivated those changes. The effect of slab participation was concluded to be greatly influenced by the level of structural drift. The changes to the code were correlated with effective slab participation at structural drifts on the order of 2%, which is consistent with performance-based design objectives. Experimental studies showed that at larger drifts, the entire width of the slab might be engaged as additional tension reinforcement to the beams subjected to hogging moments. The study recommended that whenever it is anticipated that structures would be taken to higher drift levels, designers should consider the effect of increased slab participation on structural stiffness, global shear demand and capacity, beam shear demand, bar cutoffs, and joint confinement. While the code changes represented the first attempt to quantify the contribution of the slab, the study proposed several other issues, such as the dependence of slab participation on pertinent indices that account for the relative stiffnesses of the beams and columns framing into the connection for future amendments. Currently, those changes which were first proposed to be included in the ACI 318-99 version are now well-established provisions in Chapter 21 in the latest version of ACI 318-11 as previously discussed in subsection 2.1.2.

2.2.2.6 *Küçükarslan (2010)*

This study used the FEA as an analytical framework for evaluating the slab contribution and effective width only in compression in T-beams. The study assumed that the distribution of compressive stress on the flange of T-beams depends on the relative dimensions of the cross-section, span length, support and loading conditions. These factors were incorporated to revisit the effective width evaluation and compare it against various codes formulas, which are expressed only in terms of span length or flange and web thicknesses and ignore the other important variables as claimed by the author.

Three-dimensional FEA was carried out using SAP2000 (2012) on continuous T-beams under different loading conditions to assess the effective flange width based on displacement

32

criterion. Eight-node brick elements were used to model the T- beams. The formulation was based on a combination of the elementary bending theory and the FEA. The beam spacing (S), beam span length (L), total depth of the beam (D), the web (b_w) and the flange thicknesses (h) were considered as independent variables. Depending on the type of loading, the numerical value of the moment of inertia of the transformed beam cross- section, and hence the effective flange width, were calculated. Next, the input data and the FE displacement results were used in a nonlinear regression analysis. Two explicit design formulas for effective flange width (b_e) were derived and proposed for two different cases of loading as follows:

- For concentrated load at mid-span:

$$\frac{b_e}{S}=0.322\times\left(\frac{S}{L}\right)^{-0.2947}\times\left(\frac{L}{D}\right)^{0.2463}\times\left(\frac{b_w}{D}\right)^{0.0913}\times\left(\frac{h}{D}\right)^{0.1698} \tag{2-13}$$

- For uniform distributed load:

$$\frac{b_e}{S}=0.2858\times\left(\frac{S}{L}\right)^{-0.3058}\times\left(\frac{L}{D}\right)^{0.2746}\times\left(\frac{b_w}{D}\right)^{0.086}\times\left(\frac{h}{D}\right)^{0.1473} \tag{2-14}$$

The two formulas were used to make comparisons with the ACI-318 (2008), Eurocode (1991), TS-500 (1984) and BS-8110 (2009) code recommendations. The following conclusions were drawn from the results obtained in this study:

- For the point load case, all codes gave highly overestimated values for the effective flange width particularly for short and deep beams when the results were compared with the analyses based either on stress criterion or deflection consideration.

- As the beam became slender, this trend changed and smaller effective flange width values were obtained for increasing values of the beam spacing. However, for all cases the recommendations given by Eurocode (1991) gave overestimated results.

- Using the curves developed from the proposed equations, it was observed that as the beam spacing S increases, b_e/S decreases. Moreover, for the same value of the beam spacing S, the ratio b_e/S increases as the span length L increases.

- The beam spacing S and the beam span length L affect the effective flange width more significantly than the other parameters.

- For beams under a uniformly distributed load, it was found that the proposed formula gave underestimated results for deep beams with respect to the code equations. However, as the beams became slender all codes yielded very conservative assessments of b_e for uniformly distributed load case except for Eurocode (1991) which gave consistently overestimated results for all cases. For most of the beams under a uniform distributed load, Eurocode values of b_e/S were very close to unity.

- Comparisons were made between the proposed deflection-based formulas and the formulation based on stress criterion. It was found that the results of the proposed equation for the uniformly distributed load case exhibited very good agreement with the results of

stress criterion when the beam spacing was small. However, as the beam spacing increased, the proposed equation produced conservative effective flange width values.

2.2.3 Effective Width for Shear Walls

While the effective width of flanged moment-frames and floor beams was extensively investigated in the past, recent studies switched the focus to flanged RC shear walls and cores. It is instructive to expose the notion of the effective flange width from a different structural element perspective here. Resembling flange behavior in floor beams, the distribution of strains in the shear wall flange, and in turn the corresponding stress distribution, is also nonlinear, which considerably complicates analysis and design. To avoid direct consideration of the shape of the nonlinear stress distribution, engineers resort to the concept of effective width in shear walls again in a similar fashion to flanged floor beams. However, the design philosophy for walls has been more dynamic than the well-established moment-frames and floor systems design philosophies. Shear walls design has recently changed from prescriptive to deformation-based and, as a consequence, the effective width provisions and the philosophy behind them also underwent a dramatic change. As recent as the UBC-94 (1994) was used, the tension effective width was required to not be greater than 1/10 of the wall height.

2.2.3.1 *Thomsen and Wallace (1996)*

Wallace (1996) and Thomsen and Wallace (1995, 2004) underlined that the effective flange width estimation should be based on the maximum expected level of building response. They based their conclusions on experimental strain variation along the flange width at different imposed drift levels to support the influence of the performance level on the amount of flange reinforcement mobilized. On the other hand, Wallace (1996) also suggested a revisited tension flange effective width of 1/4 the wall height, which was subsequently adopted in the 1999 ACI 318 seismic provisions. Several studies followed the ACI 318-99 amendments that continued to focus on improving the design code provisions. One comprehensive study amongst those studies is by Hassan and El-Tawil (2003) and summarized next.

2.2.3.2 *Hassan and El-Tawil (2003)*

This study was concerned mainly with questioning and revisiting the ACI 318-02 simple expression, which is a function of story height, for estimating tension flange effective width in flanged RC shear walls. Other influential variables such as drift level, wall width, and the level of axial load were not addressed in the ACI expression and thus were the focus of the study. In addition, the motivation for their research stemmed from the fact that coupled walls can be subjected to axial forces that vary during an earthquake as a result of the coupling action. Under seismic conditions, the net axial force acting on a wall can become quite high and can possibly reverse direction subjecting the wall to axial tension. Therefore, the purpose of the study was to quantify the effect of axial load (including tension) along with other parameters on the tension flange effective width for better code provisions evaluation. Hassan and Eltawil (2003) used a detailed FE model to investigate the effect of drift level, wall width, and the level of axial load on the tension flange effective width. The FE model was developed using DIANA and accounted for nonlinear steel and concrete behavior. The model was validated through comparisons to available test data from literature. The analytical results showed that the tension flange effective

width is dependent on the studied parameters. Implications of the study data regarding existing guidelines were discussed and provisions were suggested for implementation in performance-based design criteria. The main conclusions adopted from the authors' summary are as follows:

- Analysis results showed that although the tension flange effective width does not vary significantly as a function of wall height, it is strongly dependent on the drift level, axial force level, and wall length.

- Comparisons between the numerical results and ACI 318-02 specifications indicate that the ACI provisions did not accurately specify the tension flange effective width, especially in the presence of compressive axial load. Another issue with the ACI provisions was that the effective width is tied to wall height and not wall length, even though wall length is a more influential variable. Although a calibration based on wall height is certainly reasonable and acceptable if wall length is proportional to wall height, in many cases such a predetermined relationship between height and length cannot be assumed. Another drawback of the ACI 318-02 fixed effective width provisions was its deficiency for an accurate evaluation of structural behavior at a specific drift level as required in performance-based design.

- Design criteria that are a function of wall length, drift, and axial force level were proposed for determining the tension flange effective width. Although more complicated than the ACI 318-02 criteria, the proposed specifications were more reasonable in that they account for the effect of important variables and more suitable for implementation in performance-based design codes. However, the authors suggest that still extensive analytical and experimental studies are needed to confirm and/or refine their proposed criteria.

2.3   REVIEW OF LITERATURE

The experimental program conducted in this study comprises the core of the study as it consists of testing two large-scale bridge subassemblies. The first specimen was tested in quasi-static cyclic loading. The second one was retrofitted with CFRP and tested using hybrid simulation technique. To conduct successful tests, several previous studies that focused on large-scale bridge components or subassembly testing were consulted. In addition, early studies that promoted bridge performance-based design and capacity design concepts were also reviewed during the course of this study. In this section, some of those relevant herein studies are summarized briefly for completeness. However, a review of the studies that utilized hybrid simulation testing technique for investigating bridge components and systems behavior is included in Chapter 7. The relevant studies briefly reviewed here are categorized and presented in two subsections: bridge component and subassembly testing and performance-based bridge design.

2.3.1   Bridge Subassembly and Component Testing

During the last few decades, investigations of bridges and infrastructure structural damage following several severe earthquakes have been one of the main priorities of several federal and different states departments of transportation such as Caltrans. That is to develop proper design

practices and better detailing of members and joints in bridges. Several research programs embarked on using experimental testing to investigate the flexural and shear behavior of columns or cap beam-column joint regions, for example, to ultimately develop design guidelines and recommendations. Some of those studies that are of most relevance to the study conducted here are briefly mentioned in the following subsections. Two studies that tested a large-scale bridge subammeblies are first presented (Seible et al. 1993 and 1994, MacRae et al. 1994). An example of a large experimental study that involved bidirectional loading is presented next (Mazzoni 1997). Two studies that extensively studied cap beam-column joint behavior and involved both large-scale bridge subassembly testing and bidirectional loading are briefly summarized as well (Natio et al. 2002 and Mosalam et al. 2002). The subsection concludes with few examples of bridge component tests that focused only on columns.

2.3.1.1   Seible et al. (*1993, 1994*)

The researchers conducted two full-scale tests in 1993 and 1994 at the Structures Laboratory in the University of California, San Diego. The second test utilized observations and results from the first test in altering the specimen design. The full-scale test specimens comprised a 5-ft diameter column along with the cap beam and portion of the box-girder superstructure from a prototype PC bridge. The tests focused on the cap beam-column connection with #18 bars and under unidirectional seismic-type loading. The research focused on investigating: (1) the anchorage behavior of straight #18 bars based on the AASHTO design guidelines, (2) determining local distress levels and failure mechanisms in the cap beam-column connection, and (3) assessing local distress and failure behavior with respect to global seismic design principles of collapse prevention and damage control and reliability. The first test (1993) showed that the cap beam-column connection was capable of forcing initial plastic hinging into the column with ductility limited by the joint and cap beam deterioration. However, no premature bond slip or joint deterioration was noticed. It was observed that nominal maximum principal tensile stress levels of 6 to 8 $\sqrt{f_c'}$ contributed to the encountered cap beam-column joint distress. This led to horizontal cap dilation measured in the longitudinal bridge direction through the joint core and significant joint shear cracking. Although such observed cracking and dilation did not cause brittle failure, yet it posed a problem for post-earthquake repair and a compromised serviceability design criteria.

Based on the observations from the first test, the design of the second specimen was slightly altered and verified by testing. The second test (1994) addressed the observed issues through increasing the cap beam width, using additional vertical and horizontal joint shear reinforcement, and adopting soffit flare. When the second test was conducted to verify the proposed design changes, it was observed that most of or nearly all the inelastic action was migrated to the column through a flexural hinge without joint shear cracking or bond slip. This is the favorable weak column-strong beam design approach that allows damage repair without significant traffic interruption. Another observation from the second test is that it provided high level of integrity to the cap beam-column region which meets serviceability requirements and functionality design limit state criteria. The proposed design changes also led to better constructability due to less reinforcement congestion as the cap beam was wider.

2.3.1.2 MacRae et al. (1994)

The researchers conducted a ¾ large-scale test of the Santa Monica Viaduct PC cap beam-column joint. The objective of the experiment was to determine the peak strength of the connection, the degradation of strength with lateral displacement, and the failure mode under reversed cyclic loading in-plane with the bent. No special shear reinforcement was provided in the cap beam-column joint. Thus, the subassemblage specimen failed primarily due to joint shear failure. However, the strength degradation was gradual with the cycles of repeated loading. Moreover, no punching was observed in the vicinity of the cap beam-column region although the column axial load was increased during the test to 1.5 times the expected maximum column axial load. It was noted also that even when the full flexural strength at the base of the prototype column is achieved, the overall bent behavior is still expected to respond reasonably. Only after a large amount of deformation, the top column connection would be effectively pinned.

2.3.1.3 Mazzoni (1997)

Up to the late 80s and early 90s, unidirectional quasi-static testing was the most common loading technique. Only few bridge component or subassembly tests were conducted under bi-directional loading. The comprehensive study by Mazzoni (1997) is one of those studies that considered both unidirectional and bidirectional loading and is presented here as an example of bridge studies that considered bidirectional loading. The study comprised an experimental program to investigate the seismic design and response of the lower-level beam-column connection in a RC double-deck bridge structure. Two 1/3-scale beam-column joints with different levels of joint shear stress demands were built according to the adopted design criteria back then and tested in the laboratory. The difference between the two specimens is related to the difference in capacity of the members framing into the joint. The nominal strength of the columns and beams of the second specimen were greater than those of the first. This resulted in a higher joint shear stress demand imposed on the beam-column joint of the second specimen.

The study focused on several design issues and parameters besides the effect of bidirectional loading. These were the yielding of columns versus beams, joint shear strength, detailing of transverse reinforcement in the joint, detailing of member longitudinal reinforcement in the joint, the effect of beams perpendicular to the loading direction, and the joint depth to bar diameter ratio. However, only the conclusion related to the effect of bidirectional loading is presented here as more dedicated studies for the bridge joint behavior is presented next. While bidirectional loading was applied first then followed by unidirectional loading, the study showed that the design strengths were reached only during the unidirectional response and were not reached during bidirectional response. However, the bidirectional cycles dissipated a significant amount of hysteretic energy, but were not found to affect the unidirectional response envelope. The effects of bidirectional loading were determined to be important in the response of the structural system in terms of incorporating better load path and residual stresses, but did not affect the design strength of the test specimens.

To acknowledge the importance of bidirectional loading in certain cases, the FEMA 461 (2007) included guidelines for conducting tests under bidirectional loading. The FEMA 461 is an important document that provides guidelines for the testing and loading protocols for determining the seismic performance characteristics of structural and nonstructural components and was consulted to develop the loading protocol for the study presented in this report. The

general FEMA-461 (2007) statement for bidirectional loading is as stated follows: "Imposed deformation or force will typically be applied in a single degree of freedom (unidirectional loading). Bidirectional loading (loading in two orthogonal horizontal directions) should be carried out whenever it is anticipated that such loading has a significant effect on any of the damage states and the associated fragility function. Written justification should be provided if it is decided in this case to apply only unidirectional loading."

2.3.1.4 *Natio et al.* (*2002*)

This study relied primarily on an extensive experimental program to investigate different designs for bridge beam-column joints. The motivation of the study was the fact that the 1989 Loma Prieta earthquake and subsequent studies resulted in higher design requirements for transverse reinforcement in bridge beam-column joints in California. The resulting reinforcement details can be congested and difficult to construct. The undertaken experimental investigation examined four large-scale interior joints with details typical of those required in California. The experimental program included tied square cross-section columns and spirally reinforced circular cross-section columns. Both conventional and headed joint reinforcement configurations were investigated. It is to be noted that another complementary study was conducted to further investigate the beam-column joint behavior but within a larger bridge subassembly involving a representative portion of the box-girder as presented in the next subsection (Mosalam et al., 2002).

The experimental results showed that the adopted design requirements back then produced joints that remain essentially elastic to relatively large drifts, whereas the columns developed inelastic rotations adjacent to the joints. The study showed also that the response of the square column subassemblies was not as stable as that of the circular column subassemblies. That was attributed to the linear (versus circular) arrangement of the column longitudinal reinforcement, which results in simultaneous slip, buckling, and eventual simultaneous fracture of several longitudinal bars. The use of headed reinforcement within the joint regions was shown to be effective in reducing congestion and thereby improving constructability while maintaining comparable structural behavior. In general, headed longitudinal column reinforcement exhibited less slip and underwent higher strain than conventional longitudinal reinforcement at similar levels of displacement demand. Finally, it was shown that the lateral transverse joint reinforcement used in the tested joints was not significantly activated, reaching less than 25% of the yield strain. This suggested that less reinforcement could be used in connections with demands similar to those of the test specimens.

2.3.1.5 *Mosalam et al.* (*2002*)

This study was the extension of the previously reviewed study (Natio et al., 2002) that comprised an experimental program that aimed at investigating the cap beam-column joint design using conventional and head rebars while considering the box-girder contribution. Thus, it is very relevant to the study presented in this report in terms of the specimens' geometry, test setup, and data reduction framework. The study presented the methodology and findings from two large-scale experiments conducted on RC bridge subassemblies. Each subassembly, very similar to the subassembly considered in this study, consisted of the middle column/cap-beam joint of a three-column bridge bent and a large part of the monolithically cast-in-place box-girder of a typical California highway bridge. The subassemblies were subjected to constant gravity load and

gradually increasing bidirectional cyclic lateral loading. One subassembly represented the later 90s common practice in California and the other considered new design using headed reinforcing bars with reduced volume of transverse reinforcement to improve joint construction. Special attention was given to proper modeling of the boundary conditions and use of instrumented supports. The effect of bidirectional loading on global damage of the box-girder slabs was considered in the study and was presented in the form of variation of the effective moment of inertia of the cap-beam cross-section with displacement ductility. Both subassemblies experienced excessive shear damage in the joint regions with ultimate failure due to pullout of column longitudinal reinforcing bars. However, the use of headed bars led to better global and local performances due to improved confinement of the joint region with less volume of reinforcement. Because of the relevancy of this study, more detailed conclusions, as stated by the authors, are presented as follows:

- Use of headed reinforcement was an efficient way to reduce reinforcement congestion within critical regions in RC bridges such as cap-beam/ column joints. The tested new design using headed reinforcement with less total amount of transverse steel was shown to lead to improved global response compared to the common design practice with conventional reinforcement. This was observed mainly from the more gradual strength degradation with cyclic loading, from the higher ultimate displacement ductilities in both of the longitudinal and transverse loading directions, and from the reduction of the average shear strain within the cap beam/column joint region.

- Caltrans estimate of the effective slab width acting with the integral bent cap in resisting flexural demands as 12 times the slab thickness is conservative up to a displacement ductility level of five. For lower ductility levels, larger contribution of the soffit and deck slabs may be used in estimating the flexural stiffness of the effective cap beam. This may have significant design implications where higher cap beam stiffness will change the seismic internal forces in the different bent sections. It is to be noted that this particular observation from that study is of great relevance to the study presented in this report and was a vital motivation for carrying out this study to better quantify the cap beam effective slab width.

- The vertical and longitudinal horizontal headed reinforcements within the joint region were effective in confining these regions as supported by the strain measurements. This was reflected in delaying the pullout of the column longitudinal bars, i.e. requiring larger number of cycles for the column longitudinal bars to pullout compared to the case with conventional design. The conventional joint reinforcement in the form of vertical hooks and stirrups and horizontal hairpins were not as effective as the corresponding headed bars due to possible slippage of these bars in relation to the surrounding concrete.

- Based on the observed mode of failure, the study recommended to further investigate the use of headed bars as longitudinal column reinforcement as a possible way of preventing the observed pullout of these rebars. In this way, significant improvement of the seismic performance of the designed bridge system (ultimate drift ratios greater than 8.5% and ultimate displacement ductility greater than 6) can be obtained. Although more than 8% drift was achieved in the experimental study, this large drift was accompanied with excessive strength and stiffness degradation. The goal of investigating the use of headed

bars as longitudinal reinforcement of the column is to eliminate the brittle mode of failure caused by bar pullout.

A general observation regarding the use of headed rebars based on the conclusions from Natio et al. (2002) and Mosalam et al. (2002) is that headed rebars are efficient in reducing joint congestion and lead to better constructability without compromising strength requirements. The same observation is supported by conclusions from earlier studies such as Ingham et al. (1995) and Thewalt and Stojadinovic (1995) that suggested that using headed reinforcement usually results in a better performance because of the enhanced anchorage. The same observation was the motivation for Hube and Mosalam (2010, 2011) to propose new design for RC box-girder in-span hinges. The use of headed rebars was shown to be effective in in-span hinges as was the case for beam-column joints.

2.3.1.6 Other Relevant Studies

The behavior of only bridge columns rather than a bridge subassembly has always been a main research area for two reasons. First, plastic hinging in bridge columns is the desired mode of failure. Second, testing single columns in a unidirection or bidirection or even on a shaking table is more convenient and relatively easier than testing a bridge system or subassembly. Thus, numerous tests were conducted on columns to verify and ensure that desired ductility at failure is achieved. In this subsection, few examples of the several column tests in the literature are briefly listed.

The lateral response of well-confined bridge columns with varying longitudinal reinforcement ratios and aspect ratios was investigated by Lehman and Moehle (1998). The results were used to outline the performance-based seismic design framework for RC bridge columns. Moreover, the behavior of RC bridge columns having varying aspect ratios and varying lengths for confinement extent was experimentally and analytically examined on four circular columns by Calderone et al. (2000). Tests to evaluate the behavior of bridge columns subjected to variable axial load and various loading patterns were conducted at the Structural Laboratory of the University of Southern California in 2002 by Esmaeily-Gh and Xiao (2002). They found that the axial load and loading pattern variation had significant effect on the flexural strength capacity, the mode of failure and damage pattern, and the ductility and deformation of the columns.

The effect of bar buckling in RC columns was studied by Brown et al. (2007). Eight circular columns, reinforced with longitudinal bars and circumferential spirals, were tested under constant axial load and cyclic lateral displacements. The goal was to generate data on bar-buckling mechanisms for developing a numerical model and for further understanding of the phenomenon. New modeling strategies for modern RC bridge columns were developed to accurately model column behavior under seismic loading, including global and local forces and deformations, as well as progression of damage (Berry and Eberhard, 2007). The models were calibrated using the observed cyclic force-deformation responses and damage progression observations of a 37-test database of spirally RC columns.

2.3.2 Performance-based Design of Bridges

This brief subsection aims at drawing the attention to how research is associated with the shift from conventional strength design methods to the performance-based design of bridges. Drastic number of research studies were conducted over the past couple of decades that focused on capacity design approach and nonlinear modeling and analysis procedures and techniques in response to the need of reliable performance-based design approach. According to ASCE-41 (2006), performance-based earthquake engineering (PBEE) is based on designing to achieve predetermined performance levels or objectives in a specific hazard environment. Performance-based design is intended to allow structures to meet specific performance objectives with greater reliability than the traditional prescriptive code approach. The design of structural components for target performance levels requires an assessment of strength, stiffness, and deformation characteristics typically into the nonlinear range of elements and subassemblies that make up the seismic-force-resisting system as advised by ACI-374.2R (2013).

Hose and Seible (1999) conducted a study as a part of an early initiative by the Pacific Earthquake Engineering Research (PEER) Center to develop and demonstrate the parametric basis for performance-based bridge engineering. The study resulted in a bridge performance database and catalog to evaluate the capacity of bridge systems and their subcomponents allowing an accurate characterization and prediction of the structural behavior. The developed database was based on observations and results from various laboratory tests, as well as damage from past earthquakes. This database was essential for the performance-based design process to advance.

Mackie and Stojadinovic (2003) defined the performance objectives in terms of annual probabilities of socio-economic decision variables being exceeded in a seismic hazard environment of the urban region and site under consideration. Further probabilistic seismic demand analysis was used to compute values of bridge-specific engineering demand parameters given ground motion intensity measures, such as peak ground acceleration. An optimal probabilistic seismic demand model (PSDM) was developed and proposed for typical highway overpass bridges. It is to be noted that probabilistic frameworks are gaining more popularity especially as PEER has been promoting full probabilistic evaluation within its PBEE methodology. Meanwhile, intensive efforts were undertaken to improve the performance, reliability, and economy of performance-based methods in extreme events. A cos-estimation approach of seismic performance was investigated in Ketchum et al. (2004). The project focused mainly on providing revised and improved empirical rules for the influence of design ground motion level on bridge construction cost.

As previously mentioned, PBEE and probabilistic approaches require extensive nonlinear analyses. Few examples of analytical studies that focused on enhancing bridge modeling and analysis practices are presented. Aviram et al. (2008) furnished a good collection of practical guidelines for nonlinear analysis and modeling of bridge structures to assist practicing engineers in the implementation of nonlinear methods for bridge design subjected to seismic loading. This collection of practical and readily implementable recommendations is primarily intended to estimate seismic demand on critical bridge components and systems. In addition, the report by Aviram et al. (2008) offers a comprehensive literature review of the current engineering practices in the US and how they relate to desired analytical methods. Another application that can significantly alter an entire bridge system response and is more feasible to tackle analytically is

the bridge abutment response along with soil–structure interaction and backfill flexibility. A performance-based evaluation of bridges on liquefiable soils with focus on abutment modeling using nonlinear inelastic analysis is presented in Kramer et al. (2008). The report provides a detailed analytical model consisting of liquefiable and non-liquefiable soils, pile foundations, abutments, and the bridge superstructure along with the model validation. The study considered the computed response under various loading conditions, and provided conclusions regarding the resulting damage and loss estimates. Further studies of RC bridge systems including soil-foundation-structure interaction are given in Dryden and Fenves (2009) and Mitoulis (2012).

3 Development of Experimental Program

Experimental framework was undertaken to investigate the structural behavior of integral bent cap beam in RC box-girder bridges subjected to earthquake loading. This chapter discusses the development of the experimental program. The determination of the prototype bridge configuration, the design of the experimental subassembly, the test setup and boundary conditions, specimens' construction, material properties, and the instrumentation techniques used for the experiments are also presented.

3.1   BRIDGE TERMINOLOGY

Due to the intersections of highways and wide avenues in the United States, bridges are indispensable for a smooth traffic flow. Several steel and RC bridge types exist in California. However, a typical California bridge system is a RC integral box-girder bridge as illustrated in Figure 3.1. This system consists of a single-level elevated highway supported on multiple bents and abutments. Each bent consists of either single or multiple columns. These columns terminate in a solid RC beam, referred to as the bent cap beam, which spans the entire bridge width. The cap beam and columns make up the transverse bridge frames which, in turn, support the highway bridge span.
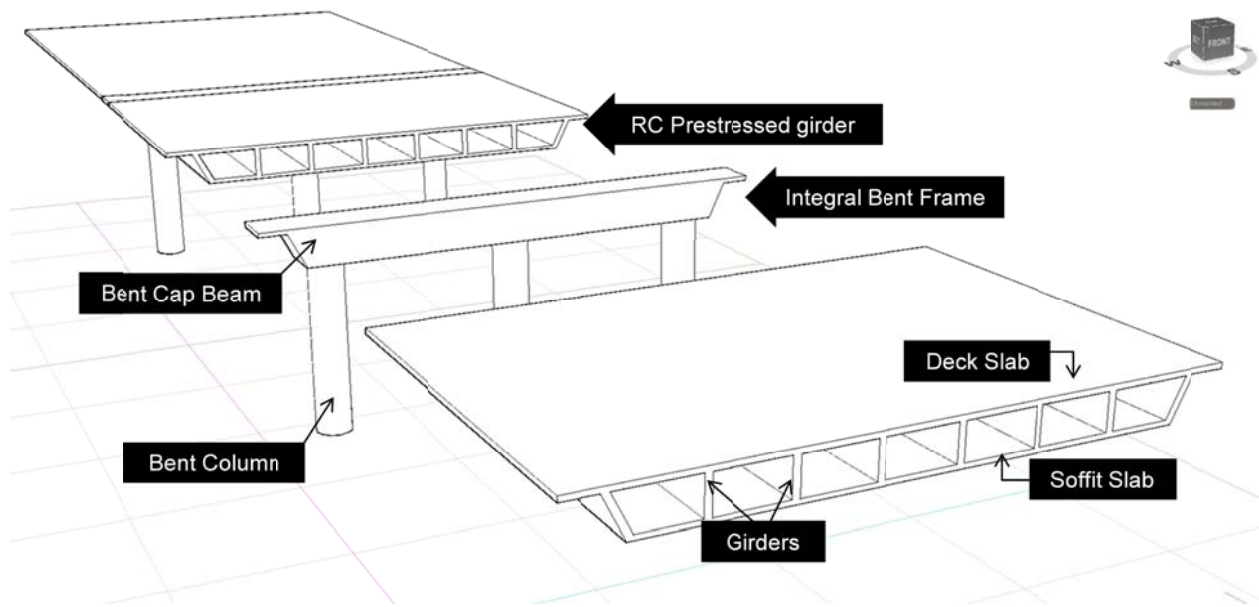
Figure 3.1 Components of a RC box-girder bridge

Many different types of structural systems may be used to span the distance between bents. They range from composite steel plate girders, which rest on top of the cap beam, to integral post-tensioned concrete box-girder systems constructed monolithically with the cap beam. A typical box-girder consists of a top deck slab, bottom soffit slab, and longitudinal webs, commonly referred to as girders. The different components of the bridge bents and longitudinal box-girder are shown in Figure 3.1. Long-span bridges are often divided into segments or frames to allow for shrinkage and expansion due to temperature variations. In monolithic construction, each frame typically consists of two to three bridge bents and their adjoining spans. Connection between adjacent longitudinal frames is accomplished through in-span hinges (seats) that are capable of transmitting vertical (and possibly transverse) forces while allowing for expansion and rotation.

Due to the nature of the test setup utilized for the experimental program conducted in this study, the specimen bridge subassembly is tested in an inverted position as discussed in a following section and illustrated in Figure 3.2. To avoid confusion, the slabs are referred to directly as soffit slab and deck slab, as per Figure 3.2, rather than top slab and bottom slab. The figure also shows the parts of the prototype bridge considered for the experimental subassembly as discussed next.
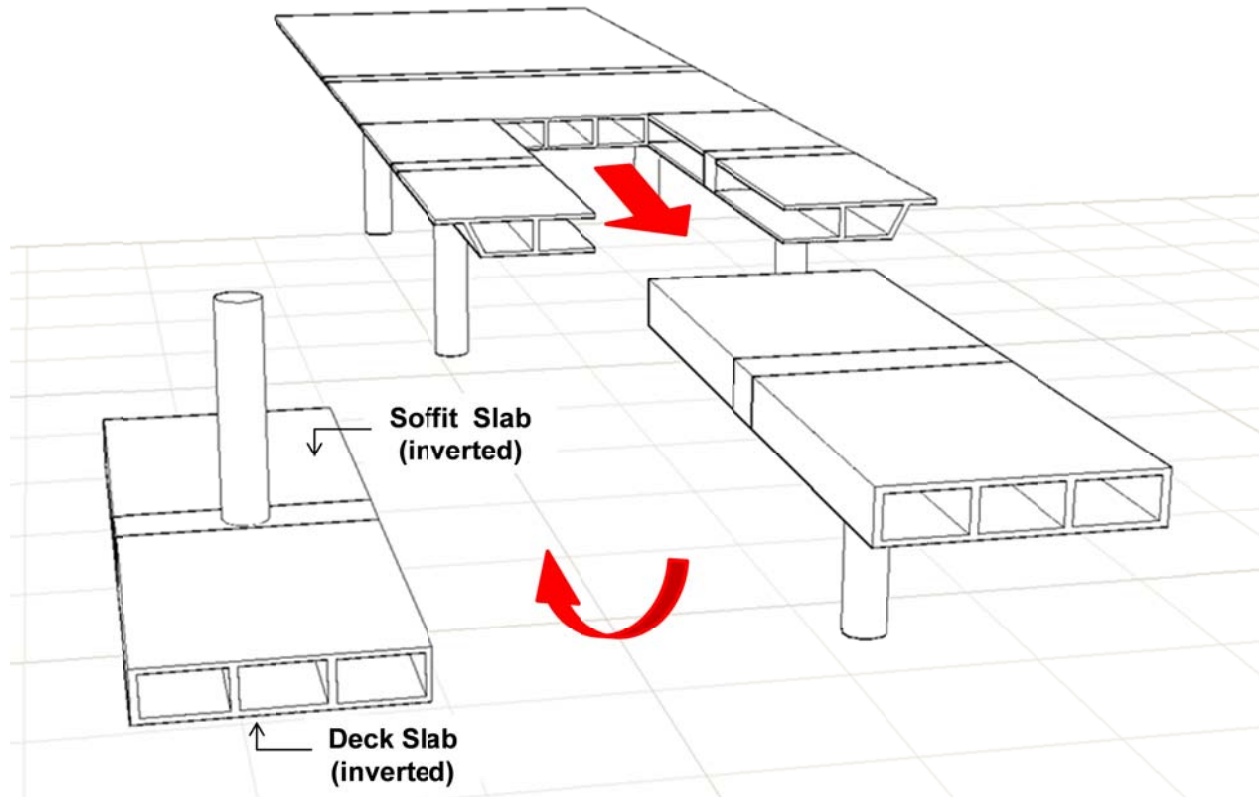
Figure 3.2 Convention of the specimens' box-girder slab terminology

3.2 PROTOTYPE

To determine the geometry and structural configuration for the test specimens, a typical California bridge construction was considered as the prototype. There are several methods for choosing a prototype bridge for research studies. One method is based on conducting a survey of existing bridges, then averaging the spans and cross-sections dimensions to generate a virtual prototype that is then considered a representative typical bridge. This method was adopted by Natio et al. (2001) where sixteen RC bridges built in California between 1985 and 1995 were evaluated. This study resulted in the selection of a representative prototype that consisted of a three-column bridge bent with an integral box girder and pinned column-to-footing connections. The prototype bridge considered average spans of 150 ft. between the bents which consisted of circular columns and a cap beam depth that is comparable to the column diameter. Another method for choosing a prototype bridge is using real existing bridges. This method is useful if a particular structural behavior is investigated or damage due to a specific loading case (e.g. specific earthquake) is analyzed. Lee and Mosalam (2014) used two existing bridges to investigate the behavior of RC columns in shear due to horizontal and vertical earthquake excitations. The two considered bridges are the Amador Creek Bridge and the Plumas-Arboga Overhead Bridge.

A different method for choosing a prototype bridge was utilized in this study which aims at investigating the structural behavior of integral bent cap beams and box-girder slab contribution in light of the AASHTO and Caltrans Seismic Design Criteria (SDC). A readily available typical California bridge that is designed by the Caltrans Bridge Academy is utilized. This bridge, which for convenience is referred to directly as Academy Bridge throughout this study, is a representative of California most common RC box-girder bridge type with integral bent cap beams. The Caltrans Bridge Academy uses the Academy Bridge as a part of the complete hands-on design exercise for junior bridge engineers and professional bridge design workshops. The Academy Bridge is modified to allow the generation of a symmetric and feasible subassembly specimen that can be accommodated at the Structures Laboratory at the University of California, Berkeley. The key features of the bridge, such as the main span, bent cap and box-girder geometry, and column diameter, are not changed or modified. However, the modifications are concerned only with the bent layout and elevation (height). A shorter column height, which still guarantee a flexural governed behavior as intended for the original Academy bridge design, and a symmetrical three-column bent that is unskewed are the main modifications applied to the Academy Bridge. The differences between the original Academy Bridge and the modified prototype are summarized in Table 3-1. The detailed geometry and dimensions of the modified Academy Bridge prototype considered throughout the course of this study are shown in Figure 3.3.

Table 3-1 Differences between the modified prototype and Academy Bridge

	Academy Bridge	Modified Prototype
Spans	3 spans: 124 ft., 168 ft., 112 ft.	3 spans: 124 ft., 168 ft., 124 ft.
Skewness	Skew at 15°	Orthogonal at 0°
Bent Height	44 ft. (aspect ratio 7.33)	30 ft. (aspect ratio 5)

Bent Layout	2 columns hinged at base	3 columns hinged as at base

ELEVATION

PLAN

TYPICAL CROSS-SECTION
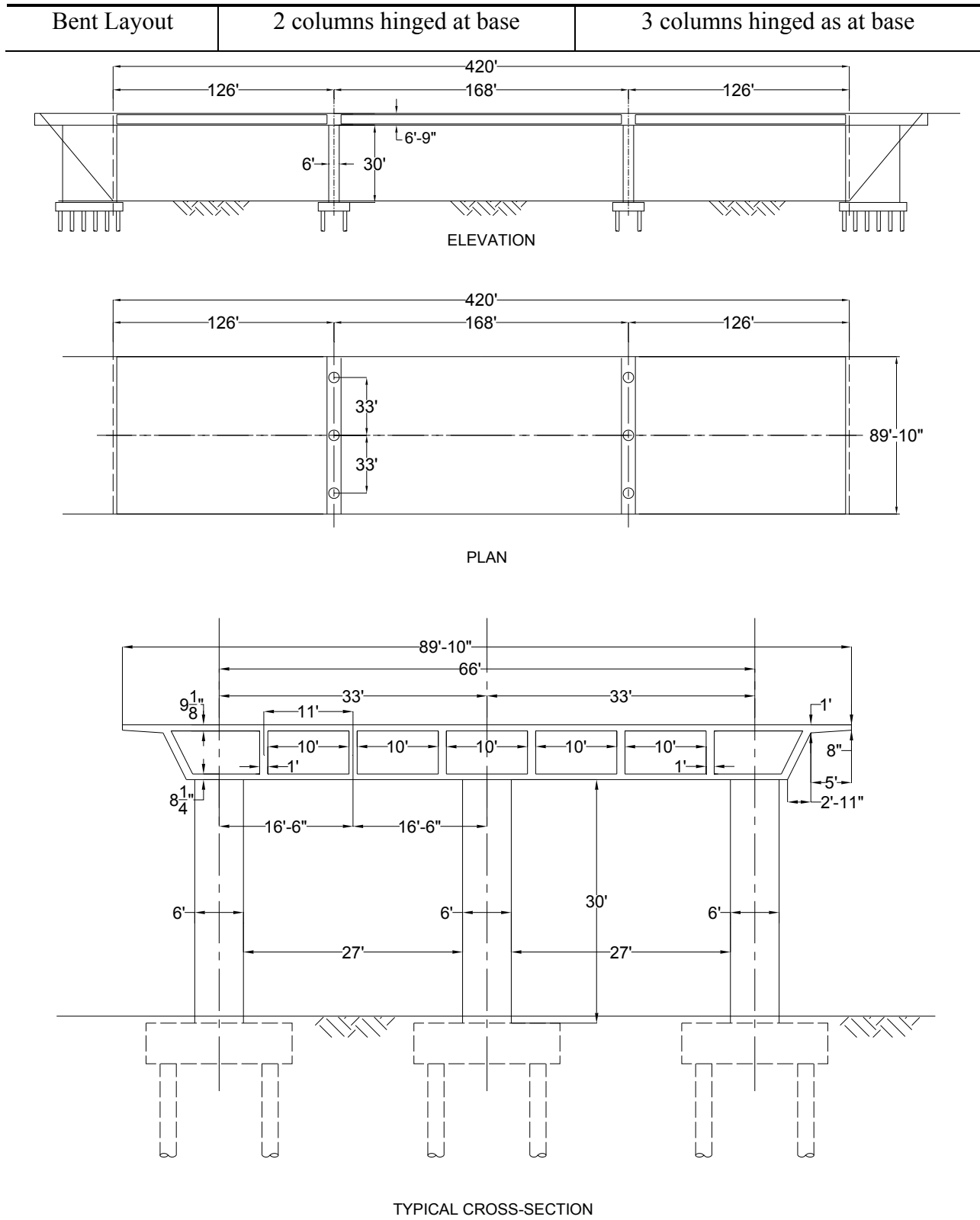
Figure 3.3 Different views of the modified Academy Bridge

46

3.3   SUBASSEMBLY DEVELOPMENT

3.3.1   Subassembly Geometry

The experimental investigation focuses on the behavior of integral bent cap beam and strain distribution in the box-girder slabs in a bridge system subjected to constant gravity loading and varying transverse (lateral) loading. Thus, representative portion of the box-girder in the longitudinal direction of the bridge is considered at both sides of the bent cap beam and column to form the subassembly was chosen for this study. The prototype bridge comprises multi-column bents where the transverse bridge frame consists of an integral bent cap supported on three columns. Only the middle column and part of the bent cap is considered in the subassembly. Figure 3.4 shows the representative portions of the bent cap beam in the transverse direction and box-girder in the longitudinal direction. The basis for choosing such representative portions is described next.

A full-scale and a complete assembly of all the bridge components would be the ideal case scenario for exact and accurate testing. However, due to practical considerations and laboratory limitations, only a reduced-scale and a representative subassembly are considered for testing. The largest possible scale is always favorable to mimic the actual behavior and avoid any scale effect bias. However, a compromise between the subassembly scale versus the considered representative portions of the bent cap and box-girder is usually part of the test subassembly design decision. The most feasible physical boundary conditions for the test subassembly is the main criterion adopted in this study for deciding on the representative bridge longitudinal and transverse span portions. On the other hand, the laboratory space available for testing as dictated by the reaction frame and the actuators capacity are the considered criteria for determining the final test subassembly scale.

The feasible boundary conditions are usually associated with minimal translational and rotational constraints i.e. provide least reactions. Meanwhile, laboratory hinged supports that allow free rotations especially for massive RC components are challenging and costly. Therefore, choosing the points of zero moments in the bridge under both vertical (gravity) and lateral cases of loading, in both transverse and longitudinal directions, leads to the most feasible boundary conditions. That is because partial fixations at zero moment locations are most likely to introduce the minimum secondary bending moments. For accurate estimation of zero moment locations in the prototype bridge, a SAP2000 (2009) elastic model for the prototype bridge was utilized. More details about the bridge model and boundary conditions verification are presented in Chapter 4.

For the bridge longitudinal direction, the bending moments and deflection inflection points are defined by gravity loads only because the lateral loads are resisted primarily by the bent cap and columns framing action. The zero moment locations along the bridge box-girder longitudinal direction are shown from the SAP2000 bridge model in Figure 3.5. It is shown that the zero moment location is at 1/4 of spans continuous from both sides and 1/3 of spans continuous only from one side. The prototype spans allow for a symmetric zero moment locations at both sides of a transverse bridge frame, which in turn results in a symmetric test subassembly dimensions. For the transverse direction, the zero moment location along the bent cap beam is controlled mainly by the direction of the lateral load as shown in Figure 3.6. It is shown that the beam zero moment location varies from approximately 1/3 to 1/2 of the span to

47

either side of the middle column as the lateral load direction is reversed. Meanwhile, the beam zero moment location varies from approximately 1/2 to 2/3 of the span adjacent to the outer columns. The test subassembly is considered for both earthquake cyclic loading and hybrid simulation with load reversals. Therefore, an approximate location of the zero moment is chosen to be at 1/2 of the beam span to account for the load reversals. The last component of the global geometry of test subassembly is the bent column. For a multi-column bent, a hinged pile cap is used as the column foundation. Therefore, the zero moment location along a hinged column is at support location, i.e. the full column height is engaged and consequently considered in the resulting test subassembly.
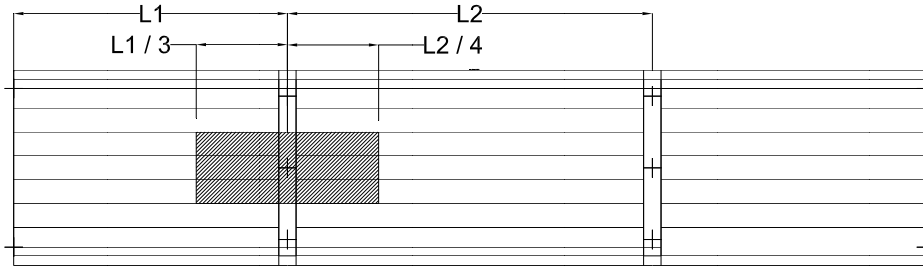
Figure 3.4 Subassembly considered for testing as identified within the prototype bridge
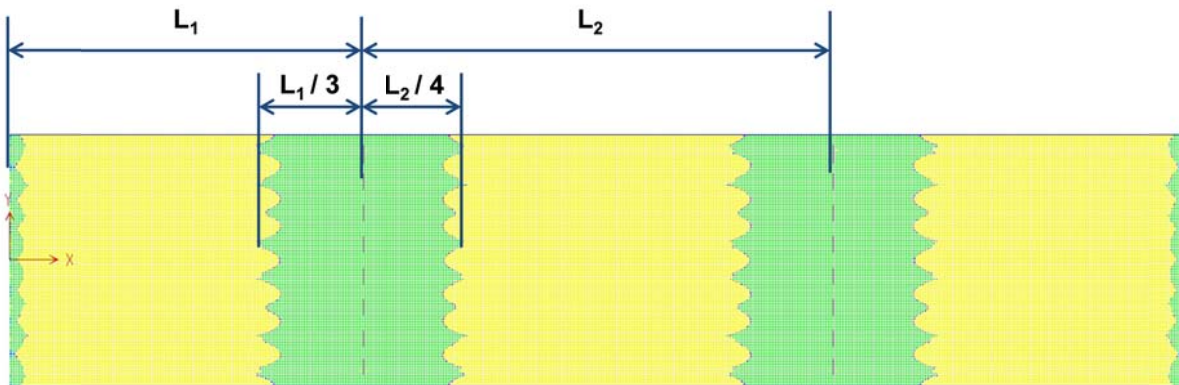
Figure 3.5 Locations of zero moments along the longitudinal direction of the prototype bridge under vertical gravity loading
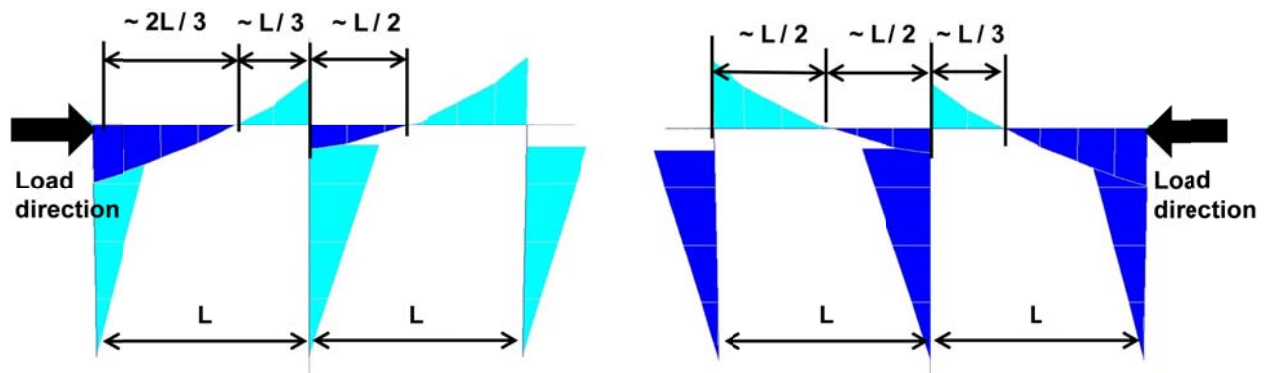
Figure 3.6 Locations of zero moments along the transverse direction of the prototype bridge under combined vertical and lateral loading

48

As a result of the identified zero moment locations for each of the column, bent cap beam, and box-girder along with the available reaction frame height and laboratory space at the Structures Laboratory at the University of California, Berkeley, a maximum scale of 1/4 is proposed for the test subassembly. The dimensions of the resulting test subassembly at 1/4-scale were found to be acceptable in light of the reaction frame dimensions and laboratory space. The expected forces required for the 1/4-scale subassembly during either the quasi-static or hybrid simulation tests were found from pre-test analyses, presented in details in Chapter 4, to be accommodated within the available actuators capacities. In addition, the 1/4-scale allows for the use of normal concrete aggregate and standard reinforcement sizes. Therefore, a reduced 1/4-scale test subassembly was finalized for the two test specimens considered in this study.

3.3.2   Boundary Conditions

To simplify the testing and the construction, the test specimen (subassembly) was oriented upside-down with the box-girder and the cap beam against the floor and the column in the air. The specimen is sought for testing under combined vertical gravity and bidirectional lateral loading. Therefore, a stable test setup would require proper boundary conditions for load application and resisting forces against the laboratory strong floor and reaction frame in the three global axes X, Y, and Z. How the boundary conditions affect the specimen geometry is only presented in this subsection while more details are discussed in the Test Setup subsection. The inverted position requires the minimal physical boundary conditions relative to the regular orientation. These physical boundary conditions are required at five locations; the column end, namely (*action*), the two cap beam ends (*reaction*), and the two box-girder ends (*reaction*) as follows:

- The vertical and lateral actuators are connected directly at the inverted column top end at the anticipated zero moment location. Thus, no footing or pile cap is needed in this orientation and only a column head that facilitates the actuators' connection to the column is considered. A hexagonal shape column head was found to be the best geometry for accommodating the connections of the vertical and lateral loading systems.

- Two vertical struts are considered at the two cap beam ends. The vertical strut provides a vertical reaction only while allowing for translation in the two horizontal directions, full rotations around the X and Y axes, and partial rotation around the Z axis. This is to mimic the reactions at the chosen zero moment location for the symmetric subassembly.

- Two seat beams are considered at the box-girder ends. The seat beams are monolithically casted with the specimen at the box-girder ends. Such monolithic setting is expected to fully restrain the three translational degrees of freedom while partially restraining the rotations. Ideally, the rotations are required to be unrestrained to allow for the desired zero moments at such locations. This partial rotational fixation is only a result of the deck slab stiffness which is much smaller relative to the seat beam, leading to a potential cracking mechanism at the interface. Such dynamic cracking mechanism, i.e. opening and closing cracks, at that slab/seat beam interface can be assumed to accommodate the very small rotations at the box-girder ends without creating undesired large bending moments. This assumption is verified analytically using a SAP2000 (2012) model for the subassembly that utilizes different hinged and fixed end supports. More details are presented in the pre-test analysis in Chapter 4.

49

Based on the framework discussed above for the evolution of the test specimen geometry, scale and boundary conditions, the final specimen components and dimensions are summarized in Table 3-2 and presented in three different views in Figure 3.7.

Table 3-2 Summary of the reduced 1/4-scale specimen dimensions

Column diameter	18 in.
Column height	90 in.
Cap beam/superstructure height	20-3/8 in.
Cap beam width	24 in.
Deck slab thickness	2-5/16 in.
Soffit slab thickness	2-1/16 in.
Box girder web thickness	3 in.
Clear width of box cell	30 in.
Clear height of box cell	16 in.
Subassembly overall length	264 in.
Subassembly overall width	102 in.
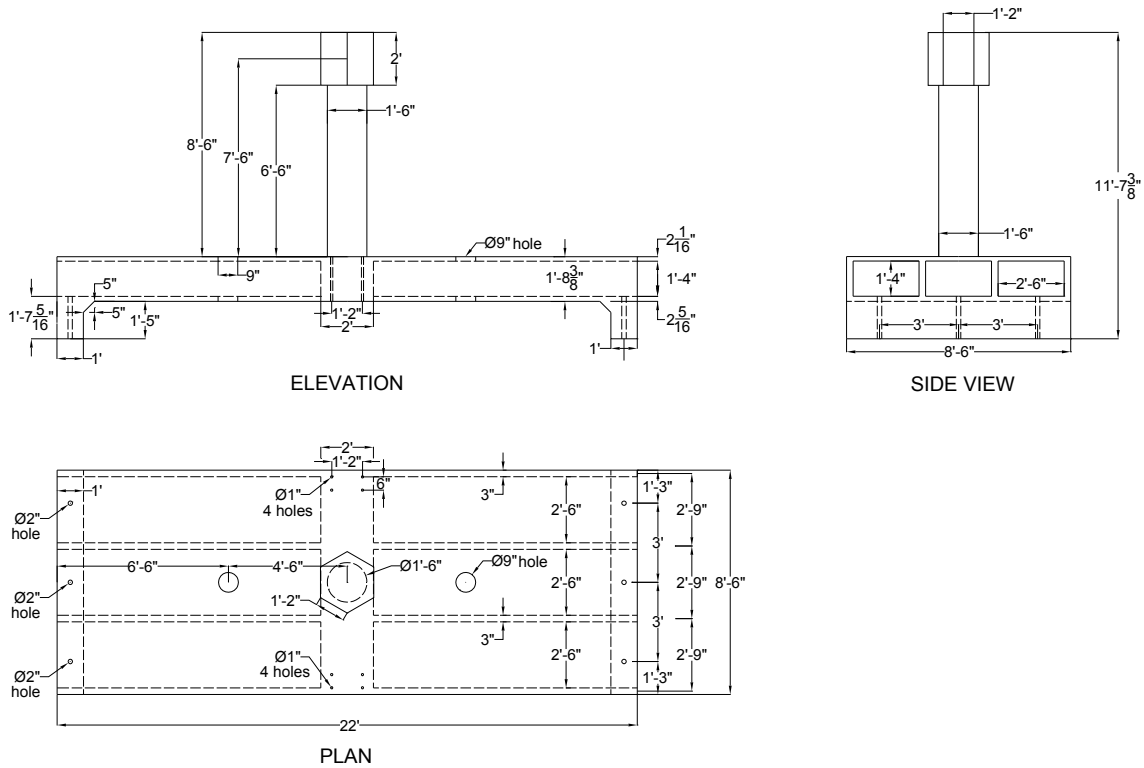
Figure 3.7 Different views of the 1/4-scale subassembly specimen

50

3.4   SPECIMEN DESIGN

Two identical specimens are considered for this study with similar design but different loading protocol as discussed in details in a following subsection. A brief summary of the specimen design and cross-section reinforcement is presented here. The details of the specimen design loads and calculations of required reinforcement are presented in Appendix A.

To calculate the design loads for the reduced-scale specimen, the SAP2000 (2012) full prototype bridge model was used to first estimate the loads and straining actions, due to dead and live loads, at relevant structural element. Next, the elements straining actions were scaled down using the proper similitude relationships and used to design the different specimen sections. In addition, the provisions of the Caltrans Seismic Design Criteria (SDC 2010) and the AASHTO LRFD Bridge Design Specifications (2007) were considered to estimate seismic design loads. The bent cap beam and box-girder superstructure are flexurally designated as capacity protected components to remain elastic when the column reaches its overstrength capacity. More details of the utilized seismic capacity design approach can be found in Appendix A.

The design of the specimen includes flexural and shear design for each of the column, cap beam, beam-column joint, box girder deck and soffit slabs, box girder webs, and the seat beams required for the specimen attachment to the strong floor of the laboratory. One assumption for the design of the box-girder is neglecting the effect of prestressing. Although the prototype bridge comprises a longitudinally post-tensioned PC box-girder, yet this study focuses only on the behavior of the cap beam and box-girder slab contribution in the bridge transverse direction. Thus, no prestressing is needed for the specimen as long as the box-girder remains elastic in the longitudinal direction. The design was made according to the following Codes and Standards: AASHTO LRFD Bridge Design Specifications (2007), Caltrans SDC (2010), and ACI-318 (2008). The reinforcement details of the main specimen's components are summarized in Table 3-3 and all of the specimen cross-sections are shown in Figure 3.8.

Table 3-3 Summary of the specimen cross-sections reinforcement

Column	16 #6 longitudinal bars
	#3 spiral at 2-1/2 in.
Cap beam	8 #5 negative reinforcement
	8 #5 positive reinforcement
	#3 stirrups with 4 branches at 5 in. spacing
Box-girder	#3 with standard hook in transverse direction at 4 in. spacing
	#3 straight bars in longitudinal direction at 2-1/2 in. spacing
	#3 single branch tie at 4 in. spacing
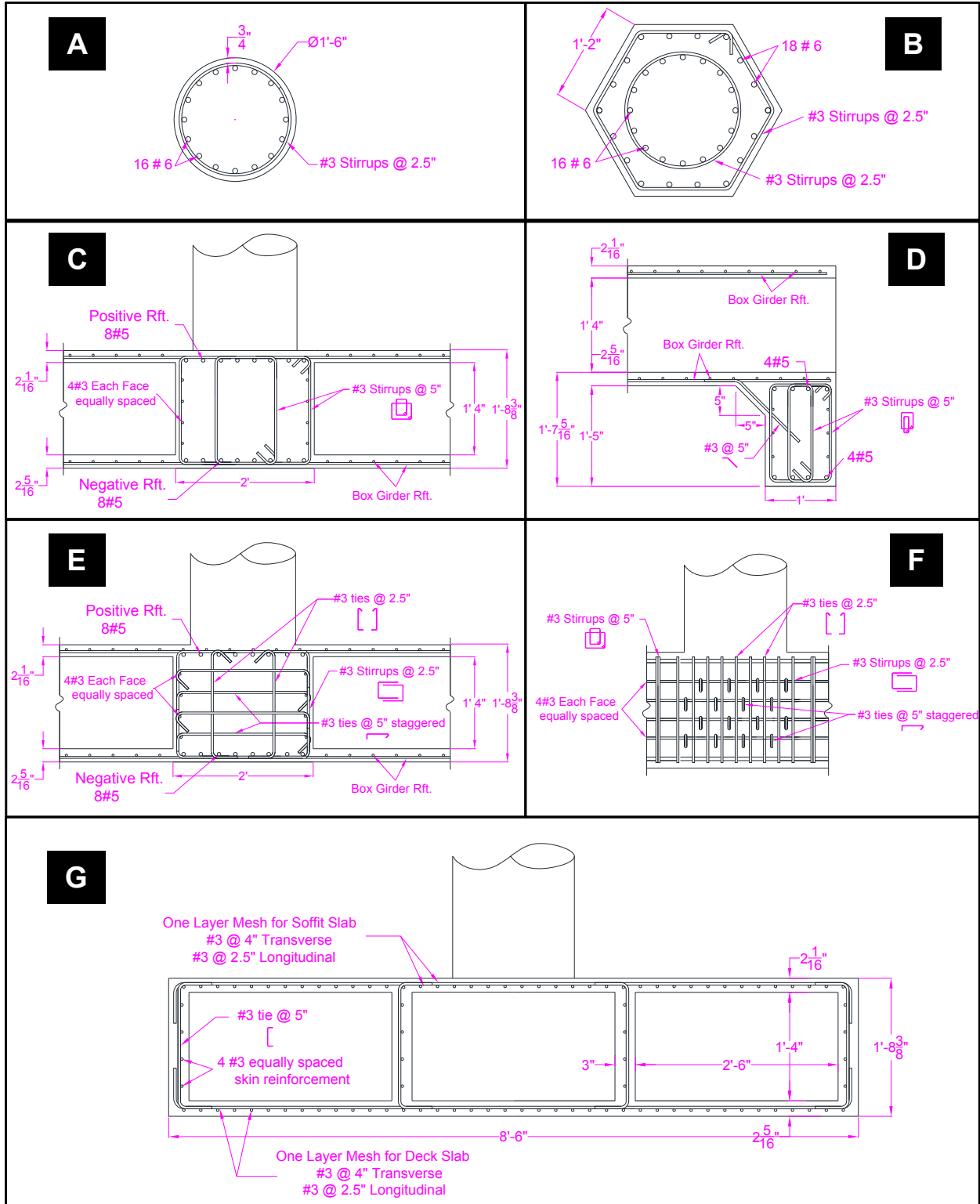
Figure 3.8 Dimensions and reinforcement details for each of the specimen components: (A) Column, (B) Column Head, (C) Cap Beam, (D) Seat Boundary Beam, (E) Joint Reinforcement in Transverse Direction, (F) Joint Reinforcement in Longitudinal Direction, (G) Box-girder

3.5   TEST SETUP

To facilitate the experimental program, the two specimens considered for this study were constructed and tested upside down. The objective of the tests is to investigate the behavior of bent cap and slab contribution under combined vertical and lateral load. Therefore, vertical and lateral loading systems were required. All loads were applied at the column end in its inverted position, while the specimen was line supported on two concrete beams at the box-girder ends and additionally point supported by two vertical struts at the cap beam ends. A schematic representation of the test setup, including the loading systems and boundary supports is shown in Figure 3.9. The detailed test setup and the relative locations of the loading actuators and supports are shown in different views in Figure 3.10 and Figure 3.11.

The gravity load was applied at the column free end, top end in the inverted position, through two vertical hydraulic actuators and a steel spreader I-beam place on top of the column head. The actuators are pulling downwards on the spreader beam through pinned connections from one end, and reacting against the laboratory strong floor also through pinned connections at the other end. All pinned connections were achieved through 3D ball-bearing clevises. Due to practical considerations, the spreader beam span had to be limited to avoid excessive flexibility and to achieve constant and stable vertical load. Thus, the vertical actuators had to pass through both of the soffit and deck slabs of the specimen's box-girder to reach the strong floor. Two 9-inch holes were made in both slabs and at the two sides of the column for the actuator rods to pass through. Special 3-inch diameter and 2-foot length rods were fabricated to allow for the extension of the actuators. In addition, 1-inch elastomeric rubber pad was used between the spreader beam and the concrete column top to avoid any stress concentration due to concrete surface imperfections and achieve a vertical uniform load application.

The lateral load was also applied at the column head using two lateral hydraulic actuators that were reacting against the laboratory steel reaction frame shown schematically in Figure 3.10. The lateral actuators setting allows for applying both cyclic loading during the quasi-static testing of first specimen, and the online computed earthquake displacement input during the hybrid simulation testing of the second specimen. The actuators were located in one horizontal plane but connected to the column head at two inclined directions rather than two orthogonal directions to provide stability during both unidirectional and bidirectional loading. Accordingly, two special considerations were required. First, geometric transformation was needed to transform the desired input displacements in X and Y directions, that correspond to the bridge subassembly transverse and longitudinal directions, respectively, to the local actuators directions. Second, the column head geometry had to be designed properly to facilitate the two inclined lateral actuators connections. Based on the attachment points of the actuators to the reaction frame and the distance between the frame and the column head, a hexagonal shape was found to be the best choice even though it was not the most ideal from the ease of construction perspective.

Similar to the vertical actuators end connections, the lateral actuators end connections were also 3D pins. The pinned nature of the actuator to the column head connection ensured the application of only lateral force without any vertical loads or bending moments. Steel plates of 1-inch thick were installed on the two opposite sides of the hexagonal column head and prestressed together. The actuators were then bolted to the front plates. Thus, when the actuators extended, the force was transferred to the column as bearing on the front face directly. When the actuators

retracted, the force was transferred through the prestressing to the other face of the column head and bearing wass achieved from the back sides.
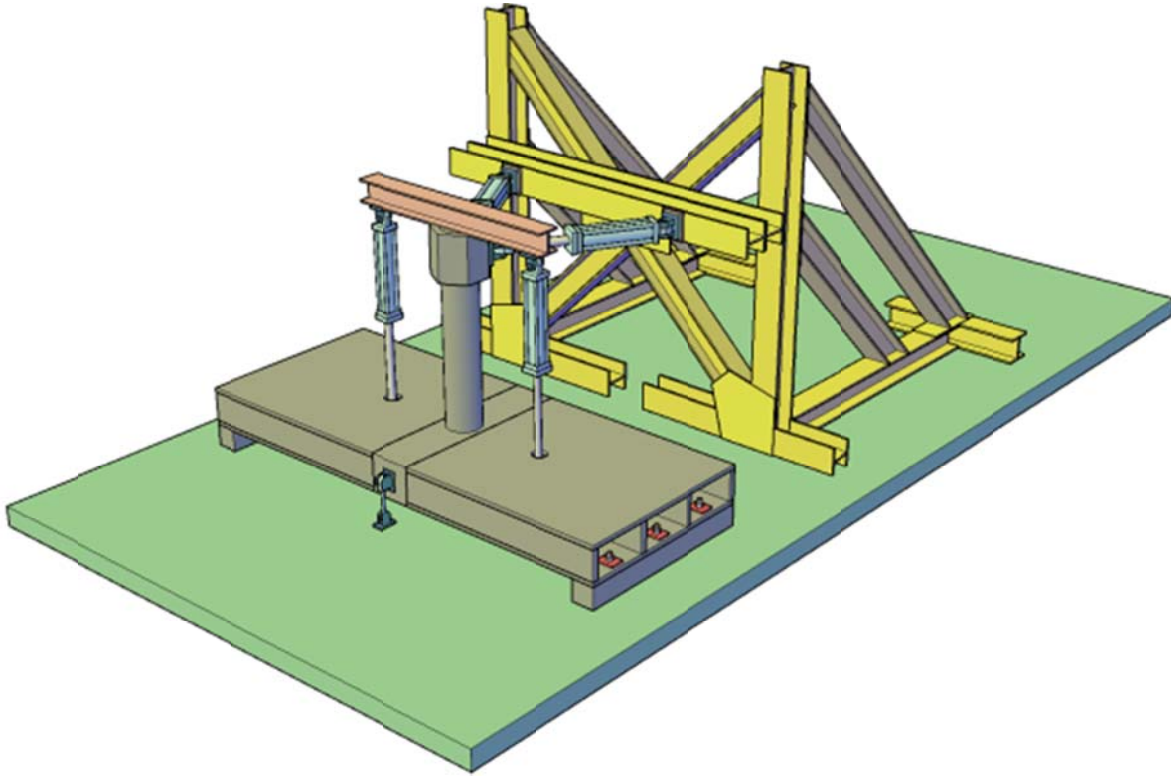
Figure 3.9 Schematic 3D view of the test setup
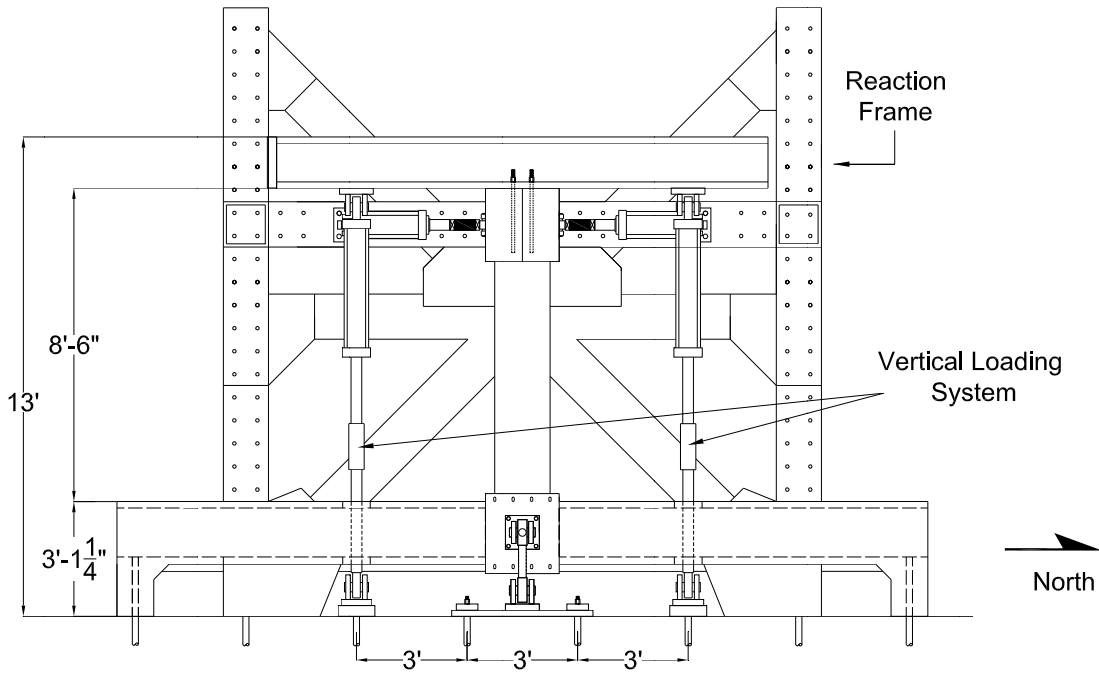
Figure 3.10 Elevation view of the test setup
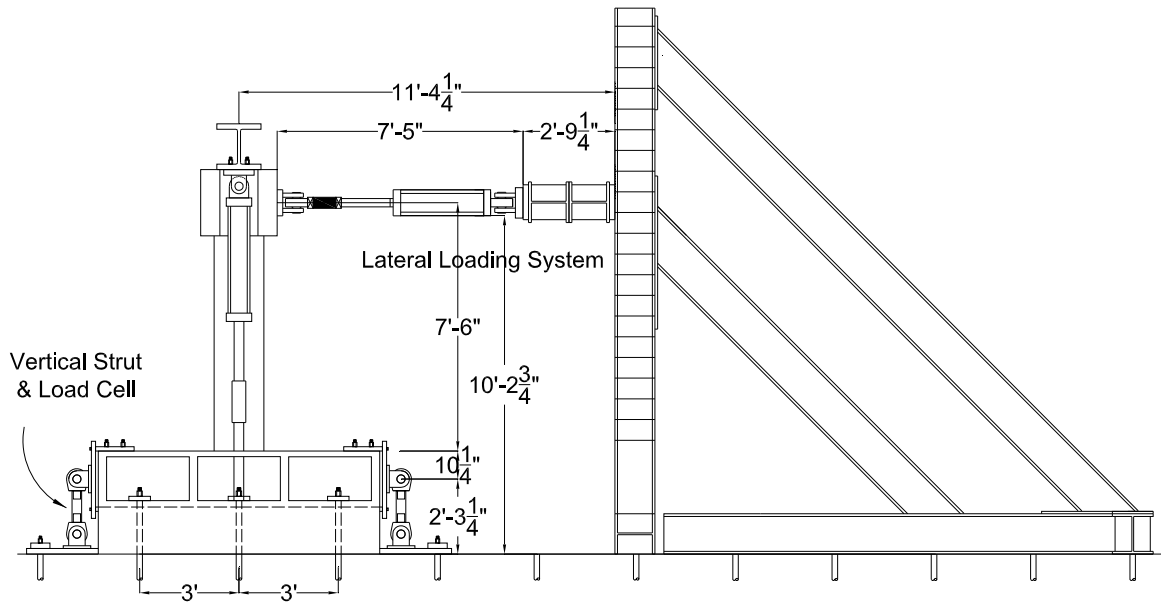
SIDE VIEW
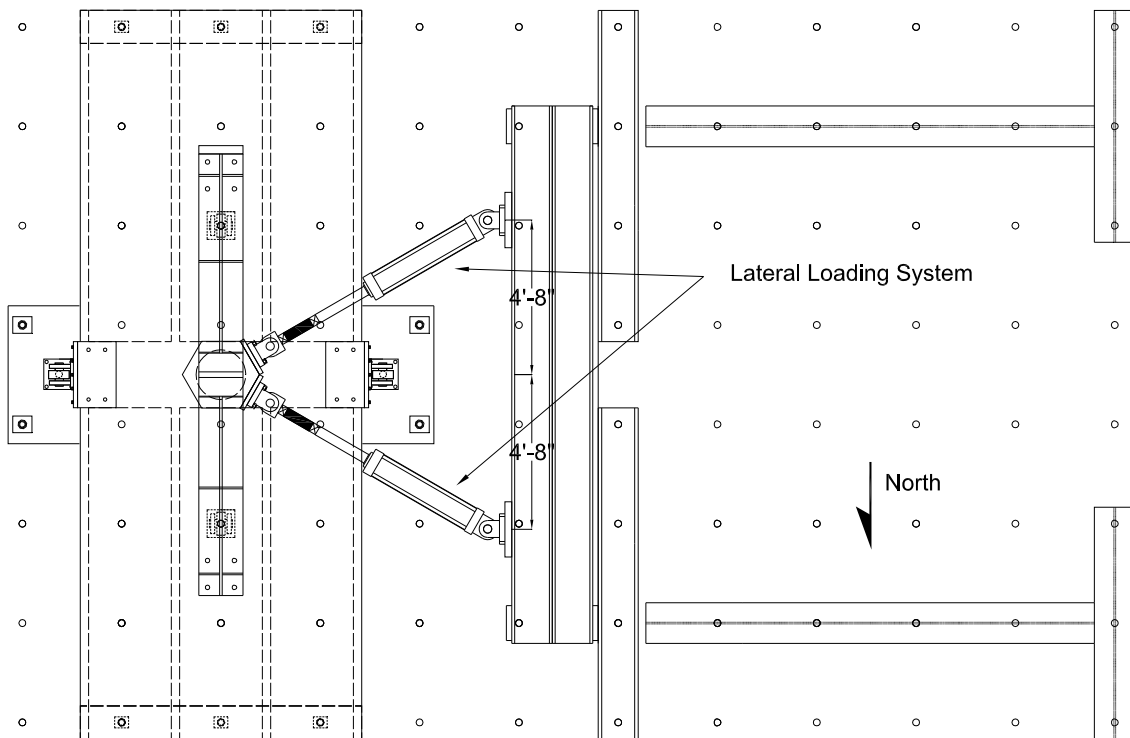
PLAN VIEW

Figure 3.11 Side and plan view of the test setup

As previously discussed, the specimen was attached to the laboratory strong floor through the seat beams and two vertical struts at the cap beam ends. The two RC seat boundary beams were cast monolithically with the specimen. Each beam had three through-pipes that were 3 foot apart and match with the laboratory strong floor hole pattern. The seat beams were hydrostoned to the strong floor then a total of six prestressing rods were used to prestress the specimen down to the strong floor. The hydrostone and prestressing guaranteed enough friction resistance with the strong floor at the bottom faces of the seat beams bottom face to provide the necessary horizontal and vertical reactions during lateral loading.

Two vertical 1D struts, designed to mimic a roller support, were also used at the cap beam ends to provide vertical reactions during both gravity and lateral load application. The strut vertical reaction was designed to be transferred to the cap beam through bearing to avoid any unnecessary shear or tensile stress states at the cap beam ends and to achieve uniform stress distribution along the entire cap beam width. The load path at the cap beam end started with the vertical force in the strut, reacting against the strong floor, and transmitted to a side plate through 4 shear bolts and small bearing edge blocks around the clevis plate. The force was then transmitted from the side plate to the top and bottom plates through 10 shear and friction bolts. The top and bottom plates were prestressed together to guarantee the only compression stresses exist at the cap beam end. It is noted also that the top and bottom plates were hydrostoned to the cap beam surface to avoid any stress concentration resulting from the surface inconsistencies. A schematic drawing of the vertical 1D strut along with the actual fabricated strut end connection are shown in Figure 3.12. A detailed catalog of photos for the test setup procedure and pieces is provided in Appendix D. The final assembled test setup is shown in Figure 3.13. This photograph was taken for the quasi-static test of the first specimen before the test started, and the same test setup was also used for the hybrid simulation test of the second specimen.
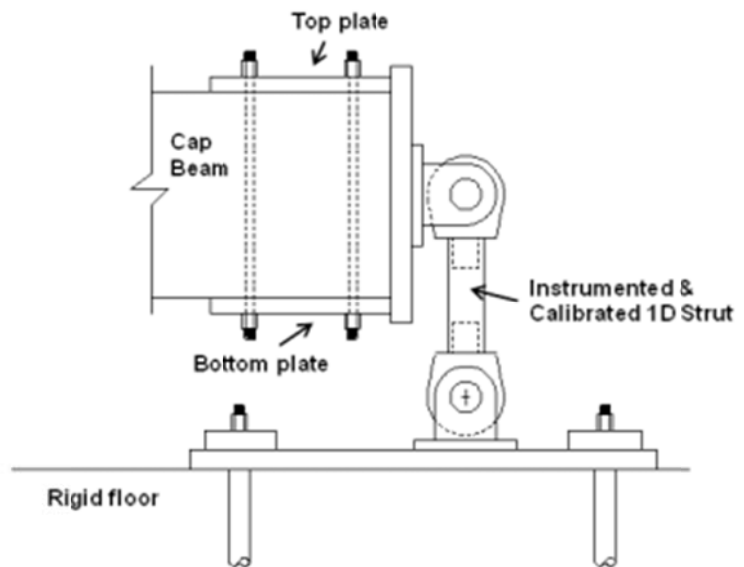
Figure 3.12 Vertical 1D calibrated strut used at the specimen's cap beam ends

Figure 3.13 Test setup for the bridge subassembly tests

3.6   EXPERIMENTAL PROGRAM

The objective of this section is to summarize the different tests that were conducted within the experimental program of this study. Two identical specimens were built and tested using two different loading and testing schemes: cyclic quasi-static testing and hybrid simulation (HS) testing. The first specimen was tested as-built under cyclic loading. After the first test was completed, it was decided to repair the tested specimen and strengthen the second specimen before it was tested. The details of the testing sequencing and basis for the repair and retrofit decisions are presented in the following subsections, while the utilized loading schemes are explained in the next section.

3.6.1   As-built Specimen One: Quasi-Static Testing

The first test in the four-test series, comprising the full experimental program, was a quasi-static test for the first specimen tested as-built under combined constant gravity load and bidirectional cyclic lateral loading. Originally, two identical specimens were planned to be tested as-built but using the two different testing techniques: cyclic loading and hybrid simulation. Thus, the quasi-static cyclic loading test of the first specimen as-built did not change from the original plan. Two different levels for gravity load were used in the first cyclic loading test such that the first level corresponded to only the dead load while the second level considered additional loads due to live loads and earthquake excitations. The bidirectional cyclic loading was applied independently in one direction at a time, i.e. a group of cycles was applied in the column-bent cap plane (transverse direction) then followed by a similar group of cycles in the box-girder longitudinal

57

direction. The observed mode of failure was the desired Caltrans SDC weak-column strong-beam (WCSB) which motivated the expansion of the experimental program. Based on that observed behavior and test results from the first test of the first specimen, it was decided to strengthen the second specimen before conducting any tests in an attempt to transfer higher moment demands to the bent cap beam. Meanwhile, the first tested specimen was decided to be repaired and re-tested twice. Description of each of these tests in the updated experimental testing program along with the objective behind the repair or retrofit decision are discussed in the following subsections.

3.6.2 Repaired Specimen One: Quasi-Static Testing

Before proceeding with further testing, a repair decision using Carbon Fiber Reinforced Polymer (CFRP) was made and pursued for the first tested specimen along with a retrofit decision for the second untested specimen. That is because it was feasible and convenient to carry out a repair job concurrently with the desired retrofit job of the second untested specimen. Moreover, the first test left the column completely damaged with several rebars rupture. Thus, a repair was useful to achieve a more stable system for the HS system development and trial tests before pursuing the second specimen's HS test. A quasi-static cyclic loading test was also sought for the repaired specimen before conducting the HS trial tests for the sake of comparison with the original as-built test.

Accordingly, the second test in the four-test sequence was a similar quasi-static test to the first test but applied to the repaired specimen. A constant gravity load that corresponded only to the second level used in the first test along with bidirectional cyclic lateral loading were adopted for the second test. Similar group of cycles as used in the first test were reapplied for the repaired specimen in the second test. However, the second test was intentionally stopped without applying the last group of cycles that were applied in the first test in both transverse and longitudinal directions group. That was to make sure that the repaired specimen would still have sufficient remaining force capacity for the HS system development trials, namely the third test.

3.6.3 Repaired Specimen One: Hybrid Simulation Development Testing

The third test utilized the first specimen that was repaired. The main objective of this test was providing a real HS test trial to verify the development of the HS system that was established particularly for this research study, but meant to be generic for future laboratory uses as well. Two main aspects of the development were verified through the third set of tests. The first is the back and forth communication between the computational and physical components of the hybrid system. It was necessary to make sure the computed input displacements passed to the actuators, and resulting forces measured at the actuators' load cells fed back to the computational platform through a robust communication loop. The second aspect of verification was concerned with the geometric transformation between global degrees-of-freedom (DOFs) used in the computational model and the actuators' local DOFs. Both aspects were successfully verified through several test runs that used the Northridge excitations recorded at both of Sylmar and Rinaldi stations. The tests were conducted with and without the application of gravity load. It is noted that the gravity load application was an essential part of the original test plan and the trials that did not involve the gravity load were only intended to check the stability of the developed HS system.

3.6.4   Retrofitted Specimen Two: Hybrid Simulation Testing

The fourth and final test in the experimental program was the HS testing of the second specimen that was already retrofitted before any testing. The retrofit aimed at strengthening the column using CFRP to amplify the moment demand on the cap beam for further bent cap capacity evaluation and exploring different modes of failure, if any. Another objective for the retrofitted HS test was to investigate whether an over-designed retrofit scheme can migrate the failure to a different part of the bridge. Moreover, the effectiveness of CFRP confinement was also explored. The HS tests involved several runs that included uni- and bi-directional testing, different scales for the lateral excitations, and different levels for the gravity load. Moreover, a new testing scheme was proposed and considered in few HS test runs to account for the P-delta effect that incorporated not only the gravity load, but also the effect of the vertical component of the earthquake excitations. The HS runs mainly used the Rinaldi record from the Northridge earthquake at various scales up to 200% and three levels for the gravity load. Two of the gravity load levels were similar to the ones used in the first quasi-static test. The third level was used to further increase the moment demands in the bent cap beam and to be compatible with the higher excitation levels. More details regarding the loading protocol are presented in the next section.

3.7   LOAD PROTOCOL

Two different types of lateral loading techniques were utilized in the experimental program conducted in this study. These are a quasi-static cyclic loading with a prescribed load pattern and an online computed earthquake response input signal applied through HS test. While the lateral loading was applied either during a cyclic loading test or a HS test, a constant gravity load was applied as well through force control throughout all the tests. Meanwhile, lateral cyclic and HS input signals were applied using slow-rate displacement control. A rate of loading of 0.02 to 0.06 in./sec was used and varied based on the loading cycle or HS signal level. The higher the loading amplitude was, the faster the loading rate became to keep the total testing time reasonable.

For the cyclic tests, the lateral loading was an offline signal adopted from the FEMA 461 (2007) guidelines. On the other hand, the input signal for the lateral loading in the HS tests was an online signal computed and updated based on a multi-DOF computational model subjected to the Rinaldi record from the Northridge earthquake. The gravity load levels for the HS tests were similar to those used in the quasi-static cyclic tests except for an additional level that was used only in the last few HS tests. More details about the gravity load levels and the FEMA 461 cyclic load pattern are presented here, while the HS loading details are included in Chapter 7.

3.7.1   Gravity Load

A constant gravity load was applied through two vertical actuators and a spreader beam at the top of the inverted column as previously discussed in the test setup. The total gravity load was split evenly between the two actuators. The vertical gravity load was applied first through force control, before any lateral loading, and remained almost constant during all tests. However, two levels of gravity load were used during cyclic tests and a third level was used in the HS tests. The lowest gravity load level used was 82-kips (approximately 5% of the column axial capacity), which was used in small-level cycles before the first yield. The second level was double the

value of the first level, i.e. 164-kips (approximately 10% of the column axial capacity). For the few HS tests that experienced a third higher level of gravity load, a total load of almost 240-kips (approximately 14.5% of the column axial capacity) was applied, which was the maximum load that could be applied by the vertical actuators.

The criteria for choosing the values and different levels of the gravity load considered the pre-test analysis results and practical considerations and axial load values from bridge engineering practice. The first level of 82-kips load was chosen to obtain initial bending moments in the bent cap beam that resembled the bending moments in the prototype bent cap under the distributed dead loads and with proper consideration of similitude relationships. However, the 82-kips value was not sufficient to mimic the prototype's corresponding value for the column axial load. Meanwhile, the effects of additional live load and the vertical component of earthquake excitations can increase both the column's axial load and the bending moments in the bent cap beam. Therefore, the second level of the gravity load at 164-kips was used for the higher levels of lateral cyclic and HS loading when it was more crucial to model accurate column axial loads for correct confinement effects. The initial gravity load level was then judged to be doubled to account for proper column axial load, consider additional live loads, and approximately account for axial force fluctuation due to the earthquake vertical excitations.

A better way of expressing the gravity load level that is more appealing to bridge engineers is to relate the gravity load value to the axial load capacity of the column. The axial capacity of the circular column can be approximately calculated as the gross sectional area times the concrete compressive strength. The actual compressive strength was available from the material tests, as discussed in Section 3.9. However, the Caltrans SDC expected compressive strength was used rather than the actual strength for consistency because the different tests were conducted at different times where concrete properties varied. In addition, engineers in practice relate the axial load to the expected compressive strength rather than the nominal 28-day compressive strength due to the lack of actual material data during design. Accordingly, an expected compressive strength of 1.30 times the 5 ksi nominal 28-day strength was used. The resulting gravity load to column axial capacity ratio, referred to as axial load ratio (ALR) for brevity, for the 82-kips and 164-kips was 5% and 10%, respectively. The third level used in last set of HS tests corresponded, in turn, to approximately 14.5% axial load ratio. An example of how the axial load ratio of 5% is calculated is shown in Equation (3-1).

$$ALR \ (\%) = \frac{P}{A_c \times f'_{expected}} = \frac{82}{254 \times 6.5} = 5\% \tag{3-1}$$

where,

$P = 82$ kips, is the gravity load (column axial load)

$A_c = \frac{\pi}{4} \times 18^2 = 254 \, \text{inch}^2$, is the gross area of the circular column

$f'_{expected} = 1.3 \times f'_c = 1.3 \times 5 = 6.5 \, \text{ksi}$, is expected compressive strength (Caltrans SDC 2011)

3.7.2 Cyclic Load Pattern

A bidirectional cyclic loading scheme was desired to represent real lateral loading conditions as in case of earthquake loading. Several options were investigated for the bidirectional interaction. A circular orbit was the first option as suggested by Hachem and Mahin (2000) after several dynamic tests. A similar option is an elliptical orbit for bidirectional loading as suggested by Terzic and Stojadinović (2010). The third option, which was the one adopted in this study, is a cross-shape orbit for bidirectional loading, i.e. alternating unidirectional cycles where a group of cycles is applied in one direction at a time. The third alternative was chosen as it was found to best serve the purpose of the test regarding the investigation of the bent cap beam. Loading in the plane of the bent cap was indispensable to better understand the box-girder slab contribution and evaluate the effective slab width. Moreover, the torsional effects on the cap beam could be still considered when loading is pursued in the orthogonal direction to the cap beam plane. Another reason for considering applying the load in one direction at a time is it becomes more suitable for FE model calibrations and post-test analyses. Finally, some of the HS tests were planned to be bidirectional with actual interaction considered through a computational model. Thus, bidirectional loading in the simple cross orbit with one direction loading at a time was finalized for the quasi-static testing program.

The second issue in finalizing cyclic loading patterns is the choice of the number and amplitude of the cycles in the different groups. Several studies in the past were dedicated only for cyclic loading histories and patterns for quasi-static tests such as Leon and Deierlein (1996), Krawinkler (1996), Clark et al. (1997) among others. However, Krawinkler (2009) compared several loading histories adopted from different standards and studies for seismic acceptance testing and performance-based design. Loading histories from ATC-24 Protocol (1992), SAC Protocol (Clark et al. 1997), SPD Protocol (Porter, 1987), CUREE (Krawinkler et al., 2000), ISO (1998) and FEMA 461 (2007) were compared. Based on this comparison, the author's opinion was that the protocols are similar and are expected to produce similar performance assessments. Consequently, the FEMA 461 (2007), loading protocol was adopted in this study because it was the latest and similar to others.

According to FEMA 461, two cycles are applied at each ductility level, and the suggested ductility levels (μ) for testing are as follows: 0.25μ, 0.35μ, 0.50μ, 0.70μ, 1.0μ, 1.4μ, 2.0μ, 2.8μ, 4.0μ, 5.6μ, and 8.0μ. The amplitudes, however, needed to be determined in displacement values for control purposes. A preliminary value of 1-inch was assumed for the column yield displacement based on hand calculations to conduct the 0.25μ to the 1.0μ level tests. Next, the strain values in the column rebars were checked at the 1.0μ level test to verify if yield took place or not. The strains were found to be less than the yield strain obtained from material tests. Therefore, another value of 1.25-inch yield displacement was used based on pre-test analysis results and indeed it corresponded to the first column yield occurred. The high-level cycles of 1.4μ, 2.0μ, 2.8μ, 4.0μ, 5.6μ, and 8.0μ were then related to the 1.25-inch yield transverse displacement and the test was conducted accordingly. A plot that summarizes both of the gravity load and all the lateral loading cycles that were applied during the full quasi-static test of the first specimen is shown in Figure 3.14. Snap shots of the loaded specimen during the test in the transverse and longitudinal directions are shown in Figure 3.15 and Figure 3.16, respectively.
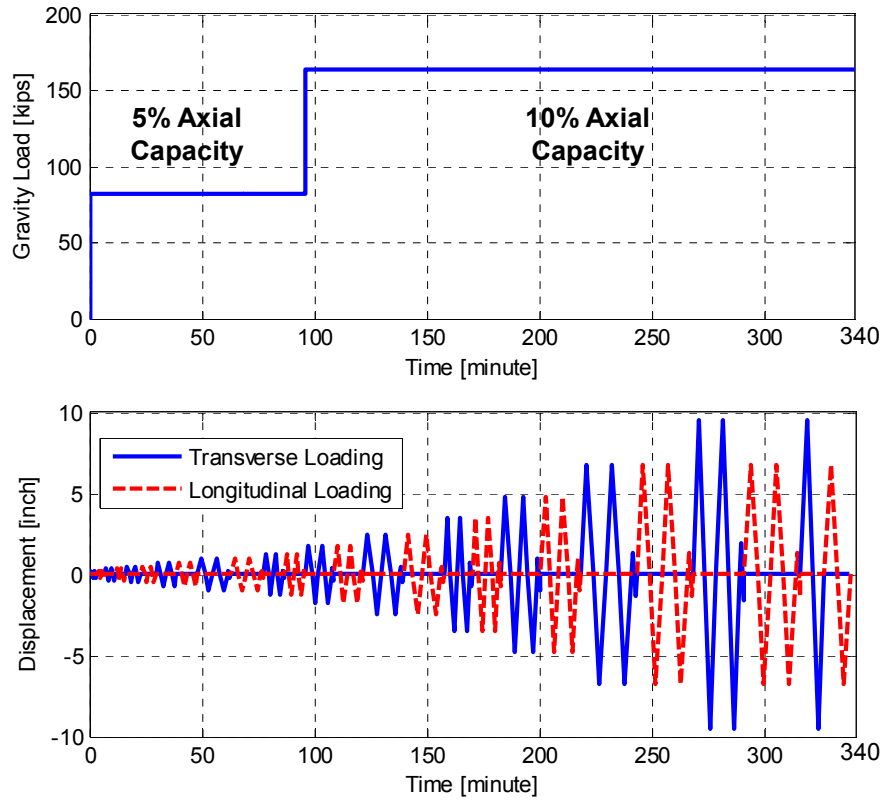
Figure 3.14 Final loading protocol used for the first specimen cyclic loading test

Figure 3.15 A view of first specimen test in progress under transverse cyclic loading.

Figure 3.16 A view of first specimen test in progress under longitudinal cyclic loading

3.8 CONSTRUCTION OF SPECIMENS

Two identical specimens were constructed simultaneously indoors in the Structures Laboratory at the University of California, Berkeley. All the construction phases were conducted by a professional construction company, and ready concrete mix was delivered to the laboratory site in three different lifts. The specimens were constructed in three phases and fresh concrete was cast at the end of each phase, which led to the existence of cold joints in the specimens. The construction phases and cold joints location were chosen to be as close as possible to real bridge construction. Similarly, the formwork and reinforcement fabrication adopted common practices in bridge construction to mimic actual construction conditions. Brief description of the different construction phases is presented here. More details of the construction are given in Appendix C.

The first construction phase included laying out the formwork for the seat beams and the box girder deck slab, furnishing the deck slab transverse and longitudinal reinforcement, constructing the column and bent cap beam steel cages, placing all the steel cages in place, and casting the first concrete lift that included the seat beams and whole deck slab. Figure 3.17 and Figure 3.18 show the deck slab reinforcement, column and cap beam cages, and casting of first concrete lift for the two specimens concurrently. Curing blankets in addition to E-CURE chemical were used for curing during the first day after concrete casting to avoid any shrinkage cracks.

63
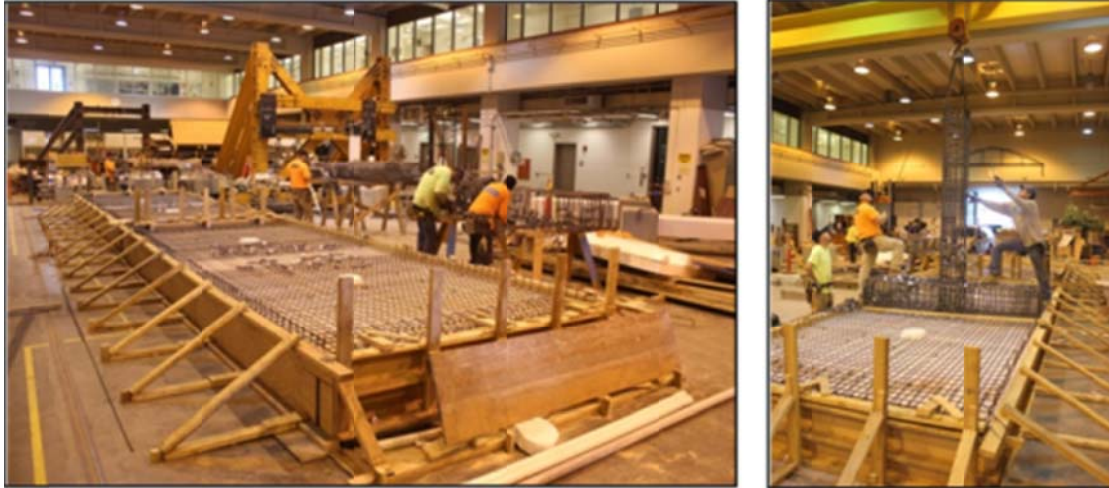
Figure 3.17 Reinforcement steel mesh for the deck slab (left) and fabrication and setting up of the column and cap beam steel cages (right)

Figure 3.18 Seat beams and box-girder deck slab concrete placement (first lift)

The second construction phase was the most complicated since it involved the construction of the rest of the box-girder including its cells and cap beam. This phase started the following day after the deck slab was initially set by placing custom-made cardboard boxes (Figure 3.19) to create the inner cells of the box-girder section. Although in real bridge construction the box-girder inner formwork is left permanently, it was desired to clear the specimens' cells for monitoring the reposnse and crack observation. That is why special cardboard formworks were used to facilitate its removal after the construction was completed. The box-girder web and soffit slab reinforcement was also laid out as part of this construction phase as shown in Figure 3.19. This phase was concluded with the second concrete lift that included cap beam and all the box-girder webs and soffit slab. The concrete surface was smoothly finished (Figure 3.20) then cured using E-CURE and curing blankets to avoid any shrinkage cracks in the thin soffit slab.

The third and last phase of construction involved the specimens' columns and column heads. A sonotube was used for the circular column construction and special timber formwork and platform was used for the hexagonal column head as shown in Figure 3.21. The last concrete lift was dedicated for the column and column head. The overhead crane at the laboratory was used to convey the hopper to the column top (Figure 3.21). After the construction was completed, all formwork removal started three weeks after the last concrete lift was cast.

64

Figure 3.22 shows the cardboard formwork removal and the final specimen configuration before placement in the test setup.
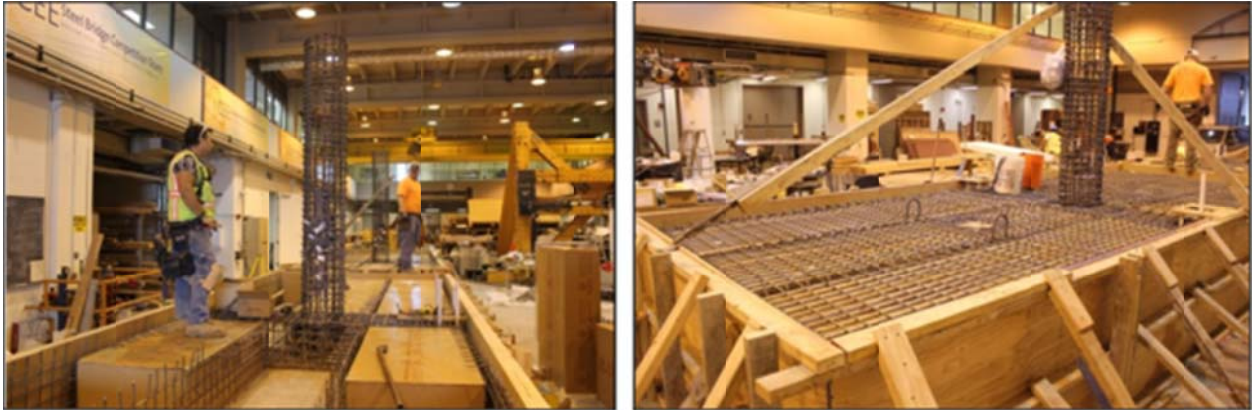
Figure 3.19 Installing custom-made cardboard boxes for box-section (left) and furnishing reinforcement steel mesh for the soffit slab (right)

Figure 3.20 Finishing the surface of the second concrete lift (left) and curing of concrete surface using curing blankets (right)

Figure 3.21 Column and column head formwork (left) and placing and vibrating the concrete of the column and column head (middle and right)

Figure 3.22 Removing the cardboard boxes used to create the box-girder cells (left) and final specimen configuration (right)

3.9 MATERIAL PROPERTIES

Extensive material testing was conducted for concrete and reinforcing steel as part of the research program. The details of the material testing are described in this section. Moreover, brief description of the materials used for the repair of the first tested specimen and the retrofit of the second specimen is included.

3.9.1 Concrete

Normal-weight concrete was used with a characteristic strength of 5 ksi and 3/8 in. maximum aggregate size because of the tight box-girder dimensions in the reduced-scale specimens. A similar concrete mix design was ordered for the three concrete lifts. A design water/cement (w/c) ratio of 0.411 was used, but each of the three lifts had a slightly different final w/c ratio that varied between 0.385 and 0.413. The detailed mix design as provided by the vendor of the ready concrete mix vendor is shown in Table 3-4. A minimum slump of 7 inch was also required to ensure proper workability and flowability of the concrete into the tight and congested box-girder and joint areas. A slump test was performed and slump value was verified every time before accepting the concrete lift to avoid any construction problems as shown in Figure 3.23. The same figure also shows concrete cylinders, prisms, and notched-beams sampling for material testing.

Samples of the three concrete lifts used in the subassembly specimens were subjected to various compressive, tensile, and flexural tests. For determining the compressive characteristics, concrete cylinders were tested to determine the characteristic strength and strength gain, compressive stress-strain relationships using load and displacement controls. For determining the tensile characteristics, concrete was tested to determine splitting tensile strength and modulus of rupture. In addition, notched-beam samples were tested to determine the fracture energy.

Table 3-4 Concrete mix design

Material	Description	ASTM	Specific Gravity	Admixtures [oz/yd]	Weight [lb]	Volume [ft³]
Cement	Type I/II/V	C-150	3.15	-	752	3.82
Aggregate p gravel	Eliot 3/8"	C-33	2.68	-	1500	8.97
Natural Sand	Eliot Sand	C-33	2.65	-	1420.9	8.59
Type A Water Reducer	Wrda 64	C-494	1	2.0 - 4.0	-	-
Type F Hige Range Water	Adva 190	C-494	1	3.0 - 15.0	-	-
City Water	Water	C-94	1	37.0 gal	308.8	4.95
Air (2.5%)	-	-	-	-	-	0.67
TOTAL	-	-	-	-	**3982**	**27.0**

Figure 3.23 Slump test (left) and concrete sampling for material tests (top and bottom right)

3.9.1.1 Compressive Tests

The compressive strength test was conducted to monitor the strength gain of concrete with time at the standard ages: 7, 14, 21 and 28 days, and at each of the two main specimens test days (average age of 128 and 308 days for the cyclic test of the first specimen and the hybrid simulation test of the second specimen, respectively. For this test, standard 6 in.×12 in. cylinders were used. The cylinders were cured next to the two subassembly specimens in same laboratory indoors conditions. The cylinders were capped with a sulfur compound and were tested in a Universal Testing Machine at the Concrete Laboratory of the University of California, Berkeley in accordance with ASTM C39-05 (ASTM 2005). The test setup and a typical tested and crushed cylinder are shown in Figure 3.24. The test results for the concrete at all different ages are listed in Table 3-5. The strength gain of the concrete versus time (age) up to the standard 28 days

characteristic strength and actual strength on test days of the subassembly specimens is shown in Figure 3.25 for all three concrete lifts.
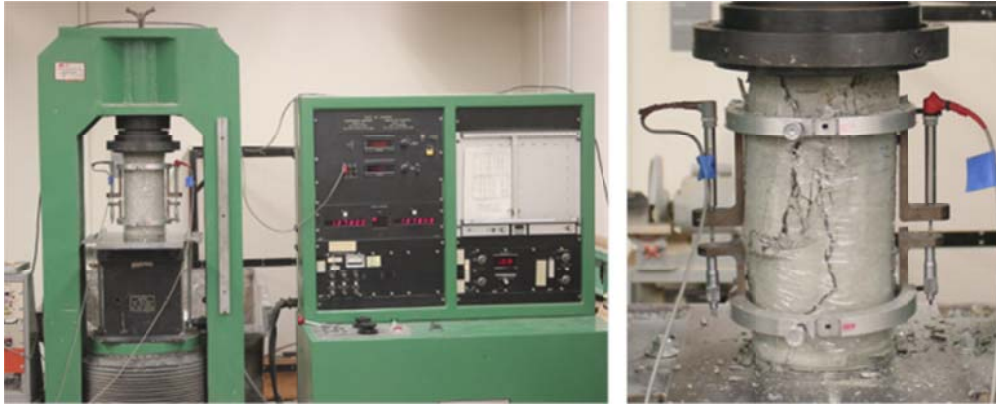
Figure 3.24 Compressive strength test setup (left) and typical mode of failure (right)

Table 3-5 Compressive strength test results

| Age [days] | Compressive Strength f_c' [ksi] | | | | | |
| | Lift 1 | | Lift 2 | | Lift 3 | |
	Mean	St. Dev.	Mean	St. Dev.	Mean	St. Dev.
7	4.21	0.62	4.66	0.76	4.54	0.29
14	5.20	0.13	5.91	0.18	5.18	0.03
21	5.47	0.13	6.33	0.48	5.81	0.14
28	6.28	0.19	6.60	0.06	5.99	0.19
128	7.15	1.03	7.68	0.23	6.85	0.36
308	7.58	0.24	8.12	0.40	7.83	0.35
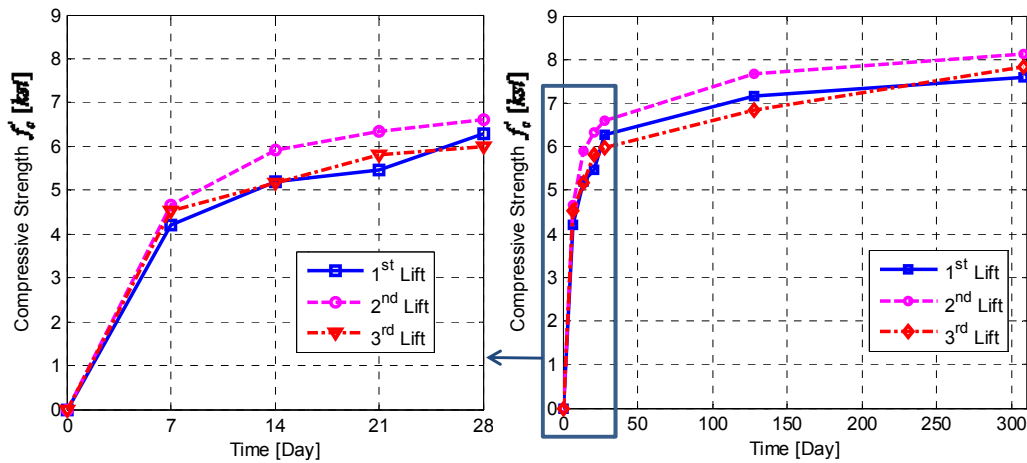
Figure 3.25 Strength gain for different concrete lifts up to 28 days (left) and up to final day of testing (right)

68

The same test setup used for determining the compressive strength is used to obtain a compressive stress-strain test under force control to determine the constitutive behavior of concrete in the compression hardening region, before the peak load. The only difference from regular compressive tests is the use of a compressometer around the cylinder to measure the strain (Figure 3.24). A sample of three cylinders from each concrete lift was instrumented with the compressometer and tested at the age of 28 days and first specimen test day (128 days) to estimate the stress-strain curve up to the failure point. The compressometer comprises two displacement transducers (LVDT) connected on the opposite sides of the cylinder to estimate average strain based on both transducers readings as seen in Figure 3.24. The summary of the test results (stress and strain at peak, and Young's modulus) is shown in Table 3-6. From the stress-strain test, the modulus of elasticity E_c of concrete was computed using the secant stiffness at $0.4\,f_c'$. A typical compressive stress-strain test results using force control from the 28 days test of the first concrete lift samples is shown in Figure 3.26.

Table 3-6 Stress-strain compressive test results using force control

	Age [days]	Stress at Peak [ksi]			Strain at Peak			Young's modulus [ksi]		
		Mean	St. Dev.	COV	Mean	St. Dev.	COV	Mean	St. Dev.	COV
lift 1	28	6.27	0.18	0.028	0.0033	0.0002	0.074	3207.4	81.9	0.026
	128	7.15	1.03	0.144	0.0033	0.0009	0.264	3116.6	81.6	0.026
lift 2	28	6.78	0.17	0.025	0.0033	0.0002	0.062	3215.7	66.3	0.020
	128	7.68	0.23	0.030	0.0029	0.0001	0.050	3565.9	84.7	0.024
lift 3	28	5.30	0.73	0.138	0.0024	0.0006	0.237	3192.9	48.3	0.015
	128	6.85	0.36	0.053	0.0026	0.0001	0.042	3238.0	142.1	0.044
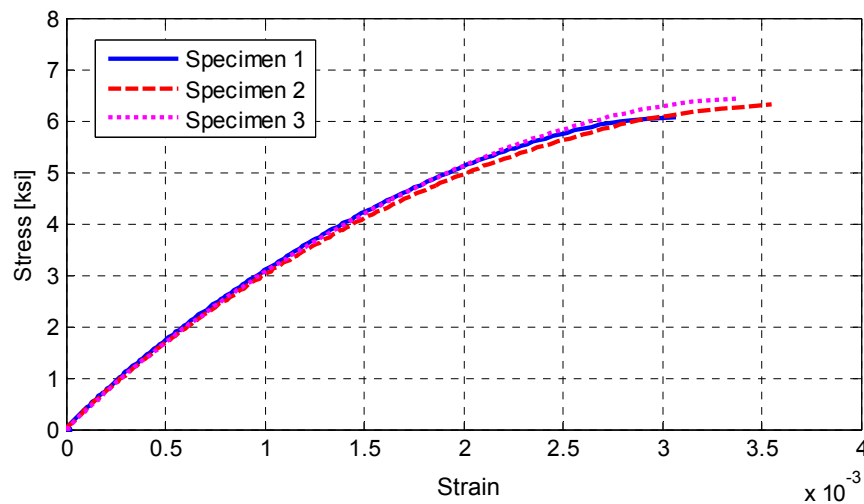
Figure 3.26 Typical concrete stress-strain relationship using a force-controlled test (results shown are for samples from first concrete lift tested at 28 days)

69

A compressive stress-strain test using displacement control was conducted to obtain a better estimate of the strain at peak and attempt to capture any of the constitutive behavior of post-peak. A displacement-control testing machine and setup at the University of California, Davis was used for this purpose as shown in Figure 3.27. A total of nine cylinders (three from each concrete lift) were tested at age of 298 days; few days before the hybrid simulation test of the second specimen. The summary of the test peak stress, strain at peak, and Young's modulus are shown in Table 3-7. Due to the nature of the loose compressometer used for such tests, the brittle failure of the cylinders displaced the compressometer significantly after failure. Thus, only a small portion of the immediate post-peak behavior and strain at peak were captured as shown in Figure 3.28.

Figure 3.27 Compressive test under displacement control at the University of California, Davis (left), compressometer (middle) and typical mode of failure (right)
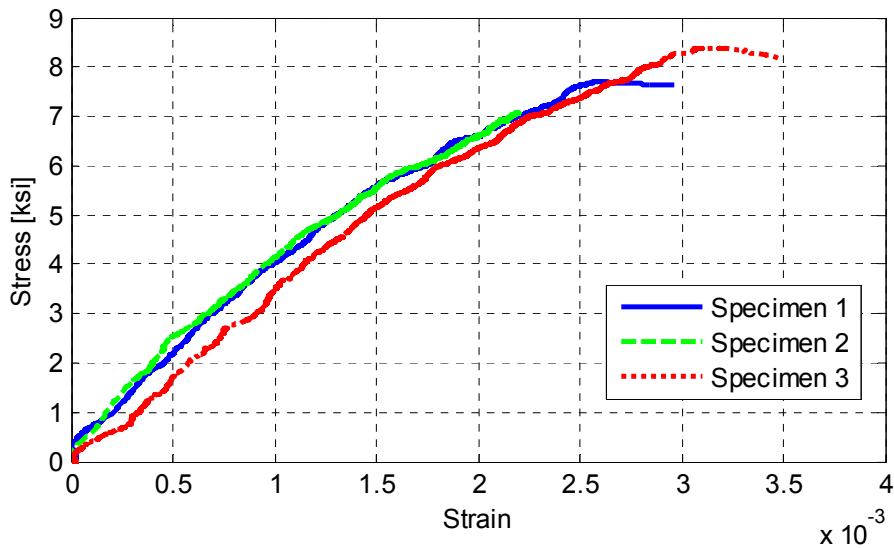
Figure 3.28 Typical concrete stress-strain relationship using a displacement-controlled test (results shown are for samples from second concrete lift at 298 days)

70

Table 3-7 Stress-strain compressive test results using displacement control

	Age [days]	Stress at Peak [ksi]			Strain at Peak			Young's modulus [ksi]		
		Mean	St. Dev.	COV	Mean	St. Dev.	COV	Mean	St. Dev.	COV
lift 1		6.84	0.31	0.045	0.0031	0.0002	0.064	3285.3	144.72	0.044
lift 2	298	7.73	0.65	0.084	0.0027	0.0005	0.188	3823.3	565.40	0.148
lift 3		7.16	0.22	0.030	0.0031	0.0002	0.071	3465.4	278.52	0.080

3.9.1.2 Tensile Tests

The splitting tensile strength represents a lower bound of the tensile strength of concrete. The test was conducted using standard 6 in.×12 in. concrete cylinders according to ASTM C496-04 (ASTM 2004a). A sample of three cylinders from each concrete lift was tested at ages of 128 and 308 days to capture actual concrete properties at the age of the subassembly specimens at day of testing. For a splitting tension test, the concrete cylinder is placed on its side and loaded in compression as shown in Figure 3.29. The maximum load P was recorded and the splitting tensile strength f_{ct} was estimated from Equation (3-2).

$$f_{ct} = \frac{2P}{\pi l d}$$

(3-2)

where l and d are the length and diameter of the standard cylinder, respectively. The test results are summarized in Table 3-8. A clear view of the concrete texture and aggregate distribution and size can be observed from the tested cylinders in splitting tension as shown in Figure 3.30.

Table 3-8 Splitting and modulus of rupture test results

	Age [days]	Splitting tension f_{ct} [ksi]			Modulus of Rupture f_r [ksi]		
		Mean	St. Dev.	COV	Mean	St. Dev.	COV
lift 1	128	0.50	0.012	0.025	0.79	0.043	0.054
	308	0.62	0.038	0.060	0.94	0.069	0.073
lift 2	128	0.54	0.090	0.165	0.93	0.045	0.048
	308	0.58	0.033	0.057	1.02	0.097	0.095
lift 3	128	0.48	0.059	0.125	0.96	0.046	0.048
	308	0.58	0.021	0.036	1.12	0.031	0.028

Figure 3.29 Splitting tension test setup (left) and typical mode of failure (right)

Figure 3.30 Close-up view of the concrete texture and aggregate size and distribution from a tested cylinder in splitting tension

The modulus of rupture test, or four-point flexural test, gives a higher estimate of the tensile capacity than the splitting strength test. The test was performed using 3 in.×3 in.×12 in. concrete beams according to ASTM C293-07 (ASTM 2007). A sample of four beams from each concrete lift was at ages of 128 and 308 days similar to the splitting tension test samples. The test requires the beam to be simply supported with span $L = 9$ in. and subjected to four-point bending, as shown in Figure 3.31. From the test, the maximum load P was recorded and the modulus of rupture f_r was computed from Equation (3-3).

$$f_r = \frac{PL}{bh^2} \tag{3-3}$$

where b and h are the width and height of the beam cross-section, respectively. The test results are summarized, along with the splitting tension test results, in Table 3-8.
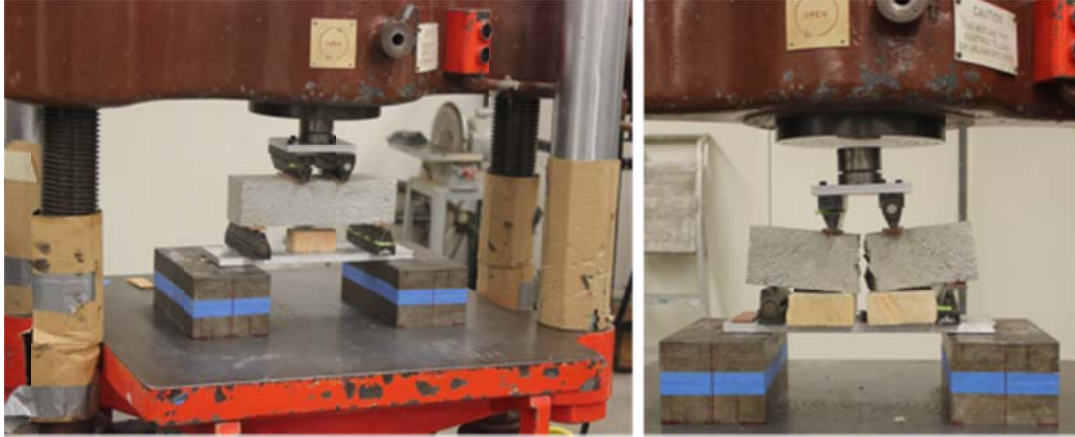
Figure 3.31 Four point bending test setup for estimating the concrete modulus of rupture (left) and typical mode of failure (right)

3.9.1.3 Notched-Beam Tests

The fracture energy tests were conducted to evaluate the amount of energy released during tensile cracking of concrete. The fracture energy is defined as the amount of energy necessary to create one unit area of crack, and it has units of energy per unit area. The fracture energy is a key parameter in nonlinear concrete constitutive modeling and continuum FEA. Thus, the values obtained from these tests were utilized in DIANA (2012) FEA subassembly model calibration and post-test analyses. The test selected for this study is conducted according to the European recommendation (Rilem 1985). For the test, 4 in. × 4 in. × 36 in. concrete beams are cast to have a middle notch for crack initiation and propagation until failure. The notch is introduced in the beam using a wooden insert in the beam formwork, such that the area of ligament above the notch A_{lig} is half of the total cross-section height, i.e. 2 in. × 4 in. The beams were simply supported at a span of 32 in. and loaded at the mid-point under displacement control. The test setup and instrumentation used for this part of the study at the Concrete Laboratory of the University of California, Berkeley is shown in Figure 3.32. The deformation of the beam was measured at the mid-point with a displacement transducer. Because of the large scatter expected in fracture energy tests, many samples were tested for an accurate determination of the mean fracture energy. A total of 15 beams were casted: three beams were casted from the first concrete lift, and six beams from each of the second and third concrete lifts. From these 15 beams, only 12 beams were tested, at approximate age of 280 days, and 3 beams were already found broken when the formwork was removed. The load-deformation information was recorded until failure as shown in Figure 3.33 for all the tested notched-beams. The area under the load-deformation relationship was estimated and used to calculate the fracture energy from Equation (3-4).

$$G_f = \frac{W_o + (m_1 + 2m_2)g\delta_0}{A_{lig}}$$

(3-4)

where W_o is the area under the load-deformation relationship, m_1 is the mass of the beam between the supports, m_2 is the mass of the loading support not attached to the machine, g is the acceleration of gravity, and δ_0 is the deformation at failure. The test results of samples of each concrete lift individually and all beams together are summarized in Table 3-9 and Table 3-10,

73

respectively. Statistics based on all beams together is useful to estimate a single mean value that is representative of the concrete lifts for FEA and concrete modeling.

Figure 3.32 Notched-beam test setup, instrumentation, and mode of failure

Table 3-9 Fracture energy from notched-beam test results (Samples from individual lifts)

	Test Response Quantity	Mean	St. Dev.	COV
Lift 1	Displacement at failure δ_o [inch]	0.083	0.019	0.230
	Peak Load P_o [lbf]	203.2	6.91	0.034
	Fracture Energy G_f [lbf/inch]	2.359	0.417	0.177
Lift 2	Displacement at failure δ_o [inch]	0.093	0.028	0.305
	Peak Load P_o [lbf]	197.9	109.2	0.552
	Fracture Energy G_f [lbf/inch]	2.289	0.734	0.321
Lift 3	Displacement at failure δ_o [inch]	0.074	0.010	0.135
	Peak Load P_o [lbf]	204.8	110.1	0.538
	Fracture Energy G_f [lbf/inch]	2.094	0.629	0.301

Table 3-10 Fracture energy from notched-beam test results (all samples together)

	Test Response Quantity	Mean	St. Dev.	COV
All Beams	Displacement at failure δ_o [inch]	0.083	0.021	0.253
	Peak Load P_o [lbf]	201.7	93.6	0.464
	Fracture Energy G_f [lbf/inch]	2.219	0.607	0.274
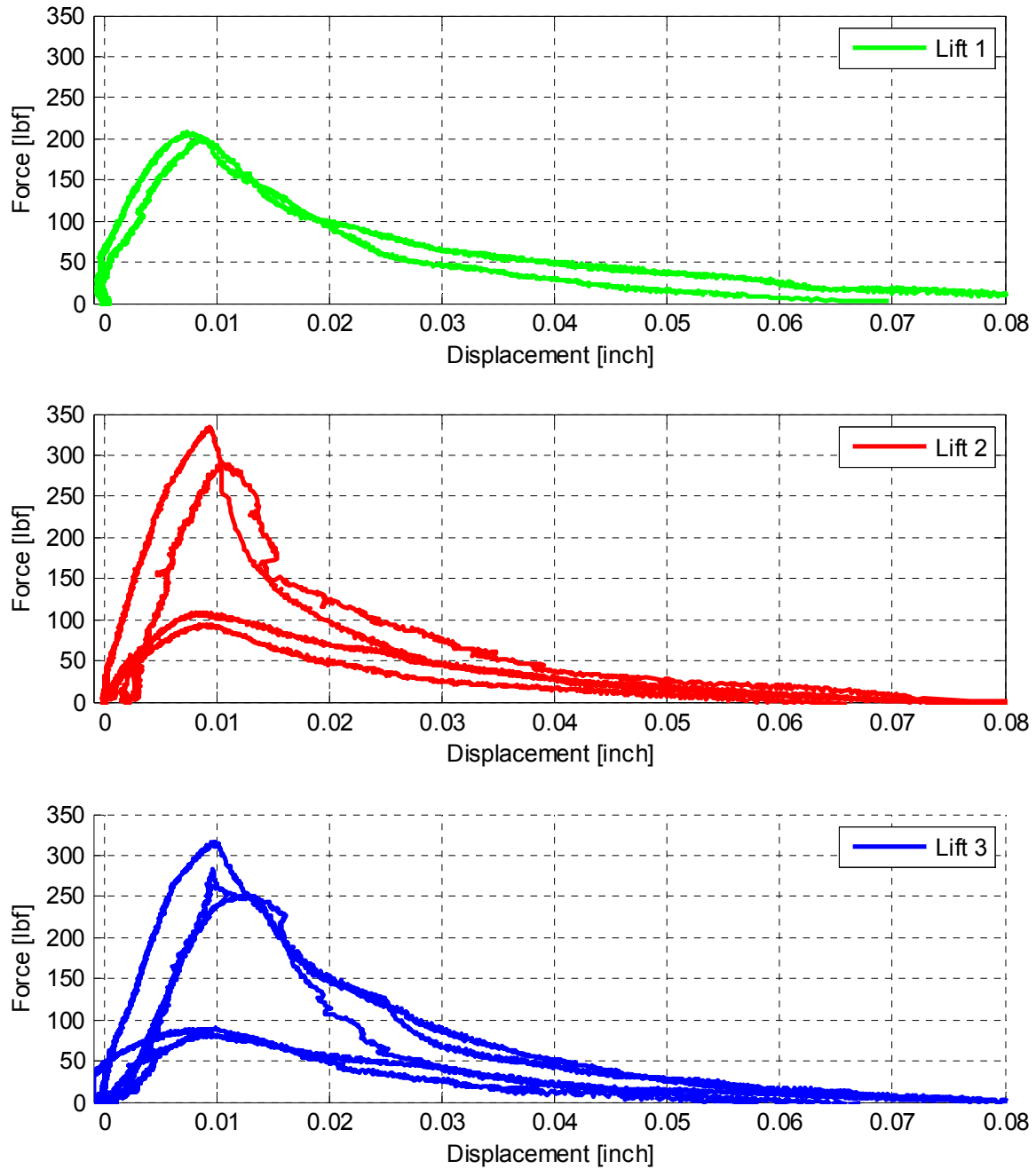
Figure 3.33 Load-deformation relationships for notched-beam tests for all concrete lifts

3.9.2 Reinforcing Steel

The reinforcing steel used in the experimental program was Grade 60, meeting the requirements of ASTM A706-04 (ASTM 2004b). Three different bar sizes were used in the specimen construction: #3, #5 and #6. However, the #3 bars were obtained from two different stocks such that all #3 longitudinal bars were from one stock, while all the #3 transverse steel used in column ties, beam stirrups, and box-girder ties were from the second stock. For each type of steel, three

coupons were tested using a Universal Testing Machine, as shown in Figure 3.34. The steel coupons were 32 in. long. To measure deformation, two displacement transducers were attached to the specimen as shown in Figure 3.34. This deformation was measured between two points separated at 2 in. The bars were loaded according to ASTM E8-04 (ASTM 2004c). All rebars were tested until rupture. From the tests, the stress and strain were calculated by dividing the total force by the nominal cross-sectional area of the reinforcing bar and the deformation by the gage length, i.e. 2 in., respectively. The test results of the reinforcing steel are summarized in Table 3-11. The stress-strain relationships obtained from all rebar tests are shown in Figure 3.35.

Table 3-11 Summary of mechanical properties of steel reinforcing bars

	#3 longitudinal		#3 stirrups		#5 longitudinal		#6 longitudinal	
	Mean	St. Dev.	Mean	St. Dev.	Mean	St. Dev.	Mean	St. Dev.
Yield Stress f_y [ksi]	67.37	0.40	66.90	0.51	66.51	0.39	68.99	0.43
Yield Stain ε_y	0.0026	0.0001	0.0026	0.0	0.0026	0.0001	0.0026	0.0
Ultimate Stress f_u [ksi]	106.73	0.23	104.37	0.31	97.43	0.21	93.90	0.22
Ultimate Strain ε_u	0.1091	0.0089	0.1088	0.0048	0.0964	0.0103	0.1265	0.0059
Young's Modulus E_s [ksi]	27383	951	28000	369	25620	732	27173	329
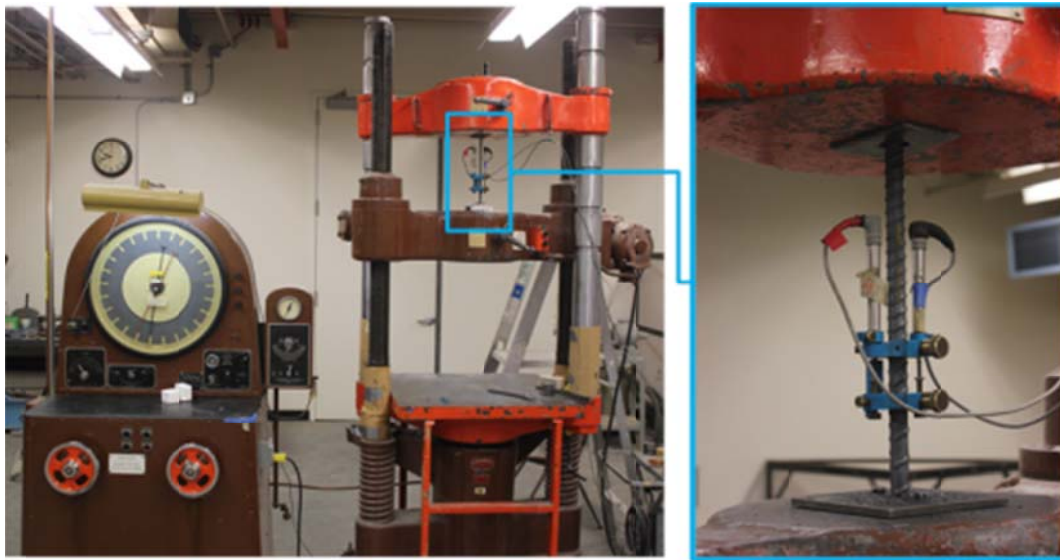
Figure 3.34 Test setup and instrumentation for tensile testing of reinforcing bars
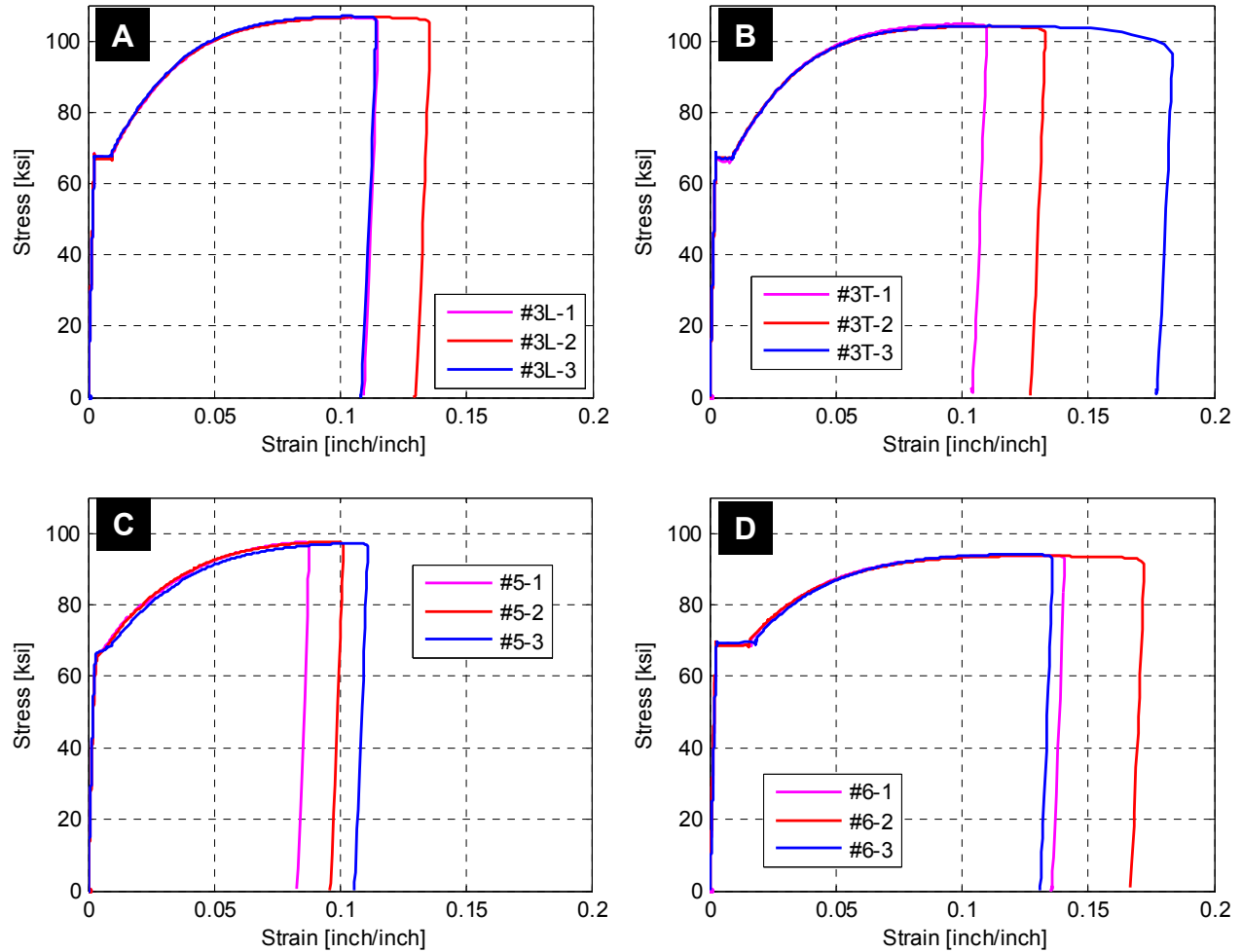
Figure 3.35 Stress-strain relationships for the different reinforcing bars coupons for: (a) #3 stirrups (b) #3 longitudinal bars (c) #5 bars (d) #6 bars

3.9.3 Repair and Retrofit Materials

The experimental program involved the repair of the first tested specimen and the retrofit of the second specimen before it was tested. Thus, it is useful to have an idea about the mechanical properties of the different materials used in both the repair and retrofit processes. Unlike concrete and reinforcing steel, testing representative material samples was not possible during the course of the study. However, nominal and characteristic properties as provided by the materials supplier are briefly listed here for completeness.

3.9.3.1 *Unidirectional Carbon Fiber Fabric*

Unidirectional carbon fiber fabric along with a two component epoxy system comprised the Fiber Reinforced Polymer (FRP) system used for both of the repair and the retrofit processes. Three layers of FC061 unidirectional carbon fiber fabric were used for each of the repaired and retrofitted specimen. It is to be noted that FC061 Structural Fabric is a standard modulus continuous-fiber unidirectional carbon fiber fabric with superior tensile strength. FC061 Structural Fabric can be impregnated with RN075 Fiber Impregnation Resin to achieve a super

strong FRP composite laminate for structural strengthening applications. The fiber fabric itself before resin application pertains very high mechanical properties with average tensile strength of 700 ksi, average tensile modulus of 34,000 ksi, and rupture strain of 1.4%.

3.9.3.2 *Two Component Epoxy System*

Epoxy or any suitable resin is the second necessary component of FRP laminates used for structural purposes. A RN075 LPL Two Component Epoxy System was used along with the carbon fabrics to compose the FRP layers. The RN075 Fiber Impregnation Resin is a 100% solids, solvent-free, and two-component moisture tolerant epoxy. It is a low viscosity epoxy for wetting and use with carbon and glass fiber fabrics for structural strengthening. The mechanical properties reported for the resin itself are: 10.5 ksi compressive strength after 7 days curing, 6 ksi tensile strength after 14 days curing, and rupture strain that varies between 2-4%. The reported properties comply with the ASTM standards for epoxy and composites.

From a structural engineering perspective, it is always more useful to report mechanical properties of a readily fabricated ply or layer of the final FRP product. The manufacturers reported an average laminate tensile strength for the FRP composite of 149 ksi with an average tensile modulus of 10,100 ksi and corresponding rupture strain of 1.2%. It is to be noted that a single ply thickness is 0.04 inch, and in turn, the final thickness of the 3-layers CFRP jacket was 0.12 inch.

3.9.3.3 *Patching Material & Structural Mortar*

While only a composite jacket of carbon fabrics and epoxy resin was used to retrofit the second specimen, several other materials were used for the repair of the damaged plastic hinge region in the first specimen. More details about the undertaken repair procedure are discussed in Chapter 6. However, an overview of the mechanical properties of the patching material and structural mortar used during the repair is presented here.

A Structural Motor SM020 was used to fill the concrete cracks wider than 0.75 inch and patch the damaged surface for proper application of the CFRP composite layer. Based on the data provided by the manufacturer, the structural mortar had an average compressive and split tensile strength of 6.3 ksi and 595 psi, respectively, after 28 days. The modulus of elasticity based on the data from the elastic regime of the stress-strain plot was 2,260 ksi. Bond and flexural strength of 0.5 ksi and 1.15 ksi, respectively, were measured after 28 days with failure noticed in the substrate.

Concrete cracks with width less than 0.75 inch were cap-sealed using GS100 gel/paste epoxy system. Compressive and tensile strength of epoxy system was 10.5 ksi and 7.2 ksi, respectively. Rupture strain of the epoxy system was about 0.85%. The average flexural strength measured after 14 days was 5.6 ksi.

3.10   INSTRUMENTATION

Several measurements techniques were adopted during each test: force, displacement, and strain. In addition, curvatures were deduced from either strains or displacements. Cameras were also

used extensively to capture cracks and damage propagation. A summary of the instruments and their layout used for these measurements is presented in this section.

3.10.1 Load Measurement

Load was measured to assist in the control of both the vertical and lateral actuators and to measure the total forces applied to the specimen for capacity estimation. Several load cells were used to measure the actuator forces: two for the vertical actuators and another two for the lateral ones. In addition, the two struts used as part of the specimen physical boundary conditions were instrumented with strain gages to work as load cells. The vertical load actuators were used to apply the gravity load under load control. Thus, the load cell measurements were indispensable to monitor the level of applied load. The lateral load actuators were run in displacement control. However, the load cell measurements were still crucial to estimate the total force applied to the specimen, base shear capacity, and to calculate the stiffness and its degradation during the experiment. The load cells were calibrated in compression using the universal testing machines available at the University of California, Berkeley. Special attention was paid to the calibration of the fabricated strut load cells as discussed in more details in Appendix F. The two different types of load cells used for both the actuators and calibrated struts are shown in Figure 3.36.
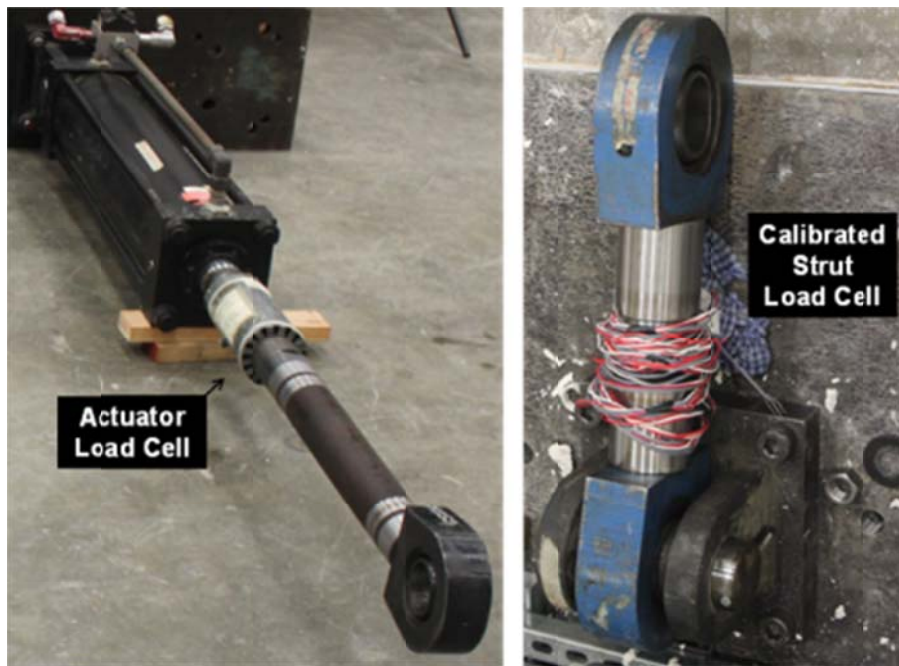
Figure 3.36 Different load cells used in testing: typical actuator load cell (left) and calibrated strut load cell (right)

3.10.2 Displacement Measurement

External deformations/displacements were measured using displacement transducers (wire potentiometers) and linear motion potentiometers. Three ranges of wire potentiometers (wirepots) were used to measure large column deformations: ±5 in., ±7.5 in., and ±15 in. The ±5 in. and ±7.5 in. range transducers were used for measuring the column deformation at mid-

79

height. The ±15 in. range was used for larger displacements at the column's top in the inverted position where lateral load was applied. The wirepots have an accuracy of 0.10% of its full range, i.e. 0.03-in. resolution for a range of ±15 in. Piano wires and strings were used to extend the wire potentiometer ends to the column. At the column mid height, the wires were connected to the concrete face through attachment to an embedded hook. At the column top, or more accurately, at the mid-height of the column's head where load was applied, the wires were attached to a steel ring that was welded to the plates used around the hexagonal column head for attaching actuators. Figure 3.37 shows the layout for the wire potentiometers mounted on the east side instrumentation frame and wires attachment to the column top. A total of 12 wirepots were used and were distributed in 2D and 3D triangulation as identified and shown in plan and side views in Figure 3.38 and Figure 3.39, respectively.

The other type of displacement transducers used in this experimental program was linear motion potentiometers or accurately referred to as Linear Variable Differential Transformer (LVDT). The LVDTs used in this study were dedicated for measuring the cap beam and box-girder displacements as they were laid out underneath the specimen in its inverted position. Another set of LVDTs was used for column curvature measurements as discussed in a following subsection. For the LVDTs underneath the specimen, two ranges were used: ±1 in. at the edges and ±2 in. at the center. Steel hooks were used to attach the LVDTs wires to the concrete face. Tiny holes were drilled, filled with epoxy, then the steel hooks were inserted in holes before the epoxy hardened to form the attachment points. Figure 3.40 shows the layout for the LVDTs underneath the specimen and how the wires were attached to the steel hooks implanted in the specimen deck slab and cap beam.
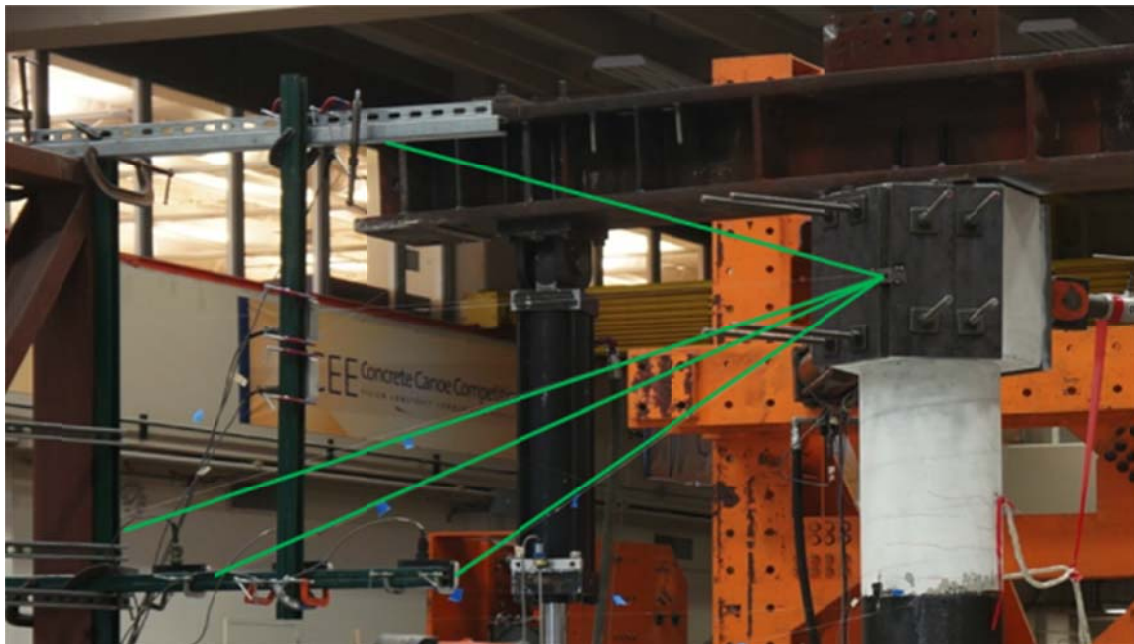
Figure 3.37 Wirepots setup at the East instrumentation frame
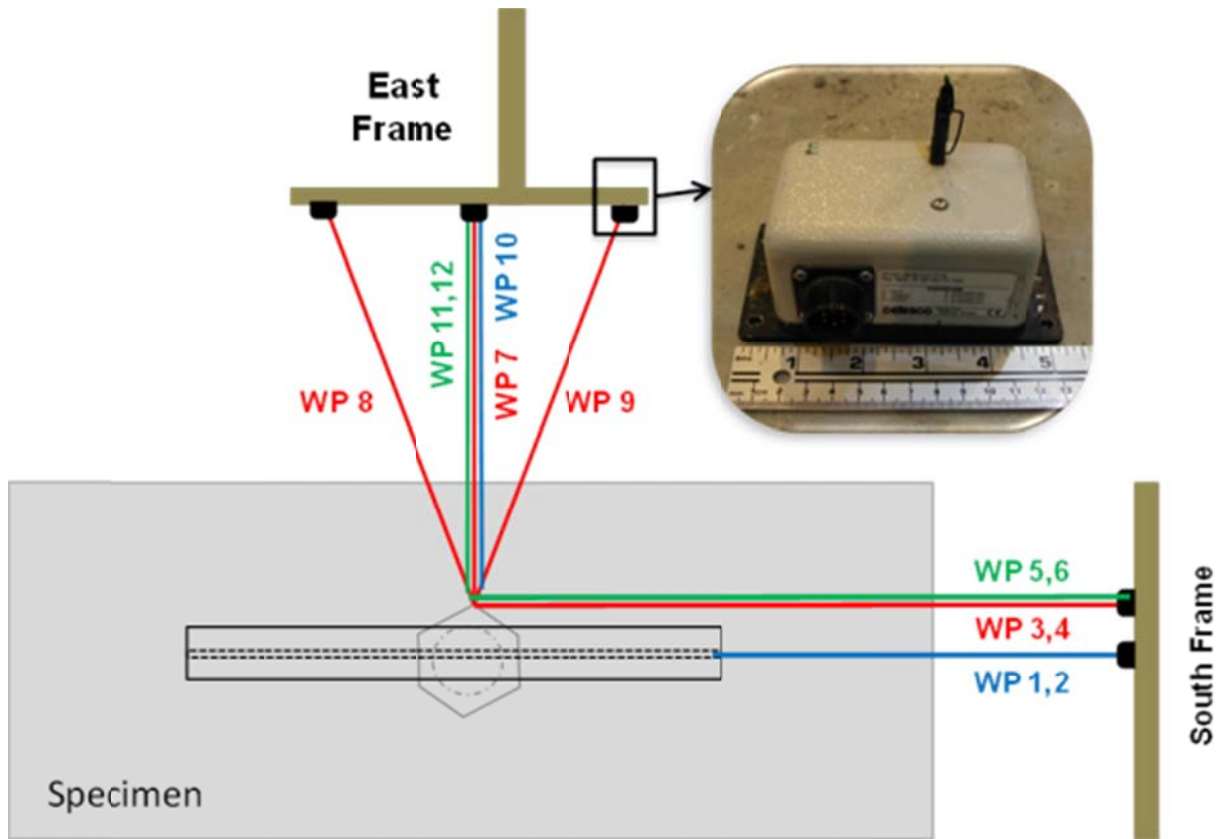
Figure 3.38 Layout of the wirepots in plan view (East and South sides are identified)
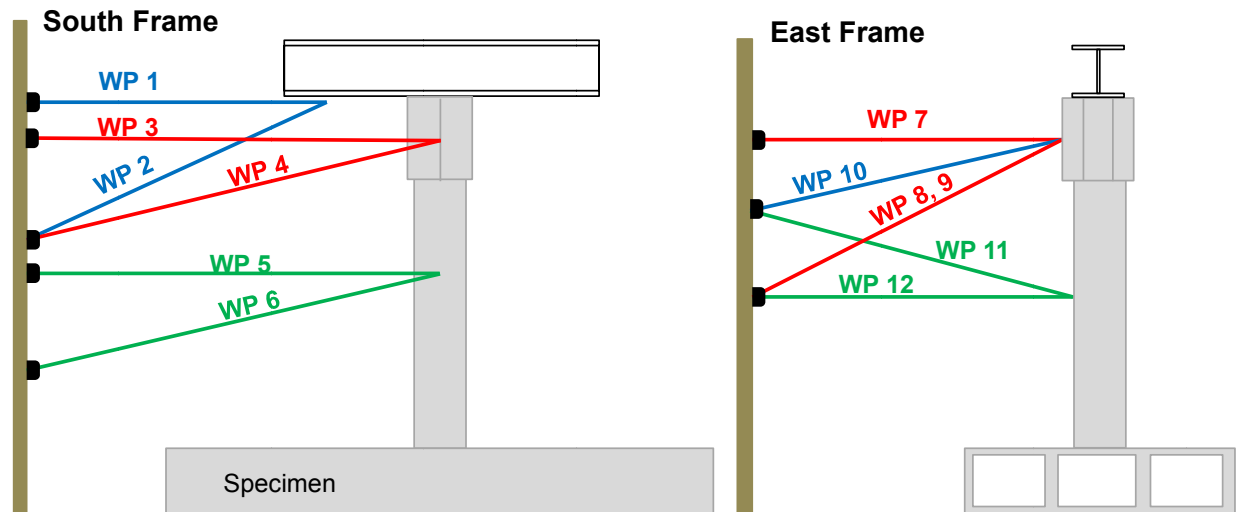
Figure 3.39 Layout of the wirepots in side view at East and South sides frames

81
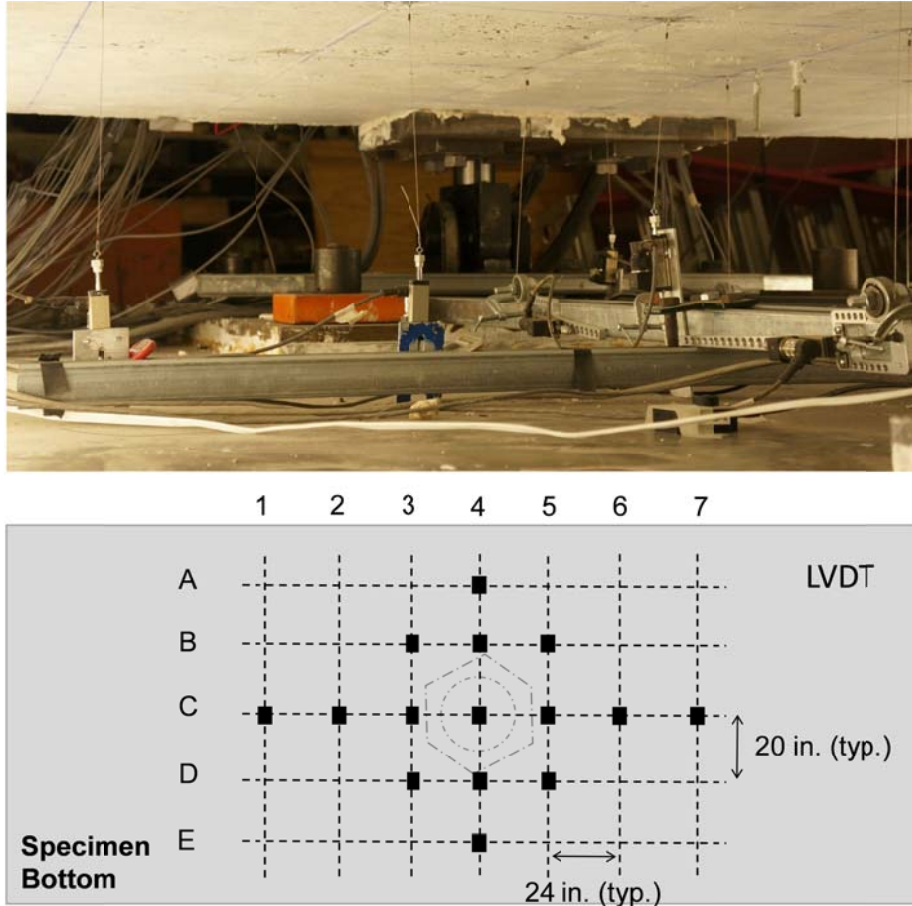
Figure 3.40 LVDTs under the specimen monitoring the deformation of the cap beam and the box-girder

3.10.3 Strain Measurement

Strains were measured locally on the reinforcement and at some local points inside the concrete or on its surface. Only reinforcement strain gages are reliable and conclusive. However, the concrete gages are useful as well in showing behavior trends rather than accurate strain readings. Reinforcement strains were measured using foil gages mounted on the surface of the reinforcement. The utilized gage size was 0.20 in. × 0.08 in. The gages were post-yield ones with a rated deformation capability of 15% strain. The bar surface deformations in the region surrounding the gage location were removed and the surface was polished. The strain gage was glued to the surface and covered by four protective coatings: air-drying polyurethane, wax, polysulfide liquid polymer compound (providing a tough flexible barrier), and vinyl mastic tape. Figure 3.41 shows various stages of the process of installing strain gages on the reinforcing bars. It is to be noted that instrumenting the rebars with strain gages is a milestone in RC components or subassembly testing. Thus, proper attention is required to be paid to minimize the chances of losing strain gages during construction. Instrumenting the rebars with more than 350 strain gages for the two specimens started two months before specimens' construction to have sufficient time for this important task. A picture of few stacks of the instrumented rebars stored in the laboratory before construction is shown in Figure 3.42.

82

Concrete strain was measured using embedded concrete gages. Only 14 embedded concrete gages were used and installed between the soffit slab transverse rebars, where it is anticipated to be the compression side, as shown in Figure 3.43. Concrete gages of 4.5 in. length were used. Another type of concrete gages used in this study is the surface concrete gages. However, the surface gages were installed only for the second specimen. That is because it was decided to use such surface gages based on the first test results were the embedded gages did not provide meaningful values. Figure 3.44 shows the layout of surface concrete gages used in the second specimen on the compression side. The last group of strain gages used in this study was dedicated for the CFRP jacket. Linear 0.20 in. × 0.08 in. foil gages similar to the ones used for the steel reinforcement were installed around the circumference of the CFRP jacket to monitor the confinement strains in the jacket. That is to judge the effectiveness of the CFRP jacket and examine the resulting circumfernical strains during either the repaired first specimen or retrofitted second one. The FRP jacket strain gages can be seen in Figure 3.44 as well.

One last note on strain gages is related to the gages arrangement and how the locations of strain gages, especially on the reinforcement, were chosen. The DIANA 3D pre-test model and analysis were utilized for the decision of the strain gages locations. More details on pre-test analysis are presented in the next chapter. The locations where maximum strain was expected in the box-girder, column, or cap beam along with locations capturing the strain distribution in the transverse direction were identified from the pre-test analysis. Figure 3.45 shows an example of the DIANA results for the strain distribution in a plan view inside the cap beam and box-girder under lateral loading. Accordingly, the strain gage arrangements in the soffit and deck slabs transverse and longitudinal reinforcement are shown in Figure 3.47 and Figure 3.48, respectively. The cap beam rebars were heavily instrumented as shown in Figure 3.46. Moreover, the strain gages used for the column longitudinal rebars and transverse hoops are shown in Figure 3.49.
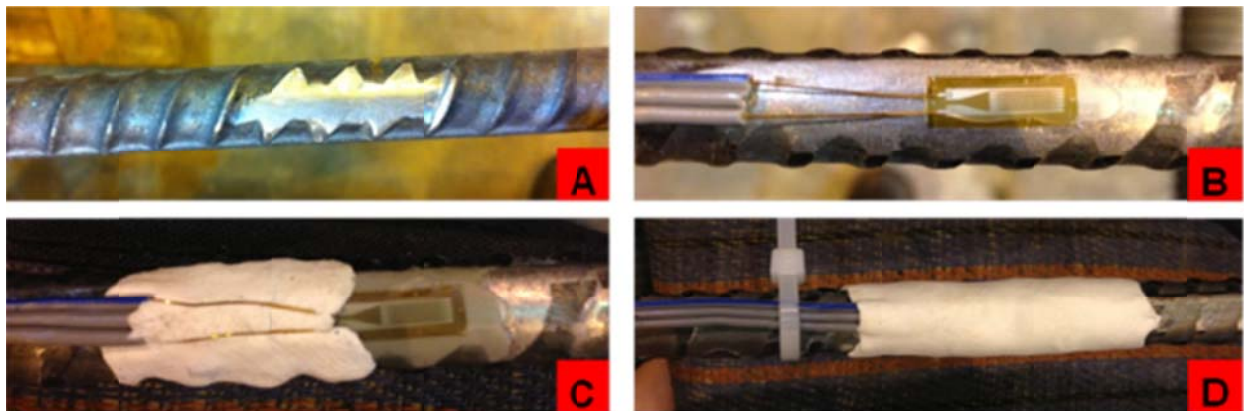
Figure 3.41 Strain gages used for reinforcing bars instrumentation where several chemical and mechanical protection layers added on top of the gages for their protection

Figure 3.42 Instrumented specimens' beam and slab reinforcement bars
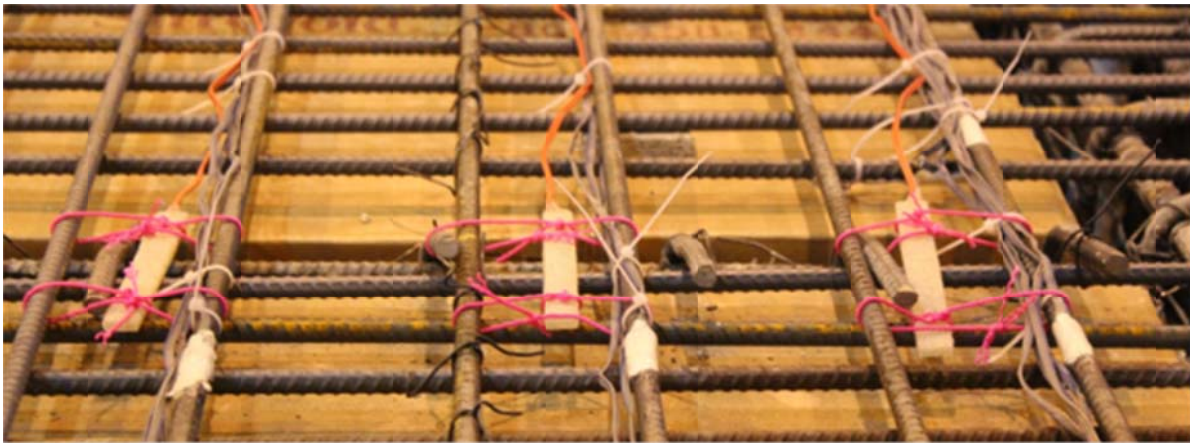
Figure 3.43 Embedded concrete strain gages used in the soffit slab part of the box-girder

Figure 3.44 Surface concrete strain gages installed on top of the soffit slab of the second specimen only (some CFRP jacket strain gages are shown also)
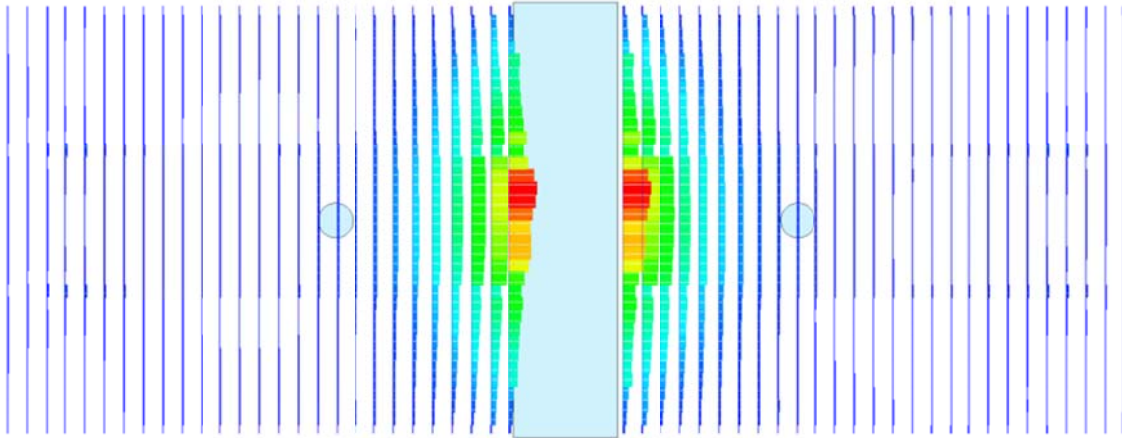
Figure 3.45 An example of strain distribution in the box-girder transverse reinforcement as obtained from DIANA pre-test analysis to decide on gages distribution
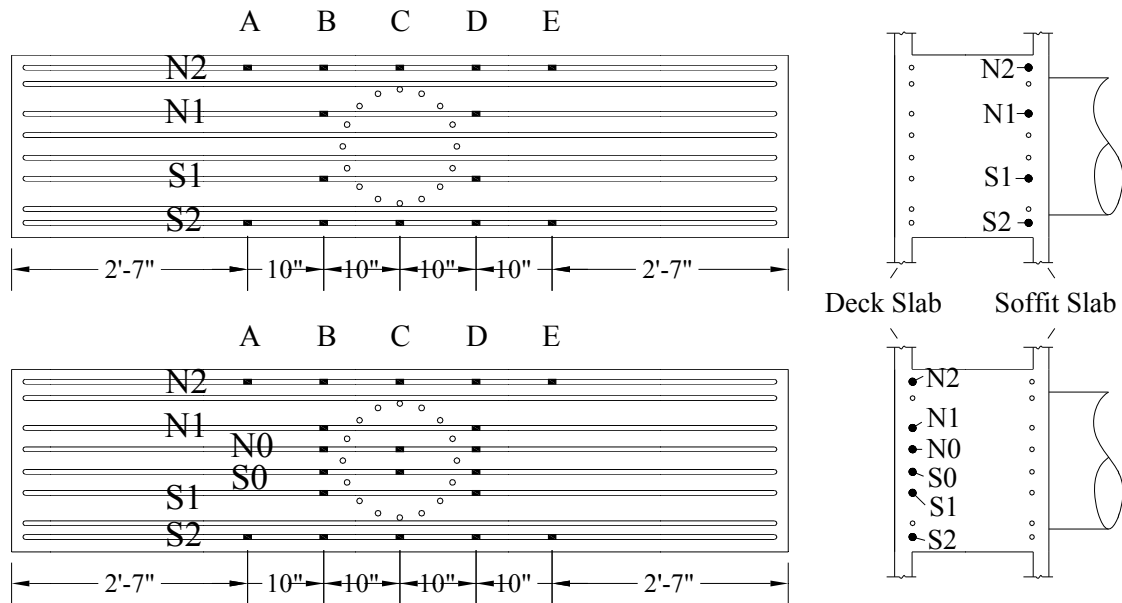
Figure 3.46 Layout of strain ages used for the cap beam reinforcement
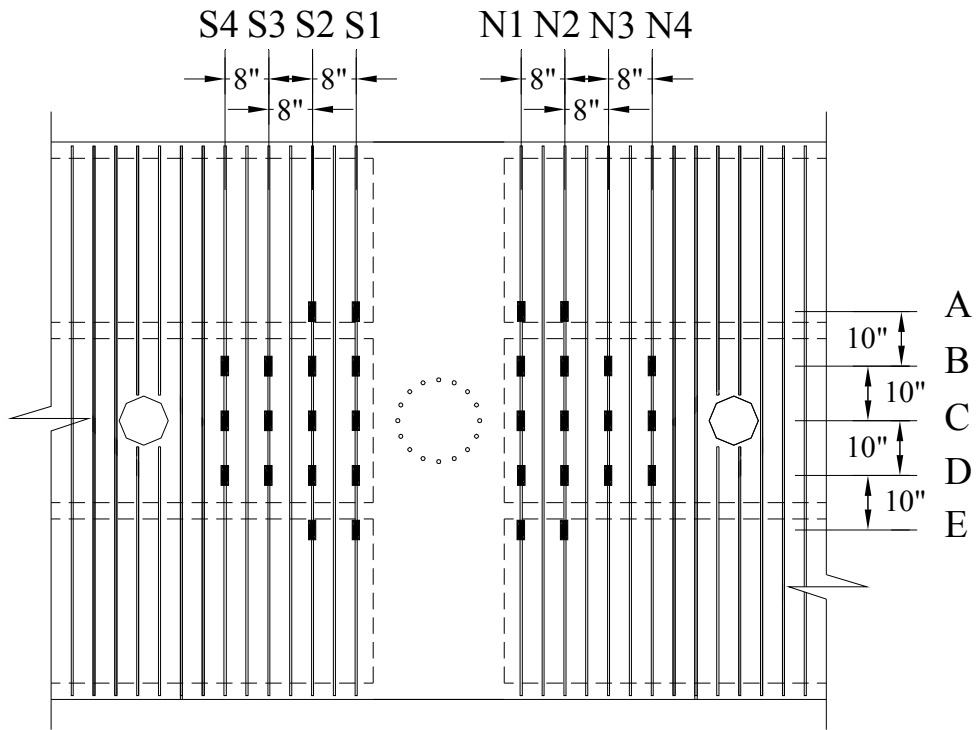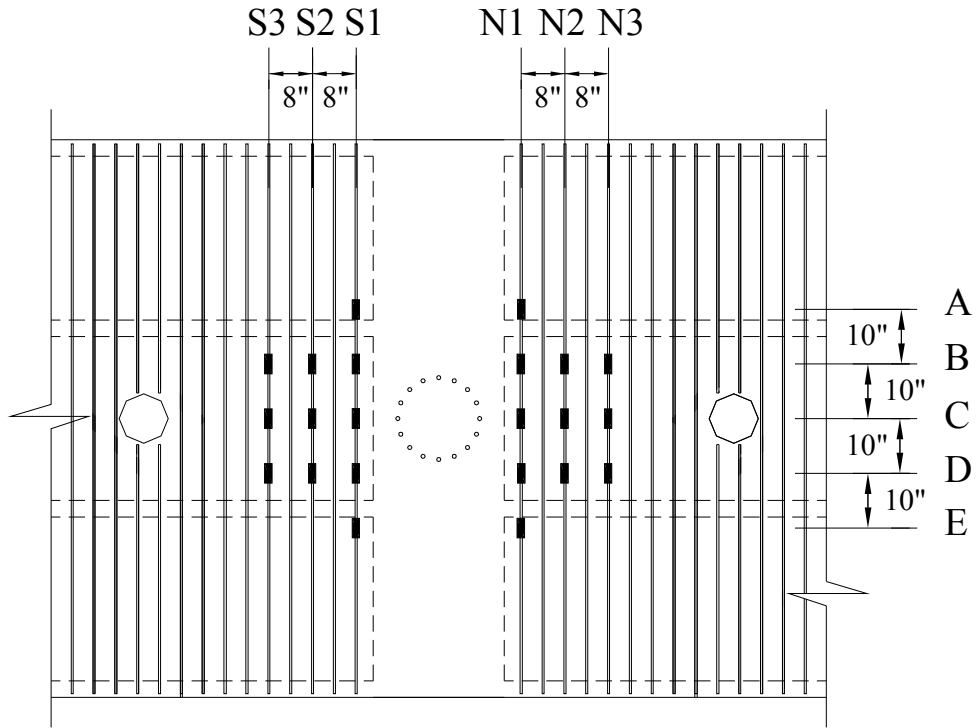
Figure 3.47 Layout of strain ages used for the box-girder soffit slab (top) and deck slab (bottom) transverse reinforcement
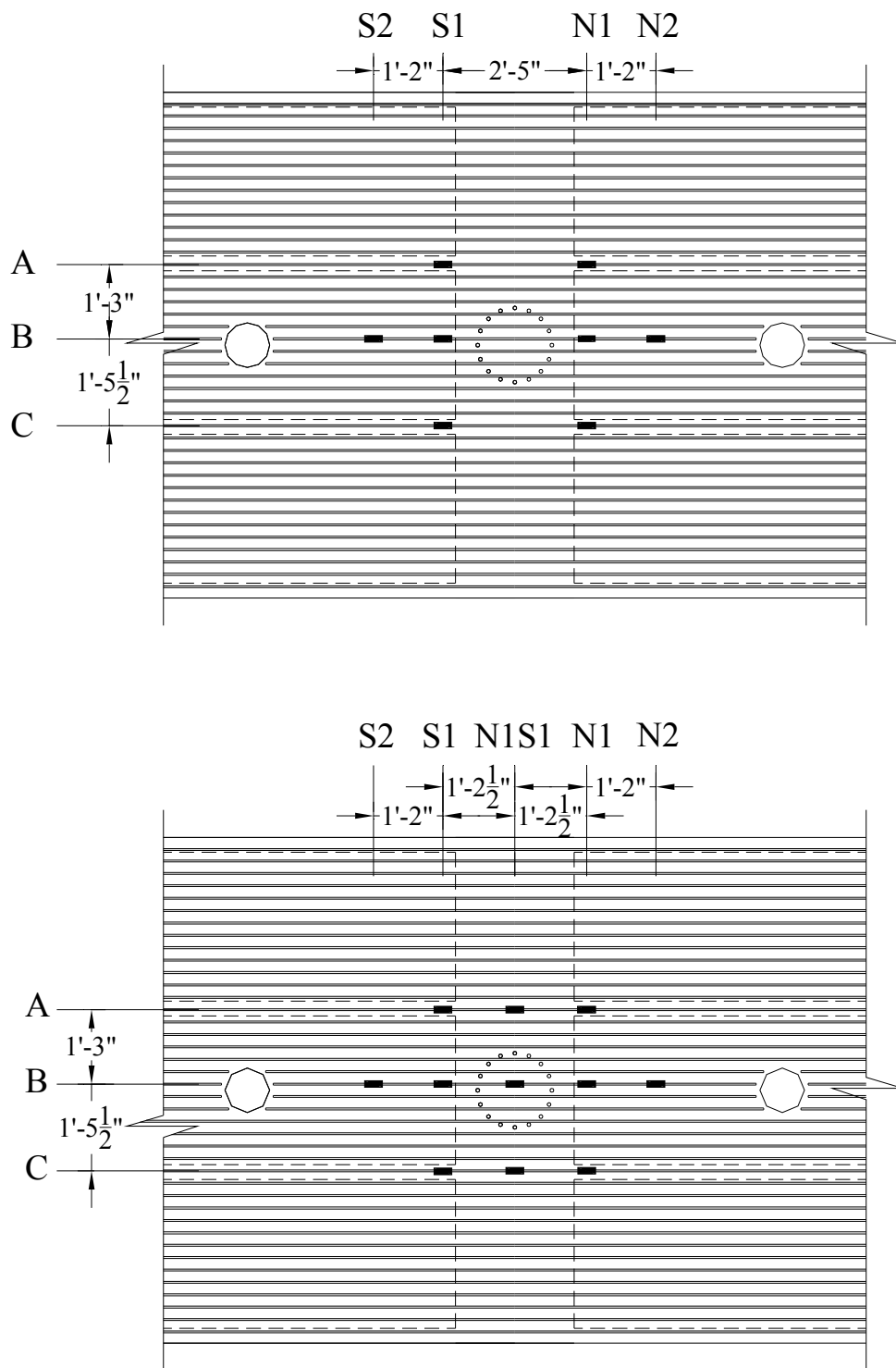
Figure 3.48 Layout of strain ages used for the box-girder soffit slab (top) and deck slab (bottom) longitudinal reinforcement
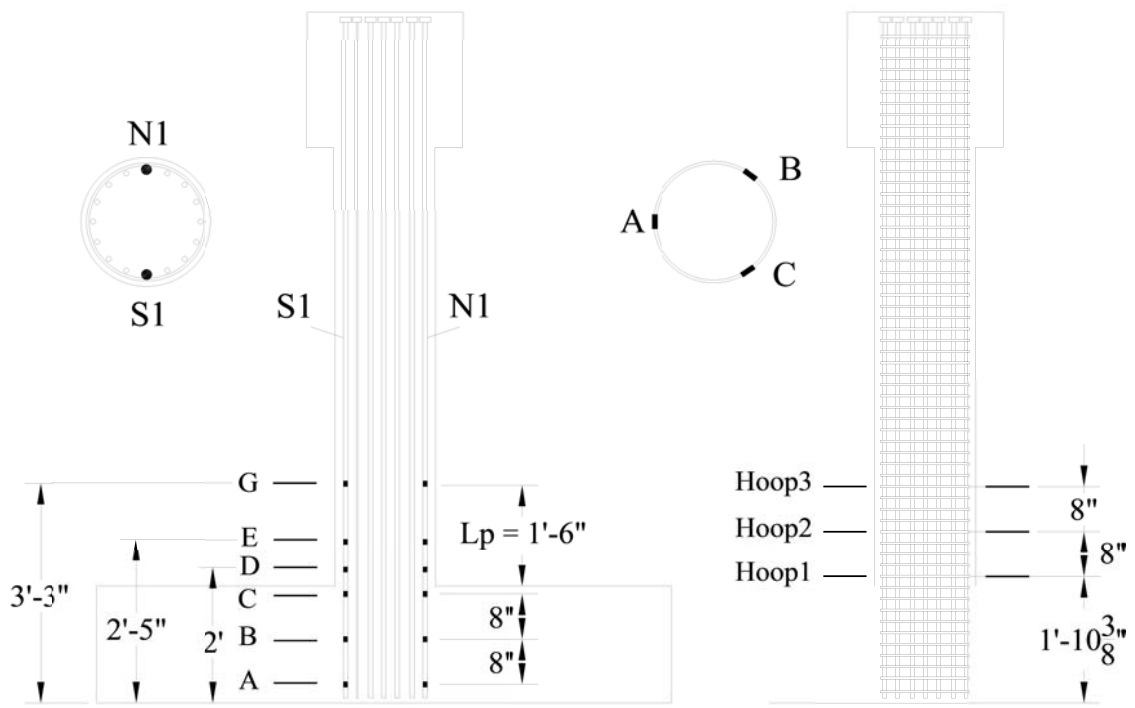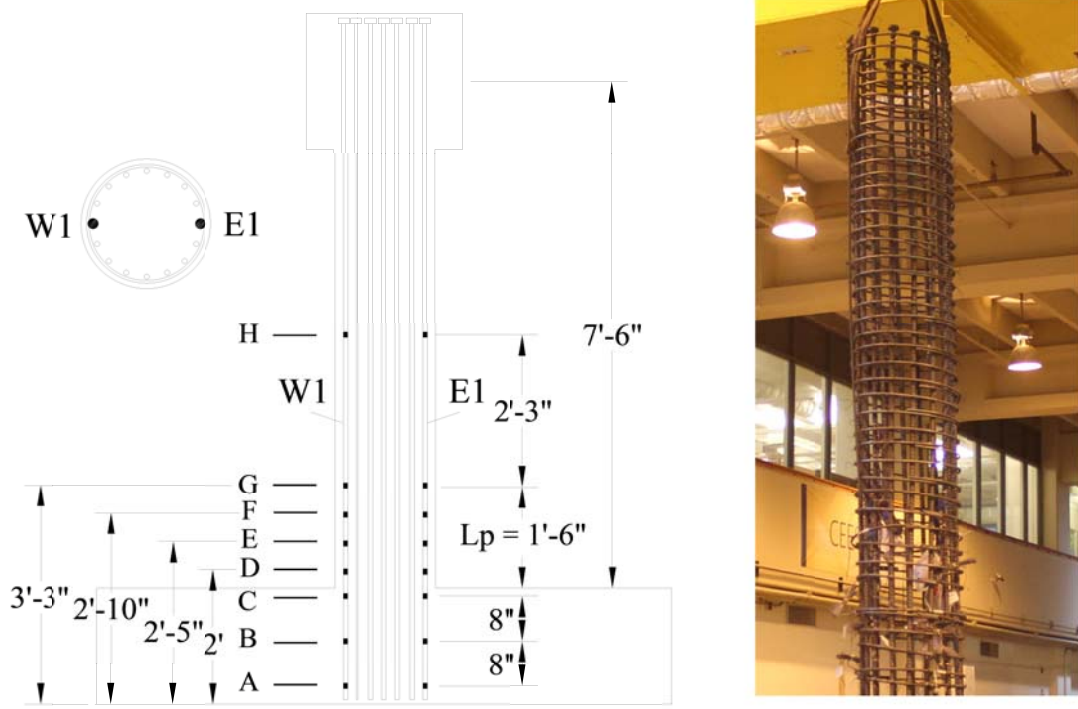
Figure 3.49 Layout of strain gages used for the column longitudinal and transverse reinforcement

3.10.4 Curvature Measurement

As previously mentioned, LVDTs were used for direct cap beam and box-girder displacement measurements under the specimen and a different set was dedicated for column curvature estimation. The curvatures were not measured directly but estimated from the LVDTs relative displacement measurements as discussed here. LVDTs are robust and reliable in calculating very small curvatures and rotation with high accuracy.

The subassembly column was instrumented with four levels of LVDTs in the North-South (longitudinal loading) direction and five levels in the East-West (transverse loading) direction. Each two opposite LVDTs at a certain level measured displacements that can be relatively associated to other levels. The relative displacements between each two measuring levels can be transformed to linear strains if the distance between the two levels is known. The linear strains at two opposite sides of the column can be then used to estimate the cross-section curvature at a given level using the horizontal distance between the two planes where the linear strains are calculated. This described process for estimating curvatures using LVDTs is illustrated in Equations (3-5) and (3-6) and Figure 3.50. The actual layout and setup of the column's LVDTs dedicated for curvature measurements are shown in Figure 3.51.

$$\kappa = \frac{\varepsilon}{L} = \frac{\varepsilon_1 + \varepsilon_2}{D + Offset_1 + Offset_2} \tag{3-5}$$

$$\varepsilon_1 = \frac{\Delta h_1}{h_1} \, , \, \varepsilon_2 = \frac{\Delta h_2}{h_2} \tag{3-6}$$

where

$\Delta h_{1,2}$: change in displacement at a given LVDT between two fixed points (direct reading of LVDT)

$h_{1,2}$: distance between two fixed points set by the threaded rods projected out of the column

$Offset_{1,2}$: initial horizontal distance between the column face and a given LVDT center line

D: column diameter [inch]
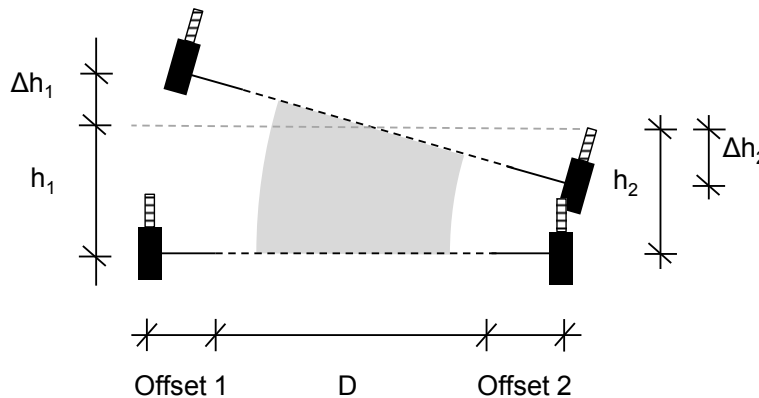
Figure 3.50 Schematic representation of paramters required to estimate the column curvatures using linear LVDTs

89
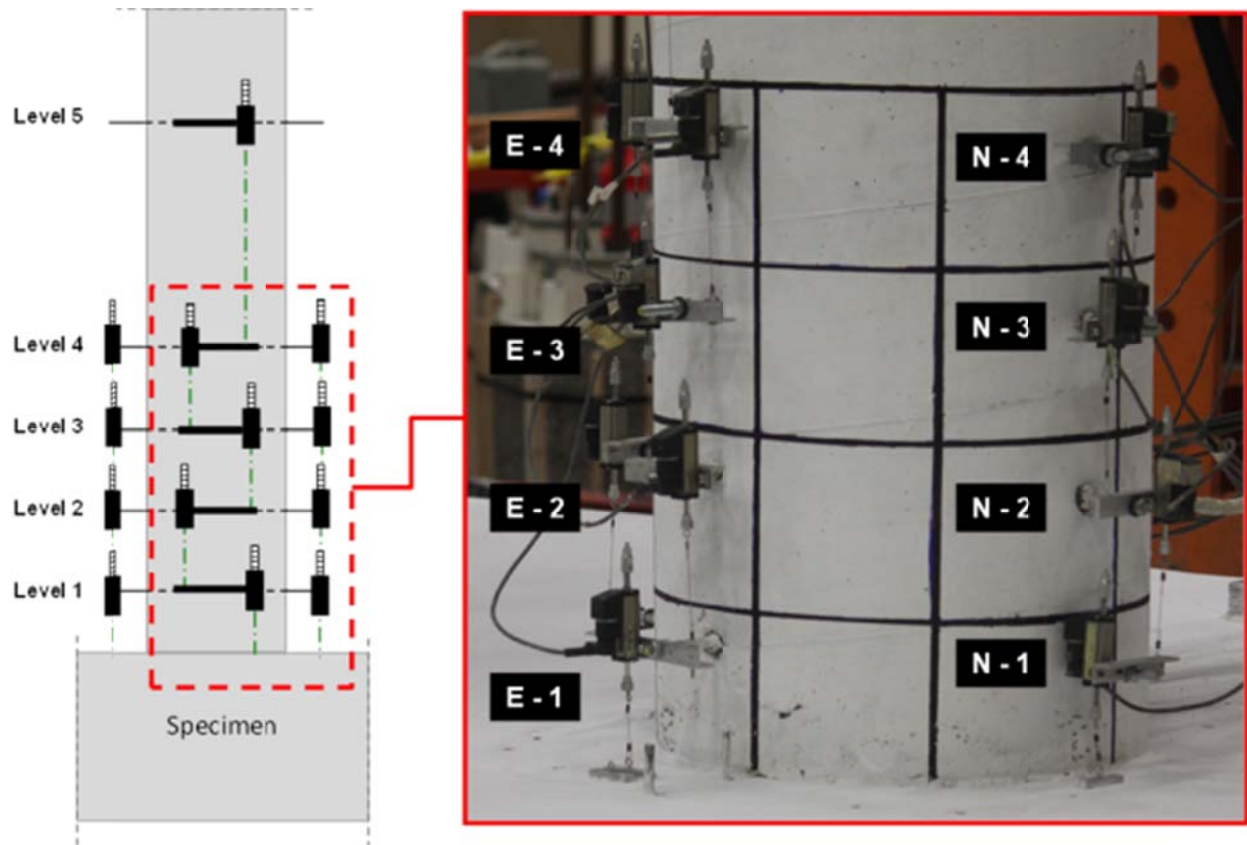
Figure 3.51 Distribution of LVDTs on the column (left) and picture of installed LVDTs (right)

3.10.5 Cameras

The final type of instruments used throughout the conducted experimental program is cameras. Figure 3.52 shows an overview of the arrangement of various cameras used during the tests. Several Digital Single-Lens Reflex (DSLR) cameras were used to capture still pictures for crack and damage propagation in all tests. A monochrome DSLR camera was installed inside the North middle cell of the box-girder to capture joint region cracking. A random speckles pattern was applied to the North side of the column-cap beam joint region, exposed to the monochrome DSLR camera, for the purpose of adopting Digital Image Correlation (DIC) measuring technique. A random speckle pattern also was applied to the east side of the specimen as observed from Figure 3.13. DIC is a novel measuring technique that is undergoing extensive development for use in structural engineering applications at the University of California, Berkeley. In DIC, high resolution still pictures can be used to estimate surface displacement and strain distributions. An example of the strain distribution during one of the conducted quasi-static tests loading cycles obtained from DIC is shown in Figure 3.53. In addition to the remote DSLR cameras, several other Gopro cameras were used underneath the specimen to capture crack pattern in the inverted box-girder's deck and the cap beam. Few Gopro cameras were used in other box-girder cells to capture direct photographs of any cracks inside the cells as seen in Figure 3.52. For better quality pictures of dark spots, laboratory shop lights and flash lights were used inside the box-girder cells and under the specimen as also seen in Figure 3.52.

90
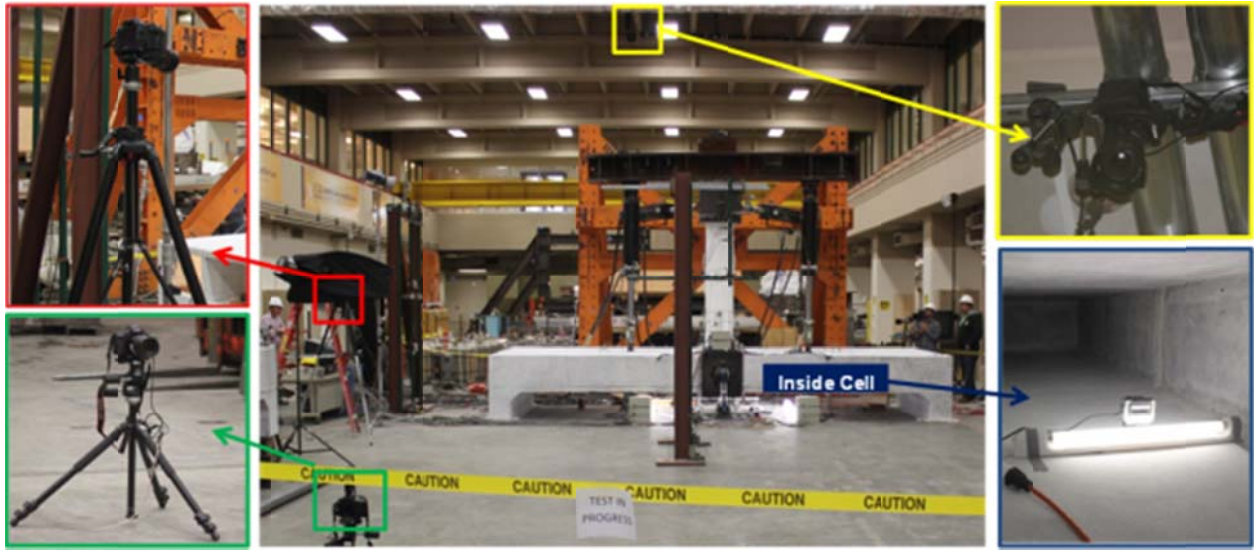
Figure 3.52 Overview of different types of cameras, their arrangement, and illumination system used during testing
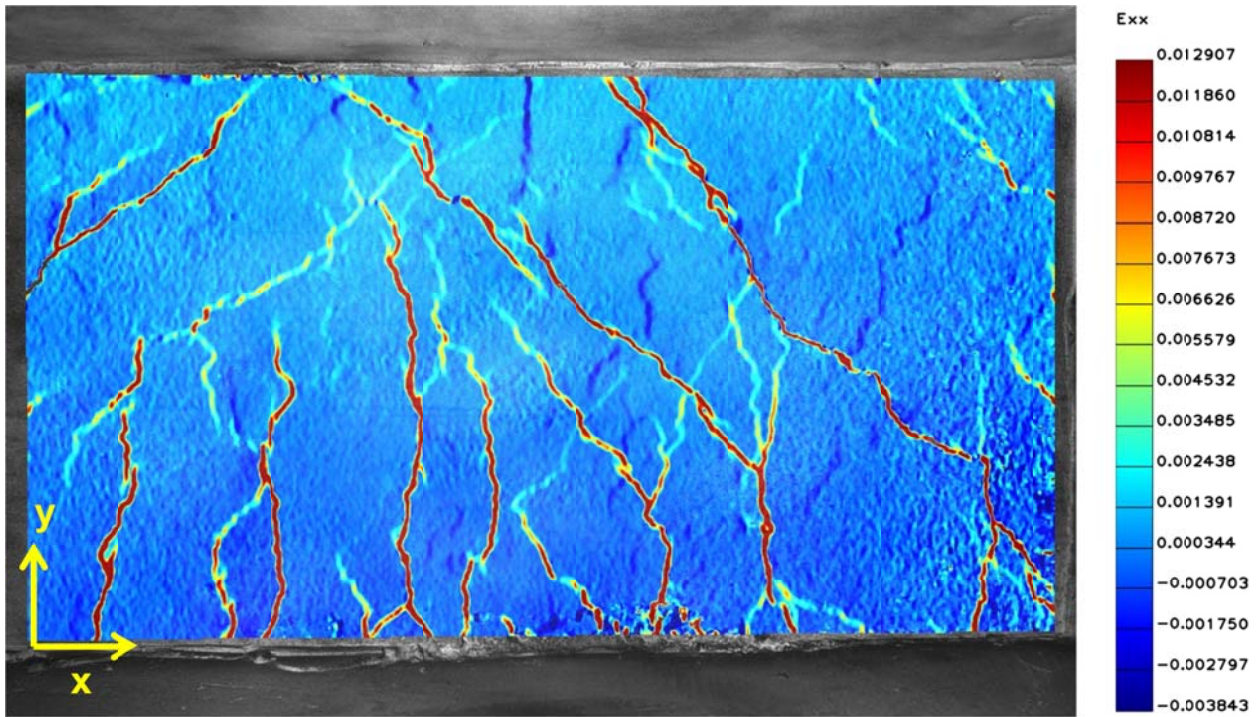
Figure 3.53 Example of strain distribution and crack pattern in the column-cap beam joint region obtained from the DIC technique during one of the cyclic loading tests

4   Pre-Test Finite Element Analysis

A computational framework was pursued to complement the undertaken experimental framework. The Finite Element Method (FEM), also referred to as Finite Element Analysis (FEA) as well, is considered for the conducted computational work throughout this study. Two main stages of FEA comprise the computational framework. These are pre-test and post-test analysis. The pre-test analysis aimed primarily at providing answers and clearing several issues that are associated with experimental work. Thus, several linear and nonlinear one-, two-, and three-dimensional models were utilized in this study to conduct the pre-test analysis before the experimental tests specimens were built or the test setup pieces were assembled. On the other hand, the post-test analysis uses some of the pre-test analysis models to calibrate them against the experimental results and carry out further analysis and a parametric study that complements the experimental work.

This chapter presents all the different FE models developed and used in the pre-test analysis. The pilot studies conducted using these models are also discussed. Three different types of models were used and categorized for the sake of this discussion according to the utilized finite elements dimensions. The first type of models utilized one-dimensional (1D) elements for modeling either the full prototype bridge or the test subassembly specimen. The Open System for Earthquake Engineering Simulation (OpenSees) was used for 1D models. The second type of models used two-dimensional (2D) elements mainly for box-girder modeling. The commercial analysis package SAP2000 (2012) was used for the 2D models. The most sophisticated level of modeling is the three-dimensional (3D) solid element modeling, which was also utilized in this study. The general purpose FEA package DIANA (DIsplacement ANAlyzer 2011) was used for creating the 3D models and performing linear and nonlinear analyses. The pre-test analysis presented in this chapter is divided into four sections. The first section is dedicated to the 1D OpenSees models. The second section focuses on the SAP2000 models. The third section provides a very brief discussion of 3D modeling of RC. The last section presents the 3D DIANA models.

The pre-test analysis had several objectives. Each of the 1D, 2D, and 3D models and FEA fulfilled one or more of the main objectives. These objectives are: (1) verify expected subassembly behavior with respect to the mode of failure, column and bent cap beam behavior; (2) finalize the loading protocol especially for the hybrid simulation test through ground motion selection and scaling; (3) estimate the expected lateral forces during cyclic and hybrid simulation loading for test setup design and checks; (4) decide on the proper locations and distribution of the instrumentation where maximum straining actions are expected. The details of how these objectives were achieved are discussed in the following sections.

4.1   1D OPENSEES MODELING

Two simple 1D OpenSees models were used as the first part of the pre-test analysis. The first model was developed for the test specimen subassembly using the geometry and reinforcement design discussed in Chapter 3. Nonlinear pushover analysis was conducted for the test specimen model at different gravity load levels. The main objectives of the test specimen pushover analysis was verifying whether the cap beam failure is expected or not and how would the gravity load level affect both of the column and cap beam behavior. The second OpenSees model was developed for the prototype bridge adopted from the Caltrans Academy Bridge as discussed in Chapter 3. The prototype bridge analysis was intended investigate any possible effects of the vertical component of the earthquake excitations on the behavior of the bent cap beam, which is the centerpiece of this study. Nonlinear time history analysis was conducted under several ground motions that considered both bidirectional horizontal components only, and combined vertical and bidirectional horizontal components. Details of the subassembly and prototype bridge analyses are discussed in the following two subsections.

4.1.1   Subassembly Specimen Analysis

The test subassembly is a simple OpenSees model that used 3 1D beam-column elements with distributed plasticity. Each of the 3 elements represents one of the subassembly components which are: column, cap beam, and box-girder. The boundary conditions used for the model and the dimensions of the idealized 1D elements of the subassembly, which coincide with the elements centerlines, are shown in Figure 4.1. The boundary conditions are roller supports at each of the cap beam ends, and a fixed-translation supports at each of the box-girder ends. In addition, one rotational degree-of-freedom (DOF) is restrained to provide the torsional stiffness of the box-girder section. Fiber sections were used for each of the 3 beam-column elements used in the model. All the material properties used in this model are nominal material properties based on a concrete characteristic strength of 5 ksi and reinforcement steel yield of 68 ksi. The 68 ksi yield stress was used for the steel rather than the typical 60 ksi yield stress because of the sensitivity of the lateral force and column capacity to the steel yield stress. Thus, the 68 ksi was used as a better estimate than the lower bound 60 ksi. Two of the available material constitutive models in OpenSees were adopted for the model: Cocnrete02 and Steel02 for the concrete and reinforcement, respectively. The Cocnrete02 models the nonlinear concrete behavior in both tension and compression. The Steel02 was calibrated to reflect elastic-perfectly plastic behavior since the model analysis is used only for preliminary behavior investigation.

Only nonlinear pushover analysis was conducted at different levels of axial load in both transverse and longitudinal directions. It is to be noted that the transverse direction is always aligned with the cap beam, while the longitudinal direction is aligned with the box-girder and this definition is fixed throughout the entire study. All loads were applied at the top of the column in the inverted position as shown in Figure 4.1. The gravity vertical load was applied under load-control, i.e. using force increments, while the lateral pushover was applied under displacement control, i.e. using displacement increments. The modified Newton-Raphson algorithm was the algorithm used most frequently for solving the nonlinear equilibrium equation, but the linear stiffness method was also used when convergence was not obtained using the Newton-Raphsoin methods. More information about the incremental-iterative nonlinear solution strategy is presented in the 3D modeling of RC section. Moreover, it is to be noted that a lumped

mass was also added at the column top since this same model was also used as part of the hybrid simulation computational model development and idealization. The discussion related to the use of this model as part of the hybrid simulation test is included with the hybrid simulation system components and development in Chapter 7. The three axial load levels considered were 5, 10 and 15%. An axial load level is the ratio between the applied gravity load to the expected axial capacity of the column based on the gross 18-inch column diameter and concrete nominal compressive strength of 5 ksi.
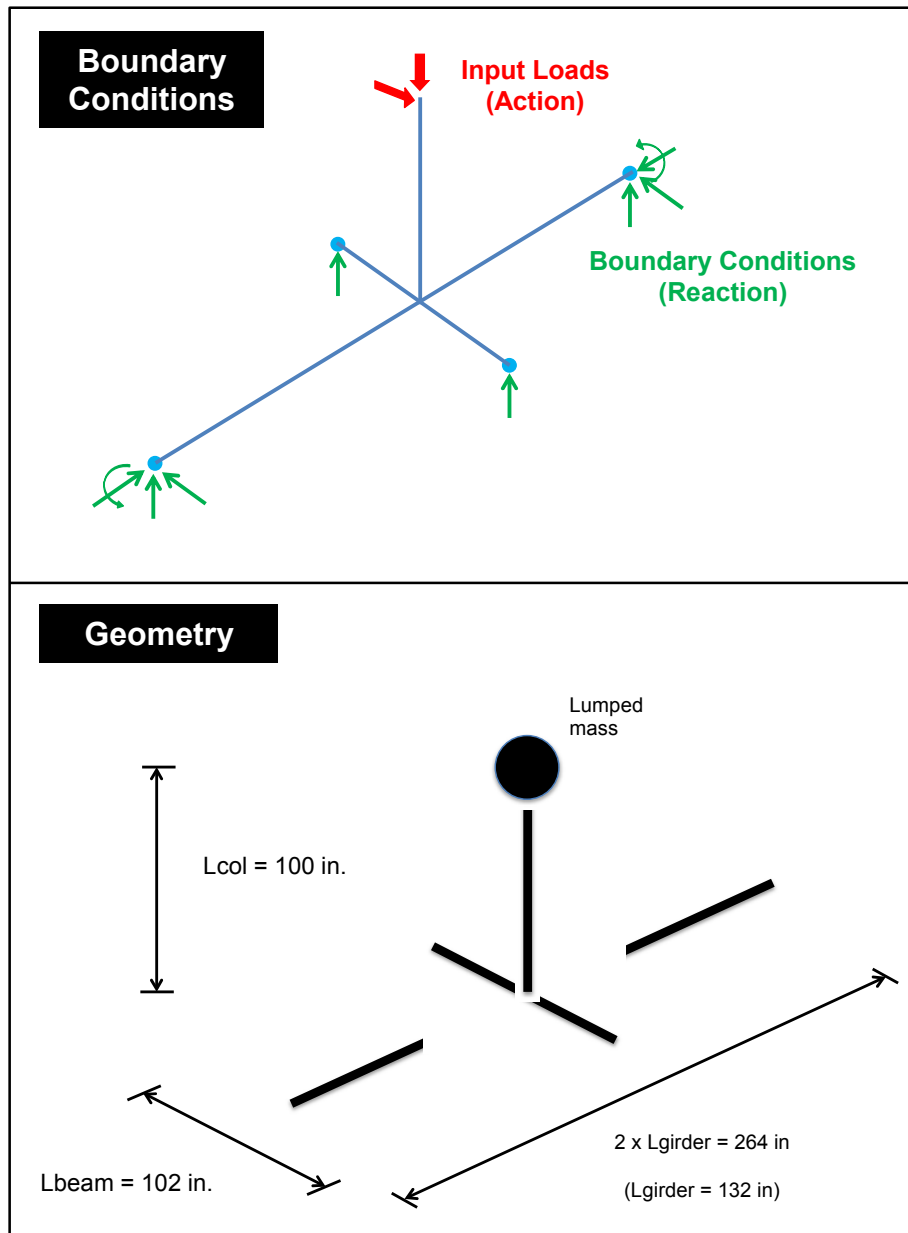
Figure 4.1 Schematic representation of features of the OpenSees model for the test subassembly specimen (boundary conditions and geometry)

Figure 4.2 shows the force-displacement relationship obtained from the lateral pushover analysis in the transverse direction under different gravity load levels. The figure shows a

noticeable increase in the lateral force capacity as the axial load level is increased. The same observation is confirmed from the column moment-curvature relationship in Figure 4.3, where the moment capacity of the column increases with the axial load level as expected. The cap beam moment-curvature relationship shown in Figure 4.4 suggests that for the 5% and 10% cases, the cap beam does not yield. However, at 15% axial load, the cap beam failed as seen from the curvature values in Figure 4.4. There is a direct relation between the gravity load level and the cap beam moments because of the nature of the setup as understood from Figure 4.5 that shows the bending moment distribution in the column-cap beam elements due to different load cases. Another way of presenting the cap beam yield at the 15% axial load is using the stress-strain relationship obtained for one of the rebars in the tension side of the cap beam (Figure 4.6). The figure also confirms that no yielding in the cap beam took place at 5% or 10% axial load. On the other hand, the column rebars yielded at all gravity load levels as seen in Figure 4.7. The results suggest the conclusion that varying the gravity load is a possible way of delaying the column plastic hinge formation while pushing the cap beam further to higher moment demands.
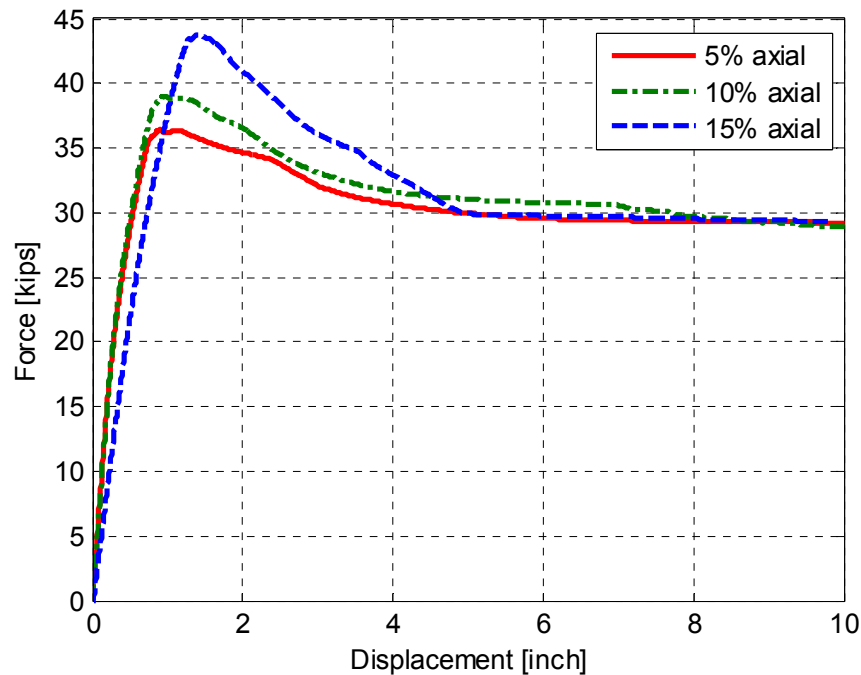
Figure 4.2 Force-displacement relationship for the OpenSees test subassembly under constant gravity load (3 levels) and lateral pushover loading in the transverse direction
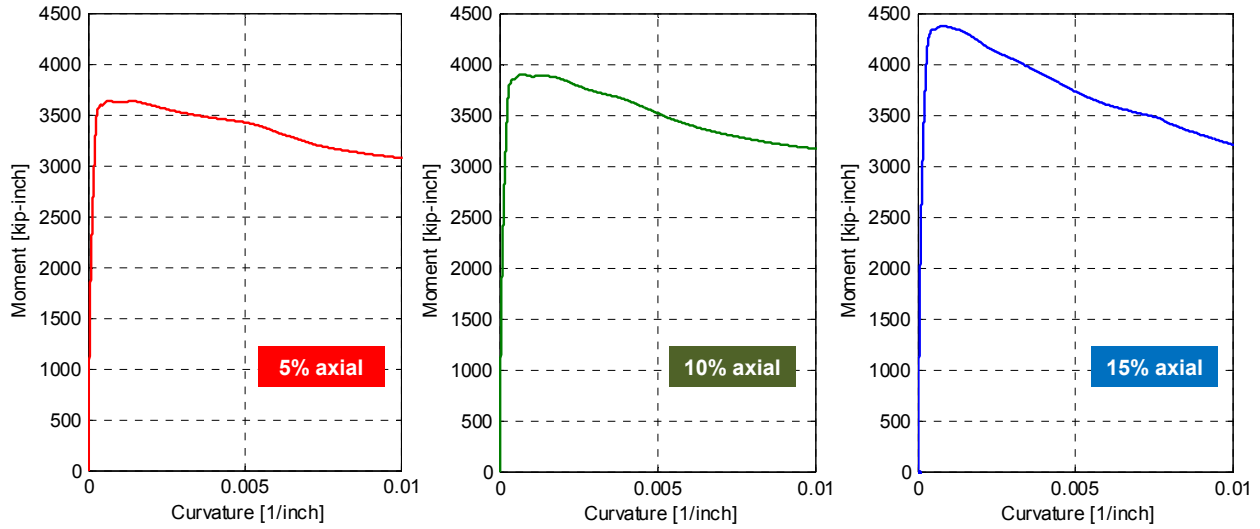
Figure 4.3 Moment-curvature relationship for the subassembly's column section under constant gravity load (3 levels) and lateral pushover loading in the transverse direction
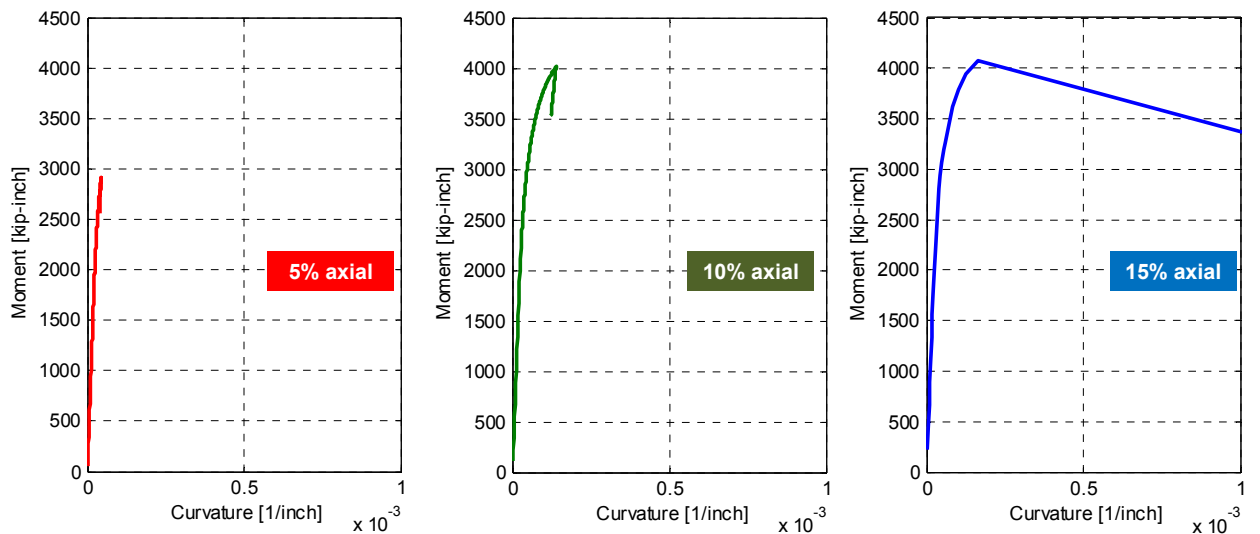
Figure 4.4 Moment-curvature relationship for the subassembly's cap beam section under constant gravity load (3 levels) and lateral pushover loading in the transverse direction
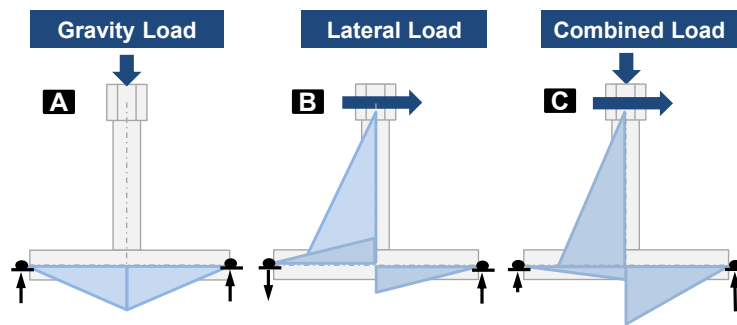
Figure 4.5 Schematic bending moment distribution along the column and bent cap beam in three load cases: (a) gravity load (b) lateral load (c) combined gravity and lateral loads
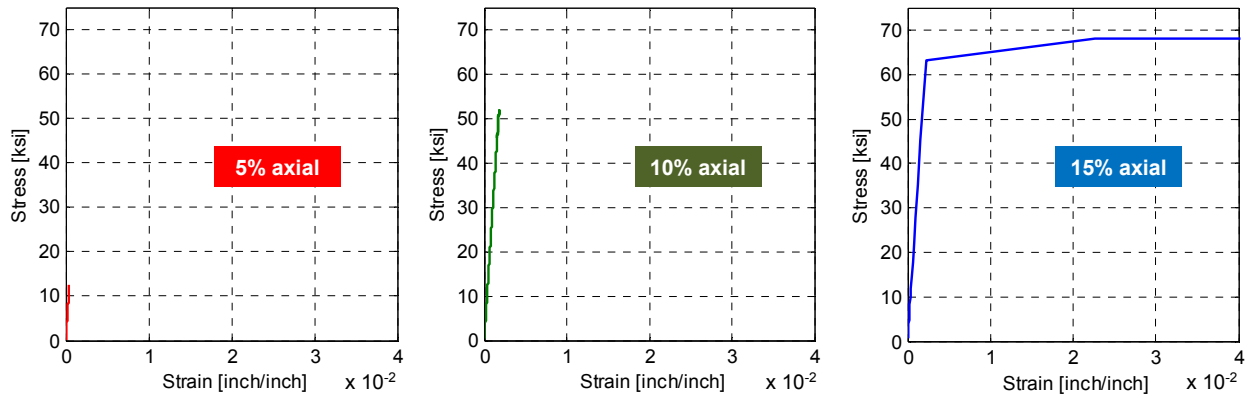
Figure 4.6 Stress-strain relationship for one of the cap beam tension side rebars under constant gravity load (3 levels) and lateral pushover loading in the transverse direction
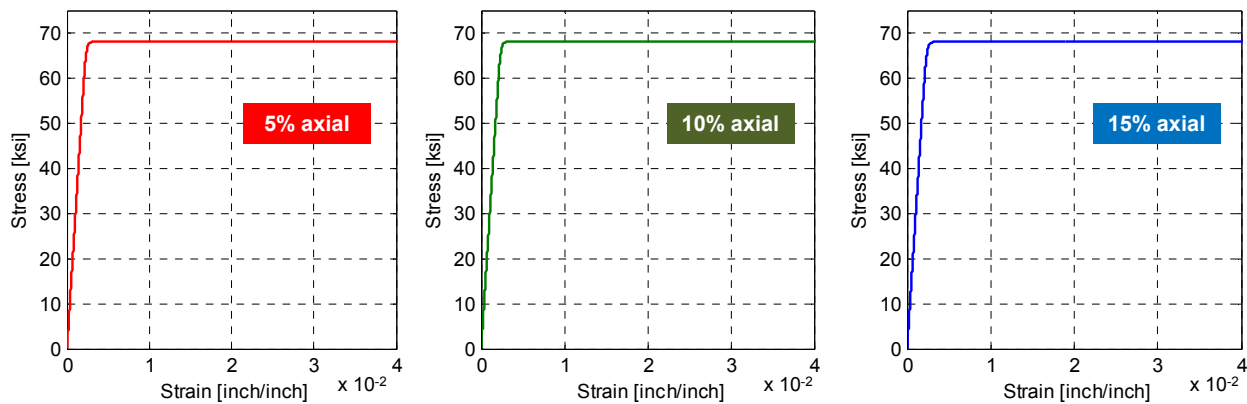
Figure 4.7 Stress-strain relationship for the outermost West rebar of the column (refer to Figure 3.11for definition of the North side) under constant gravity load (3 levels) and pushover loading towards east

4.1.2 Prototype Bridge Analysis

The OpenSees was further used to perform a full prototype bridge nonlinear time history analysis. The full-scale prototype bridge, previously discussed in Chapter 3 and identified in Figure 3.3, was modeled using 1D beam-column elements. A preliminary design was performed according to AASHTO (2007) and Caltran SDC (2010) to estimate the reinforcement in the bents columns and cap beams. Approximate reinforcement for the box-girder was estimated as well and taken as percentage of the box-girder area based on practical recommendations from Caltrans engineers. Similar element types and model characteristics as the subassembly OpenSees model were utilized in the full bridge model. In summary, fiber sections were used for the columns, cap beams and box-girder beam-column elements used in the model. In addition, the 5 ksi nominal concrete characteristic strength was used in the Concret02 model, and 68 ksi yield stress was used for Steel02 model that was calibrated to resemble an elastic-perfectly plastic behavior. The total bridge mass was distributed along the full lengths of the box-girder and bent cap beams. This distribution was checked to make sure it led to accurate distribution of the actual bending moments due to bridge own weight (gravity loading). Moreover, the periods

and modes of vibrations obtained from the Opensses model were compared against a more detailed SAP2000 bridge model (presented in the next subsection) to also verify the mass distribution. The boundary conditions used for the bridge model were hinged base for all columns and roller supports with additional torsional restraints at the two abutments locations. A schematic representation of the OpenSees bridge model showing the elements dimensions and mass distribution is shown in Figure 4.8.
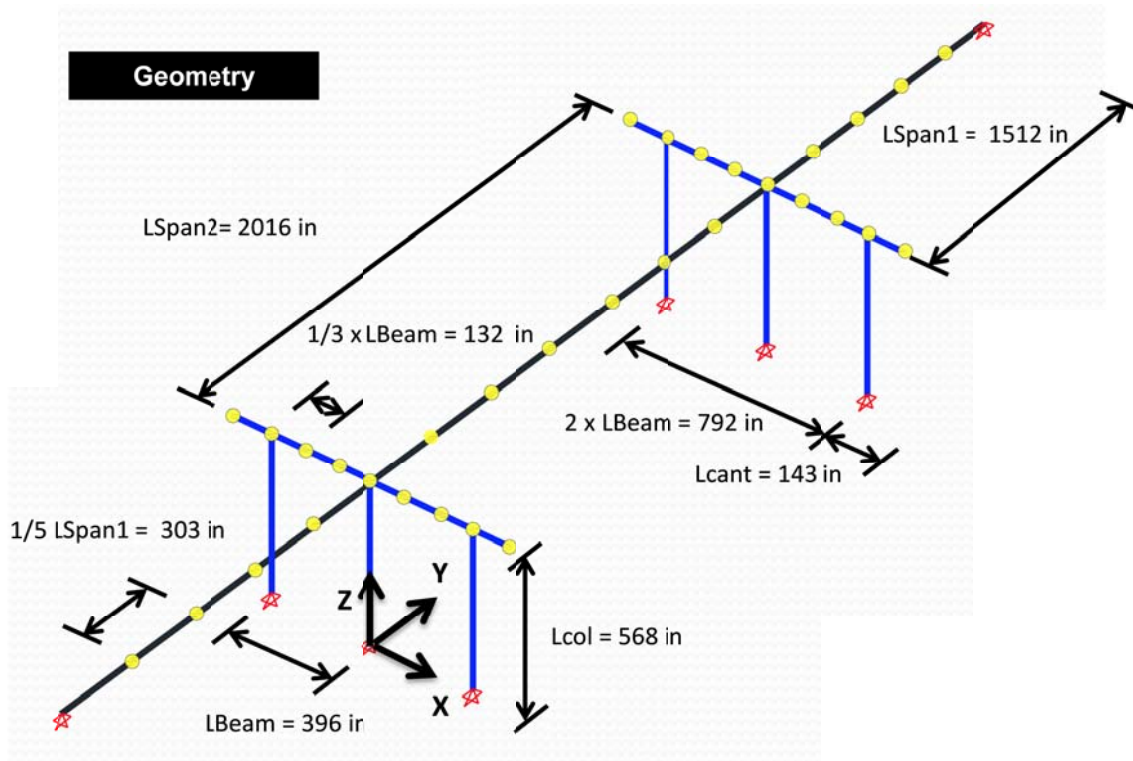
Figure 4.8 Schematic representation of OpenSees model of the modified Academy Bridge

The main type of analysis carried out for the bridge model is nonlinear time history analysis. The objective of this bridge analysis was investigating the possible effects of vertical component of ground motions on the bent cap beam behavior. This was done at an early stage of the study to decide if the vertical excitations should be considered in the hybrid simulation (HS). It was decided that it is impractical to apply a vertical excitation during the HS test because of setup limitations. However, the conducted nonlinear time history analysis for the bridge was very beneficial in choosing a short list of ground motions for further detailed pre-test analysis and final ground motion selection for the HS test. Another outcome of the bridge analysis was estimating the axial load fluctuation in the bridge columns due to the vertical excitations. In summary, a large number of ground motions were selected (discussed in the following paragraph) and used to conduct two sets of nonlinear time history analysis on the OpenSees prototype bridge model. The first set used only the two horizontal components of the selected ground motions. The second set used both of the two horizontal components and the vertical component as well of the selected ground motions. Comparisons were made between the results of these two sets of ground motions to investigate whether the vertical component exerts significant additional demands in bending moment for the cap beam and in axial force for the column.

The PEER Next Generation Attenuation (NGA) strong ground motions database (2005) was used to select the ground motions for this study. The main criterion to select a pool of ground motions was the relative significance of the recorded vertical component. Several previous studies focused on the vertical-to-horizontal component scaling of ground motions and attenuation relationships for the vertical component response spectra, e.g. Campbell and Bozorgnia (2003); Bozorgnia and Campbell (2004). These studies suggest that only near-fault records for relatively large magnitude earthquakes would feature relatively large vertical accelerations. Accordingly, earthquakes of magnitude 6.50 or larger and stations that were within 10 km from the fault were selected to prepare the list of ground motions considered in this study. The 6.5 magnitude and 10 km distance to fault are not fixed value set by the literature, but rather a choice of the author to develop a reasonable list of ground motions that still includes all the large recorded vertical excitations. Therefore, a total of 88 records, each comprise two horizontal and one vertical components, were selected from the PEER NGA database to be used in this study as summarized in Table 4-1. It is to be noted that Table 4-1 shows 6 highlighted ground motions in which comprise the short list of ground motions where the vertical component was found to significantly increase the moment demands on the cap beam of this particular bridge model.

As previously mentioned, the list of the 88 ground motions was used to run two sets of nonlinear time history analysis; one set did not include the vertical component while the other included both horizontal and vertical components. That is to compare the results obtained from a given ground motion record with (w/) and without (w/o) the vertical component. A total of 6 ground motions (highlighted in Table 4-1, and summarized in Table 4-2) were found to have the most significant effect on the bent cap beam due to the consideration of the vertical component of the ground motion. The considered significant effect means the occurrence of large curvatures at several sections in both of the bent column and cap beam. A large curvature in the bent cap beam was accompanied by the beam reaching its moment capacity, i.e. causingreflects a cap beam plastic hinge formulation. Selected sample results from two of the most severe 6 ground motions are shown here. Results from the Kobe ground motion runs (ID #5 in Table 4-2) are presented to show the effect of the vertical component on the cap beam moment and curvature demands. In addition, the results from Northridge Sylmar ground motion runs (ID #4 in Table 4-2) show the axial force fluctuation with and without vertical component inclusion. The cap beam and column critical sections used to plot the selected sample results are shown in Figure 4.9.

Firstly, to investigate the effect of the vertical excitation on the cap beam demands, the results from 30% Kobe ground motion runs are presented. Figure 4.10 shows the comparison between the moment-curvature for the bent column section 1 (Figure 4.9) with and without the vertical excitation. It is shown that the column failed in both cases whether the vertical excitation is considered or not. It is also noticed that the column moment capacity in the case of the vertical component included is higher than that without vertical excitations. This can be attributed to the effect of the additional compression axial load which, as shown before in the test subassembly study (Figure 4.2 and Figure 4.3), can lead to a higher moment capacity. The detailed effects of vertical excitations, however, are not the focus of this analytical study, but the reader is referred to studies, e.g. Lee and Mosalam (2014), for a comprehensive investigation of the effect of vertical excitation on bridge columns axial and shear capacities. The relevant part of this study is what shown in Figure 4.11 and Figure 4.12 for the moment-curvature of the bent cap beam at

sections 2 and 3, respectively. These figures show that the vertical excitation led to the failure of the cap beam by causing significantly larger curvature demands.

Table 4-1 List of ground motions (GMs) used in OpenSees bridge time history analysis

ID	NGA Sequence	Earthquake				Station	
		Name	Magnitude	Year	Fault Type	Name	Distance (km)
1	77	San Fernando	6.61	1971	RV	Pacoima Dam (left abut)	1.81
2	126	Gazli, USSR	6.8	1976		Karakyr	5.46
3	143	Tabas, Iran	7.35	1978	RV	Tabas	2.05
4	158	Imperial Valley-06	6.53	1979	SS	Aeropuerto Mexicali	0.34
5	159	Imperial Valley-06	6.53	1979	SS	Agrarias	0.65
6	160	Imperial Valley-06	6.53	1979	SS	Bonds Corner	2.68
7	165	Imperial Valley-06	6.53	1979	SS	Chihuahua	7.29
8	170	Imperial Valley-06	6.53	1979	SS	EC County Center FF	7.31
9	171	Imperial Valley-06	6.53	1979	SS	EC Meloland Overpass	0.07
10	173	Imperial Valley-06	6.53	1979	SS	El Centro Array #10	6.17
11	179	Imperial Valley-06	6.53	1979	SS	El Centro Array #4	7.05
12	180	Imperial Valley-06	6.53	1979	SS	El Centro Array #5	3.95
13	181	Imperial Valley-06	6.53	1979	SS	El Centro Array #6	1.35
14	182	Imperial Valley-06	6.53	1979	SS	El Centro Array #7	0.56
15	183	Imperial Valley-06	6.53	1979	SS	El Centro Array #8	3.86
16	184	Imperial Valley-06	6.53	1979	SS	El Centro Differential	5.09
17	185	Imperial Valley-06	6.53	1979	SS	Holtville Post Office	7.65
18	189	Imperial Valley-06	6.53	1979	SS	SAHOP Casa Flores	9.64
19	284	Irpinia, Italy-01	6.9	1980	N	Auletta	9.55
20	285	Irpinia, Italy-01	6.9	1980	N	Bagnoli Irpinio	8.18
21	495	Nahanni, Canada	6.76	1985	RV	Site 1	9.6
22	497	Nahanni, Canada	6.76	1985	RV	Site 3	5.32
23	753	Loma Prieta	6.93	1989	RV-OBL	Corralitos	3.85
24	763	Loma Prieta	6.93	1989	RV-OBL	Gilroy - Gavilan Coll.	9.96
25	765	Loma Prieta	6.93	1989	RV-OBL	Gilroy Array #1	9.64
26	779	Loma Prieta	6.93	1989	RV-OBL	LGPC	3.88
27	802	Loma Prieta	6.93	1989	RV-OBL	Saratoga - Aloha Ave	8.5
28	821	Erzican, Turkey	6.69	1992	SS	Erzincan	4.38
29	825	Cape Mendocino	7.01	1992	RV	Cape Mendocino	6.96
30	828	Cape Mendocino	7.01	1992	RV	Petrolia	8.18
31	879	Landers	7.28	1992	SS	Lucerne	2.19
32	949	Northridge-01	6.69	1994	RV	Arleta - Nordhoff Fire	8.66
33	983	Northridge-01	6.69	1994	RV	Jensen Filter Plant	5.43
34	1004	Northridge-01	6.69	1994	RV	LA - Sepulveda VA	8.44
35	1013	Northridge-01	6.69	1994	RV	LA Dam	5.92
36	1044	Northridge-01	6.69	1994	RV	Newhall - Fire Sta	5.92
37	1045	Northridge-01	6.69	1994	RV	Newhall - W Pico Can	5.48
38	1050	Northridge-01	6.69	1994	RV	Pacoima Dam (downstr)	7.01
39	1051	Northridge-01	6.69	1994	RV	Pacoima Dam (upper)	7.01
40	1052	Northridge-01	6.69	1994	RV	Pacoima Kagel Canyon	7.26
41	1063	Northridge-01	6.69	1994	RV	Rinaldi Receiving Sta	6.5
42	1084	Northridge-01	6.69	1994	RV	Sylmar - Converter Sta	5.35

Table 4-1 (continued) List of ground motions (GMs) used in OpenSees bridge time history analysis

ID	NGA Sequence	Earthquake				Station	
		Name	Magnitude	Year	Fault Type	Name	Distance (km)
43	1085	Northridge-01	6.69	1994	RV	Sylmar - Converter East	5.19
44	1086	Northridge-01	6.69	1994	RV	Sylmar - Olive View	5.3
45	1106	Kobe, Japan	6.9	1995	SS	KJMA	0.96
46	1111	Kobe, Japan	6.9	1995	SS	Nishi-Akashi	7.08
47	1119	Kobe, Japan	6.9	1995	SS	Takarazuka	0.27
48	1120	Kobe, Japan	6.9	1995	SS	Takatori	1.47
49	1165	Kocaeli, Turkey	7.51	1999	SS	Izmit	7.21
50	1176	Kocaeli, Turkey	7.51	1999	SS	Yarimca	4.83
51	1182	Chi-Chi, Taiwan	7.62	1999	RV-OBL	CHY006	9.77
52	1193	Chi-Chi, Taiwan	7.62	1999	RV-OBL	CHY024	9.64
53	1197	Chi-Chi, Taiwan	7.62	1999	RV-OBL	CHY028	3.14
54	1231	Chi-Chi, Taiwan	7.62	1999	RV-OBL	CHY080	2.69
55	1244	Chi-Chi, Taiwan	7.62	1999	RV-OBL	CHY101	9.96
56	1489	Chi-Chi, Taiwan	7.62	1999	RV-OBL	TCU049	3.78
57	1490	Chi-Chi, Taiwan	7.62	1999	RV-OBL	TCU050	9.51
58	1491	Chi-Chi, Taiwan	7.62	1999	RV-OBL	TCU051	7.66
59	1492	Chi-Chi, Taiwan	7.62	1999	RV-OBL	TCU052	0.66
60	1493	Chi-Chi, Taiwan	7.62	1999	RV-OBL	TCU053	5.97
61	1494	Chi-Chi, Taiwan	7.62	1999	RV-OBL	TCU054	5.3
62	1495	Chi-Chi, Taiwan	7.62	1999	RV-OBL	TCU055	6.36
63	1499	Chi-Chi, Taiwan	7.62	1999	RV-OBL	TCU060	8.53
64	1501	Chi-Chi, Taiwan	7.62	1999	RV-OBL	TCU063	9.8
65	1503	Chi-Chi, Taiwan	7.62	1999	RV-OBL	TCU065	0.59
66	1504	Chi-Chi, Taiwan	7.62	1999	RV-OBL	TCU067	0.64
67	1505	Chi-Chi, Taiwan	7.62	1999	RV-OBL	TCU068	0.32
68	1507	Chi-Chi, Taiwan	7.62	1999	RV-OBL	TCU071	5.31
69	1508	Chi-Chi, Taiwan	7.62	1999	RV-OBL	TCU072	7.03
70	1510	Chi-Chi, Taiwan	7.62	1999	RV-OBL	TCU075	0.91
71	1511	Chi-Chi, Taiwan	7.62	1999	RV-OBL	TCU076	2.76
72	1512	Chi-Chi, Taiwan	7.62	1999	RV-OBL	TCU078	8.2
73	1515	Chi-Chi, Taiwan	7.62	1999	RV-OBL	TCU082	5.18
74	1519	Chi-Chi, Taiwan	7.62	1999	RV-OBL	TCU087	7
75	1521	Chi-Chi, Taiwan	7.62	1999	RV-OBL	TCU089	8.88
76	1528	Chi-Chi, Taiwan	7.62	1999	RV-OBL	TCU101	2.13
77	1529	Chi-Chi, Taiwan	7.62	1999	RV-OBL	TCU102	1.51
78	1530	Chi-Chi, Taiwan	7.62	1999	RV-OBL	TCU103	6.1
79	1545	Chi-Chi, Taiwan	7.62	1999	RV-OBL	TCU120	7.41
80	1546	Chi-Chi, Taiwan	7.62	1999	RV-OBL	TCU122	9.35
81	1550	Chi-Chi, Taiwan	7.62	1999	RV-OBL	TCU136	8.29
82	1551	Chi-Chi, Taiwan	7.62	1999	RV-OBL	TCU138	9.79
83	1605	Duzce, Turkey	7.14	1999	SS	Duzce	6.58
84	1611	Duzce, Turkey	7.14	1999	SS	Lamont 1058	0.21
85	1612	Duzce, Turkey	7.14	1999	SS	Lamont 1059	4.17
86	1615	Duzce, Turkey	7.14	1999	SS	Lamont 1062	9.15
87	1617	Duzce, Turkey	7.14	1999	SS	Lamont 375	3.93
88	1618	Duzce, Turkey	7.14	1999	SS	Lamont 531	8.03

Table 4-2 Short list of GMs with most significant effect of vertical excitation on the considered bridge cap beam response

ID	NGA Seq. #	Earthquake				Station	
		Name	Magn.	Year	Fault Type	Name	Distance-to-fault (km)
1	495	Nahanni, Canada	6.76	1985	Reverse	Site 1	9.60
2	779	Loma Prieta	6.93	1989	Reverse-Oblique	LGPC	3.88
3	1063	Northridge-01	6.69	1994	Reverse	Rinaldi	6.50
4	1084	Northridge-01	6.69	1994	Reverse	Sylmar	5.35
5	1119	Kobe, Japan	6.90	1995	Strike-Slip	Takarazuka	0.27
6	1505	Chi-Chi, Taiwan	7.62	1999	Reverse-Oblique	TCU068	0.32
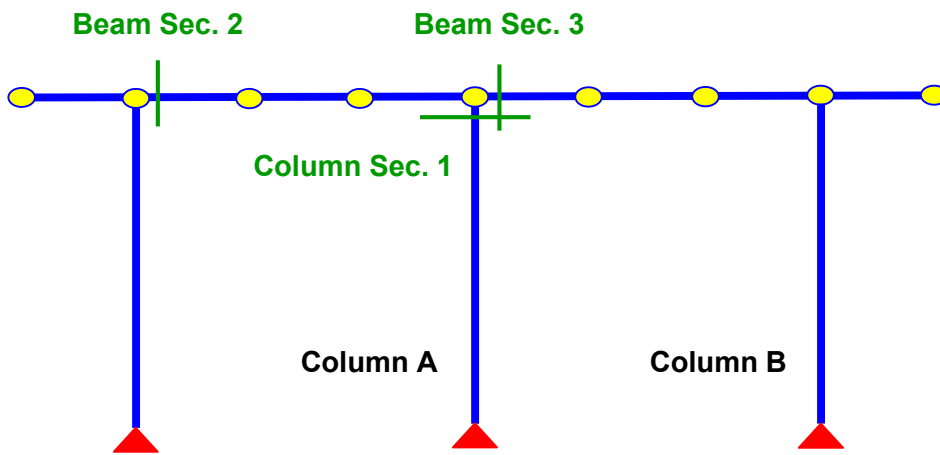
Figure 4.9 Bridge bent with critical cross-sections identified
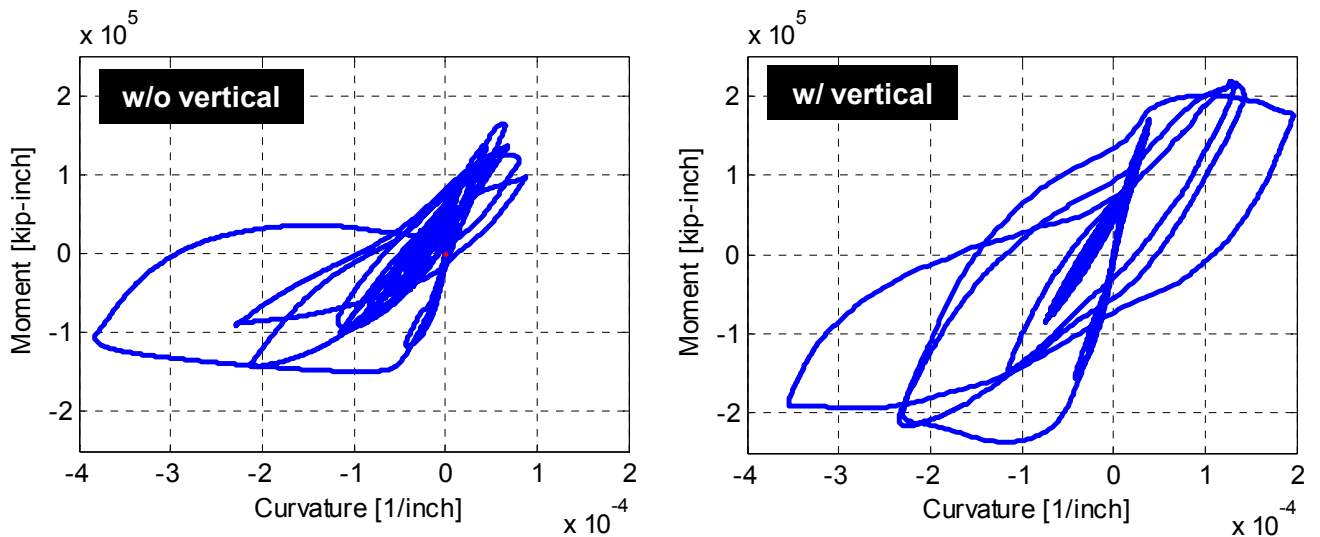
Figure 4.10 Moment-curvature relationships for bridge column (Section 1 in Figure 4.9) subjected to 30%-scale Kobe GM with and without vertical excitation component

102
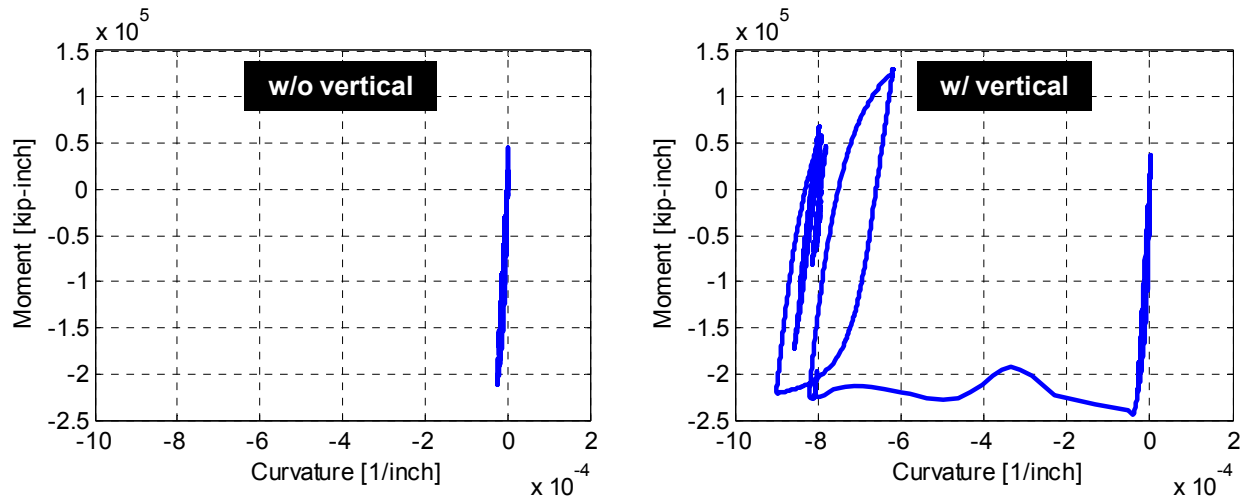
Figure 4.11 Moment-curvature relationships for bridge cap beam (Section 2 in Figure 4.9) subjected to 30%-scale Kobe GM with and without vertical excitation component
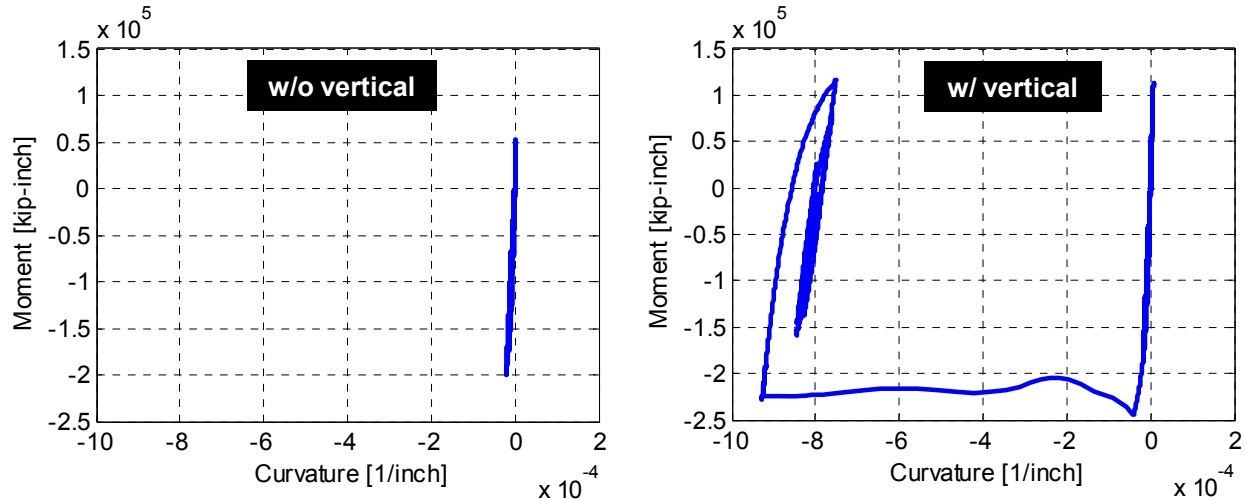
Figure 4.12 Moment-curvature relationships for bridge cap beam (Section 3 in Figure 4.9) subjected to 30%-scale Kobe GM with and without vertical excitation component

The presented preliminary observation of the effect of vertical excitations was useful on deciding which ground motion would have a more significant effect on the modified Academy Bridge prototype considered in this study. Clearly, a future study that would consider different bridge configurations for investigating the effects of vertical excitation on the cap beams is useful. Another interesting aspect of the vertical excitation response is the resulting fluctuation in the columns axial load. As mentioned before, this study does not aim at identifying the effects of vertical excitation on the axial or shear capacity of the columns. Only the fluctuation in axial load from a seismic demand perspective is considered in this study to inform the experimental program load protocol decisions. Figure 4.13 and Figure 4.14 show the axial load due to 100% Sylmar record of the Northridge ground motion in the bent interior column A and exterior column B, as identified in Figure 4.9, respectively. It is to be noted that the axial load in the interior column is fluctuating around an approximate value of 3200 kips versus a 1500 kips for the exterior column. This reflects directly the level of gravity load due to the bridge own-weight and other superposed dead loads. When vertical excitation is included the axial load was

increased at some instances by almost 60% in case of interior column and 100% in case of exterior column. This was observed for most of the ground motions and not only the presented sample. Therefore, an increase of 50% to 100% in the gravity load during the course of the conducted experimental program was adopted to address the effect of vertical excitation not only on the column axial force, but the cap beam demands as well. This is because the additional gravity load due to the vertical excitation in the used test setup also translates into additional moments in the cap beam and axial force in the column (refer to Figure 4.5).
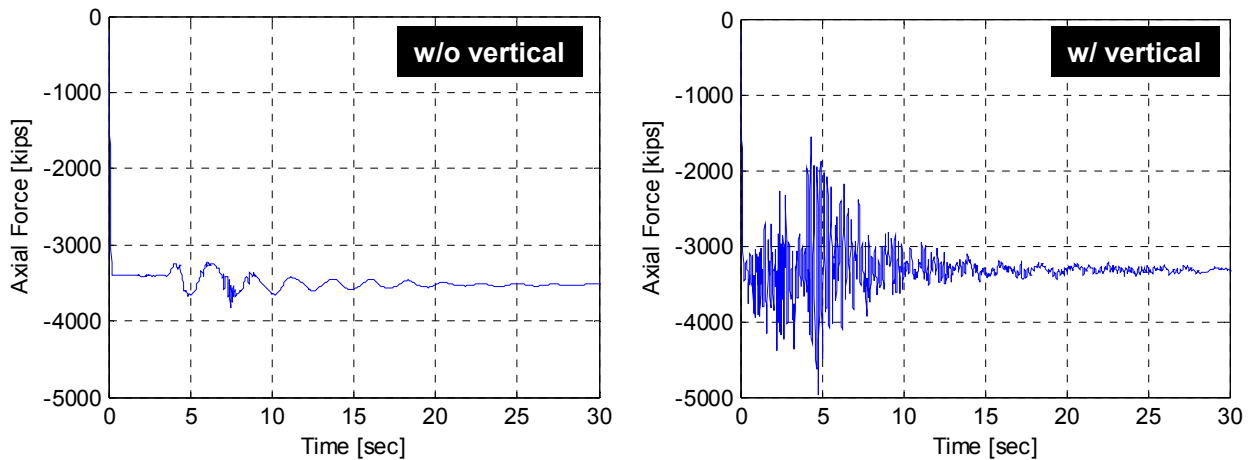
Figure 4.13 Axial load fluctuation in bridge interior column A (Figure 4.9) subjected to 100%-scale Northridge Sylmar GM with and without vertical excitation component
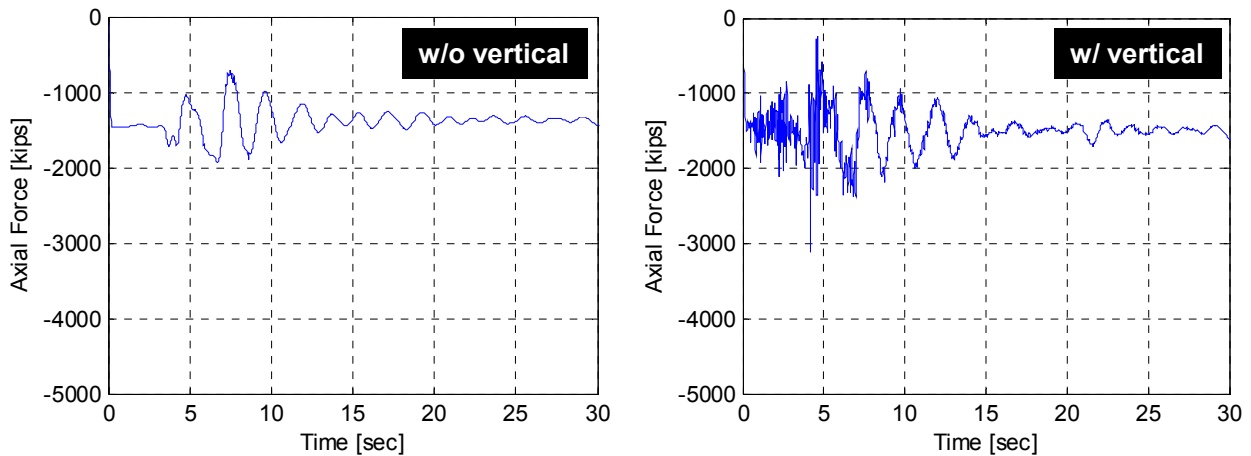
Figure 4.14 Axial load fluctuation in bridge exterior column B (Figure 4.9) subjected to 100%-scale Northridge Sylmar GM with and without vertical excitation component

4.2   2D SAP2000 MODELING

Nonlinear modeling and analysis of bridges is useful and could be required at times during seismic checks. However, elastic linear models and simplified analysis under vertical and lateral

loads is essential for any bridge design process. Therefore, a detailed bridge model for the prototype considered in this study was developed using the commercial software SAP2000 (2012) to provide several necessary response quantities that were utilized throughout the study. The prototype SAP2000 model was mainly used to determine the design forces and bending moments for the test specimen design as previously discussed in Chapter 3. Moreover, it was used to provide reference modes of vibration and periods ofvibrations that were utilized for the calibration of the OpenSees full bridge model and HS computational model. The elastic SAP2000 bridge model was also used to decide on the test specimen subassembly geometry development and boundary conditions, refer to discussion in Chapter 3. For the particular objective of finalizing the experimental test specimen boundary condition, a simple SAP2000 model was also developed for the test specimen subassembly. Discussion of the specimen model is presented first then followed by the full bridge elastic model discussion in the following two subsections.

4.2.1   Subassembly Specimen Analysis

A simple linear elastic model for the test subassembly was developed using SAP2000. The model used 1D beam-column elements for the bent cap beam and the column and 2D plane stress shell elements for the box-girder. Two different views of the developed subassembly model are shown in Figure 4.15. Linear analysis under vertical and lateral concentrated loads at the column top in the inverted position of the test subassembly was carried out. The purpose of the linear analysis was to try different boundary conditions and compare the forces and bending moment distribution in the different subassembly components against the corresponding full bridge case. Four different cases of boundary conditions were investigated as shown in Figure 4.16. A sample of the analysis results for the third case of the boundary conditions is shown in Figure 4.17 and Figure 4.18. When compared to the prototype bridge, it was found that either case 3 or 4 gave better match for bent cap beam response. Also the effect of the whether using full fixation or hinges at the box-grader ends was minimal relative to bent cap beam response. It was concluded that whether the seat beams sought for the specimen boundary conditions were too stiff or not, they did not alter the behavior in the vicinity of the bent cap beam.
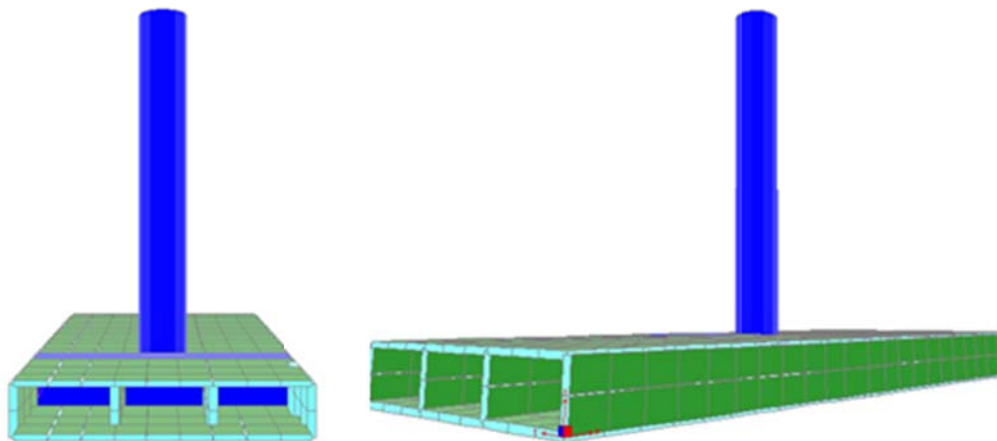
Figure 4.15 Test subassembly SAP2000 model

105
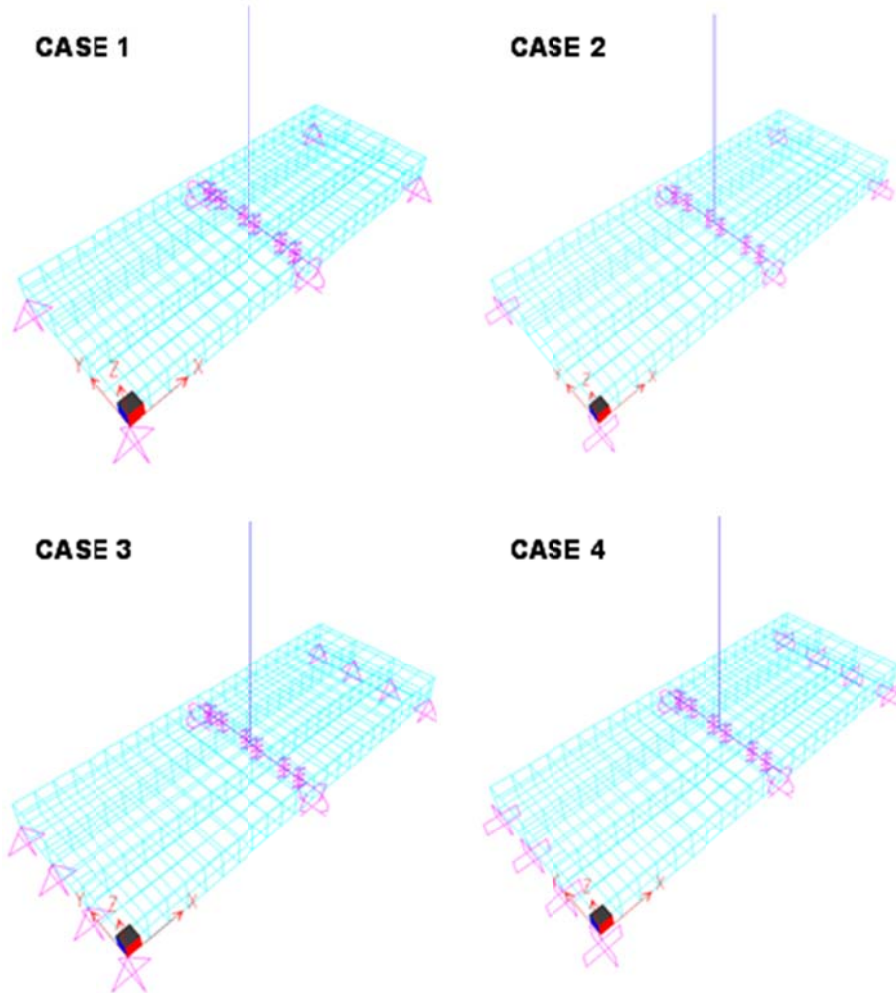
Figure 4.16 Investigated boundary conditions of the test subassembly
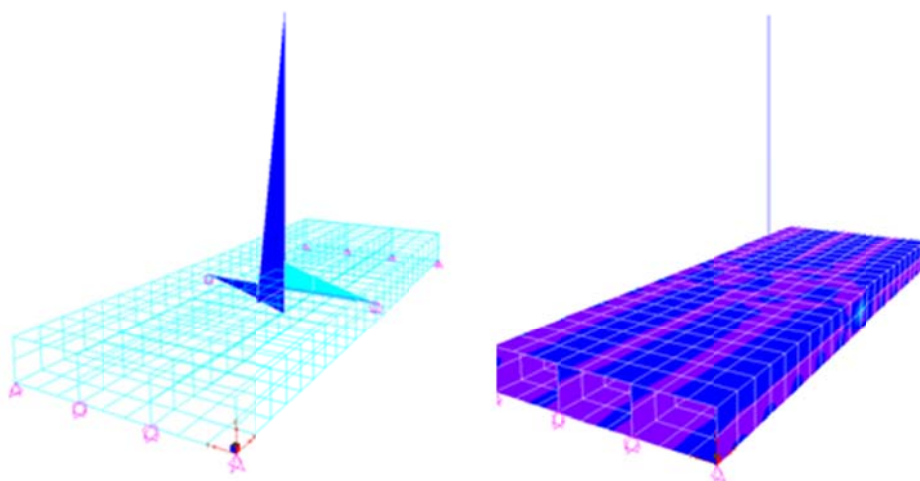
Figure 4.17 Sample of linear analysis results of subassembly model due to lateral transverse loading: moment distribution in the cap beam and column (left); moment distribution in the subassembly deck in the transverse direction (right)
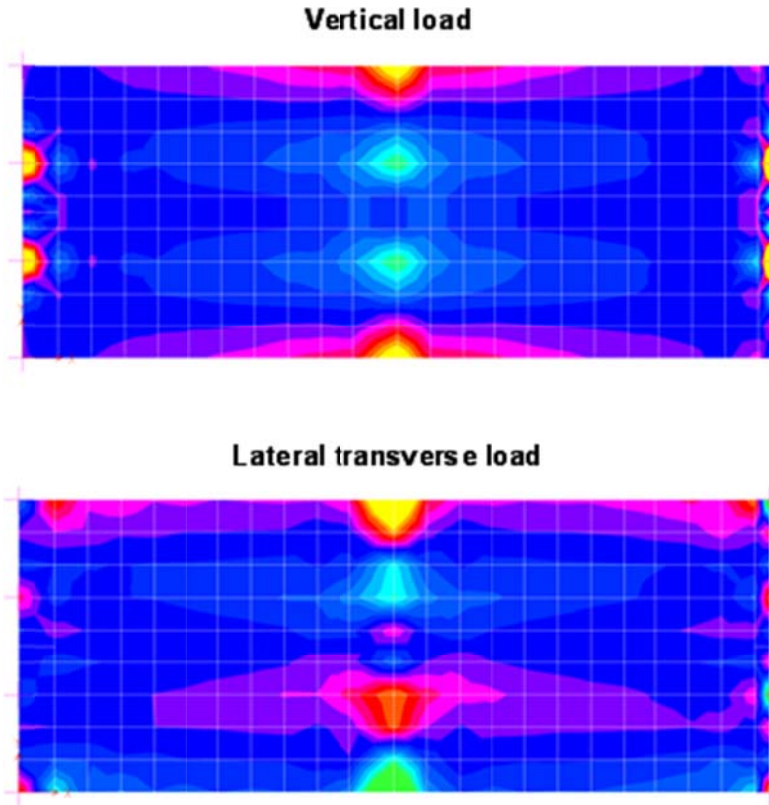
Figure 4.18 Stress distribution in the deck slab due to two different load cases

4.2.2 Prototype Bridge Analysis

As previously mentioned, the prototype bridge SAP2000 model was used as the reference for designing the subassembly geometry, boundary conditions, and reinforcement. The bridge model used 2D shell elements for the box-girder superstructure and beam-column elements for the bent columns and cap beam as illustrated in Figure 4.19. The full prototype bridge was analyzed under gravity, i.e. dead weight and live traffic loads, and lateral loads to provide design forces and bending moments for the reduced-scale test specimen as discussed in details in Appendix A. It is to be noted that proper similitude relationships were adopted for scaling the straining actions. The linear analysis of the prototype was used to also determine locations of zero-moments for choosing the subassembly geometry and dimensions. A sample of the bridge analysis under gravity and lateral transverse load is shown in Figure 4.20.

Moreover, an eigen solution analysis was performed using the SAP2000 prototype bridge model. For its accuracy in defining the full superstructure mass and proper lateral stiffness of the bridge bents, the obtained periods and modes of vibration from this analysis were considered the reference for all dynamic aspects that followed throughout the study. The main three modes of vibrations and corresponding periods for the full prototype bridge in the transvers, longitudinal, and vertical directions are shown in Figure 4.21. The obtained periods were used in calibrating the lumped mass values for the OpenSees prototype bridge model and the DIANA test subassembly model used to conduct dynamic time history analyses. These periods were utilized as well in the experimental program to calibrate the mass used in the computational part of the HS.

107
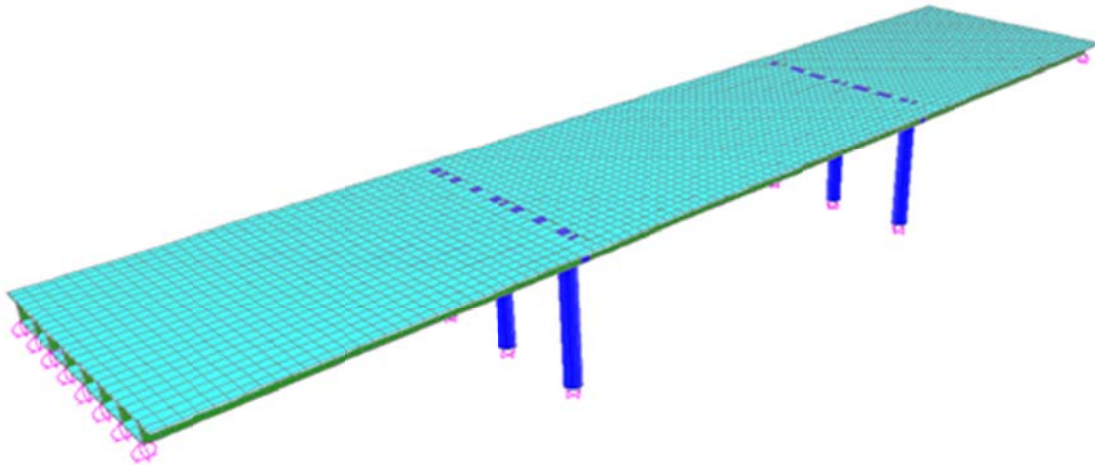
Figure 4.19 Three-dimensional view of the prototype SAP2000 model.

Vertical load
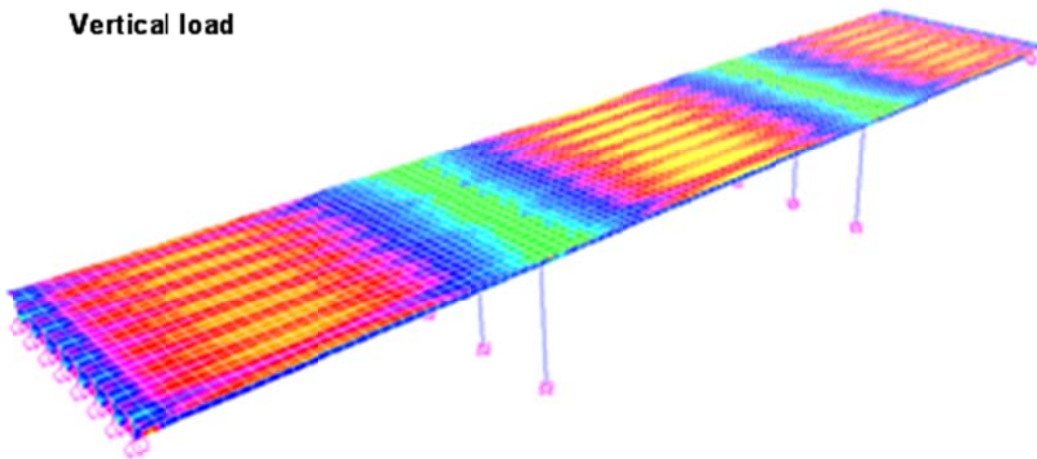
Lateral transverse load
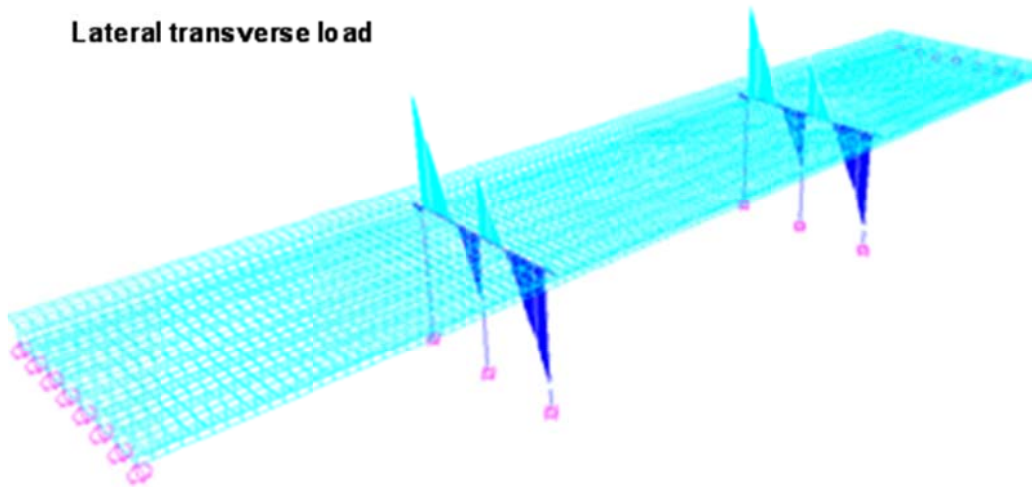
Figure 4.20 Sample of linear analysis results of prototype model: moment distribution in bridge deck in the longitudinal direction (top), and moments in bent cap beam (bottom)

$T_{trans} = 1.22$ sec
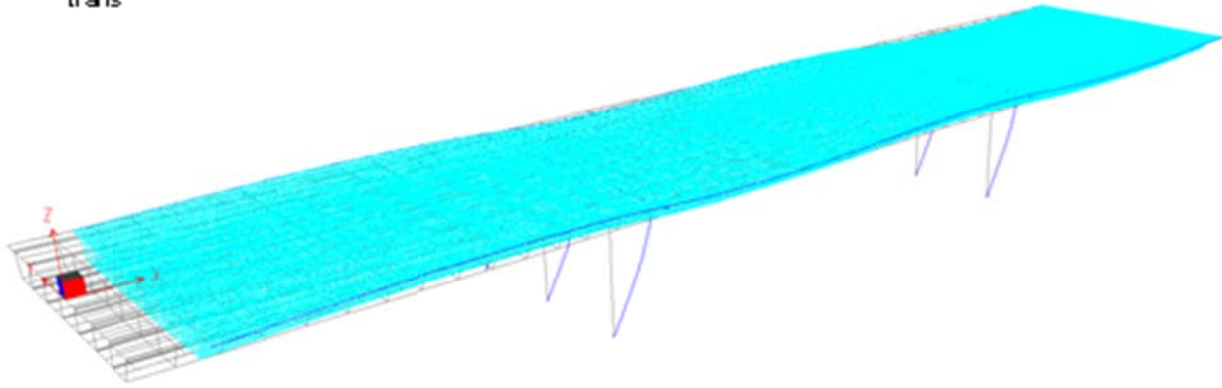
$T_{long} = 1.02$ sec
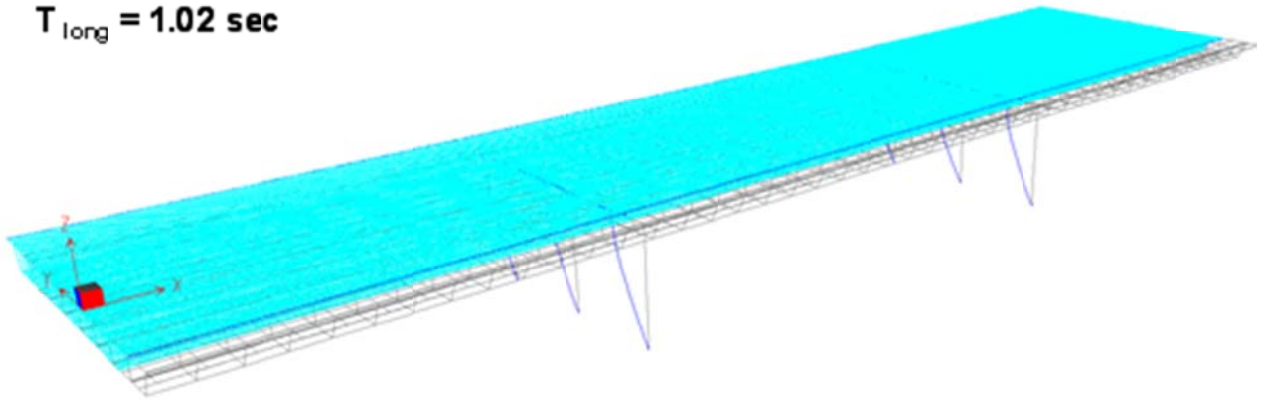
$T_{vertical} = 0.40$ sec
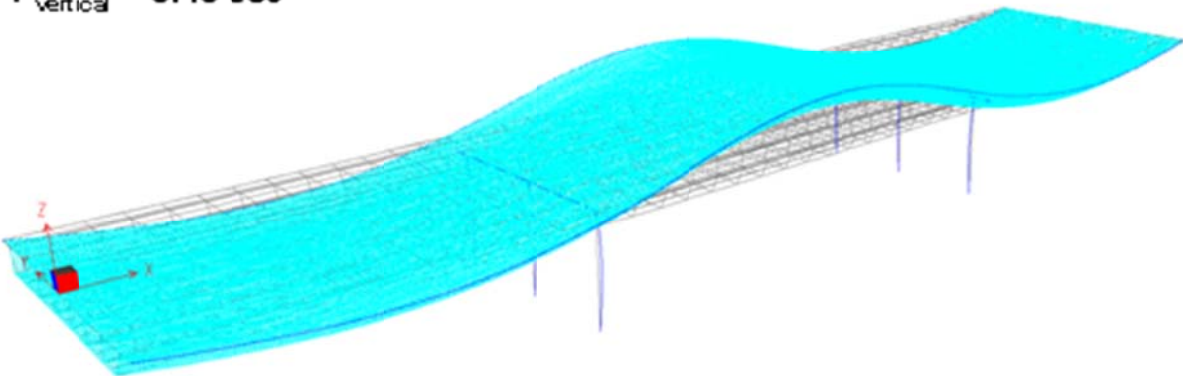
Figure 4.21 Three main modes of vibration and corresponding periods for the prototype bridge in the transverse, longitudinal, and vertical directions

4.3   3D MODELING OF REINFORCED CONCRETE

Accurate modeling of the stress states and damage of a highly non-homogeneous material such as RC has always been challenging. It becomes more challenging when macro structural system models that feature different cases of static and dynamic loading are sought as a part of structural analysis and design procedures. Many computational methods exist for 3D modeling of the structural systems; how well these models reflect the actual behavior of RC bridges, particularly systems subjected to combined gravity and lateral loading, is not clear. Therefore, the third type of models developed in this study using 3D solid elements in DIANA (2014) was first utilized in the pre-test analysis phase, but calibrated later as part of the post-test analysis phase against the experimental results to gain confidence on how the actual behavior is reflected through the computational modeling.

Advanced constitutive modeling of RC is the essence of the detailed 3D DIANA FE models. A discussion of the basics of 3D modeling of RC using FE formulation and using DIANA is presented in this section. The discussion is divided into three subsections that cover concrete modeling, reinforcing steel, and the nonlinear solution strategies utilized throughout this computational research. A short note on the FE formulation is presented first for completeness. A standard FE displacement formulation was adopted in this project. Displacement vector, $\{u\}$, within each element is interpolated from the vector of nodal degrees of freedom, $\{d\}$, using specific shape functions that depend on element type, $[N]$, as given in Equation (4-1).

$$\{u\} = [\mathrm{N}]\{d\} \tag{4-1}$$

The strain vector within the element, $\{\varepsilon\}$, is obtained from the displacement by differentiation as in Equation (4-2).

$$\{\varepsilon\} = \partial\{\mathrm{u}\} \tag{4-2}$$

where ∂ is the usual differential operator used in the case of small deformation. Combining Equations (4-1) and (4-2), the strain can be evaluated directly from the nodal displacements as given in Equation (4-3) using the strain shape function, $[B]$.

$$\{\varepsilon\} = \partial[\mathrm{N}]\{\mathrm{d}\} = [\mathrm{B}]\{\mathrm{d}\}. \tag{4-3}$$

Using the principle of virtual work, the element stiffness matrix can be computed from Equation (4-4) such that:

$$\text{External Work = Internal Work} \rightarrow \quad \delta\{u\}^T \{r\} = \int_V \delta\{\varepsilon\}^T \{\sigma\} \ dV \tag{4-4}$$

where $\{r\}$ is the vector of element external loads, δ indicates a virtual quantity, $\{\sigma\}$ is the stress vector within the element, and V represents the element volume. From Equations (4-3) and (4-4), the element stiffness matrix, $[k]$, can be derived as given by Equation (4-5).

$$[k] = \int_V [\mathrm{B}]^T [E][\mathrm{B}] \ dV \tag{4-5}$$

where $[E]$ is the constitutive matrix. In this study, only the nonlinear behavior due to material damage is reflected in the matrix $[E]$ whereas the nonlinear geometry due to large displacements is not considered. Finally, using standard FEM assembly procedure, the global stiffness matrix of the structure, $[K]$, is assembled. Similarly, the global nodal loads vector, $\{R\}$, is assembled leaving the global nodal displacements $\{D\}$ the only unknown in Equation (4-6).

$$[K]\{D\}=\{R\} \tag{4-6}$$

More details on the considered element types, the concrete and reinforcing steel material models, and the solution method of the above nonlinear system of equations are presented next.

4.3.1 Modeling of Concrete

4.3.1.1 Element Types

Two different types were used in the developed 3D DIANA models according to the meshing algorithm used. Auto-meshing algorithms in DIANA generate only tetrahadron (pyramid) elements. However, extruding quadrilateral faces or surface elements produces the brick elements. Auto-meshing was first used for preliminary analysis and then a revised version of the model that utilized brick elements was developed. Only the brick element based-models are considered for model calibration and post-analysis phases. The first type of elements used is the 12 DOFs pyramid TE12L element, Figure 4.22(a), which comprises four nodes with 3 DOFs per node and three sides and uses the isoparametric formulation. It is based on linear interpolation in terms of the natural coordinates ξ, η, and ζ given by Equation (4-7), and uses numerical Gauss integration. The linear polynomials yield a constant strain and stress distribution over the element volume. For numerical integration, DIANA by default applies a 1-point integration scheme over the volume. However, 4- and 5-point integration schemes are available too for TE12L elements.

$$u_i(\xi,\eta,\zeta) = \alpha_0 + \alpha_1\,\xi + \alpha_2\,\eta + \alpha_3\,\zeta \tag{4-7}$$

where $i = 1$ to 12 and α_0 to α_3 are constants determined by standard FEM.

The second type of elements used in this study is the eight-node isoparametric 24 DOFs solid brick HX24L element shown in Figure 4.22(b). Similar to the TE12L, the brick element is based on linear interpolation and Gauss integration. The polynomials for the translation displacement field use tri-linear interpolation as expressed by Equation (4-8).

$$u_i(\xi,\eta,\zeta) = \alpha_0 + \alpha_1\,\xi + \alpha_2\,\eta + \alpha_3\,\zeta + \alpha_4\,\xi\eta + \alpha_5\,\eta\zeta + \alpha_6\,\zeta\xi + \alpha_7\,\xi\eta\zeta \tag{4-8}$$

where $i = 1$ to 24 and α_0 to α_7 are constants determined by standard FEM.

Typically, a rectangular brick element approximates the strain and stress distribution over the element volume as follows. The strain ε_{xx} and stress σ_{xx} are constant in x direction and vary linearly in y and z direction. The strain ε_{yy} and stress σ_{yy} are constant in y direction and vary

linearly in x and z direction. The strain ε_{zz} and stress σ_{zz} are constant in z direction and vary linearly in x and y direction. By default DIANA applies a $2 \times 2 \times 2$ integration scheme. A $1 \times 1 \times 1$ scheme is an available option. For either element type, the nonlinear material behavior of the concrete is incorporated using nonlinear constitutive model.

| Tetra-hadron (pyramid) TL12L | Tri-linear brick HX24L |
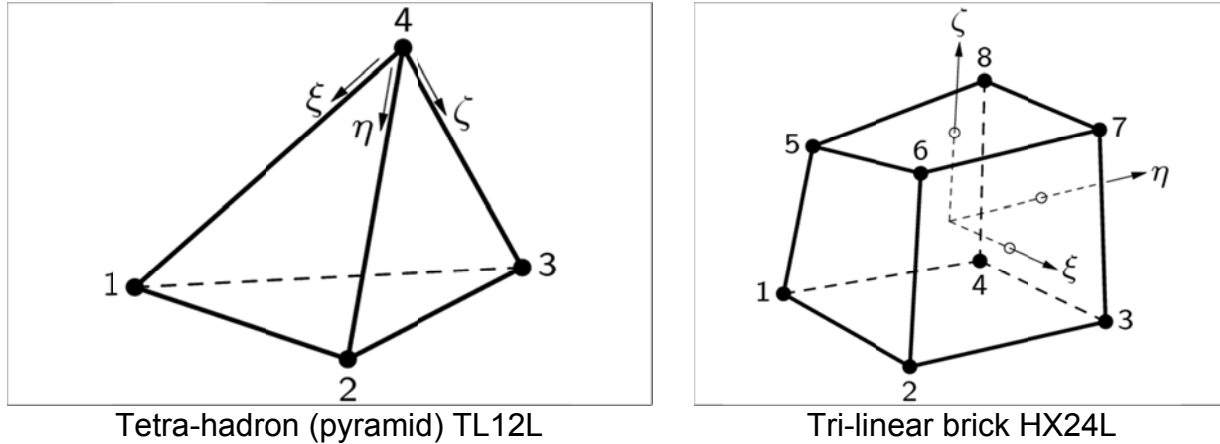
Figure 4.22 Used element types in the 3D DIANA models

4.3.1.2 Constitutive Models

Concrete is a complex material with different tensile and compressive behavior, which depends on the confinement. When concrete reaches its tensile strength, it cracks with diminishing strength as the crack width increases. The cracks are geometrical discontinuities that separate the material. To model the cracking behavior of materials, there are two basic approaches, the discrete crack approach and the smeared crack approach (Rots 1991; Bažant and Planas 1998). The discrete crack approach reflects the final damaged state most closely. It models the crack directly via a displacement-discontinuity in an interface element that separates two solid elements. The discrete approach does not fit the nature of the FE displacement method. In addition, it is computationally more convenient to employ a smeared crack approach. In this latter approach, a cracked solid element can be still considered a continuum but requires proper account of the stiffness change according to certain stress-strain relationships. This second approach is the one utilized throughout this computational research. It is worth noting that the underlying assumption of displacement continuity in smeared cracking contradicts the nature of the geometrical discontinuities that occurs across a crack. This assumption in some cases is known to cause stress locking (Rots 1991) and mesh bias.

Furthermore, the concrete behavior using the smeared crack approach can be modeled using either a multi-directional fixed-crack method or a total strain rotating-crack method. The multi-directional fixed-crack method considers that the orientation of the cracks remain constant, and in turn, the stress-strain relationships are evaluated in a fixed coordinate system that is set once cracking initiates. On the other hand, the total strain rotating-crack method considers that the orientation of the cracks rotates with the directions of the principal strains. Only the total strain method, which was developed along the lines of the 2D modified compression field theory (Vecchio and Collins 1986) and extended to 3D by Selby and Vecchio (1993), is utilized in this study. The total strain formulation follows the coaxial stress-strain concept, which is also known as the rotating crack model, where the stress-strain relationships are evaluated in the principal

112

directions of the strain vector. The basic concept of the total strain-based crack models is that the stress is evaluated in the directions given by the crack directions. The strain vector $\{\varepsilon\}_{xyz}$ in the element coordinate system xyz at iteration $i+1$ at time (or pseudo-time for nonlinear static loading) $t+\Delta t$ is updated with the strain increment $\{\Delta\varepsilon\}_{xyz}$ according to Equation (4-9).

$$
{}^{t+\Delta t}_{i+1}\{\varepsilon\}_{xyz} = {}^{t}\{\varepsilon\}_{xyz} + {}^{t+\Delta t}_{i+1}\{\Delta\varepsilon\}_{xyz}
$$

(4-9)

This strain vector is subsequently transformed to the crack coordinate system nst (refer to the insert in Figure 4.23) with the continuously-varying strain transformation matrix ${}^{t+\Delta t}_{i+1}[T] = \left[T\left({}^{t+\Delta t}_{i+1}\{\varepsilon\}_{xyz}\right)\right]$ according to Equation (4-10).

$$
{}^{t+\Delta t}_{i+1}\{\varepsilon\}_{nst} = {}^{t+\Delta t}_{i+1}[T] \; {}^{t+\Delta t}_{i+1}\{\varepsilon\}_{xyz}
$$

(4-10)

The strain transformation matrix is determined by calculating the eigen vectors of the strain tensor. During loading, the concrete is subjected to both tensile and compressive stresses, which may result in cracking and crushing of the material. The deterioration of the material due to cracking and crushing in 3D structures is monitored with six internal damage variables $\alpha_k, k=1,\ldots,6$ (Figure 4.23). The loading-unloading-reloading conditions are monitored with unloading constraints $r_k, k=1,\ldots,6$ (Figure 4.23), which model the stiffness degradation in tension and compression separately. These constraints for tension and compression are expressed as given in Equations (4-11) and (4-12), respectively.

$$
r_k = \begin{cases} 0 & \text{if } {}^{t+\Delta t}_{i+1}\varepsilon_k > \alpha_k \\ 1 & \text{if } {}^{t+\Delta t}_{i+1}\varepsilon_k \leq \alpha_k \end{cases}, \quad k = 1,2,3
$$

(4-11)

$$
r_k = \begin{cases} 0 & \text{if } {}^{t+\Delta t}_{i+1}\varepsilon_{k-3} < \alpha_k \\ 1 & \text{if } {}^{t+\Delta t}_{i+1}\varepsilon_{k-3} \geq \alpha_k \end{cases}, \quad k = 4,5,6
$$

(4-12)

With the assumption of no damage recovery, the stress in direction j is given by Equation (4-13).

$$
\sigma_j = f_j\left(\{\alpha\},\{\varepsilon\}_{nst}\right) \times g_j\left(\{\alpha\},\{\varepsilon\}_{nst}\right)
$$

(4-13)

where f_j is the uniaxial stress-strain relationship and g_j is the loading-unloading function. If unloading and reloading is modeled with a secant approach, g_j is given by Equation (4-14).

$$
g_j = \begin{cases} 1 - \dfrac{\alpha_j - \varepsilon_j}{\alpha_j} & \text{if } \varepsilon_j > 0 \\ 1 - \dfrac{\alpha_{j+3} - \varepsilon_j}{\alpha_{j+3}} & \text{if } \varepsilon_j < 0 \end{cases}
$$

(4-14)
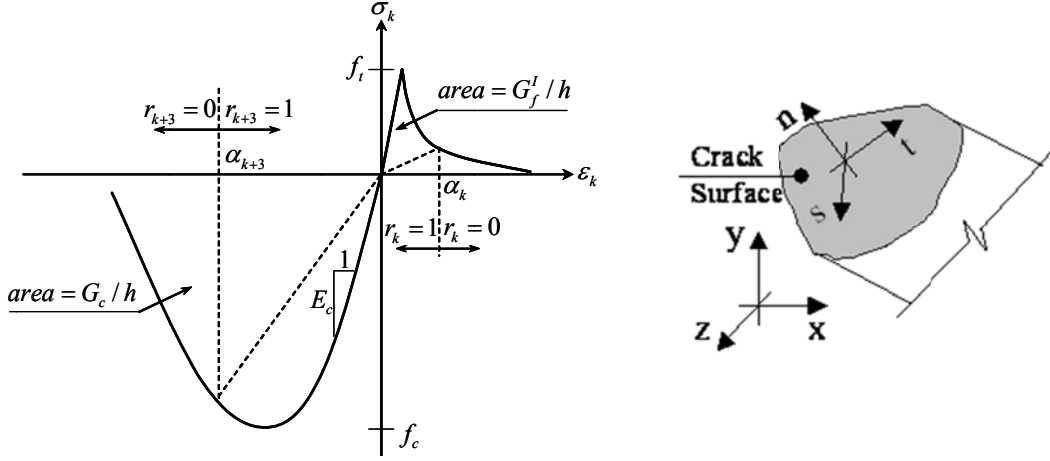
Figure 4.23 Rotating crack surface and unidirectional concrete material model in principal directions

For the incremental-iterative solution scheme, the constitutive model should define the stiffness matrix, which is utilized to achieve equilibrium. In this study, a secant stiffness matrix approach is adopted. This approach has proven to be robust and stable in RC structures with extensive cracking. For this purpose, the secant stiffness terms in the j-th direction are presented in Equations (4-15) and (4-16) for the tensile and compressive regimes, respectively.

$$\overline{E}_j = f_j\big(\{\alpha\},\{\varepsilon\}_{nst}\big)/\alpha_j \qquad \text{(for tension regime)} \tag{4-15}$$

$$\overline{E}_j = f_j\big(\{\alpha\},\{\varepsilon\}_{nst}\big)/\alpha_{j+3} \qquad \text{(for compressin regime)} \tag{4-16}$$

These secant stiffness terms can be geometrically interpreted as the slopes of the dashed inclined lines shown in Figure 4.23. The secant stiffness matrix in the *nst* coordinate system is given by Equation (4-17) which corresponds to the stiffness matrix of an orthotropic material with zero Poisson's ratio in all directions.

$$D_{secant} = \begin{bmatrix} \overline{E}_1 & 0 & 0 & 0 & 0 & 0 \\ 0 & \overline{E}_2 & 0 & 0 & 0 & 0 \\ 0 & 0 & \overline{E}_3 & 0 & 0 & 0 \\ 0 & 0 & 0 & \overline{G} & 0 & 0 \\ 0 & 0 & 0 & 0 & \overline{G} & 0 \\ 0 & 0 & 0 & 0 & 0 & \overline{G} \end{bmatrix} \tag{4-17}$$

where $\overline{G} = \beta_s G$ and the parameter β_s ($0 \leq \beta_s \leq 1$) is a non-dimensional shear retention factor that reduces the elastic shear modulus G of concrete after cracking to the constant value $\overline{G}$. For the full definition of all components and parameters of total strain crack model in DIANA, the basic properties, e.g. Young's modulus, are complemented with input for the compression, tension,

and shear behavior. For behavior in compression, the uniaxial stress-strain relationship for the concrete is based on elastic-perfectly-plastic behavior, shown in Figure 4.24(a), and governed by the concrete compressive strength f_c. The tensile relationship is based on linear tension softening, shown in Figure 4.24(b). The tensile behavior depends on the concrete tensile strength f_t and the fracture energy G_f^I from crack opening mode, i.e. mode I. The areas under the compressive and tensile stress-strain relationships control the ultimate compressive strain and the crack strain beyond which the concrete loses its entire respective capacities. These areas depend on the band-width (h), i.e. localization size, of plastification or damage due to cracking which is expressed as $h = \sqrt[3]{V_e}$ where V_e is the volume of the FE. It is to be noted that for the pre-test analysis, expected material properties were used for f_c and f_t as defined by Caltrans SDC (2013) based on nominal concrete properties. Meanwhile, the fracture energy, G_f^I, was related to other concrete materials using the CEB-FIP Model Code recommendation (1993). However, for the post-test analysis actual material properties were used including that for the fracture energy.
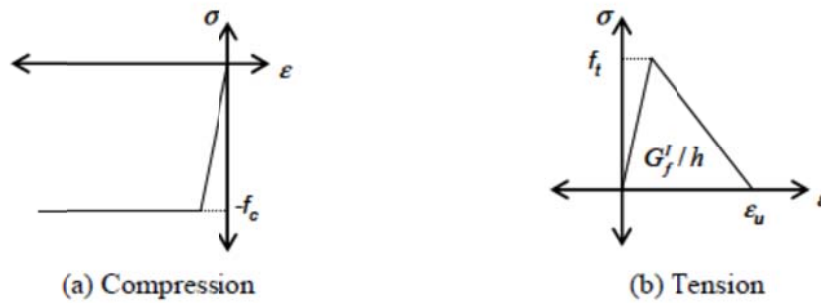
Figure 4.24 Concrete stress-strain relationships

4.3.2   Modeling of Steel Reinforcement

Modeling of steel reinforcement, including any prestressing tendons, using FE is commonly performed by one of two different methods (DIANA 2014, Naito et al. 2001). The first method, which is less computationally demanding, involves the use of embedded or smeared reinforcement within the concrete. The embedded reinforcement action is introduced in the concrete element through which it passes, and the stiffness of the concrete element is modified accordingly. The embedded reinforcement formulation implies perfect bond between the concrete and the reinforcement. However, bond-slip reinforcement could be used as well, which is the second method used for modeling reinforcement. The bond-slip reinforcement is more computationally demanding and involves separate discretization of the reinforcement from the surrounding concrete, i.e. the reinforcing bar is internally modeled using 1D discrete truss or beam elements, which are connected to the mother concrete elements by line-solid interface element. These interface elements between the concrete element edge and the reinforcement line element is what is needed to model the bond-slip effects. A schematic of both of the embedded and discrete reinforcement in a parent element is shown in Figure 4.25 (a) and (b), respectively. One drawback of the discrete method is the additional nodes and DOF required. For example, Figure 4.25 suggests that when embedded reinforcement is adopted, two brick elements with total of 36 DOF can be used. On the other hand, discrete representation of reinforcement requires the use of eight brick elements for concrete and two 1D elements for the reinforcement in

115

addition to interface elements between the steel and the concrete to represent the slip and dowel actions. This latter modeling technique requires solving for 90 DOF. Another drawback for discrete reinforcement is that the concrete mesh is restricted by the reinforcement locations. This restriction makes the concrete mesh difficult to generate, particularly in situations such as the sough test specimen which has high reinforcement ratios and tight box-girder dimensions. Therefore, only embedded reinforcement was considered for the pre-test analysis. It is worth noting that no bond-slip was observed from the experiments, so embedded reinforcement was used in post-test analysis as well. More details about embedded reinforcement formulation and constitutive modeling are presented next.

a) Embedded reinforcement   b) Discrete reinforcement
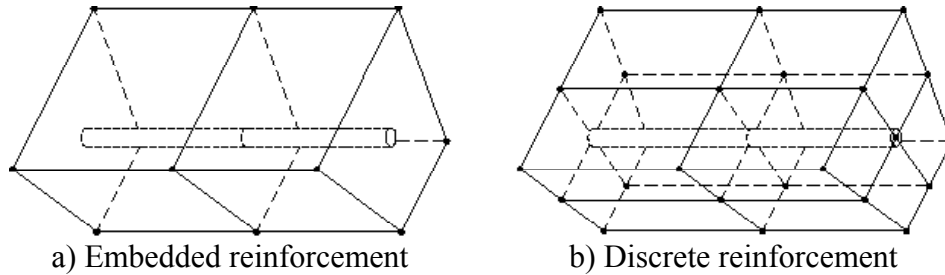
Figure 4.25 Reinforcement elements in FEA

4.3.2.1 Embedded Reinforcement

Embedded reinforcement is introduced within the concrete element through which it passes, referred to as the parent element. The stiffness of this "parent element" is then modified based on the path of the reinforcement through the element. As a result, the assumption is made that there exists perfect bond between the concrete and the reinforcement. For the simple case where a uniform quantity of reinforcement is distributed across the element at a certain angle from the element natural coordinate system, the additional stiffness terms are easily computed. Given that the element displacements are computed from the nodal displacements, the reinforcement displacements, $\{u\}^r$, can be found using the same shape functions matrix, [N] as those for the concrete elements as given by Equation (4-18).

$$\{u\}^r = [\text{N}]\{d\} \tag{4-18}$$

However, the reinforcement displacements are evaluated at the isoparametric coordinates of the reinforcement integration points, e.g. using 2-point Gauss integration scheme. The strain vector of the reinforcement can accordingly be evaluated by Equation (4-19).

$$\{\varepsilon\}^r = [\text{B}]^r \{d\} \tag{4-19}$$

where $[\text{B}]^r$ is the strain–displacement matrix evaluated at the reinforcement integration points. Standard transformation techniques are used to obtain the reinforcement strain vector in the same orientation as the parent element strain vector. Making use of transformation, reinforcement constitutive equations, and usual FE procedure, one can obtain the contribution of reinforcement to the stiffness of the parent element and the corresponding internal force vector of the reinforcement. Accordingly, the stiffness and internal force contributions of the reinforcement

116

are accounted for in a similar manner as the concrete element stiffness and internal forces with only the exception that integration is performed at the reinforcement integration points rather than at the element integration points.

4.3.2.2 Constitutive Model

Reinforcing steel material is modeled assuming elasto-plastic behavior based on Von-Mises yield criterion with modulus of elasticity E_s and yield strength f_y. Two models were considered for hardening. The first is a simple uniaxial elastic-perfectly-plastic model with identical compression and tension behavior and no hardening as shown in Figure 4.26(a). The simple model is a reasonable approximation for the pre-test analysis where generic behavior trends and approximate force capacity values are sought. However, for more accurate analysis during the post-test analysis phase, the hardening rule followed the Voce (1948) equation available in DIANA, which is schematically shown in Figure 4.26(b) and presented by Equation (4-20).

$$f(\varepsilon) = \begin{cases} \varepsilon E_s \leq f_y & \varepsilon \leq \varepsilon_y + \varepsilon_{pl} \\ f_y + (f_u - f_y)\left(1 - \exp\left[-\dfrac{\varepsilon - \varepsilon_y - \varepsilon_{pl}}{\varepsilon_{po}}\right]\right) & \varepsilon \geq \varepsilon_y + \varepsilon_{pl} \end{cases} \qquad (4\text{-}20)$$

where f_y is the yield stress, f_u is the ultimate stress, E_s is the steels' Young's modulus, ε_{pl} is the plateau strain, and ε_{po} is a parameter to adjust the strain-hardening regime. For post-test analysis the Voce equation parameters (assumed to be the same for tension and compression) were calibrated against the actual reinforcing steel material properties presented in Chapter 3.
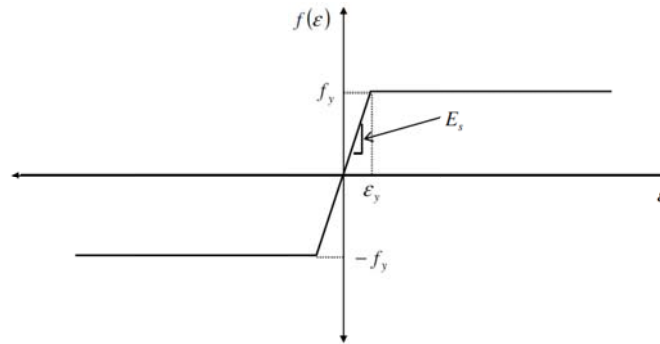
(a) Elastic-perfectly plastic
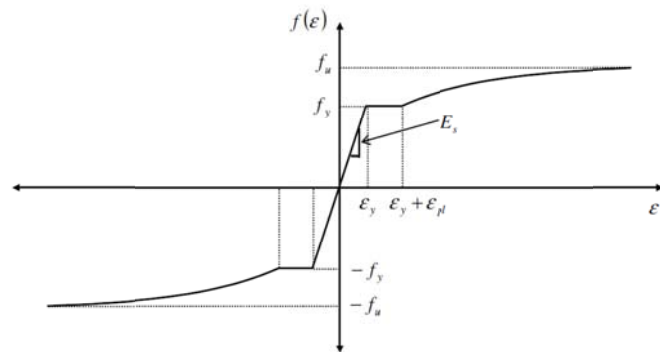
(b) Voce

Figure 4.26 Reinforcing steel stress-strain relationships

4.3.3   Nonlinear Solution Strategy

In nonlinear FEA, the relation between the force vector and displacement vector, in the weak-form of equilibrium or FE formulation, is no longer linear. Similar to the linear FEA, it is desired to calculate a displacement vector that equilibrates the internal and external forces in nonlinear FEA. To determine the state of equilibrium in nonlinear cases, the problems are not discretized only in space (with finite elements), but also in time (with increments). The time increments used can be real time increments, for creep or dynamic analysis, or pseudo-time increments to describe sequence of events, i.e. provide a counter function. To achieve equilibrium at the end of a given event (increment), iterative solution algorithm is used. When all the events (increments) are considered, the combination is called an incremental-iterative solution procedure. A brief discussion of the iterative and incremental procedures considered in this study is presented.

4.3.3.1   *Iterative Procedures*

Several iterative methods are available in DIANA. Three pure iterative procedures are available, which are the Newton-Raphson method, the Quasi-Newton method, and the Linear Stiffness method. Moreover, DIANA offers two variations that can be used in combination with any of the pure iterative procedures, which are the Continuation method and the Line Search method. Finally, several criteria to stop the iteration loop are discussed. Another variation of the iteration algorithm is the Arc-length method. The idea behind all the iterative methods is to generate a sequence of approximations u_i for the solution, i.e. the displacement vector $\{u\}$ is determined through the recovered formula given by Equation (4-21).

$$\{u_{i+1}\} = \{u_i\} + \gamma_i \left(P_f - [K]\{u_i\}\right) \tag{4-21}$$

where P_f is the assembled load vector and γ_i is an integration constant that defines the iterative solver such that eventually the residual, which is written as $(P_f - [K]\{u_i\})$, converges to zero. The three iterative procedures, mentioned above, were all used in this study and they are discussed in more details in the following:

Newton-Raphson (regular and modified)

The regular and modified Newton-Raphson methods are illustrated schematically in Figure 4.27 (a) and (b), respectively. For the regular Newton-Raphson strategy, the tangent stiffness is calculated for every iteration within a given increment. This strategy yields a quadratic convergence, which means that the iteration process converges with a few iterations. The modified Newton-Raphson strategy computes the tangent stiffness at the start of the load increment and uses this same stiffness for all the iterations within this load increment. This method usually requires more iterations than the regular Newton-Raphson, but the computations are faster for each iterations, since the tangent stiffness matrix is formulated, assembled, and decomposed only once at the beginning of each load increment. Generally, in FEA, regular Newton iteration can be used when minimal nonlinear behavior and damage (cracking or plasticity) in each increment is expected. For moderate levels of damage, the modified Newton iteration is better for convergence as it avoids calculating the stiffness of the moderately damaged elements at each iteration.

(a) Regular Newton-Raphson Method   (b) Modified Newton-Raphson Method
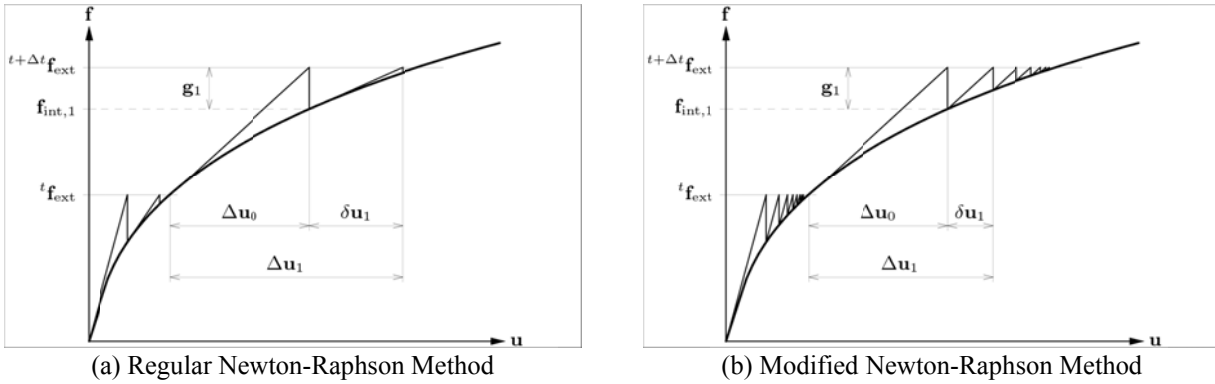
Figure 4.27 Schematic representation of ititartive nonlinear solvers (DIANA 2014)

Quasi-Newton

The Quasi-Newton method, also called "Secant method", essentially uses the information of previous solution vectors and out-of-balance force vectors during the increment to achieve a better approximation as illustrated in Figure 4.28. Unlike Regular Newton-Raphson, the Quasi-Newton method does not set up a completely new stiffness matrix at every iteration. The stiffness of the structure is rather determined from the known positions at the equilibrium path. Three different methods are available in DIANA for assembling the Quasi-Newton stiffness matrix. These are the Broyden, the Broyden-Fletcher-Goldfarb-Shanno (BFGS), and the Crisfield methods. Only the Broyden method was used in this study as it demonstrated the least rate of divergence in runs with large number of DOF.

Linear Stiffness

The Linear and Constant Stiffness iteration methods can be used if the other methods become unstable, or if it is desirable to keep certain characteristics. The linear strategy uses the initial linear stiffness matrix for all the iterations in all the load increments as illustrated in Figure 4.29. The linear stiffness method is usually very robust, especially in nonlinear dynamic analysis but it is possible that the system follows an unstable equilibrium path after bifurcations (DIANA 2014). For situations where high nonlinearity is encountered, the linear solution strategy can be used. This procedure requires many iterations to reach a converged solution. However, the cost of each iteration is low since the tangent stiffness matrix is formulated, assembled, and decomposed only once at the beginning of the analysis.
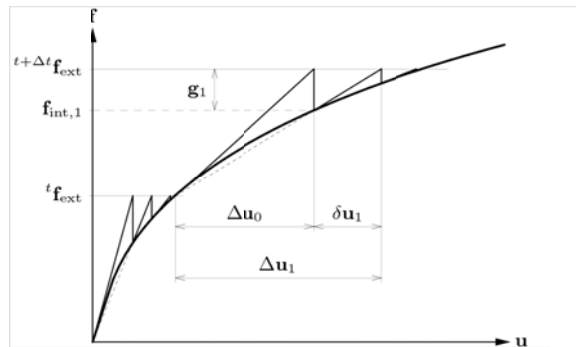
Figure 4.28 Schematic representation of Quasi-Newton iterations (DIANA 2014)

119
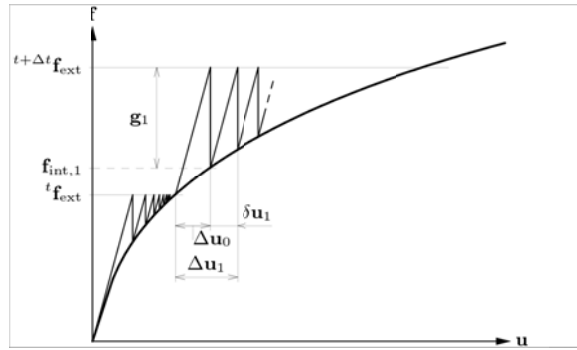
Figure 4.29 Schematic representation of Linear Stiffness iterations (DIANA 2014)

4.3.3.2 *Incremental Procedures*

The second part of the incremental-iterative solution procedure consists of the incremental procedures. The initial choice of the step size for every increment is an important factor in the incremental-iterative process. There are several methods that can be sued to determine step sizes. For instance, fixed increments, such as prescribed force increments, can be used versus adaptive increments, such as the Arc-length method where the step size is adapted based on the results of a current step. Only incremental methods that used fixed steps either in load control or displacement control were used in this study. When iterations are in process, the external force, f_{ext}, vector can be increased directly at the start of each increment. This is usually called "load control" and schematically represented in Figure 4.30(a**)**. Another way to put an external load on a structure is to prescribe certain displacements at each increment, which is called `displacement control' and shown in Figure 4.30(b).
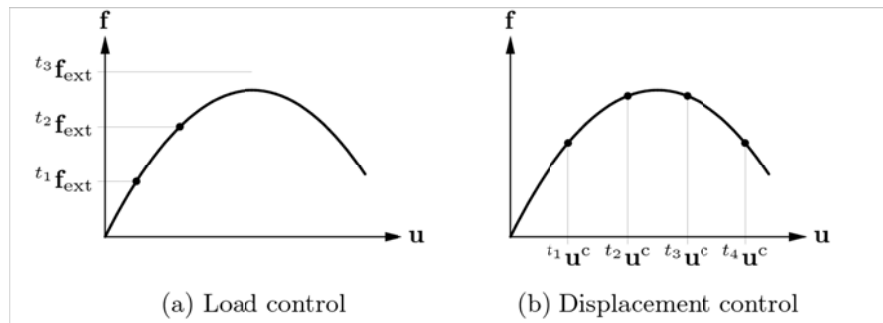
Figure 4.30 Load and displacement controls for the incremental procedure (DIANA 2014)

120

4.4 DIANA PRE-TEST ANALYSIS

The 3D modeling and analysis of the test specimen using DIANA (2014) was the most accurate and detailed model that satisfied most of the pre-test analysis objectives. The DIANA pre-test analysis aimed at: (a) estimating the subassembly column and bent cap behavior and mode of failure under different gravity and lateral load combinations, (b) estimating the expected lateral forces for accurate test setup design, and (c) determining the location and distribution of the instrumentation. Two main types of nonlinear analyses were conducted, namely pushover and time history analysis. More details about the developed DIANA 3D FE models and meshes, and selected analyses results are discussed in this section.

4.4.1 Mesh Development

Two versions of the test specimen model that used different element type were developed in DIANA (2014). The first model used the auto-meshing readily available algorithms in DIANA to create the mesh for the test specimen model. The resulting mesh composed of tetrahedron pyramid elements (TH12L). The auto-meshing resulted in a total of 7050 nodes that composed 17526 TH12L elements only for the concrete mesh elements. Additional 392 bar elements were used for the embedded reinforcement. A better mesh was developed using manual 3D meshing that started with quadrilateral 2D surface mesh at different levels that was then carefully extruded at different levels to form the final 3D mesh. This meshing process resulted in a mesh that comprised only of brick elements (HX24L). Accordingly, a total of 14347 nodes encompassing 8326 HX24L elements for the concrete mesh elements were obtained. In addition, the embedded reinforcement mesh created 348 bar elements. More details about the embedded reinforcement and the two element types used in concrete meshing were included in the previous section. A view of the two test specimen meshes that used tetrahedron and brick elements is shown in Figure 4.31 and Figure 4.32, respectively. The embedded reinforcement mesh used for both models is shown in Figure 4.33.

The tetrahedron mesh was meant to develop a quick preliminary model. Thus, the boundary conditions used in that model were mainly a full fixation at the bottom nodes of the two seat beams and two vertical roller supports at the two middle nodes in the ends of the bent cap beam portions of the model. Lateral displacement loading was applied in that model directly at the very top of the column in its inverted position. On the other hand, the brick element model was more accurate and was planned for the post-test analysis calibration and parametric study. Accordingly, the bent cap beam side plates and clevises assemblages were modeled to better account for the physical boundary conditions. The seat beams where fixed in the three translational DOFs to reflect the lateral friction at the hydrostone interface between the seat beams and the strong laboratory floor. Moreover, loading in the brick elements model was applied at the correct locations at the column head to resemble the actual testing. It is worth noting that a rectangular column head was used to replace the actual hexagonal head for simplicity of modeling and load application. Both models used the total strain crack model and an idealized elastic-perfectly plastic constitutive model, previously discussed, for modeling the concrete and the reinforcement, respectively. Nominal material properties that used the Caltrans SDC (2011) expected material properties definitions were used in defining the concrete and reinforcement material models parameters. For the case of time history analysis, a lumped mass was defined at the column head portion of the model that was calibrated to maintain similar

dynamic properties, namely the natural frequencies, as the prototype bridge, but following the proper similitude relationships.
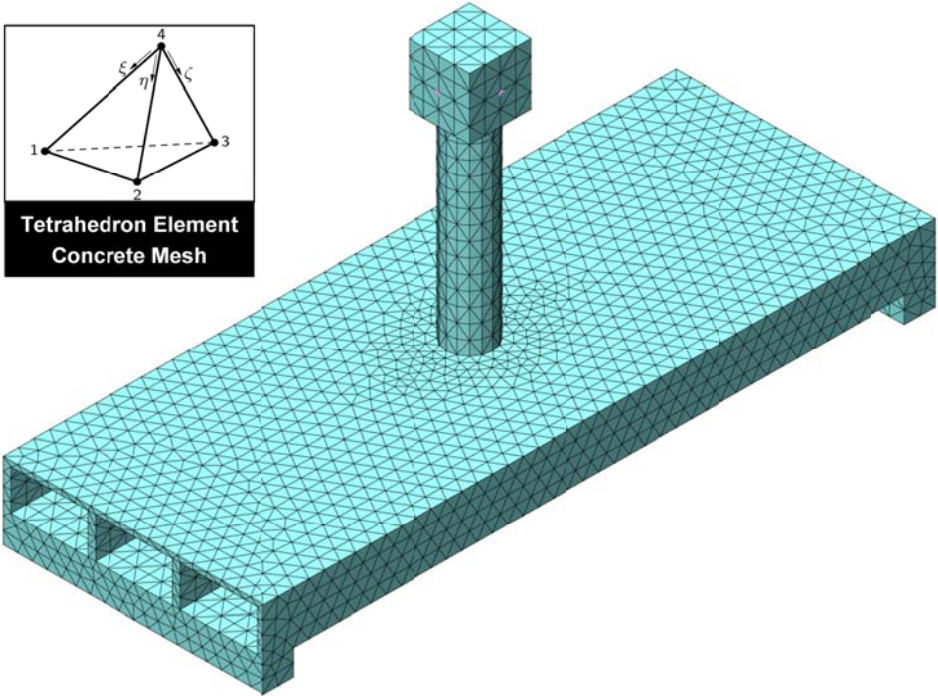
Figure 4.31 DIANA tetrahedron-element concrete mesh used for modeling the test specimen subassembly
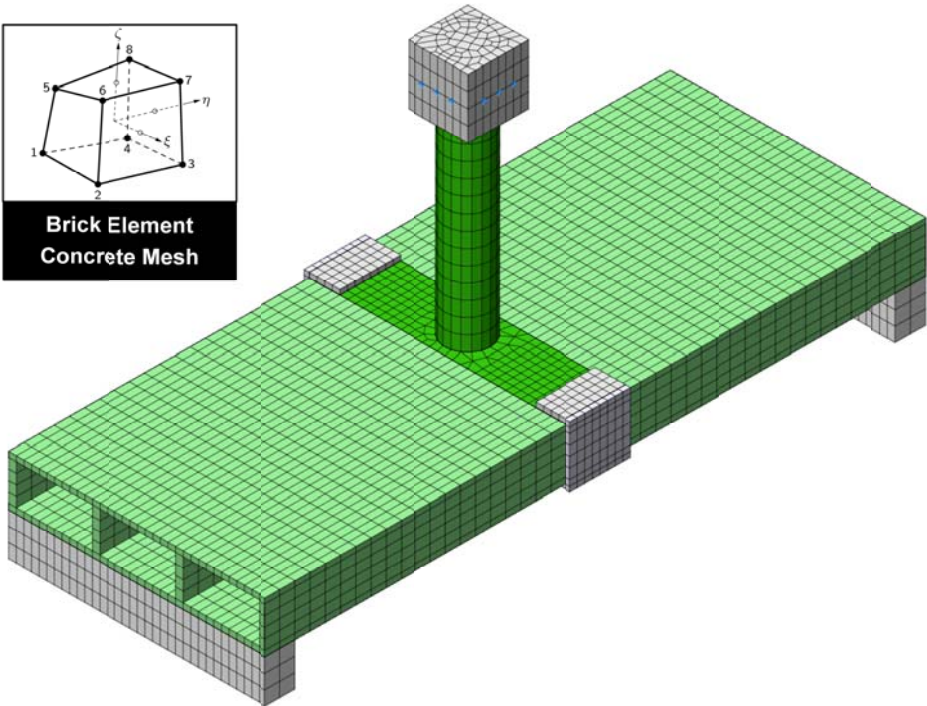
Figure 4.32 DIANA brick-element concrete mesh used for modeling the test specimen subassembly
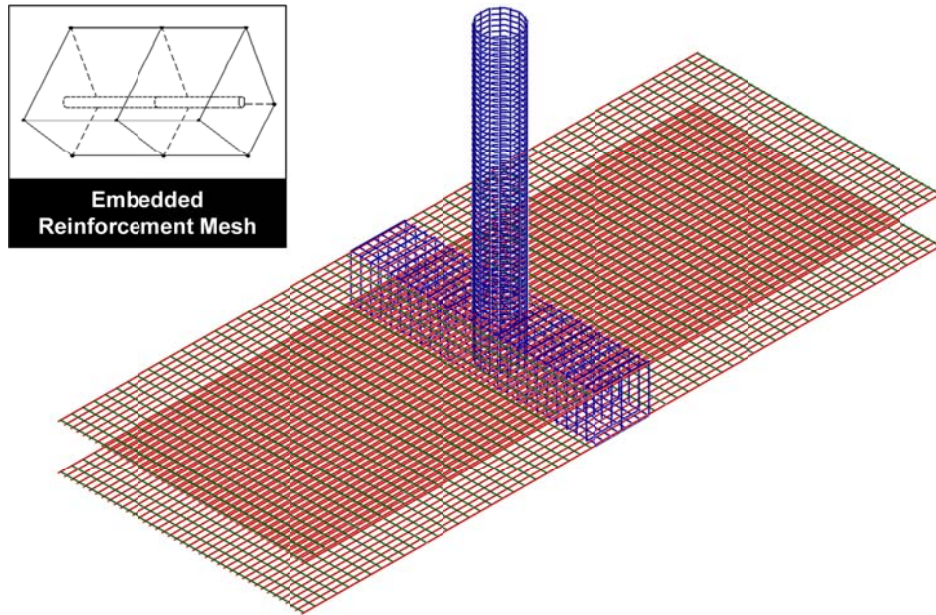
Figure 4.33 Embedded reinforcement mesh used for both DIANA 3D models of the test specimen subassembly

4.4.2 Pushover Analysis

Different sets of lateral pushover analyses were conducted at different levels of gravity loads to determine how the subassembly force capacity and mode of failure changed. It is always beneficial to first explore the expected bending moment distribution in the specimen's column and bent cap using first principals. A schematic representation for that moment distribution was previously shown in Figure 4.5 in the OpenSees analysis discussion. This bending moment distribution was the basis for conducting a series of pushover analyses. First, a vertical displacement pushover was performed to identify the capacity of the specimen subassembly in the vertical direction. The vertical capacity is dictated by the lesser flexural capacity of either the box-girder or the bent cap beam. From the specimen design (Appendix A) and sectional analysis of both sections, the box-girder in the test subassembly is expected to have a much higher capacity than the bent cap beam. Therefore, the mode of failure obtained from the vertical pushover is expected to be only attributed to the bent cap beam failure. The extensive yielding and elevated concrete crack strain values in the cap beam relative to the box-girder as obtained from the vertical pushover analysis confirm that the capacity is dictated by the bent cap failure. The vertical force-displacement relationship from the vertical pushover analysis and schematic representation of the mode of failure are shown in Figure 4.34. Moreover, the crack pattern and deformed shape of the subassembly before yield and at the final damaged state as obtained from the DIANA vertical pushover analysis are shown in Figure 4.35 and Figure 4.36, respectively.

A total of seven lateral pushover analysis sets under different constant gravity load were conducted. The seven levels of the gravity load were related to the nominal column axial capacity to obtain the following gravity load ratios (ALR) : 0%, 6%, 11%, 17%, 19%, 21%, and 23%. These values were chosen based on convenient number of load steps and number of nodes to apply equal vertical forces to eventually apply the total gravity load under force control. The

application of each of these seven gravity load cases was followed by a lateral displacement pushover in the transverse direction along the bent cap direction, which is the main focus of this study. According to the analyses, three different modes of failure were obtained, namely a failure in the column only (mode 1), failure in both of the column and the bent cap (mode 2), failure in the bent cap only (mode 3). Mode 1 of failure was observed for three cases that experienced gravity load ratios of 0%, 6%, and 11%. The crack pattern and deformed shape due to a typical mode 1 column failure is shown in Figure 4.37. The pushover force-displacement relationship for the three cases and the schematic mode of failure, mode 1, are shown in Figure 4.38. Similarly, Figure 4.39 and Figure 4.40 show the pushover curves and schematic mode of failure for the cases that experienced failure modes 2 and 3, respectively.
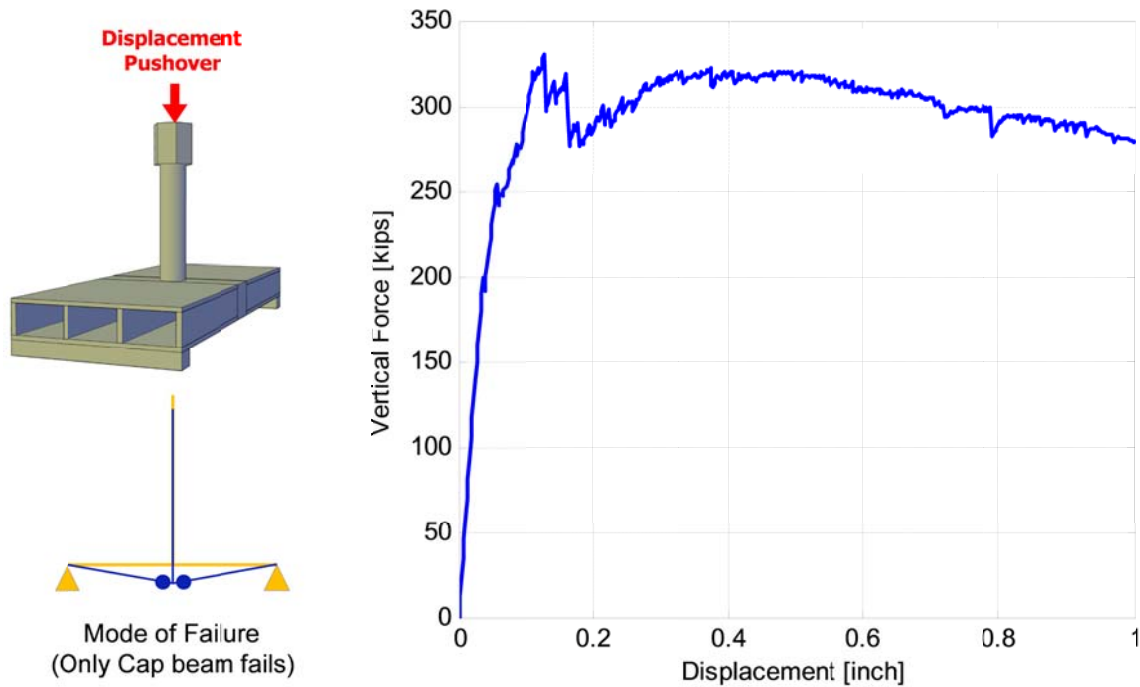
Figure 4.34 Vertical force-displacement relationship due to vertical pushover and schematic representation of the resulting mode of failure; only the cap beam fails
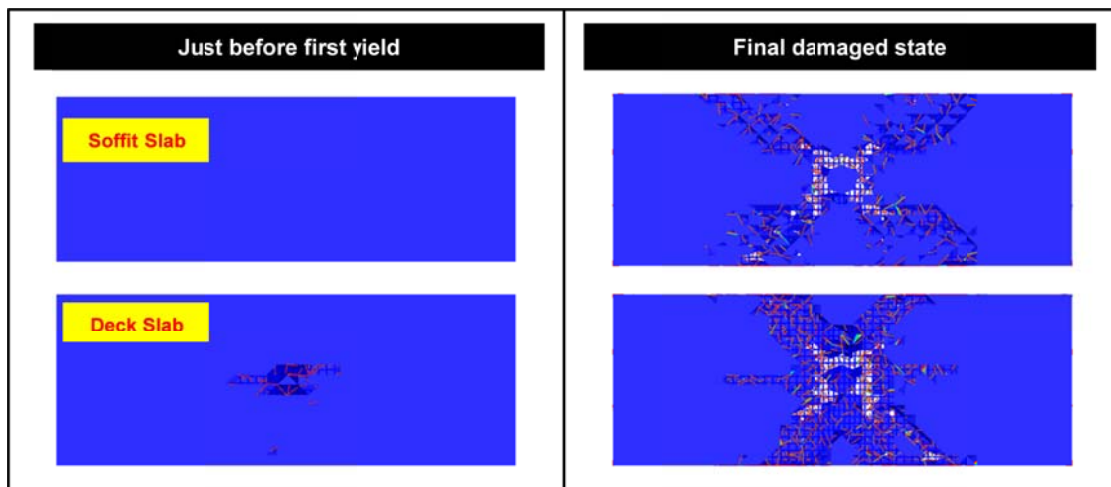
Figure 4.35 Crack pattern (DIANA) in box-girder and bent cap due to vertical pushover
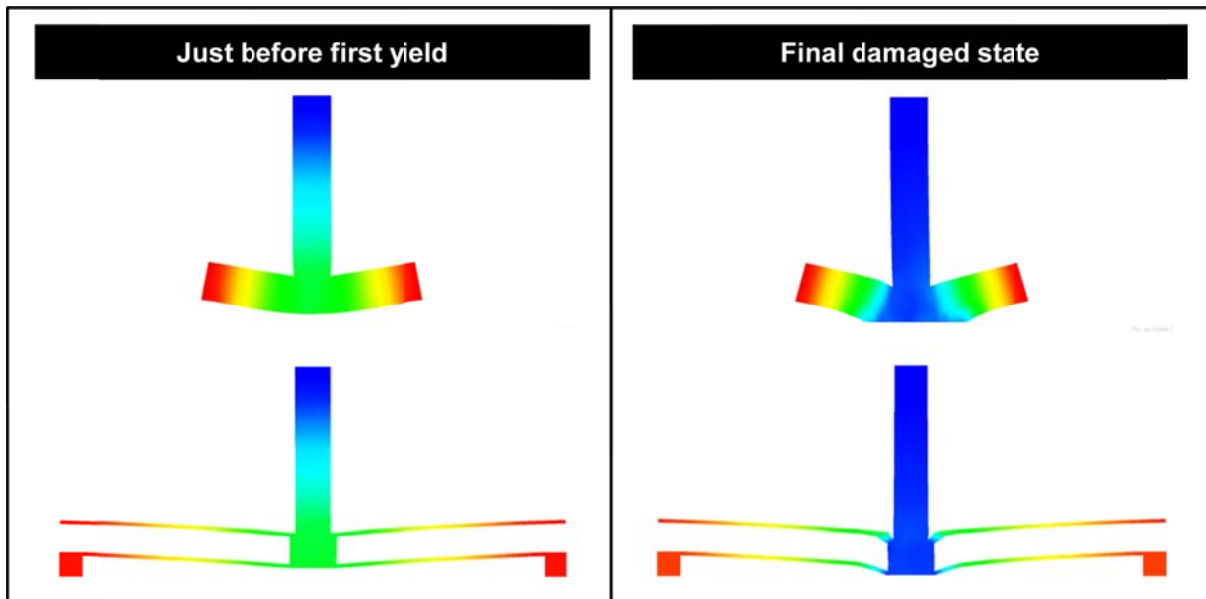
Figure 4.36 Deformed shape (DIANA) of the subassembly due to vertical pushover
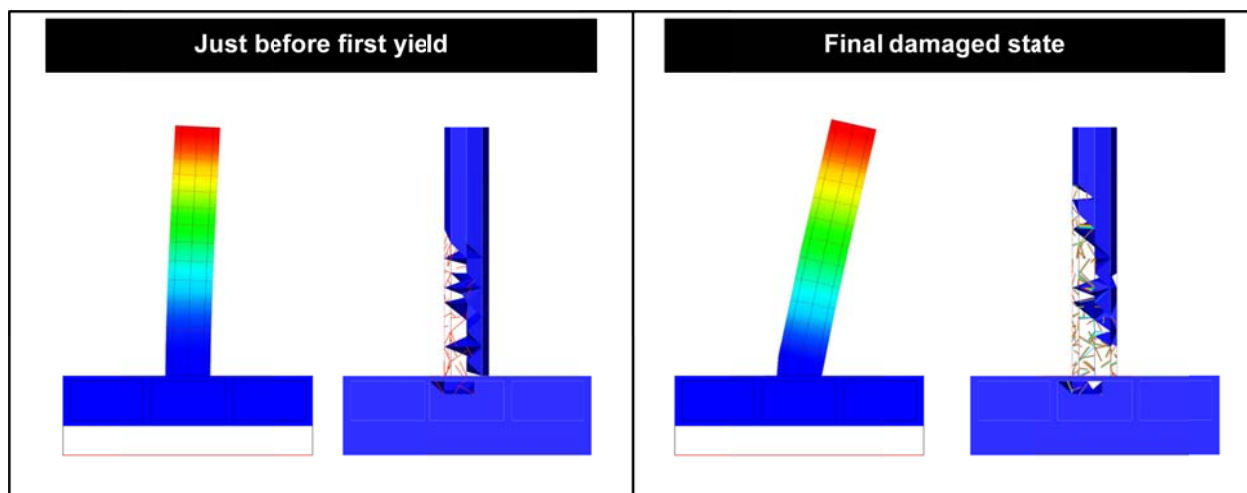
Figure 4.37 Typical crack pattern and deformed shape (DIANA) due to lateral pushover

The analyses results from the vertical pushover and the seven lateral pushover analyses were compiled together in a gravity load-lateral (vertical-horizontal) capacity interaction diagram as shown in Figure 4.41. The figure also identifies the three flexural modes of failure previously identified, i.e. plastic hinge in column only (mode 1); plastic hinge in both the column and bent cap (mode 2), and plastic hinge in bent cap only (mode 3). It is worth noting that only ductile flexural modes of failure are allowed in capacity design approach, and specifically, the first mode of failure of plastic hinge in columns only is allowed by the bridge seismic design provisions, e.g. Caltrans SDC (2013). It can be observed from the schematic moment distribution in Figure 4.5 and the envelop interaction diagram in Figure 4.41 that the gravity load directly increases the moment demand in the bent cap in this test specimen setting and may cause its failure.
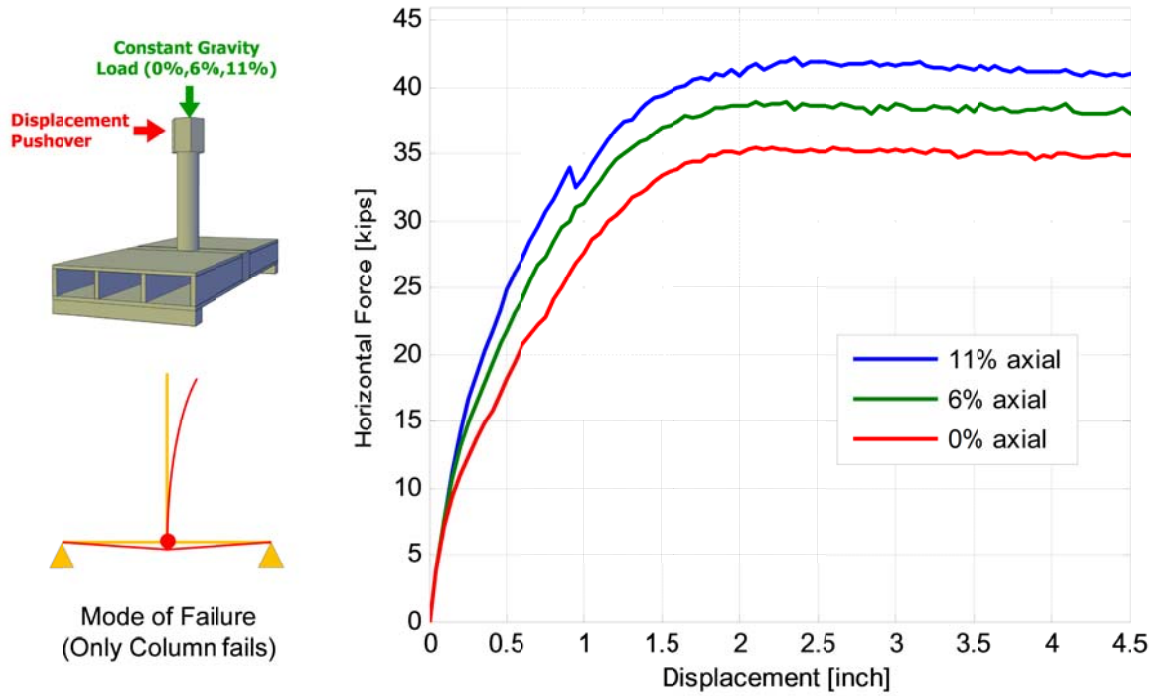
Figure 4.38 Lateral force-displacement relationship at different axial load levels (0%, 6%, and 11% of column axial capacity) and schematic representation of the resulting mode of failure; only the column fails
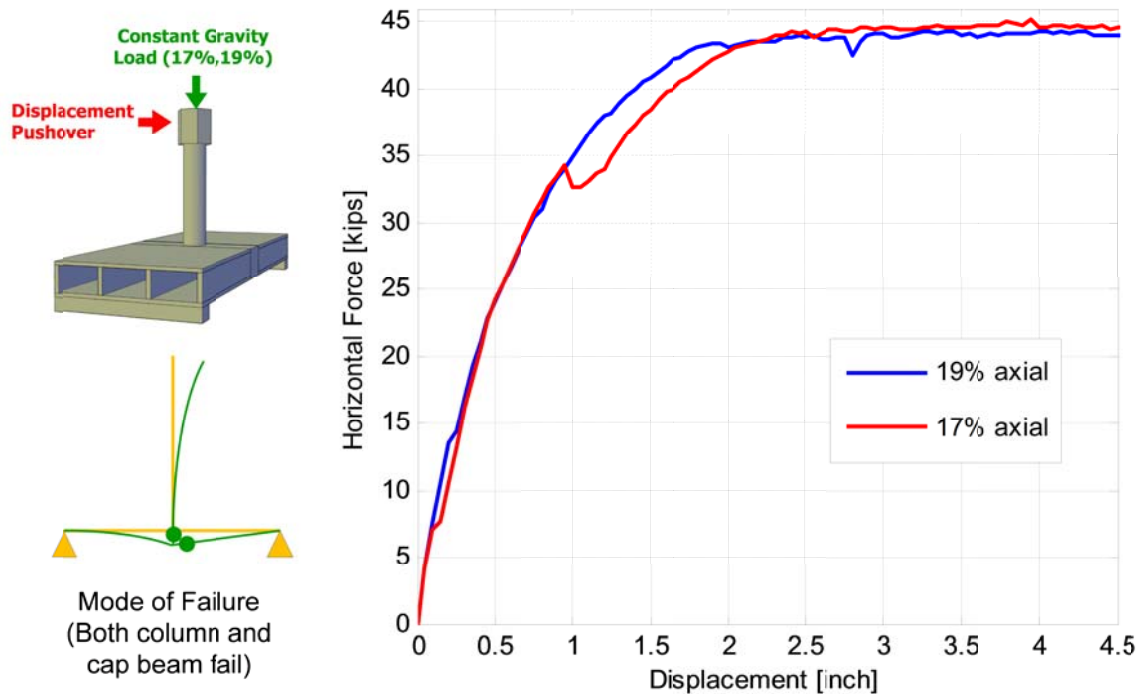
Figure 4.39 Lateral force-displacement relationship at different axial load levels (17% and 19% of column axial capacity) and schematic representation of the resulting mode of failure; both the column and cap beam fail

126
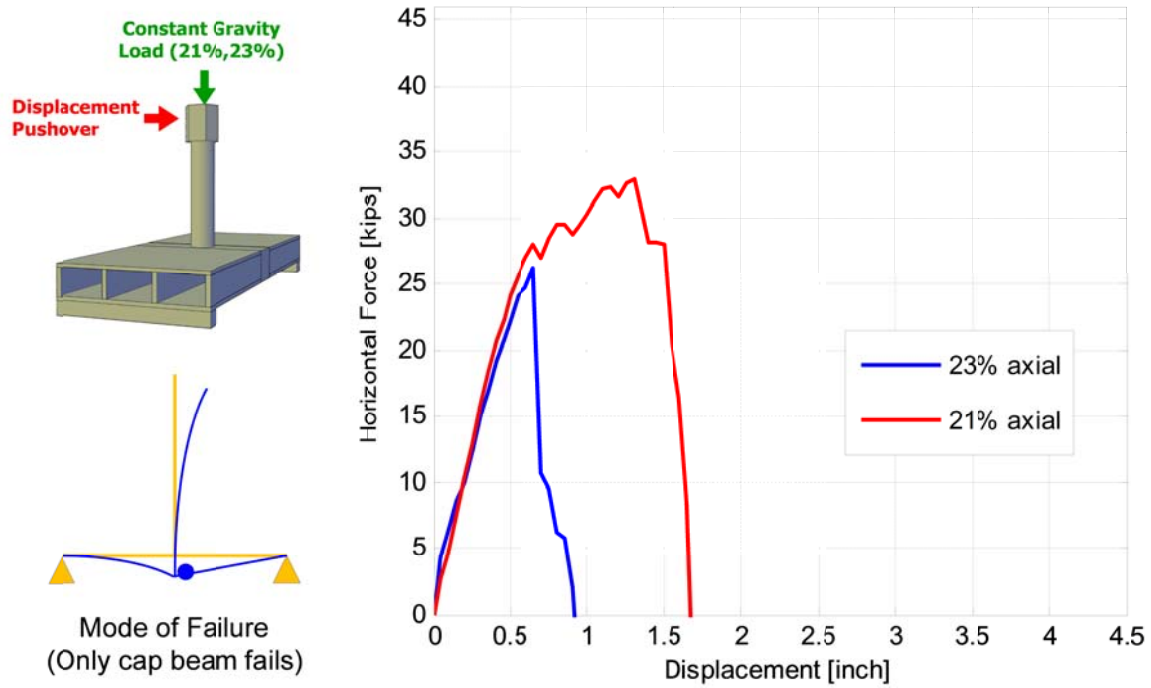
Figure 4.40 Lateral force-displacement relationship at different axial load levels (21% and 23% of column axial capacity) and schematic representation of the resulting mode of failure; only the cap beam fails
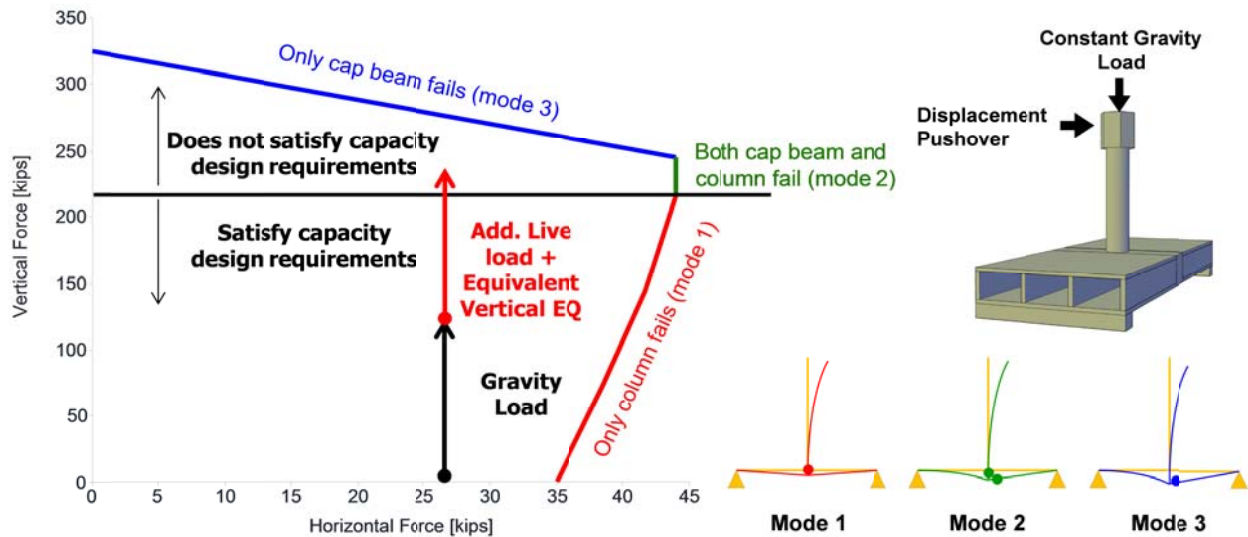
Figure 4.41 An envelope of the horizontal and vertical load values at failure which summarizes the different pushover analysis cases and the corresponding modes of failure from DIANA specimen model

Based on the insight provided by the detailed set of pushover analyses, it was desired to apply the gravity loading in the conducted tests such that it represents as many of the above-mentioned modes of failure as possible. However, due to the capacity of the actuators used in the experimental testing, it was concluded that the 6% and 11% were appropriate for the as-built first specimen (SP1) test which was meant to evaluate the bent cap behavior and modes of failure that

followed from adopting the latest code provisions. However, for the retrofitted second specimen (SP2) test, increasing the demands on the bent cap was the main goal to investigate the behavior of the bent cap into the inelastic range. Thus, an additional gravity load level that corresponded to the 17% gravity load ratio case discussed above was used. It is to be noted that for actual testing, the absolute gravity load values were related to the Caltrans axial column capacity that was based on the expected concrete strength rather than the actual one. Accordingly, the final 3 gravity load ratios (ALR) from the tests were 5%, 10%, and almost 15% which corresponded to the 6%, 11%, and 17% from the analysis that used the expected concrete strength. These gravity load levels were tied to the vertical excitation resulted from the time history analysis as discussed in the next subsection.

4.4.3 Time History Analysis

The two detailed DIANA models were used to conduct different nonlinear time history analyses. Several gravity load levels were combined with different ground motions that were selected from the short list adopted from the OpenSees prototype bridge analysis (Table 4-2). Different components of the ground motions were used in the analysis. A preliminary set of analyses that used two horizontal components besides the vertical one were conducted first to understand the behavior of the test specimen subassembly under the effect of 3D ground motion. However, more dedicated analyses focused on using only one horizontal component in the transverse direction, and compare it to the case when the same transverse horizontal component was used with the corresponding vertical component. The latter two cases are schematically shown in Figure 4.42. Only sample of the several runs are shown here for brevity. First, the analysis under 25% Loma Prieta ground motion at 11% gravity load using the transverse horizontal and the vertical components are shown. Figure 4.43 and Figure 4.44 show the displacement history, force history, and force-displacement relationship in the lateral transverse and vertical directions, respectively. Another example is the 50% Northridge ground motion recorded at Sylmar station at 23% gravity load when only transverse horizontal component is included, where Figure 4.45 and Figure 4.46 show the lateral and vertical response of this other example, respectively. For comparison purposes, the response from 50% Northridge ground motion at 23% gravity load but using both horizontal and vertical components is presented in Figure 4.47 and Figure 4.48 for the lateral and vertical response, respectively.
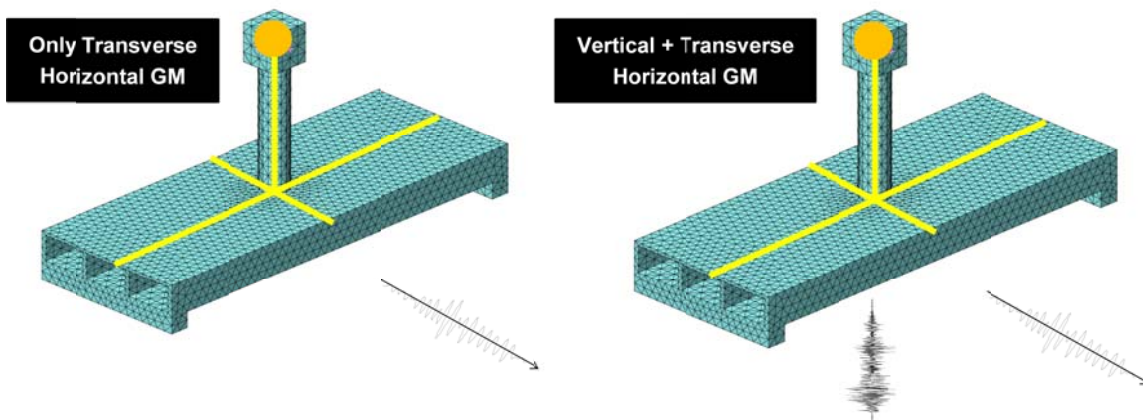
Figure 4.42 Schematic representation of the test specimen DIANA model with lumped mass at column top and tetrahedron elements for two different time history analysis cases
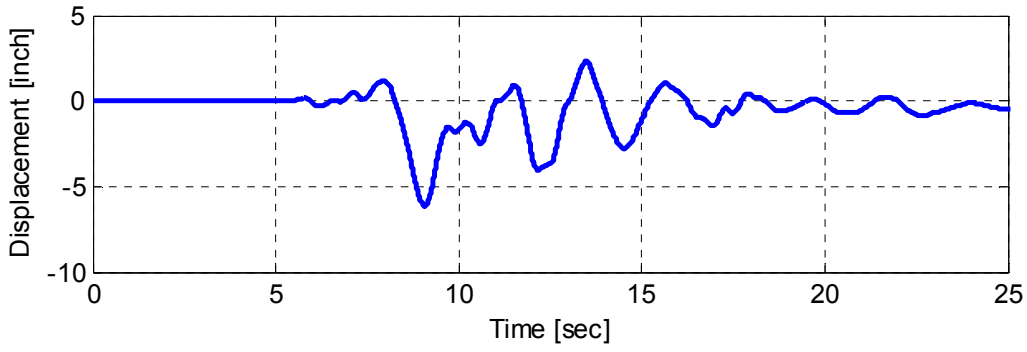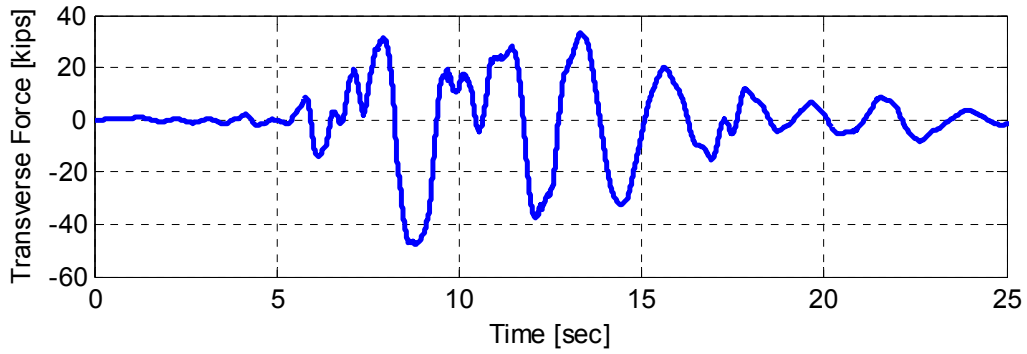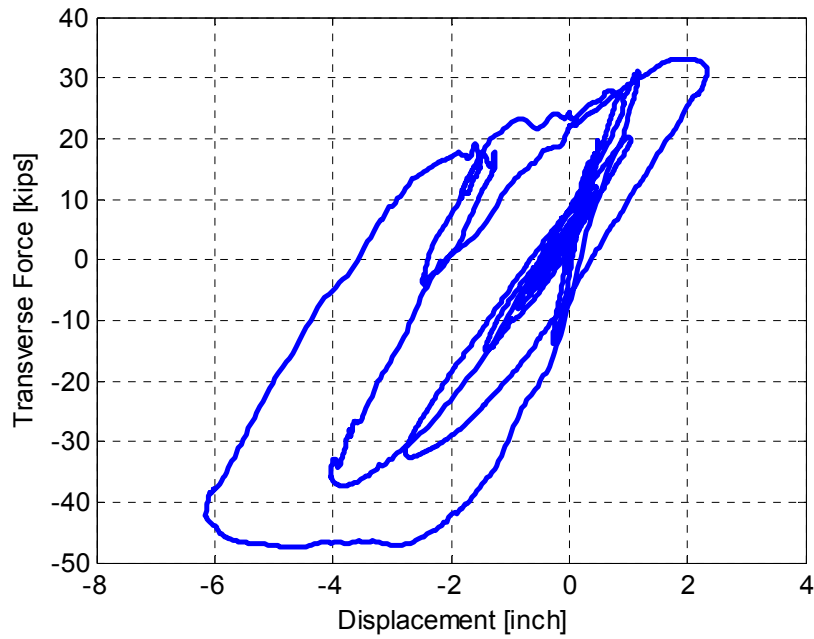
Figure 4.43 Analysis results for the case of 25% Loma Prieta GM (transverse and vertical components) and 11% constant gravity load of column axial capacity: (a) Lateral displacement history (b) Lateral force history (c) Lateral force-displacement relationship
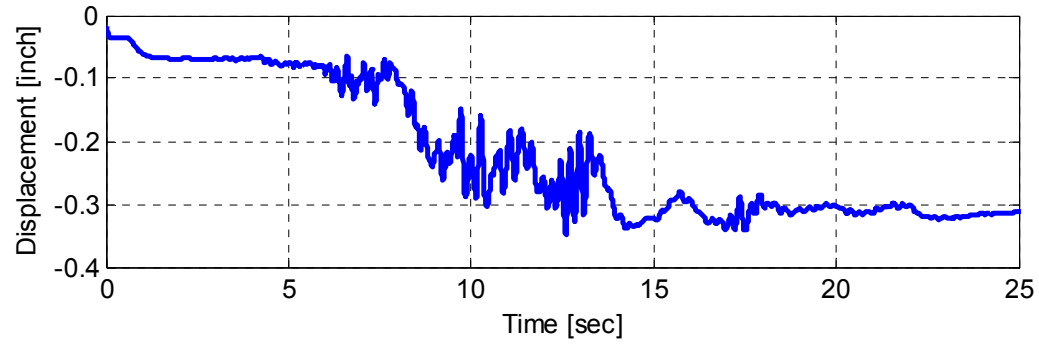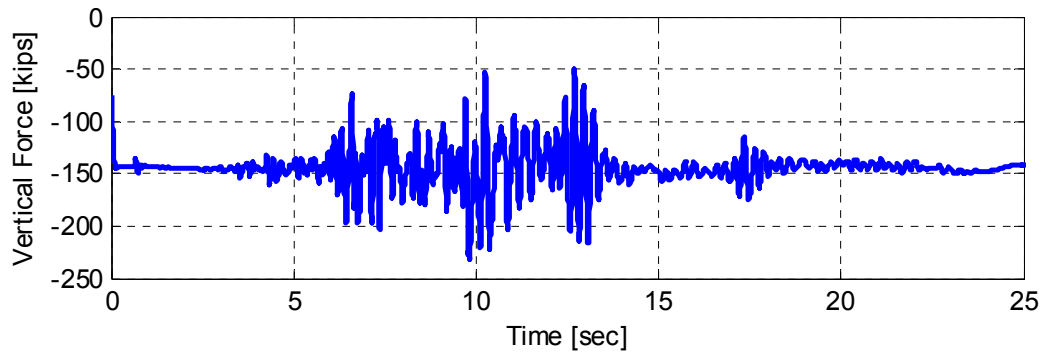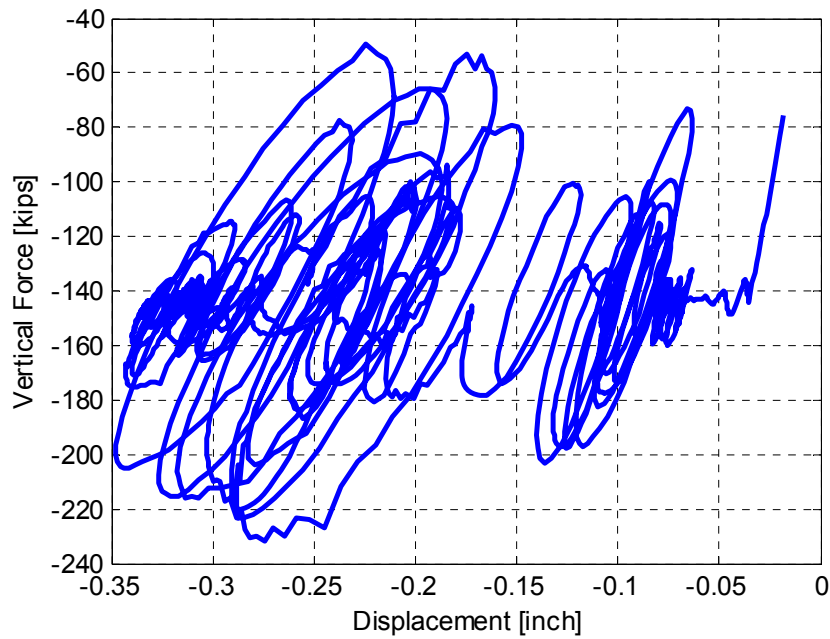
Figure 4.44 Analysis results for the case of 25% Loma Prieta GM (transverse and vertical components) and 11% constant gravity load of column axial capacity: (a) Vertical displacement history (b) Vertical force history (c) Vertical force-displacement relationship
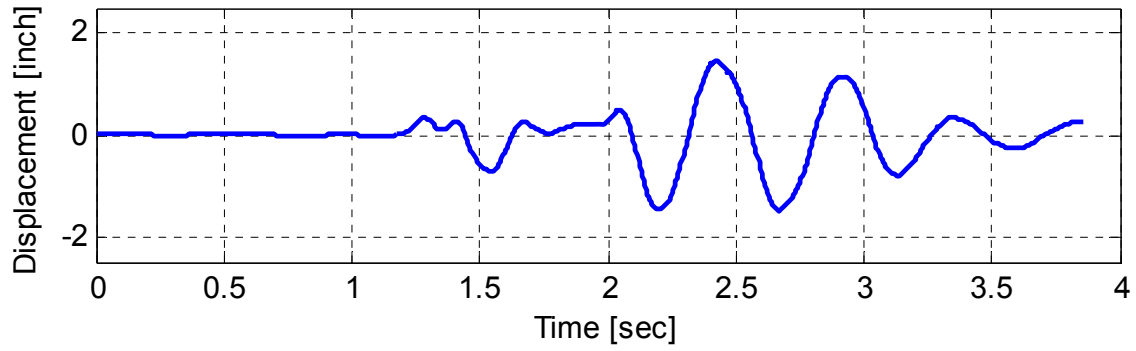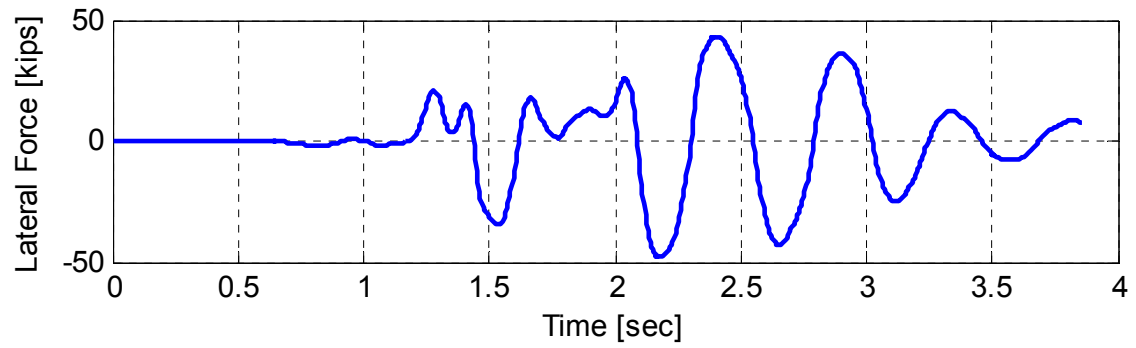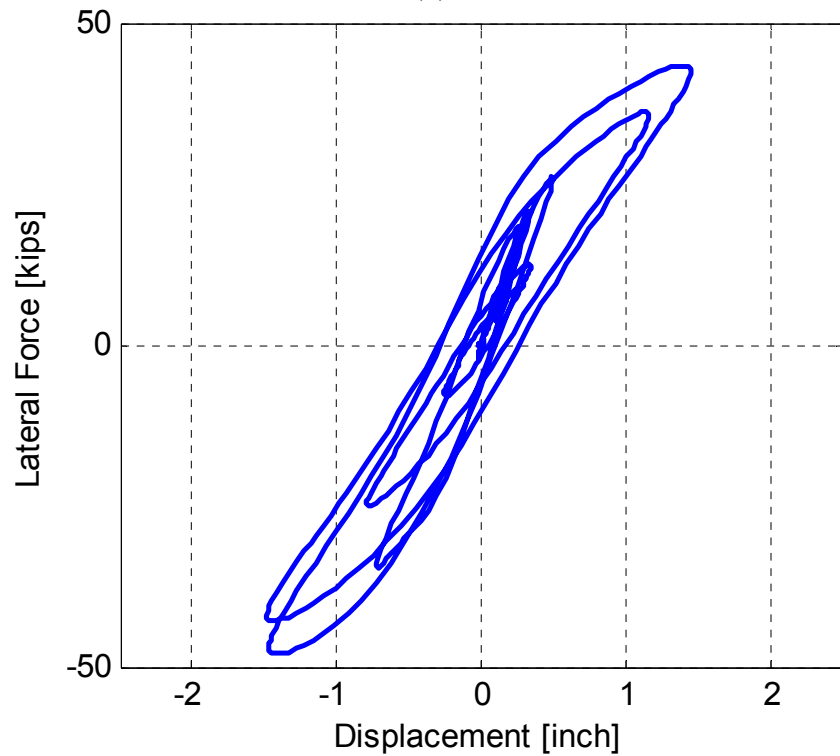
Figure 4.45 Analysis results for the case of 50% Northridge GM (Sylmar record) with only horizontal excitation and 23% constant gravity load of column axial capacity: (a) lateral displacement history, (b) lateral force history, (c) lateral force- displacement relationship

131
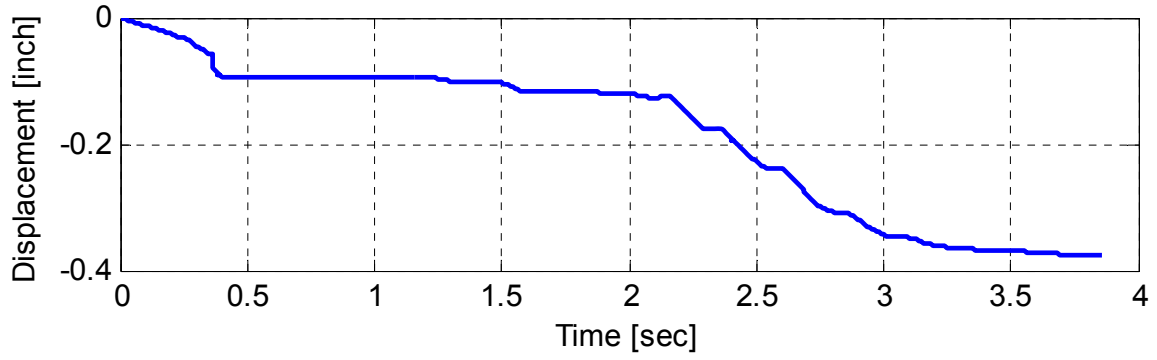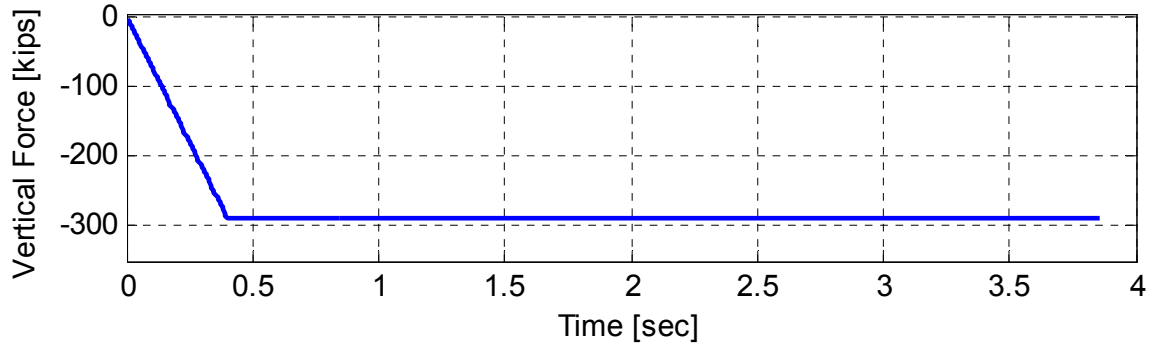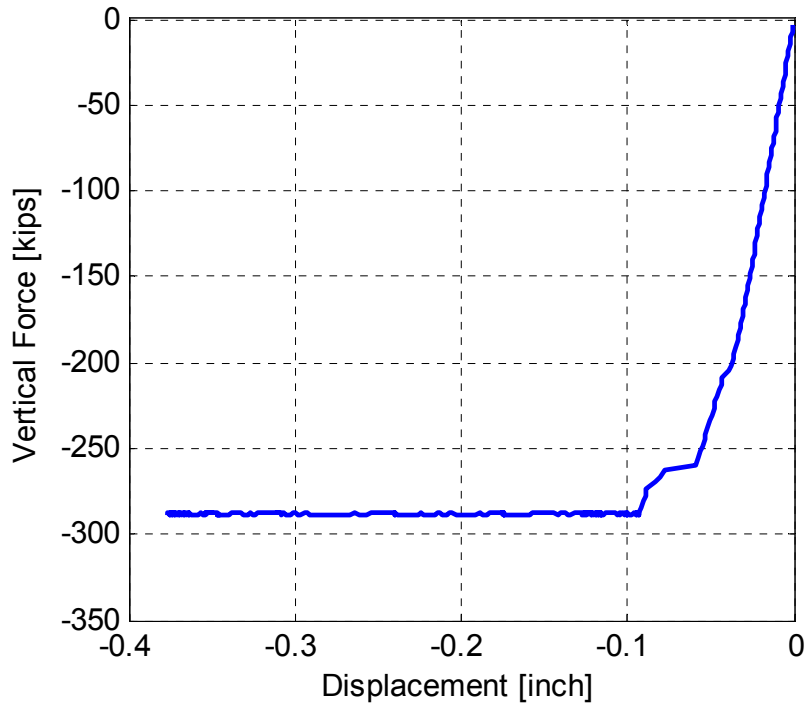
Figure 4.46 Analysis results for the case of 50% Northridge GM (Sylmar record) with only horizontal excitation and 23% constant gravity load of column axial capacity: (a) vertical displacement history, (b) vertical force history, (c) vertical force-displacement relationship

132
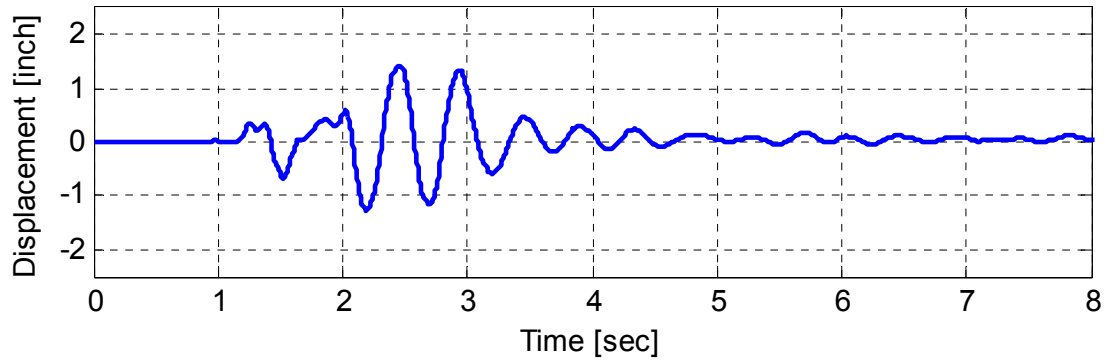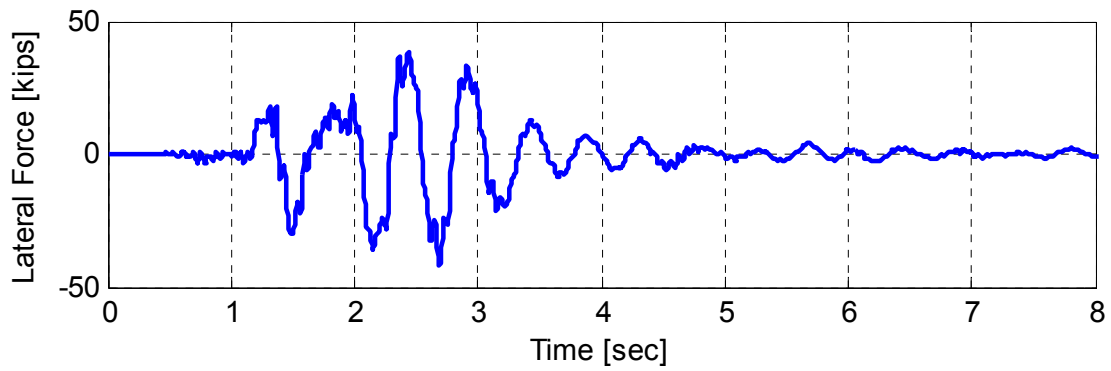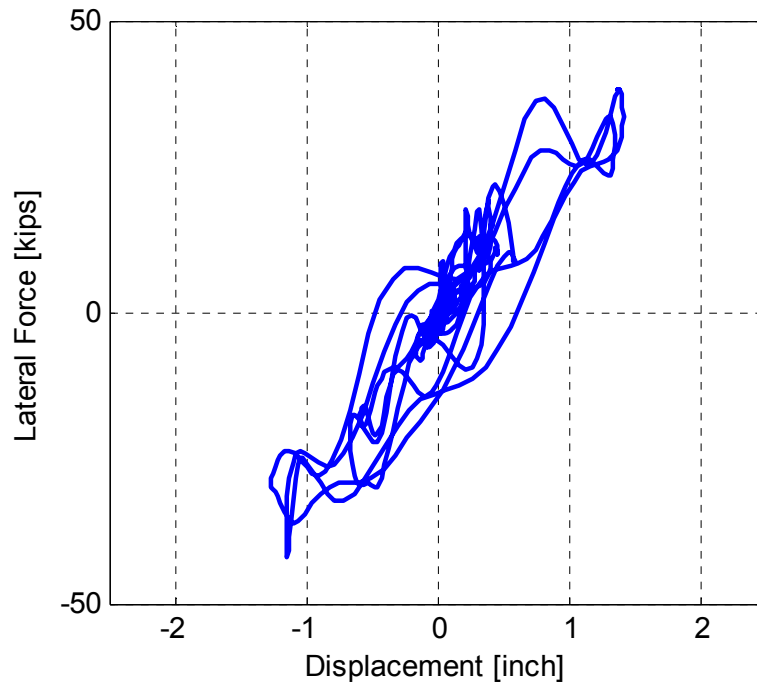
Figure 4.47 Analysis results for the case of 50% Northridge GM (Sylmar record) with both vertical and horizontal excitations and 23% constant gravity load of column axial capacity: (a) lateral displacement history, (b) lateral force history, (c) lateral force-displacement relationship

133
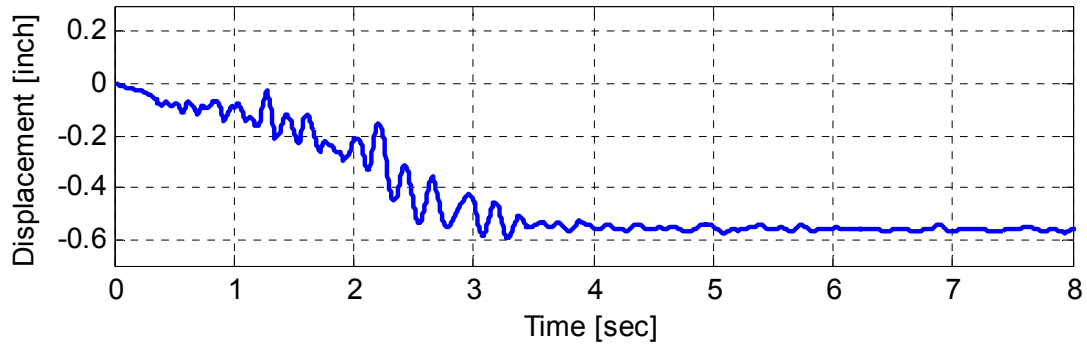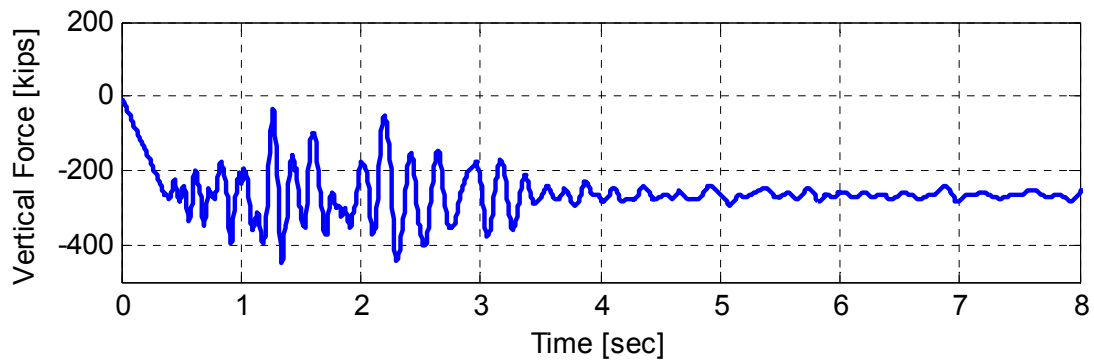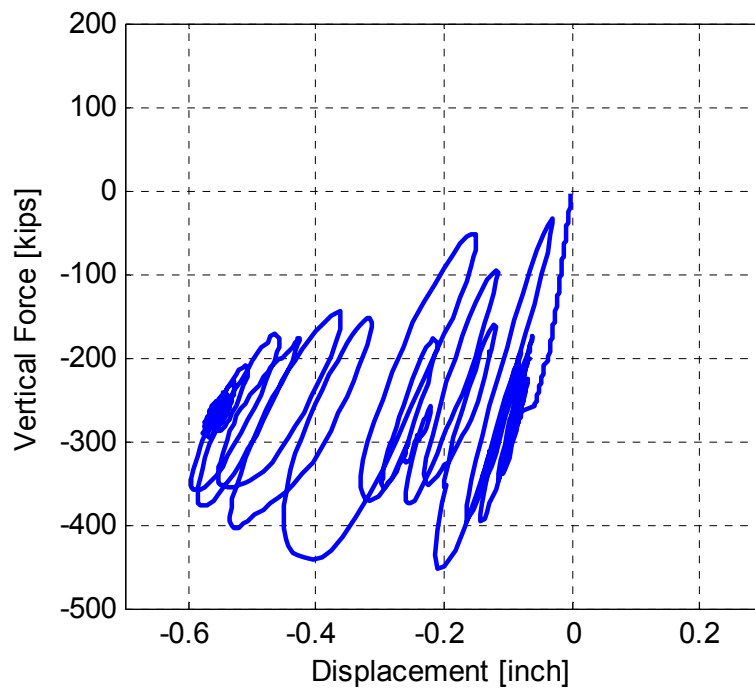
Figure 4.48 Analysis results for the case of 50% Northridge GM (Sylmar record) with both vertical and horizontal excitations and 23% constant gravity load of column axial capacity(a) vertical displacement history (b) vertical force history (c) vertical force-displacement relationship

The lateral behavior in the transverse direction, i.e. in the cap beam plane, and the vertical system behavior were shown for all the selected three cases of time history analyses. The force values were capped when either the column or cap beam capacity was reached. The lateral force capacity from the different time history analysis runs agreed with the pushover analysis. However, a higher vertical force capacity was observed from the time history than the case of the vertical pushover because of the effect of the lateral dynamic loading that produced moments opposite in sign to those resulting from the vertical loading moments. Moreover, it is implied from the vertical force fluctuation shown in Figure 4.44 and Figure 4.48 for cases that involved vertical excitation, that the vertical excitation can increase the vertical load demand by almost 100% of the gravity load. This justifies to some extent the selected gravity load levels to account for the effect of vertical excitations. On the other hand, the obtained displacement values from the dynamic analysis helped in identifying the mode of failure and overall system ductility, which was beneficial input for the second specimen HS testing. In summary, it was observed that the higher the initial gravity load was, the less was the lateral ductility in case of vertical excitation inclusion. That is because the vertical excitation along with higher gravity load caused the failure of the bent cap beam directly without obtaining significant damage in the column. Thus, it was concluded that 10% gravity is the most appropriate starting point for the case of HS tests to obtain higher ductility levels. Meanwhile, the HS tests could accommodate an increase in the gravity load level up to 15% to account for higher vertical excitation effects compatible with higher ground motion scale to obtain the expected failure in both column and bent cap simultaneously. It is to be noted that the 15% was a conservative estimate mainly because the conducted tests were all static tests where the gravity load was maintained for prolonged times. However, the actual increase in the gravity load due to vertical excitation as obtained from the analysis demonstrated a dynamic effect that took place only for a short period of time, i.e. the effect of the instantaneous increase in dynamic gravity loads should not be as excessive as the static load. Thus, the 15% axial load considered for the tests was conservative because it represented a more severe case.

4.4.4   Input for Test Setup and Instrumentation

The detailed DIANA FE pre-test analysis was utilized to develop informed decisions for the test setup design forces and the instrumentation of the transverse slab reinforcement necessary to measure the strain distribution for effective width determination. First, the largest expected lateral force from the pushover analyses and maximum observed reaction in the cap beam end struts were noted for test setup design. The maximum lateral force in the transverse direction was found to be almost 45 kips as noted from the vertical-lateral force interaction diagram shown in Figure 4.41. It is to be noted that a closer value was obtained for the capacity in the longitudinal direction form the preliminary analysis. This is mainly because the capacity was dictated by the column capacity which is almost the same in both transverse and longitudinal directions. The 45 kips limit was verified to be much less than the combined horizontal actuators capacity and the lateral shear capacity of the prestressing rods used to hold down the specimen to the laboratory strong floor. Meanwhile, the maximum observed reaction in the cap beam end roller supports was found to be in the vicinity of 140 kips under combined lateral and gravity loads. The two vertical struts were then designed to remain elastic up to 200 kips each to provide accurate and meaningful strain readings for reaction calibration.

135

The pre-test analysis was used to determine the stress and strain distributions in the transverse slab reinforcement adjacent to the bent cap beam in both soffit and deck slabs for informed instrumentation decisions. A view of the strain profile in both soffit and deck slabs in elevation is shown in Figure 4.49 for a typical lateral pushover analysis case. In addition, the strain profile observed in the deck slab from more loading cases: vertical pushover analysis, a typical lateral pushover, and a typical time history analysis is shown in plan view in Figure 4.50 (a), (b), and (c), respectively. It was determined that the strain decays within about 2 feet from the cap beam face in case of deck slab and close to 1-1/2 foot in the soffit slab. Thus 4 bars were instrumented at each side of the cap beam in the deck slab and 3 bars were instrumented at each side of the cap beam in soffit slab as previously shown in Chapter 3. The strain distribution was also assessed in respect to the two special holes that had to be constructed for vertical actuators rods as shown in Figure 4.50 and Figure 4.49. it is noted that the strain decays and almost reach zero away from the holes. Thus, confidence was gained that the holes would not influence the stress/strain distributions. In summary, the pre-test FEA described in this chapter confirmed that the sought test setup is adequate to conduct the experimental program and obtain the desired behavior and mode of failure. Moreover, it is confirmed that the experimental setup is able to apply the required maximum loads and deformations to the test specimens. Moreover, the FEA described in this chapter was improved using actual material properties to match the experimental results in the post-test analysis as discussed in details in Chapter 9.
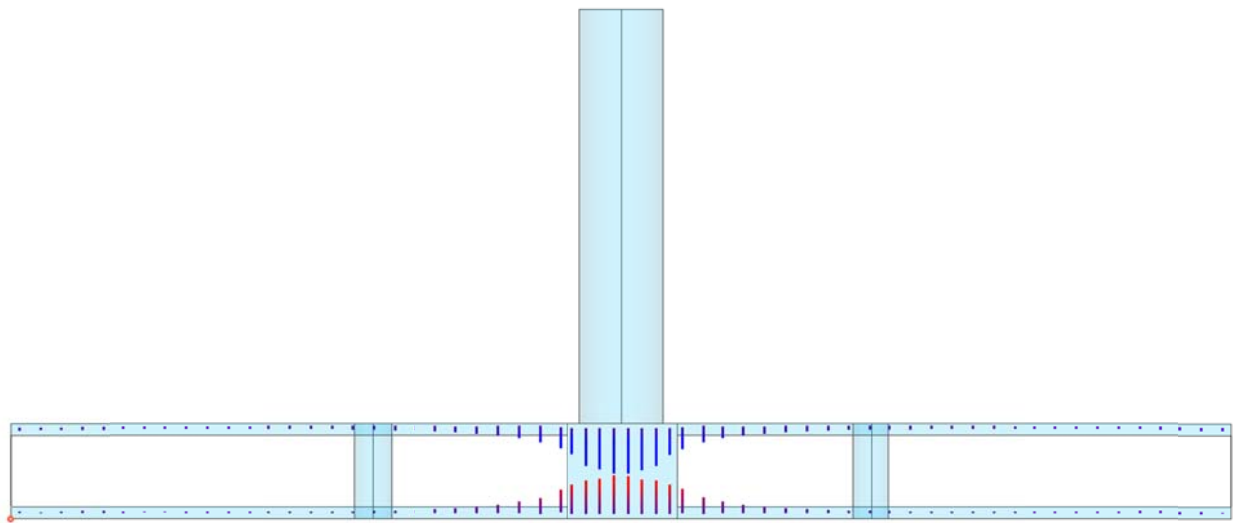
Figure 4.49 Strain distribution in the reinforcement along the cap beam and transverse slab cross-section for DIANA specimen model subjected to lateral pushover and constant gravity load
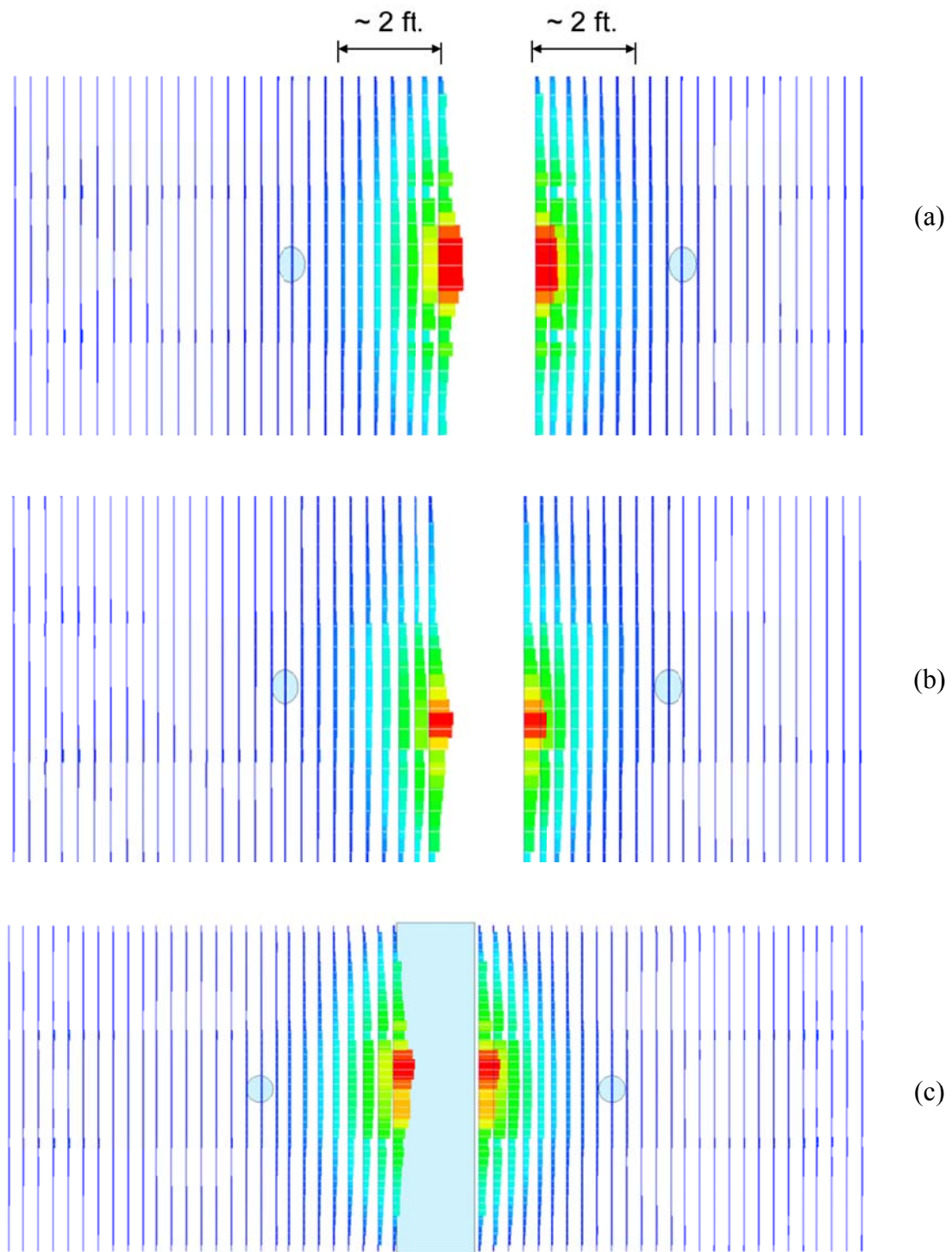
Figure 4.50 Strain distributions in the transverse slab reinforcement from the DIANA specimen model under two cases of loading: (a) vertical pushover, (b) lateral pushover with constant gravity load, (c) time history analysis using Kobe ground motion at 50%

137

5   Quasi-Static Testing: As-Build Specimen One

The first specimen SP1 tests encompassed a major part of the experimental program as it was utilized in three different test sets. It was first tested in the as-built condition under a quasi-static cyclic loading. After the cyclic test was completed, the column was heavily damaged as it lost its force capacity and stiffness. Thus, it was decided to repair the column of the tested specimen SP1 to restore partial capacity and stiffness for use the specimen in HS verification. However, the repaired specimen was tested under same cyclic loading history as the original as-built specimen test for response comparison, which comprised the second set of tests. The HS trial tests were carried out afterwards in the third set of tests that used SP1. The discussion of the first set of tests is the focus discussed in this chapter. The second set of tests is discussed in the next chapter, and the HS trials are presented in Chapter 7 as part of the HS system verification.

The first as-build test is extremely important for several reasons. First, the test original objective was to investigate the structural response of the bent cap beam and the bridge subassembly, and determine the contribution of the box-girder slabs under lateral loading. Next, the results from the as-built test provide a datum for comparing the behavior of both of the repaired system that was retested and the retrofitted second specimen SP2 that was tested using HS. Therefore, special attention is given to the post-processing of the first specimen as-built test results for its importance. A comprehensive framework for presenting and discussing all key observations and results of first test are presented in this chapter.

As previously mentioned in Chapter 3, the first test conducted in the experimental program was a quasi-static cyclic loading test of the first as-built specimen. The test was conducted under constant gravity load and 12 bidirectional lateral loading groups. The complete set of all loading groups was achieved in 2 full days of testing. All the runs in both of the transverse and the longitudinal directions were compiled together. Thus, the time history used throughout this chapter presents the net time of actual testing, i.e. active loading. It is to be noted that that the data acquisition was split between two DAQ systems; the Pacific Instruments[2] (PI) which can record all channels readings continuously while the loading is active or paused, and the NEFF[3] which records the data only during active loading. Therefore, two time scales can be observed from the different response histories presented in the following sections. These are approximately a total time of 465 minutes for all data recorded at the PI, and 260 minutes for data recorded on the NEFF. The 200 minutes difference reflects the total accumulated time of pauses during the tests when crack and damage propagation were documented.

---

[2] Pacific Instruments (www.pacificinstruments.com)
[3] NEFF Instruments, founded by Glyn Neff (www.neff.com)

The postprocessing presented here for SP1 quasi-static test results and discussions consist of six main parts. The first part discusses the global behavior of the bridge subassembly specimen in terms of lateral forces, displacements, and stiffness in both transverse and longitudinal directions. The second part focuses on the local behavior of the column in terms of reinforcement strains, section curvatures, and bending moments. Similar discussion for the local behavior of the bent cap beam strains, curvatures, and bending moments is presented in the third part. The fourth and fifth parts comprise the effective width discussion in tension and compression sides, respectively. The effective width is a key outcome of the experimental study that aims at revisiting the box-girder slabs contribution to the bent cap beam stiffness and moment capacity. The chapter concludes with the sixth part of the results framework discussion which emphasizes other response quantities that are of relevance to the final conclusions from the test.

5.1   PROGRESSION OF TESTING AND DAMAGE

The as-built SP1 cyclic loading tests involved bidirectional loading in both transverse and longitudinal directions. Figure 5.1 and Figure 5.2 show the test setup and progression of the loading from a top view in the transverse and longitudinal directions, respectively.
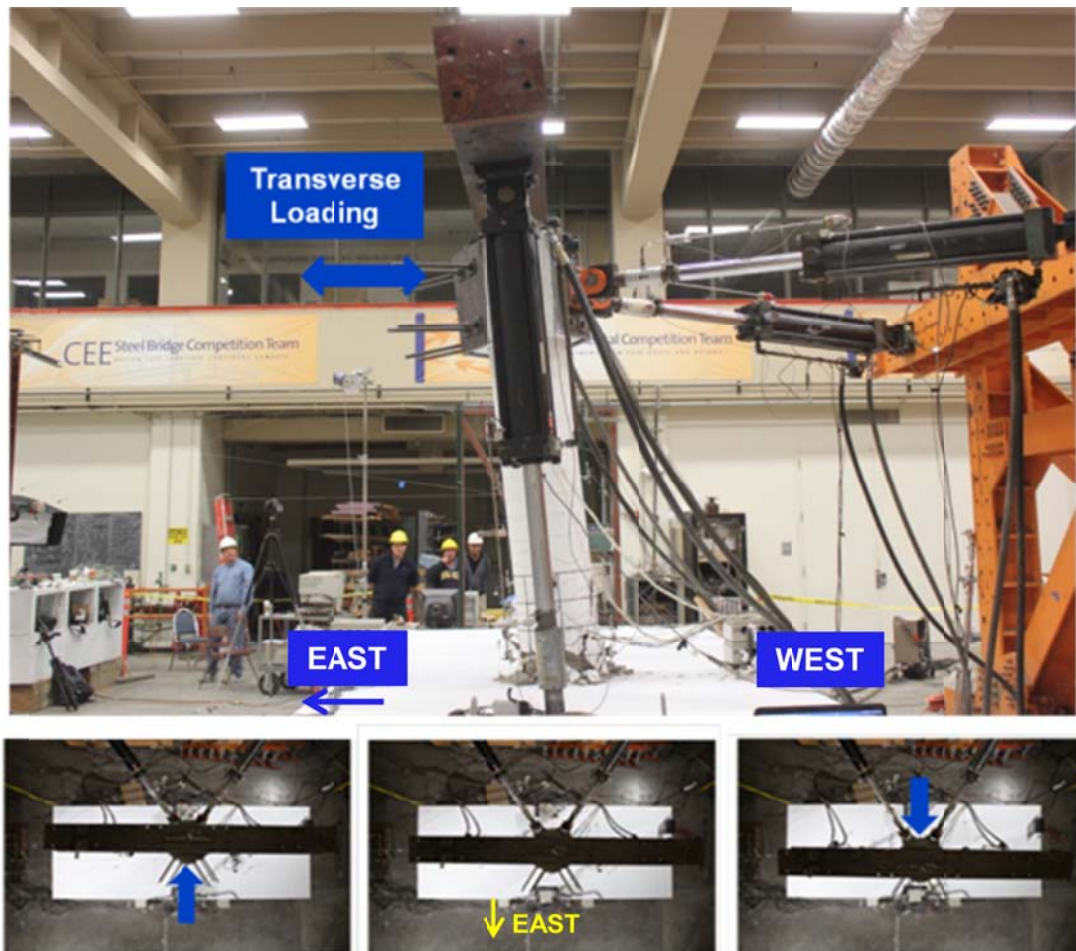
Figure 5.1 As-built SP1 test setup and progression of loading in the transverse direction

139
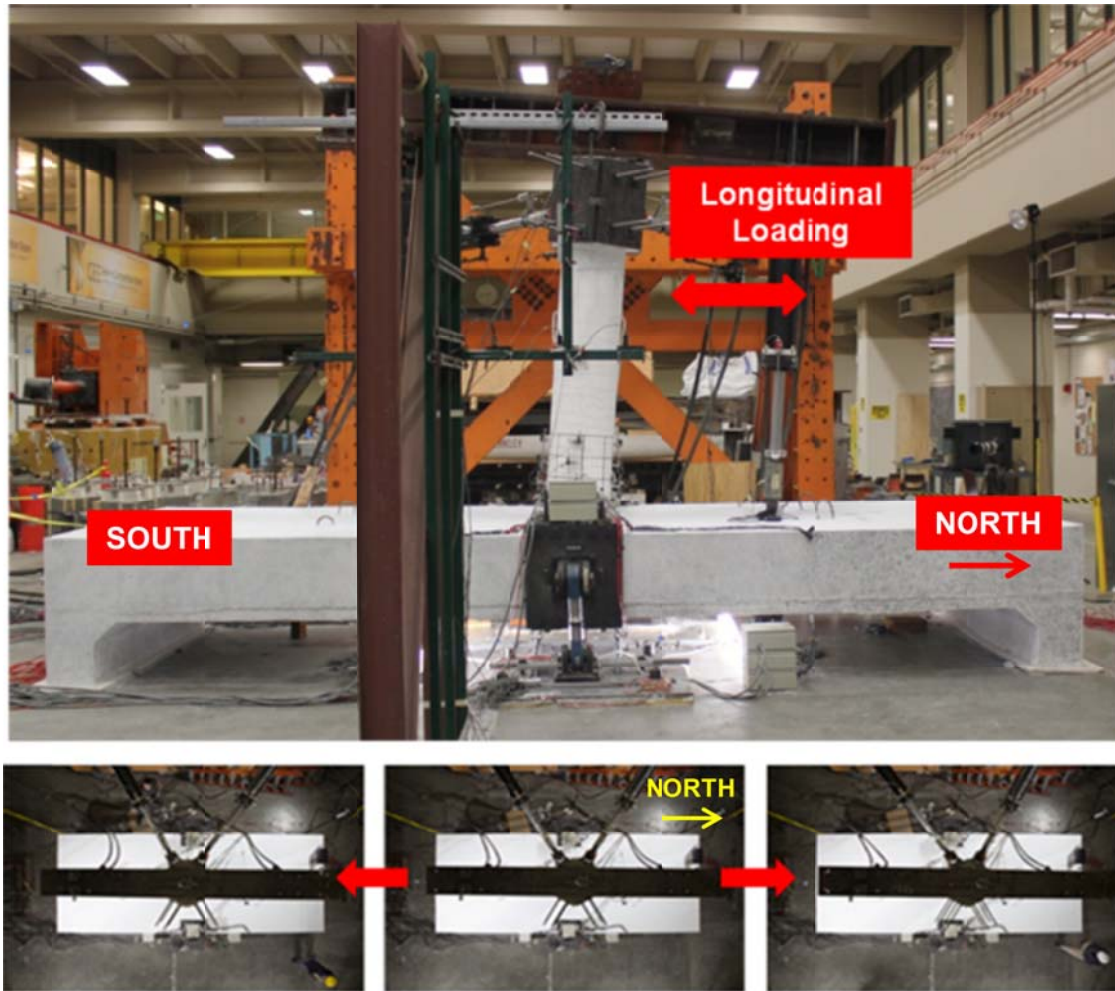
Figure 5.2 As-built SP1 test setup and progression of loading in the longitudinal direction

A convention notion that is very important for all the test results discussion that follows is the direction of loading. Throughout this study, the loading in the transverse direction refers to loading in the direction of the bent cap beam centerline, i.e. the East-West direction as defined in Figure 5.1. Whenever loading is pushing towards the East, it is designated as the positive transverse loading direction, and in turn, the negative transverse loading direction is pulling towards the West. On the other hand, the longitudinal direction is loading in the North-South direction, i.e. along the box-girder centerline as shown in Figure 5.2. Pushing towards the North defines the positive longitudinal loading while pulling towards the South is the negative longitudinal direction. These different ways of defining the loading direction are used interchangeably throughout the discussion.

The observed damage during the as-built SP1 cyclic loading test is discussed in this section as well. All the damage was concentrated in the column, which experienced a flexural plastic hinge mode of failure. No shear failure or extensive shear cracking were observed during the test. Only minor shear cracking was observed in the column-bent cap joint region as shown in Figure 5.3, which shows the joint region crack pattern at transverse loading cycles that correspond to 1.0 and 7.6 ductility levels. More information about the ductility levels obtained from the pursued cyclic loading pattern is presented in the next section. Minor flexural cracks

140

were also observed in the tension side of the box-girder and bent cap, which is the bottom face of the specimen in the inverted position, as shown in Figure 5.4. This figure was compiled from 4 fisheye-lens cameras that were installed underneath the specimen to observe the tension cracks. The longitudinal cracks are aligned with the box-girder centerline and no permanent flexural cracks were observed along the bent cap beam. However, the longitudinal cracks were observed to open wider when lateral transverse loading was progressing then reduced in width again after lateral loading was completed. This indicates that the final permanent crack pattern is mainly due to the applied concentrated gravity load rather than due to the application of any of the transverse or longitudinal lateral loading.
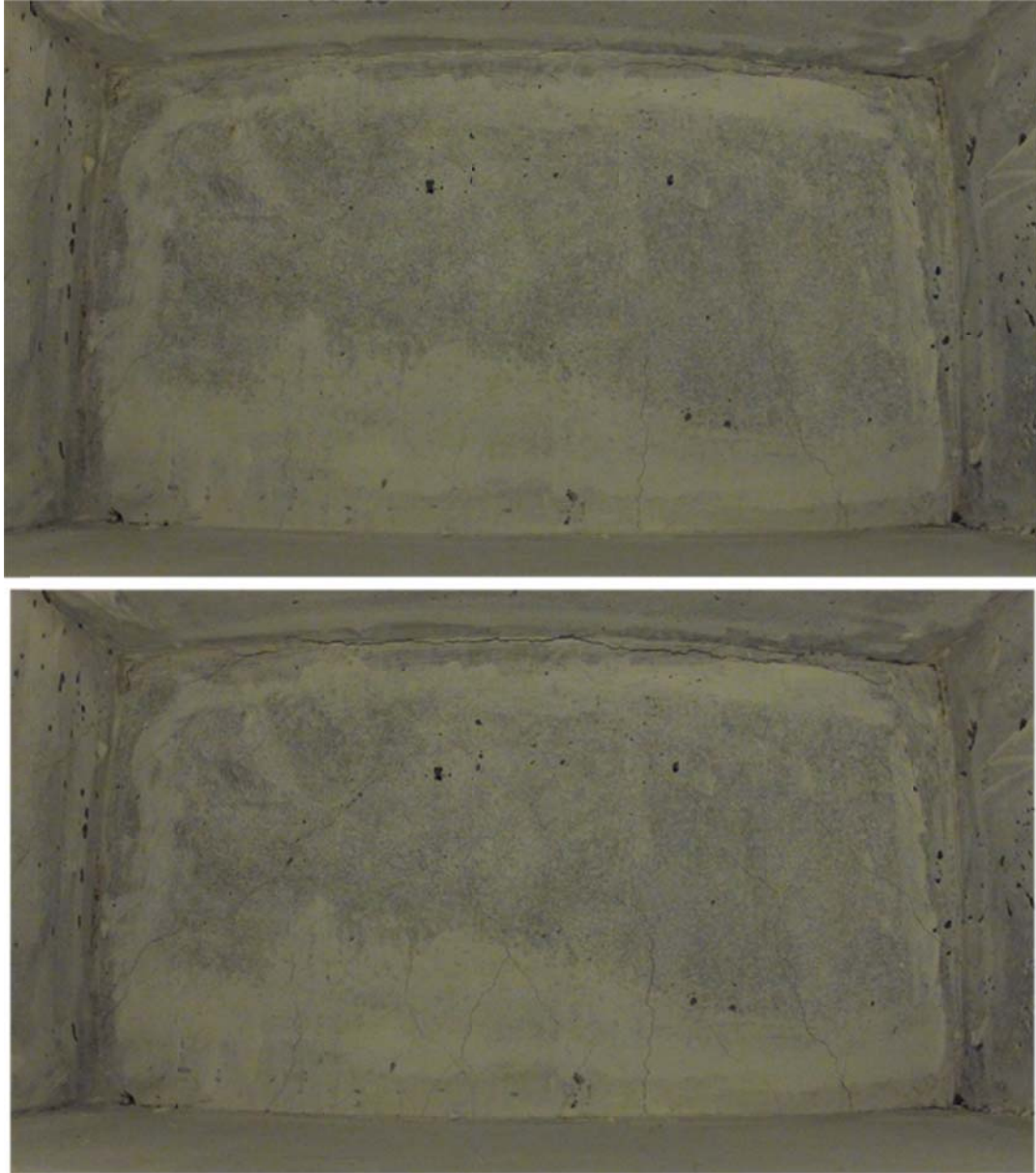
Figure 5.3 Minor shear cracking in the column-bent cap joint region at transverse loading cycles that correspond to 1.0 (top) and 7.6 (bottom) ductility levels

Figure 5.4 Minor flexural longitudinal cracks in the deck slab, i.e. bottom face of the inverted specimen, after all loading cycles. The horizontal line in the figure coincides with the box-girder center line

The main damage was observed in the column, where a flexural plastic hinge was developed. Figure 5.5 shows the progression of cracking, spalling, and concrete damage in the plastic hinge region of the column. Moreover, Figure 5.6 shows the final damaged state of the column and illustartes the buckled and ruptured reinforcing bars after all the spalling concrete

parts were removed. All the column longitudinal rebars buckled and six of them were ruptured during the as-built SP1 cyclic tests as shown in Figure 5.6.
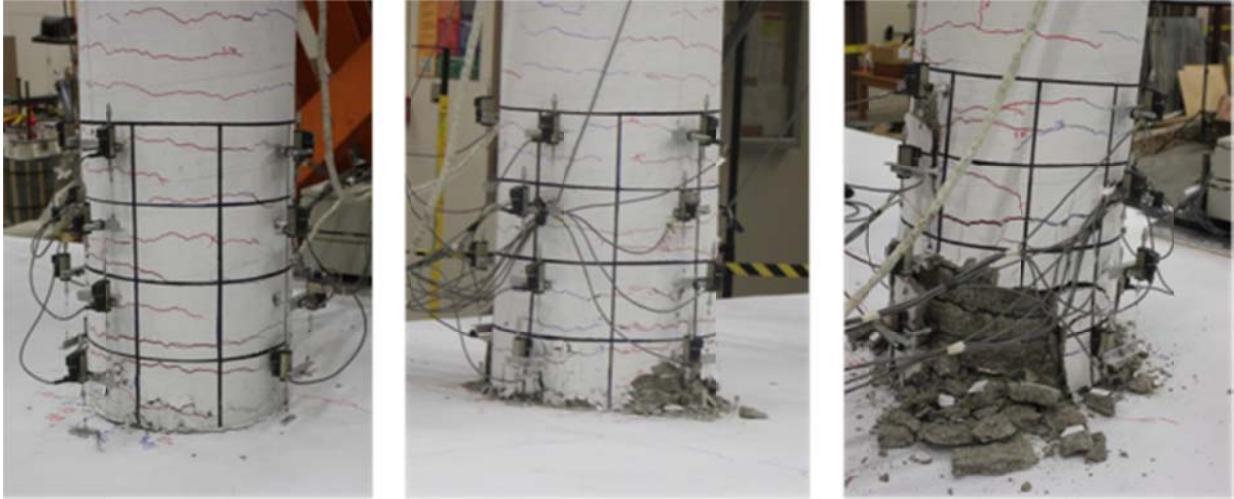
Figure 5.5 Propagation of the column cracking and spalling in the plastic hinge zone

Figure 5.6 Final damaged state of the as-built SP1 column: all the rebars were exposed and buckled, and six rebars were ruptured

5.2   GLOBAL BEHAVIOR

The global behavior of the tested specimen refers to the forces, displacements, and lateral stiffness acquired from the test results. Each of these quantities is discussed in details in the following subsections.

5.2.1   Force History

The full loading cyclic history was applied in 2 days of testing. The reasons for splitting the test over two days are the slow nature of the load application and the need for experimentally revising the cyclic groups when the first rebar yield is observed. That is because the progressive cyclic loading groups are multiples of the yield displacement as recommended by FEMA 461 (2007). It was decided to apply two different levels of the gravity load as previously discussed in Chapter 3. The first level corresponds to approximately 5% of the column axial capacity for a total of 82 kips. This was maintained until the first yield was observed for the low-level lateral cycles: 0.25, 0.35, 0.5, 0.7, 1.0 and 1.25 inch top displacement in both transverse and longitudinal directions. The gravity load was then increased to 10% (164 kips) to account for additional live load and possible effect of vertical excitations as discussed in Chapter 4. That was the case for the larger loading groups of 1.75, 2.45, 3.5, 4.8, 6.8, and 9.5 inch in transverse direction, and 1.75, 2.45, 3.5, 4.8, 6.8 (repeated twice) inch in the longitudinal direction. Before concluding the first test program, the gravity load was increased further to 12% (190 kips) and one small displacement cycle was applied to see if the damaged column can still transfer moments to the bent cap beam. The actual full history of the gravity load and its three different levels applied during all the cyclic test runs is shown in Figure 5.7.
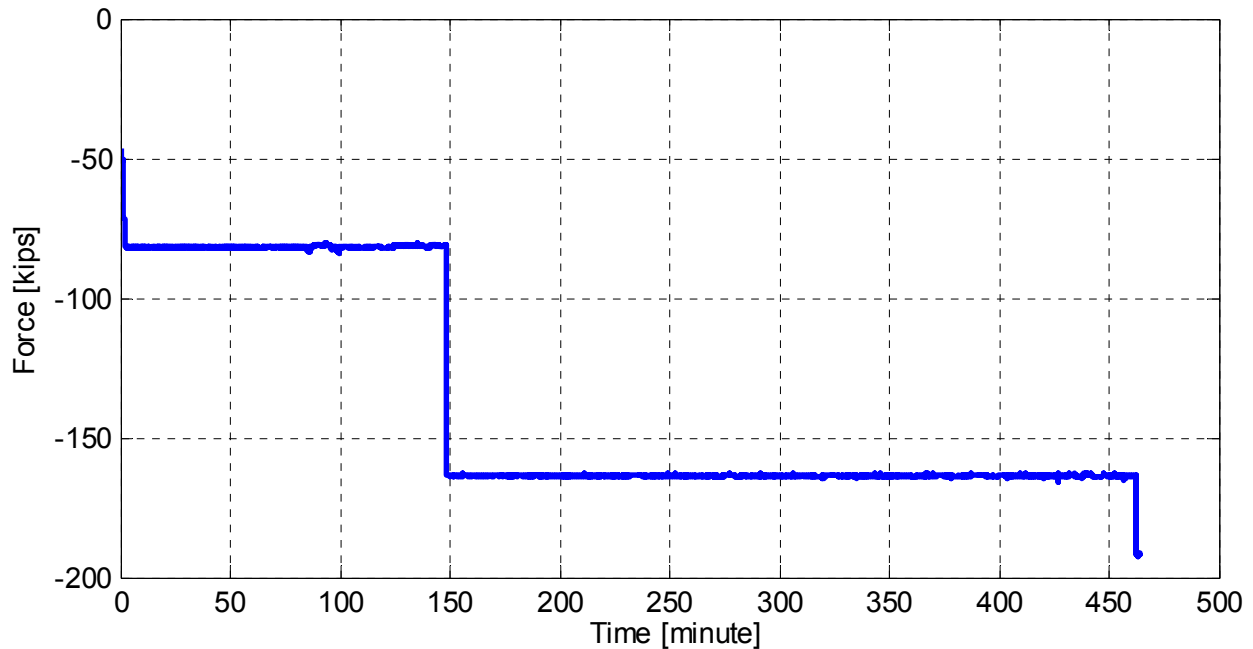
Figure 5.7 History of the gravity load applied during the first specimen (SP1) cyclic test runs

144

The lateral force that develops in the actuator as a prescribed displacement is applied is one of the key response quantities that are monitored in a RC bridge subassembly test. The observed force is often recognized as the column base shear, and is utilized to estimate the column bending moment. Therefore, as a cyclic test progresses, the forces are recorded to capture the base shear and bending moment capacities. In a flexural-controlled bridge column, the moment capacity is reached first, and the observed base shear is dictated by such moment capacity. The resultant forces observed in transverse (f_x) and longitudinal (f_y) directions are shown in Figure 5.8. These are computed from the actual recorded actuators load cells forces. The exact geometry and configurations of the lateral actuators were used to compute the resultant f_x force during transverse loading cycles, and to compute the resultant f_y force during longitudinal loading cycles. The history of the two lateral actuators measured forces, designated as North and South actuators according to their location relative to the test setup, and the resultant force in each of the transverse and longitudinal directions is shown in Figure 5.9. It can be observed from the figure that the actuators forces have approximately similar values and direction during a transverse loading cycle. On the other hand, during longitudinal loading cycles, the actuators forces have opposite directions and different values. A close-up look at all the forces for only one transverse and one longitudinal loading groups is shown in Figure 5.10.
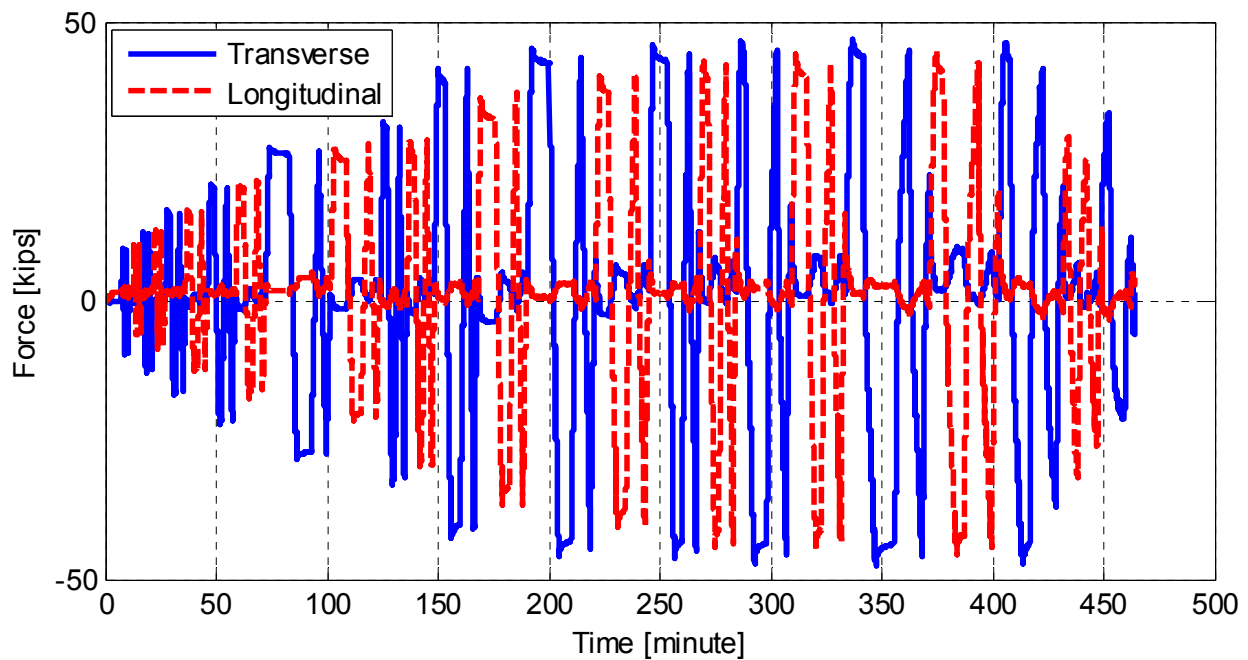
Figure 5.8 History of the force in both transverse and longitudinal directions (estimated from lateral actuators load cells) for all first specimen test runs

145
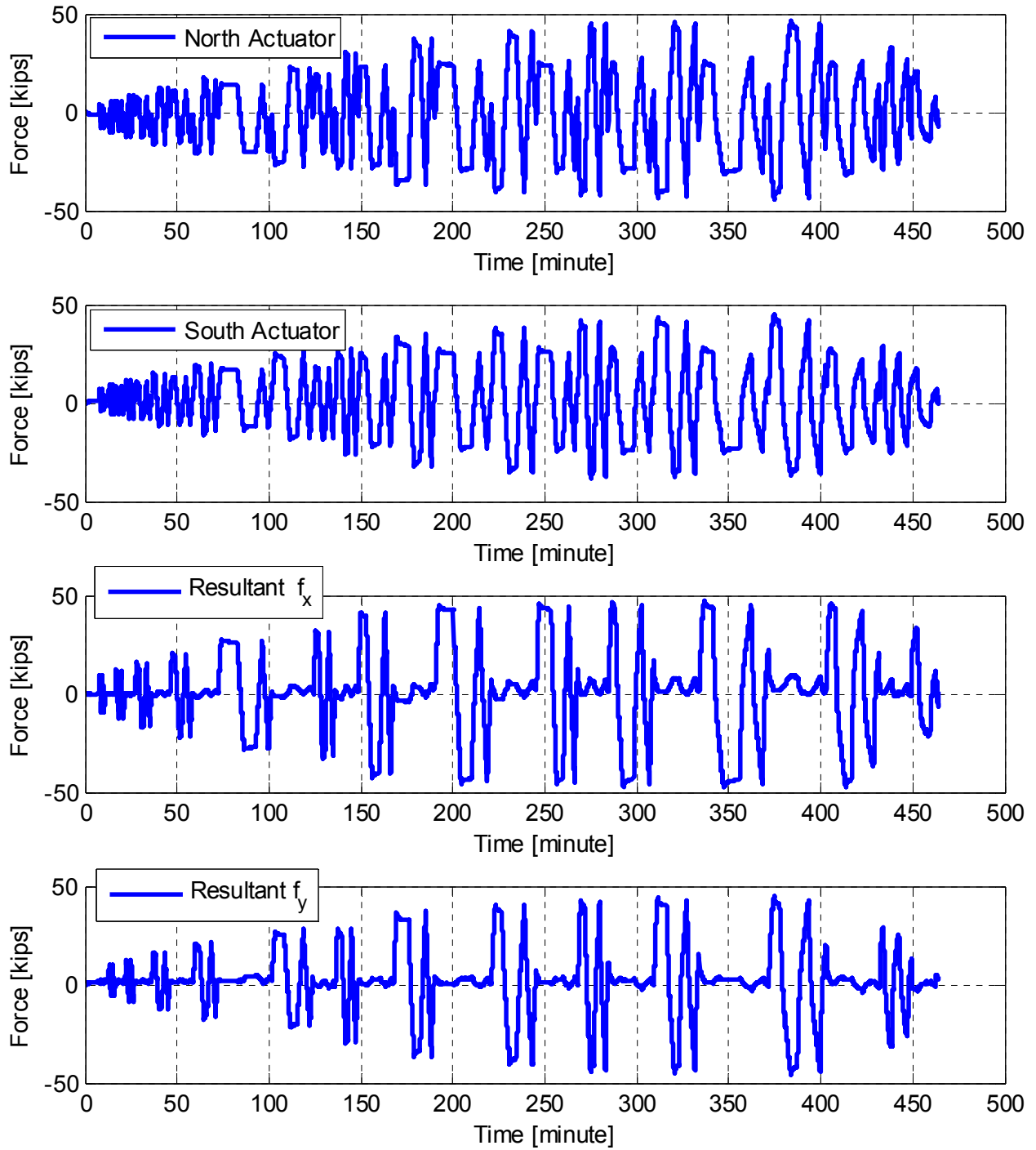
Figure 5.9 History of both of the North and South lateral actuators load cells measurements and the corresponding resultant forces in the transverse (f_x) and the longitudinal (f_y) directions for all cyclic loading groups

146
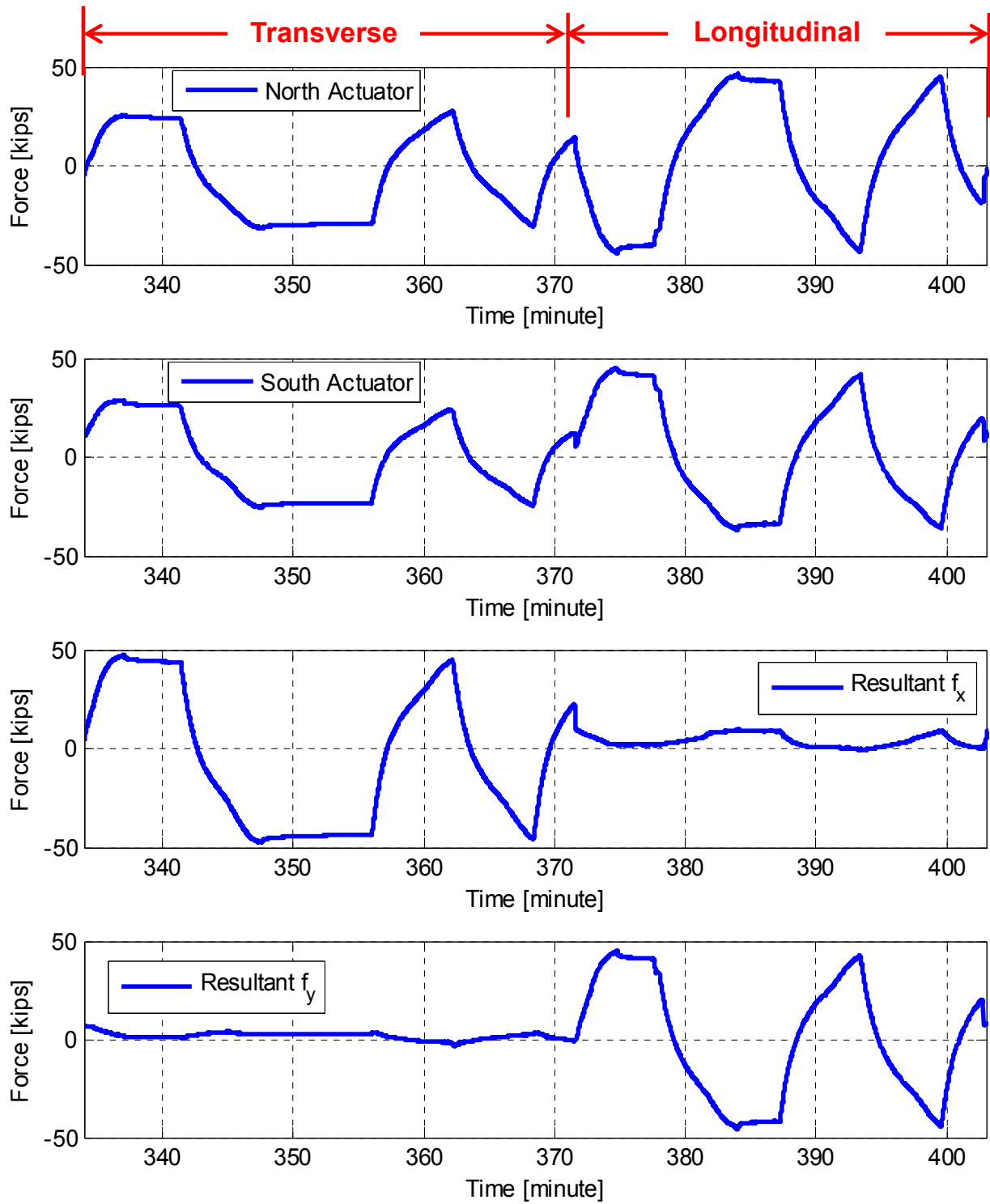
Figure 5.10 Zoomed-in view of the history of both of the North and South lateral actuators load cells measurements and the corresponding resultant forces in the transverse (f_x) and the longitudinal (f_y) directions for one transverse and one longitudinal loading groups

147

5.2.2 Displacement History

For a cyclic loading test under displacement control, prescribed displacements are the primary input to the actuators. These desired prescribed displacements are usually required in meaningful directions such as the bridge subassembly transverse and longitudinal directions. For practical reasons, the actuators configuration is not aligned with the transverse and the longitudinal directions of the specimen (bridge subassembly). Accordingly, the actuators displacement input is transformed such that the resulting column head motion agrees with the desired transverse (u_x) or longitudinal (u_y) displacements. The actual obtained displacements during the test were tracked in the actuators local direction through temposonic transducers, and in the global transverse and longitudinal directions through wire potentiometers (wirepots). The geometry and actuators configuration were used to transform the actuators local motion to the corresponding global transverse and longitudinal directions. The transformed actuators temposonic measurements were compared to the wirepots displacements to check the quality of measurements and transformations. It was found that the displacements computed from the exact actuators geometry and temposonic measurements are the most accurate. Thus, only the most accurate displacement histories obtained from transformed temposonic measurements are presented here.

The final obtained displacements in both transverse (u_x) and longitudinal (u_y) directions for all loading groups are shown in Figure 5.11. The flat parts of the plot at given displacement peaks represent the pausing time as the research team investigated the specimen's crack and damage propagation. The column head displacement orbit during all the test runs is presented in Figure 5.12. This figure emphasizes that the displacement loading was obtained at only one direction at a time as desired, i.e. either transverse direction only or longitudinal direction only. The independent bidirectional loading tests are generally more useful in uncoupling and understanding the bridge system behavior in each direction separately. This is favorable for the case of investigating the bent cap beam effective width and box-girder slab contribution. However, since a realistic concurrent bidirectional loading has its own benefits of being more representative to earthquake loading, the second specimen (SP2) was tested using both independent and concurrent bidirectional hybrid simulation loading schemes. It is to be noted that a larger displacement cycle at 9.5 inch column top displacement was only possible in the transverse direction because of the setup limitations of the vertical loading system. Thus, the last displacement group at 6.8 inch was repeated again rather than applying the 9.5 inch cycles. It is also useful throughout this discussion to relate the applied displacements to the corresponding column drift ratio and/or displacement ductility level. The drift ratio is calculated by the ratio of the displacement at the column head (either u_x or u_y) to the 90-inch column height. The ductility level is calculated by the ratio of the column head displacement, either u_x or u_y, to the displacement at the first experimentally-determined yield (Δ_{yield}), which was found to be 1.25 inch. The input displacements and corresponding drift ratio and ductility are shown in Table 5-1.

The history of the actual recorded temposonic displacements for each of the North and South actuators along with the resulting displacements in both transverse and longitudinal directions is shown in Figure 5.13. The two actuators move together with similar direction and values when only u_x is desired and the directions are reversed when only u_y is applied. The zoomed-in view in Figure 5.14 shows clearly how the actuators actual displacements relate to the desired (and observed) displacements. It is also observed that displacements are, unlike forces, well-controlled. When only u_x is applied, the corresponding u_y value is almost zero, and vice-

versa. In the force histories, previously shown in Figure 5.9 and Figure 5.10, some residual forces were still observed in one direction while loading was proceeding in the other orthogonal direction.

Table 5-1 Summary of input displacement and corresponding drift ratio and ductility level

Displacement [inch]	0.25	0.35	0.50	0.70	1.00	1.25	1.75	2.45	3.50	4.80	6.80	9.50
Drift Ratio [%]	0.28	0.39	0.56	0.78	1.11	1.39	1.94	2.72	3.89	5.33	7.56	10.56
Ductility Level [μ]	0.20	0.28	0.40	0.56	0.80	1.00	1.40	1.96	2.80	3.84	5.44	7.60
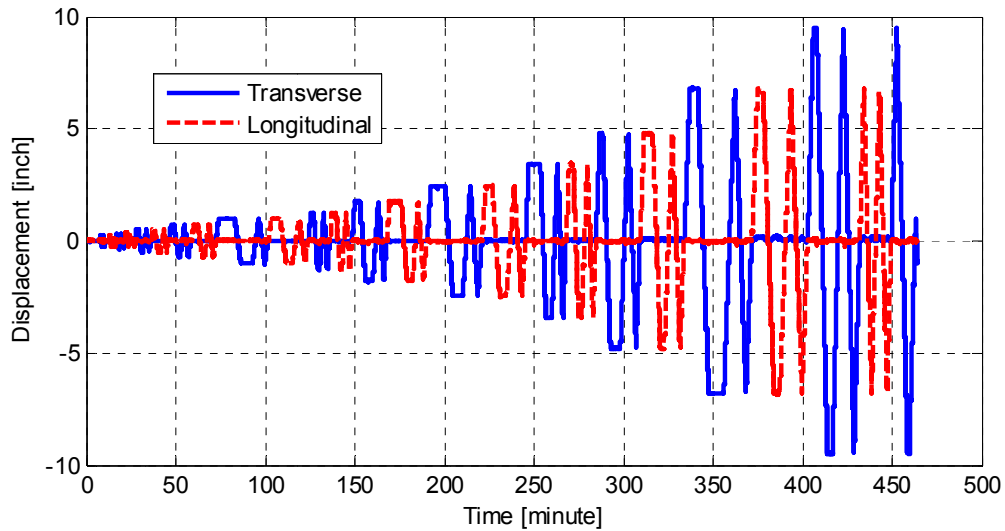
Figure 5.11 History of obtained displacements in both transverse (u_x) and longitudinal (u_y) directions for all cyclic loading groups
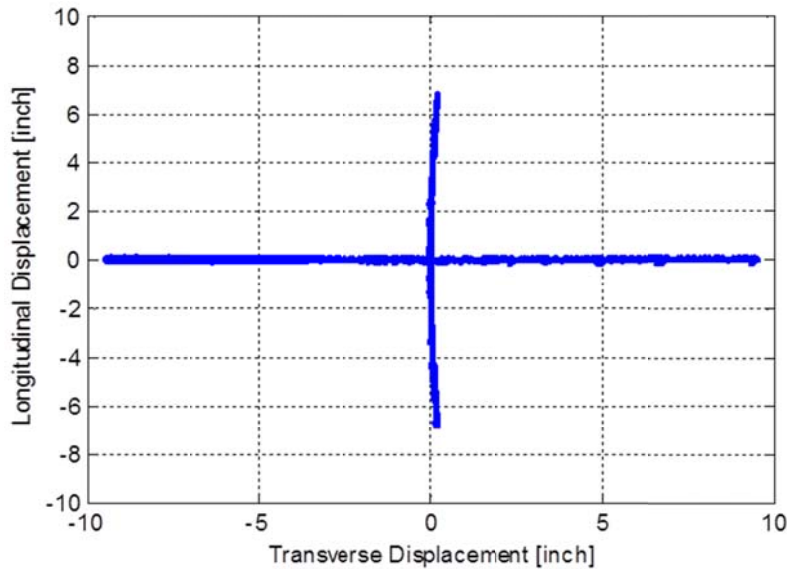
Figure 5.12 Displacement orbit of the specimen's column head for all cyclic loading groups (transverse displacement u_x versus longitudinal displacement u_y)

149
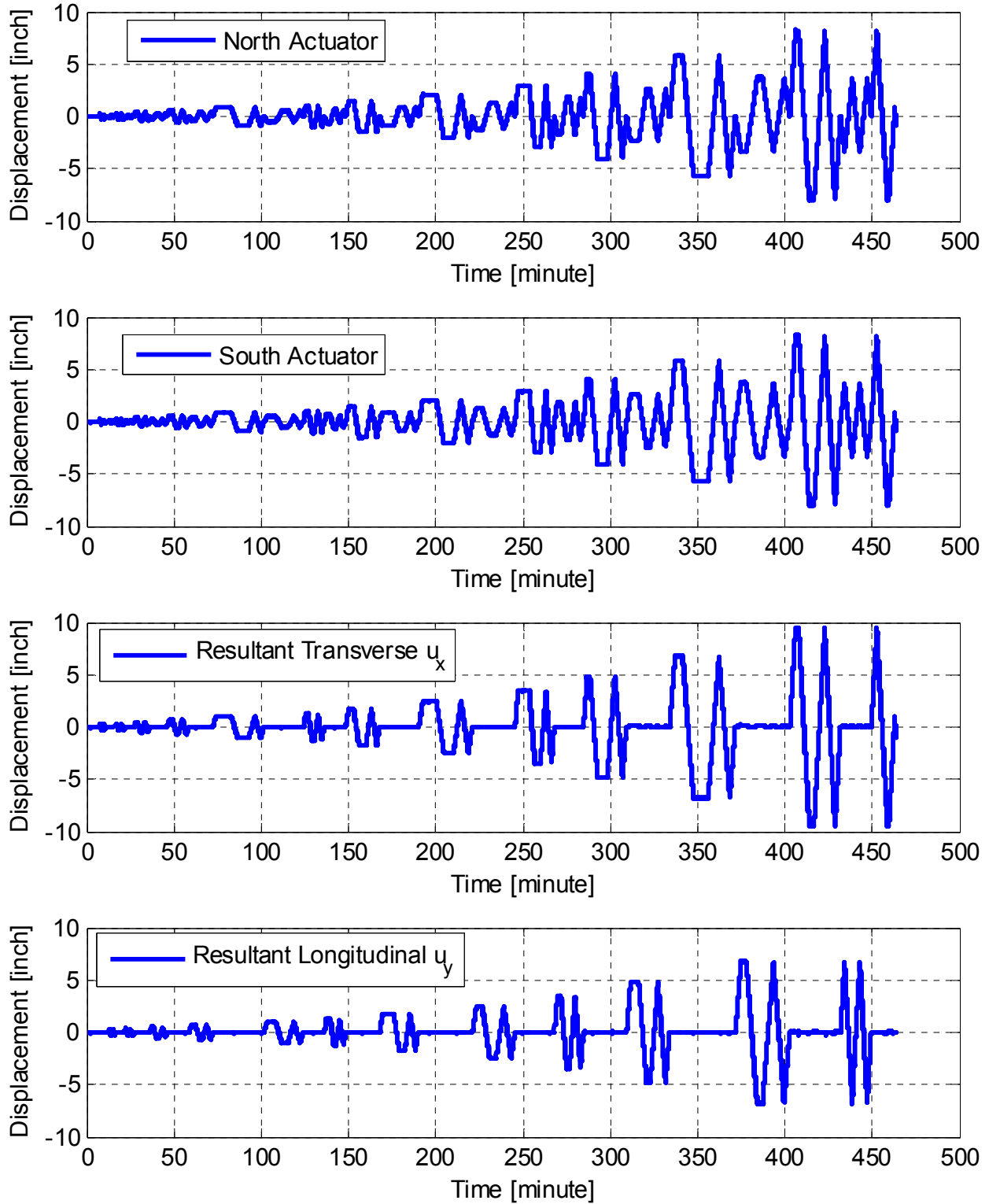
Figure 5.13 History of both of the North and South lateral actuators temposonics measurements and the corresponding resultant displacement in the transverse (u_x) and the longitudinal (u_y) directions for all cyclic loading groups
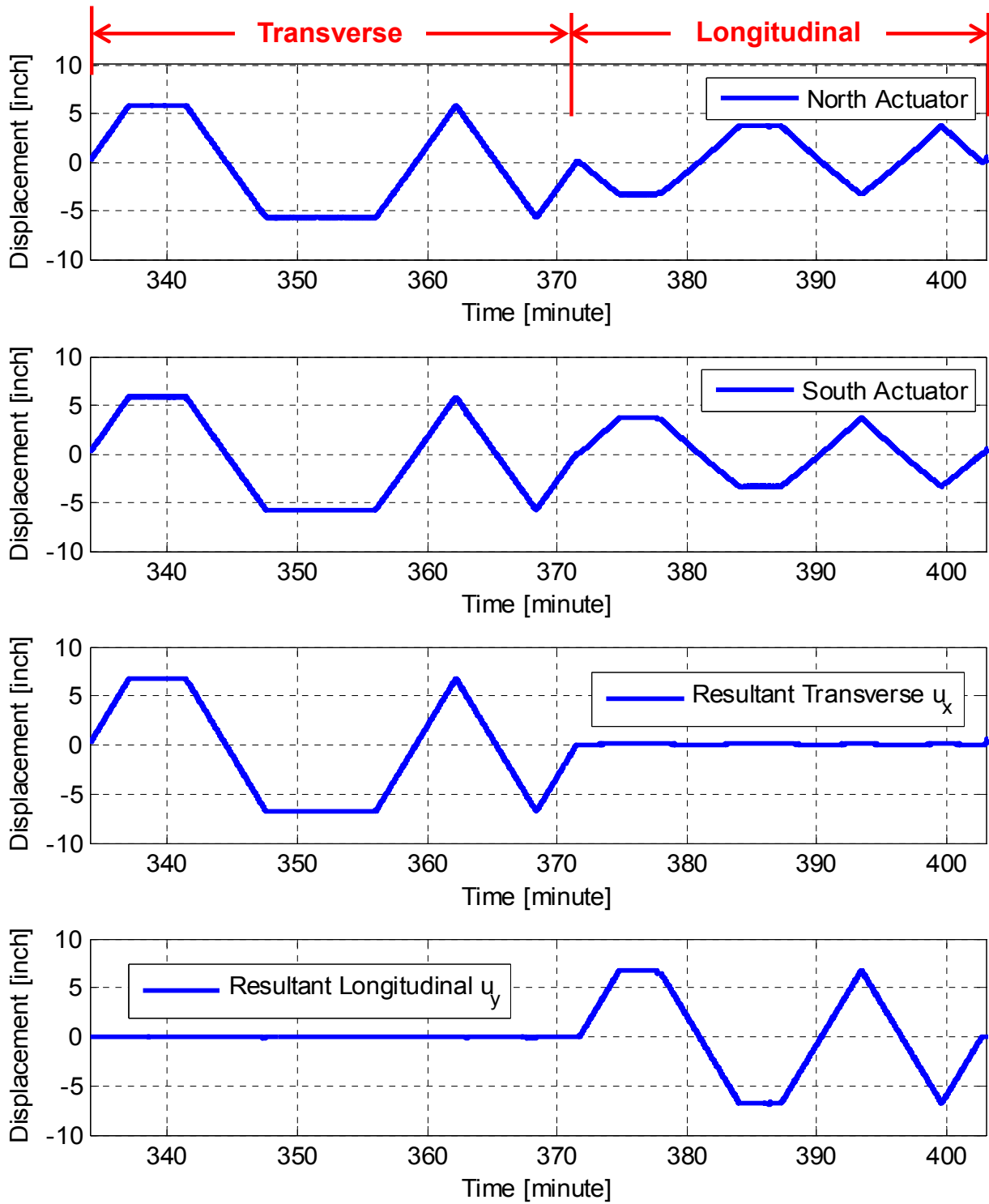
Figure 5.14 Zoomed-in view of the history of both of the North and South lateral actuators temposonics measurements and the corresponding resultant displacement in the transverse (u_x) and the longitudinal (u_y) directions for all cyclic loading groups

151

5.2.3 Force-Displacement

The final obtained forces and displacements in the specimen's transverse and longitudinal directions, designated as X and Y, respectively. Relationships are utilized in this subsection to obtain the force-displacement relationships for the tested bridge subassembly. The force-displacement response is considered a whole system response rather than a single column response. That is because of the nature of the column-to-superstructure (bent cap and box-girder) connection. It is also to be noted that a given cyclic loading group was applied first in the transverse direction then the longitudinal. It is expected accordingly to observe different behavior in the two directions.

The force-displacement relationships for all the cyclic loading groups in both transverse (f_x versus u_x) and longitudinal direction (f_y versus u_y) are shown in Figure 5.15 and Figure 5.16, respectively. For a convenient way of capturing the obtained force capacity and corresponding displacement, the envelops of each of the force-displacement relationships in the transverse and the longitudinal directions are shown in Figure 5.17 and Figure 5.18, respectively. The response obtained in both directions is also compared in Figure 5.19. From these figures, it is observed that the force capacity in the longitudinal direction is slightly less than the corresponding value in the transverse direction. These values are 44.70 kips versus 47.00 kips for positive loading (i.e. actuators pushing the column head), and -45.55 kips versus -47.50 kips for negative loading (i.e. actuators pulling the column head) in the longitudinal and transverse directions, respectively. All the capacity or maximum recorded force values were obtained at the first peak of the 11th loading cycle (6.8 inch applied displacement) which corresponds to a drift ratio of 7.52% and a displacement ductility level of 5.42. The notation of the first peak of a given cyclic loading groups can be shown in the inserts of Figure 5.17 or Figure 5.18. This reflects the fact that each cyclic loading group consisted of two full cycles which were individually recognized in two different envelop curves. The maximum obtained forces in each loading cycle in each of the transverse and longitudinal directions and the corresponding displacements are respectively summarized in Table 5-2 and Table 5-3 in the next subsection.

The force-displacement curves show the ductile behavior of the column as desired in a strong beam-weak column design philosophy adopted for bridge designs. The column maintained almost full capacity up to a drift ratio of almost 10% and ductility level of 7. The capacity degradation occurred in the last loading cycle in each direction due to rebars rupture. Each sudden drop in the force-displacement relationship indicates a rebar rupture which typically occurred for the buckled rebars as the load is being reversed. A total of 6 rebars ruptured; 4 at the east side of the column and 2 at the west side. The East direction is the positive loading in the transverse direction, while is the West is the negative loading direction. The rupture of the first and second rebars occurred during the second cycle of the 9.5 inch group in the transverse direction. Accordingly, the capacity dropped significantly when loading was resumed in the longitudinal direction as seen from the force-displacement relationships at the second set of 6.8 inch group. In addition, 2 rebars were then ruptured during the final longitudinal loading group. It was decided to proceed with another single-cycle 9.5 inch transverse loading cycle to see how the capacity degradation proceeds further. The last 2 rebars rupture occurred during that final transverse loading cycle as observed from the force-displacement curve in the transverse direction.
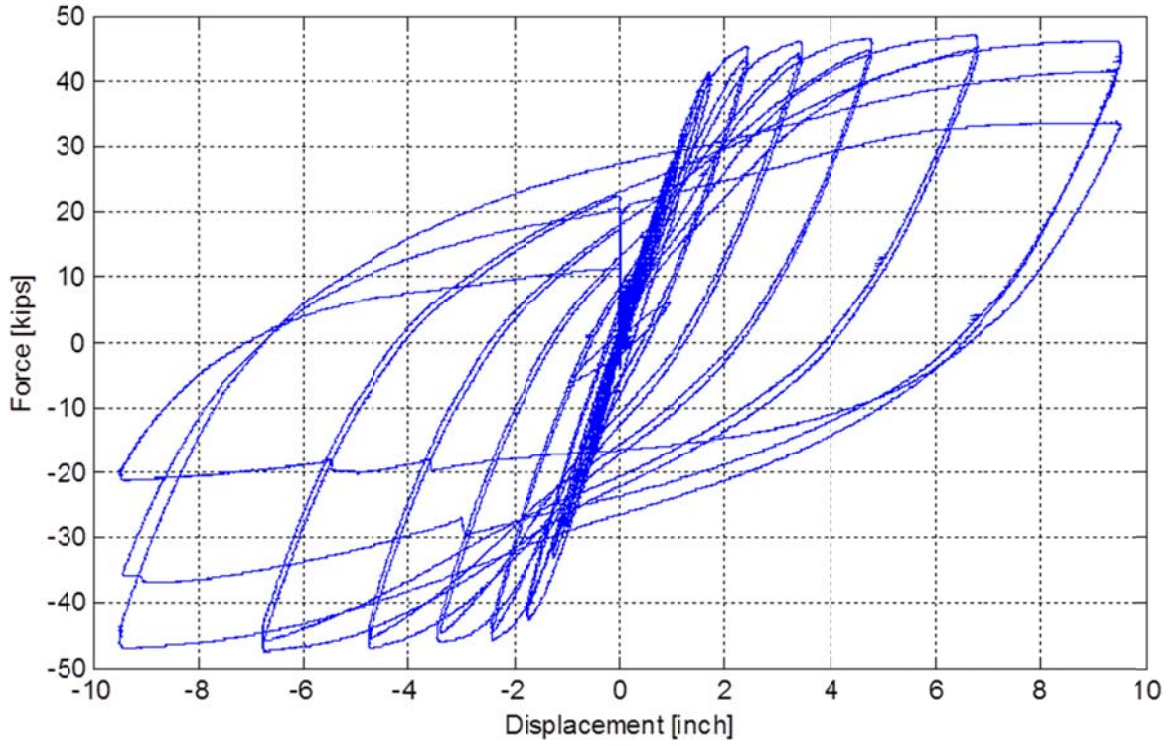
Figure 5.15 Force-displacement relationship for all cycles groups in transverse direction
(f_x versus u_x)
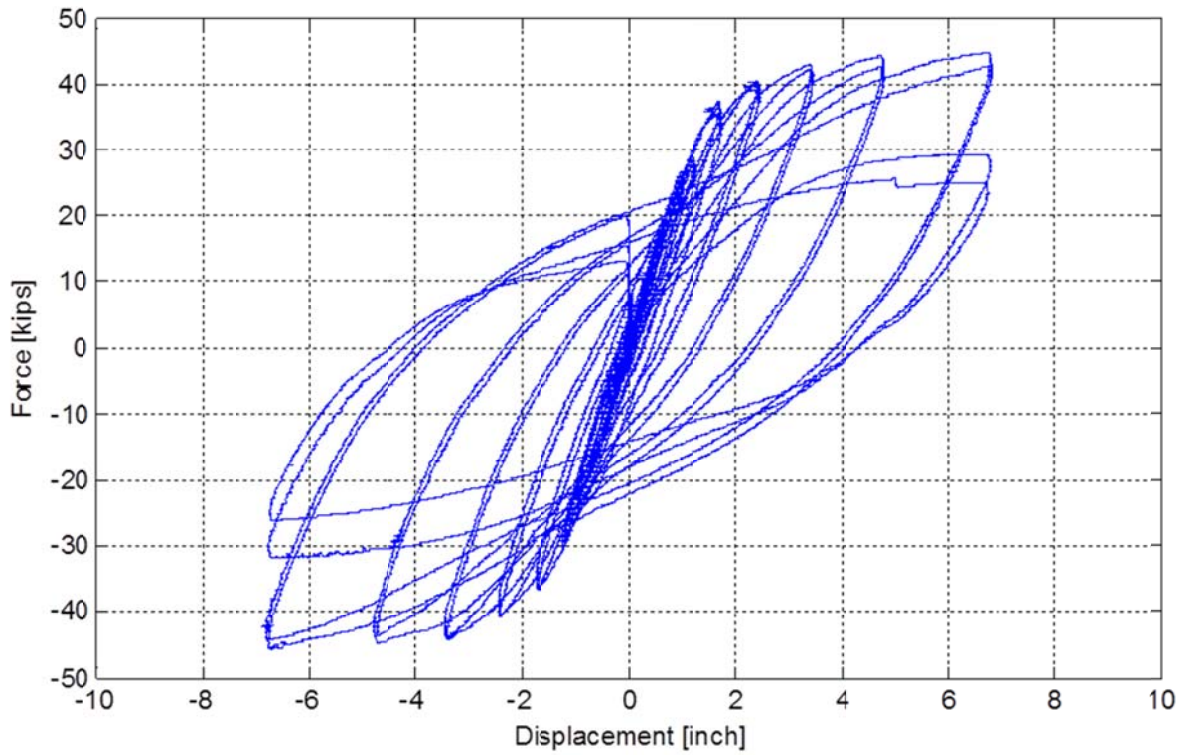
Figure 5.16 Force-displacement relationship for all cycles groups in longitudinal direction
(f_y versus u_y)

153
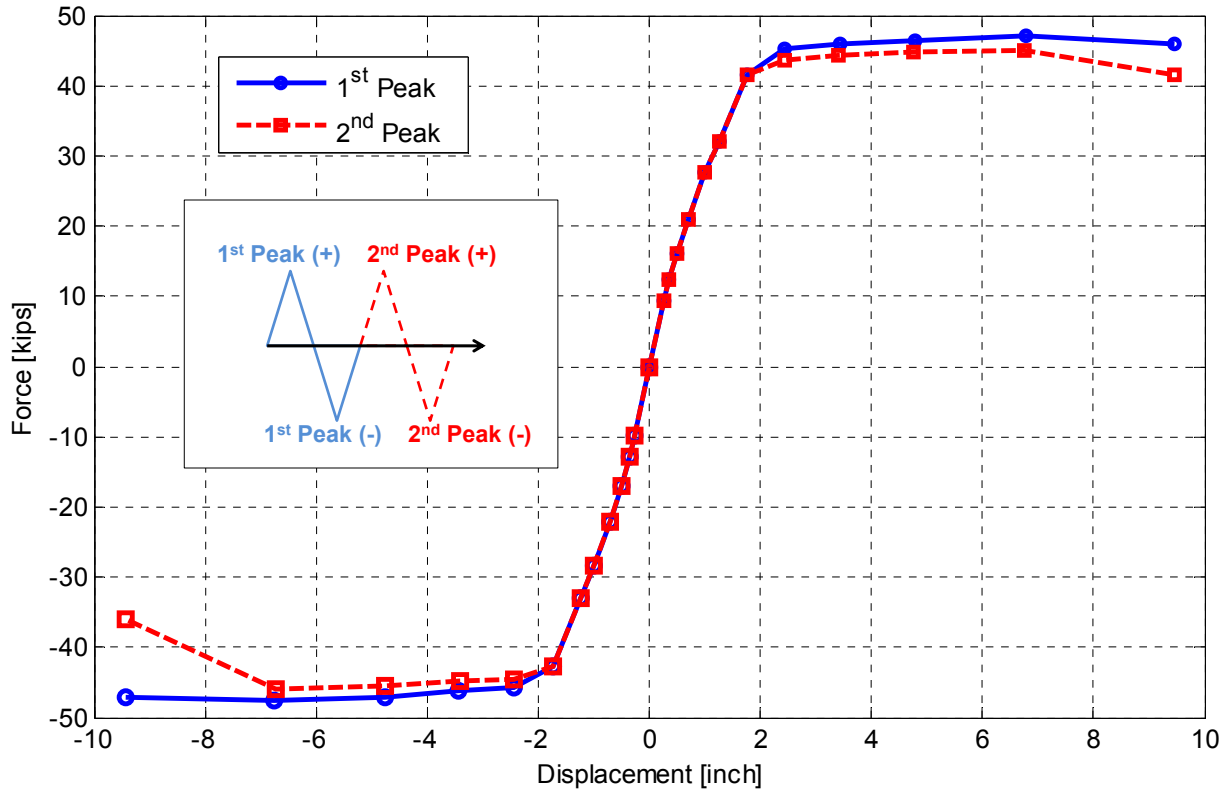
Figure 5.17 Force-displacement envelop for all cycles groups in transverse direction
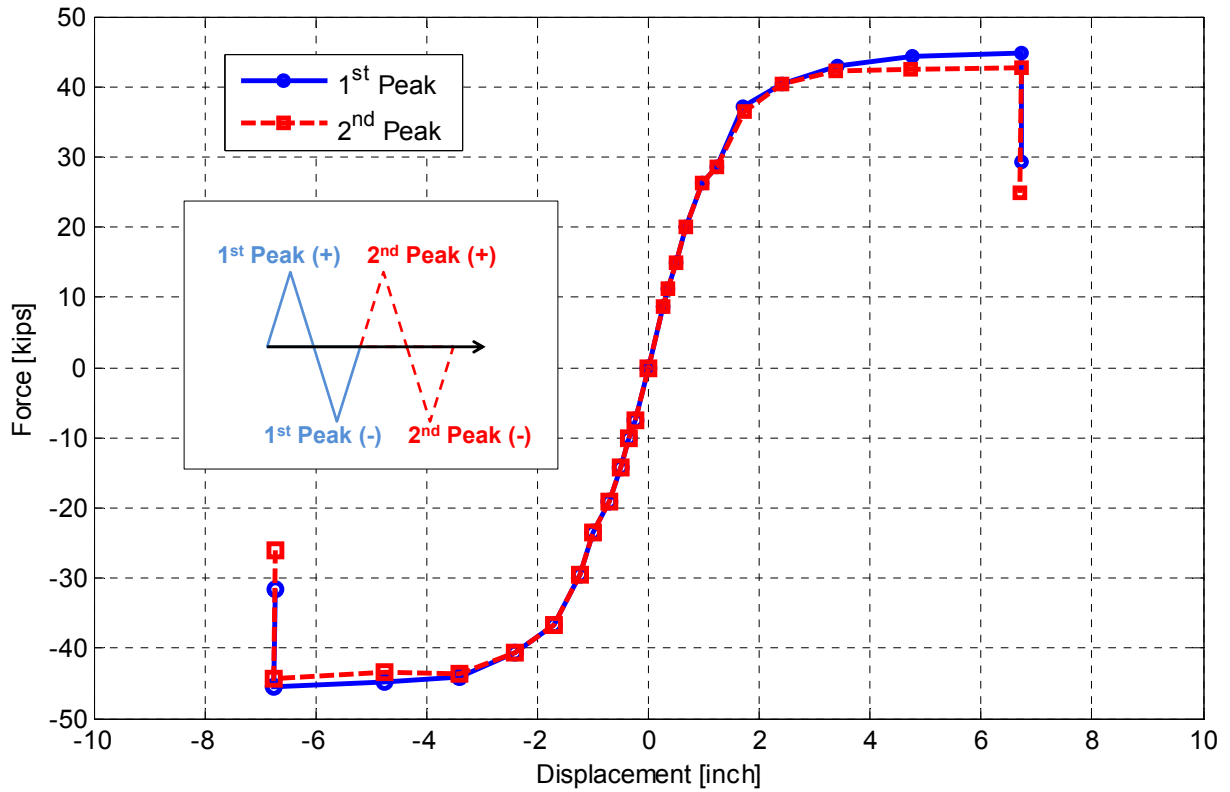
Figure 5.18 Force-displacement envelop for all cycles groups in longitudinal direction

154
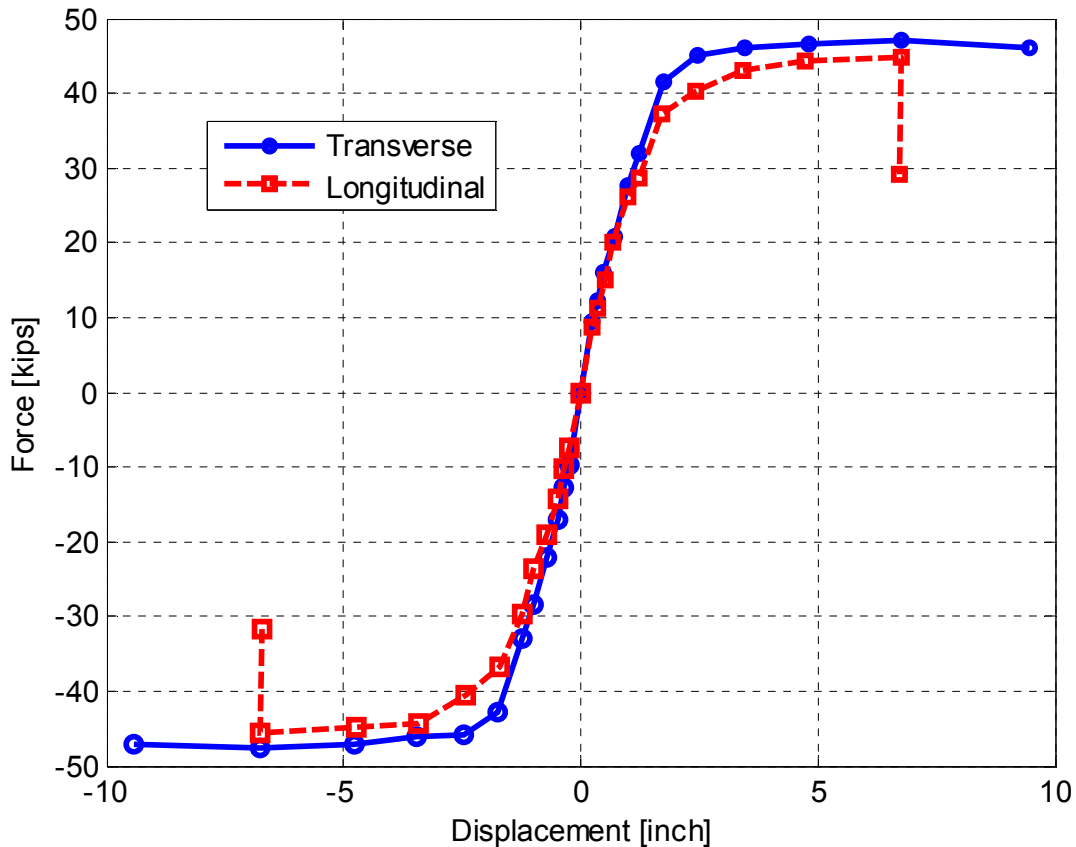
Figure 5.19 Comparison of force-displacement envelops (cycles 1ˢᵗ peak) in both transverse and longitudinal directions

5.2.4 Stiffness Determination

Using the recorded force and displacement values during each of the loading cycles in both transverse and longitudinal directions, the lateral stiffness of the bridge subassembly was estimated. Several ways were used to estimate the stiffness after each loading cycle. A linear regression was best fit to the force-displacement loop obtained from each cyclic loading group. The secant stiffness at the maximum recorded force and its corresponding displacement was estimated twice from positive and negative loading for each loading group. An example for computing the secant stiffness for one of the 9.5 inch transverse cycling loading groups is shown in Figure 5.20. A summary of the estimated best fit, positive and negative stiffness values along with the observed maximum force and displacements is listed in Table 5-2 and Table 5-3 for the transverse and longitudinal directions, respectively. The tables also list the corresponding drift ratio and ductility level for each loading group. The degradation of the secant stiffness, calculated from both positive and negative loading cases, is plotted against the drift ratio and ductility level in Figure 5.21 and Figure 5.22 for the transverse and longitudinal directions, respectively.

To obtain another estimate of the stiffness, a small loading cycle (20% of the preceding cycle's amplitude) was applied after each of the main test loading groups in both directions. The initial stiffness was then obtained from those small cycles to judge the stiffness degradation as

155

loading progresses. A comparison between the stiffness degradation in both transverse and longitudinal directions using the previously mentioned secant stiffness and the stiffness values obtained from the small cycles is presented in Figure 5.23 and Figure 5.24, respectively. It is observed that the stiffness in the longitudinal direction is consistently less than that in the transverse direction at a given drift ratio or ductility level. This can be attributed to two main reasons. First, the loading always started in the transverse direction first before it resumes in the longitudinal direction for a given group of loading cycles. Accordingly, the cracking and nonlinearity happening during the transverse loading results in a relative reduction in the stiffness when the longitudinal loading takes place. The second reason for the observed less stiffness in the longitudinal direction can be a result of the relative flexibility of the column/box-girder statical system in the longitudinal direction relative to the column/cap beam statical system in the transverse direction.
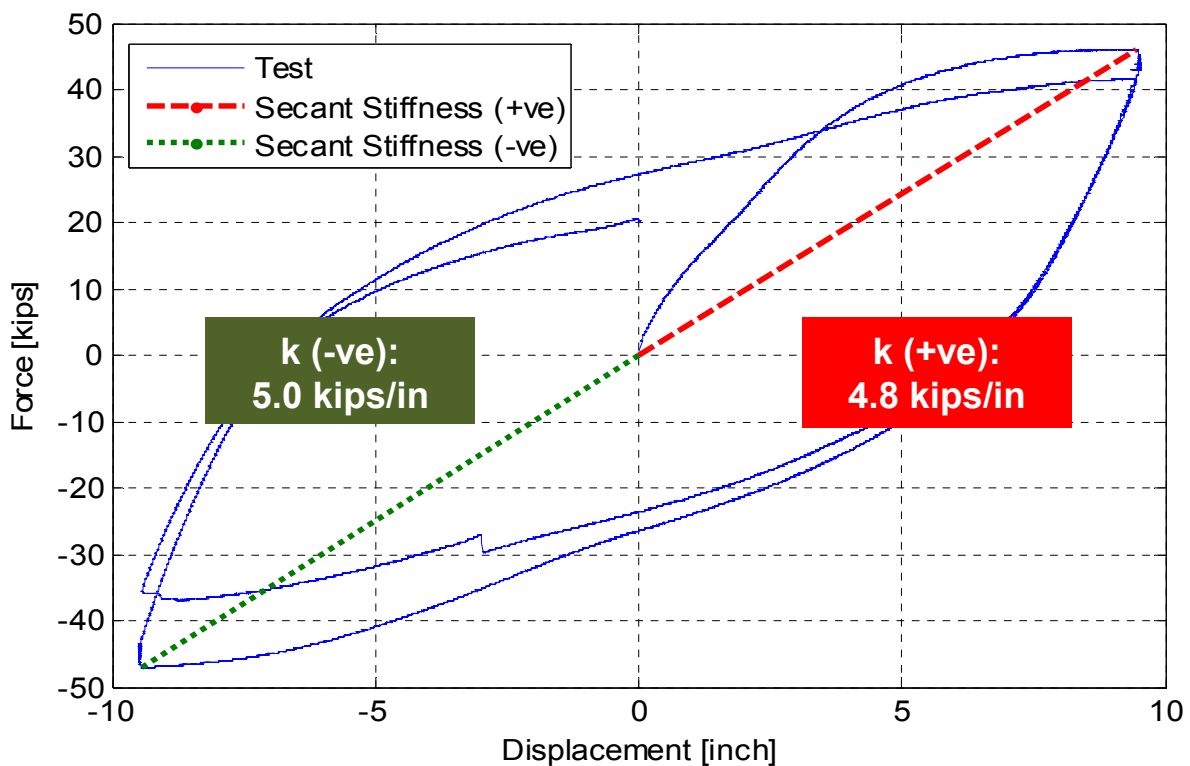
Figure 5.20 Example of secant stiffness calculation in positive and negative loading directions for the 9.5 inch transverse displacement cyclic loading group

156

Table 5-2 Summary of displacement, force, stiffness, ductility, and drift ratio values for all runs in transverse direction (X)

Run #	Disp. u_x [inch]		Force f_x [kips]		Stiffness [kips/inch]			Drift Ratio [%]	Ductility [μ]
	+ve	-ve	+ve	-ve	Best Fit	Secant +ve	Secant -ve		
1	0.25	-0.25	9.35	-9.76	37.70	37.40	39.04	0.28	0.20
2	0.34	-0.35	12.30	-12.76	35.40	36.18	36.99	0.38	0.27
3	0.49	-0.49	16.12	-16.96	33.00	33.24	34.61	0.54	0.39
4	0.70	-0.70	20.86	-22.13	29.81	29.80	31.61	0.78	0.56
5	1.00	-1.00	27.60	-28.40	26.98	27.60	28.40	1.11	0.80
6	1.25	-1.24	32.00	-32.95	25.13	25.60	26.57	1.39	1.00
7	1.75	-1.74	41.50	-42.72	23.25	23.71	24.55	1.94	1.40
8a	2.45	-2.45	45.20	-45.80	17.71	18.45	18.69	2.72	1.96
8b	2.45	-2.45	43.60	-44.50	17.71	17.80	18.16	2.72	1.96
9a	3.45	-3.45	46.00	-46.18	12.48	13.33	13.39	3.83	2.76
9b	3.40	-3.42	44.30	-44.80	12.48	13.03	13.10	3.78	2.72
10a	4.80	-4.76	46.50	-47.10	8.80	9.69	9.89	5.33	3.84
10b	4.76	-4.76	44.70	-45.60	8.80	9.39	9.59	5.29	3.81
11a	6.77	-6.76	**47.00**	**-47.50**	6.12	6.94	7.03	7.52	5.42
11b	6.75	-6.74	45.00	-46.00	6.12	6.67	6.82	7.50	5.40
12a	9.46	-9.44	46.00	-47.10	3.86	4.86	4.99	10.51	7.57
12b	9.45	-9.42	41.60	-35.93	3.86	4.40	3.81	10.50	7.56
13	9.45	-9.40	33.72	-21.25	2.22	3.57	2.26	10.49	7.56
14	0.97	-0.97	6.30	-0.62	6.28	6.53	0.65	1.07	0.77

Table 5-3 Summary of displacement, force, stiffness, ductility, and drift ratio values for all runs in in longitudinal direction (Y)

Run #	Disp. u_x [inch]		Force f_x [kips]		Stiffness [kips/inch]			Drift Ratio [%}	Ductility [μ]
	+ve	-ve	+ve	-ve	Best Fit	Secant +ve	Secant -ve		
1	0.25	-0.24	8.59	-7.46	30.50	34.36	31.08	0.28	0.20
2	0.34	-0.34	11.33	-10.18	29.80	33.32	29.94	0.38	0.27
3	0.50	-0.49	14.90	-14.15	28.20	29.80	28.88	0.56	0.40
4	0.69	-0.70	20.00	-19.05	26.00	28.99	27.21	0.77	0.55
5	0.98	-0.99	26.20	-23.60	23.50	26.73	23.84	1.09	0.78
6	1.23	-1.24	28.70	-29.60	22.30	23.33	23.87	1.37	0.98
7a	1.71	-1.71	37.20	-36.70	19.70	21.75	21.46	1.90	1.37
7b	1.72	-1.71	36.40	-36.60	19.70	21.16	21.40	1.91	1.38
8a	2.42	-2.42	40.30	-40.60	15.60	16.65	16.78	2.69	1.94
8b	2.42	-2.42	40.30	-40.60	15.60	16.65	16.78	2.69	1.94
9a	3.40	-3.40	43.00	-44.20	11.60	12.65	13.00	3.78	2.72
9b	3.39	-3.40	42.20	-43.70	11.60	12.45	12.85	3.77	2.71
10a	4.75	-4.75	44.25	-44.77	8.23	9.32	8.97	5.28	3.80
10b	4.74	-4.75	42.50	-43.50	8.23	8.97	9.16	5.27	3.79
11a	6.74	-6.76	**44.70**	**-45.55**	5.62	6.63	6.33	7.49	5.39
11b	6.73	-6.75	42.60	-44.30	5.62	6.33	6.56	7.48	5.38
12a	6.72	-6.73	29.25	-31.70	3.30	4.35	4.71	7.47	5.38
12b	6.71	-6.73	25.00	-26.00	3.30	3.73	3.86	7.46	5.37
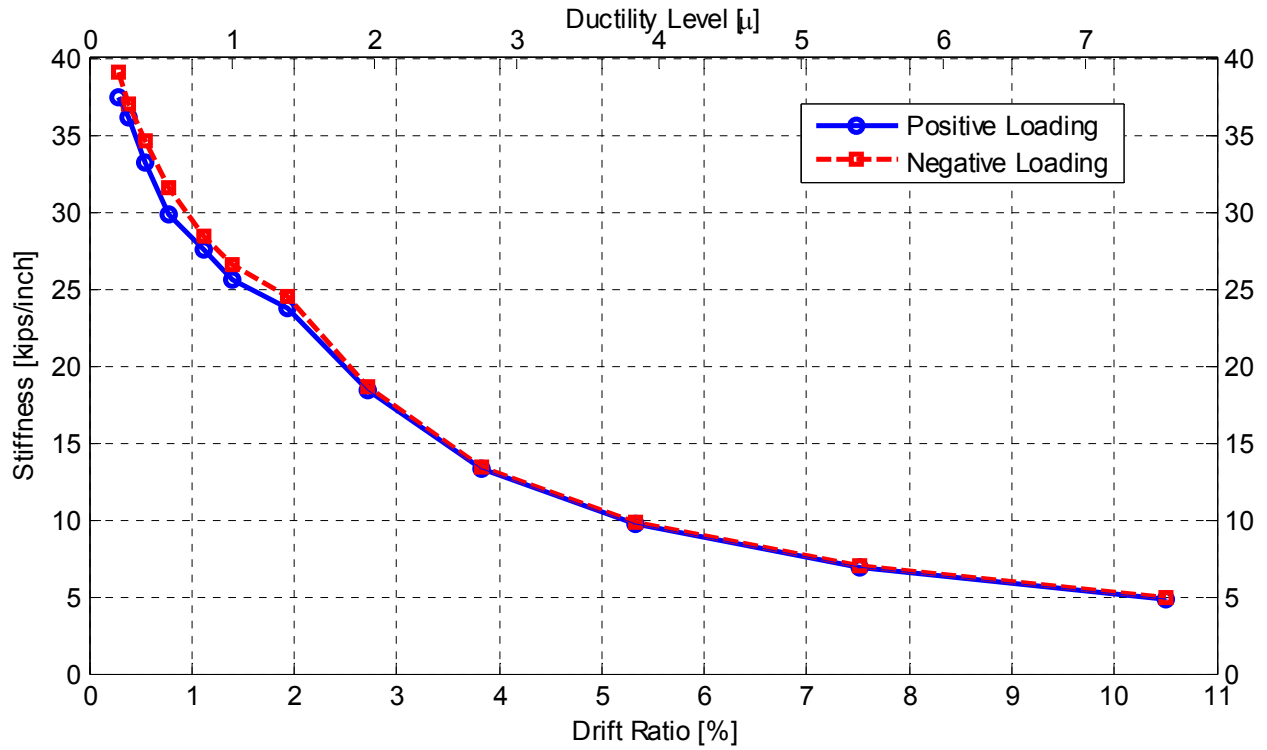
Figure 5.21 Lateral secant stiffness degradation in transverse direction
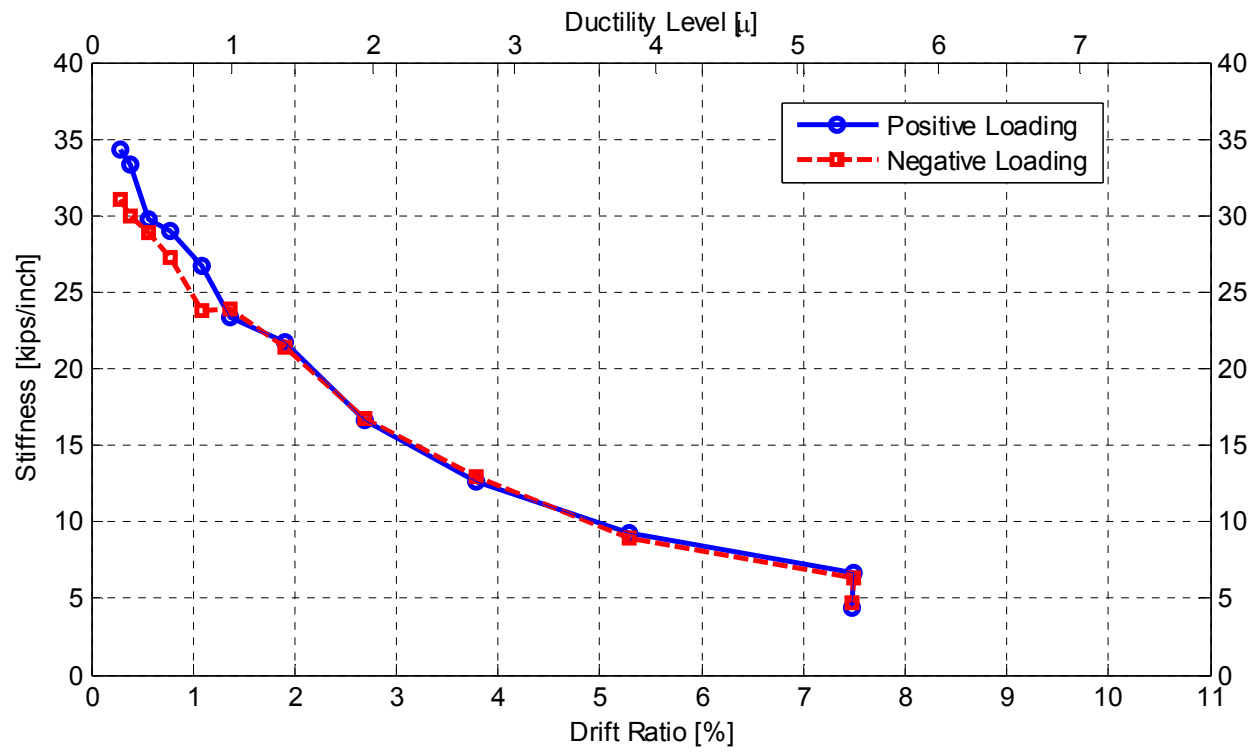
Figure 5.22 Lateral secant stiffness degradation in longitudinal direction

159
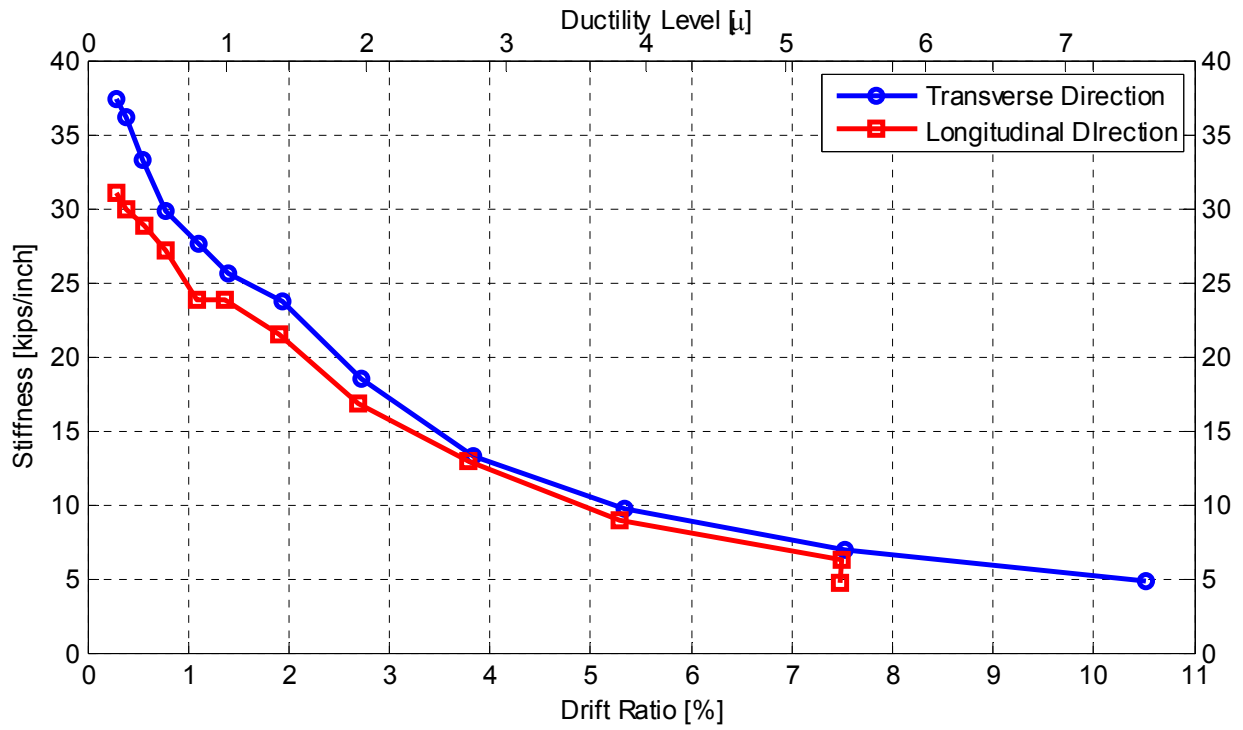
Figure 5.23 Comparison of stiffness degradation in both transverse and longitudinal directions using the secant stiffness values
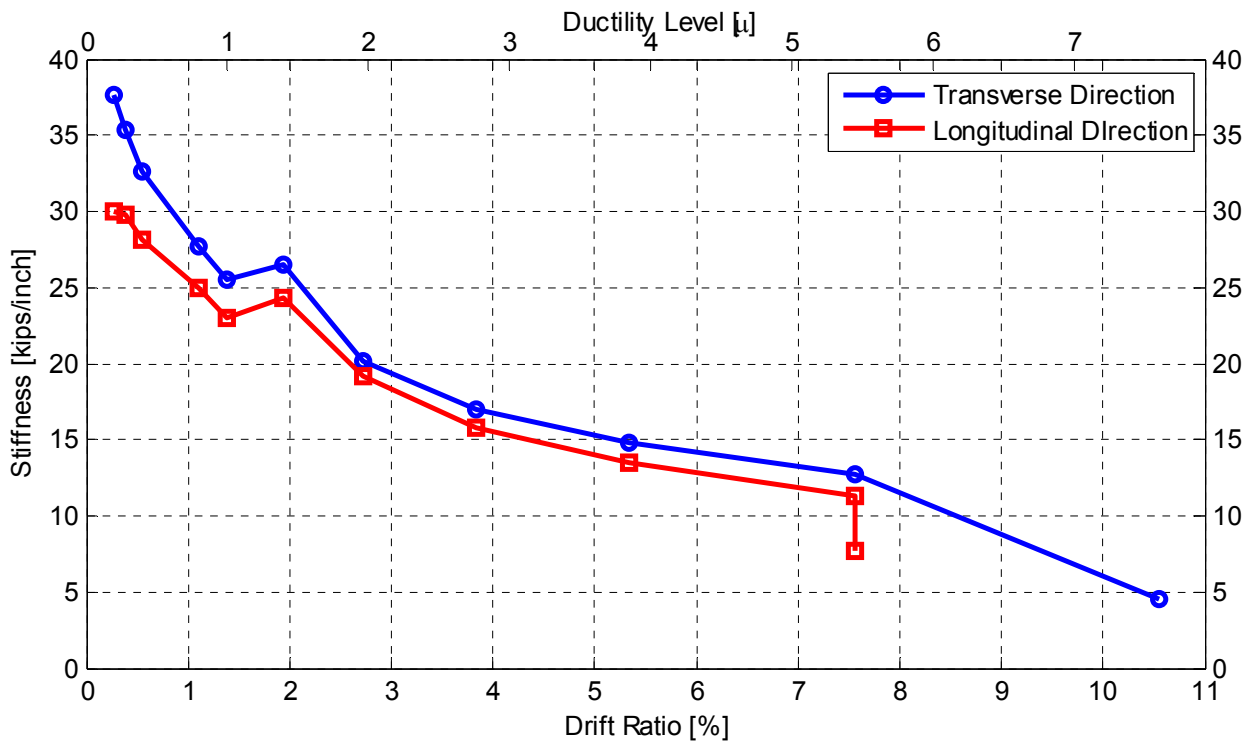
Figure 5.24 Comparison of stiffness degradation in both transverse and longitudinal directions using the stiffness values estimated from the small cycles that followed the main test loading groups

160

5.3   COLUMN LOCAL BEHAVIOR

The main objective of the experimental program pursued in this study is to evaluate the bent cap beam behavior and effective width. However, the local column behavior was extensively studied for better understanding of the overall bridge system response and to evaluate the column repair and strengthening schemes undertaken after the first specimen test was completed. The discussion of the local column behavior presented in the following three subsections focuses on the strain and curvatures recorded at different levels in the column plastic hinge zone, and the column section's moment-curvature relationship in both transverse and longitudinal directions. The column data and observed response are also useful for populating the existing database of column tests and possible future studies that focus on analytical and FE modeling.

5.3.1   Strain Behavior

Strain ages were installed at various levels along the four rebars that experienced the largest strains according to the adopted loading directions. The outermost north and south ones experienced the largest strains during longitudinal (N-S) loading, while the outermost east and west ones experienced the largest values during transverse (E-W) loading. The notation of loading direction is presented along with the four instrumented column rebars in Figure 5.25. The history of the strain measured in each of those four rebars is shown in Figure 5.26. The used strain gages were capable of recording the strain measurements almost throughout the test until a rebar rupture as seen from the east rebar strain history for instance. A maximum strain of almost 8% (0.08) was recorded in the north rebar which unlike the east and west rebars, did not rupture during the test. A close-up view of the different rebars strain history is shown in Figure 5.27. The figure shows how the strain develops only in east and west rebars during transverse loading, and north and south rebars during longitudinal loading. The shown strain histories were recorded at the strain gages at the maximum column moment location in the plastic hinge zone, i.e. slightly above the beam face. However, the strain profile in each of the four instrumented rebars along the column height is also presented here. Figure 5.28 through Figure 5.35 show the strain profile for each of the four instrumented rebars captured at three different loading levels, 2.7%, 5.3% and 7.5% drift ratio, at both of the positive and negative amplitudes of the loading cycles. The strain profile agrees with the expected bending moment distribution along the column height. However, a nonlinear distribution is shown in the plastic hinge zone due to excessive yielding and damage.
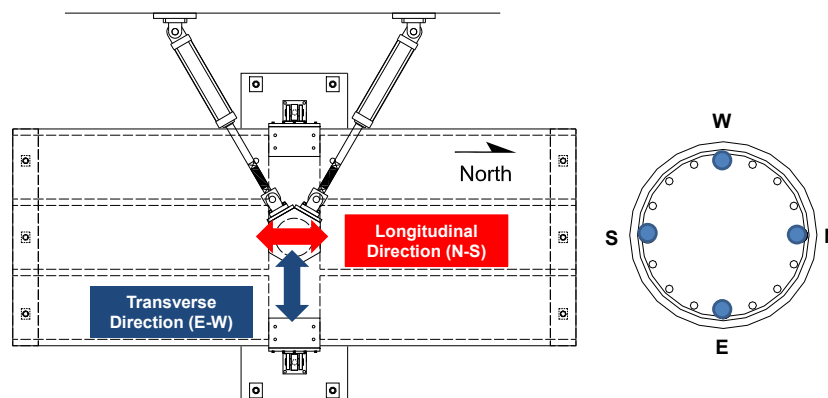
Figure 5.25 Notation of loading direction and layout of instrumented column rebars
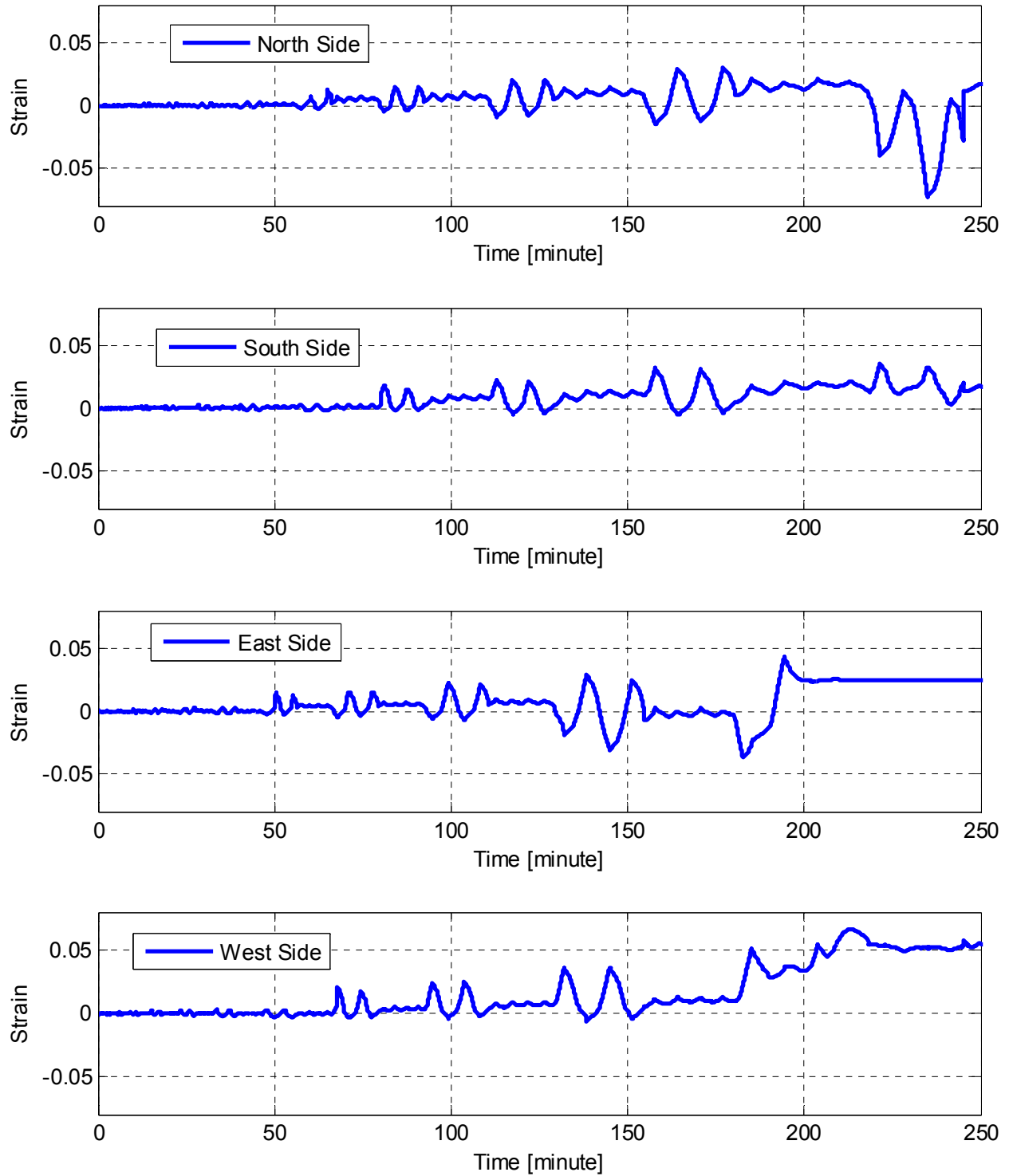
Figure 5.26 History of the column rebars strains at lowest section in the plastic hinge where maximum strain is expected for all loading cycles
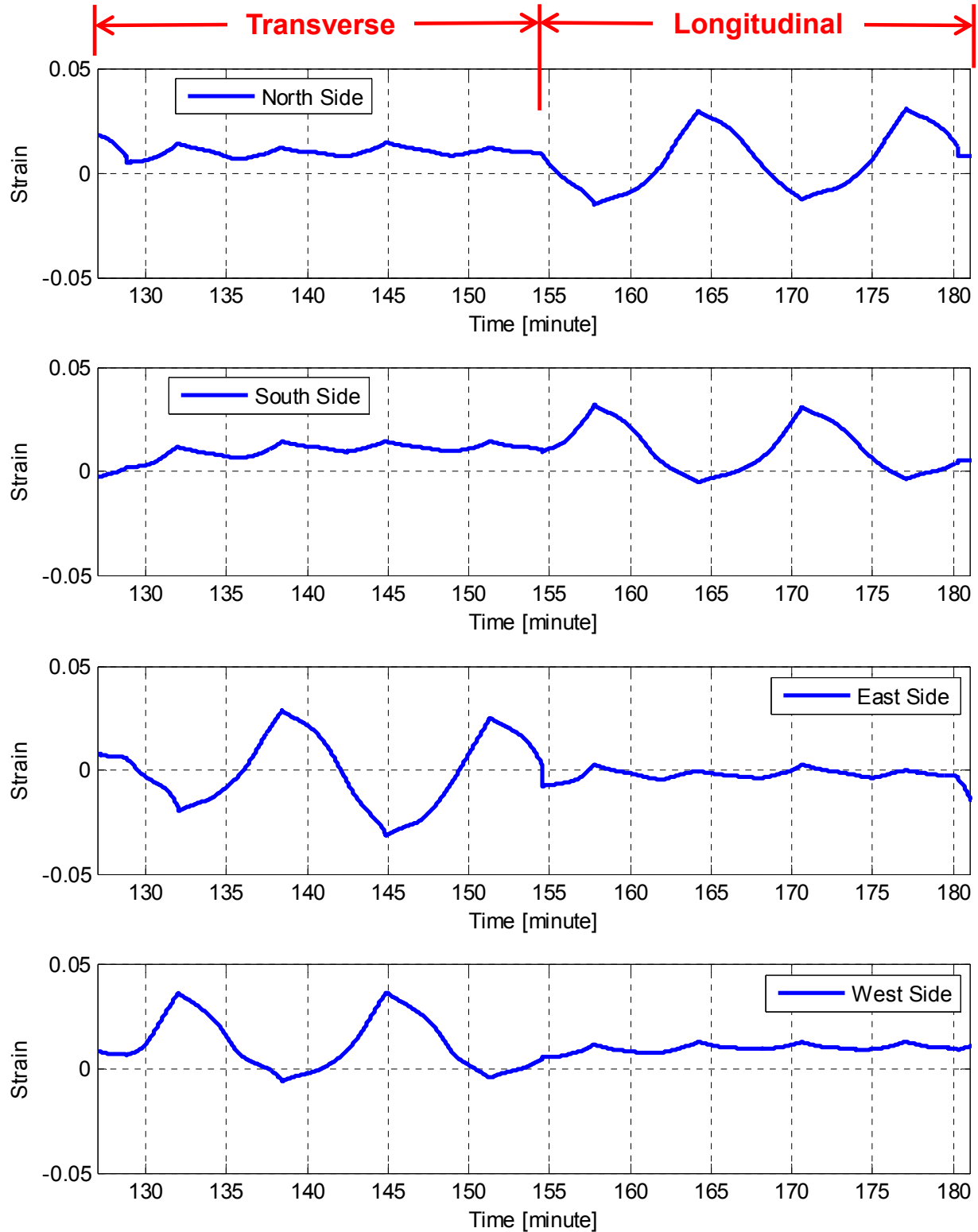
Figure 5.27 Zoomed-in view of the history of the column rebars strains at lowest section in the plastic hinge where maximum strain is expected for one group of transverse and one group of longitudinal loading cycles
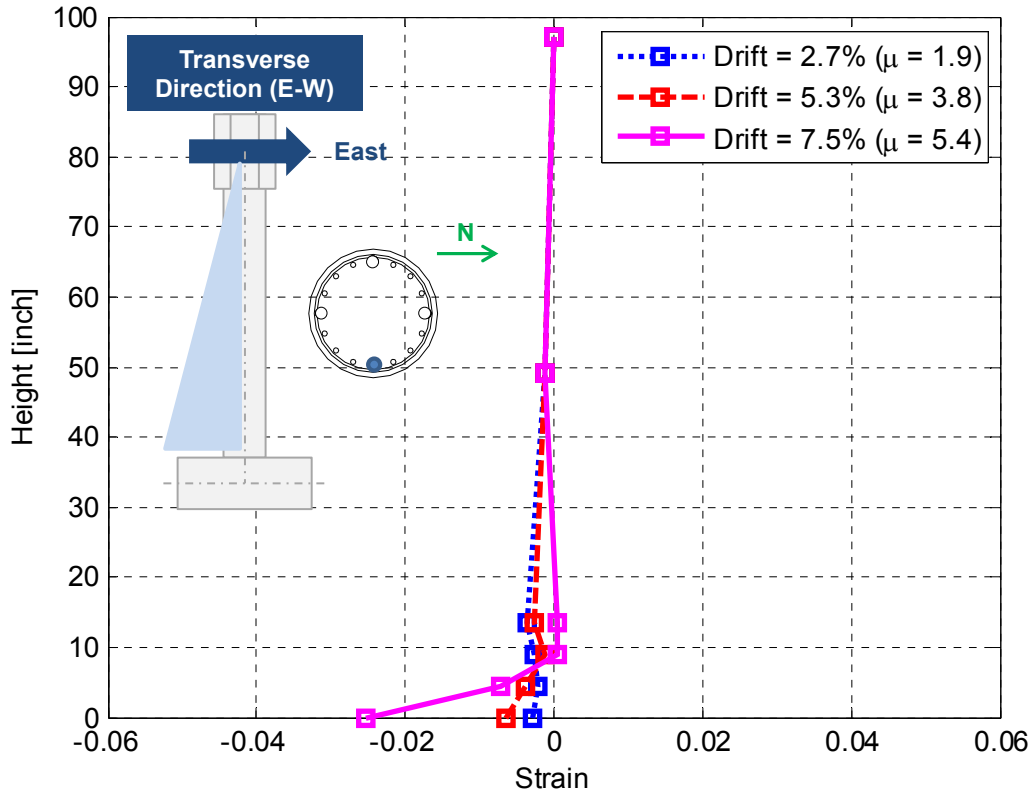
Figure 5.28 Strain distribution along EAST side rebar when loading is towards EAST
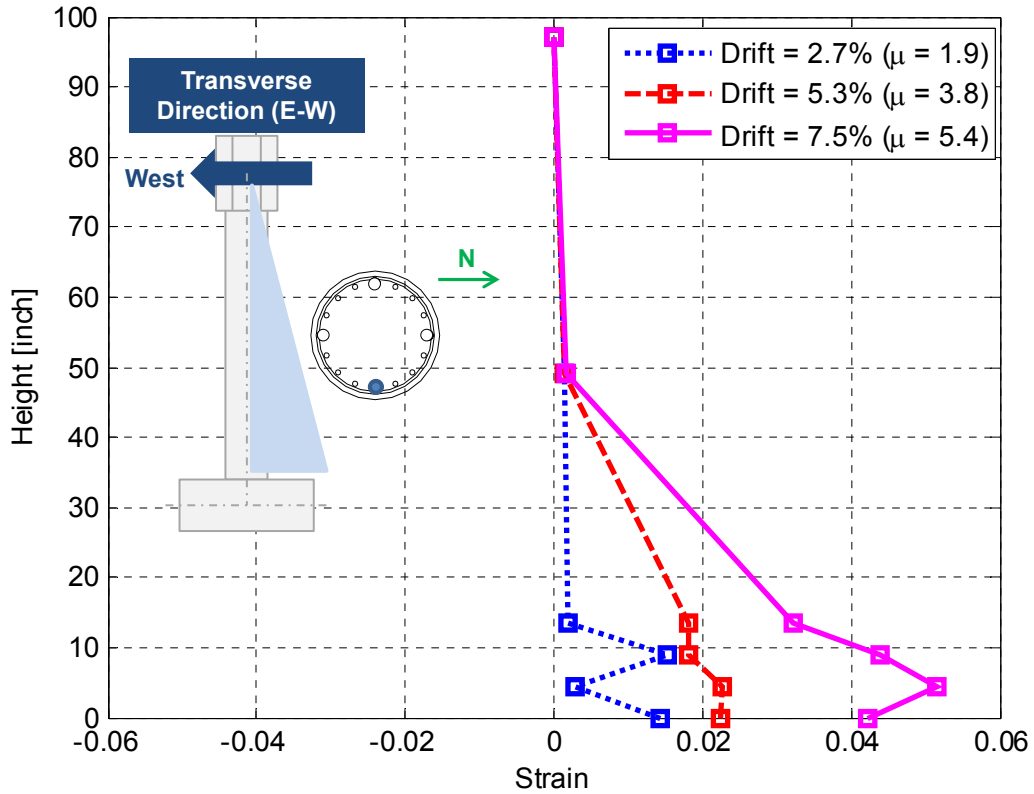
Figure 5.29 Strain distribution along EAST side rebar when loading is towards WEST
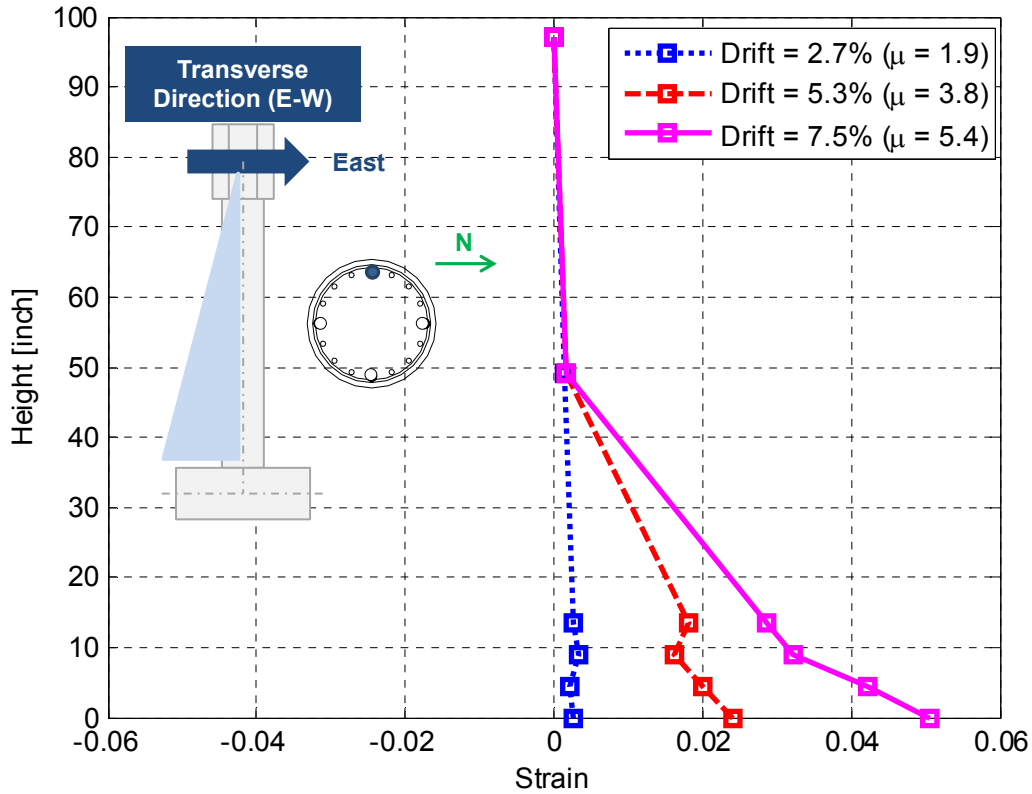
Figure 5.30 Strain distribution along WEST side rebar when loading is towards EAST
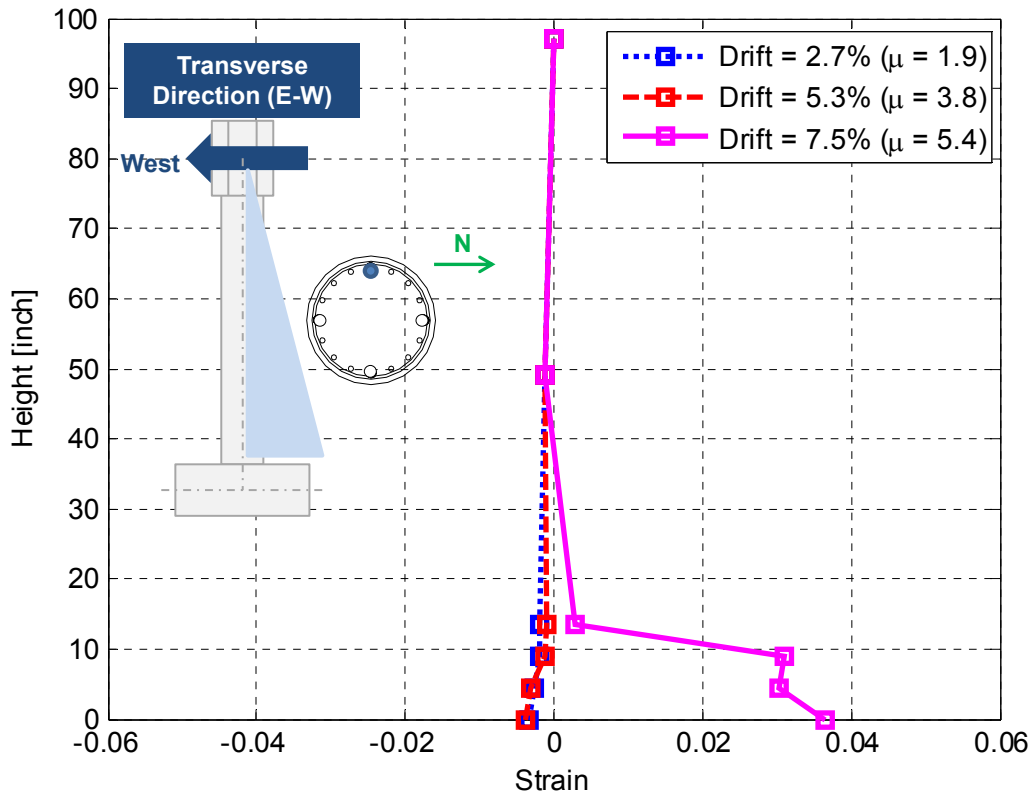
Figure 5.31 Strain distribution along WEST side rebar when loading is towards WEST

165
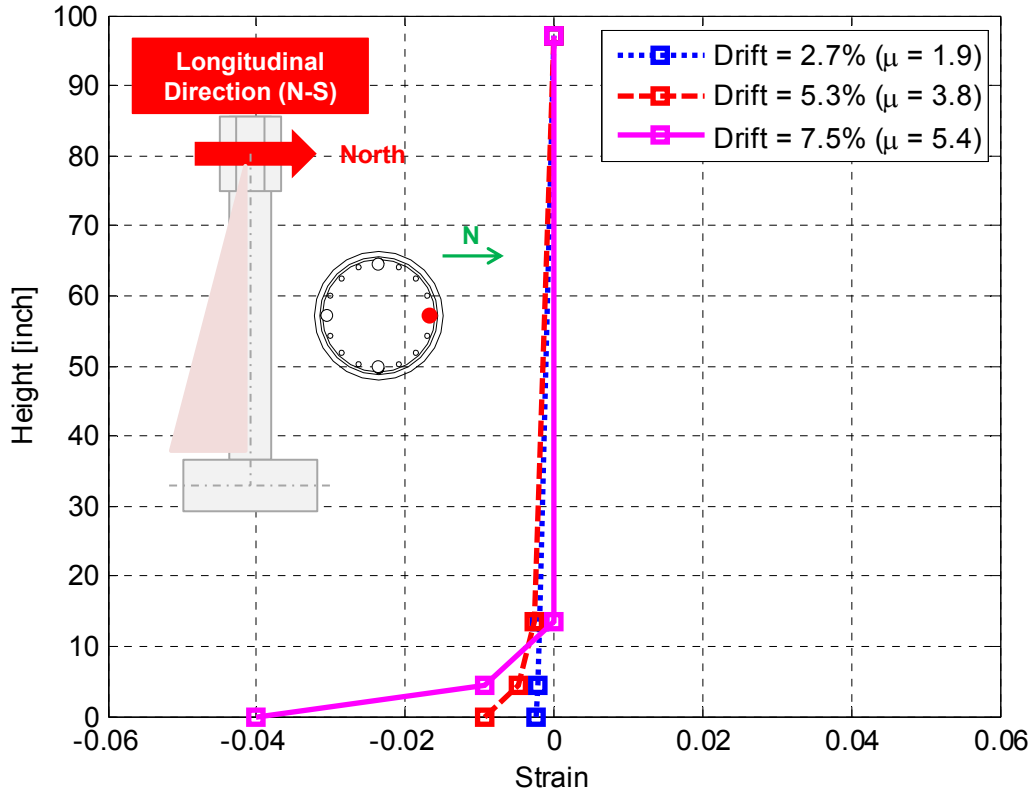
Figure 5.32 Strain distribution along NORTH side rebar when loading is towards NORTH
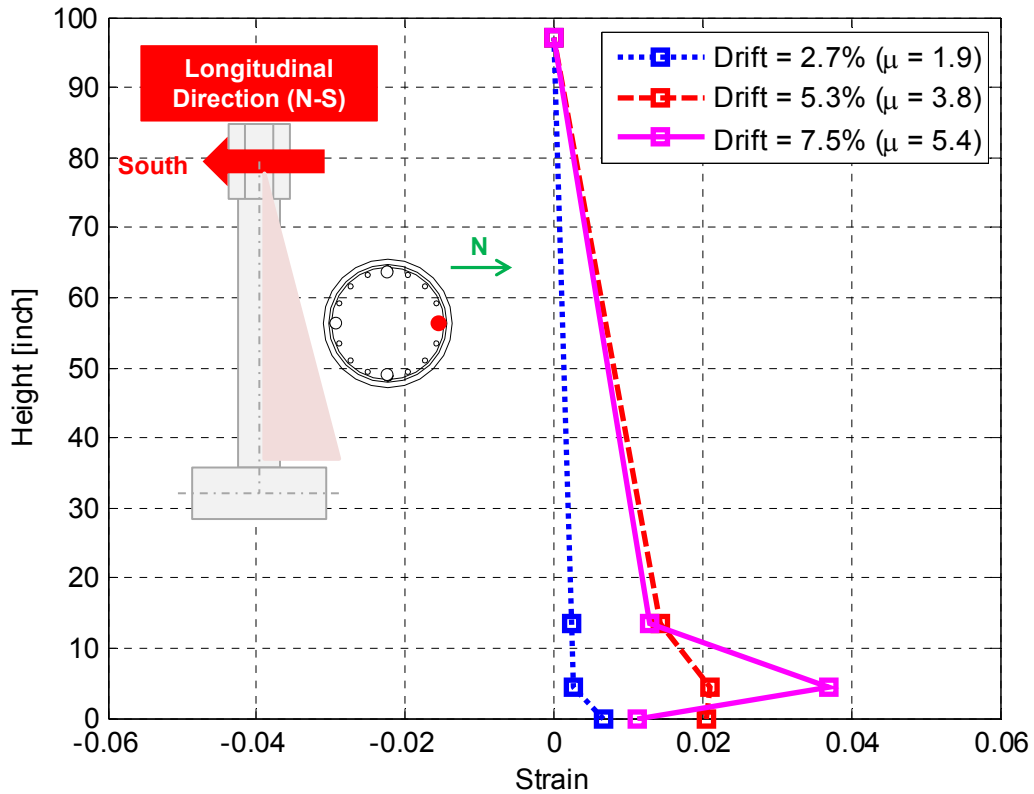
Figure 5.33 Strain distribution along NORTH side rebar when loading is towards SOUTH

166
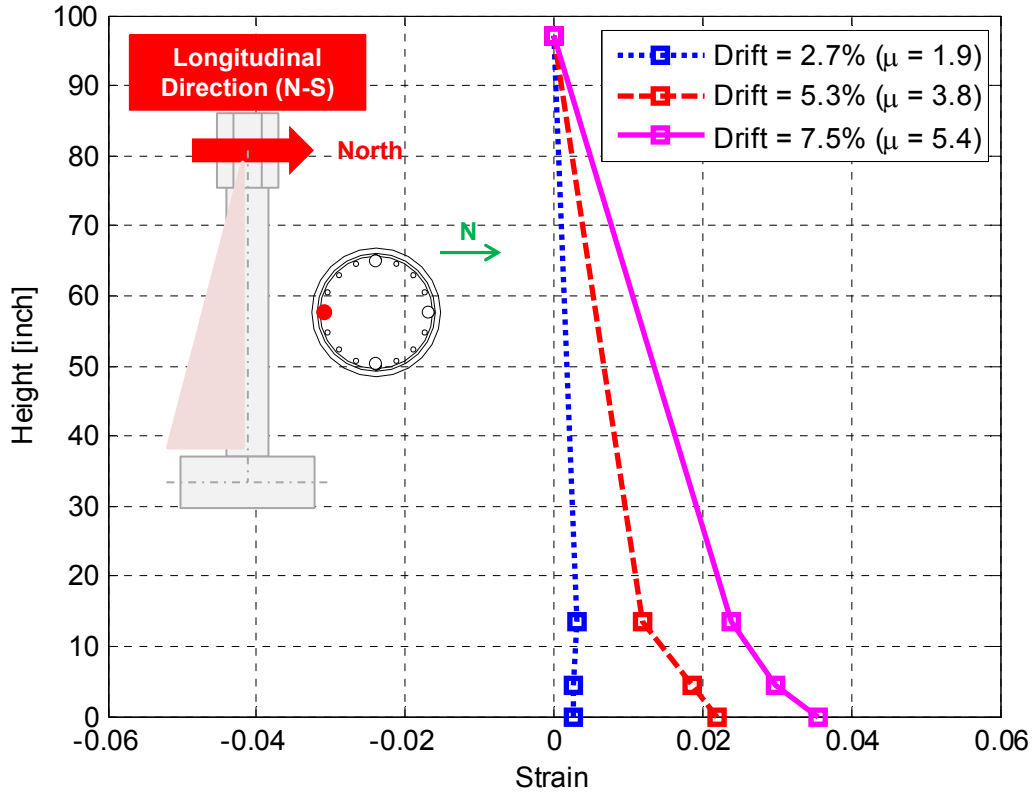
Figure 5.34 Strain distribution along SOUTH side rebar when loading is towards NORTH
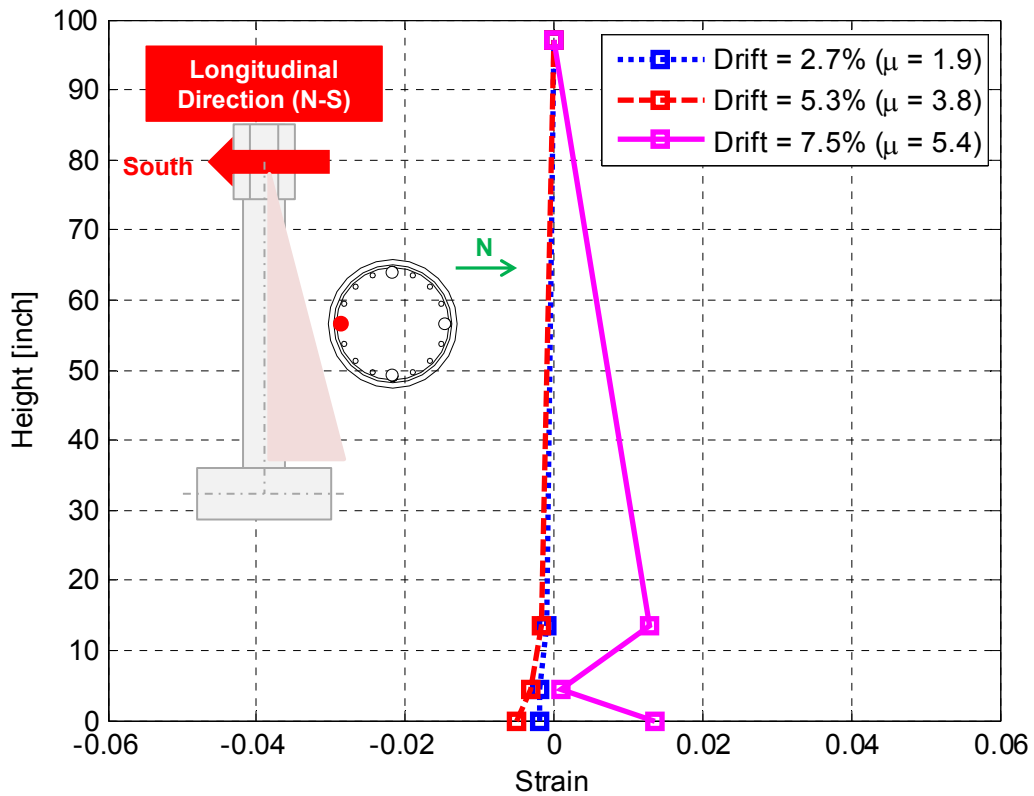
Figure 5.35 Strain distribution along SOUTH side rebar when loading is towards SOUTH

167

5.3.2   Curvature Behavior

Curvatures are important behavior metric especially for desired flexural-control ductile behavior. The plastic hinge rotations, and curvatures in turn, increase significantly relative to the other locations outside the desired column plastic hinge region. The subassembly column's curvatures were captured during the test using dedicated LVDTs as previously discussed in the instrumentation section in Chapter 3. The history of the measured curvature at the lowest level in the column's plastic hinge zone, i.e. close to the beam face, is shown in Figure 5.36 for both of the transverse (E-W) and longitudinal (N-S) directions. A close-up view of the curvature history is shown in Figure 5.37 to emphasize that most of the column rotations are planer with the load. This means that when loading is in the transverse direction, the column rotation and curvature is only in the E-W direction and vice versa in the longitudinal direction.
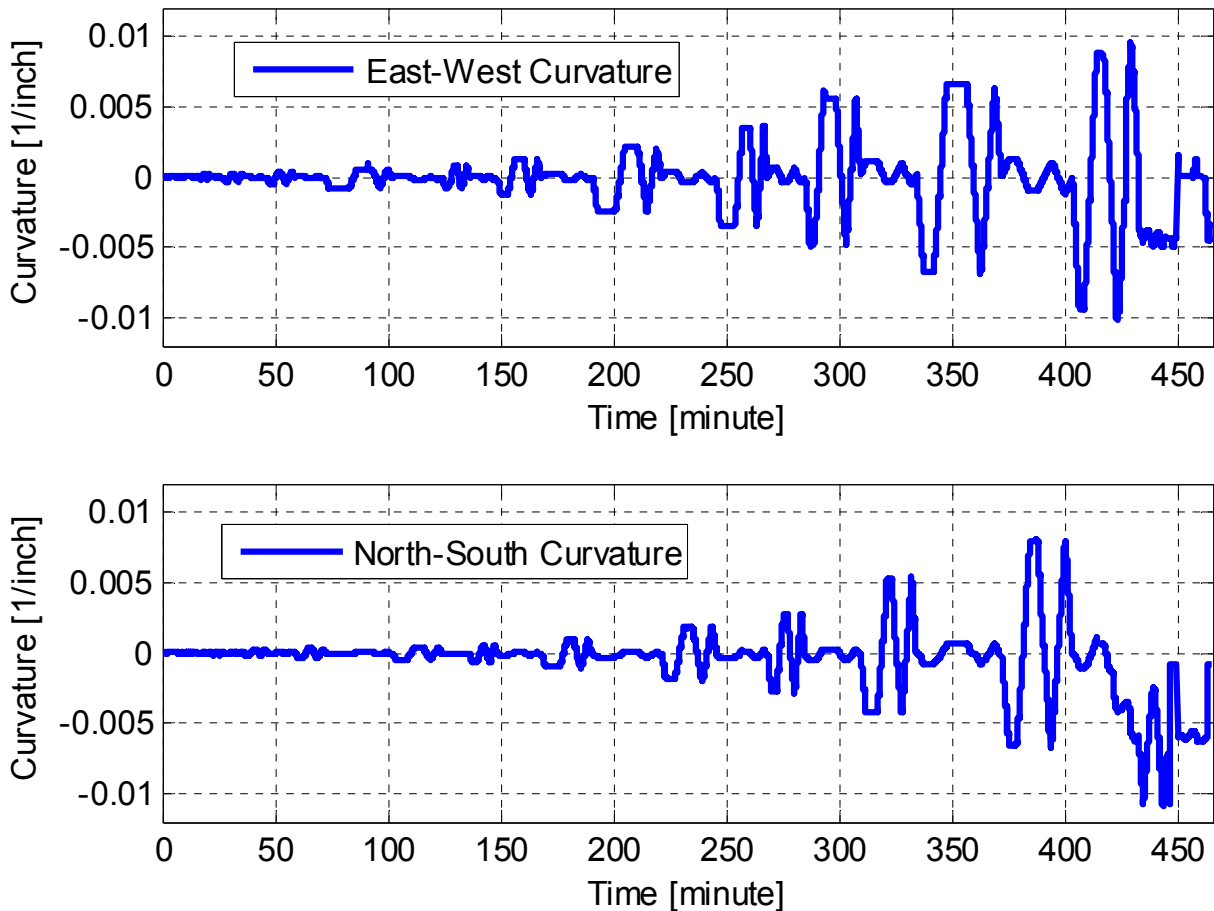
Figure 5.36 History of column curvature at the lowest section in the plastic hinge zone in both east-west (transverse) and north-south (longitudinal) directions for all loading cycles

168
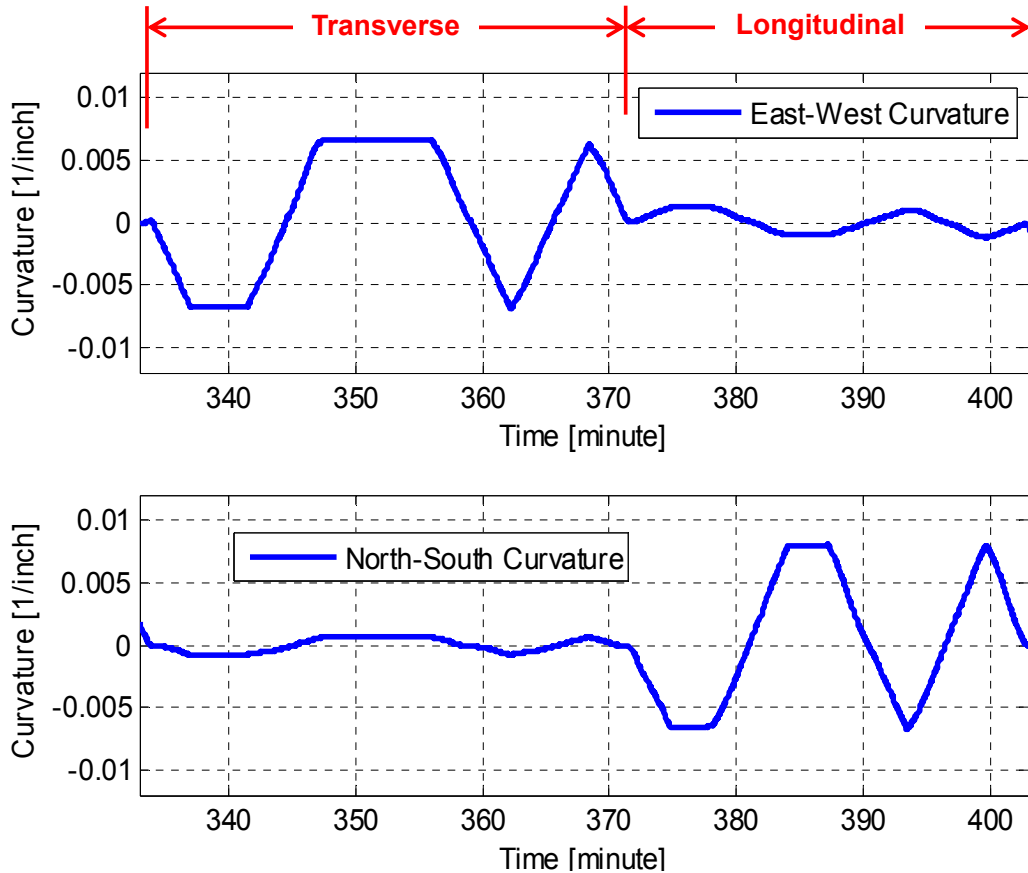
Figure 5.37 Zoomed-in view of the history of the column curvature at the lowest section in the plastic hinge zone in both east-west (transverse) and north-south (longitudinal) directions for one group of transverse and one group of longitudinal loading cycles

The distribution of curvatures along the column height is also of interest to investigate the column behavior. As previously mentioned, it is desired to concentrate the damage in the plastic hinge zone that is designed to be ductile enough to accommodate large rotations and avoid any collapse at elevated lateral loading demands. Such desired behavior was observed during the test. The curvature profile along the column height is shown in Figure 5.38 and Figure 5.39 for four levels of loading in the transverse direction when loading is in east and west directions, respectively, i.e. the curvature recorded at the loading cycle positive and negative amplitudes. Similarly, the curvature distribution in the column's longitudinal direction for loading in north and south directions is shown in Figure 5.40 and Figure 5.41, respectively. The four levels of loading included in these figures are the 1.0%, 2.7%, 5.3%, and 7.5% drift ratios, which correspond to ductility levels of 1.0, 1.9, 3.8, and 5.4, respectively. A maximum curvature value of almost 0.01 in.$^{-1}$ was recorded before the LVDT instrumentation slipped because of the extensive concrete spalling. Considering a yield curvature of 0.00034 in.$^{-1}$ as estimated from sectional analysis, the observed maximum curvature denotes a curvature ductility of 29.4. Meanwhile, the maximum curvature value corresponds to plastic rotation of approximately 0.15 radians (8.6 degrees) using a 15-inch plastic hinge length as calculated by Caltrans SDC provisions. The plastic rotation and curvature ductility values show that the column designed according to the latest Caltrans SDC and AASHTO provisions is more ductile than the minimum code requirements.

169
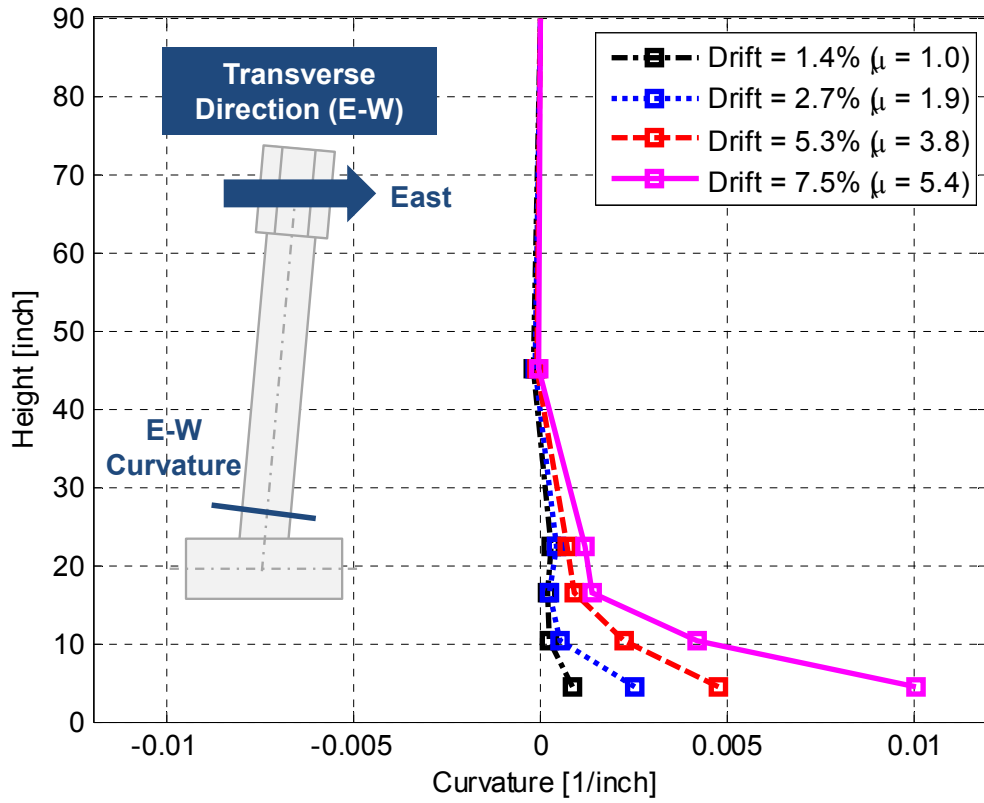
Figure 5.38 Curvature distribution along column height when loading is towards East
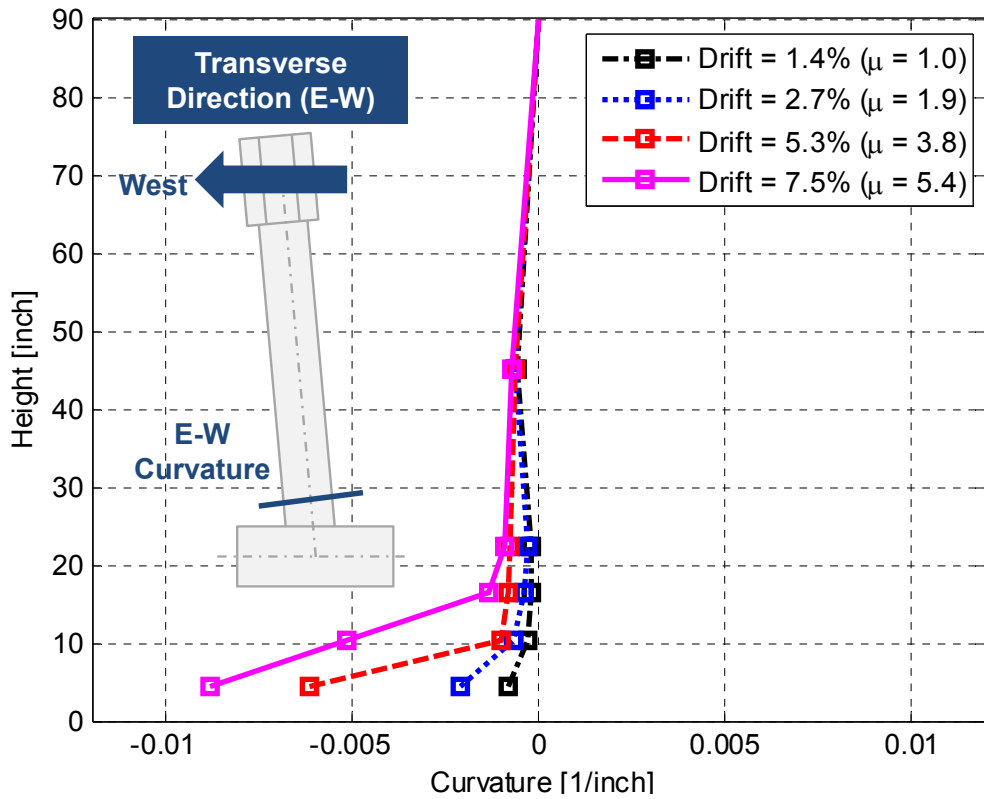
Figure 5.39 Curvature distribution along column height when loading is towards West

170
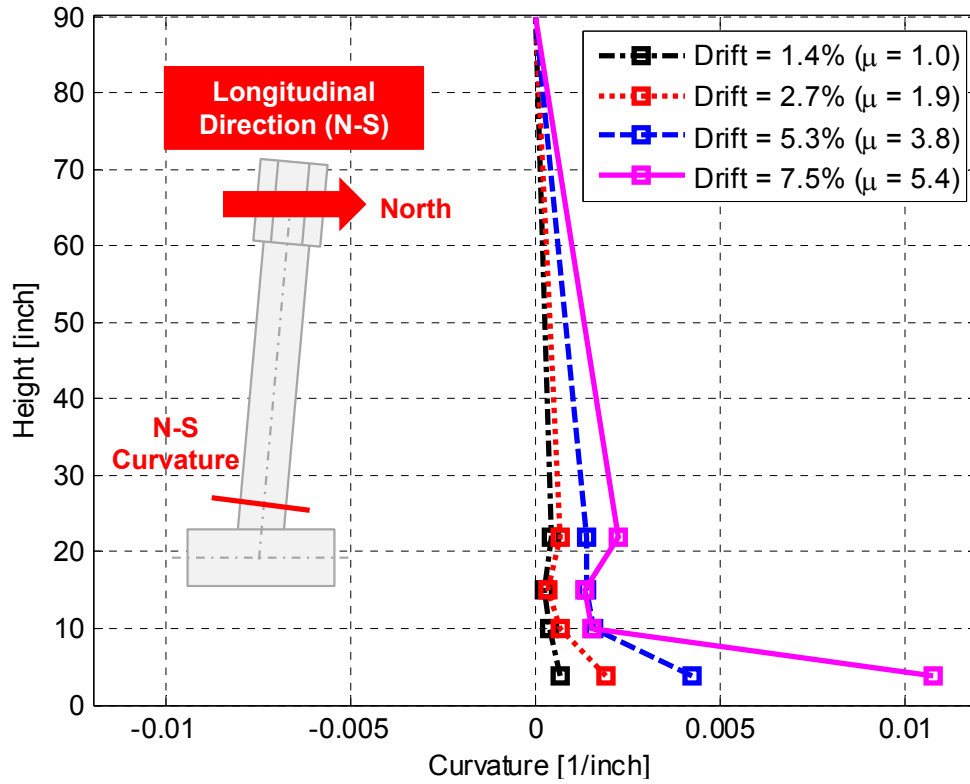
Figure 5.40 Curvature distribution along column height when loading is towards North
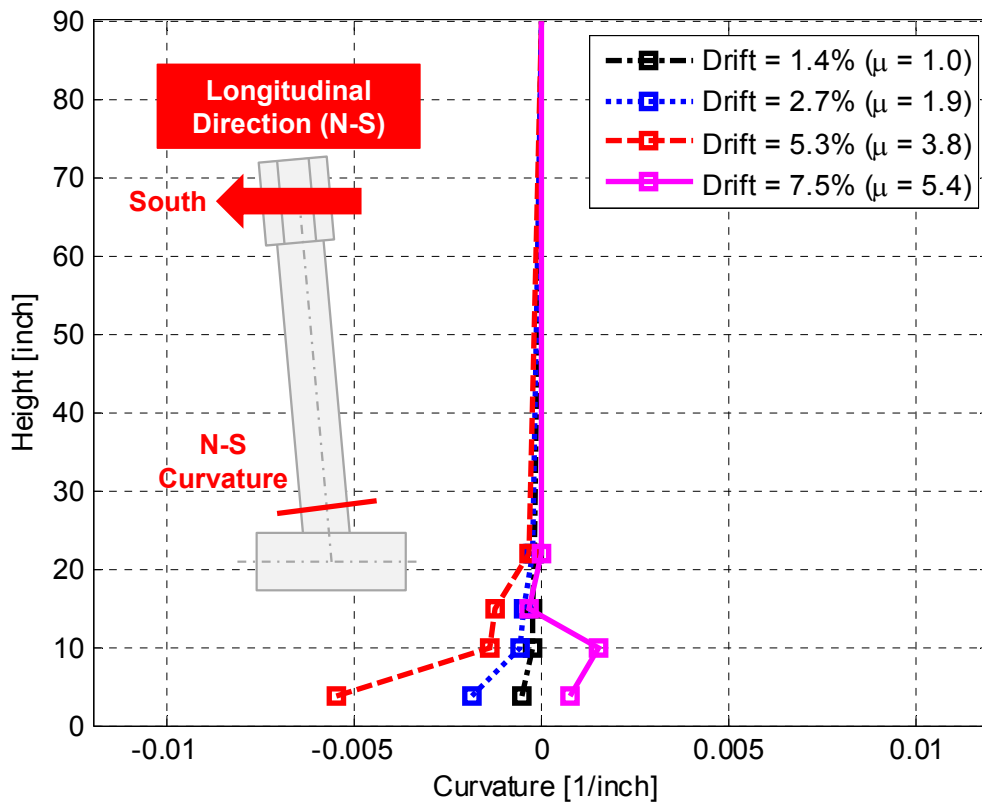
Figure 5.41 Curvature distribution along column height when loading is towards South

171

5.3.3 Moment-Curvature Relationships

Based on the previous discussion of the observed column curvatures, it is favorable to relate such curvatures to the corresponding bending moments to obtain the moment-curvature relationships. To estimate the column's curvatures, one way is to use the LVDTs dedicated to measure relative displacements to calculate strains and then curvatures. However, strains recorded in the column rebars can also be used to calculate curvatures as long as each two opposite strain gages (SG) at a given level are used and linear strain distribution (plane section remaining plane hypothesis) is assumed. The moment-curvature relationships obtained at different sections in the transverse direction are compared when LVDT-based and SG-based curvatures are utilized as shown in Figure 5.42 through Figure 5.46. At small-loading levels or linear elastic regime of the column, the curvature calculations from either the LVDTs or SGs compare well. However, at elevated loading levels and large plastic hinge rotations and deformations, the curvatures calculated from the LVDTs are more accurate and reliable. The SG-based curvatures are under estimated as shown in Figure 5.45 and Figure 5.46 at the plastic hinge maximum rotation/curvature region. Therefore, only LVDT-based curvatures were used to plot the moment-curvature relationships in the longitudinal direction. Figure 5.47 through Figure 5.50 show the moment-curvature at four different sections in the longitudinal direction. The moment-curvature relationships at the lowest section in the plastic hinge where the maximum curvatures were determined are compared for the transverse and longitudinal directions in Figure 5.51.
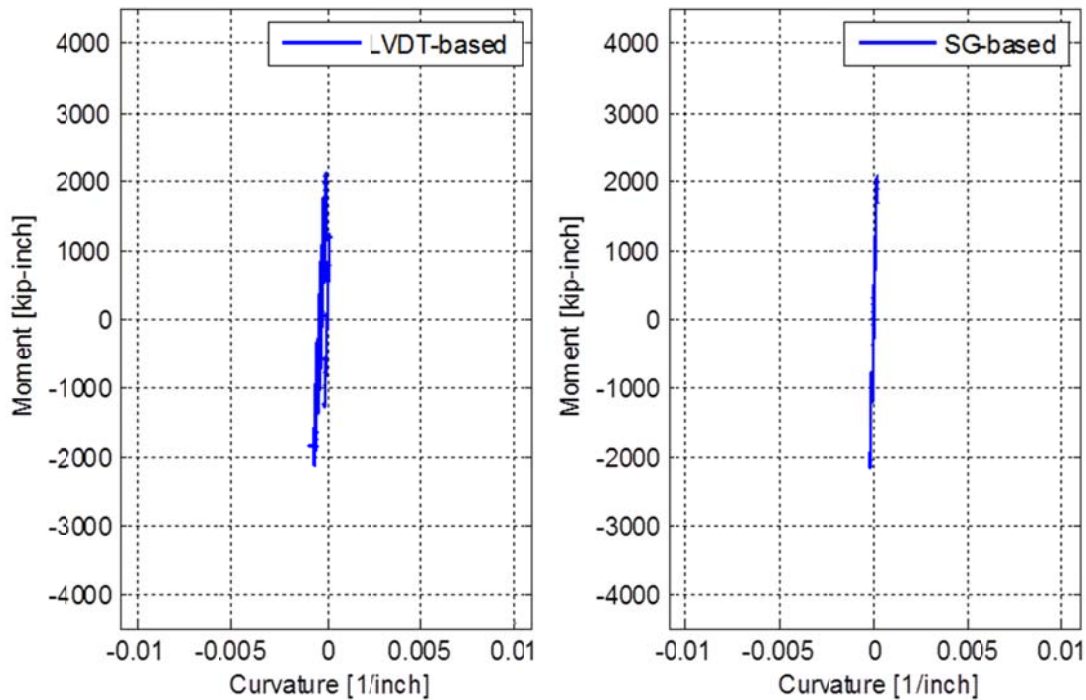
Figure 5.42 Comparison of LVDT-based and strain-based column moment-curvature relationship at section 5 (mid-height, refer to Figure 3.51) due to all transverse loading cycles
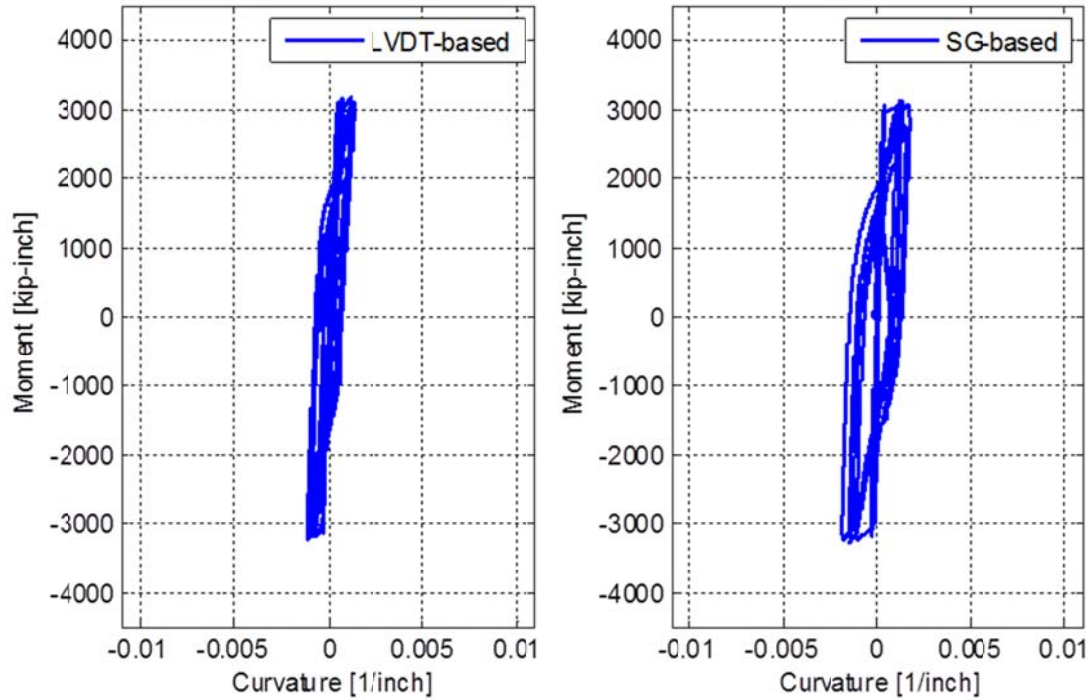
Figure 5.43 Comparison of LVDT-based and strain-based column moment-curvature relationship at section 4 (22 inch from beam face, refer to Figure 3.51) due to all transverse loading cycles
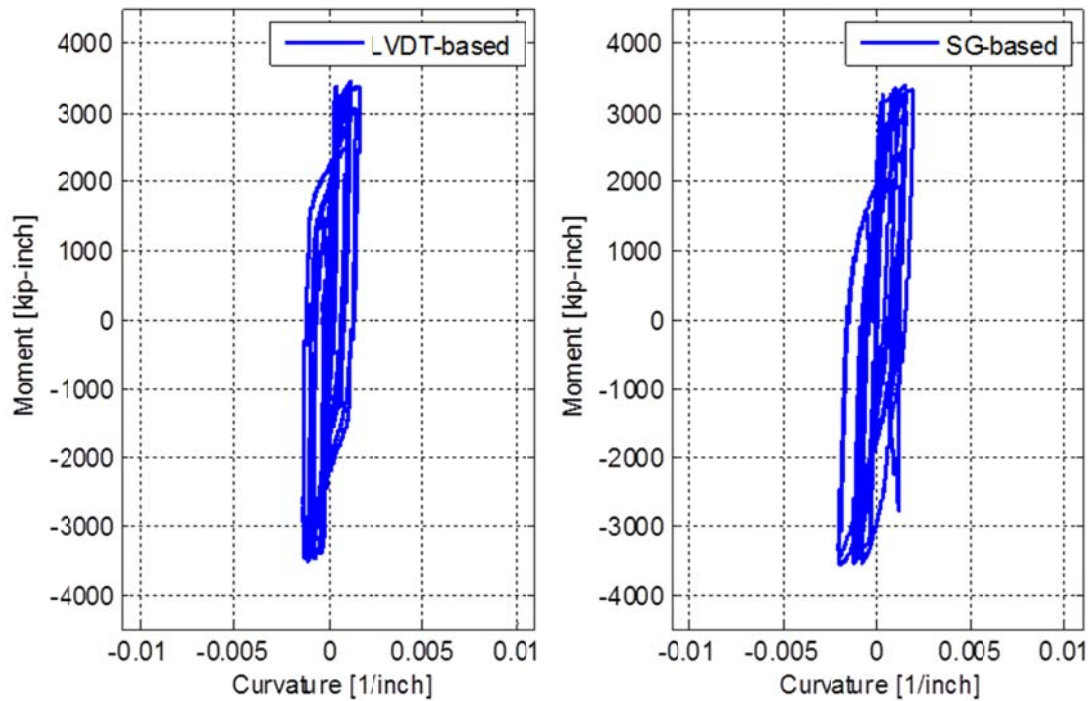
Figure 5.44 Comparison of LVDT-based and strain-based column moment-curvature relationship at section 3 (16 inch from beam face, refer to Figure 3.51) due to all transverse loading cycles
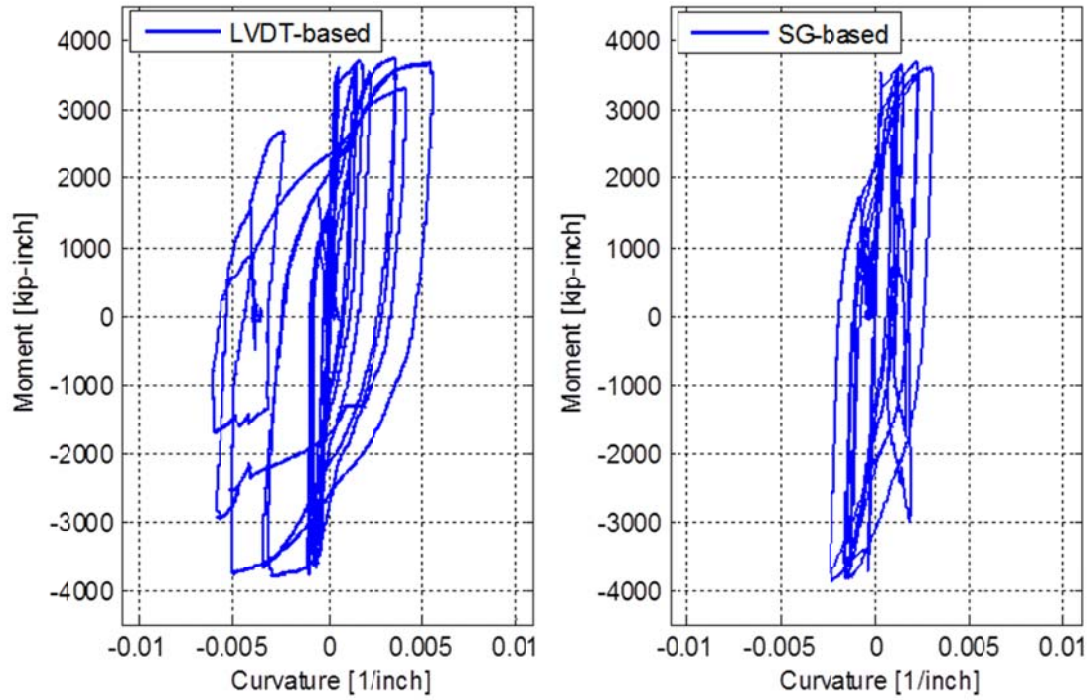
Figure 5.45 Comparison of LVDT-based and strain-based column moment-curvature relationship at section 2 (10 inch from beam face, refer to Figure 3.51) due to all transverse loading cycles
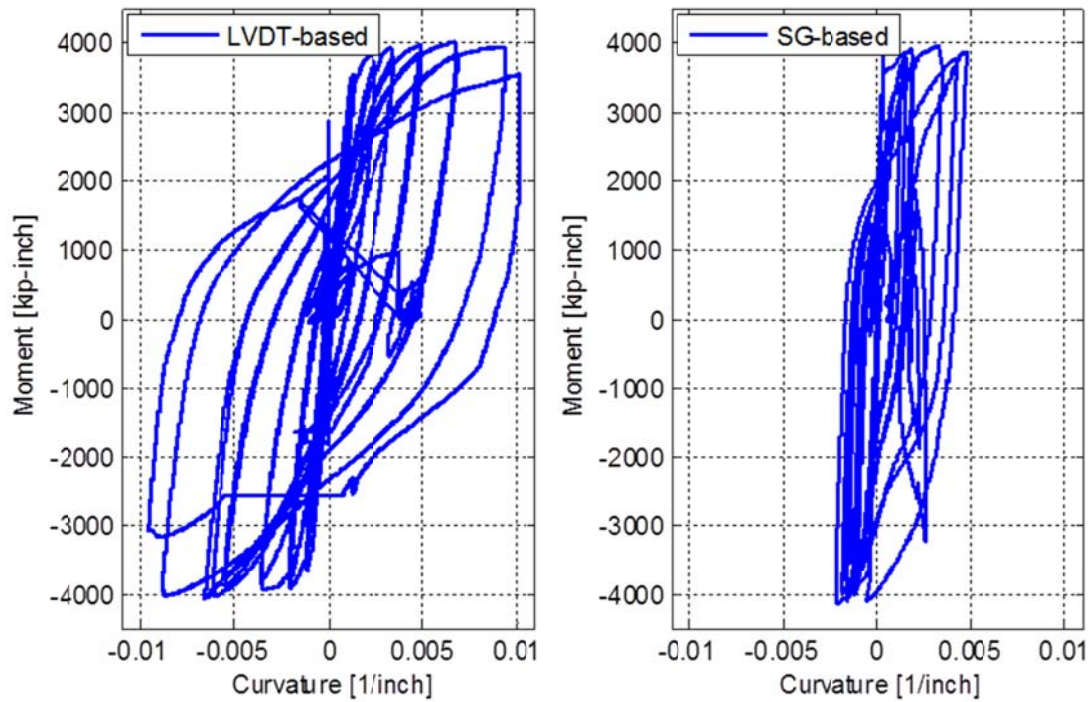
Figure 5.46 Comparison of LVDT-based and strain-based column moment-curvature relationship at section 1 (4 inch from beam face, refer to Figure 3.51) due to all transverse loading cycles

174
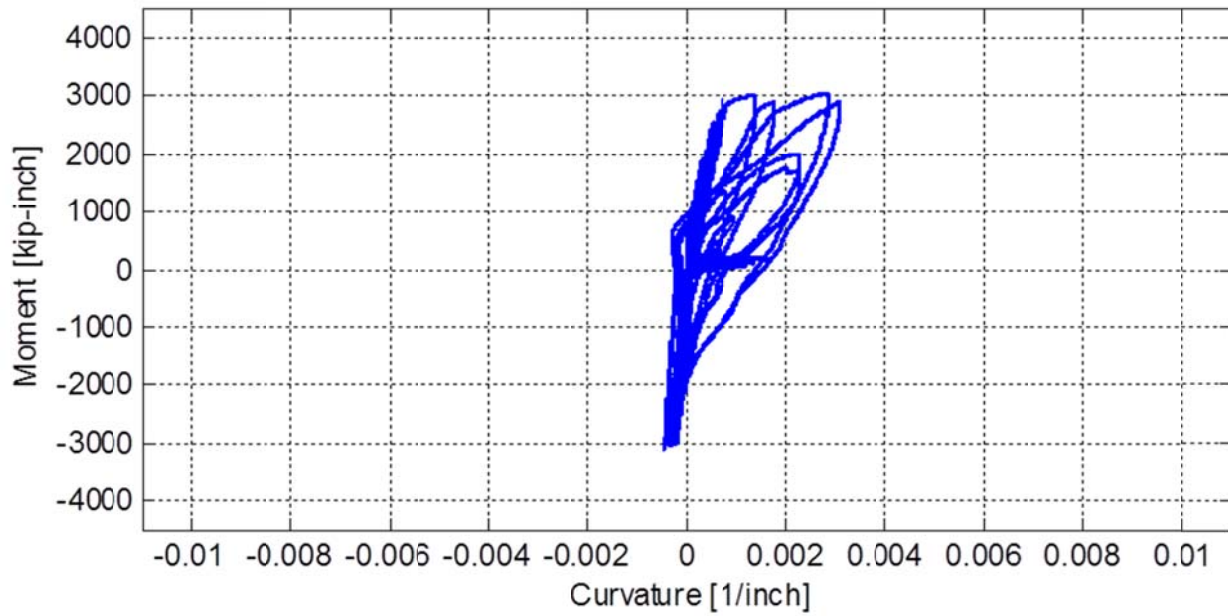
Figure 5.47 LVDT-based column moment-curvature relationship in N-S direction at section 4 (22 inch from beam face, refer to Figure 3.51) due to all longitudinal loading cycles
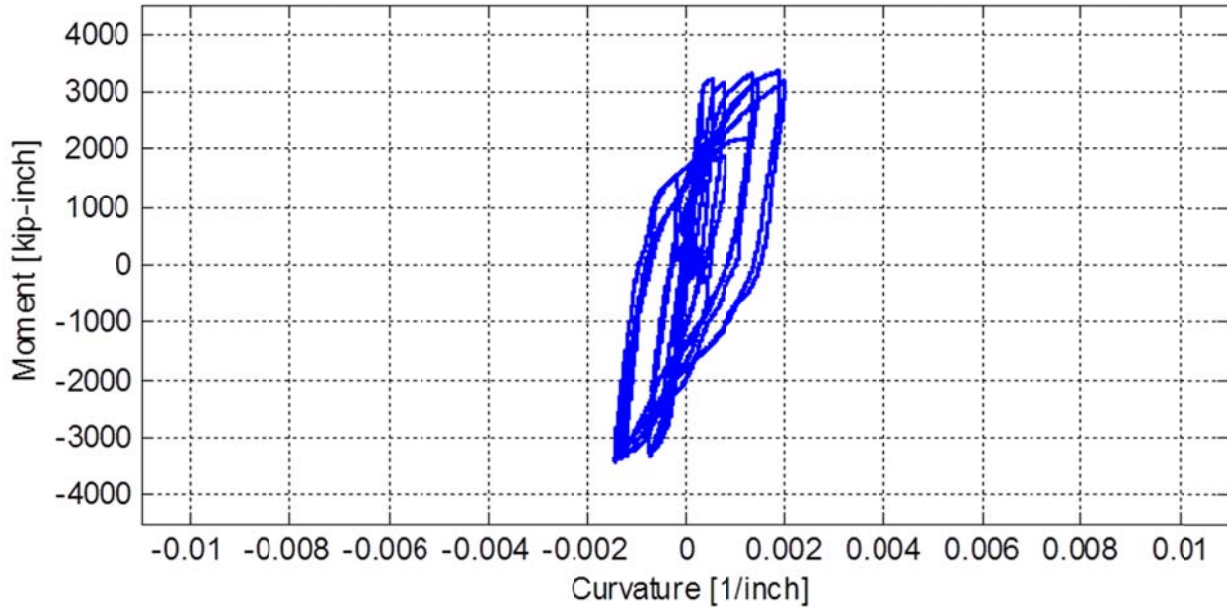
Figure 5.48 LVDT-based column moment-curvature relationship in N-S direction at section 3 (16 inch from beam face, refer to Figure 3.51) due to all longitudinal loading cycles
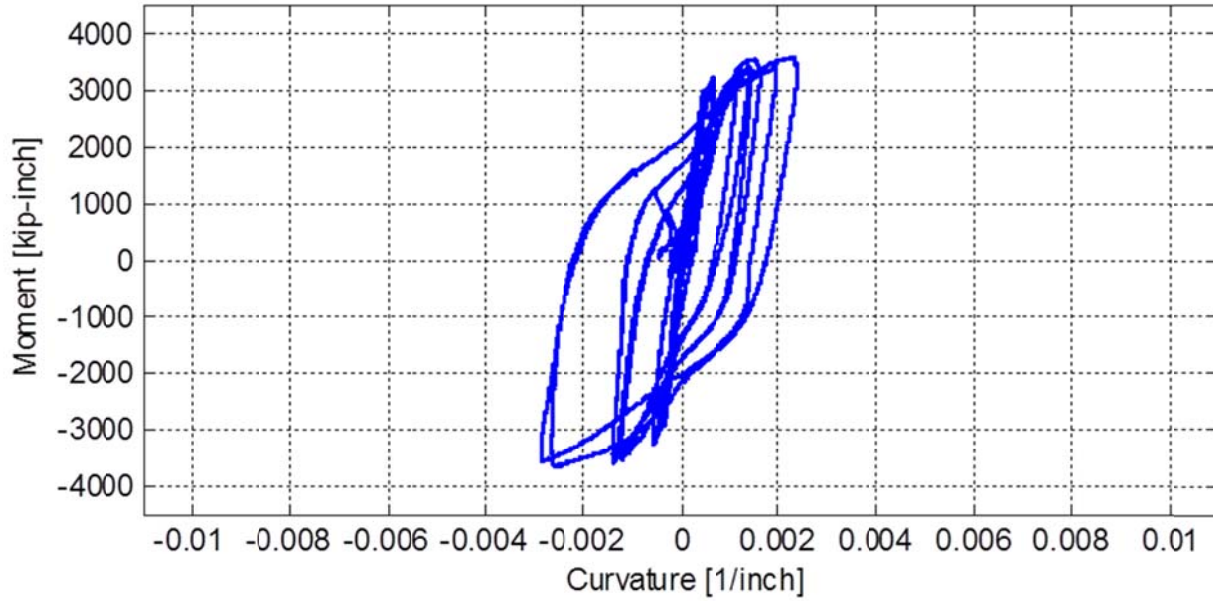
Figure 5.49 LVDT-based column moment-curvature relationship in N-S direction at section 2 (10 inch from beam face, refer to Figure 3.51) due to all longitudinal loading cycles
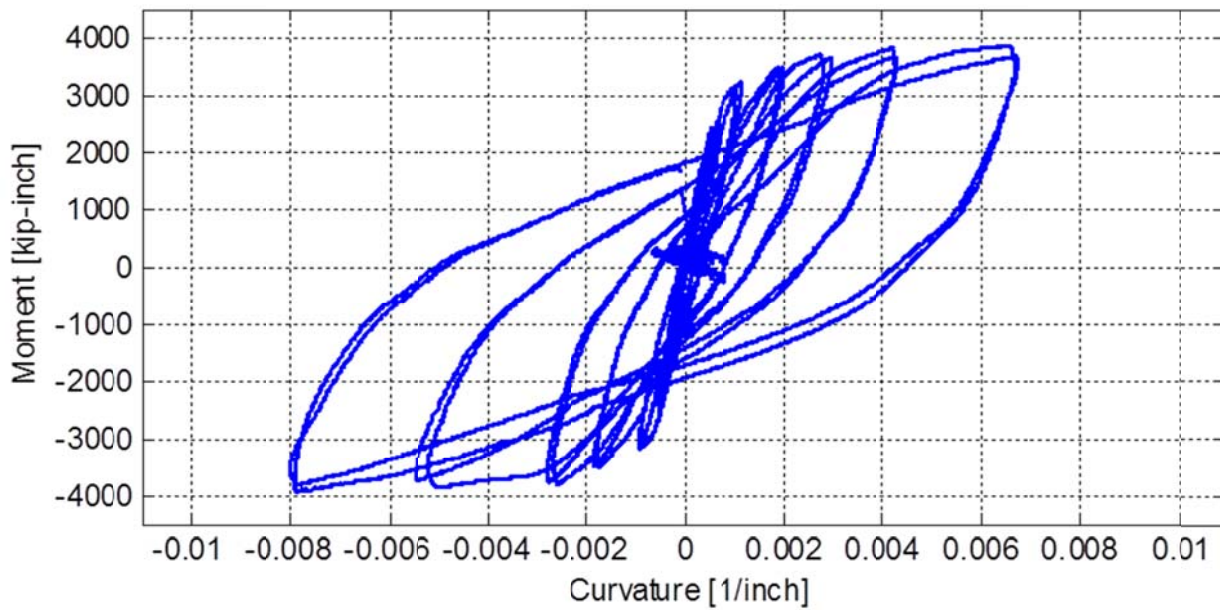
Figure 5.50 LVDT-based column moment-curvature relationship in N-S direction at section 1 (4 inch from beam face, refer to Figure 3.51) due to all longitudinal loading cycles

176
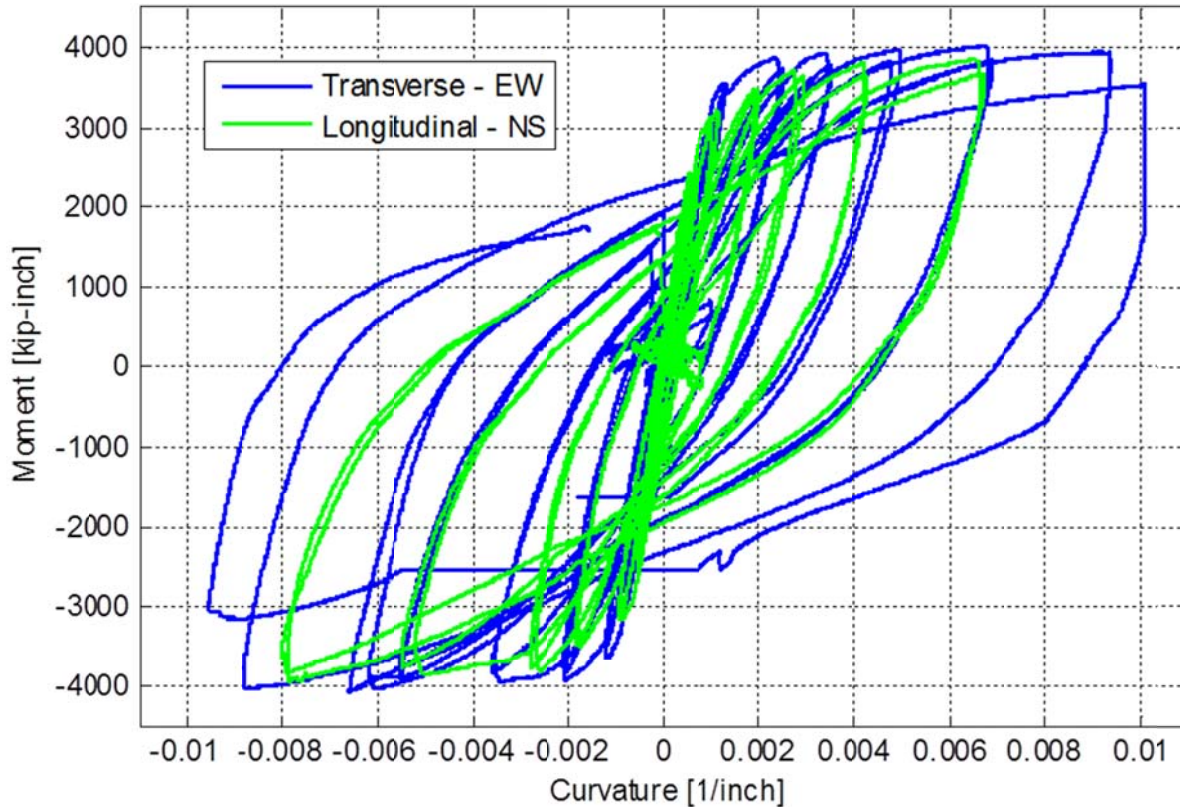
Figure 5.51 Comparison of column moment-curvature relationship in both transverse (E-W) and longitudinal (N-S) directions at section 1)4 inch from beam face, refer to Figure 3.51)

5.4   BENT CAP LOCAL BEHAVIOR

The structural behavior of the bent cap beam under combined gravity and lateral loading is central to the undertaken experimental study. The main objective of this study is to evaluate the contribution of the box-girder slabs to the cap beam stiffness, the capacity of the cap beam and its mode of failure, if any. To study the behavior of the cap beam, the strain at various locations in several rebars was measured. The strains were used to estimate the section curvatures. In addition, the instrumented vertical struts used as part of the specimen boundary conditions were used to estimate the bending moments in the cap beam. An important notation that is referred to continuously throughout this section and the subsequent sections as well is the designated sections B and D where all the cap beam and box-girder slabs behavior was monitored. The bending moment distribution in the cap beam is important to show and relate to sections B and D responses. Figure 5.52 schematically shows the bending moment distribution along the cap beam in the tested subassembly specimen under different cases of loading. Sections B and D are also shown in Figure 5.52. The figure shows a more exact sketch for the moment distribution considering the column and cap beam continuity and cross-section width rather than the center line. The strains, curvatures, bending moments, and moment-curvature relationships for the bent cap beam are discussed in this section.
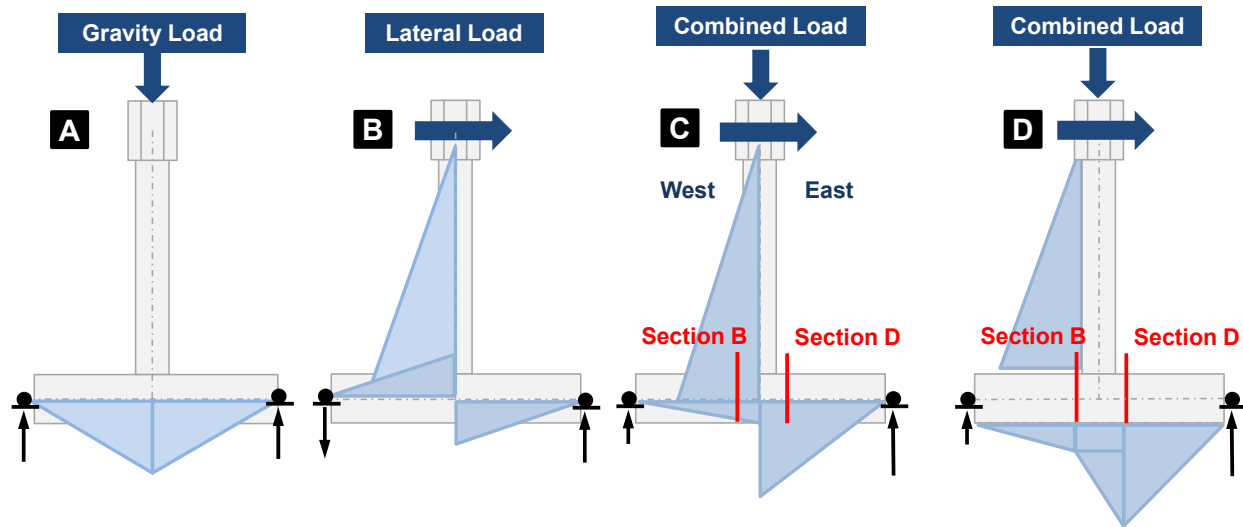
Figure 5.52 Schematic bending moment distribution along the bent cap beam center line in three cases of loading: (a) gravity load only (b) lateral load only (c) combined gravity and lateral loads, and (d) a more accurate distribution considering the column and beam actual cross-section width rather than center lines

5.4.1 Strain Behavior

The first response quantity discussed in this subsection is the cap beam rebars strain where only positive strains at the tension side of the bent cap beam are presented. A useful convention to keep in mind is that the tension side of the bent cap consistently occurred at the bent cap beam bottom in the inverted position. The subassembly specimen SP1 cap beam had 8 longitudinal rebars for both positive and negative reinforcement. According to the inverted specimen orientation and moment distribution previously shown, the negative reinforcement (i.e. tension side) is at the bottom, while the top reinforcement is the positive reinforcement (i.e. compression side). Four of the top and six of the bottom rebars were instrumented with strain gages at sections B and D identified in Figure 5.52. However, strain gages were installed along 5 sections, A through E, for top and the bottom rebars as shown in Figure 3.46. The recorded maximum positive strain at each of those 5 sections in one of the beam bottom bars (tension side) at the positive (loading east) and negative (loading west) peaks of the 0.8μ transverse loading cycle are shown in Figure 5.53 and Figure 5.54, respectively. The figures also schematically show the expected bending moment distribution according to the loading direction. The strain profile agrees with the moment distribution, which gives more confidence in the strain gages readings.

As the strain profile along the cap beam length is verified, it is useful to check the history of the measured strains. Representative strain history plots in one of the cap beam bottom rebars (tension side) for all loading cycles at sections B and D, where maximum strains along the beam length were recorded, are shown in Figure 5.55 and Figure 5.56, respectively. An important observation from these figures is the almost invariable strain readings while loading in the longitudinal direction. However, excessive progression in strain values was observed at the start of each transverse loading group of cycles. This is attributed to the fact that transverse loading directly alter the cap beam bending moment, while the longitudinal loading causes only torsion in the cap beam which minimally alter the cap beam longitudinal strain values. It is to be noted

178

also that while up to 8% strain was observed in the column rebars as the plastic hinge accumulated damage, only strains up to 1.3% were recorded and observed in the bent cap beam. This is expected because the bridge design philosophy calls for an essentially elastic superstructure and bent cap beams.
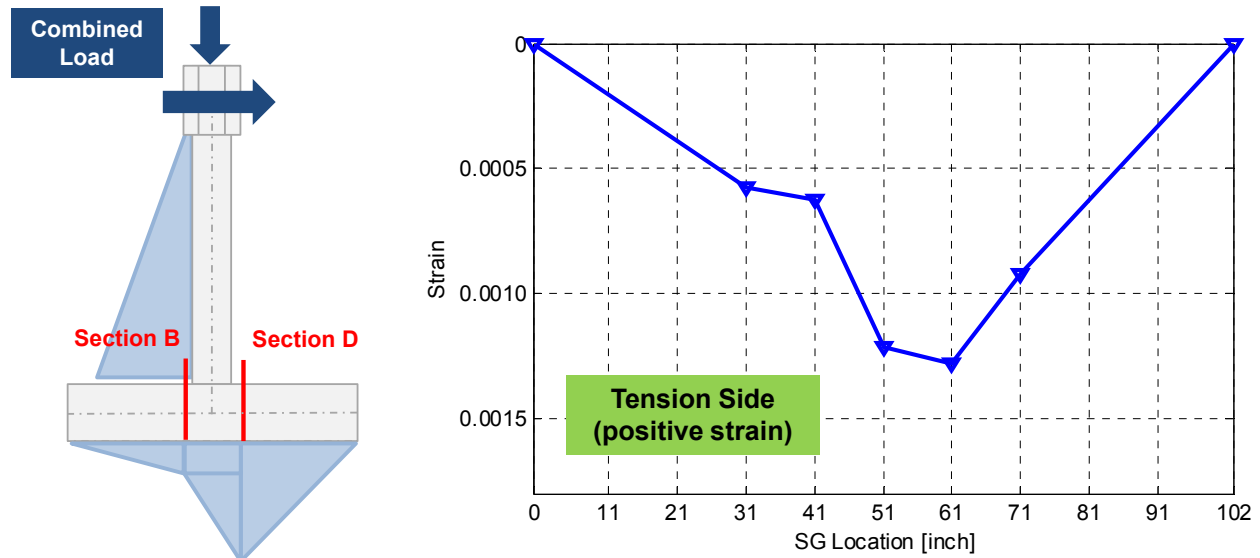
Figure 5.53 Strain profile along one of the cap beam tension side rebars due to combined gravity and one of the lateral transverse loading cycles in East direction
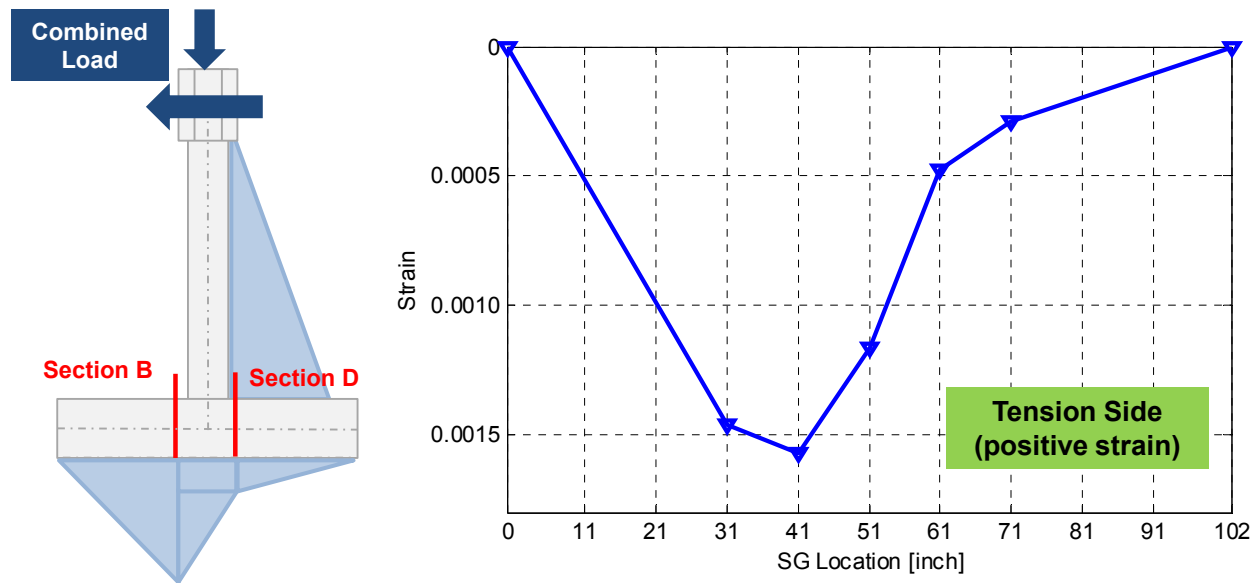
Figure 5.54 Strain profile along one of the cap beam tension side rebars due to combined gravity and one of the lateral transverse loading cycles in West direction

Another way of looking at the measured strains in the cap beam is by plotting them against the progressing lateral load. The maximum strains measured at sections B and D are plotted against the lateral transverse force in Figure 5.57 and Figure 5.58, respectively. The strain increase at zero lateral force (marked with arrows) corresponded to the increase of strains resulting from gravity load application. The gravity load was applied at two levels as previously

179

discussed. The first gravity load level was followed by all the small-level lateral loading cycles, which resulted in almost linear elastic strain in the cap beam rebars as suggested by Figure 5.57 and Figure 5.58. The cap beam rebars started yielding after the second level of gravity load was applied followed by the first high-level (1.4μ which corresponded to 1.94% drift ratio) cycle. Once the rebars yielded, they became very sensitive to loading and every new transverse loading cycle excessively increased the cap beam rebars strains especially as loading was increasing towards the first peak in a given cycle. The longitudinal loading did not cause any significant increase in the rebars strain. The observed strain during longitudinal loading is shown in the figures in the form of small loops around the zero transverse force value at the end of each of the main loops after each transverse loading group of cycles.
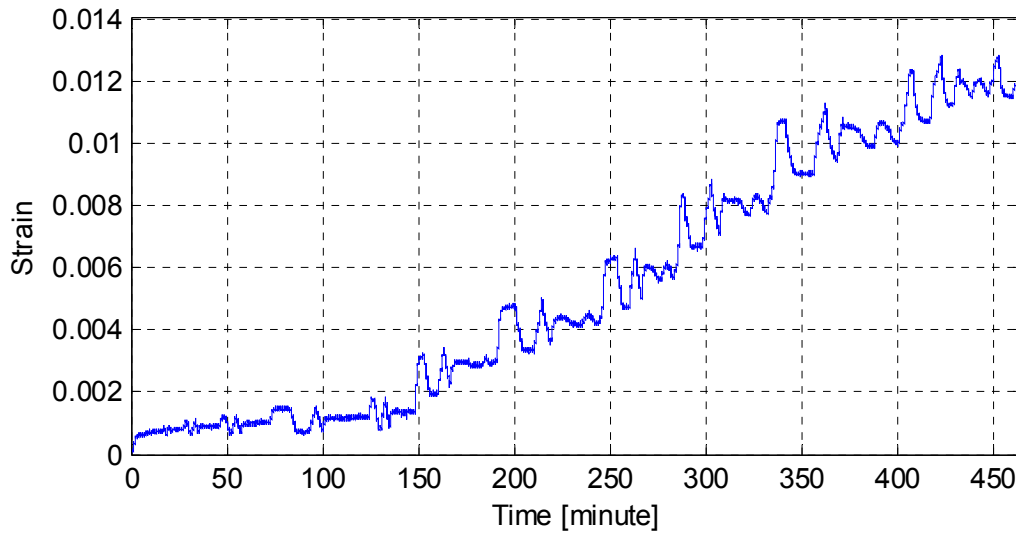
Figure 5.55 History of strain at bent cap beam maximum strain location at section B for all loading cycles
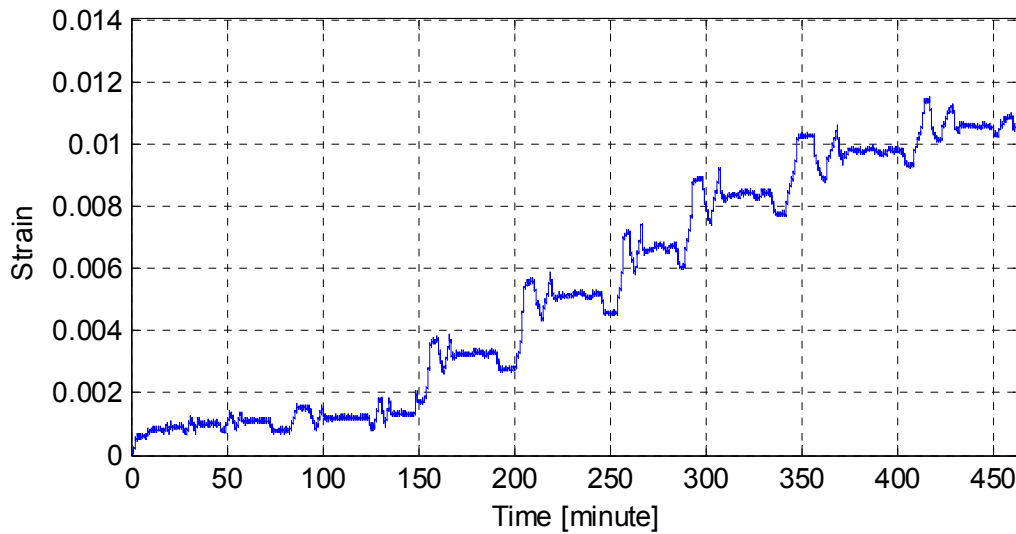
Figure 5.56 History of strain at bent cap beam maximum strain location at section D for all loading cycles
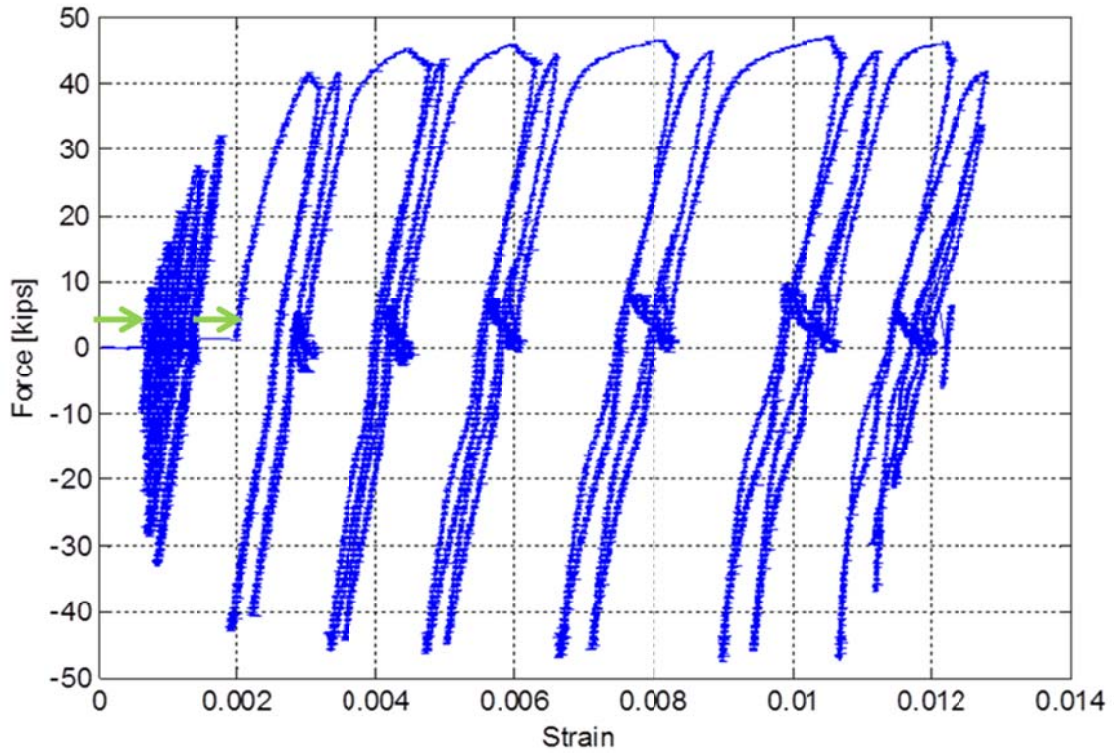
Figure 5.57 Lateral transverse force versus bent cap beam maximum strain at Section B for all loading cycles
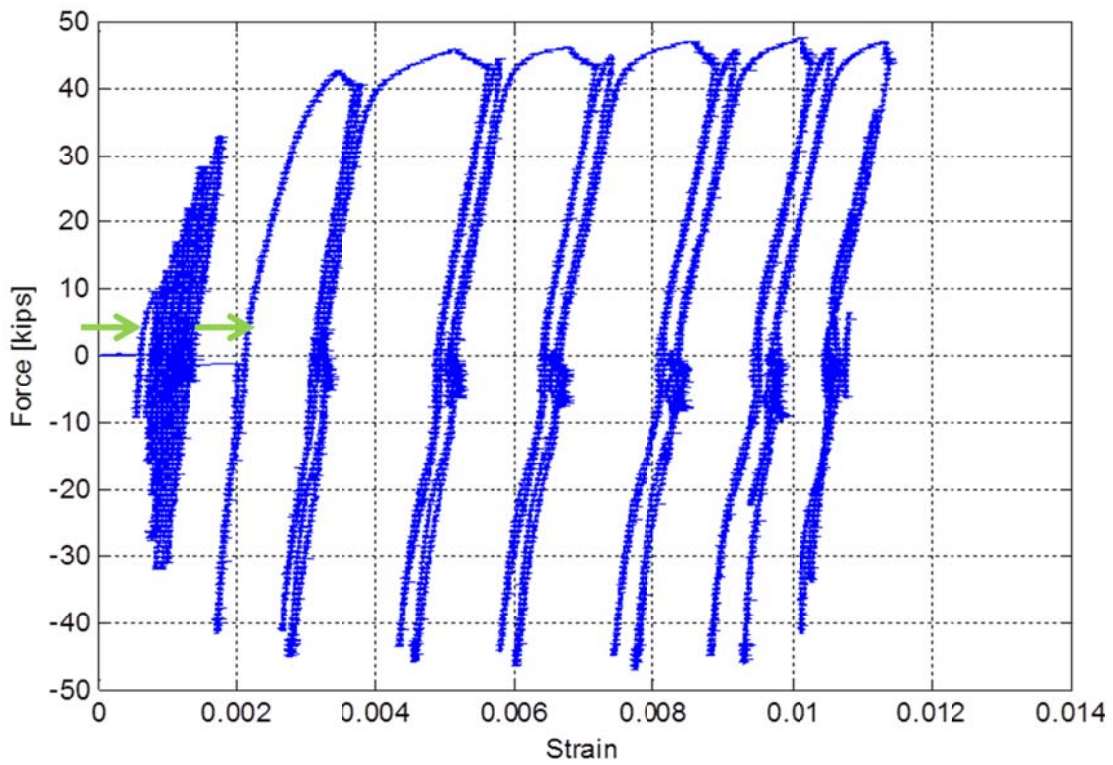
Figure 5.58 Lateral transverse force versus bent cap beam maximum strain at Section D for all loading cycles

181

Irrespective of the high post-yield recorded strain values, the bent cap beam can be still considered essentially elastic. This argument is supported by several evidences. Firstly, while all rebars yielding occurred only in the tension side, no concrete spalling was observed or associated with the increased cap beam strain values. Only minor cracks at the bottom of the cap beam were observed. In addition, no concrete crushing or extensive cracking was observed in the compression side of the cap beam. It is to be noted that a plastic behavior in a concrete element is associated with extensive concrete cracking and spalling because of either rebars buckling or concrete reaching crushing strain value reached. In conclusion, the concrete in the cap beam was found to be almost elastic throughout the test where no major cracking in the tension side and no even minor cracking in the compression side took place. This conclusion is the main reason why the decision to strengthen the second specimen (SP2) was taken. That is to increase the column moment capacity and accordingly, pass higher moment demands to the cap beam in an attempt to understand the plastic behavior of the cap beam. While column strengthening of the second specimen was pursued, it was convenient and feasible to partially repair the first specimen to be retested again. The repaired specimen test led to the second evidence that the cap beam remained essentially elastic even though the rebars extensively yielded before. When the specimen was unloaded and the repaired specimen test was conducted, linear elastic and much less strains were observed in the cap beam. More details are presented in Chapter 6.

On the other hand, the onset of a plastic cap beam response was reported from the HS retrofitted SP2 test. While the second specimen column was strengthen and well-confined, a conventional plastic hinge in the column was avoided and concrete crushing in the cap beam compression side was observed before the test ended. The reader is referred to Chapter 8 for the full discussion of the second specimen strengthening and HS tests. A reminder is that the cap beam plastic behavior is not a design objective in the recent performance-based or capacity bridge design philosophies. However, observing at least the onset of the cap beam plastic behavior is useful in fully quantifying the effective slab width and for accurate capacity estimation. A more economic design of the cap beam can be consequently achieved when the contributions of the box-girder slabs and slab transverse reinforcement are fully utilized.

5.4.2 Curvature Behavior

As previously mentioned in the column local behavior discussion, curvatures can be either estimated from a set of LVDTs properly aligned together or from the rebars strains at two opposite sides. In the case of the bent cap beam, using LVDTs was not practical. Thus, each two opposite strain gages at a top and corresponding bottom cap beam rebar were used to estimate the cap beam curvature at both sections B and D. The history of the estimated curvatures from using one set of rebars at sections B or D are shown in Figure 5.59 and Figure 5.60, respectively. Based on the sectional analysis results of the test specimen bent cap beam (shown in Figure 5.65 in a later subsection), the yield curvature value was found to be 0.00017 in.$^{-1}$. Thus, it can be noticed from the experimentally-determined curvatures shown in the figures that the bent cap beam yielded during SP1 cyclic loading tests, which was previously observed from the strain values at the bent cap tension side. However, based on the visual evidence of no damage, the yielded bent cap beam remained essentially elastic even when the strain in the tension side and the cross-section curvatures reached almost six times their yield values.
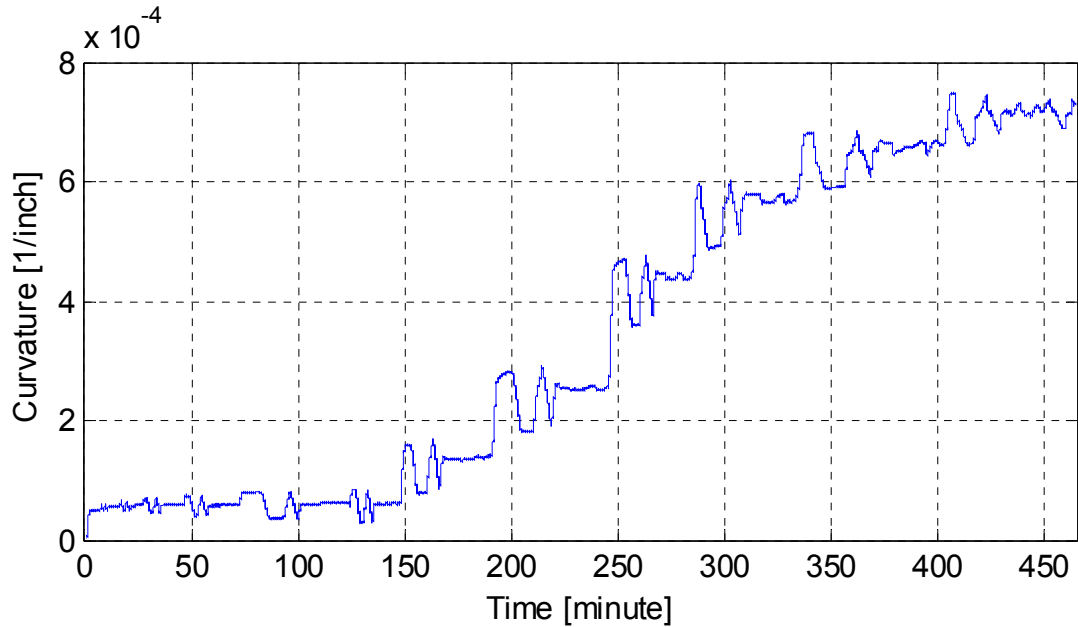
Figure 5.59 History of the curvature at cap beam section B due to all lateral loading cycles
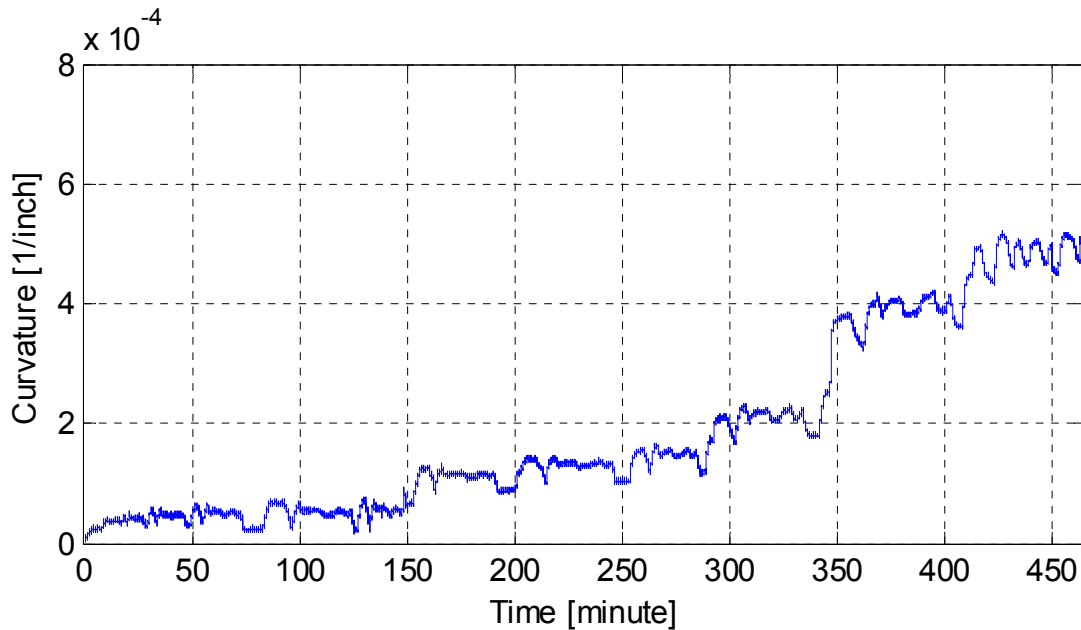
Figure 5.60 History of the curvature at cap beam section D due to all lateral loading cycles

5.4.3   Bending Moment Behavior

Investigating the bent cap beam bending moment behavior and capacity, if possible, is a central objective of this study as it is tied to the box-girder slab contribution. To determine the bending moment in the cap beam where the maximum moments were expected at sections B and D, the two instrumented vertical struts were utilized. The moment history at both sections due to lateral loading only and due to combined lateral and gravity loading is shown in Figure 5.61. It is to be noted that the vertical reactions at the beam end struts were always the total reactions due to both

gravity and lateral loading. However, to isolate the beam moments due to the lateral load only, the reaction recorded at the end of the gravity load application was subtracted from the total reaction recorded during the lateral load cycles that followed.
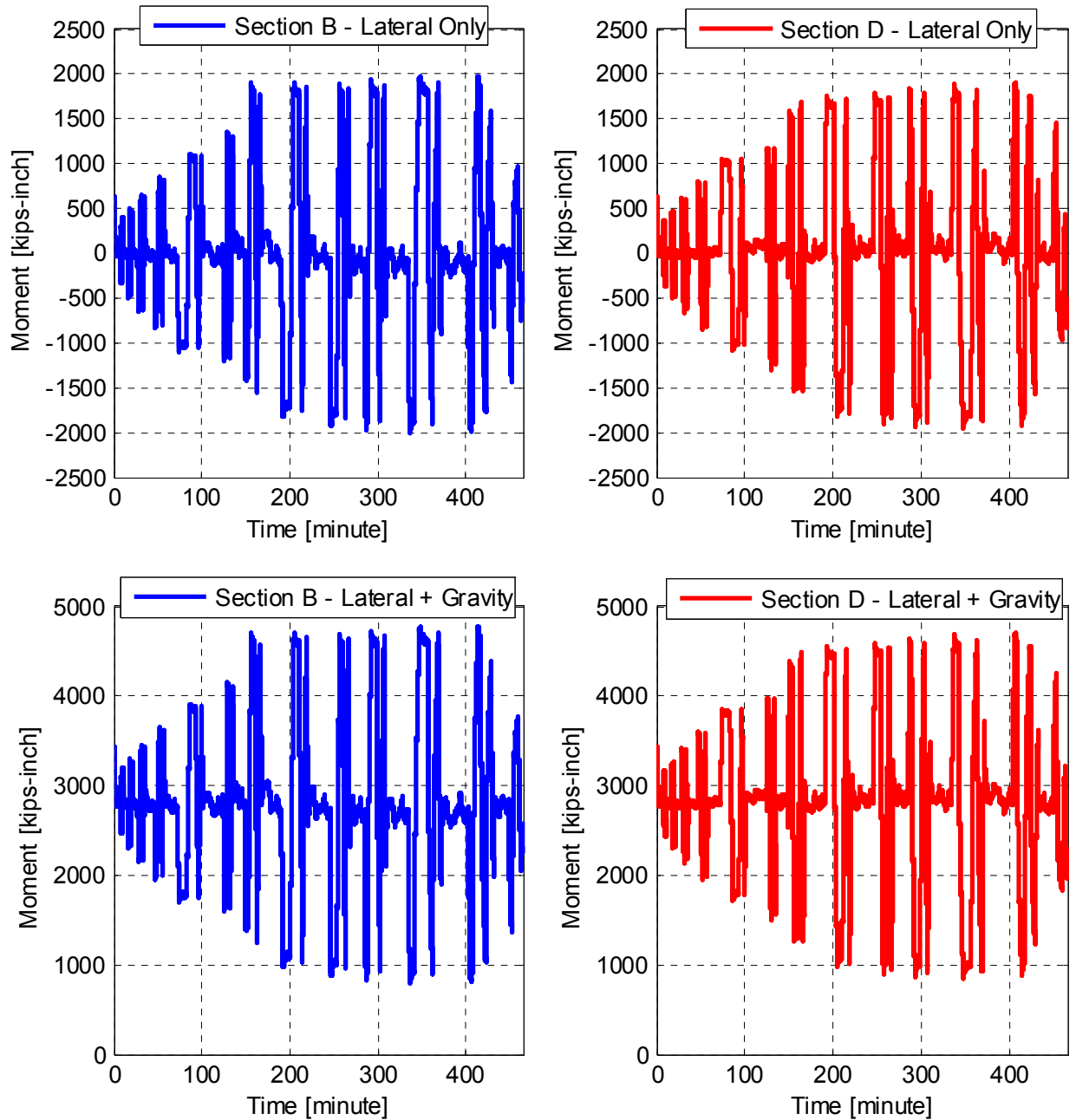
Figure 5.61 History of cap beam bending moment at sections B and D due to lateral loading only and combined lateral and gravity loading for all loading cycles

The moments due to lateral loading only were of interest because they were used to verify the accuracy of the procedure that used the vertical reaction at an end strut multiplied by its distance to either the location of section B or D to estimate the moment directly. The verification relied on satisfying the moment equilibrium at the joint region due to the lateral

loading case only. In this case, the bent cap beam moments at sections B and D, the box-girder twist moment, and the column moment should sum up to zero. If the box-girder twist is relatively small and negligible, the total cap beam moment from sections B and D due to lateral load only should approximately neutralize the column moment, designated as M_{col}, which was verified in Figure 5.62. The figure shows that the sum of the moments at sections B and D, designated as M_{beam}, is comparable to the column moment with difference that did not exceed 250 kip-inch, i.e. less than 5% of the column moment value.
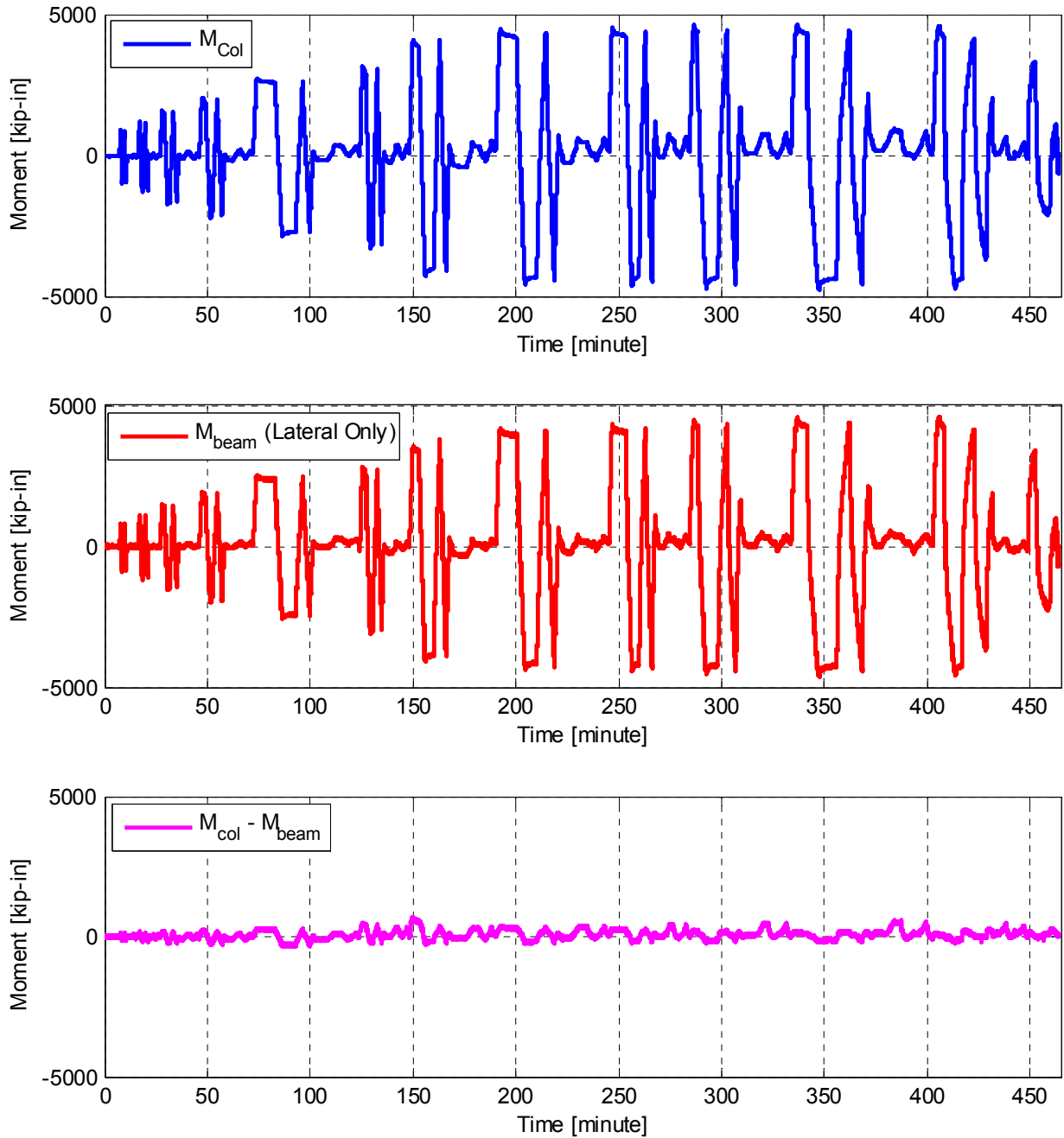
Figure 5.62 Comparison of column moment and sum of cap beam moments at sections B and D (M $_{beam}$ = M $_{section B}$ + M $_{section D}$) due to lateral loading only

It was crucial to verify whether the bending moments calculated from the vertical struts are correct for the importance of this issue in affecting the main conclusions from this study. It is implied from Figure 5.62 that the box-girder twist moment due to loading in the bent cap plane is almost negligible, and the vertical struts provided correct moment values for the bent cap beam. Similar observation was also reported in a previous study by Mosalam et al. (2002). A subassembly specimen, similar to the one tested in this study, was tested under bidirectional loading as well but all the boundary conditions at both box-girder and cap beam ends were instrumented and calibrated. Accordingly, it was possible to quantify the load path in the subassembly components using the estimated reactions at all boundary conditions. They concluded that the bent cap beam moment can be directly calculated from the beam end struts vertical reactions. Moreover, they found that the effect of the reactions at the end of the box-girder resulting from the box-girder torsional stiffness have negligible effect on the bent cap beam moment value calculated directly from the cap beam end struts.

5.4.4 Moment-Curvature Relationships

The cap beam bending moments were discussed and verified in the previous subsection. A beneficial use of the bending moment to investigate the overall bent cap response is to plot it against the section curvatures, which were also estimated as discussed in an earlier subsection. Figure 5.63 and Figure 5.64 show the moment-curvature relationships for the bent cap beam for all the cyclic loading cases at sections B and D, respectively. The analytical nominal moment-curvature relationship obtained from classical sectional analysis is shown in Figure 5.65 for comparison purposes. The results from the moment-curvature analysis, such as the yield moment, the ultimate moment…etc., are also reported in Figure 5.65.
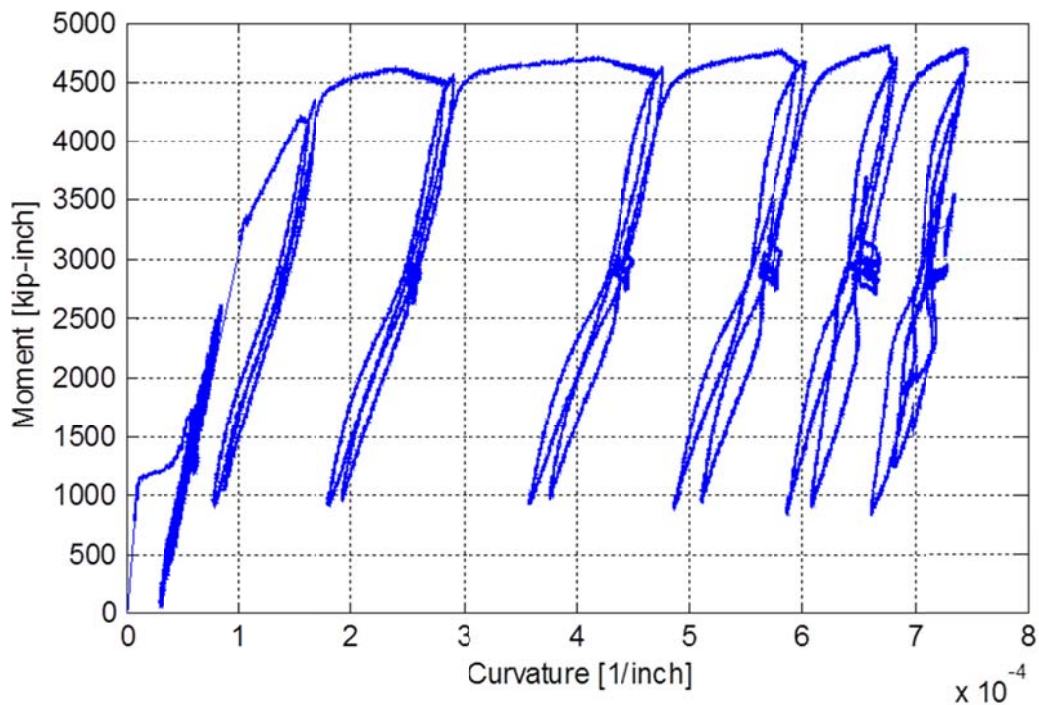
Figure 5.63 Moment-curvature relationship for the bent cap at section B for all the loading cycles in both transverse and longitudinal directions

186
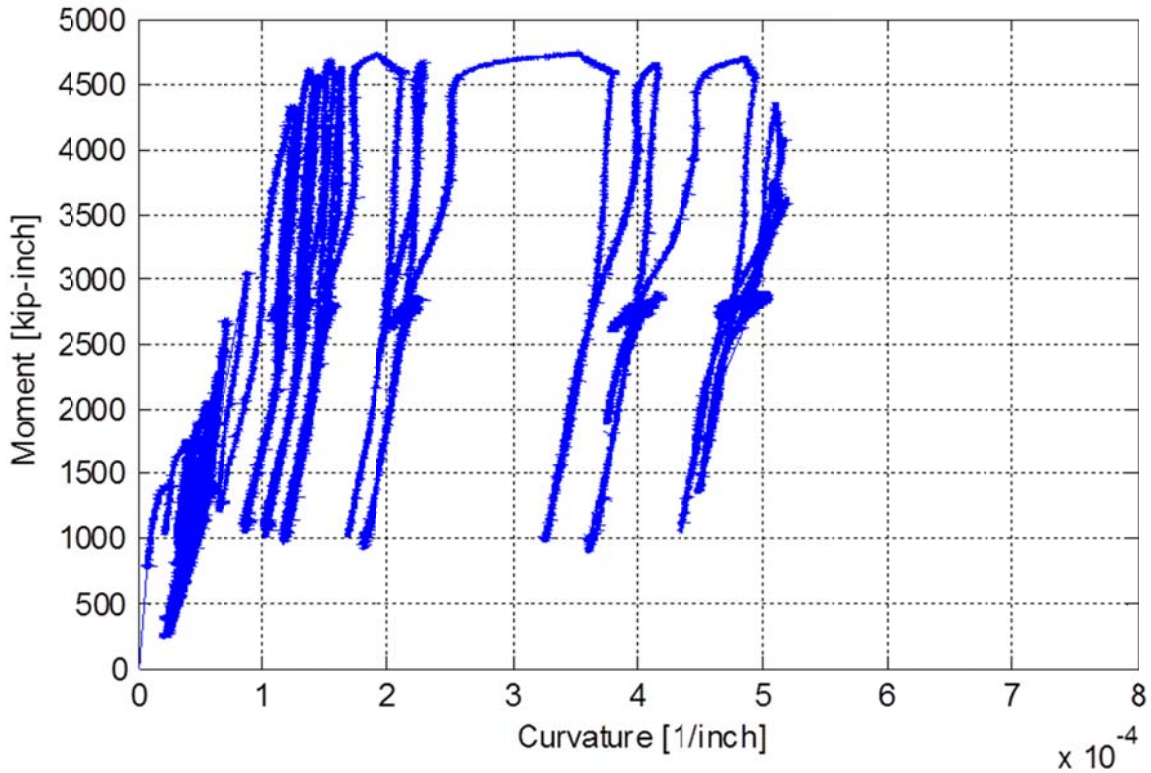
Figure 5.64 Moment-curvature relationship for the bent cap at section D for all the loading cycles in both transverse and longitudinal directions

Curvature at First Yield:	-.1618E-3 1/in
Ultimate Curvature:	-4.539E-3 1/in
Moment at First Yield:	-3719 kip-in
Ultimate Moment:	-5024 kip-in
Centroid Strain at Yield:	.9580E-3 Ten
Centroid Strain at Ultimate:	40.22E-3 Ten
N.A. at First Yield:	-5.923 in
N.A. at Ultimate:	-8.862 in
Energy per Length:	19.96 kips
Effective Yield Curvature:	.1724E-3 1/in
Effective Yield Moment:	3963 kip-in
Over Strength Factor:	-1.268
EI Effective:	2.30E+7 kip-in^2
Yield EI Effective:	243.0E+3 kip-in^2
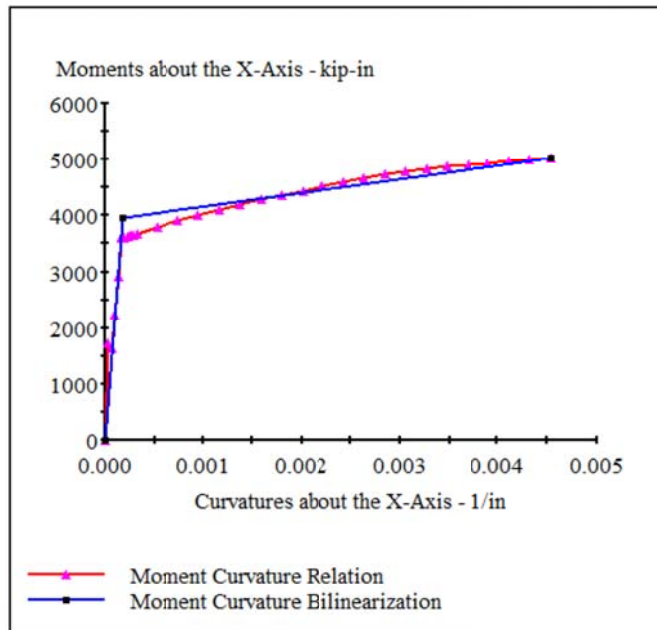
Figure 5.65 Moment-curvature relationship for cap beam estimated from sectional analysis (XTRACT, 2002) using the Caltrans SDC integral bent cap effective flanged section

187

It is observed from the experimentally determined moment-curvature relationships that the moment is capped in both sections B and D at a value slightly higher than 4500 kip-inch. When tied with the observed column behavior and damage, it is understood that the bent cap moment was capped because of the reached column capacity that capped the demand at the bent cap beam. However, the extensive curvature increase at this capped moment causes the yielding of the cap beam, which has been confirmed already from the strain values. It is noted that the experimental value for the yield moment when curvature values started increasing significantly is about 4500 kip-inch. The analytical value determined from sectional analysis as shown in Figure 5.65 is 3719 kip-inch. The sectional analysis considered the Caltrans SDC effective flange width, but included the tension steel in the slab as well although it is not part of the code requirement. The underestimated analytical value is indicative that the tension steel within the effective slab width should be included and larger effective width value might be needed for accurate cap beam moment capacity estimation. A more extensive discussion of the bent cap beam moment capacity is included in the HS test results and post-test analysis discussion in Chapters 8 and 9.

Another useful use of the moment-curvature relationship is to determine the effective EI for the bent cap cross-section at different loading levels. The change in the effective EI reflects the change of the overall bent cap beam stiffness. Figure 5.66 and Figure 5.67 show how the effective EI at the respective sections B and D deteriorates with the loading level, expressed in terms of drift ratio and ductility level. The moment-curvature from two different sets of top and bottom rebars were used for each section and shown in the figures. A normalized value for the effective EI was used where all the values are related to the effective EI determined from the slope of the moment-curvature relationship at first small-cycle. The absolute values for the effective EI were found much less than the recommended Caltrans value that is based on a 0.5-0.75 of the gross flanged section inertia. However, the relative change in the normalized effective EI still serves the purpose of investigating how the bent cap beam stiffness deteriorates at higher drift ratios and ductility levels.
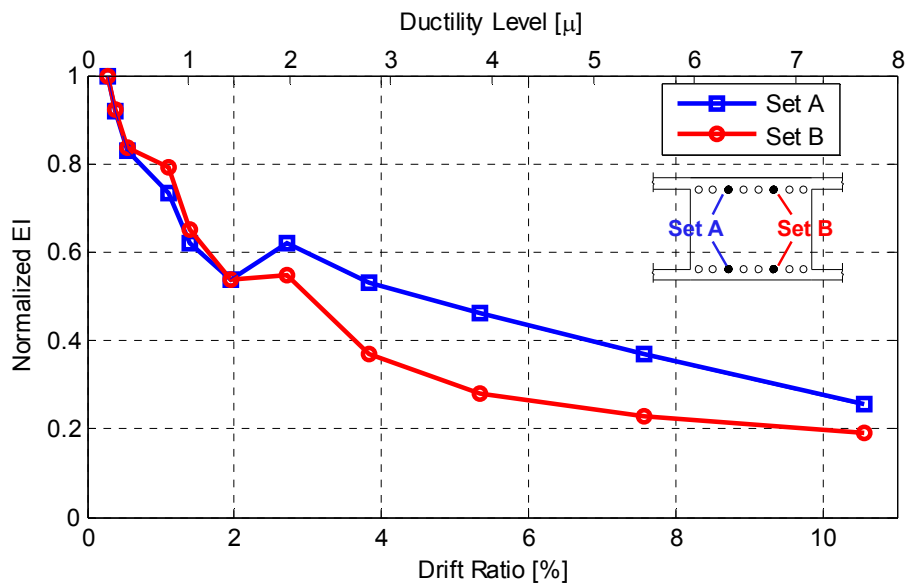
Figure 5.66 Degradation in the cap beam stiffness expressed in terms of normalized effective EI at different drift ratios and ductility levels calculated using curvatures from two different top and bottom rebar sets at Section B
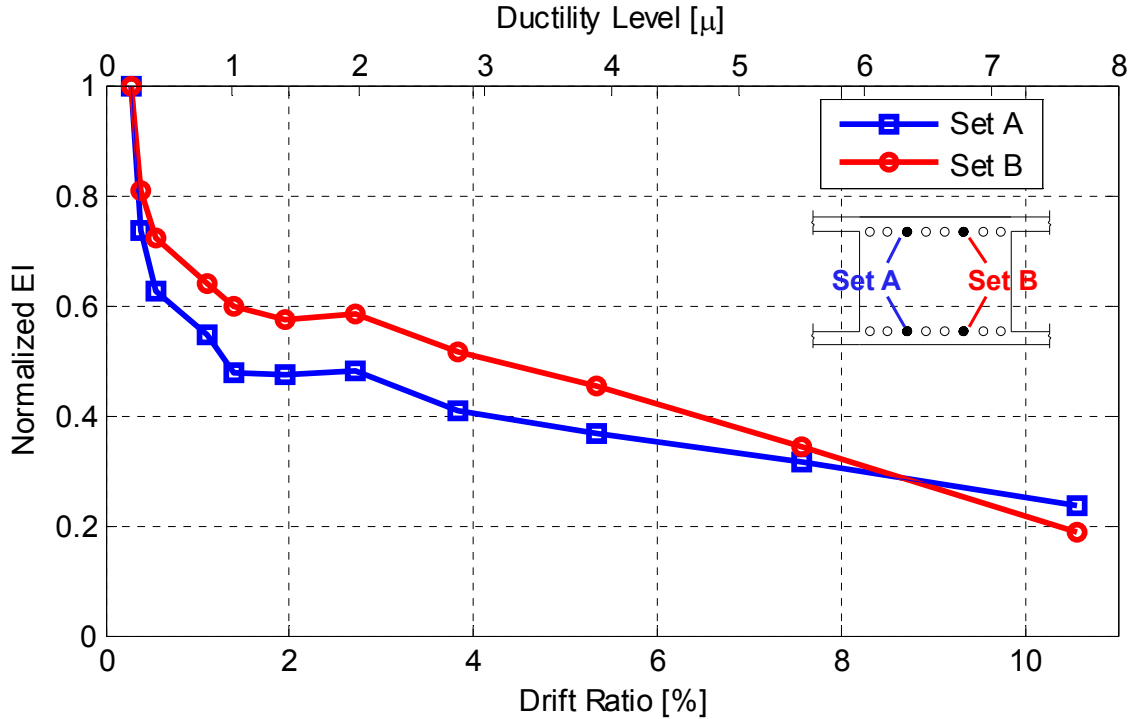
Figure 5.67 Degradation in cap beam stiffness expressed in terms of normalized effective EI at different drift ratios and ductility levels calculated using curvatures from two different top and bottom rebar sets at Section D

5.5   EFFECTIVE SLAB WIDTH (TENSION SIDE)

Caltrans SDC and AASHTO LRFD guidelines for seismic design require considering a flanged section with an effective slab (thickness = t_s) width $12t_s$ for integral RC bent cap beams for balanced stiffness check and seismic capacity check. The effective slab width that is typically based on the equivalent strain block concept is revisited in this study. The strain distribution in the bent cap beam reinforcement and the adjacent transverse (with respect to bridge box-girder axis) slab reinforcement from both sides of the beam is determined for all the as-built SP1 cyclic tests at both tension and compression sides. In bent caps, the negative moment side that requires the tension reinforcement at the bent columns and supports is usually the top side, i.e. deck slab side in integral bent caps. This is the case in the prototype and the specimen used in this study. However, in the specimen's inverted position, the top of the cap beam is facing the laboratory floor, and so is the deck slab. Thus, the tension side is the lower side of the beam in the inverted position. The strain distribution in the tension side was found more reliable than the compression side, which was very sensitive to the concentrated gravity load applied through the column. The results from the tension side strain distribution and revisited effective slab width are presented in this section. The compression side results are also briefly discussed in the next section.

This section presents and discusses the strain distribution, equivalent strain block, and corresponding effective slab width at both sections B and D, previously identified in Figure 5.52. A simple procedure to determine the effective slab width based on the concept of an equivalent strain block was devised as illustrated in Figure 5.68. The strain distribution was experimentally

obtained and spatially extended at the two tails to determine the intercept at zero strain. The area under the strain distribution was computed and transformed to an equivalent strain block with an effective width where two strain values were used, namely the minimum and the mean strain among the used six gages at a given cross-section in the cap beam reinforcement. The maximum strain was not used to avoid effects of the concentrated gravity load and scaling that caused highly localized strain values in the cap beam reinforcement.
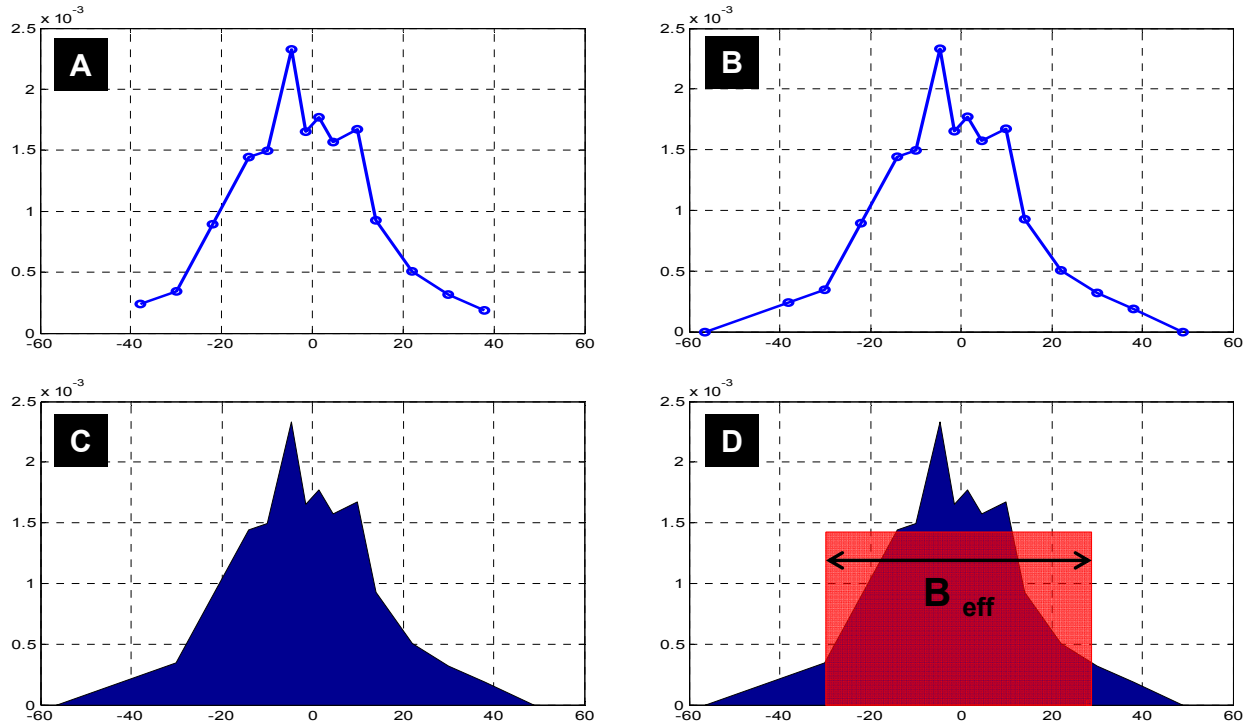
Figure 5.68 Summary of the four main steps of the procedure used to estimate the bent cap effective slab width

5.5.1   Section B: Distribution

The strain distribution at different sections across the bent cap and transverse slab reinforcement based on different strain gage readings was recorded continuously throughout all the loading cycles in both transverse and longitudinal directions. Only strain values acquired at loading cycles' peaks were considered. It is worth noting that each level of loading comprised two full cycles with total of 4 peaks, which were previously identified in Figure 5.17 and Figure 5.18 before as 1st positive peak, 1st negative peak, 2nd positive peak, and 2nd negative peak. Only results obtained from 2nd positive and 2nd negative peaks are shown for brevity since the other two cases were found very similar. Moreover, the most meaningful results were obtained when loading was in the transverse direction. That is because the longitudinal loading influenced mainly the box-girder flexural behavior rather than the bent cap beam. Therefore, all results shown in the reminder of this chapter were compiled from the strain readings at the 2nd positive and negative peaks of the transverse loading cycles, which were related to the drift ratio and ductility level (μ).

The strain distribution at section B is presented in this subsection. Figure 5.69 and Figure 5.70 show the distribution at different loading levels when the transverse load was pushing towards the East side, which is designated as the positive loading direction. Figure 5.69 presents the distribution at the small-level cycles, i.e. before any of the reinforcing bars in the cap beam or even the column, yielded, i.e. drift ratios 0.4%, 0.8%, 1.1%, and 1.4%, which corresponded to μ of 0.27, 0.56, 0.80, and 1.0, respectively. Figure 5.70 presents three high-level cycles along with the last small-level cycle to show how the distribution changed as yielding took place. The four drift levels considered in Figure 5.70 are 1.4%, 2.7%, 5.3%, and 10.5% which corresponded to μ of 1.0, 1.96, 3.84, and 7.57, respectively. On the other hand, Figure 5.71 and Figure 5.72 show the strain distribution at section B for similar levels but for cases when loading was pushing towards the West side, i.e. reversed load in the negative direction.
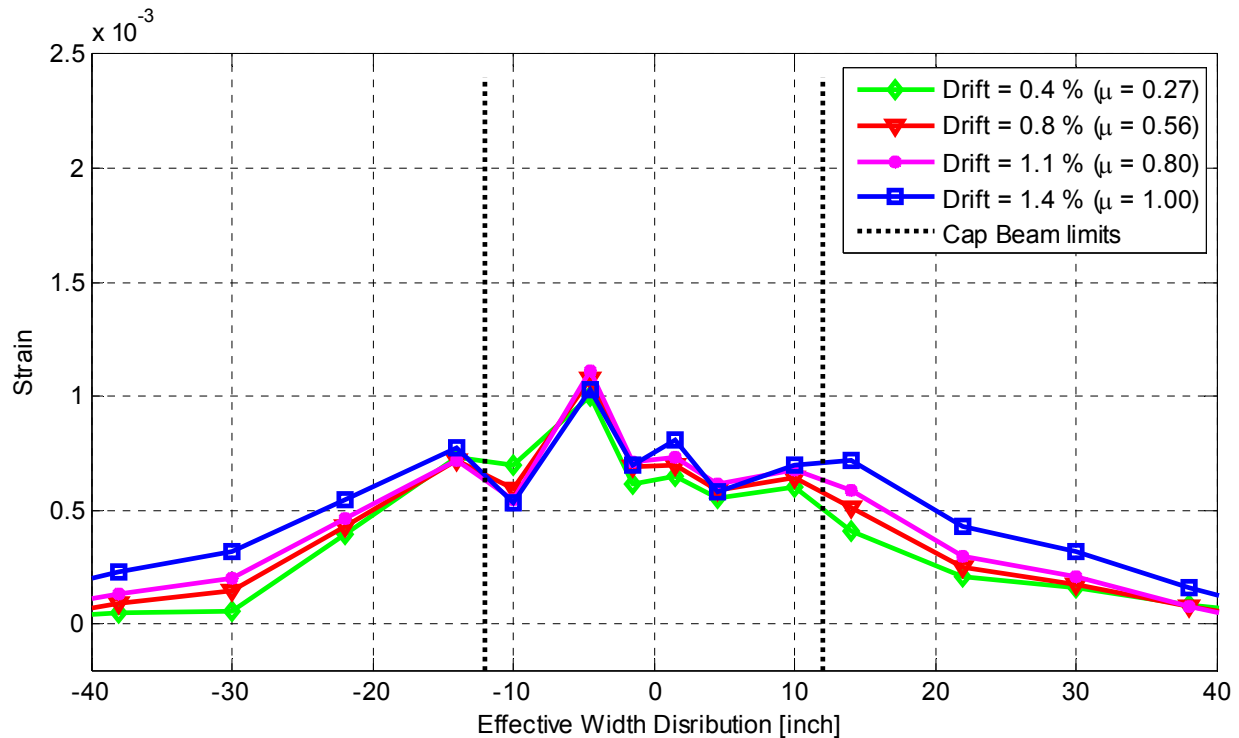
Figure 5.69 Strain distribution along cap beam and box-girder transverse deck slab reinforcement at Section B for different small-level loading cycles before yielding (loading is in positive EAST direction)

191
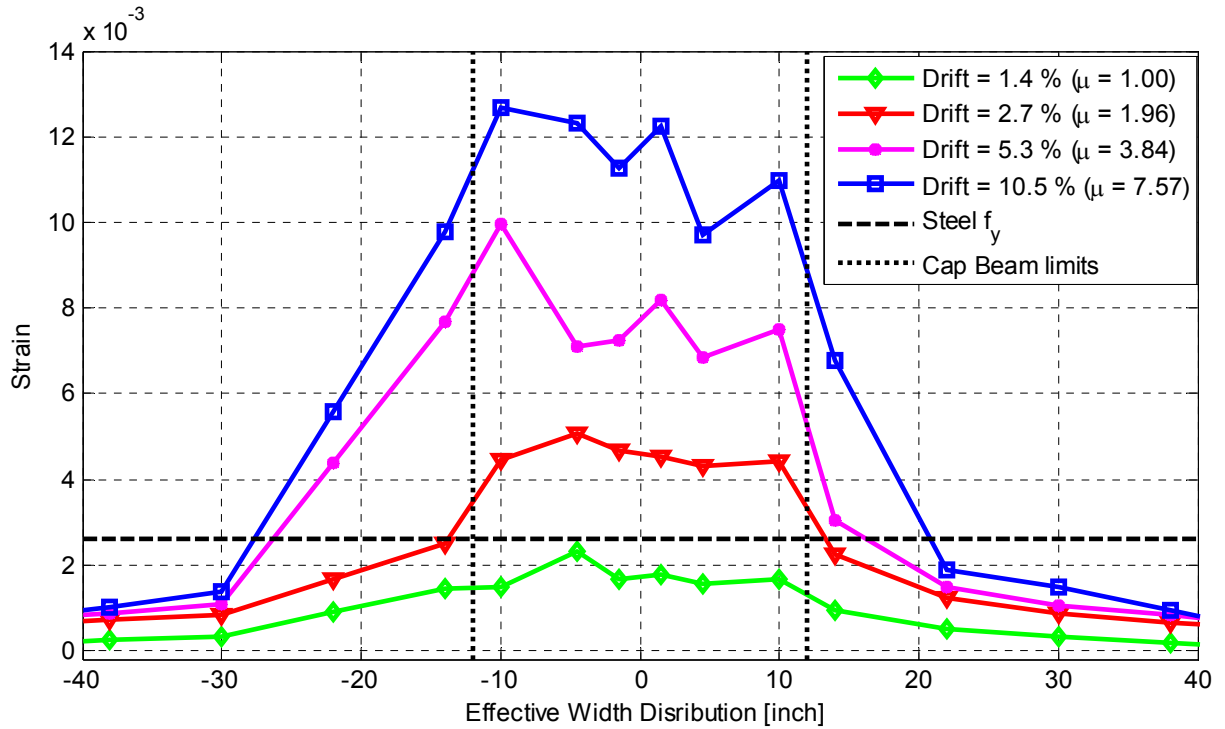
Figure 5.70 Strain distribution along cap beam and box-girder transverse deck slab reinforcement at Section B for different high-level loading cycles after yielding (loading is in positive EAST direction)
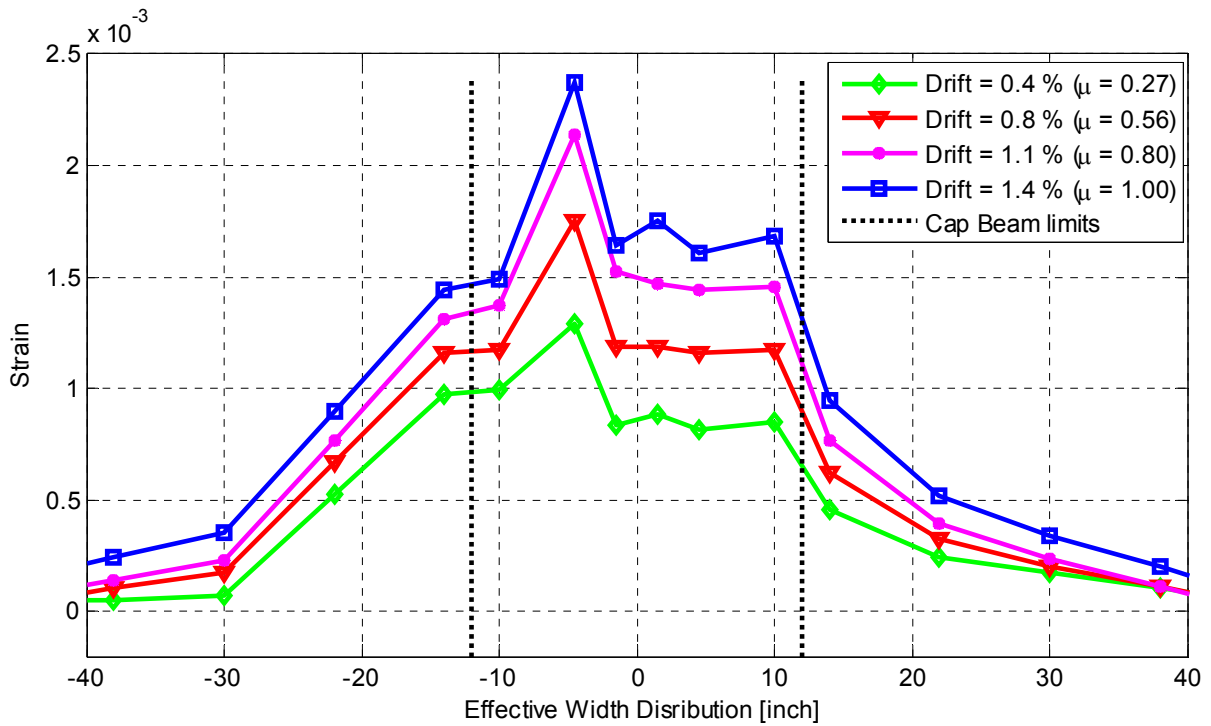
Figure 5.71 Strain distribution along cap beam and box-girder transverse deck slab reinforcement at Section B for different small-level loading cycles before yielding (loading is in negative WEST direction)

192
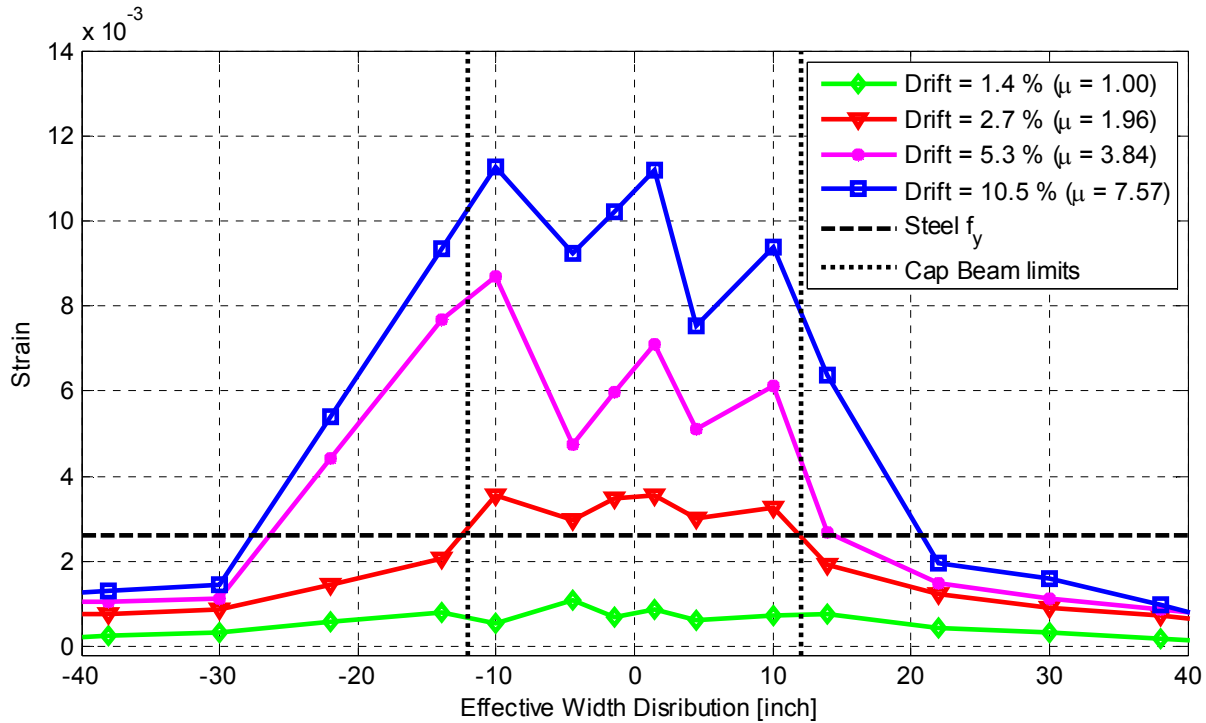
Figure 5.72 Strain distribution along cap beam and box-girder transverse deck slab reinforcement at Section B for different high-level loading cycles after yielding (loading is in negative WEST direction)

5.5.2   Section D: Distribution

Similar to the strain distribution shown at section B, different loading levels and loading direction were considered to plot the strain distribution at section D that is presented in this subsection. Figure 5.73 and Figure 5.74 show the distribution at different loading levels when the transverse load was pushing in positive direction towards the East side, while Figure 5.75 and Figure 5.76 show the distribution in case of loading in the negative direction towards the West. Strain distributions at section D at small-level cycles before any yielding in any of the reinforcing bars at drift ratios 0.4%, 0.8%, 1.1%, and 1.4%, which corresponded to μ of 0.27, 0.56, 0.80, and 1.0, respectively, are shown in Figure 5.73 and Figure 5.75 for loading in positive and negative directions, respectively. On the other hand, distributions at larger loading levels at 1.4%, 2.7%, 5.3%, and 10.5% which corresponded to μ of 1.0, 1.96, 3.84, and 7.57, respectively, are shown in Figure 5.74 and Figure 5.76 for loading in positive and negative directions, respectively.

It is to be noted that all plots in this subsection and the former one showed only the recorded strain values at locations that ranged between -40 and +40 inch according to the instrumented reinforcing bar location. The spatially extended tails that aimed at capturing the intercept at zero strain as part of determining the effective slab width, Figure 5.68b, were not shown in the strain distribution presented in Figure 5.69 through Figure 5.76. However, sample strain distribution that show the fully extended the distribution until the zero strain point are presented in the following subsections.
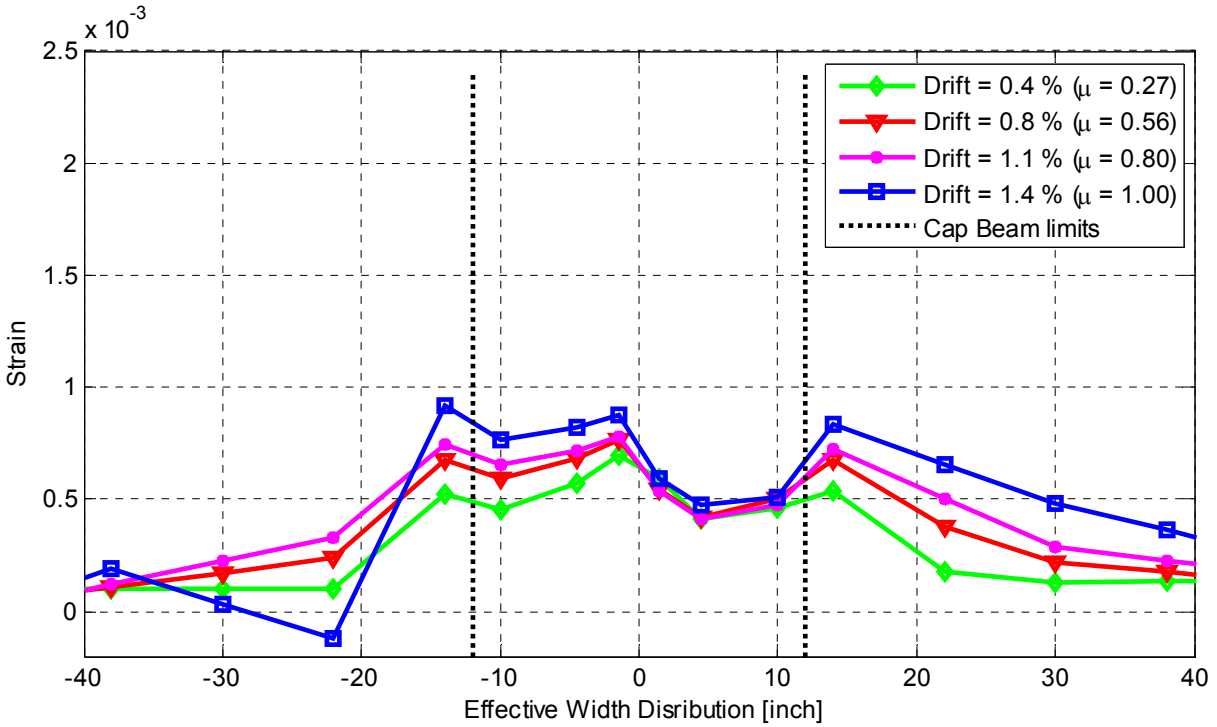
Figure 5.73 Strain distribution along cap beam and box-girder transverse deck slab reinforcement at Section D for different small-level loading cycles before yielding (loading is in positive EAST direction)
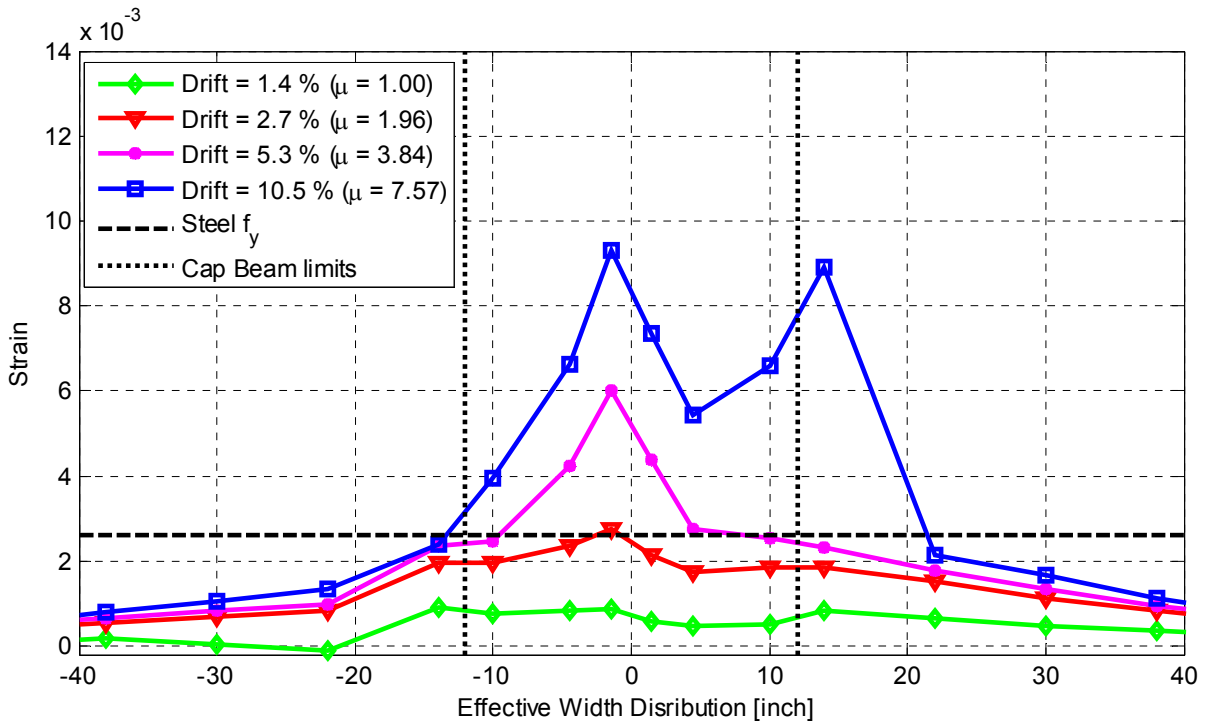
Figure 5.74 Strain distribution along cap beam and box-girder transverse deck slab reinforcement at Section D for different high-level loading cycles after yielding (loading is in positive EAST direction)
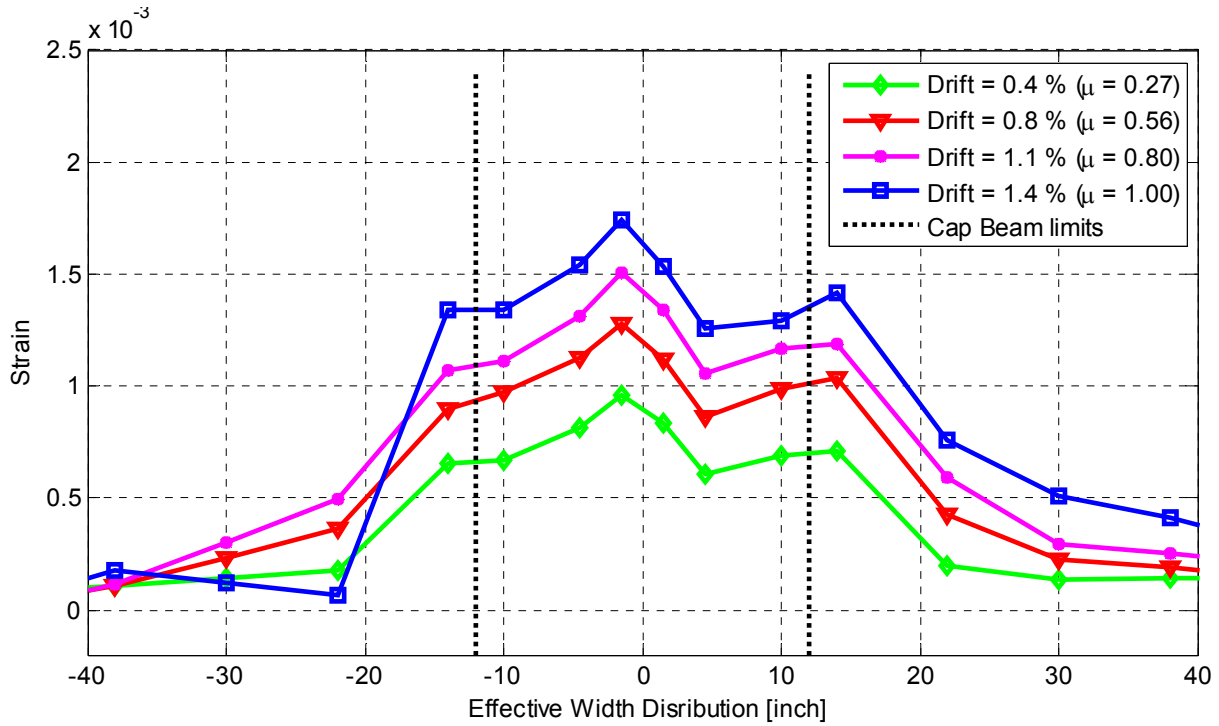
Figure 5.75 Strain distribution along cap beam and box-girder transverse deck slab reinforcement at Section D for different small-level loading cycles before yielding (loading is in negative WEST direction)
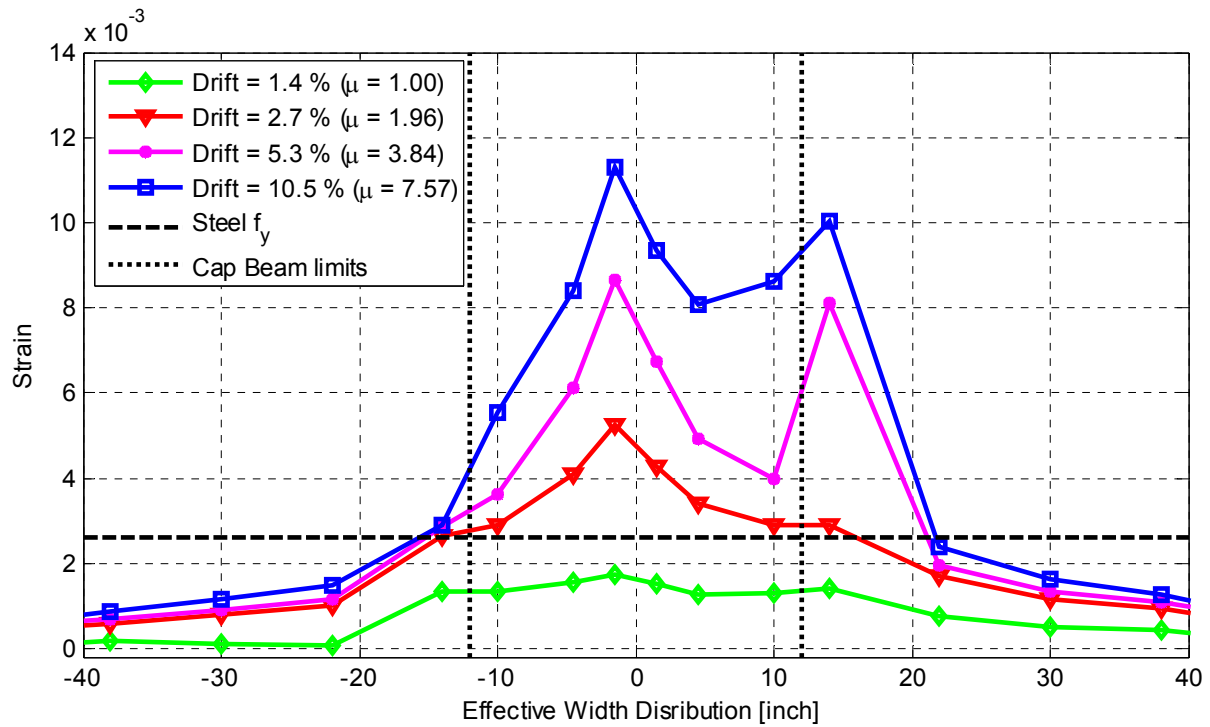
Figure 5.76 Strain distribution along cap beam and box-girder transverse deck slab reinforcement at Section D for different high-level loading cycles after yielding (loading is in negative WEST direction)

195

5.5.3   Section B: Effective Slab Width

As previously mentioned, the effective slab width is determined using the equivalent strain block concept and the simple procedure shown in Figure 5.68. The strain distributions shown in a previous subsection are utilized to estimate the effective slab width at section B at different loading levels and directions. Two values for the bent cap beam strain value were used to define the equivalent strain block (B_{eff}) throughout this study. These are the minimum and the mean of the six instrumented rebar strain gage readings at a given cross-section in the cap beam. In a prototype bridge, the full scale bent cap beam reinforcement under distributed vertical loads experience uniform strain. In this reduced-scale inverted specimen, the bent cap reinforcement did not have a uniform strain because of the concentrated gravity load and the scaling effect which made the loading zone of almost comparable size to the beam cap beam. Therefore, the minimum and mean values were both considered to harmonize the cap beam strain. The maximum value was avoided because it represented a localized unrealistic high strain values. An example of how the strain block was determined using the strain distribution at section B and using the minimum and mean cap beam strain values is shown in Figure 5.77

The total flange effective slab width, i.e. equivalent strain block width B_{eff}, was calculated for all loading cycles applied in the transverse direction at the peak of each loading cycle as mentioned before. This calculation process was repeated 4 times at the 4 peaks of each loading cycle group; 1st positive, 1st negative, 2nd positive, and 2nd negative peaks, and referred to as group I, II, II, and IV, respectively. A summary of the calculated B_{eff} at section B using both cap beam minimum (ε_{min}) and mean (ε_{mean}) strain values is shown in Figure 5.78 and Figure 5.79 for loading in the positive direction (groups I and III), respectively. Moreover, the calculated B_{eff} summary for loading in the negative direction (groups II and IV) is shown in Figure 5.80 and Figure 5.81, respectively. All figures show also the B_{eff} that is estimated in light of the Caltrans SDC provisions for the integral bent cap beam flanged section, which is directly referred to as Caltrans value for brevity.

Another way of summarizing the same data presented in Figure 5.78 through Figure 5.81 is given in Table 5-4 and Table 5-5 to conveniently read the calculated B_{eff} values directly. Moreover, the tables relate the calculated B_{eff} values to the slab thickness (t_s) and bent cap beam width (b_{beam}) through a slab contribution constant (C) which quantifies the slab contribution as multiples of t_s given by Equation (5-1).

$$B_{eff} = b_{beam} + C \times t_s \tag{5-1}$$

Table 5-4 summarizes the B_{eff} and the slab contribution C for different loading levels and direction when the minimum cap beam strain value is used, while Table 5-5 presents the case of using the mean cap beam strain value. The mean values for B_{eff} and slab contribution C for all loading cycles are listed in the same tables.

196
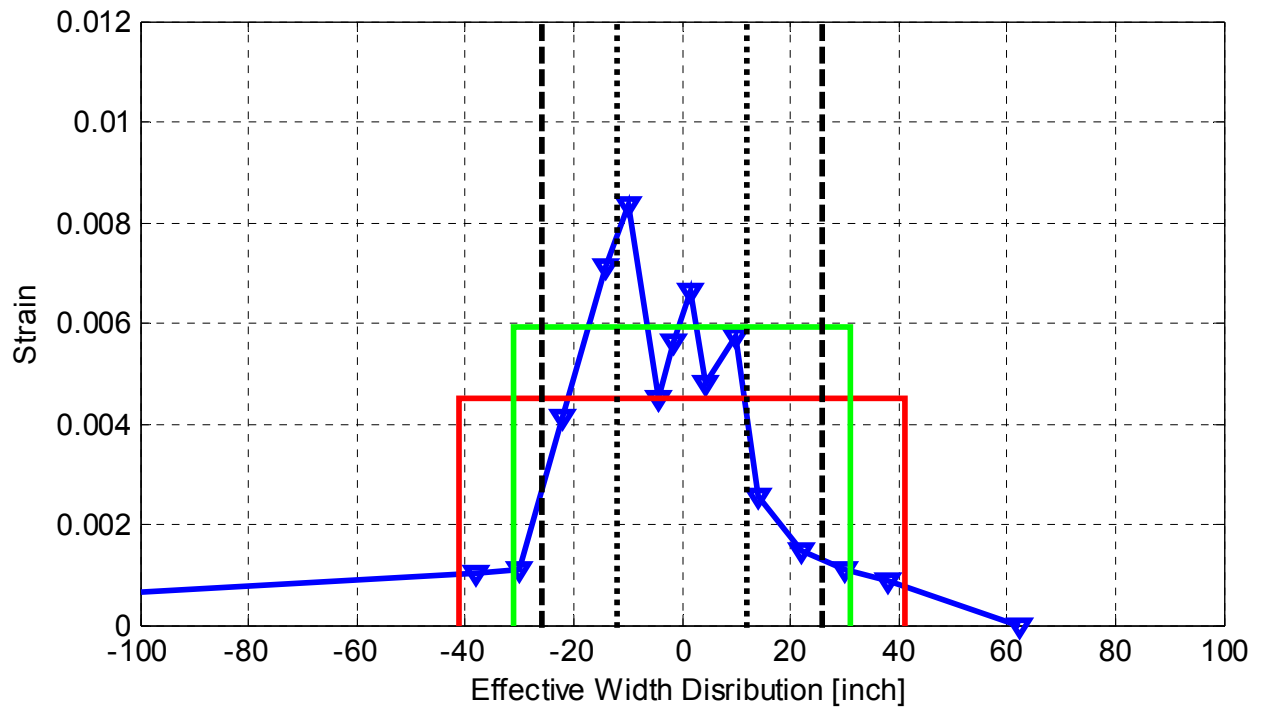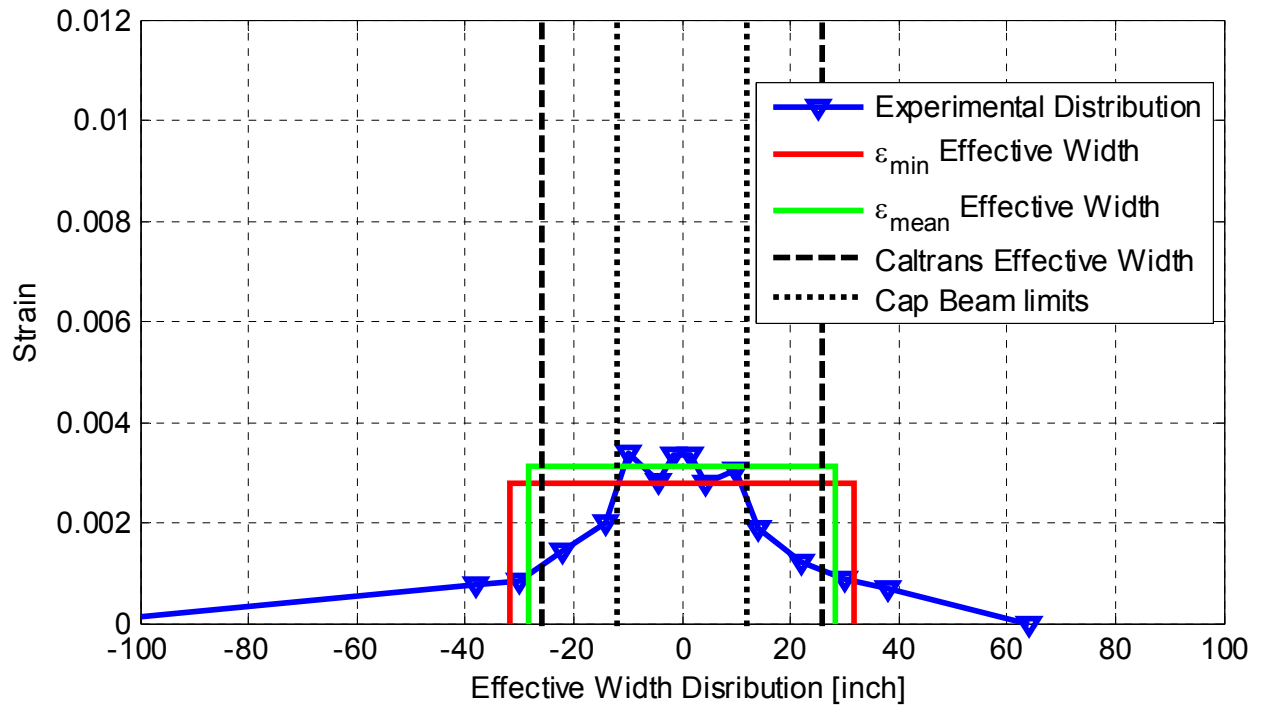
Figure 5.77 Generating effective width strain block using the strain distribution at Section B for a small- (top) and high-level (bottom) loading cycles using the observed cap beam minimum (ε_{min}) and mean (ε_{mean}) strain values
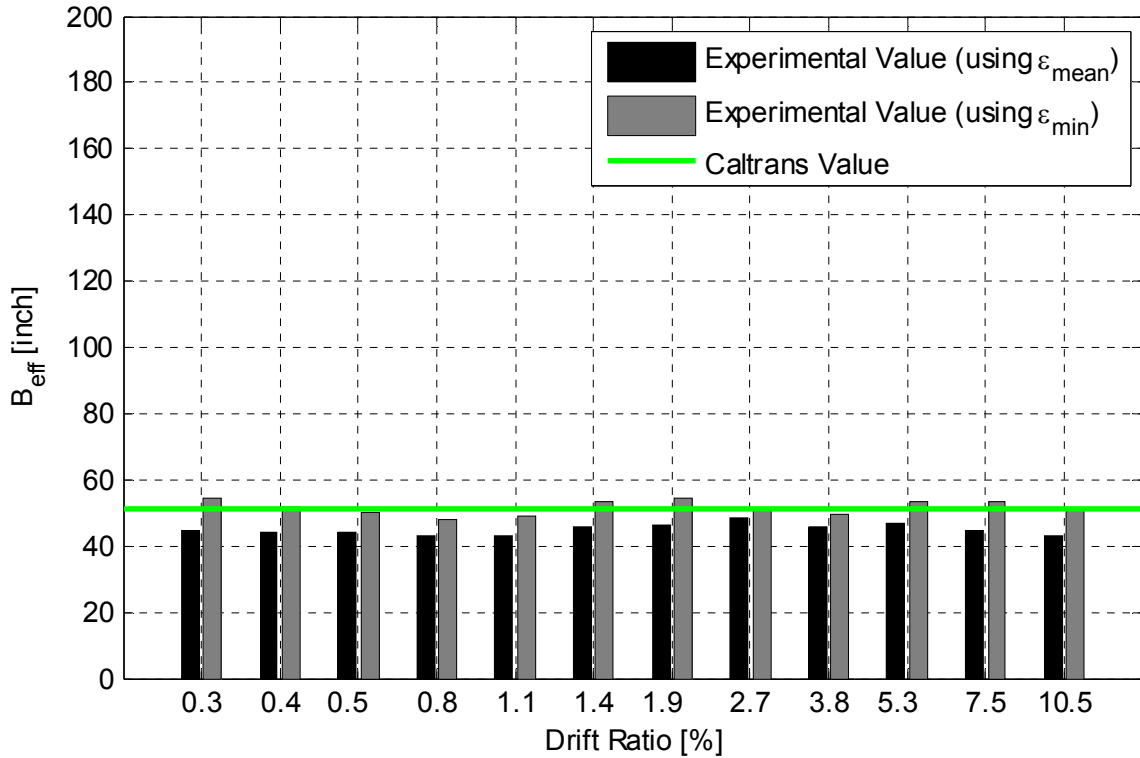
Figure 5.78 Summary of the estimated cap beam effective width at Section B at different drift ratios (group I: 1st positive peak of each transverse cyclic loading group)
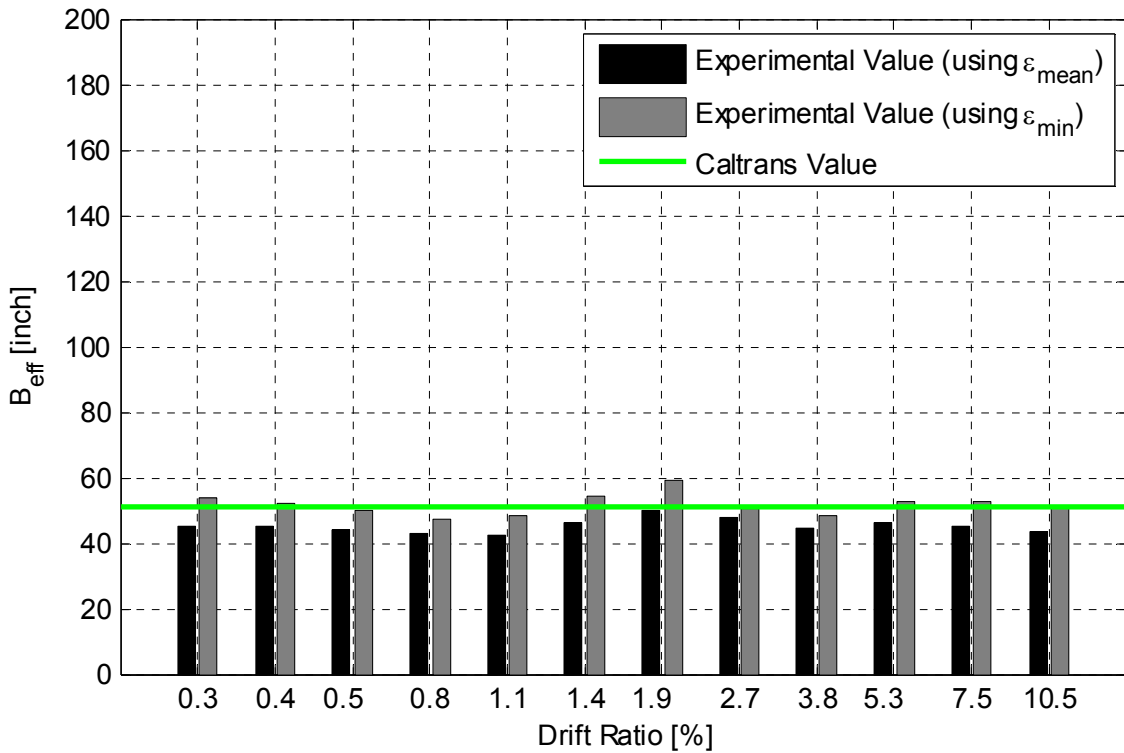
Figure 5.79 Summary of the estimated cap beam effective width at Section B at different drift ratios (group III: 2nd positive peak of each transverse cyclic loading group)
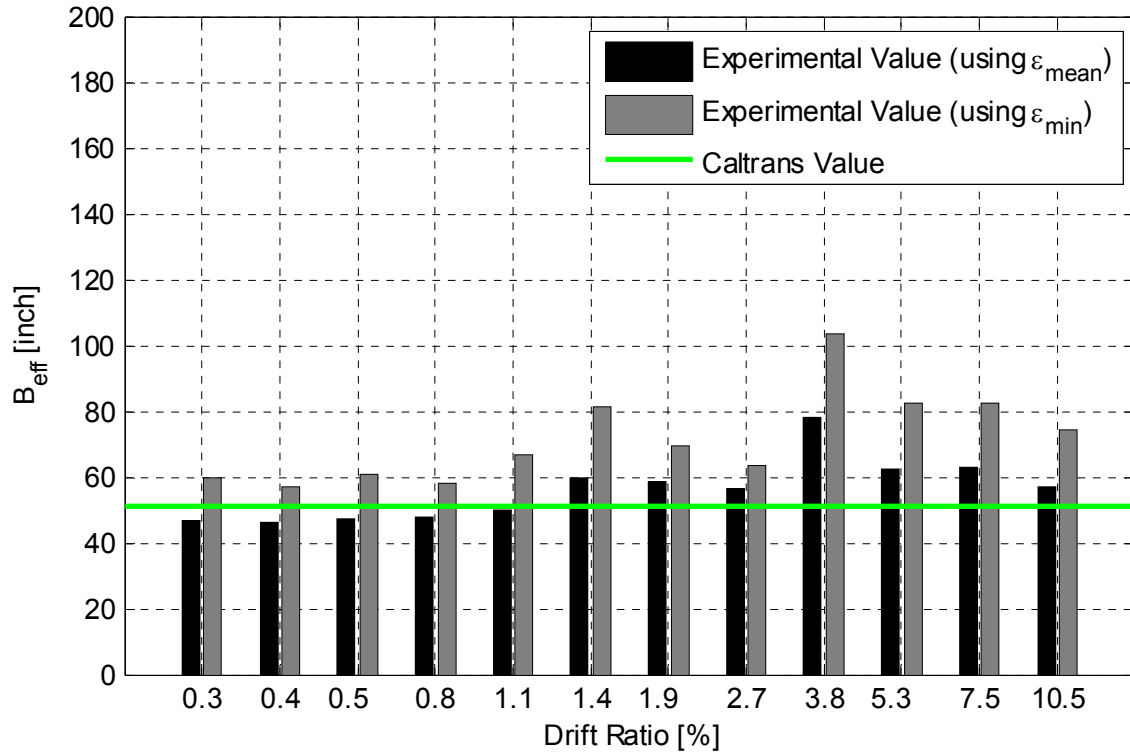
Figure 5.80 Summary of the estimated cap beam effective width at Section B at different drift ratios (group II: 1st negative peak of each transverse cyclic loading group)
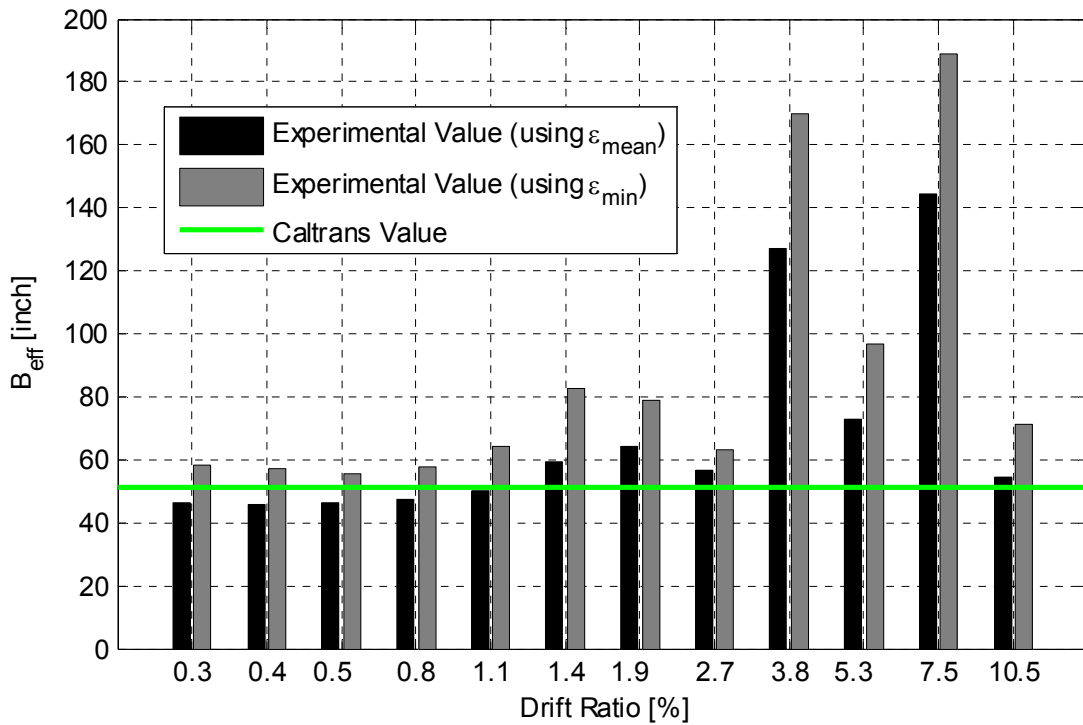
Figure 5.81 Summary of the estimated cap beam effective width at Section B at different drift ratios (group IV: 2nd negative peak of each transverse cyclic loading group)

Table 5-4 Section B effective slab width at different load levels calculated using cap beam ε_{min}

Run #	Drift Ratio [%]	Ductility [μ]	Positive loading direction (groups I and III)				Negative loading direction (groups II and IV)			
			Strain block width, B_{eff} [inch]			Slab contribution (C)	Strain block width, B_{eff} [inch]			Slab Contribution (C)
			1st cycle	2nd cycle	mean		1st cycle	2nd cycle	mean	
1	0.28	0.20	54.5	53.9	54.2	13.4	59.9	58.3	59.1	15.6
2	0.38	0.27	52.0	52.2	52.1	12.5	57.1	57.0	57.1	14.7
3	0.54	0.39	50.3	50.0	50.1	11.6	60.6	55.4	58.0	15.1
4	0.78	0.56	47.9	47.4	47.6	10.5	57.9	57.9	57.9	15.1
5	1.11	0.80	48.8	48.5	48.7	11.0	66.7	64.5	65.6	18.5
6	1.39	1.00	53.3	54.3	53.8	13.3	81.3	82.8	82.0	25.8
7	1.94	1.40	54.6	59.2	56.9	14.6	69.5	78.9	74.2	22.3
8	2.72	1.96	51.3	50.5	50.9	12.0	63.3	63.1	63.2	17.4
9	3.83	2.76	49.8	48.4	49.1	11.2	103.6	170.1	136.8	50.1
10	5.33	3.84	53.1	52.4	52.8	12.8	82.4	96.5	89.4	29.1
11	7.50	5.40	53.4	52.9	53.2	13.0	82.7	188.9	135.8	49.7
12	10.50	7.56	51.3	51.0	51.2	12.1	74.1	71.2	72.7	21.6
13	10.49	7.56	51.0	51.0	51.0	12.0	59.0	59.0	59.0	15.6
14	1.07	0.77	53.9	53.9	53.9	13.3	53.5	53.5	53.5	13.1
Mean for all loading cycles:					**51.8**	**12.4**			**76.0**	**23.1**

Table 5-5 Section B effective slab width at different load levels calculated using cap beam ε_{mean}

Run #	Drift Ratio [%]	Ductility [μ]	Positive loading direction (groups I and III)				Negative loading direction (groups II and IV)			
			Strain block width, B_{eff} [inch]			Slab contribution (C)	Strain block width, B_{eff} [inch]			Slab Contribution (C)
			1st cycle	2nd cycle	mean		1st cycle	2nd cycle	mean	
1	0.28	0.20	44.6	45.1	44.9	9.3	46.6	46.2	46.4	10.0
2	0.38	0.27	44.2	45.0	44.6	9.1	46.0	46.0	46.0	9.8
3	0.54	0.39	44.0	44.2	44.1	8.9	47.2	46.5	46.9	10.2
4	0.78	0.56	43.1	43.2	43.1	8.5	47.7	47.6	47.7	10.5
5	1.11	0.80	43.0	42.4	42.7	8.3	50.0	50.2	50.1	11.6
6	1.39	1.00	45.6	46.1	45.8	9.7	59.7	59.2	59.5	15.8
7	1.94	1.40	46.3	50.1	48.2	10.7	58.6	64.4	61.5	16.7
8	2.72	1.96	48.3	47.7	48.0	10.7	56.5	56.8	56.6	14.5
9	3.83	2.76	45.8	44.3	45.1	9.4	77.9	127.1	102.5	34.9
10	5.33	3.84	46.6	46.4	46.5	10.0	62.3	72.8	67.5	19.3
11	7.50	5.40	44.7	44.9	44.8	9.2	62.8	144.3	103.5	35.3
12	10.50	7.56	43.2	43.3	43.3	8.6	56.8	54.7	55.7	14.1
13	10.49	7.56	43.2	43.2	43.2	8.5	46.1	46.1	46.1	9.8
14	1.07	0.77	44.9	44.9	44.9	9.3	44.0	44.0	44.0	8.9
Mean for all loading cycles:					**44.9**	**9.3**			**59.6**	**15.8**

5.5.4 Section D: Effective Slab Width

A similar framework as before is used to present the effective slab width results at section D. One example of how the strain block was determined using the strain distribution at section D using the minimum and mean cap beam strain values is shown in Figure 5.82. A summary of the calculated B_{eff} at section D using both cap beam minimum and mean strain values is shown in Figure 5.83 and Figure 5.84 for loading in the positive direction (groups I and III), respectively. Moreover, the calculated B_{eff} summary for loading in the negative direction (groups II and IV) is shown in Figure 5.85 and Figure 5.86, respectively. The Caltrans value for B_{eff} is shown in all figures as well. The same data are presented differently in Table 5-7 and Table 5-8 to summarize B_{eff} and the slab contribution C for the different loading levels and direction when the minimum and mean cap beam strain values are used, respectively.
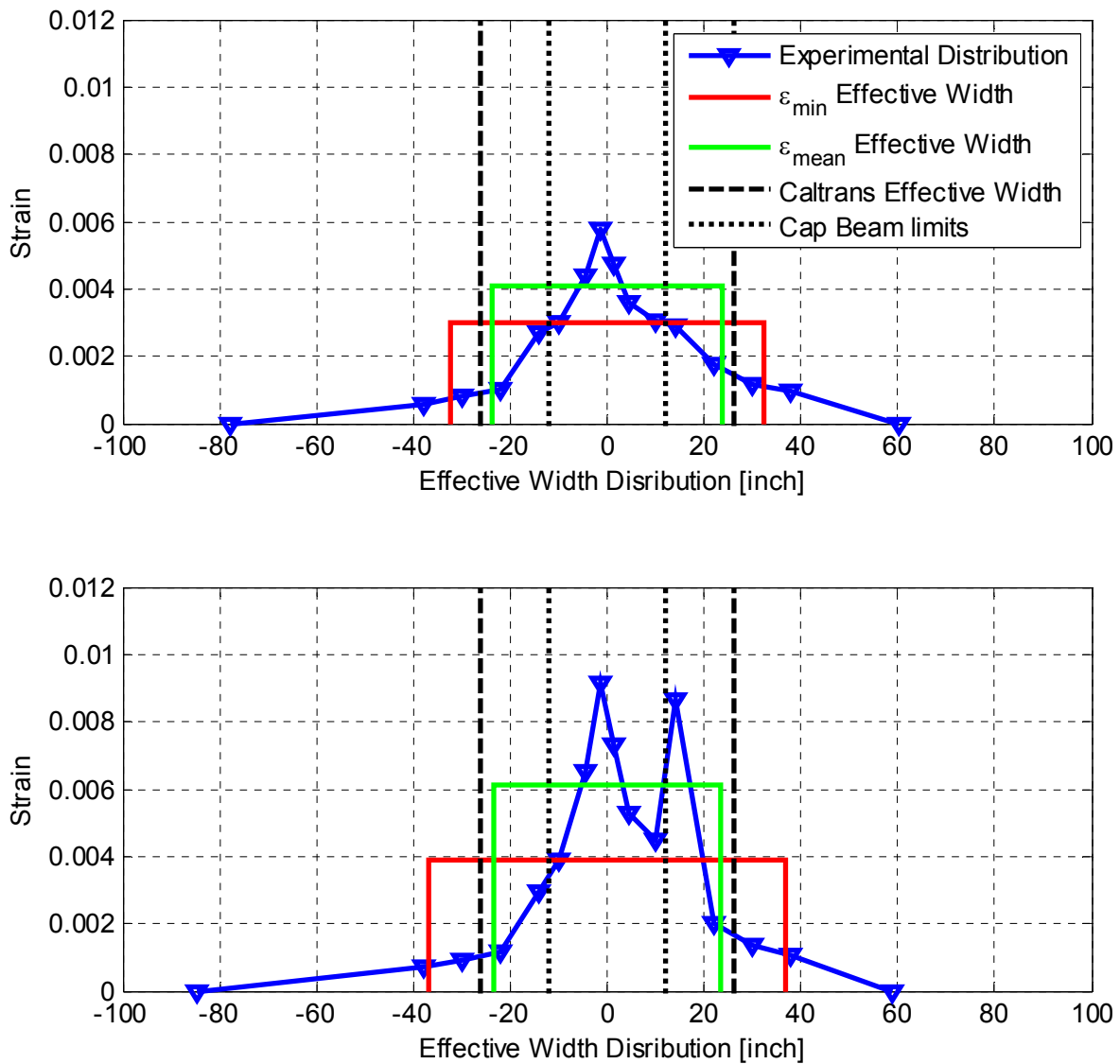
Figure 5.82 Generating effective width strain block using the strain distribution at Section D for a small- (top) and high-level (bottom) loading cycle using the observed cap beam minimum (ε_{min}) and mean (ε_{mean}) strain values

201
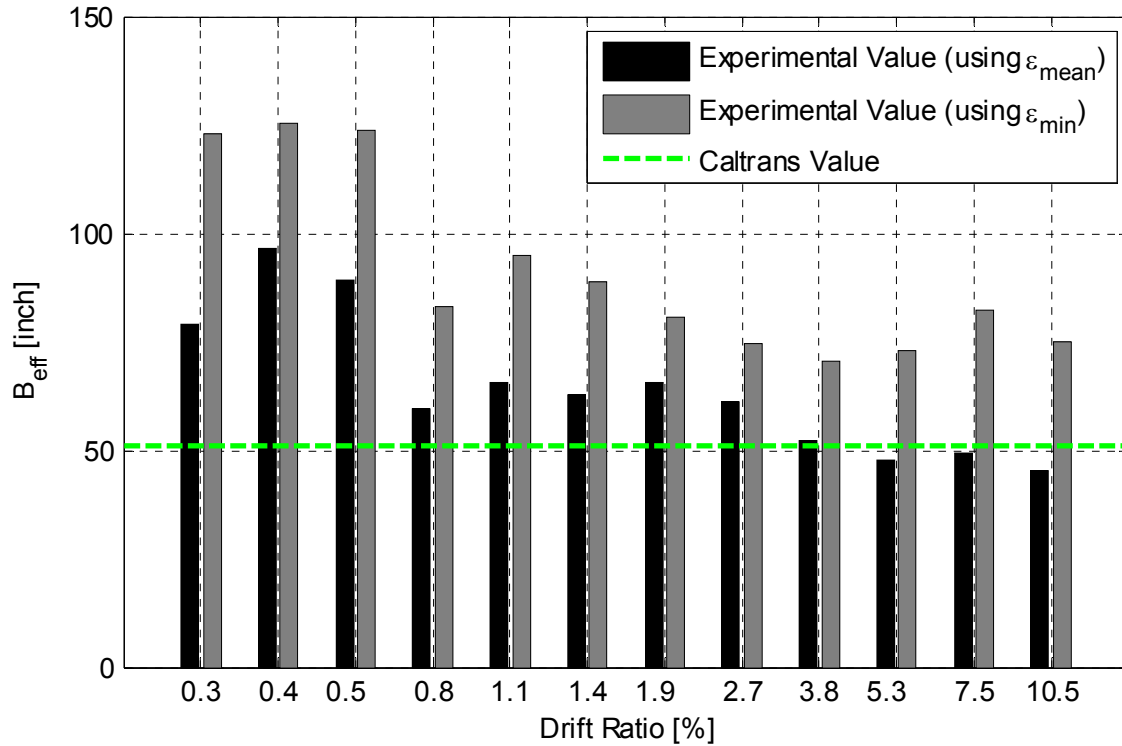
Figure 5.83 Summary of the estimated cap beam effective width at Section D at different drift ratios (group I: 1st positive peak of each transverse cyclic loading group)
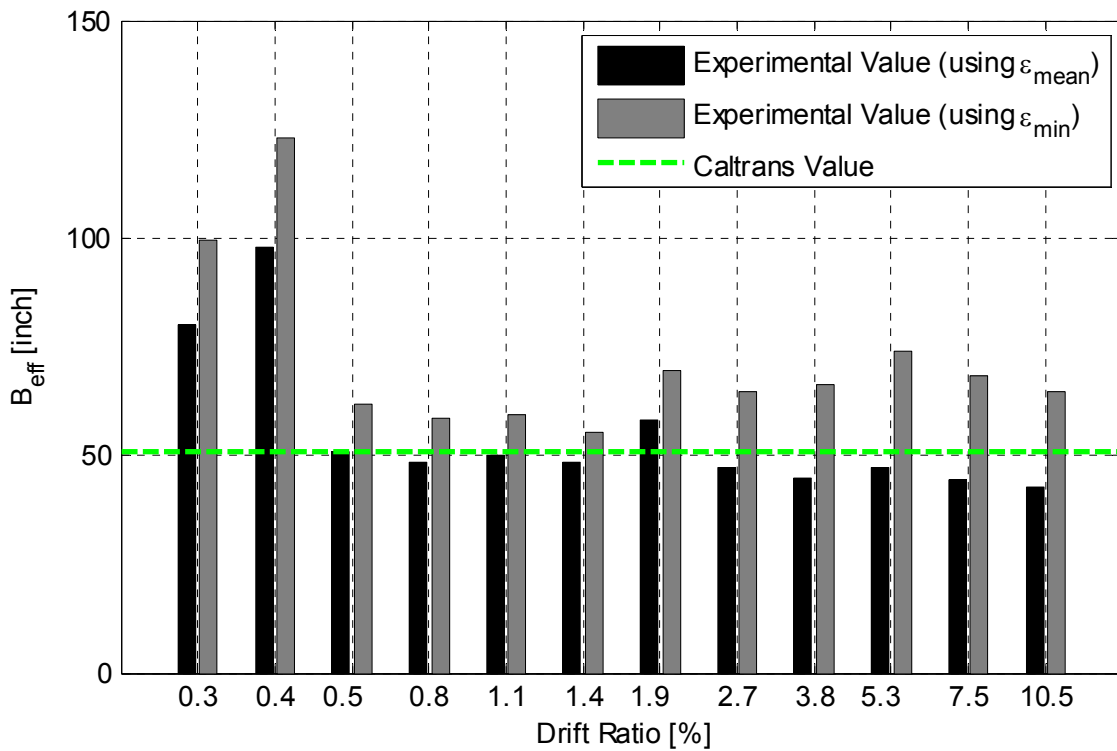
Figure 5.84 Summary of the estimated cap beam effective width at Section D at different drift ratios (group III: 2nd positive peak of each transverse cyclic loading group)
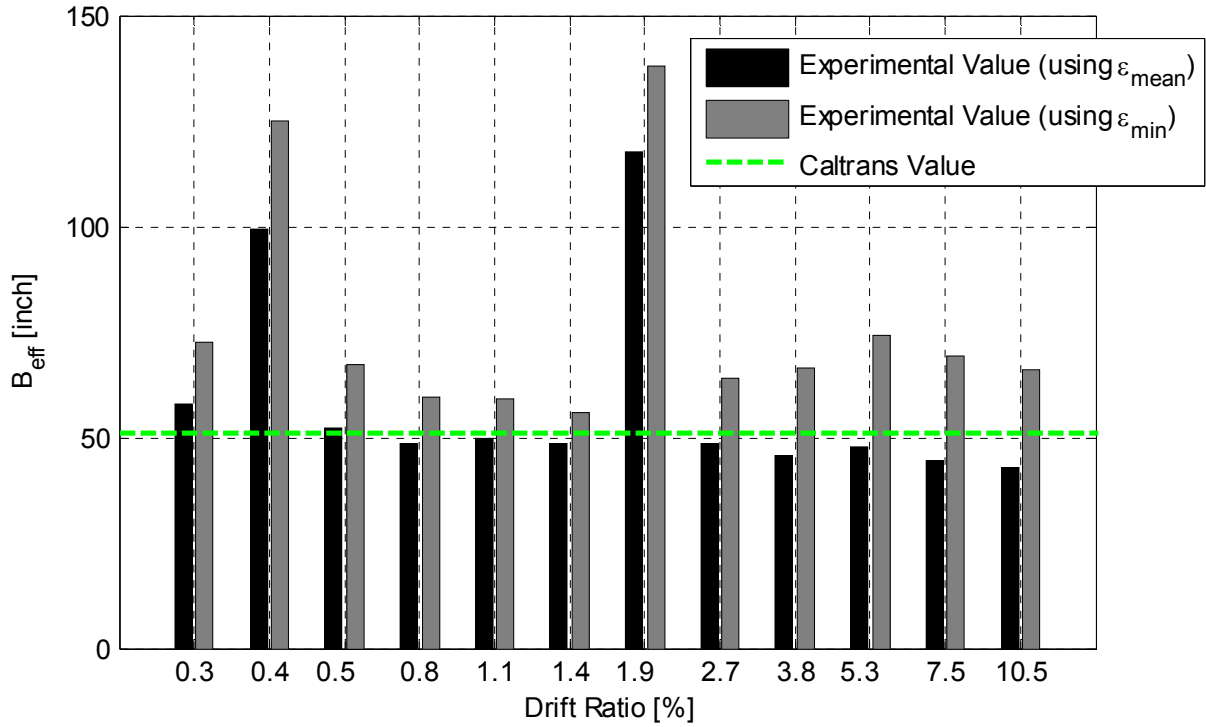
Figure 5.85 Summary of the estimated cap beam effective width at Section D at different drift ratios (group II: 1ˢᵗ negative peak of each transverse cyclic loading group)
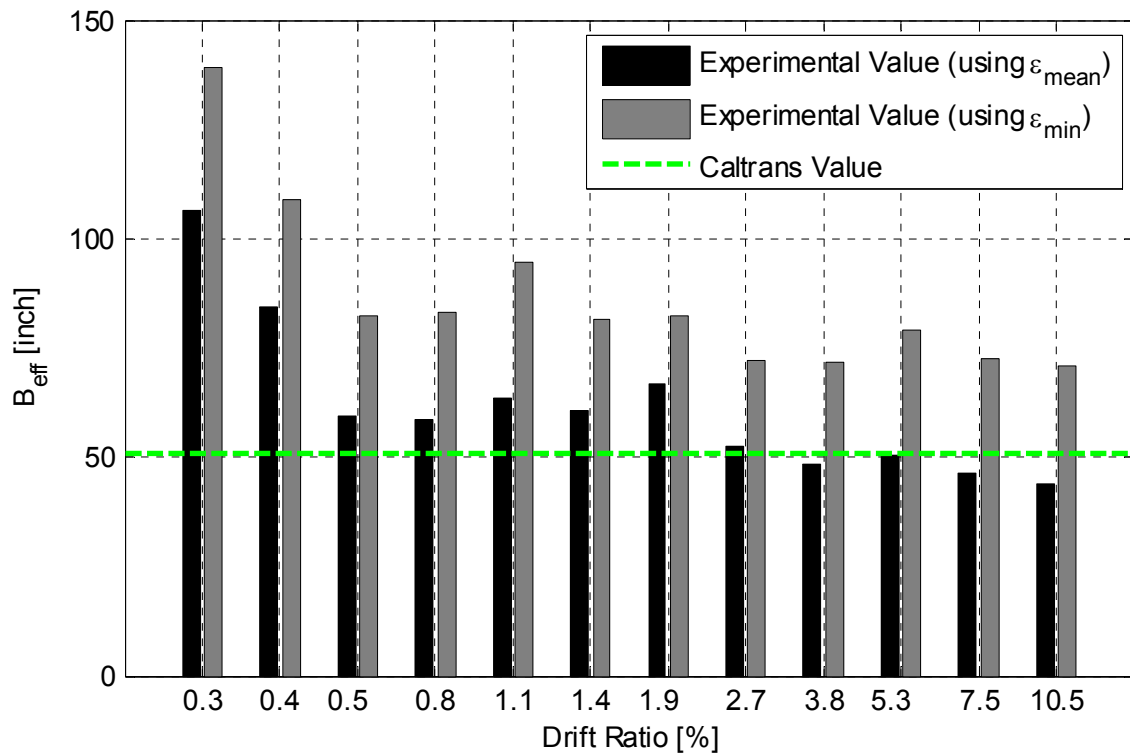
Figure 5.86 Summary of the estimated cap beam effective width at Section D at different drift ratios (group IV: 2ⁿᵈ negative peak of each transverse cyclic loading group)

Table 5-6 Section D effective slab width at different load levels calculated using cap beam ε_{min}

Run #	Drift Ratio [%]	Ductility [μ]	Positive loading direction (groups I and III)				Negative loading direction (groups II and IV)			
			Strain block width, B_{eff} [inch]			Slab contribution (C)	Strain block width, B_{eff} [inch]			Slab Contribution (C)
			1st cycle	2nd cycle	mean		1st cycle	2nd cycle	mean	
1	0.28	0.20	123.0	139.3	131.2	47.6	72.5	99.7	86.1	27.6
2	0.38	0.27	125.3	108.8	117.0	41.3	125.1	123.1	124.1	44.5
3	0.54	0.39	123.8	82.5	103.1	35.2	67.3	62.0	64.7	18.1
4	0.78	0.56	83.0	83.1	83.0	26.2	59.6	58.6	59.1	15.6
5	1.11	0.80	95.1	94.4	94.8	31.5	59.0	59.2	59.1	15.6
6	1.39	1.00	88.7	81.7	85.2	27.2	56.0	55.1	55.5	14.0
7	1.94	1.40	80.7	82.4	81.5	25.6	137.9	69.7	103.8	35.5
8	2.72	1.96	74.7	72.0	73.3	21.9	63.9	64.7	64.3	17.9
9	3.83	2.76	70.7	71.7	71.2	21.0	66.6	66.4	66.5	18.9
10	5.33	3.84	72.9	79.2	76.1	23.1	74.4	73.8	74.1	22.3
11	7.50	5.40	82.2	72.6	77.4	23.7	69.4	68.2	68.8	19.9
12	10.50	7.56	74.8	70.7	72.8	21.7	66.2	64.8	65.5	18.4
13	10.49	7.56	69.1	69.1	69.1	20.0	63.5	63.5	63.5	17.6
14	1.07	0.77	66.4	66.4	66.4	18.9	65.4	65.4	65.4	18.4
Mean for all loading cycles:					**85.9**	**27.5**			**72.9**	**21.7**

Table 5-7 Section D effective slab width at different load levels calculated using cap beam ε_{mean}

Run #	Drift Ratio [%]	Ductility [μ]	Positive loading direction (groups I and III)				Negative loading direction (groups II and IV)			
			Strain block width, B_{eff} [inch]			Slab contribution (C)	Strain block width, B_{eff} [inch]			Slab Contribution (C)
			1st cycle	2nd cycle	mean		1st cycle	2nd cycle	mean	
1	0.28	0.20	78.9	106.5	92.7	30.5	57.9	80.0	69.0	20.0
2	0.38	0.27	96.7	84.6	90.6	29.6	99.3	98.0	98.7	33.2
3	0.54	0.39	89.2	59.4	74.3	22.4	52.4	50.9	51.6	12.3
4	0.78	0.56	59.5	58.5	59.0	15.5	48.6	48.4	48.5	10.9
5	1.11	0.80	65.5	63.6	64.5	18.0	49.8	49.9	49.8	11.5
6	1.39	1.00	62.8	60.6	61.7	16.8	48.5	48.3	48.4	10.8
7	1.94	1.40	65.5	66.8	66.2	18.7	117.8	58.4	88.1	28.5
8	2.72	1.96	61.0	52.4	56.7	14.5	48.8	47.4	48.1	10.7
9	3.83	2.76	52.3	48.5	50.4	11.7	45.9	44.8	45.3	9.5
10	5.33	3.84	47.9	50.3	49.1	11.1	47.6	47.1	47.3	10.4
11	7.50	5.40	49.4	46.4	47.9	10.6	44.6	44.3	44.5	9.1
12	10.50	7.56	45.2	43.9	44.6	9.1	42.8	42.8	42.8	8.3
13	10.49	7.56	43.0	43.0	43.0	8.4	42.0	42.0	42.0	8.0
14	1.07	0.77	42.3	42.3	42.3	8.1	42.4	42.4	42.4	8.2
Mean for all loading cycles:					**60.2**	**16.1**			**54.7**	**13.7**

5.5.5   Overall Effective Width in Tension Side

For more comprehensive conclusions, the calculated effective slab width is additionally averaged out from cases of loading in positive and negative directions together at both sections. Furthermore, the overall average for both sections together was calculated such that the mean value for all the loading cases renders a single number that summarizes all the experimentally determined effective slab width values. The average B_{eff} values for each group of loading and overall average for all groups combined is shown first for each of sections B and D separately in Figure 5.87 and Figure 5.88, respectively. The averages for all the groups calculated using both the minimum (ε_{min}) and mean (ε_{mean}) cap beam strain values are also plotted against the Caltrans value for both sections in Figure 5.87 and Figure 5.88. It is noted from the figures that the Caltrans value is conservative relative to what has been observed from the experiments.

The average values from all groups are tabulated as well in Table 5-8 and Table 5-9 for cases of using the minimum and mean cap beam strain values, respectively. Table 5-8 shows respectively for all loading groups of sections B and D an average effective flange width, B_{eff}, of 63.9 inch and 79.4 inch versus an estimated value from the Caltrans SDC flanged section of 51inch. These values correspond to slab contributions $17.7t_s$ and $24.6t_s$ versus the well-known $12t_s$ Caltrans value. However, when the mean cap beam strain value is used instead, Table 5-9 suggests that the former numbers drop to $12.6t_s$ and $14.9t_s$. In addition, the overall average of both sections B and D together is calculated and denoted in the tables. When all the loading cases and sections B and D were considered, a mean value for the slab contribution was determined to be $21.2t_s$ and $13.7t_s$ based on a minimum and mean cap beam strain values, respectively. It is concluded that the $12t_s$ is conservative and a larger value is recommended to be considered for bent cap beam capacity estimation as discussed in more details in Chapter 9.
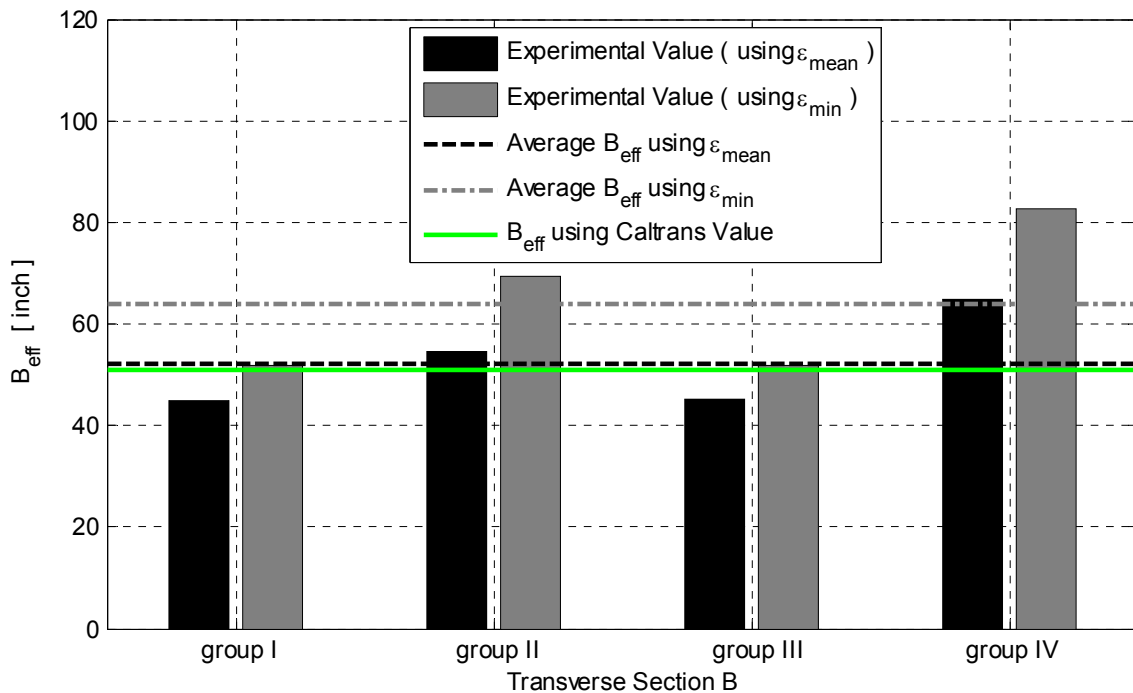
Figure 5.87 Mean effective width from all loading cycles in each group (bar chart) and overall average effective width from all loading cycles and groups (dashed lines) at Section B as compared to Caltrans SDC effective width value
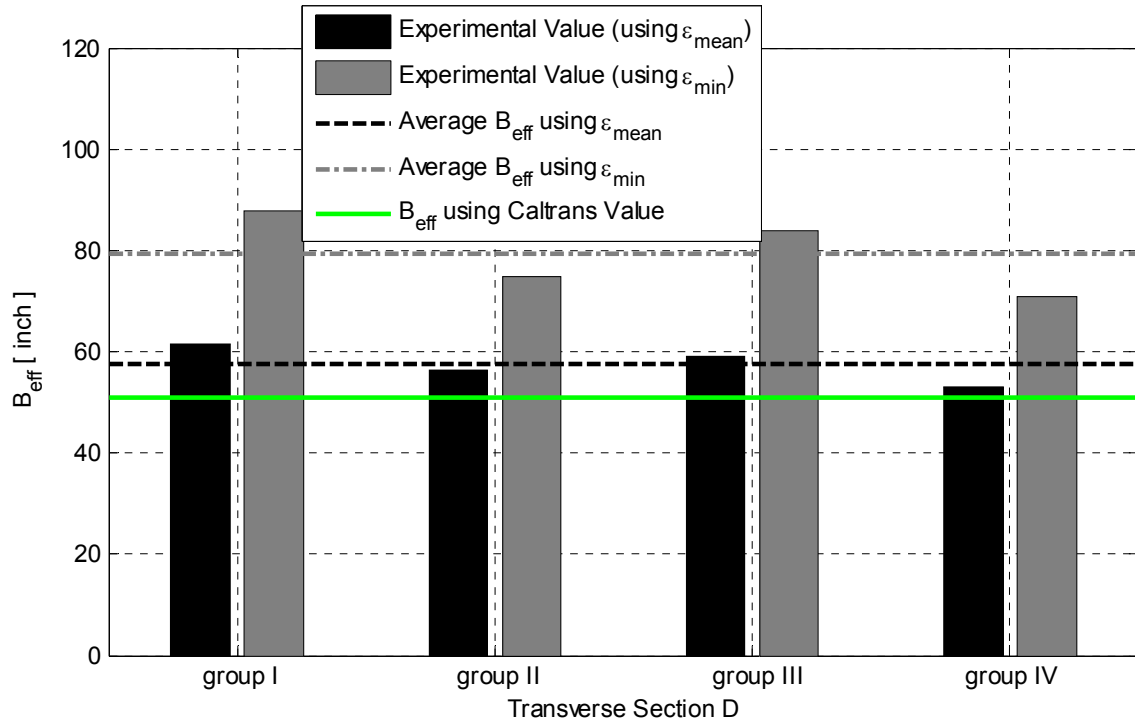
Figure 5.88 Mean effective width from all loading cycles in each group (bar chart) and overall average effective width from all loading cycles and groups (dashed lines) at Section D as compared to Caltrans SDC effective width value

Table 5-8 Summary of overall effective slab width mean calculated using cap beam ε_{min}

Run #	Drift %	Ductility	All groups I, II, III, IV mean (section B)		All groups I, II, III, IV mean (section D)		Overall mean for both sections	
			B_{eff} [inch]	Slab contribution (C)	B_{eff} [inch]	Slab contribution (C)	B_{eff} [inch]	Slab contribution (C)
1	**0.28**	**0.2**	56.6	14.5	108.6	37.6	82.6	26.1
2	0.38	0.27	54.6	13.6	120.6	42.9	87.6	28.3
3	0.54	0.39	54.1	13.4	83.9	26.6	69	20
4	0.78	0.56	52.8	12.8	71.1	20.9	61.9	16.9
5	1.11	0.8	57.1	14.7	76.9	23.5	67	19.1
6	1.39	1	67.9	19.5	70.4	20.6	69.2	20.1
7	1.94	1.4	65.5	18.5	92.7	30.5	79.1	24.5
8	2.72	1.96	57.1	14.7	68.8	19.9	62.9	17.3
9	3.83	2.76	93	30.7	68.8	19.9	80.9	25.3
10	5.33	3.84	71.1	20.9	75.1	22.7	73.1	21.8
11	7.5	5.4	94.5	31.3	73.1	21.8	83.8	26.6
12	10.5	7.56	61.9	16.9	69.1	20.1	65.5	18.5
13	10.49	7.56	55	13.8	66.3	18.8	60.6	16.3
14	1.07	0.77	53.7	13.2	65.9	18.6	59.8	15.9
Mean for all loading cycles			**63.9**	**17.7**	**79.4**	**24.6**	**71.7**	**21.2**

206

Table 5-9 Summary of overall effective slab width mean calculated using cap beam ε_{mean}

Run #	Drift %	Ductility	All groups I, II, III, IV mean (section B)		All groups I, II, III, IV mean (section D)		Overall mean for both sections	
			B_{eff} [inch]	Slab contribution (C)	B_{eff} [inch]	Slab contribution (C)	B_{eff} [inch]	Slab contribution (C)
1	**0.28**	**0.2**	45.6	9.6	80.8	25.3	63.2	17.4
2	0.38	0.27	45.3	9.5	94.7	31.4	70	20.4
3	0.54	0.39	45.5	9.6	63	17.3	54.2	13.4
4	0.78	0.56	45.4	9.5	53.8	13.2	49.6	11.4
5	1.11	0.8	46.4	10	57.2	14.7	51.8	12.4
6	1.39	1	52.7	12.7	55	13.8	53.9	13.3
7	1.94	1.4	54.8	13.7	77.1	23.6	66	18.7
8	2.72	1.96	52.3	12.6	52.4	12.6	52.4	12.6
9	3.83	2.76	73.8	22.1	47.9	10.6	60.8	16.4
10	5.33	3.84	57	14.7	48.2	10.8	52.6	12.7
11	7.5	5.4	74.2	22.3	46.2	9.9	60.2	16.1
12	10.5	7.56	49.5	11.3	43.7	8.7	46.6	10
13	10.49	7.56	44.7	9.2	42.5	8.2	43.6	8.7
14	1.07	0.77	44.5	9.1	42.4	8.2	43.4	8.6
Mean for all loading cycles			**52.3**	**12.6**	**57.5**	**14.9**	**54.9**	**13.7**

5.6   EFFECTIVE SLAB WIDTH (COMPRESSION SIDE)

The behavior of the reinforcing steel bars in the tension side in RC flanged sections under flexure is more representative of the effective slab width and slab contribution than that in the compression side. That is because all concrete in tension is cracked at both service and limit states and only steel is assumed effective in carrying the loads. However, in the compression side, the concrete contributes significantly to the flexural capacity. Thus, it is useful to acquire strain, or stress if possible, distribution in the compression zone especially if the contribution of the slabs is required. Unfortunately, using embedded concrete gages to measure concrete strain directly is not very reliable. Therefore, the compression steel was instrumented such that the strain of the surrounding concrete can be assumed the same as the steel as long as perfect bond between the steel and concrete is maintained. The sections that have been used for exploring strain distributions, namely sections B and D, are far away from the beam end and it is a safe assumption to consider that no bond slip took place at those sections.

As implied from above, embedded concrete strain gages and compression steel strain gages were both used to acquire the strain distribution at the compression side. However, the data recorded at the compression side was noisy and extremely sensitive to the applied concentrated gravity load. Accordingly, the compression side strain data, from both concrete and steel gage types, were not conclusive but briefly shown here for completeness. Moreover, for investigating the bent cap beam capacity in the post-test analysis, a similar effective width to that obtained from the tension side was considered for the compression side.

5.6.1   Reinforcement Strain Distribution

Several reinforcing bars in the bent cap beam compression side and adjacent transverse soffit slab bars were instrumented to obtain a similar strain distribution to what was presented in previous section for the tension side. The strain distribution from the different strain gage readings was recorded continuously throughout all the loading cycles in both transverse and longitudinal directions. Only results obtained from 2nd positive and 2nd negative peaks of each group of transverse loading cycles are shown for brevity. The results were selected for small-level cycles of drift ratios 0.4%, 0.8%, 1.1%, and 1.4%, which corresponded to μ of 0.27, 0.56, 0.80, and 1.0, respectively. Meanwhile, the 1.0 ductility level (1.5% drift ratio) results along with 1.96, 3.84, and 7.57 ductility levels (2.7%, 5.3%, and 10.5% drift ratio) comprised the selected high-level cycles. Figure 5.89 and Figure 5.90 show the distribution in the compression side at section B at the small-levels and high-levels of loading, respectively, when the transverse load was pushing towards the East, i.e. positive loading direction side. Figure 5.91 and Figure 5.92 show the strain distribution at section B for similar levels when loading was pushing towards the West side, i.e. reversed load in the negative direction. On the other hand, Figure 5.93 through Figure 5.96 show the distribution in the compression side for different levels and loading direction but for section D. It is observed from all the figures that the strain values in the soffit slab transverse reinforcement did not almost change with the increased lateral loading levels. Only the cap beam reinforcement strain was varying with lateral loading and in certain loading directions; negative loading direction for section B, and positive loading for section D. Accordingly, the area under the distribution could not be accurately calculated because some strain values are negative, due to compression, and others are positive due to overriding tension.
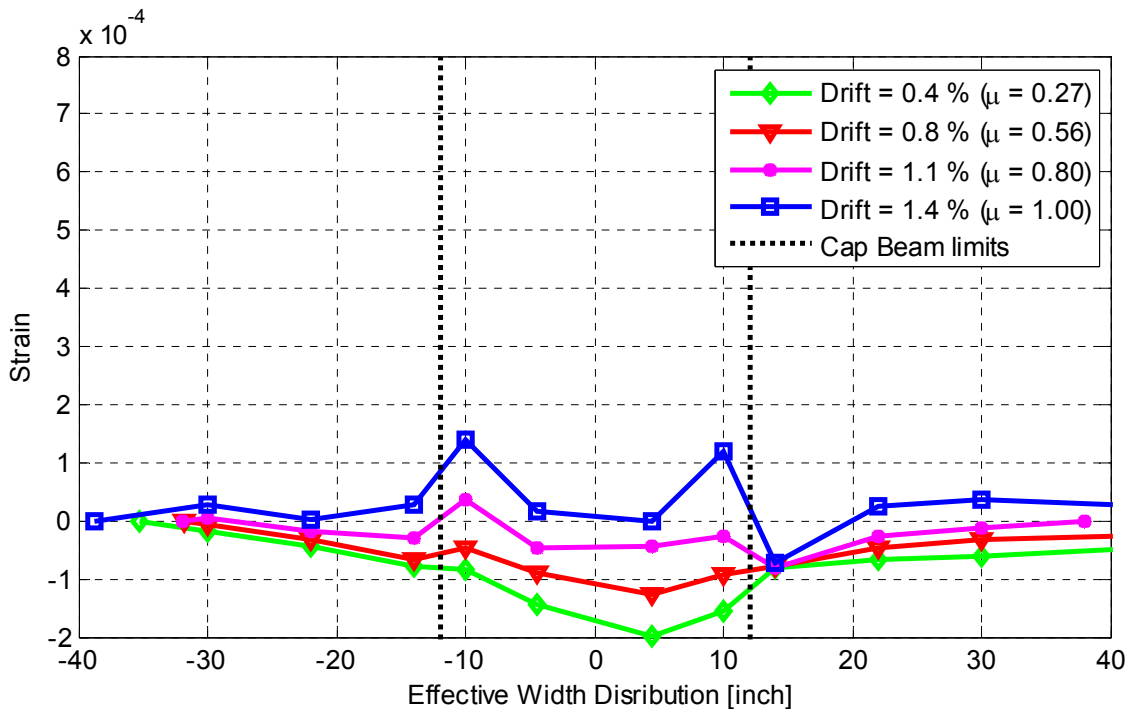
Figure 5.89 Strain distribution along cap beam and box-girder transverse soffit slab reinforcement (compression side) at Section B for different small-level loading cycles (strain values recorded at loading cycle peak when loading is in EAST direction)

208
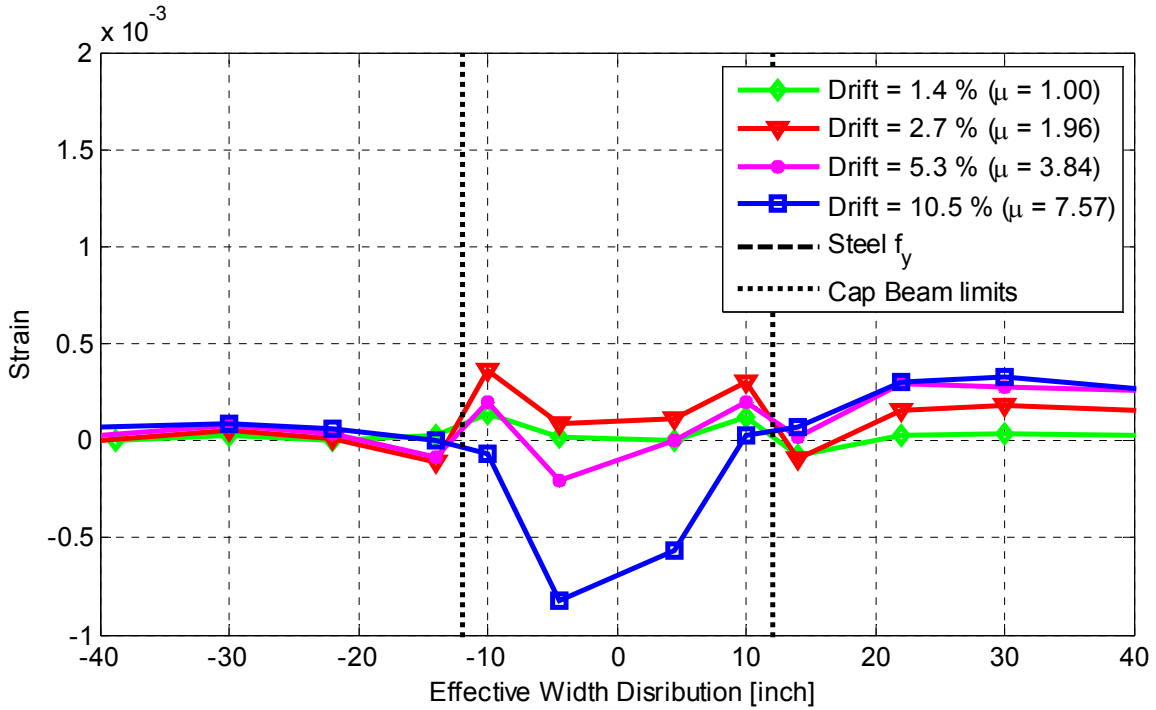
Figure 5.90 Strain distribution along cap beam and box-girder transverse soffit slab reinforcement (compression side) at Section B for different high-level loading cycles (strain values recorded at loading cycle peak when loading is in EAST direction)
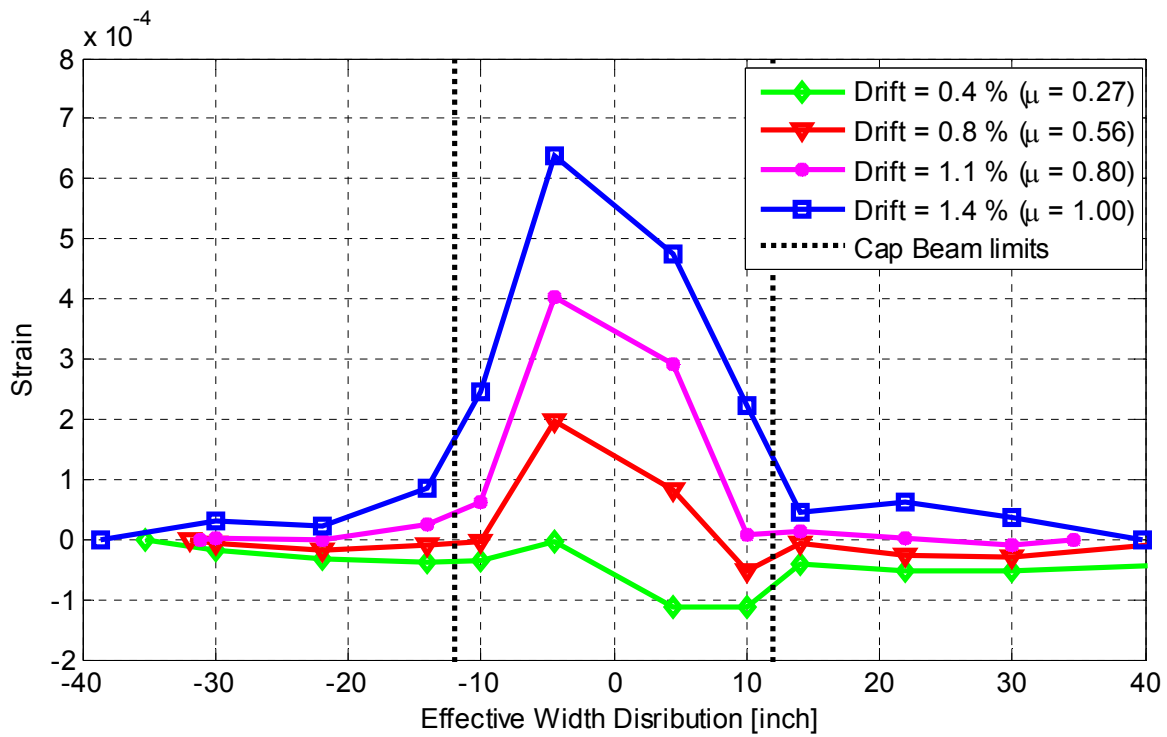
Figure 5.91 Strain distribution along cap beam and box-girder transverse soffit slab reinforcement (compression side) at Section B for different high-level loading cycles (strain values recorded at loading cycle peak when loading is in WEST direction)

209
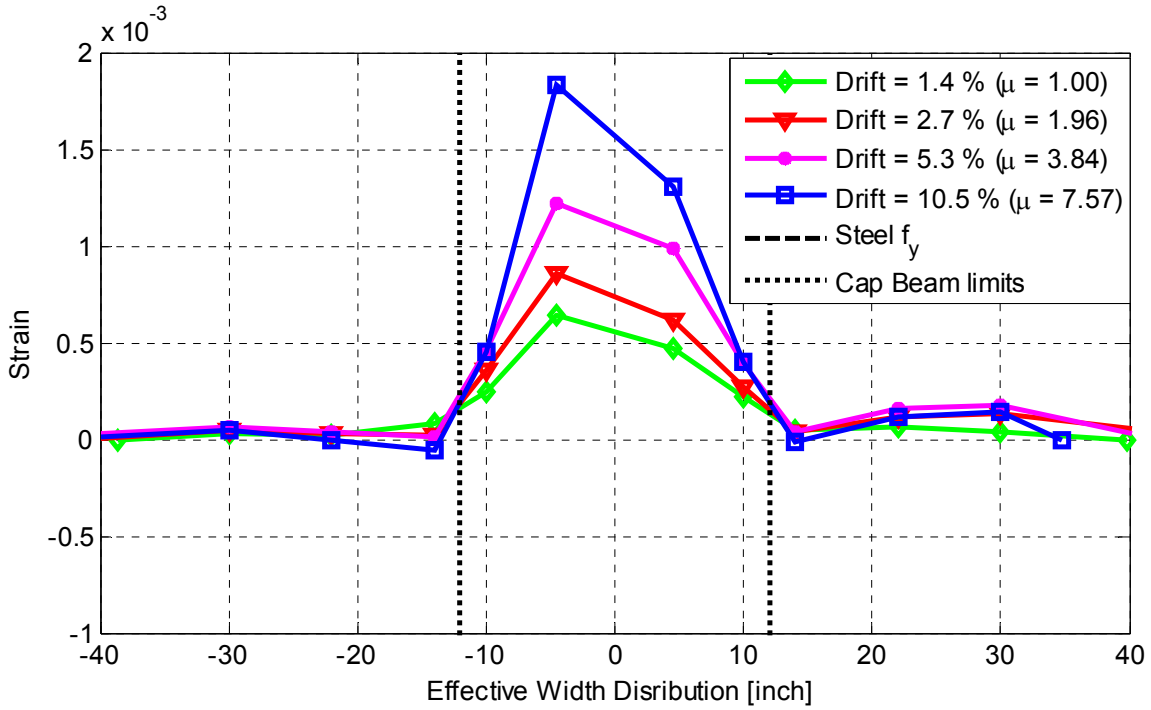
Figure 5.92 Strain distribution along cap beam and box-girder transverse soffit slab reinforcement (compression side) at Section B for different high-level loading cycles (strain values recorded at loading cycle peak when loading is in WEST direction)
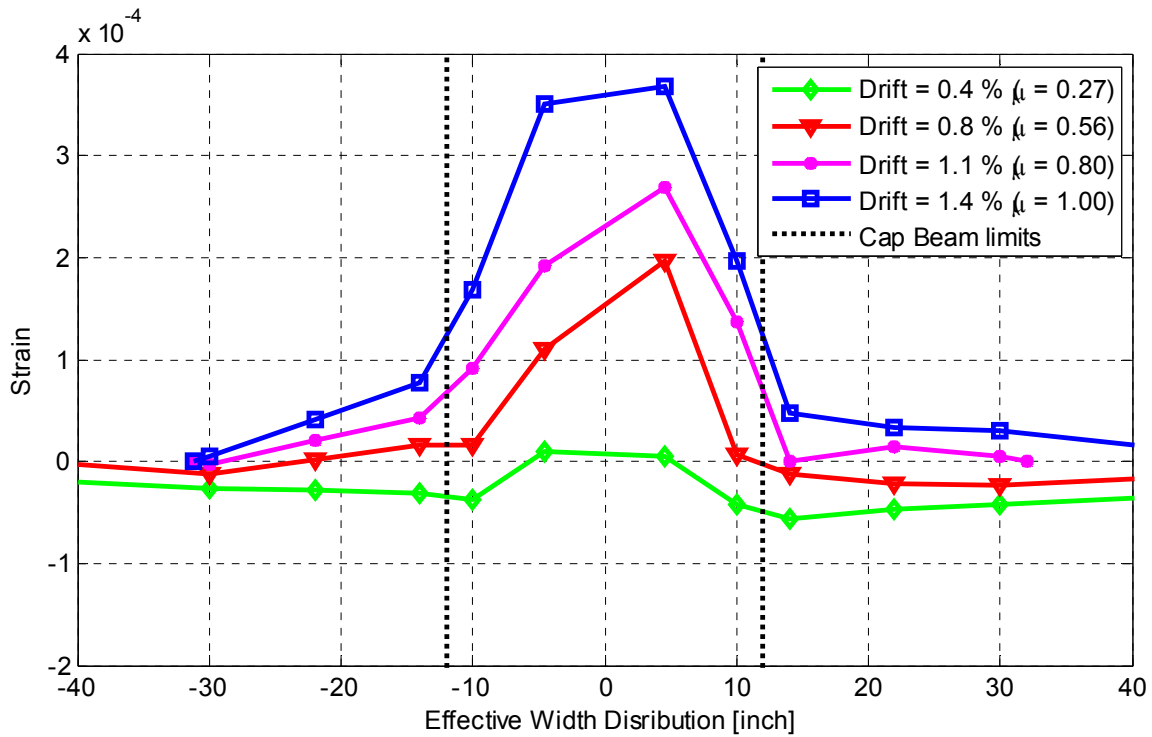
Figure 5.93 Strain distribution along cap beam and box-girder transverse soffit slab reinforcement (compression side) at Section D for different small-level loading cycles (strain values recorded at loading cycle peak when loading is in EAST direction)
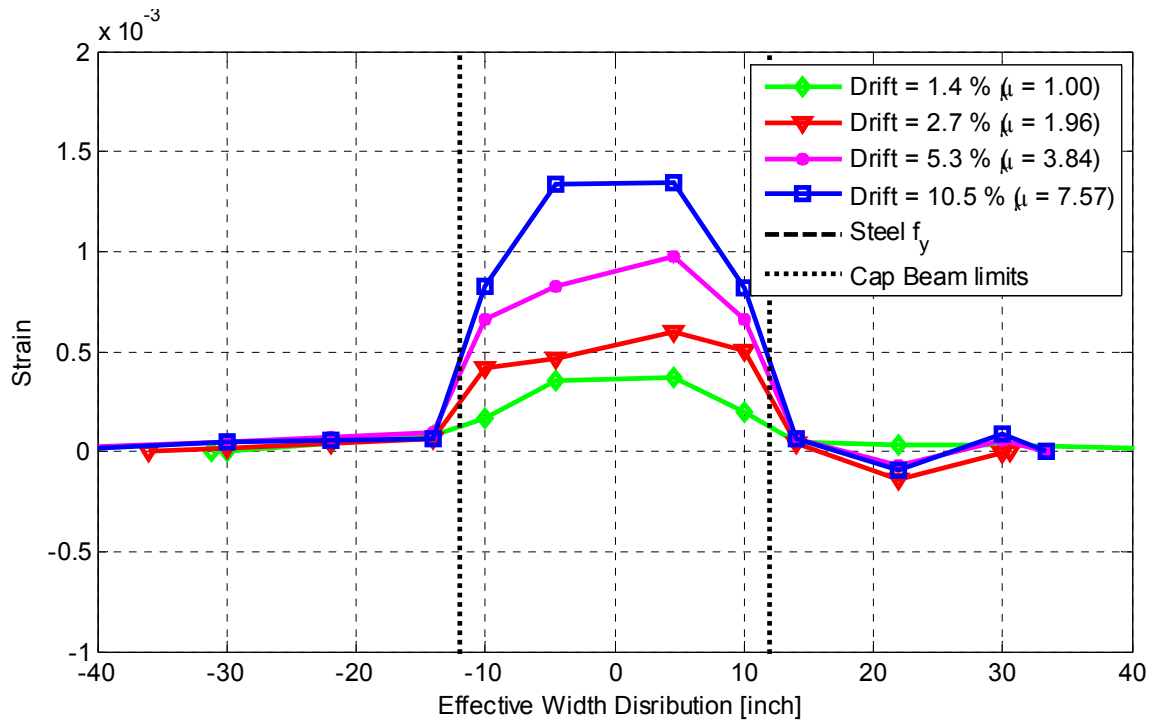
Figure 5.94 Strain distribution along cap beam and box-girder transverse soffit slab reinforcement (compression side) at Section D for different high-level loading cycles (strain values recorded at loading cycle peak when loading is in EAST direction)
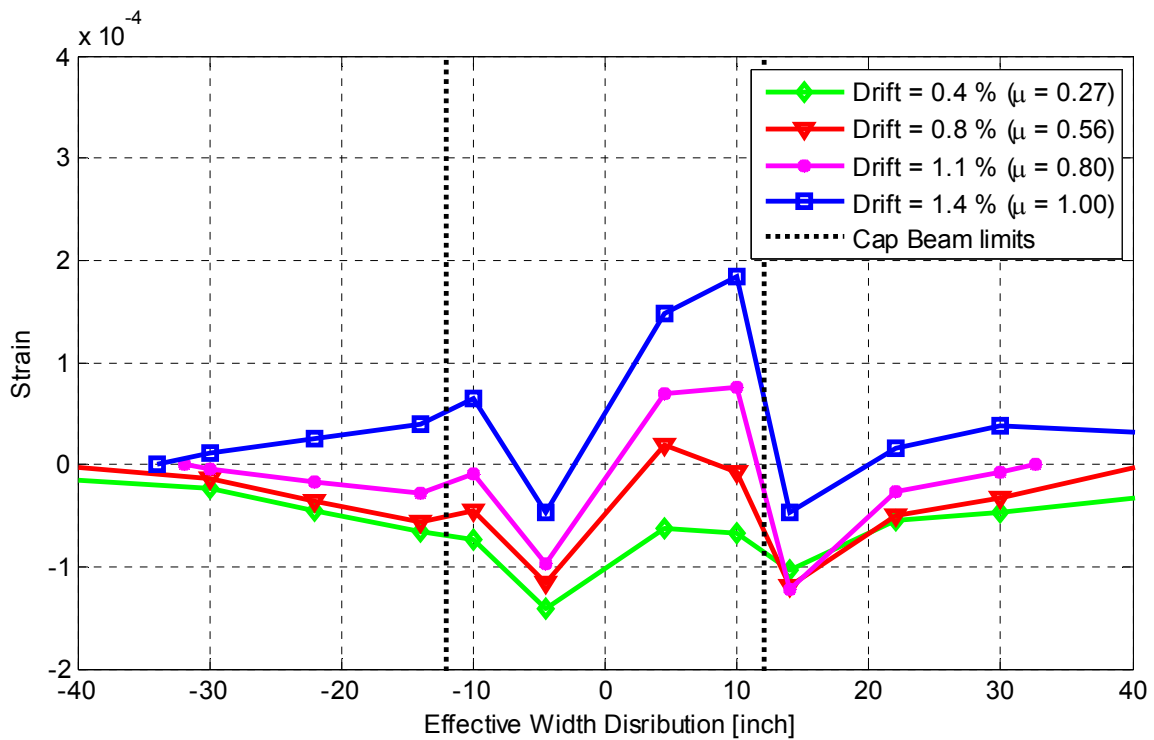
Figure 5.95 Strain distribution along cap beam and box-girder transverse soffit slab reinforcement (compression side) at Section D for different small-level loading cycles (strain values recorded at loading cycle peak when loading is in WEST direction)
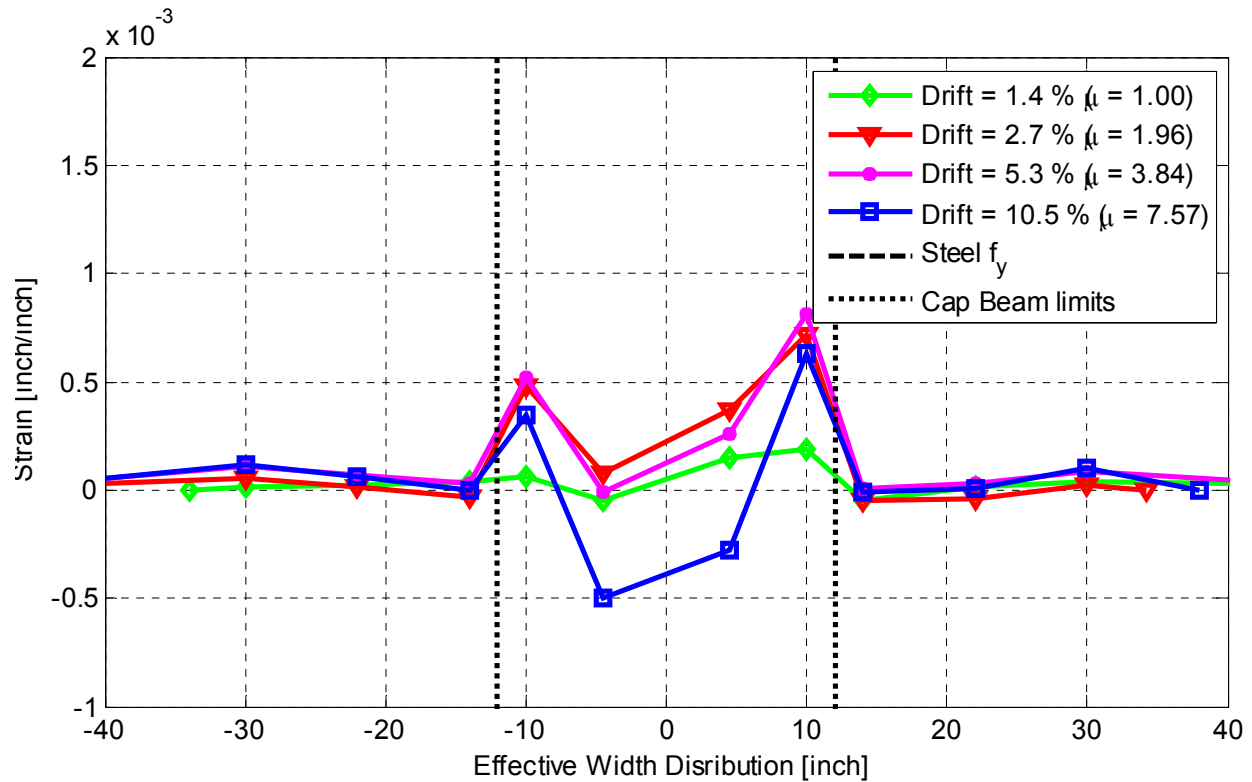
Figure 5.96 Strain distribution along cap beam and box-girder transverse soffit slab reinforcement (compression side) at Section D for different high-level loading cycles (strain values recorded at loading cycle peak when loading is in WEST direction)

5.6.2 Concrete Gage Strain Distribution

The strain distribution in the compression side based on the instrumented compression steel rebars was not conclusive. It did not allow estimating an effective slab width at the compression side as in the case of the tension side because the measurements were sensitive to the concentrated gravity load. The concrete gages measurements were even noisier and more sensitive to the concentrated load. A reasonable strain distribution was not possible to obtain from the embedded concrete gages. Figure 5.97 shows a sample of four embedded concrete gages stain history at section B during all the loading cycles. It is obvious from the figure that the concrete gage reading are noisy and could not accurately capture the different loading cycles and reversals. As a result of the unreliable data obtained from the embedded concrete gages, a different type of gages was used for the second phase of testing that involved HS testing of the retrofitted specimen SP2. This included the use of surface concrete gages that did not need to be installed during the construction as the embedded concrete gages. Instead, surface concrete gages were attached directly to the surface of the concrete from the soffit slab side where compression is expected. A discussion of the surface concrete gages sample measurements is presented in Chapter 8 together with the HS full test discussion.

212
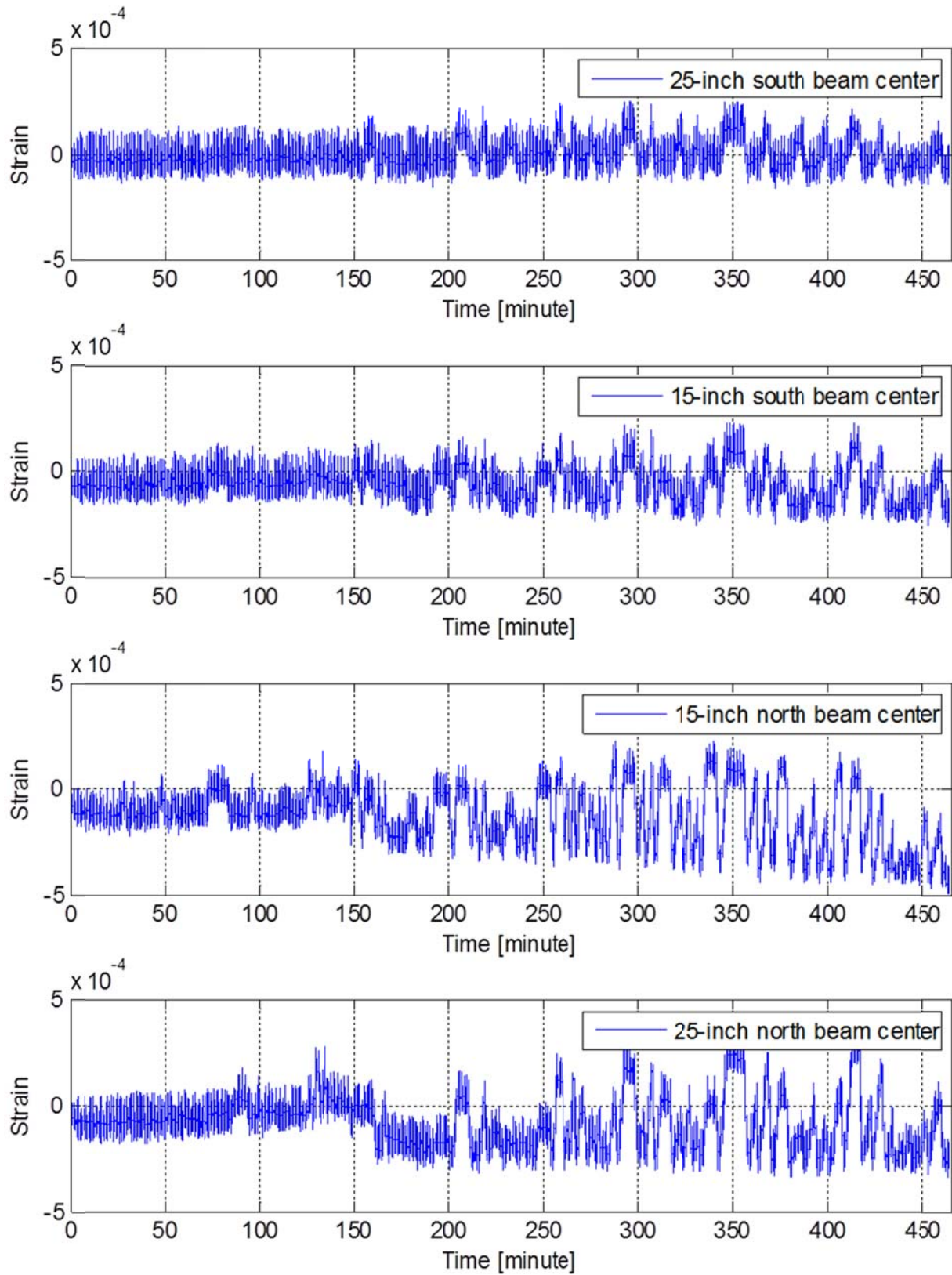
Figure 5.97 Sample of four concrete strain gages history located at the compression zone from both sides of the bent cap beam at Section B

213

5.7   OTHER RESPONSE QUANTITIES

The main focus of the experimental program was the bent cap beam behavior, the box-girder contribution, and overall system response to combined gravity and bidirectional lateral loading. Complimentary response quantities from the box-girder longitudinal rebars and various transverse shear reinforcement that support the experimental test observations are presented here.

5.7.1   Longitudinal Slab Strain

The as-built SP1 cyclic loading tests involved bidirectional lateral loading in both of the transverse and longitudinal directions. Loading in the longitudinal direction caused flexural bending in the box-girder. The strain values in the longitudinal box-girder reinforcing steel were monitored and observed to make sure that the box-girder remained essentially elastic as required for all superstructure components by the Caltrans SDC. Figure 5.98 shows the strain history at two sections in the box-girder deck slab in a longitudinal rebar, which was almost aligned with the box-girder center line, just at the two sides of the bent cap beam where maximum moments were expected. Moreover, Figure 5.99 shows the strain history at similar sections but in a different rebar that was aligned with one of the box-girder webs. Both figures show that the yielding strain of 0.0026 observed from material tests, Chapter 3, was not reached in the longitudinal box-girder rebars. Accordingly, it is safe to conclude that the box-girder remained elastic during the testing as no yielding was observed. It is worth noting that these strain values were recorded at the NEFF data acquisition system, which did not record the application of gravity load or the pausing times. Thus, a shorter total testing time is recorded versus the PI data acquisition responses.
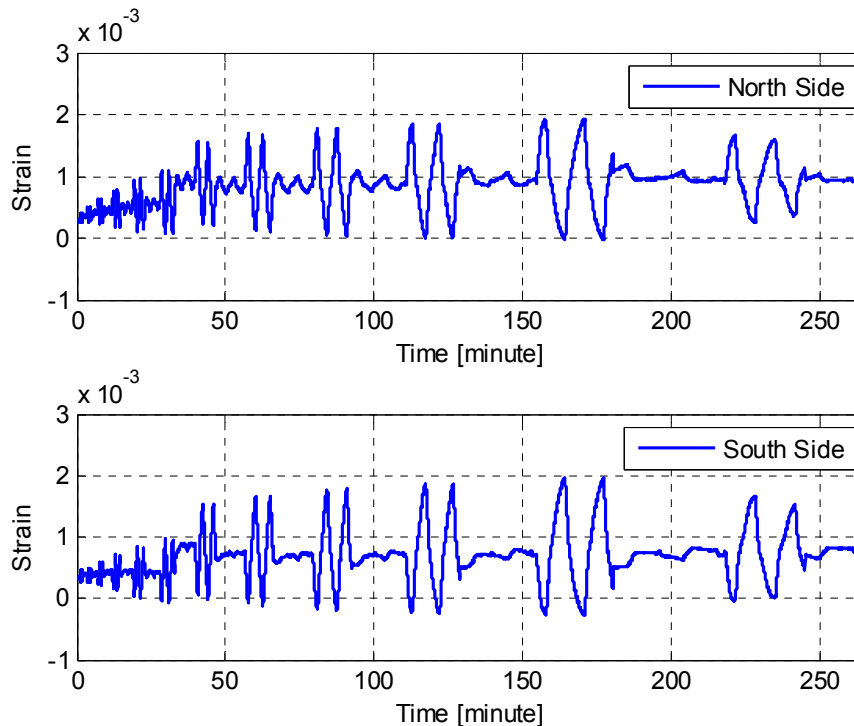
Figure 5.98 History of box-girder deck longitudinal reinforcement strain measured in the rebar at the middle of the box-girder at north and south sides of the column for all cycles

214
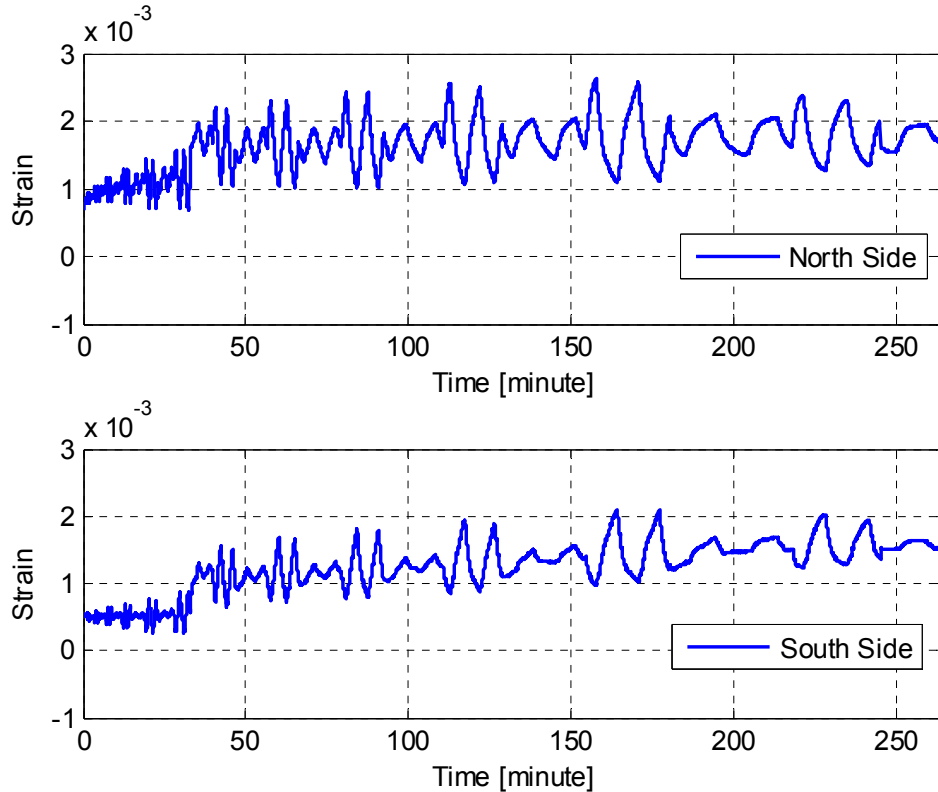
Figure 5.99 History of box-girder deck longitudinal reinforcement strain measured in a rebar aligned with a box-girder web at north and south sides of the column for all cycles

5.7.2 Box-Girder Web Tie Strain

In addition to monitoring the longitudinal rebars strain in the box-girder, the web tie (transverse) reinforcement strain was monitored as well. The strain at the most critical sections was observed to make sure that no shear yielding took place in any of the box-girder webs. The strains in the ties where the maximum shear forces were expected right at the two sides of the column, i.e. North and South sides of the column, are plotted in Figure 5.100 and Figure 5.101 for an inner and outer box-girder webs, respectively. None of the monitored box-girder webs shear strain exceeded the 0.0026 yield limit of the reinforcement as expected from the design. It is worth noting that the capacity design is extended to cover the shear checks for all superstructure components (Caltrans SDC 2013) in addition to the strength check against the column overstrength moments.

5.7.3 Joint Reinforcement Strain

The joint region is one of the most critical regions in the bridge superstructure that has to remain essentially elastic in case of extreme events from earthquakes. A brittle shear failure is not allowed by the Caltrans SDC seismic capacity design approach. It was visually observed that only minor cracks were developed in the specimen joint region during as-built SP1 cyclic tests as previously discussed. However, the strains in critical horizontal and vertical joint tie reinforcement were observed to make sure no yielding took place as shown in Figure 5.102.

215
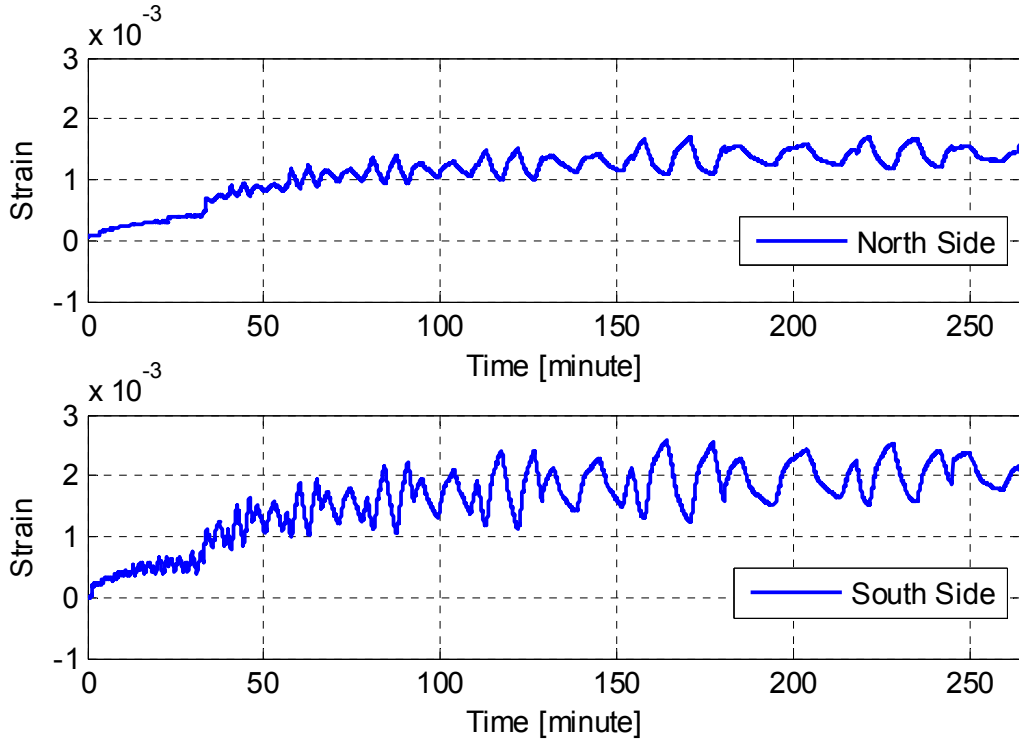
Figure 5.100 History of box-girder web tie reinforcement strain measured at the first tie in an inner web from both the north and south sides of the column for all cycles
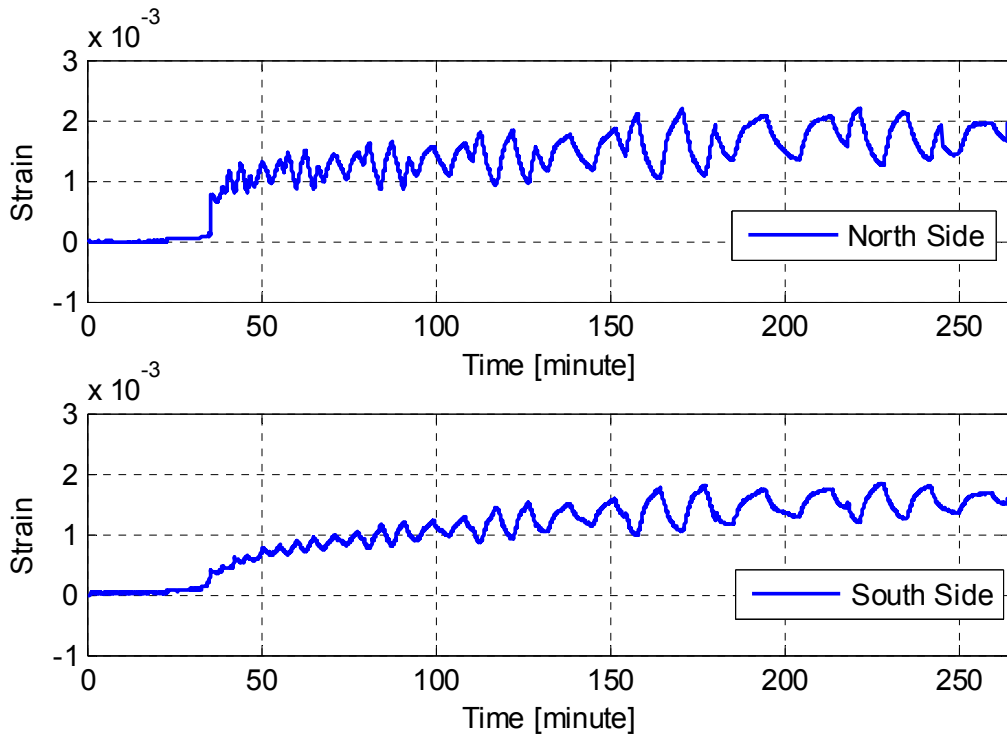
Figure 5.101 History of box-girder web tie reinforcement strain measured at the first tie in an outer web from both the north and south sides of the column for all cycles
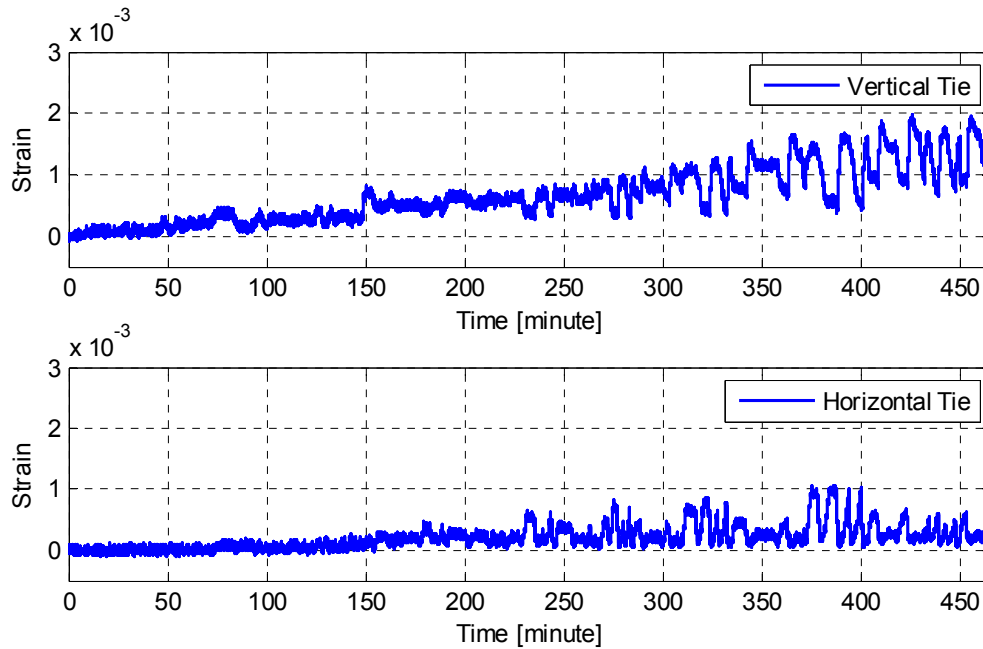
Figure 5.102 Strain history of selected critical joint vertical and horizontal cross-ties

5.7.4 Cap Beam Stirrups Strain

Shear failure is not allowed in the bent cap beam. For the test specimen's relatively wide cap beam, four-branch stirrups were used for transverse shear reinforcement. The strain monitored in the inner branches and the outer branches of one of the stirrups at maximum expected shear force location did not reach yield as shown in Figure 5.103. Thus, it is concluded that all the shear reinforcement in the tested SP1 did not yield and no brittle shear failure took place as observed.
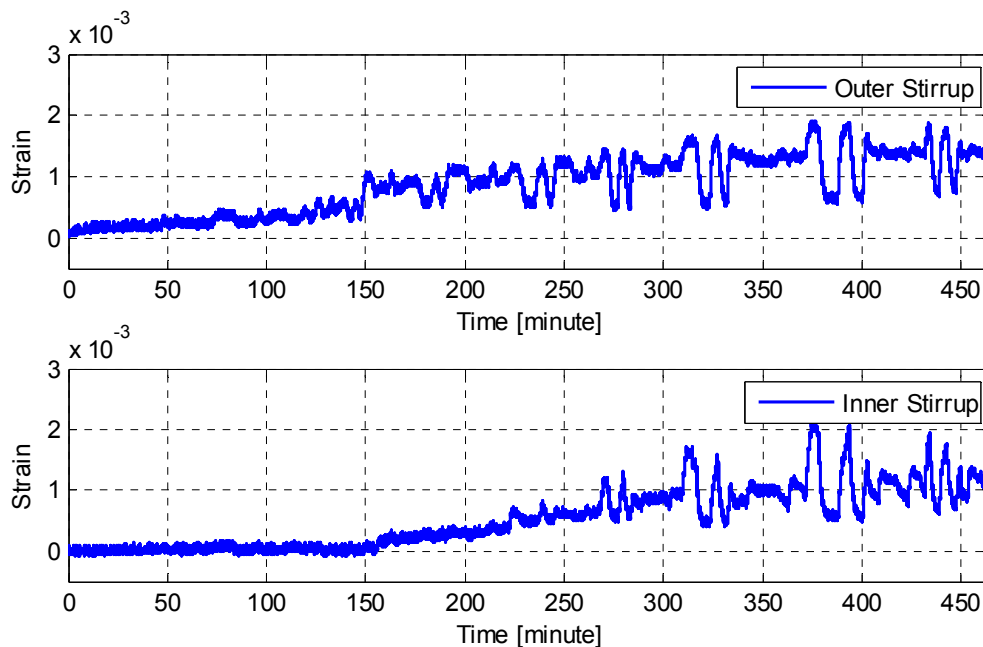
Figure 5.103 Strain history of selected bent cap outer and inner transverse stirrups

217

6 Quasi-Static Testing: Repaired Specimen One

The first specimen (SP1) was tested as-built in a quasi-static cyclic loading test as extensively discussed in Chapter 5. Next, SP1 was repaired and tested twice. The first set of tests on the repaired SP1 is a quasi-static cyclic loading test similar to the as-built set of tests. The objective of such repaired specimen cyclic loading tests was to check the repaired column capacity and verify whether the cap beam remained essentially elastic as required by the Caltrans SDC (2013). That is because the main goal of the repair was conducting HS trials to validate the developed new HS communication system rather than pursuing a full repair or retrofit to restore the full capacity of the system. Thus, the HS trials comprised the second set of tests that utilized the repaired SP1. Only the first set of tests is presented here while the HS trial tests are discussed in Chapter 7 next. In this chapter, brief discussions of the undertaken rapid repair procedure and key results from the cyclic loading tests of the repaired SP1 are presented. The results are compared against the original as-built test for insight regarding the effectiveness of the repair.

6.1 REPAIR PROCEDURE

The repair of the already tested SP1 focused only on the damaged column, and particularly, the plastic hinge region that experienced extensive concrete spalling, reinforcing steel buckling, and several bar ruptures. The repair involved replacing the damaged concrete regions with high-strength mortar, injecting all cracks with high-strength epoxy, adding few polymer reinforcing bars next to the ruptured original reinforcing steel bars, and wrapping the column with three layers of unidirectional Carbon Fiber Reinforced Polymer (CFRP) layers. All the material properties for the different materials used in the repair that were provided by the repair company were discussed in Chapter 3. More details of the step-by-step repair procedure are presented along with several illustrative photographs.

The first step required cleaning and removing all loose concrete chunks using hammering as shown in Figure 6.1. The prepared clean plastic hinge region is shown also in the same figure. A drilling machine was used to drill holes along the cracks lines at adequate spacing carefully in the cracked regions to be used for epoxy injection. The drilling procedure and final holes pattern viewed from the east side of the column are shown in Figure 6.2. Figure 6.3(a) shows all the drilled holes occupied with plastic injection ports and the application of a sealant layer of epoxy that covered the cracked zones and around the injection ports to avoid any epoxy leakage during injection. The exposed parts of the reinforcing bars were cleaned from any dust from the drilling process or concrete small portions using a wire brush. A special type of epoxy for bonding and corrosion protection (BC-020) was used to cover the rebars to enhance the bond with other repair materials. The final prepared reinforcing bars are shown in Figure 6.3(b). Subsequently, high-

strength mortar was used to patch and fill the large voids (wider than 0.75 inch) and cover all the exposed rebars, Figure 6.4(a).

In a typical repair job that follows extensive rebars buckling and rupture, the column cross-section is usually increased and new reinforcing steel dowels are implanted. However, in this part of the study, no new steel rebars were implanted in order not to alter the bent cap or the cap-column joint region, especially in a reduced-scaled test specimen. That is mainly to check whether cap beam is essentially elastic in its actual condition after the as-built test. Moreover, a partial repair was more feasible to obtain a reasonable enough force capacity for the HS test trials. Accordingly, the repair was limited to restore the original 18-inch column diameter and a rapid fabricated in-site form of polymer reinforcing bars were used as part of the repair. Eight of these polymer reinforcing bars were used and placed next to the ruptured steel rebars. For this purpose, vertical holes that are 8-inch deep were drilled for installing in the desired polymer reinforcing bars as shown in Figure 6.4(b).

| (a) | (b) |
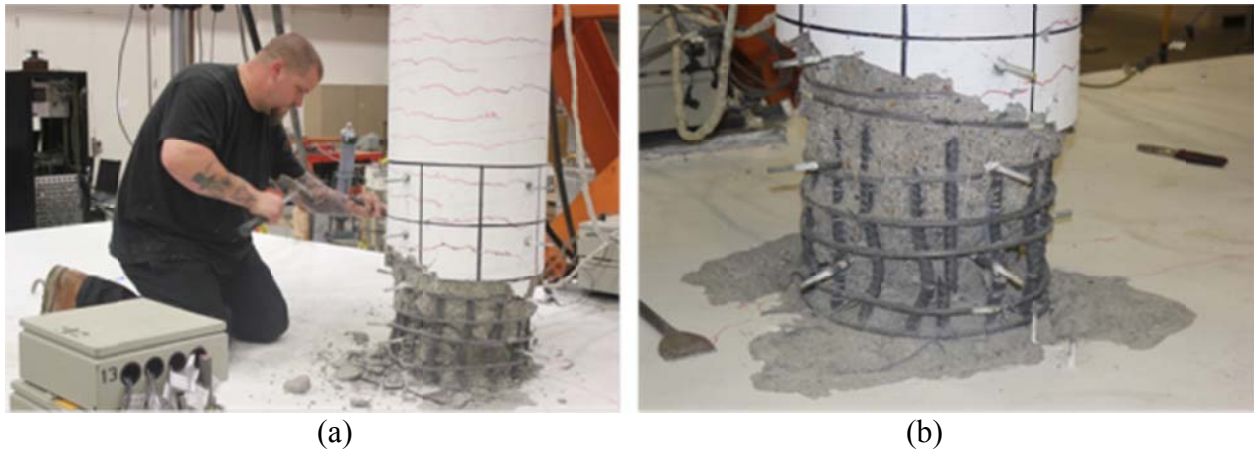
Figure 6.1 (a) Hammering loose concrete in the plastic hinge zone in the tested specimen; (b) final damaged state of the tested specimen after removal of all loose concrete chunks

| (a) | (b) |

Figure 6.2 (a) Drilling holes along the cracks for epoxy injection; (b) final holes pattern for cracks injection

(a)

(b)

Figure 6.3 (a) Installing the injection ports along the cracks and patching the concrete surface around the ports; (b) exposed rebars coated with epoxy primer for better bond

(a)

(b)

Figure 6.4 (a) Patching the column damaged core with high-strength mortar in the plastic hinge zone; (b) 8-inch deep vertical holes to add polymer reinforcing bars

A typical polymer reinforcing bar used in the repair procedure applied in this study consisted of a 20-inch long strip of the unidirectional carbon fiber sheets that was rolled longitudinally and soaked with epoxy resin, Figure 6.5(a). The drilled vertical holes were filled with the same epoxy used in soaking the polymer rolled bars before the wet polymer bars were inserted as in Figure 6.5(b). It is worth noting that the polymer bars gain their longitudinal tensile strength when they dry. The step that followed installing the CFRP bars was fixing the column-bent cap interface. This region had to undergo additional damage and cracking as the vertical holes were drilled. A mixed sand-epoxy paste was used to fill all the voids and restore a flat bent cap top surface around the column undergoing the repair as shown in Figure 6.6. After all major voids were patched and the CFRP bars were installed, only a final layer of sand-epoxy mixture was needed to compensate for all the lost concrete cover, and more importantly, restore the column circular shape to facilitate the application of the CFRP jacket. A sonotube formwork was assembled around the column to restore the 18-inch circular column diameter as shown in Figure 6.7(a). Before any paste was poured inside the sonotube formwork, the injection ports were connected to the epoxy pump to proceed with cracks injection. A fluid RN151 structural epoxy was injected in all cracks through multi-port injection system, Figure 6.7(b), and with a relatively low pressure to prevent cracks widening or any further damage to the cracked concrete.

(a)　　　　　　　　　　　　　　　　　(b)

Figure 6.5 (a) Preparation of 20-inch long CFRP bars using carbon fiber sheets coated with epoxy resin; (b) installing the wet CFRP bars in the holes drilled into the cap beam

(a)　　　　　　　　　　　　　　　　　(b)
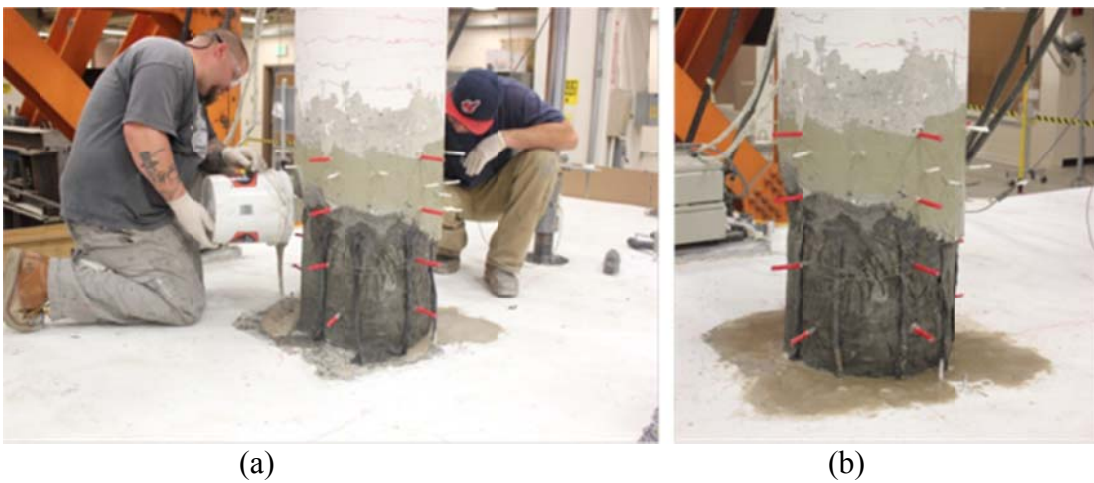
Figure 6.6 Partially fixing the column-bent cap interface using a sand-epoxy mixture; (b) overview of the partial repaired column after installing all injection ports, CFRP reinforcing bars, and patching the damaged parts in column core and at the column-bent cap interface

(a)　　　　　　　　　　　　　　　　　(b)

Figure 6.7 (a) Installing sonotube around the damaged zone to restore the column's circular shape; (b) injecting fluid epoxy into the cracks using the installed injection ports

The next step after injecting all cracks, installing the added CFRP bars, and patching all damaged parts was to prepare the column for the CFRP wrapping. A sand-epoxy mixture that is similar to the one used for fixing the column-bent cap interface was poured inside the sonotube formwork, Figure 6.8(a). One day later the formwork was removed and all the injection ports that were still in place were removed and the surface was grinded. A view of the column after the sonotube removal and grinding the surface is shown in Figure 6.8(b). It is to be noted that the rods sticking out of the column in Figure 6.8 are the instrumentation rods that were used for installing the LVDTs and are not any remaining injection ports. Figure 6.8(b) also shows that some voids remained as the poured sand-epoxy did not fill all the voids. Therefore, a final layer of the high-strength mortar, previously used in patching the column core damaged parts, was applied to fill any remaining voids and finalize the circular column restoration for efficient CFRP wrapping, Figure 6.9(a). The final surface was then cleaned of any dust or debris and one coat of RN075 primer was applied to the surface as seen in Figure 6.9(b). Finally, a total of three layers of FC061 unidirectional carbon fiber sheets were impregnated with RN075 structural epoxy system to form the column CFRP jacket. Each layer was 0.04-inch thick, i.e. three layers comprised a jacket that is 0.12-inch thick, and the jacket was extended up to the column's mid-height. Installing the first layer of the wet carbon fiber sheets at the column lower section and installing the last layer at the column middle section are shown in Figure 6.10(a) and (b), respectively. Figure 6.11 shows the final repaired column after all CFRP layers were installed.

(a) (b)

Figure 6.8 (a) Pouring sand-epoxy mixture inside the sonotube formwork to restore the column shape; (b) view of the partially repaired column after the sonotube was removed

(a) (b)

Figure 6.9 (a) A final layer of high strength mortar was applied to patch any remaining voids; (b) applying a primer epoxy coat to the surface before applying the CFRP sheets

(a)   (b)
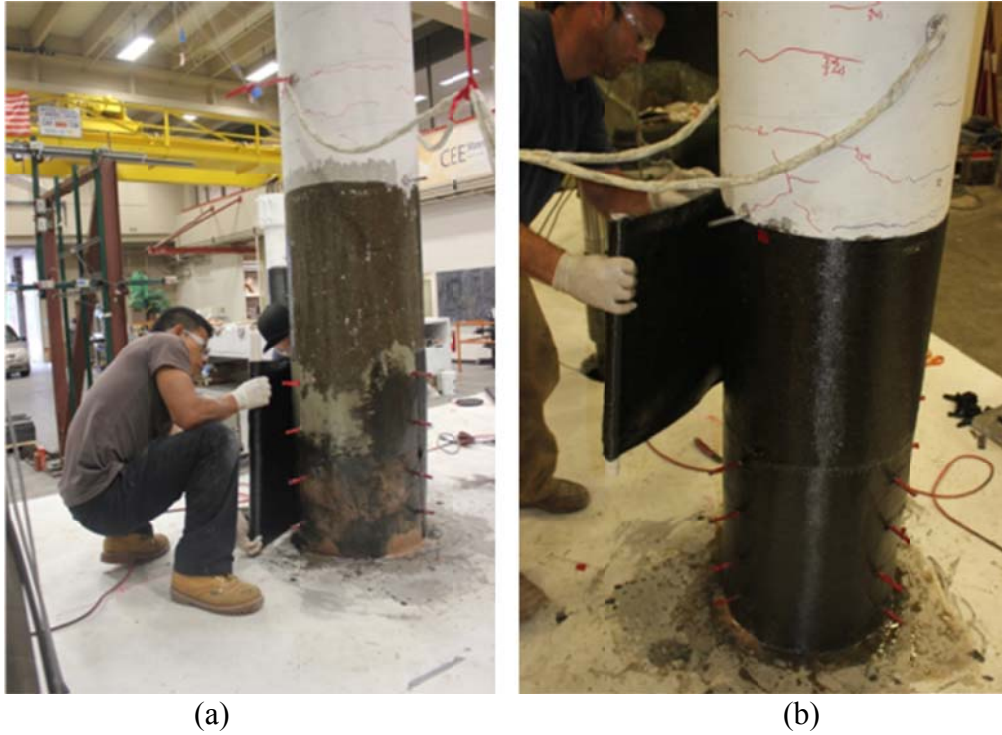
Figure 6.10 (a) Applying the first epoxy-coated CFRP layer at the bottom section of the column; (b) applying the last CFRP layer at the middle section of the column

Figure 6.11 Final repaired column after it was wrapped by three CFRP layers

6.2 PROGRESSION OF TESTING AND DAMAGE

The first set of tests that used the repaired SP1 was a replica of the previously conducted cyclic test of the original as-built specimen. The only difference is that the cyclic loading tests of the repaired specimen stopped at the 5.44-ductility level to maintain minimal force capacity for further HS trial tests and meanwhile have enough cycles at various ductility levels to compare the repaired specimen behavior to the as-built one. The same setup was used and a view of the test while transverse and longitudinal loadings were in progress are shown in Figure 6.12 and Figure 6.13, respectively.

Unlike the original unconfined specimen, no concrete spalling or damage were observed in the repaired specimen tests due to the CFRP jacket confinement. However, popping sounds of steel reinforcing bars rupture were heard during the tests indicating that the already buckled rebars from previous test were ruptured. The ruptured steel rebars explain the significant drop in the force capacity observed in both transverse and longitudinal direction as discussed in the next section. The only visually observed damage was the opening-closing crack at the column-bent cap beam interface as loading progressed. A snap shot of the interface cracking that occurred at the peak of the last loading cycle in the transverse direction, which corresponded to 5.44μ-ductility level, is shown in Figure 6.14.
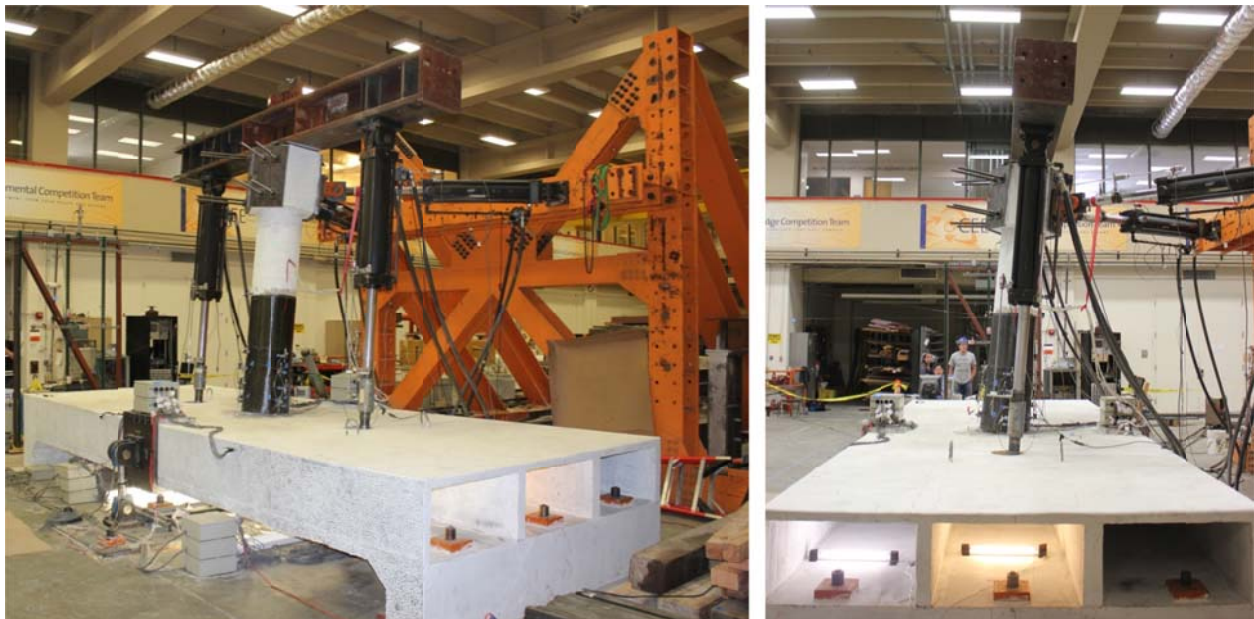
Figure 6.12 Overview of repaired SP1 cyclic loading test setup when loading is in progress and applied in transverse direction

Figure 6.13 Overview of repaired SP1 cyclic loading test setup when loading is in progress and applied in longitudinal direction

Figure 6.14 Circumferencial tear in the CFRP jacket and cracking at the column-bent cap interface as lateral loading progressed

6.3 GLOBAL BEHAVIOR

An extensive framework for post-processing the data acquired from the as-built SP1 cyclic tests was utilized to present the test results and discussion in Chapter 5. For the repaired SP1 tests, only selected results that serve the purpose of comparing the behavior of the repaired and as-built specimen are presented and discussed here. This section presents the global forces and displacements obtained from the repaired specimen tests. The computed stiffness in both transverse and longitudinal directions are also discussed. The column and bent cap beam moment-curvature behavior along with selected results of the CFRP jacket strains are presented in the following sections.

The repaired SP1 cyclic tests were carried out under a single constant gravity load level of 164 kips, which corresponded to 10% of the axial column capacity. It is to be noted that the as-built SP1 tests were conducted under two levels of gravity load but for the repaired specimen testing, only the second level of gravity load was used (10%). The force applied through each of the two vertical actuators along with the total resulting gravity load throughout the full course of the repaired SP1 cyclic tests is shown in Figure 6.15. The total vertical reactions at the two struts at the ends of the bent cap beam as compared to the total gravity load are shown in Figure 6.16. The total reactions at the struts are almost 70% of the total gravity load (115 kips to 164 kips ratio), i.e. the box-girder ends where the specimen was supported on the two cast-in-place beams attracted the remaining 30% of the gravity load. Meanwhile, it is observed that the total reaction at the two struts is almost constant throughout the transverse and longitudinal lateral loading. This confirms that two equal but opposite reactions always existed at the two struts during the lateral transverse loading. Also, no additional reactions were generated during lateral longitudinal loading because the resulting moment is out of the bent cap beam plane and did not generate any vertical reactions at the struts.

To further verify that the intended load pattern was applied correctly, the displacement orbit of all the loading cycles in both transverse and longitudinal directions is shown in Figure 6.17. The cross displacements orbit illustrates that both transverse and longitudinal loadings were applied independently, i.e. one direction at a time. However, at extreme longitudinal displacements, a small transverse displacement was obtained, which can be observed from Figure 6.17, due to the triangular actuator setup flexibility in the longitudinal direction. The displacement history that reflects the FEMA 461 load pattern for all repaired SP1 cyclic tests in transverse and longitudinal directions is shown in Figure 6.18. Only one cycle of loading was applied in the last group of cycles in both transverse and longitudinal directions. The testing was then stopped to avoid extensive damage to the repaired SP1 and maintain a reasonable residual force capacity for the HS trials. The history of the measured forces is shown in Figure 6.19. It is obvious that the force capacity was decreasing significantly as testing proceeded, which could be tied to the popping reinforcing steel rupture noise heard during the test. The test stopped when the residual force capacity was about 10 kips in one side and 20 kips in the other side. This was a reasonable force capacity to preserve for pursuing the HS trials.
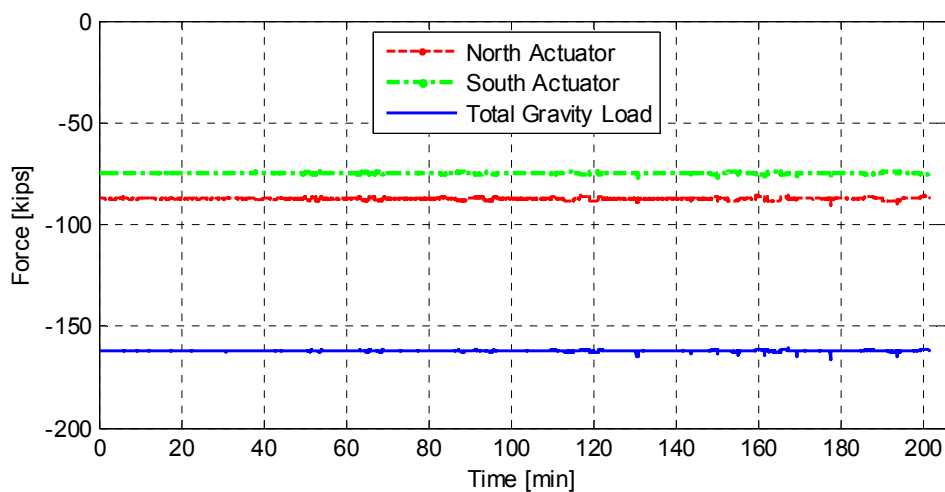
Figure 6.15 Gravity load history at both vertical actuators and total applied gravity load throughout the repaired SP1 transverse and longitudinal cyclic loading tests

226
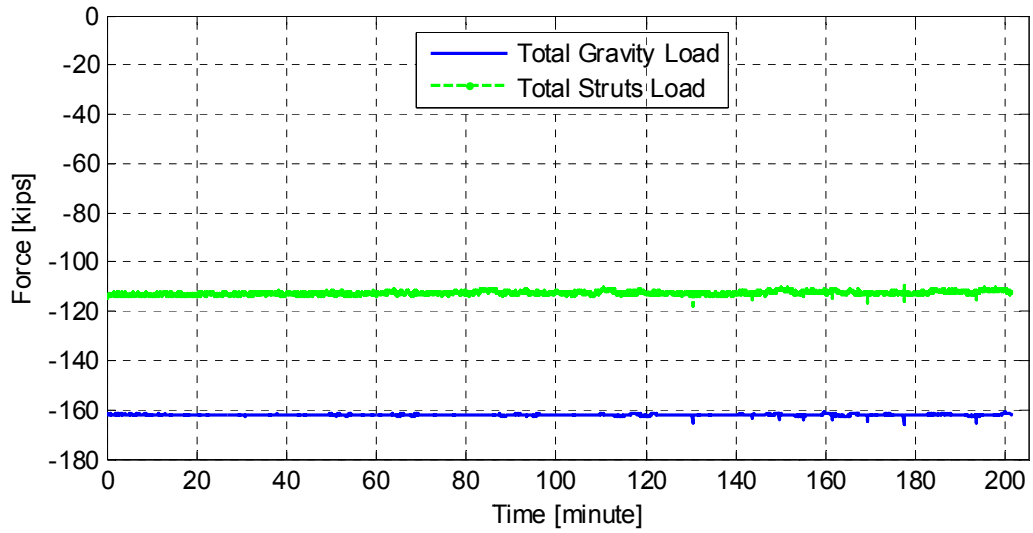
Figure 6.16 Total vertical reaction at the two bent cap end struts versus the total applied gravity load throughout the repaired SP1 transverse and longitudinal cyclic loading tests
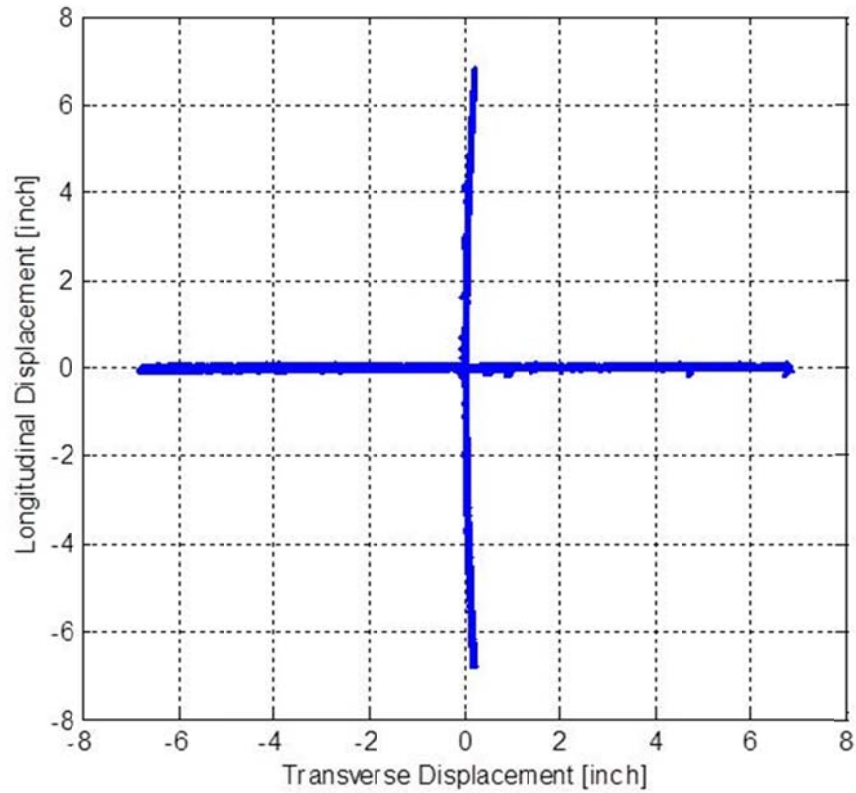
Figure 6.17 Displacement orbit (plan view) of the lateral loading pattern applied to the repaired SP1
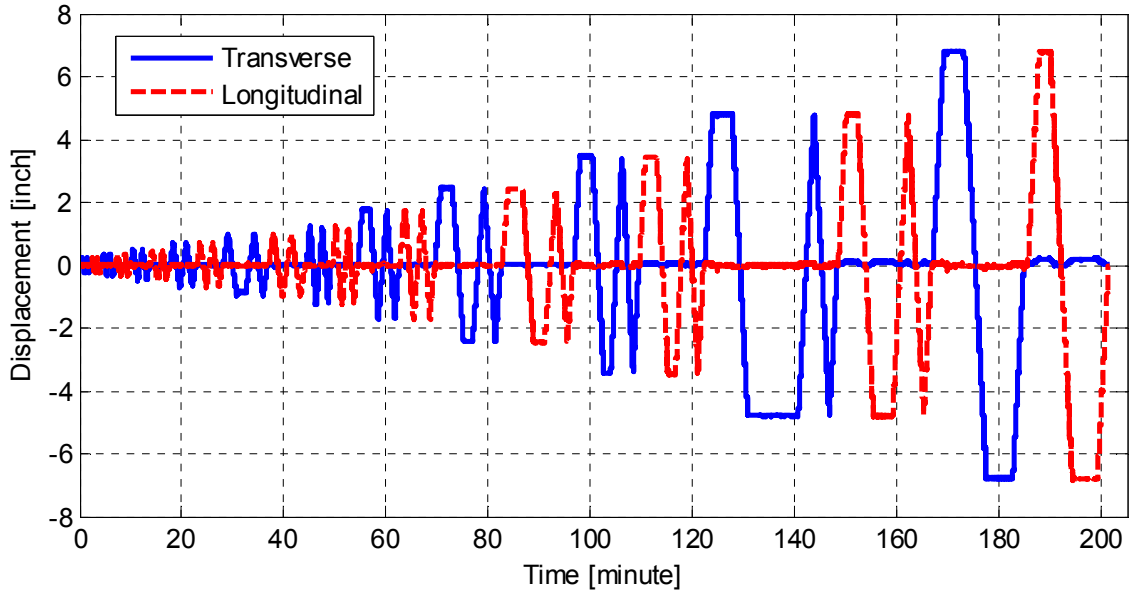
Figure 6.18 Displacement history of the lateral cyclic loading pattern applied during the repaired SP1 tests in transverse and longitudinal directions
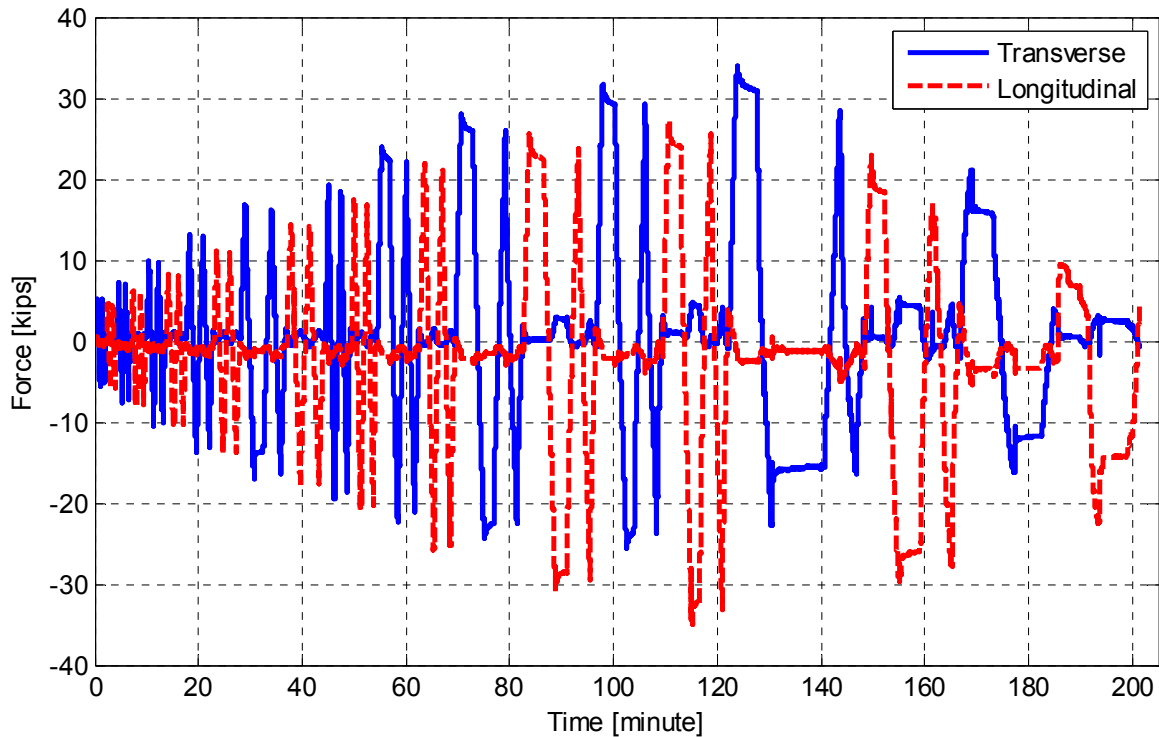
Figure 6.19 Lateral force history measured during testing the repaired SP1 under lateral cyclic loading in transverse and longitudinal directions

To evaluate the effectiveness of the undertaken rapid repair procedure, both as-built and repaired specimen global and local behaviors were compared. For a meaningful comparison, the overall residual force and secant stiffness, obtained from the last loading cycle of the as-built specimen, are compared to the maximum corresponding quantities from the repaired specimen

tests in both transverse and longitudinal directions. That is to explore how the repair scheme enhanced the global behavior from the final state reached after the as-built SP1 tests were concluded. A summary of the as-built and repaired SP1 force and stiffness comparison is shown in Table 6-1. The ratio of the increase in the force capacity and secant stiffness from the final as-built state due to the repair is computed and shown in the table as well. The overall force-displacement relationship for all as-built and repaired SP1 cyclic loading test runs in both transverse and longitudinal directions are compared in Figure 6.20. Meanwhile, the stiffness degradation as loading proceeded in both as-built and repaired SP1 tests is compared as represented by the secant stiffness value against the loading cycle ductility level in both transverse and longitudinal directions in Figure 6.21.

From Table 6-1 and Figure 6.20, it is observed that the repair led to a 22% and 25% increase of the force capacity from the last residual force obtained from the as-built tests when loading progressed in the North longitudinal and West transverse directions, respectively. Meanwhile, the repair did not enhance the force at all or just slightly increased it when the specimen was loaded in the East transverse and South longitudinal directions. This is attributed to the fact that the CFRP reinforcing bars that replaced the ruptured steel reinforcing bars were added mainly in the East and South sides of the column. It is to be noted that when reinforcement is added in one side, e.g. East side, of the column, it enhances the moment capacity when the column is pushed in the opposite side, i.e. West side. The force increase can be attributed also to the confinement effect that helped engage the buckled rebars before they ruptured.

While only a maximum of 25% increase in column capacity was obtained in one side, a significant increase of the stiffness was observed due to the repair. It is expected that the moment of inertia, and in turn, the stiffness of the column should increase because the column full cross-section was restored and well-confined. A huge improvement in the stiffness well above 300% of the final soft state that was reached at the end of the as-built tests is observed from Table 6-1. It is observed from Figure 6.21 that the initial stiffness obtained from the first loading cycle is slightly higher in the transverse direction than the longitudinal direction. This observation is consistent in both as-built and repaired specimen tests. It is noticed also that the final stiffness estimated for the last loading cycle of the repaired specimen tests is lower than what was estimated for the as-built specimen test. This can be tied to the observed crack at the column-bent cap interface, Figure 6.14, that led to this softer behavior at the end of loading.

Table 6-1 Repaired SP1 improved force and stiffness relative to the as-built residuals

Direction of Loading		Force [kips]			Stiffness [kip/inch]		
		As-built Residual	Repair	Increase Ratio [%]	As-built Residual	Repair	Increase Ratio [%]
Transverse	West	-20.68	-25.91	25.3	5	22.3	346.0
	East	33.63	33.58	-0.1			
Longitudinal	South	-25.06	-26.09	4.1	4.8	20	316.7
	North	24.79	30.35	22.4			
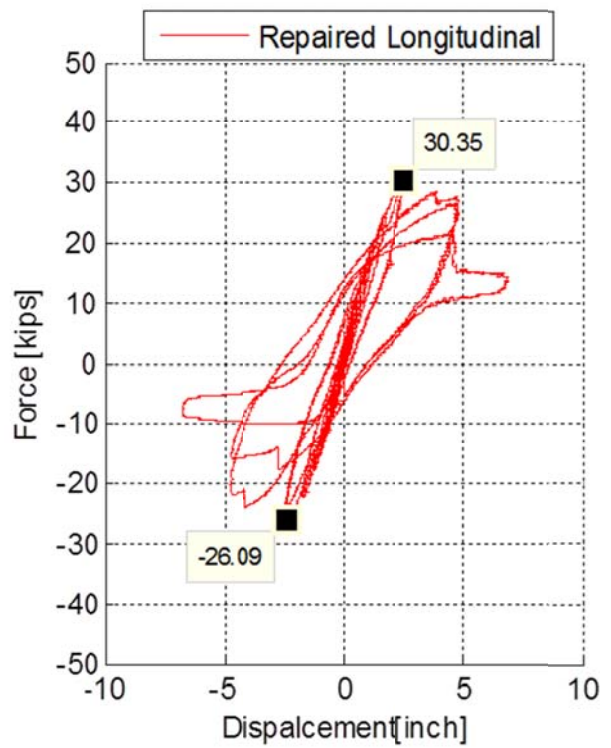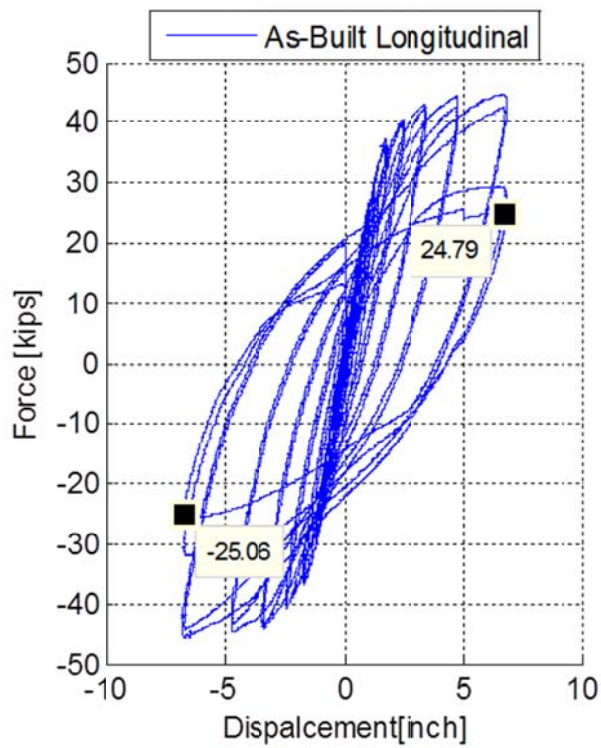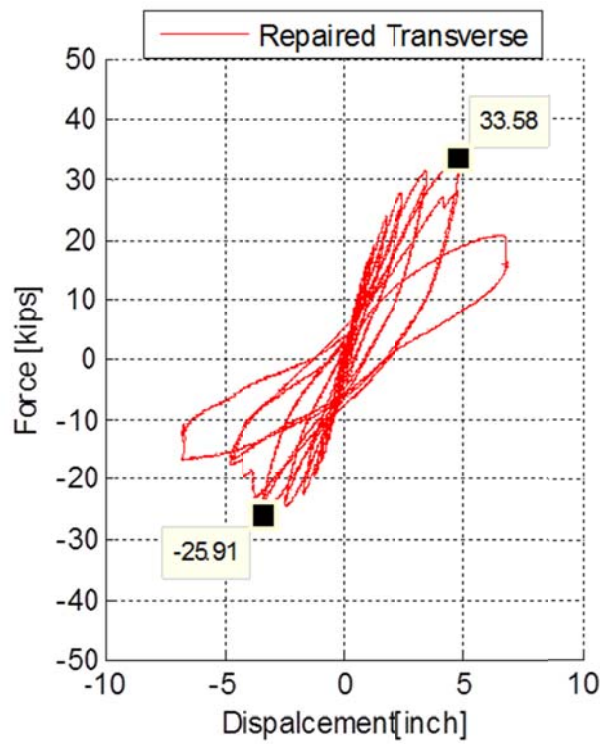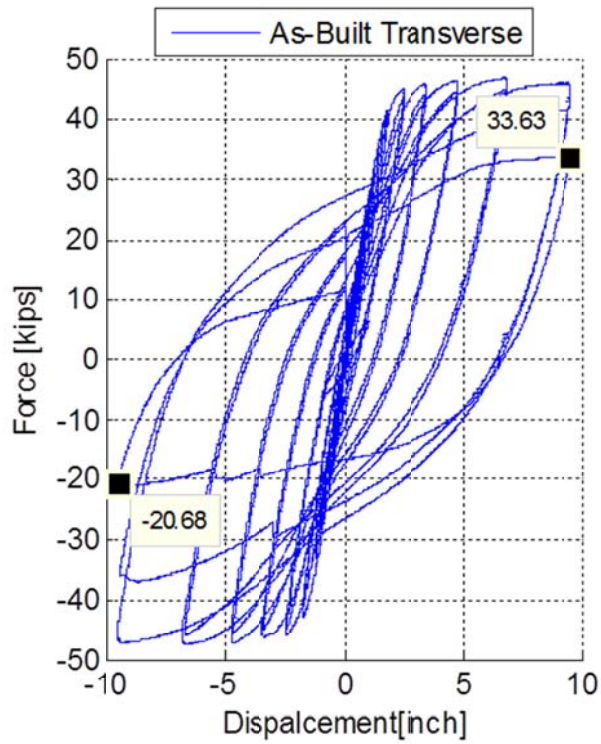
Figure 6.20 Comparison of force-displacement relationships for the as-built and repaired SP1 cyclic loading tests in both transverse and longitudinal directions
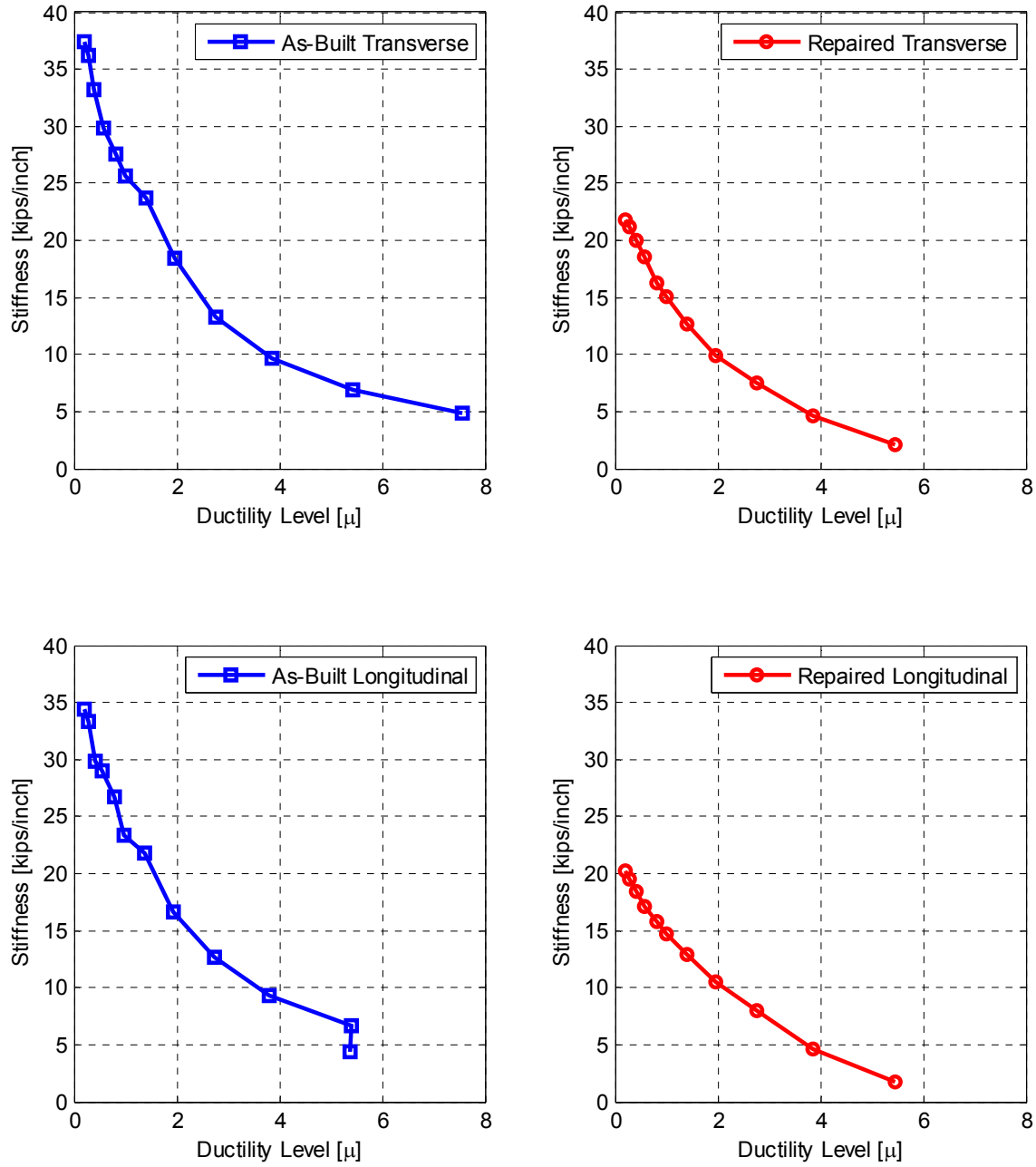
Figure 6.21 Comparison of secant stiffness degradation relative to the ductility levels for the as-built and repaired SP1 cyclic tests in both transverse and longitudinal directions

6.4 COLUMN LOCAL BEHAVIOR

Similar observations can be drawn from the column local behavior as global behavior. That is because the overall column-cap beam-box girder behavior was mainly governed by the column behavior which agrees with the Caltrans SDC seismic capacity design objective. The moment-curvature behavior of the column for the as-built and repaired specimen tests was compared and shown in Figure 6.22. The figure shows that comparable curvature capacity was obtained from the repaired specimen as the as-built test. It is to be noted that the residual moment capacity from the as-built tests were not shown in the figure as only up to the runs that corresponded to correct curvature values were plotted. That is because the last run in both transverse and longitudinal direction of the as-built tests, which were excluded from the plots, experienced extensive spalling and bar ruptures that displaced the LVDTs and led to incorrect curvature estimates. Nevertheless, the increase in the moment capacity is proportional to the increase in the force capacity as previously discussed.

Another aspect of comparing the column behavior is how the moment-curvature distribution varied at different height levels inside or outside the plastic hinge zone. The moment-curvature relationships obtained at 4 different levels are shown in Figure 6.23 and Figure 6.24 for the transverse and longitudinal directions, respectively. The reader is referred to Chapter 3 (particularly Figure 3.51) for more information about the location of curvature measurement levels. It can be noticed from both figures that unlike the as-built case, all the curvatures were concentrated in the repaired specimen tests in level 1, which is the closest to the column-bent cap interface. This implies that in the regular column plastic hinge mode of failure, the damage extends throughout the plastic hinge zone. However, in case of the well-confined repaired specimen column, all the damage was tied to an opening gap and separation that took place at the column-bent cap interface. Thus, the whole repaired column was experiencing a rigid body rotation as illustrated in Figure 6.25. A quick check to verify the rigid column rotation is to compute the rotation at the column's base from the estimated curvature and tie it to the column's top displacement. The rotation of the column in the last transverse loading cycle was found to be 4.2°. The corresponding displacement at the column's point of loading is roughly estimated using the column's height as shown in Figure 6.25. A lateral displacement of 6.59 inch is associated to a 4.2°-rigid column rotation, which is compared against the 6.8 inch actual applied displacement for this loading cycle. The only 3% difference between the actual displacement and that corresponding to a rigid column rotation supports the experimental observation that the well-confined column limits the damage to its interface with the cap beam.

The rigid column rotation observation can be tied to rocking column behavior in other bridge configurations. In this study, the column and bridge superstructure were tested in an inverted position, i.e. all the column damage that was observed would be located at the column top in the correct orientation. Moreover, the specimen's prototype bridge is a three-column bent with pinned pile caps at the supports. Thus, although the column in this study is not a rocking column for the acknowledged reasons, yet useful observations can be extended to rocking columns. In bridge configurations where the pile caps provide full fixation, a CFRP jacket that well-confines the plastic hinge zone of the column at the bottom could promote a rocking column behavior. It is to be noted that most of the recent studies that focused on resilient bridge columns tied the resiliency to the rocking behavior that is achieved using different techniques, e.g. self-centering prestressing, or hybrid fiber RC, or dual shell (Torono et al., 2014 among

others). A CFRP jacket could be another technique to obtain resilient columns that is worth further investigations through future studies.
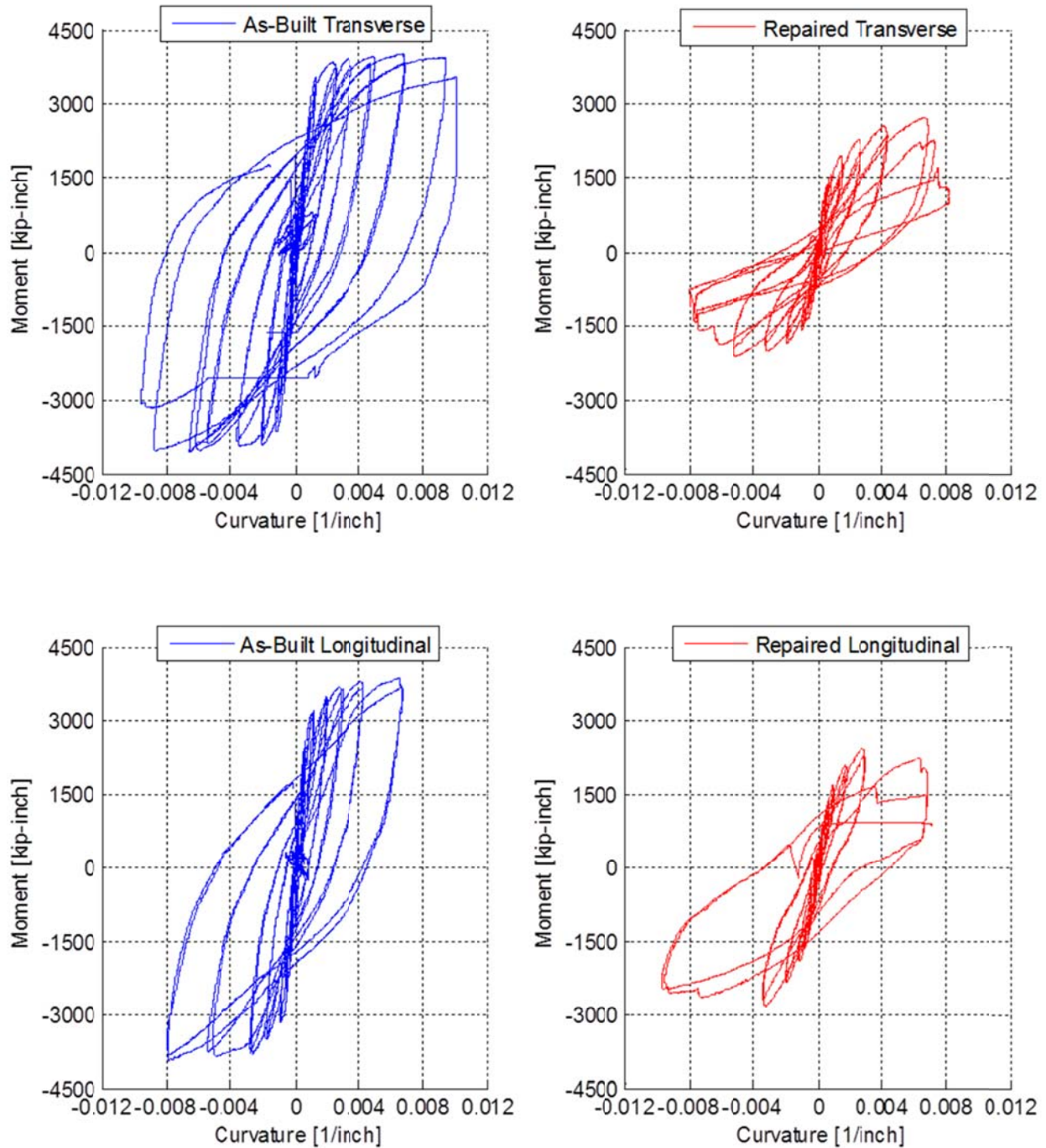
Figure 6.22 Comparison of moment-curvature relationships at the base of the column from the as-built and repaired SP1 cyclic loading tests in transverse and longitudinal directions
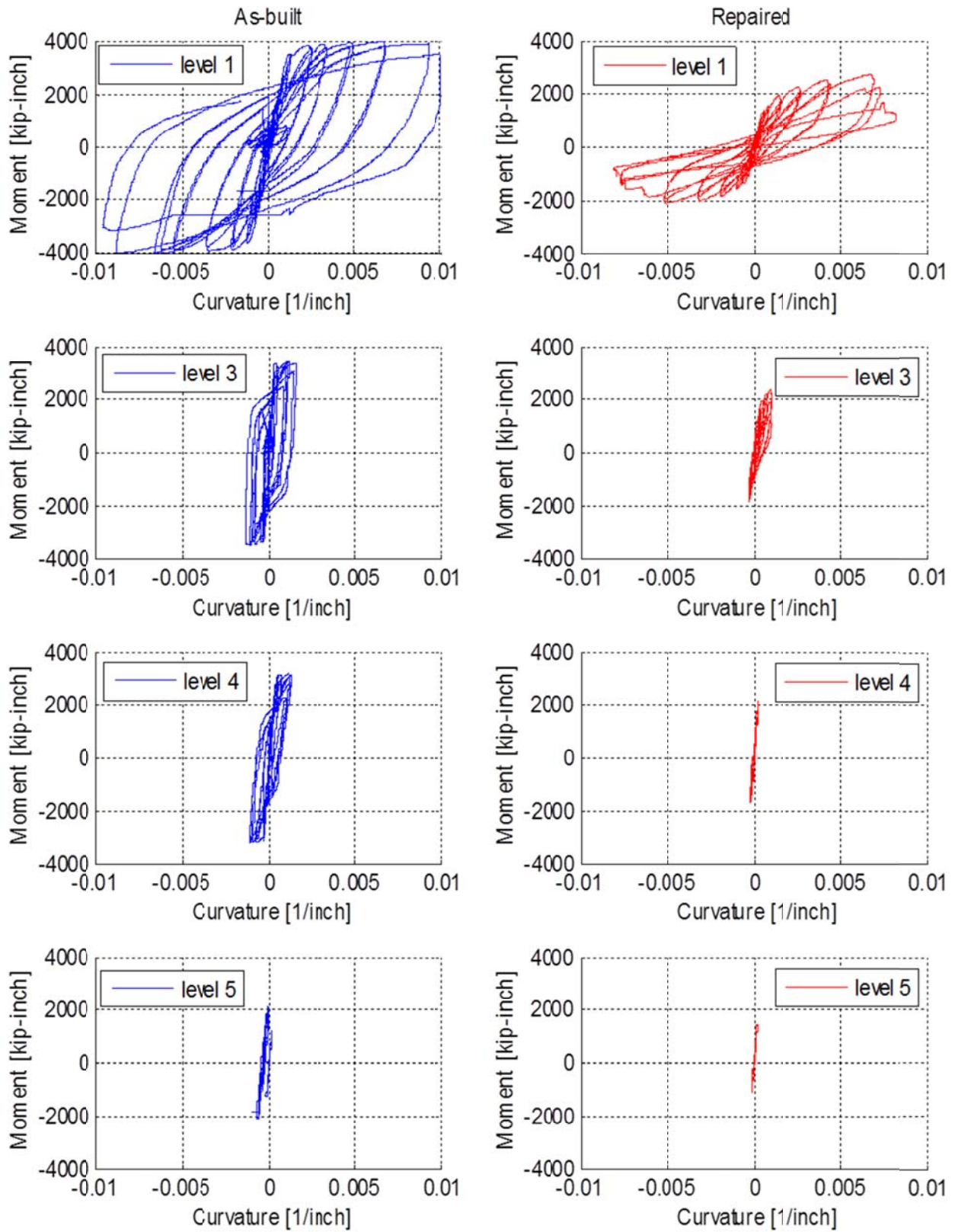
Figure 6.23 Comparison of moment-curvature relationships at different levels of the column from the as-built and repaired SP1 cyclic loading tests in transverse direction

234
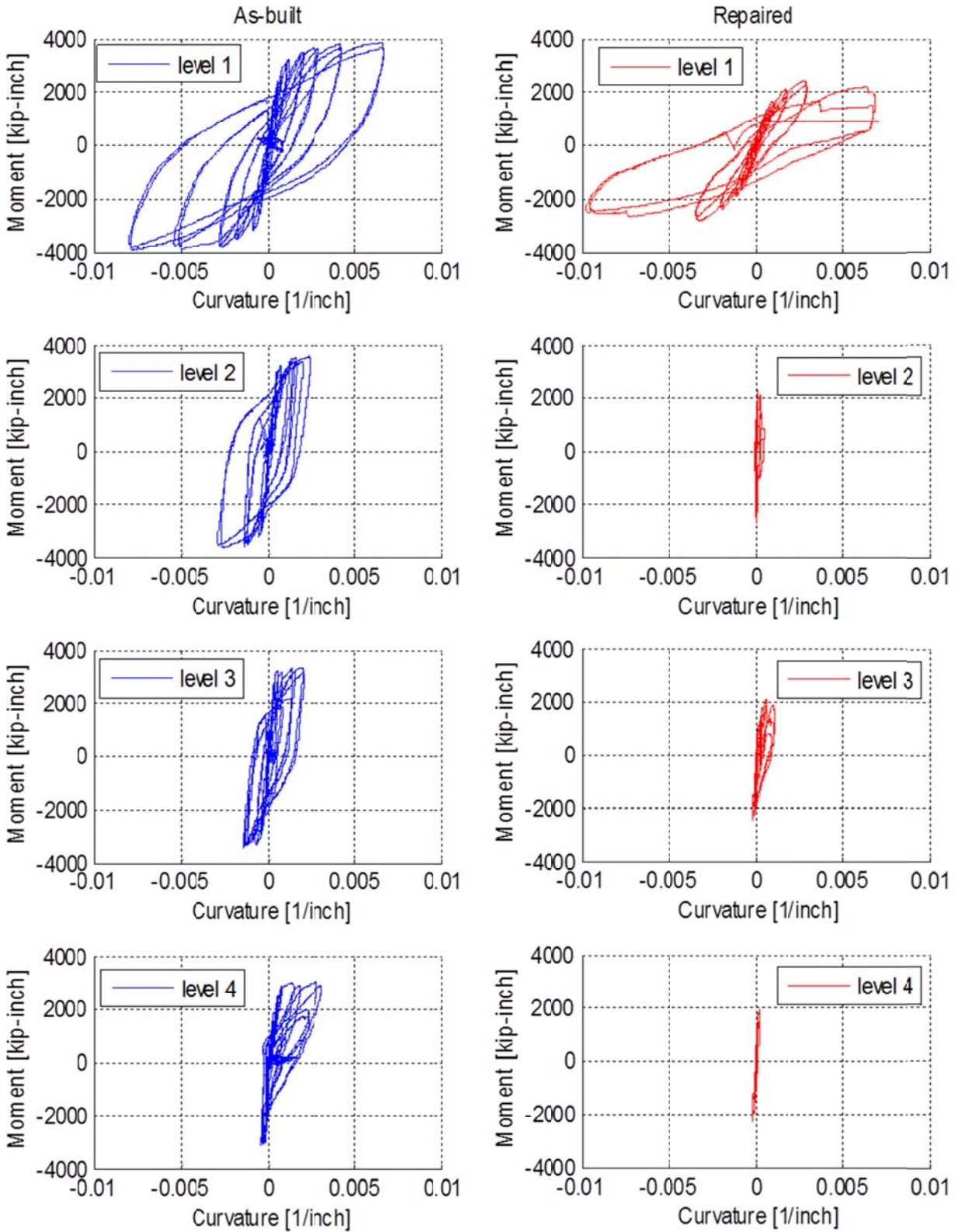
Figure 6.24 Comparison of moment-curvature relationships at different levels of the column from the as-built and repaired SP1 cyclic loading tests in longitudinal direction

235
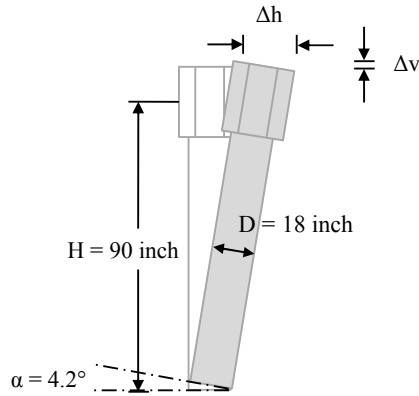
$$\Delta h(\alpha) = H * \sin(\alpha)$$
$$\Delta h(\alpha = 4.2°) = 90 * \sin(4.2°)$$
$$\Delta h(\alpha = 4.2°) = \mathbf{6.59} \text{ inch}$$

$$\Delta v(\alpha) = D * \sin(\alpha)$$
$$\Delta v(\alpha = 4.2°) = 18 * \sin(4.2°)$$
$$\Delta v(\alpha = 4.2°) = \mathbf{1.32} \text{ inch}$$

Figure 6.25 Calculation of the column head displacement for rocking as a rigid body around the base

6.5   CAP BEAM LOCAL BEHAVIOR

One of the main reasons to carry out a set of cyclic loading tests on the repaired SP1 similar to that of the as-built was to verify the essentially elastic cap beam behavior. It has been mentioned several times that a bridge seismic capacity design approach limits all damage to the column and the bent cap beam has to stay essentially elastic. All the test results and discussion in Chapter 5 shows that the as-built specimen behavior complied with the Caltrans SDC requirements. However, it was desired to further involve the bent cap beam in a second set of cyclic loading to verify whether it is still elastic after all the extensive yielding observed from the as-built tests. The reactions observed at the beam end struts were used to calculate the cap beam moments, while the strains measured in the cap beam top and bottom reinforcement were used to estimate the curvature. To verify that the moment values are correct, moment equilibrium at the column-bent cap joint due to lateral loading only was sought. The total cap beam moment from both sides of the joint along with box-girder torsion due to lateral transverse loading should sum up to the column moment. From pre-test analysis, the component from the box-girder torsion, especially for the case of extensively cracked section, is negligible. Thus, the total cap moment should be approximately the same as the column moment, which is verified in Figure 6.26 for the repaired SP1 and similar to Figure 5.62 for the as-built SP1. The two individual components that contributed to the total bent cap beam moment, namely the moment at sections B and D, are shown in Figure 6.27.

The obtained cap beam moments from the repaired specimen tests were also compared with the as-built to verify the essentially-elastic state of the bent cap beam. The moment history for the cap beam at section B is shown in Figure 6.28 for both as-built and repaired SP1 cases. Furthermore, the criterion used to judge whether the cap beam is elastic or not is the moment-curvature relationship at different loading levels and reversals. The moment-curvature relationships for the as-built and repaired SP1 tests are compared at both sections B and D in Figure 6.29 and Figure 6.30, respectively. The residual strains from the as-built test were not picked up again at the start of the repaired specimen tests due to possible load relaxation and instrumentation and data acquisition reset. Thus, the curvature values that were estimated from the strains were set to zero as starting point of the repaired specimen tests' plots in Figure 6.29 and Figure 6.30. However, this should not change the way those plots are interpreted because the

main objective was to see how the moment-curvature approximately relate as loading progressed and its direction reversed. From the figures, it is shown that the cap beam in the repaired specimen tests showed linear elastic behavior at all loading cycles and reversals in both transverse and longitudinal loading directions. Also it is noted that the cap beam experienced less moment demands during the repaired specimen tests and did not reach the yielding moment value. Sample plots of the instrumented bent cap beam reinforcing steel bars strain history at sections B and D are presented in Figure 6.31 and Figure 6.32, respectively. Given a yielding strain value of 0.0026 (=2600 µstrain), it is noted from the Figure 6.31 and Figure 6.32 that the cap beam rebars either slightly yielded or did not yield at all. Although the cap beam extensively yielded during the as-built specimen tests, it did not yield at all in the repaired specimen tests due to the reduced demand. Therefore, the behavior of the bent cap beam that was observed in the as-built specimen testing is experimentally verified to be essentially elastic because the cap beam did not yield or show any plastic or residual strain when it was retested through the repaired specimen tests.
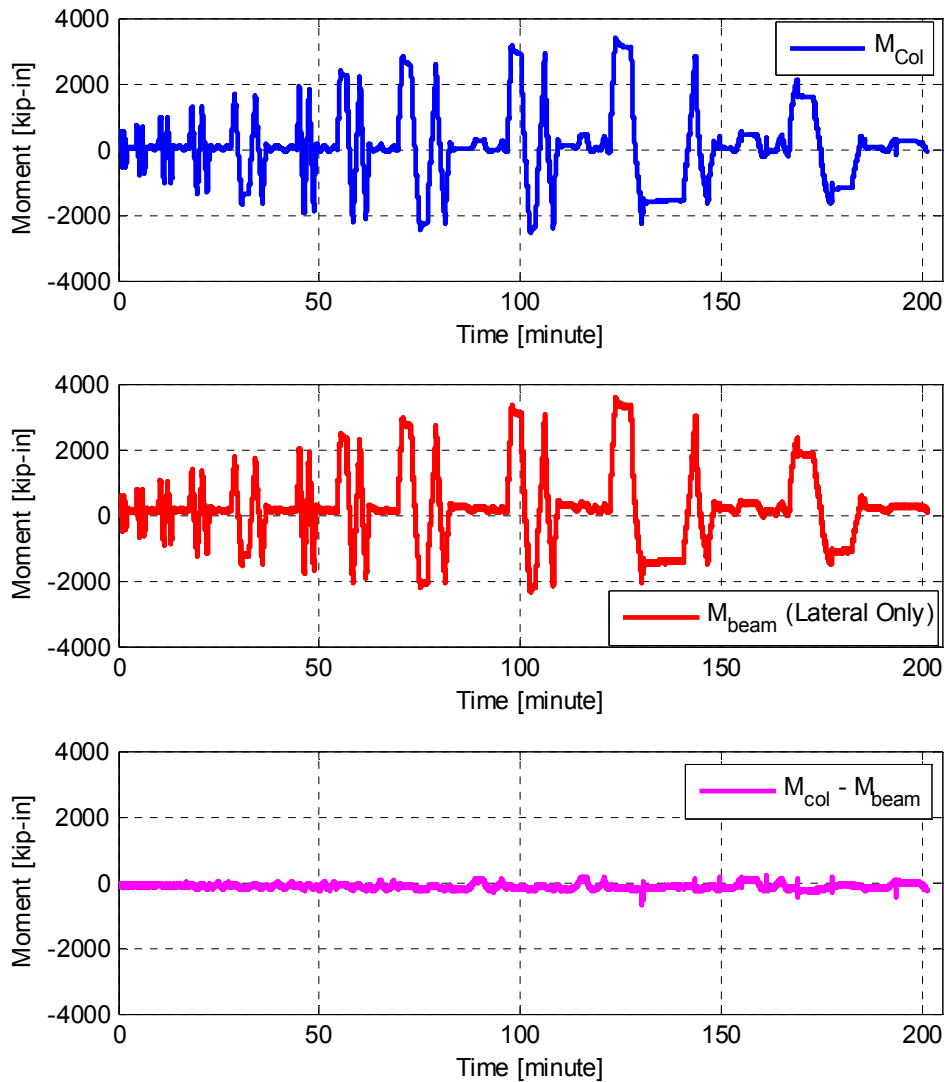
Figure 6.26 Column and total bent cap beam moment history for all repaired SP1 cyclic loading tests in both transverse and longitudinal directions

237
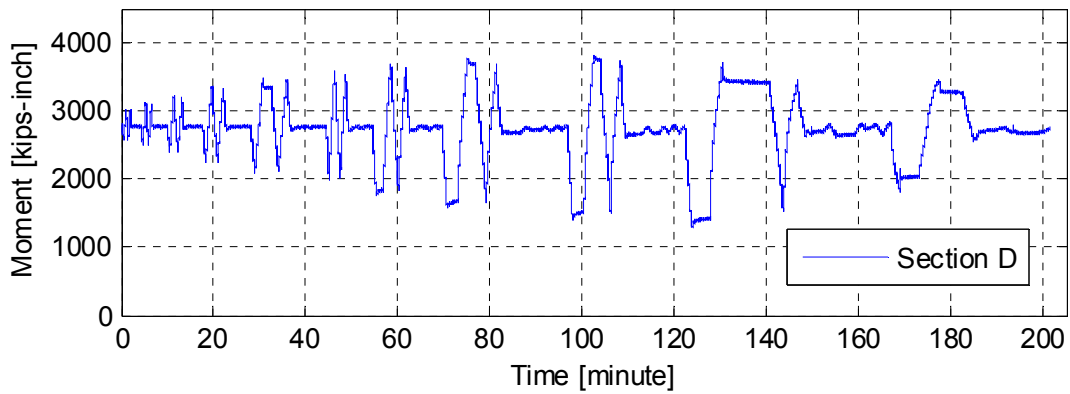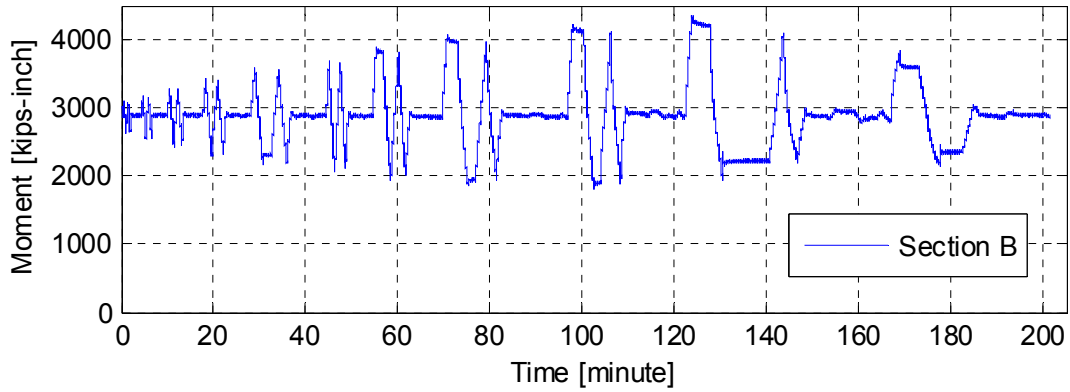
Figure 6.27 Bent cap beam moment history at both sections B and D for all repaired SP1 cyclic loading tests in both transverse and longitudinal directions
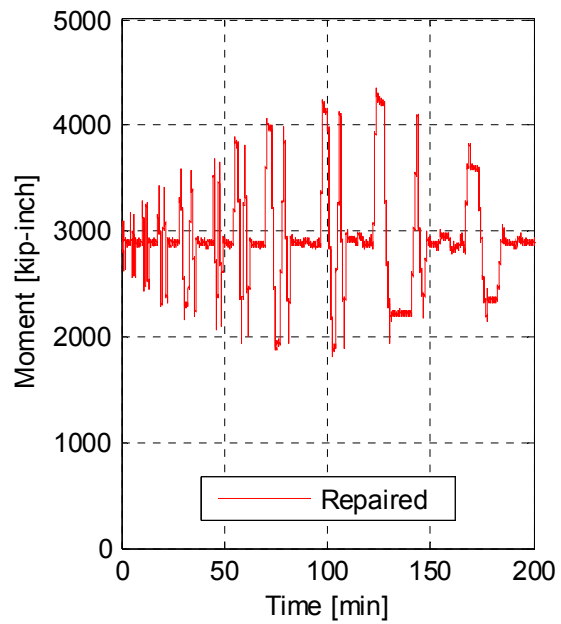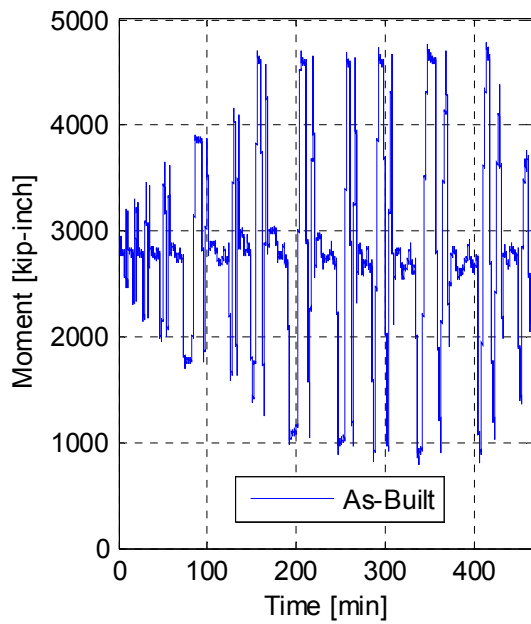
Figure 6.28 Comparison of bent cap beam moment at section B for all as-built and repaired SP1 cyclic loading tests in both transverse and longitudinal directions

238
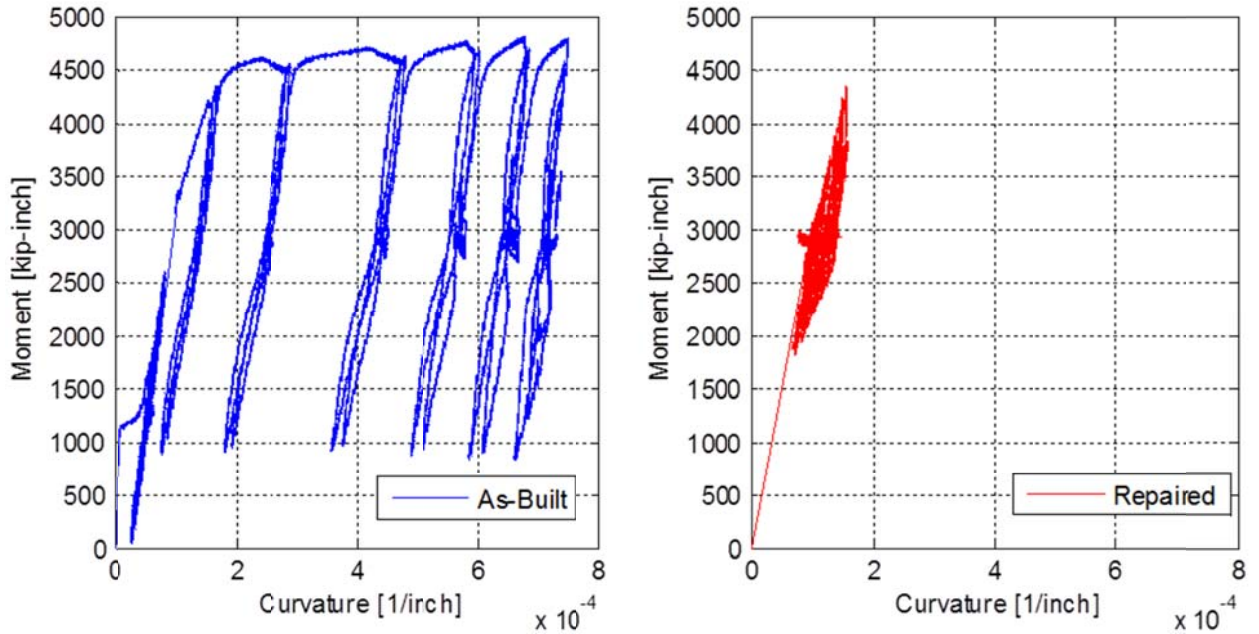
Figure 6.29 Cap beam moment–curvature relationship comparison between SP1 as-built and repaired tests at Section B
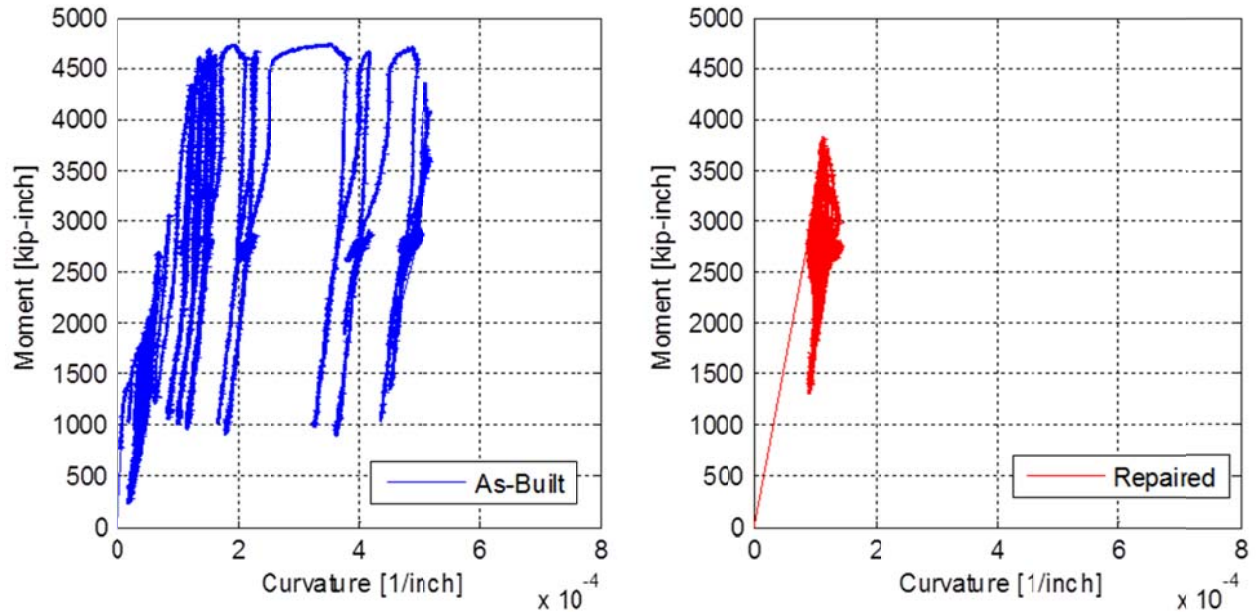
Figure 6.30 Cap beam moment–curvature relationship comparison between SP1 as-built and repaired tests at Section D
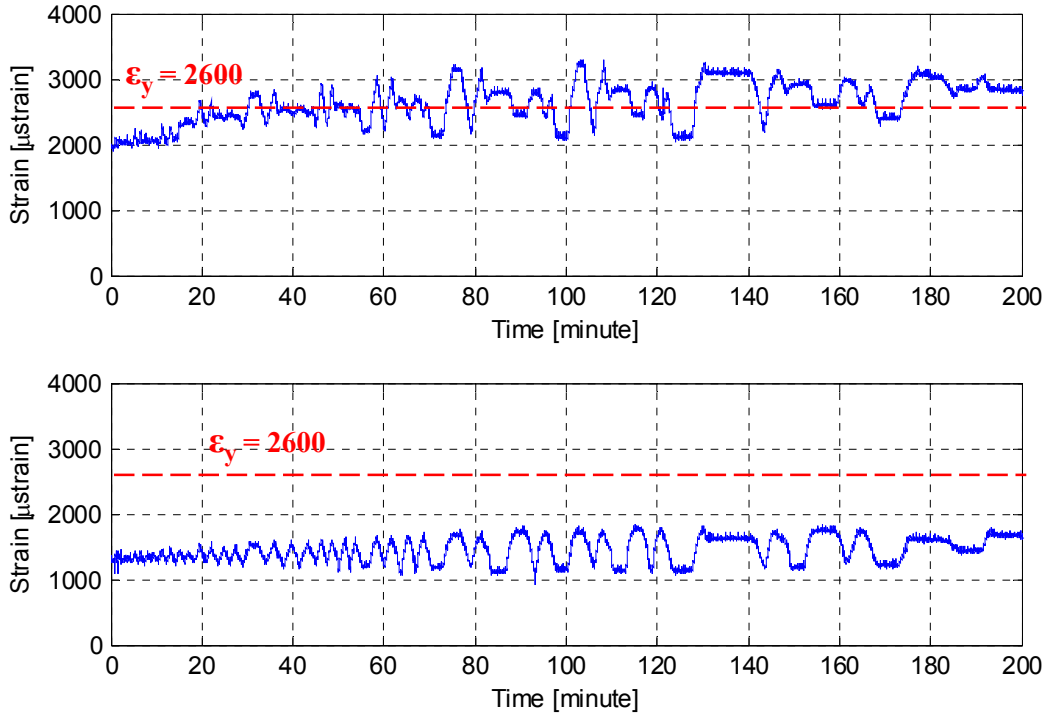
Figure 6.31 Sample of two of the six instrumented cap beam reinforcing bars strain history at Section B for all repaired SP1 cyclic tests
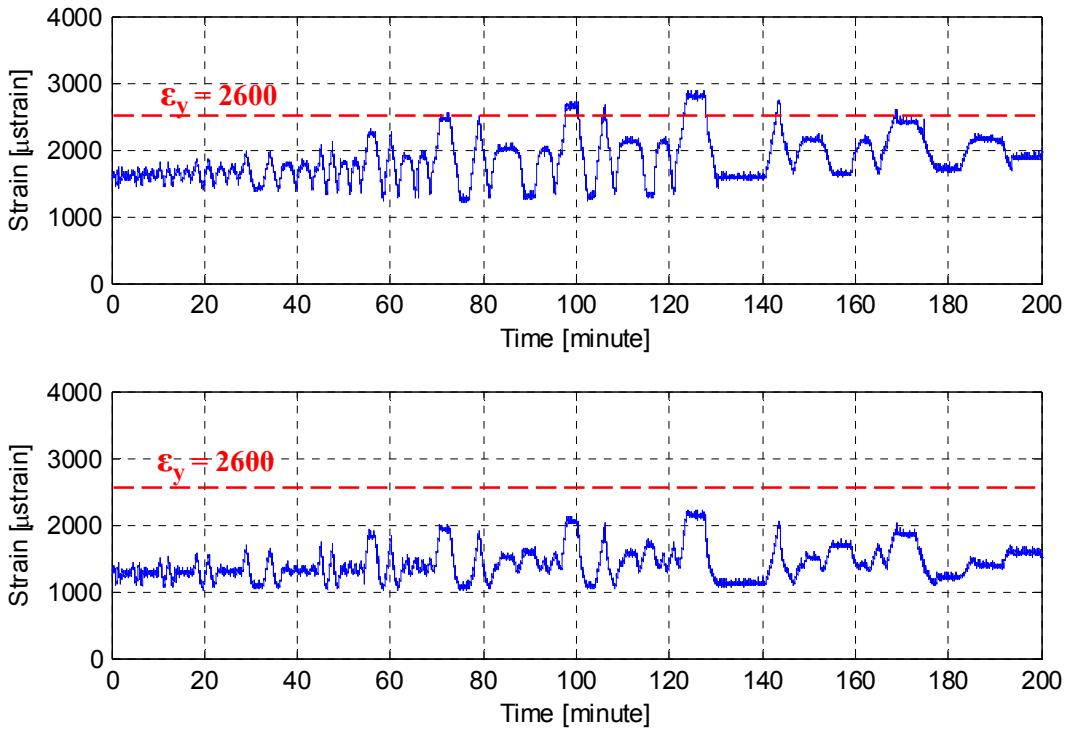
Figure 6.32 Sample of two of the six instrumented cap beam reinforcing bars strain history at Section D for all repaired SP1 cyclic tests

6.6   FRP JACKET STRAIN

One last metric to judge the effectiveness of the CFRP jacket confinement and the repair scheme is the jacket circumferential strain. A progressing circumferential jacket strain typically reflects a dilating column that is resisted by a counter confining action. The dilation is more localized in the compression zone, especially at elevated loading levels where the reinforcing bars could be buckling and displacing the concrete cover but stopped by the confining jacket. To monitor this phenomenon during the repaired specimen cyclic loading tests, several strain gages were installed around the circumference of the CFRP jacket at 8 locations. The circumferential strain history at the transverse loading's two principal sides, namely East and West sides of the column, are shown in Figure 6.33. The figure shows that the strain gage is actively engaged only when loading is aligned with the strain gages plane, i.e. transverse loading (E-W) in this case. Meanwhile, the circumferential strain is sensitive to the loading and unloading as load is reversed. When loading is towards the West, only the strain gage in the West side, where compression occurred, is picking up higher strains, while the East side gage maintains an almost constant strain, and vice versa. This confirms that dilation is localized in the compression zone, and more importantly, the CFRP jacket is effectively confining the column regardless of all the extensive damage that the column experienced before the repair.
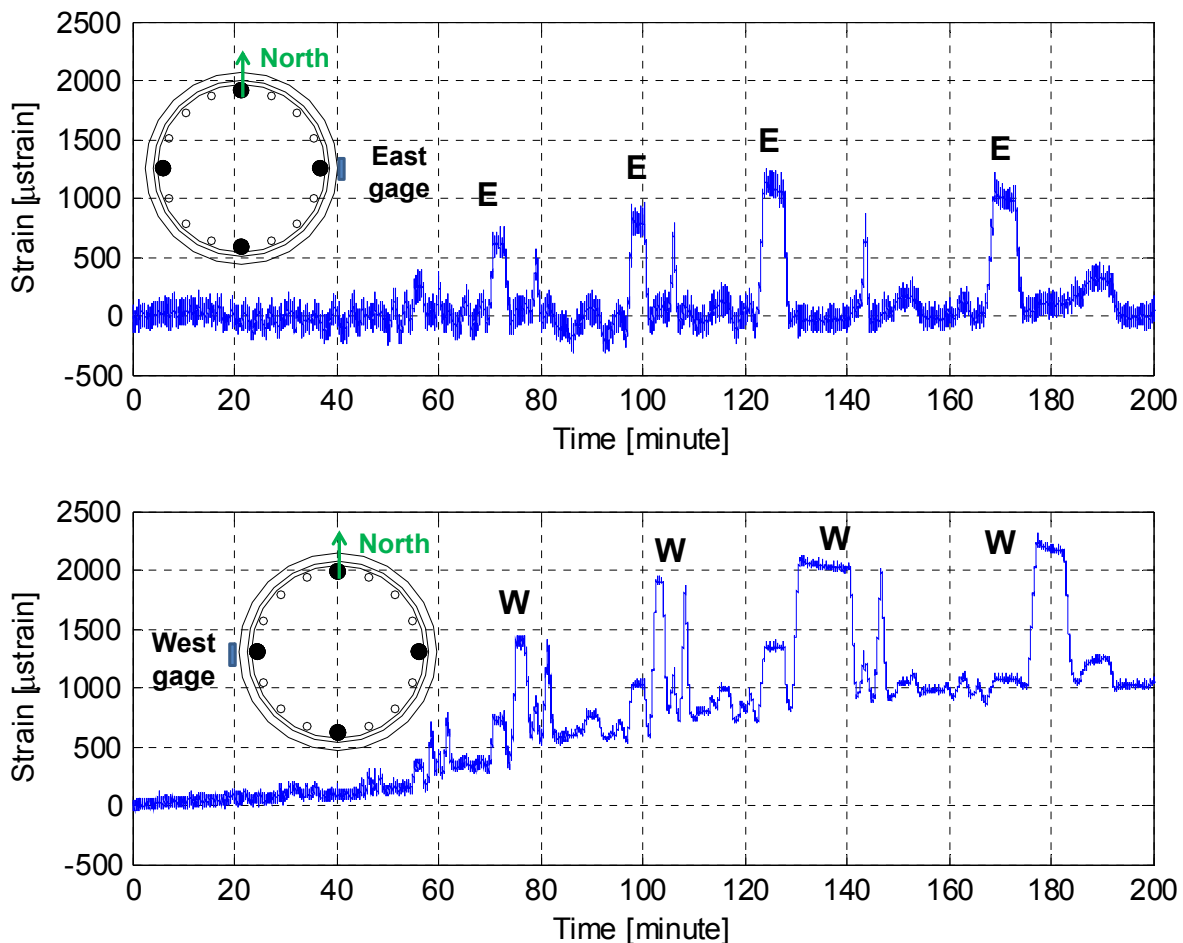
Figure 6.33 Circumferential CFRP jacket strain history in the column East and West sides for all repaired SP1 cyclic loading tests in transverse and longitudinal directions

241

Furthermore, the recordings of two strain gages at 45-degrees from transverse loading plane are shown in Figure 6.34. The strain values in this case are much less and not very sensitive to the loading direction as they are away from the main dilated regions.
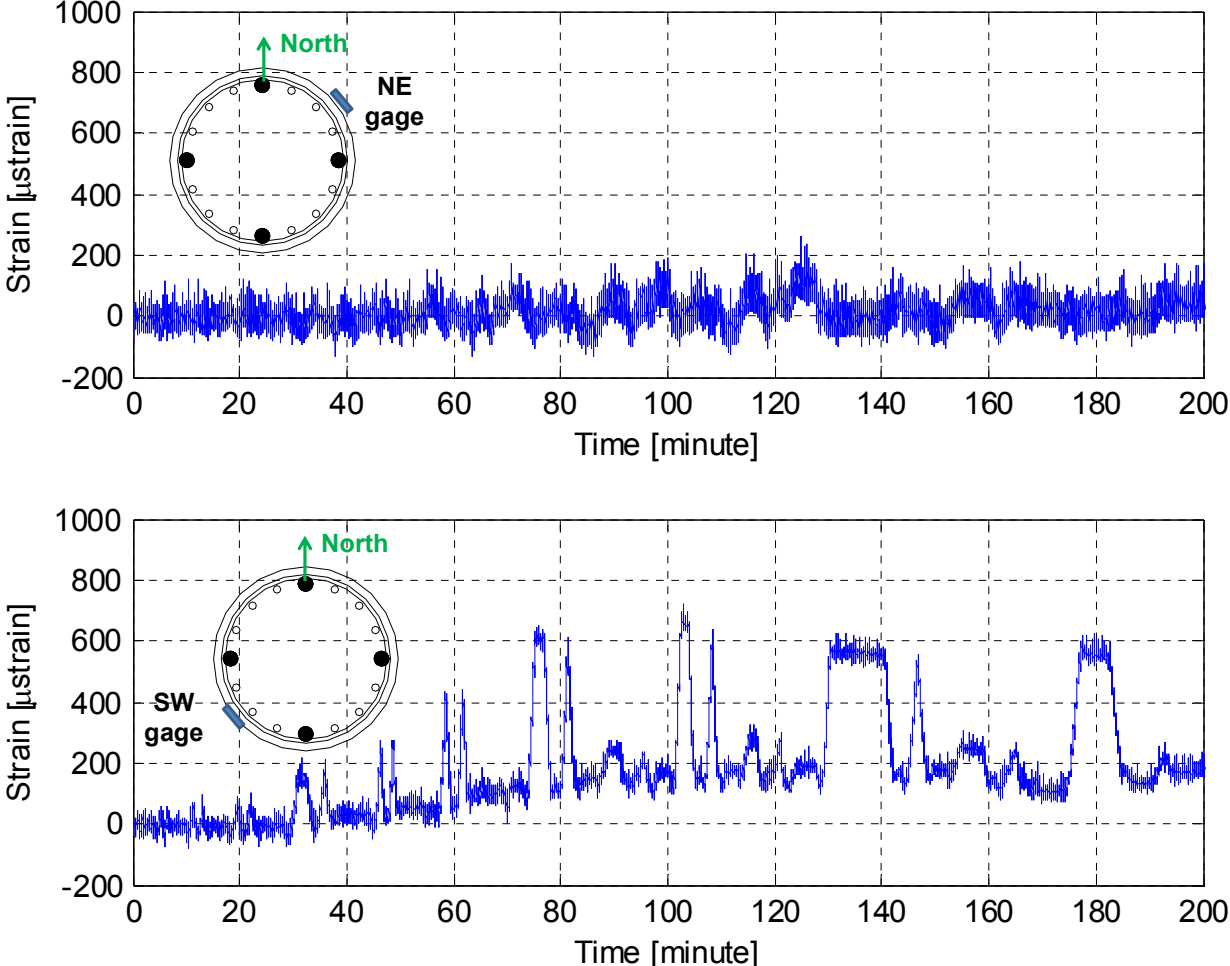
Figure 6.34 Circumferential CFRP jacket strain history in the column North-East (top) and South-West (bottom) sides for all repaired SP1 cyclic loading tests in transverse and longitudinal directions

7 Hybrid Simulation: Development and Verification

Hybrid Simulation (HS) is a mixed computational/physical testing technique that can replace shaking table tests. The essence of HS is to use an online computational substructure to update the earthquake input signal at each time step based on the force feedback from the physical substructure. A complementary objective of this study was to develop a practical HS system that utilizes readily available laboratory data acquisition systems along with inexpensive TCP/IP-Ethernet connections to establish the communication between the physical and computational substructures. The main development in this study is the PI interface to communicate with OpenFresco (2008) from the computational side, through an inexpensive Ethernet connection to replace expensive shared memory communication cards such as SCRAMNet, and the DSP card from the experimental side to control the laboratory hardware and receive the physical substructure feedback. Another development is implementing a new test setup component in OpenFresco that is capable of performing geometric transformations between the global degrees-of-freedom (DOFs) in the computational model and the actuators local DOFs for the command displacements and force feedbacks. A set of verification tests were conducted that used single and double actuators that were not attached to any specimens. A complete HS test was conducted using the repaired SP1 to validate the whole system. A brief background of HS, the main components and developments of the HS system, and verification tests are presented in this Chapter. The successfully validated HS system was utilized for conducting the retrofitted SP2 HS tests as discussed in the next chapter.

7.1 BACKGROUND

HS was first mentioned by Takanashi et al. (1975), who referred to the testing method as "online test". In the next decade, there were significant development efforts in the US that included the works of Mahin and Williams (1980), Mahin and Shing (1985), Mahin et al. (1989) at UC Berkeley, and Takahashi and Nakashima (1987) and Nakashima et al. (1988) in Japan. Previous research on HS investigated different areas that included, but not limited to, development of suitable integration methods, study of the effect of experimental errors, and real-time HS. The following sub-sections briefly discuss basic procedures in HS including numerical integration methods, errors in HS, real-time HS, and brief survey of previous relevant HS bridge tests. It is to be noted that targeted HS tests were slow tests but a very brief discussion of the real-time HS is provided for completeness.

7.1.1 Integration Methods

A wide spectrum of numerical integration methods, such as Newmark methods, generalized-alpha methods, predictor-corrector methods, and Runge-Kutta methods, exists for solving the governing equations of motion, which are discretized in time domain for different structural dynamics problems. Not all of the numerical integration methods can be used directly for solving the equations of motion in HS testing. Thus, one of the main areas of HS-related research concerns with adopting and/or modifying the existing integration methods, or developing new specialized integration methods, for HS purposes. A brief survey of the work conducted in this field is presented with broad classification of the numerical integration methods. The most common classification of numerical integration methods and algorithms is explicit versus implicit methods. It is to be noted that an explicit integration scheme was utilized for all the tests conducted in this study, but a full discussion is given for completeness. Generally, explicit formulations use already available information at a given time-step to predict the new displacement value for the next step (to be imposed on the physical test specimen in HS tests). On the other hand, implicit formulations require information from both previous and current times, and hence an iterative approach is needed. More details about explicit and implicit integration methods are presented in the following paragraphs.

7.1.1.1 Explicit Integration Methods

For an explicit algorithm, the new solution at time step ($i+1$) can be expressed entirely by known terms such as the current solution state at time step (i) or even previous step (i-1) as in Central Difference Method (CDM) for example, i.e. $u_{i+1} = f\left(u_i, \dot{u}_i, \ddot{u}_i, u_{i-1}, \dot{u}_{i-1}, \ddot{u}_{i-1}\right)$. Explicit integration methods are usually conditionally stable, meaning that the integration time step (Δt) should be smaller than the shortest natural period of a structure (T_n) divided by a factor (α) to yield a stable and accurate solution ($\Delta t \leq T_n/\alpha$). Also the new solution for the next time step can often be determined in a single calculation step without the knowledge of the tangent stiffness matrix.

Two well-known examples of explicit integration methods are CDM and explicit Newmark method. Although the equations involved in each method are not specifically mentioned herein, it can be shown that the CDM can be reproduced from Explicit Newmark when the integration parameter ($\gamma = 0.5$). Generally, the explicit Newmark method is used more often in HS than CDM for the following reasons: it does not require any quantities before the start time (i.e. at $t = 0$), the velocities and accelerations are directly obtained as the solution advances (there is no need to be calculated separately as in the CDM), and it has more favorable error-propagation characteristics as shown by Shing and Mahin (1983).

The advantages of explicit methods are that they are computationally very efficient, easy to implement, and fast in their execution. On the other hand, a limiting factor for the application of the explicit methods is their stability criteria. Hence, they are not suitable for stiff problems (short periods) and cannot even be used at all for infinitely stiff problems. Although this limitation can be overcome by choosing smaller integration time steps, the integration time step might need to be reduced to an extent that the application of explicit methods to HS becomes impractical. The implicit methods are sought in these cases. It is worth noting that some attempts have been conducted to develop unconditionally stable explicit methods such as the one proposed by Chang (2002).

244

7.1.1.2 Implicit Integration Methods

For an implicit algorithm, the solution at time step (i+1) not only depends on known quantities from the current and previous time steps, but also on the solution itself, i.e. $u_{i+1} = f(u_{i+1}, \dot{u}_{i+1}, \ddot{u}_{i+1}, u_i, \dot{u}_i, \ddot{u}_i)$. Because of this, implicit algorithms contain algebraic formulas that need to be solved iteratively in order to determine the solution at the end of a time step. Many implicit integration methods are generally unconditionally stable, thus ideal for stiff and infinitely stiff problems. This also means that only the accuracy of the algorithm needs to be considered when determining the time step size, since the method is stable for any step size. Usually this permits the selection of larger analysis time steps as compared to the explicit methods.

Implicit methods are well suited for large problems with many DOFs or for infinitely stiff problems, which arise when structural DOFs with no mass are present. However, they are computationally more demanding because they require iterative solution schemes, and they can introduce spurious loading and unloading cycles on the physical parts of the HS. A comparison of the features of explicit and implicit integration methods is shown in Table 7-1.

Table 7-1 Comparison between explicit and implicit integration methods

Item	Explicit Methods	Implicit Methods
Required input	$u_{i+1} = f(u_i, \dot{u}_i, \ddot{u}_i, u_{i-1}, \dot{u}_{i-1}, \ddot{u}_{i-1})$	$u_{i+1} = f(u_{i+1}, \dot{u}_{i+1}, \ddot{u}_{i+1}, u_i, \dot{u}_i, \ddot{u}_i)$
Iterations	not required	Required
Tangential stiffness	not required	required at each time step
Stability	conditionally stable: $\Delta t \le T_n/\alpha$	generally unconditionally stable
Computational cost	easy to implement, and computationally efficient	harder to implement, and computationally expensive due to iterative schemes
Execution time	generally faster	generally slower because of iterations
When to use	- When only physical specimen is tested, and analytical part consists of mass and damping only; - For MDOF systems with non-singular mass matrix (all DOFs have nonzero masses).	- Stiff or infinitely stiff problems with short periods; - For MDOF systems with singular mass matrix (some DOFs have zero masses such as rotational DOFs, without considering the associated mass moment of inertia, in moment resisting frames)

A short survey of how the integration methods were adopted and developed in previous studies is presented. Most of the first-generation HS testing and research focused on the use of explicit methods to avoid iterative implicit methods in HS testing involving nonlinear seismic behavior of structures. In the first documented application of HS by Takanashi et al. (1975), the CDM (explicit method) was used, while Mahin and Williams (1980) were the first to use explicit Newmark scheme. Other examples where explicit methods were employed are the works of Nakashima and Masaoka (1999) and Magonette (2001).

To overcome the limitations of stability in explicit methods, Dermitzakis and Mahin (1985) proposed another approach where explicit and implicit methods were employed for the experimental and analytical substructures, respectively. Nakashima et al. (1990) proposed a specialized Operator-Splitting (OS) method for HS based on the non-iterative implicit-explicit predictor-corrector scheme of Hughes et al. (1979). This integration method was later employed by Mosalam et al. (1998) for the HS of steel frames infilled with unreinforced concrete block masonry.

Thewalt and Mahin (1987) developed the first implicit integration method for HS based on the alpha-method by Hilber et al. (1977). Another application of a specialized implicit integration method is an integration scheme that was based on the implicit Newmark method wimh sub-stepping in an inner loop (Dorka and Heiland 1991, Dorka 2002, Bayer et al. 2005). The implicit integration method developed by Shing et al. (1991) based on the alpha-method (Hiber et al. 1977) was used in HS of concentrically braced frames (Shing et al. 1994). Recently, Schellenberg et al. (2009) developed several specialized integration algorithms for HS, including a specialized implicit Newmark method with constant number of iterations and uniform displacement increments for the iterations of an integration time step.

An approach that is associated with numerical integration methods is related to adopting numerical damping to provide numerical energy dissipation for higher modes since the effect of experimental errors is more dominant for the higher modes. Hence, some of the previous research developed integration methods that damp out the spurious higher mode participations. Two of these methods are the modified Newmark explicit methods proposed by Shing and Mahin (1983) and by Chang (1997). An example of an implicit method providing numerical energy dissipation is developed by Bonelli and Bursi (2004) based on the generalized alpha-methods by Chung and Hulbert (1993).

7.1.2 Errors in HS Testing

Due to the nature of the multi-component of HS system (HSS), there are numerous possibilities for error sources either in the computational part or the experimental part especially in the controller and boundary conditions. Elimination or at least minimizing these errors is necessary for a valid and reliable HSS. Errors in HS can be categorized into three groups. The first group is the errors due to structural modeling such as the structural idealization that consists of replacing a continuous system by a discrete number of DOFs. The second group consists of the errors due to the numerical methods. Experimental errors constitute the third group, which can be further classified as random and systematic errors. The numerical and random errors were found insignificant in contaminating the results, and thus typically ignored. However, due to the propagation and accumulation of systematic experimental errors, attention was directed to better understand the nature of these errors in order to either eliminate or minimize them or correct the results by compensating for such errors to achieve a more reliable system.

A brief survey of HS errors-related previous research is presented. Mosqueda (2003) provided a comprehensive summary of the nature and sources of HS errors and available error compensation techniques. The effect of experimental errors has always been an important area of HS research especially before the advent of modern digital controllers and closed loop control of hydraulic actuators. In two of the earliest works, the propagation of random and systematic errors was evaluated by Mahin and Williams (1980) and Shing and Mahin (1983). The cumulative

nature of experimental errors introduced by the control and data acquisition systems in HS tests using explicit numerical integration algorithm was studied by Shing and Mahin (1987). Reliability of the HS method was investigated by Yamazaki et al. (1989) where experimental error behavior was examined based on an elastic test of a six-story steel structure. Thewalt and Roman (1994) presented several parameters for identifying errors and quantifying their magnitude and effect. Mosqueda (2003) simulated the experimental errors, such as the random noise in the load cells and displacement lag errors, using Simulink models and derived linear transfer functions for time delay errors and for the dynamic behavior of experimental setups including the specimen, the transfer system, and the reaction wall.

Research aimed at reducing the effect of errors on HS. As an example of such work, Chang et al. (1998) proposed solving the momentum equation of motion which is obtained by integrating the force equation of motion. In this approach, the measured forces are filtered by the integration algorithm before being used in the numerical solution. Horiuchi et al. (1999) measured the time lag of the actuator response, i.e. the difference between command and feedback displacements, and predicted the command of the actuator by advancing the current time with the delay time using a polynomial extrapolation procedure. Alternatively, Elkhoraibi and Mosalam (2007) overcame this time lag by developing a feed-forward error compensation scheme based on the modification of the displacement command with an error term which is a function of the actuator velocity. Stoten and Magonette (2001) have investigated the effect of improvement of the hardware components, such as the use of digital controllers and digital transducers in order to achieve better experimental results. Development of integration methods aimed at damping out the spurious higher mode participations can also be classified in this category of research related to reducing the effect of errors on HS.

7.1.3 Real-time Hybrid Simulation

A HS test is said to be conducted in real-time when the experimental substructure (physical specimen) is loaded with the actual calculated velocities and accelerations. Therefore, highly variable loading rates are expected in real-time tests. Conventional HS with slow rates of loading, which is similar to the tests conducted in this study, is sufficient in most of the cases where rate effects are not important such as reinforced concrete components. However, for rate-dependent specimens, such as triple friction pendulum bearings, real-time HS becomes essential. Another relevant application is the use of real-time HS for testing rate-dependent composite (polymer) insulator posts (Mosalam et al. 2012).

The first progress in real-time HS was achieved by Nakashima et al. (1992) when dynamic actuators and a digital servo-mechanism were used. After the development of actuator-delay compensation methods by Horiuchi et al. (1999), research on real-time HS gained momentum. Darby et al. (1999, 2001) developed various real-time partitioned HS utilizing control system approaches. Nakashima and Masaoka (1999) employed a digital signal processor (DSP) for the first time to separate the actuator signal generation from the target displacement computation. Nowadays, the rapid development of computing technologies and control methods increases the number of real-time HS research activities for different applications. For example, a large amount of work was conducted on electrical switches using real-time HS (Günay and Mosalam 2014).

7.1.4 Previous HS Bridge Tests

Large portion of the studies that involved HS focused more on the development side and robustness of the testing method as briefly presented in the previous subsections. However, several studies utilized HS directly in different applications. A short discussion of the most recent studies that focused on HS application rather than development, mainly relevant studies of HS bridge tests, is presented. Some of the research projects involved whole bridge systems, especially for the computational substructure, and other focused only on bridge components as discussed next.

Large-scale hybrid simulations of full bridge structures were tied to geographically distributed HS testing in the past years. In the US, several institutions and laboratories are already connected with high performance networks to explore the benefits of integrating their resources. Collaboration between the Kyoto University and the University of California, Berkeley (Takahashi et al., 2008) aimed at examining the seismic response of a two span continuous bridge with C-bent column. The study showed confidence in using a HS system where OpenFresco (2008) and OpenSees (2000) can simulate a complicated structural system with the most appropriate model. This framework was very stable even in strong nonlinear cases. The distributed HS was found to be a powerful tool for the evaluation of structural systems.

Seismic design and research have been mainly concentrating on horizontal earthquake excitation whereas the vertical component has generally been neglected. However, the awareness of the significance of vertical ground motion has gradually been increasing due to results from studies and field observations, which confirm the possible destructive effect. This study discussed the preliminary effects of vertical excitations as part of the pre-test analysis earlier in Chapter 4. The effects of vertical ground motions on RC structures and bridge columns have been studied in Kim and Elnashai (2008) using a combined analytical-experimental research approach. For the experimental investigation, sub-structured pseudo-dynamic and cyclic static tests were employed using the NEES (Network for Earthquake Engineering Simulation) multi-axial full-scale sub-structured testing and simulation (MUST-SIM) facility at the University of Illinois at Urbana-Champaign (UIUC).

Further research projects focused on initiatives to build up a standardized platform for the efficient setup of network-based multi-site hybrid experiments, and standardized protocol procedures for efficient data exchange. Chang (2008) established a robust standardized procedure for laboratories at multiple sites to network their testing facilities in order to perform collaborative experiments. A collaborative research project was established between Canada and Taiwan to develop modules for control and instrumentation based on the use of standardized software interfaces. The Internet-based Simulation for Earthquake Engineering (ISEE) platform (Yang et al. 2007, Wang et al. 2007) was employed for the communication between the laboratories. A large-scale application to use the platform involved a hybrid model for a four-pier bridge system with prototype columns, which were tested at three remote sites over long distance. The tests progression and 3D visualization of the test results, such as deformed prototype bridge, were broadcast through the Internet in real-time. This experiment was considered the first cross-continent collaborative-networked hybrid test on large-scale specimens and has successfully demonstrated the potentials and future direction of experimental research of large-size structures and civil infrastructure systems. The experiment investigated the behavior of double–skin concrete filled tubular (DSCFT) columns. Three DSCFT columns, which is an

innovative design for resilient bridge piers in high seismicity areas, were numerically and experimentally tested at three remote sites. Local buckling of the external steel tube was observed with one test specimen and occurred due to de-bonding between the steel tube and the filled concrete. No cracks were observed on the confined concrete core at the cut section, 1 inch above the bulge due to local buckling, which rendered the double-skinned steel tubes efficient for confinement and prospect resilient bridge designs.

In China an internet-based platform NetSLab has been developed for data transmission and collaborative control among distributed laboratories during the tests. Xin-jiang and Shi-zhu (2009) conducted a seismic HS test of a multi-span bridge, in which two FRP retrofitted RC columns were tested physically, and three columns were simulated numerically. Both tested columns had different lengths and were retrofitted to prevent either shear or flexural damage to the column. The results showed that the failure modes were all ductile flexural failure besides an observed pinching phenomenon and significant stiffness degradation after yielding, which demonstrated the confining effects of the FRP retrofit in increasing the column ductility.

One of the most relevant recent studies that used a similar HS test setup to the present study, and was conducted also at UC Berkeley, is the investigation of post-earthquake traffic capacity of modern bridges in California using HS by Terzic and Stojadinovic (2010). In California, the modern highway bridges designed using the Caltrans SDC are expected to maintain at minimum a gravity load carrying capacity during both frequent and extreme seismic events. However, no validated, quantitative guidelines for estimating the remaining load carrying capacity of such bridges after an earthquake event exist. This was the motivation for the study in (Terzic and Stojadinovic 2010) to combine experimental and analytical methods to evaluate the post-earthquake traffic load carrying capacity of a modern California highway overpass bridge. An experimental study on models of circular RC bridge columns was performed to investigate the relationship between earthquake-induced damage in bridge columns and the capacity of the columns to carry axial load in a damaged condition. The test results were then used to calibrate a FE model of a bridge column. This bridge column model was incorporated into a hybrid model of a typical California overpass bridge and tested using the HS technique. A multi-DOF HS tests were conducted that used 2 translational and 2 rotational experimental DOF for the test, which required a new experimental setup element in OpenFresco; similar to what is developed in the present study. The FE model of the typical California overpass bridge was validated using the data from the HS tests.

The validated model of the typical bridge was used to evaluate its post-earthquake truck load capacity in an extensive parametric study that examined the effects of different ground motions and bridge modeling parameters such as the boundary conditions imposed by the bridge abutments, the location of the truck on the bridge, and the amount of bridge column residual drift. Terzic and Stojadinovic (2010) concluded that a typical modern California highway bridge is safe for traffic use after an earthquake if no columns failed and the abutments are still capable of restraining torsion of the bridge deck about the longitudinal axis. If any of the columns failed, i.e. if fractured column reinforcing bars are discovered in an inspection, the bridge should be closed for regular traffic. Emergency traffic with weight, lane, and speed restrictions may be allowed on a bridge whose columns failed if the abutments can restrain torsion of the bridge deck. These findings pertain to the bridge configuration investigated in the study.

A novel complex hybrid experimental test of a curved four-span bridge was performed at the NEES MUST-SIM facility at UIUC in 2013 (Frankie et al. 2013). The bridge was partitioned

into two analytical and one experimental substructure and loaded with a multidirectional earthquake excitation. The capabilities of the testing facilities at UIUC allowed controlling the boundary conditions of the pier in six DOFs. Furthermore, the experimental test program was novel in the fact that it accurately accounted for various geometric, loading, and boundary characteristics of a curved bridge structure. The project compared the experimental results with a preliminary numerical model. Large discrepancies between the experimental results and the model were observed and indicated the inadequacy of existing analytical solutions. Accordingly, the authors recommended HS testing for such complex system.

One of the latest large HS tests was conducted within the NEES facilities and presented by Mosqueda et al. (2008). The earthquake response of a six-span bridge model with five remote experimental and a numerical column substructure distributed within the NEES facilities was investigated. A multithread simualtion coordinator control strategy was applied to simultaneously load multiple remote substructures at different sites. The event-driven remote site controller allowed for the implementation of continuous HS algorithms on distributed models where computation, network communication, and other tasks may have had random completion times. This project reflected the progress of HS over the past years. The simulation time was reduced from five hours to less than one-third of an hour. In addition to the time savings, the reliability of the results were improved by minimizing the force relaxation and other strain-rate-related errors in the experimental substructures.

7.2   HYBRID SIMULATION SYSTEM

To perform a HS test, several key components including software and hardware are necessary. Schellenberg et al. (2009) provided a comprehensive overview of the key components of a generic HSS as shown in Figure 7.1. The components of the specific HSS utilized in this study in addition to the computational and experimental substructures used are discussed in this section. A brief discussion of a P-delta correction scheme that was devised and used in some of the HS tests is presented as well.
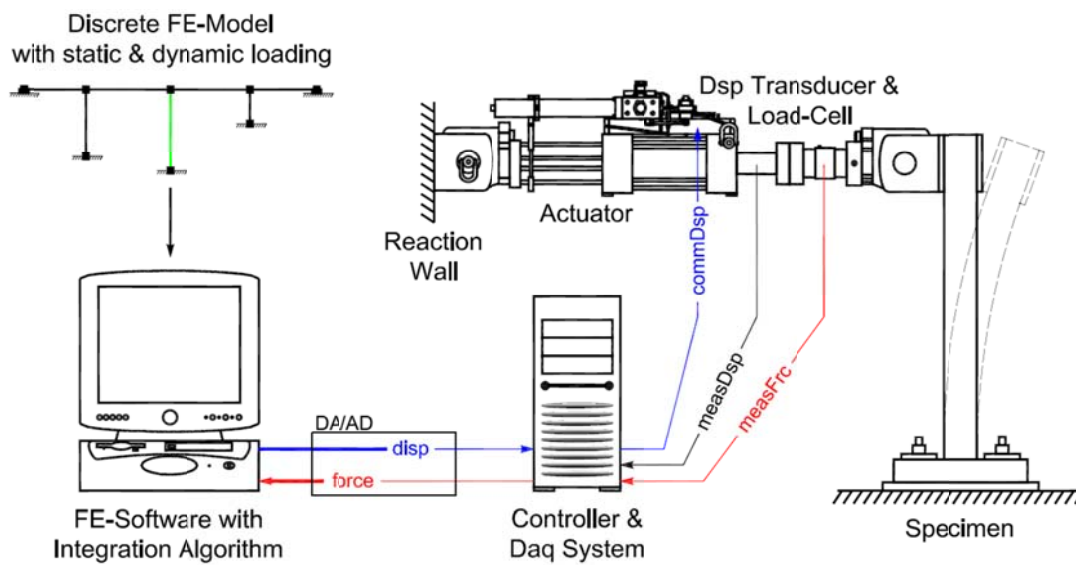
Figure 7.1 Key components of a hybrid simulation system (Schellenberg et al. 2009)

7.2.1 HSS Components and Connectivity

Four main components comprise a typical HSS. The first component is a discrete model of the structure to be analyzed on a computer, including the static and the dynamic loading. The FE method is used to discretize the problem spatially and a time-stepping integration algorithm is then used for the solution of the equations of motion with time discretization. The resulting dynamic equations of motion for the finite number of discrete DOF are a system of second-order ordinary differential equations in time that are initialized and expressed as shown in Equations (7-1).

$$\mathbf{M}\ddot{\mathbf{U}}_{i+1} + \mathbf{C}\dot{\mathbf{U}}_{i+1} + \mathbf{P}_r(\mathbf{U}_{i+1}) = \mathbf{P}_{i+1} - \mathbf{P}_{o,i+1}$$

$$\mathbf{U}_{i=0} = \mathbf{U}_0 \tag{7-1}$$

$$\dot{\mathbf{U}}_{i=0} = \dot{\mathbf{U}}_0$$

where $\ddot{\mathbf{U}}$, $\dot{\mathbf{U}}$, and $\mathbf{U}$ are the acceleration vector, the velocity vector, and the displacement vector at the structural DOFs, respectively. $\mathbf{M}$ is the mass matrix assembled from the nodal and element mass matrices, $\mathbf{C}$ is the viscous damping matrix, $\mathbf{P}_r$ are the assembled element resisting forces (which depend on the displacements), $\mathbf{P}$ are the externally applied nodal loads, and $\mathbf{P}_o$ are the assembled "equivalent" element loads.

The second required component is a transfer system consisting of a controller and static or dynamic actuators, so that the incremental response (generally the displacements) determined by the time-stepping integration algorithm can be applied to the physical portions of the structure. For slow tests such as the ones conducted in this study, quasi-static testing equipment can be used. Thus, the same controllers and static actuators that were used in the cyclic loading tests of SP1 were utilized again in SP2 HS tests. The third major component of the HSS is the physical specimen that is being tested in the laboratory and a support system (e.g. reaction wall or frame) against which the actuators of the transfer system can react. The fourth and last component is a data acquisition system including displacement transducers and load cells. The data acquisition system is responsible for measuring the response of the test specimen and returning the resisting forces to the time-stepping integration algorithm to advance the solution to the next analysis step.

A vital feature of HS is to connect the above mentioned four components together to achieve vigorous two-way communication for sending the displacement input and receiving the force feedback. The major components and connectivity pieces of the utilized HSS at the Structures Laboratory at UC Berkeley are shown in Figure 7.2. The main pieces identified in this figure are: (a) A computational platform where the numerical integration of the governing equations of motion is performed (OpenSees was used in this case), (b) OpenFresco (2008) generic middleware that communicates with the computational platform, (c) New interface software developed within the Pacific Instruments (PI) data acquisition system (DAQ) that communicates, in turn, with OpenFresco through TCP/IP connection, (d) Digital Signal Processing (DSP) card that further complements the communication loop with the laboratory hardware, and (e) digital controllers that command the hydraulic actuators in displacement control. The main development in this study is the PI interface to communicate with OpenFresco from the computational side, and the DSP card from the experimental side. Another development

was implementing a new geometric transformation test setup component in OpenFresco. More details about these developments and their verification are reported later in this chapter. A further discussion of the computational and experimental substructures is presented in the following subsections.
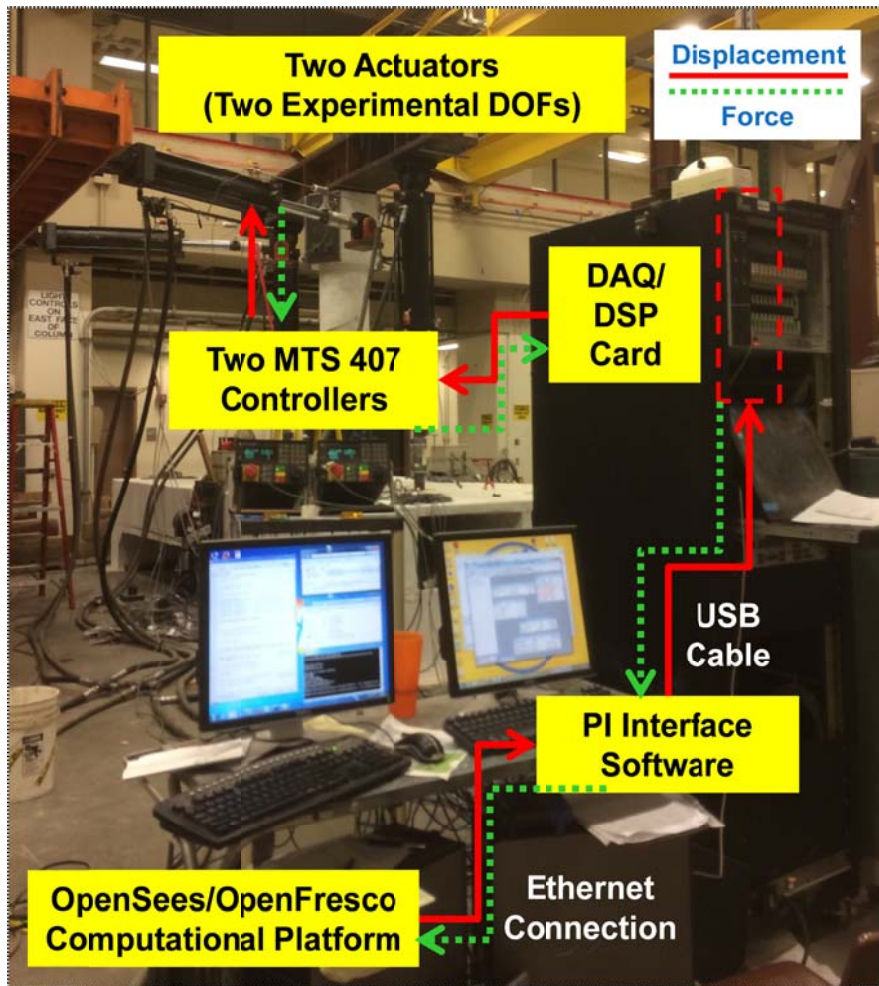
Figure 7.2 Overview of the main components and connectivity of the HSS at the Structures laboratory of UC Berkeley

7.2.2 Computational Model

The computational model consisted of multi-DOF with mass and damping. The lumped mass used in the computational model was calibrated such that comparable modes of vibration to the prototype bridge (Chapter 4) are obtained when the proper similitude relationships were applied. Damping is modeled as Rayleigh Damping with damping coefficients determined by using 5% damping ratio for periods corresponding to the transverse and longitudinal modes of vibration. A larger computational substructure of the full prototype bridge could have been used in the considered HS tests. However, the main objective of the HS test was to evaluate the bent cap beam behavior and the contribution from the test specimen box-girder slabs rather than an overall bridge behavior, i.e. a localized behavior of the test specimen and a global behavior of the test subassemblage considering the column-bent cap-box girder interaction rather than the

full bridge behavior. Accordingly, the computational model was a multi-DOF column with lumped mass at the top. The Open System for Earthquake Engineering Simulation, OpenSees (2000), previously used in the pre-test analysis, was used again in the HS tests as the FE software to analyze the computational substructure of the test specimen and solve the dynamic equation of motion to solve for the displacement at each time step. Meanwhile, OpenSees was used along with the middleware Open-source Framework for Experimental Setup and Control, OpenFresco (Schellenberg 2008), to connect the FE model with the control and data acquisition software. OpenFresco was designed in an object-oriented structure that is similar to that of OpenSees, and shares common classes and subroutines for element types and numerical integration methods for instance. Therefore, OpenFresco is most conveniently used with OpenSees as the FE platform even though OpenFresco has the capabilities to communicate with a variety of other FE software programs. Accordingly, a single OpenSees/OpenFresco input file that is prepared using the Tool Command Language (TCL) is used to define the computational model and the communication settings. The specimen is represented in OpenSees using the Generic Element type.

The HS tests were conducted using a transverse-only or bidirectional horizontal components of the ground motion. Again, the vertical component of the ground motion was used only in the tests that incorporated the P-delta correction where the total fluctuating axial load, due to both of the gravity load and vertical excitation, was used to correct for the lateral force feedback. As previously discussed in Chapter 3, a short list of six ground motions were found to cause the largest demands in the bent cap. Only the Northridge earthquake record at the Rinaldi station, out of the short list of six records previously identified in Chapter 4, was used in the actual SP2 HS tests as it was representative of a California earthquake where the used prototype is considered. Figure 7.3 shows the three components of the 100% Rinaldi record.

The above discussion is concerned mainly with the computational model considered for the intended HS tests of SP2. However, for the HSS verification tests that used the actuators only without any attached specimen, a more generic and much larger DOF model was used with a variety of ground motion records. That is to validate the HSS for larger computational models and different cases. The HSS verification tests used different ground motions with more cycles and harmonic nature, such as the El Centro record, and pulse-like nature, such as the Rinaldi record. Moreover, a multi-story multi-bay frame was used as the computational model where one of the first story columns was replaced by the experimental element. A simulation experimental element, available in OpenFresco and based on input material and geometric properties, was used rather than an actual experimental physical substructure. This was very beneficial where a multiplier (assumed stiffness) of the displacement of the free actuators in the HS verification tests was fedback as a virtual force feedback to the system to check the communication loop against the pure simulation results. More details are presented in the single actuator verification tests.
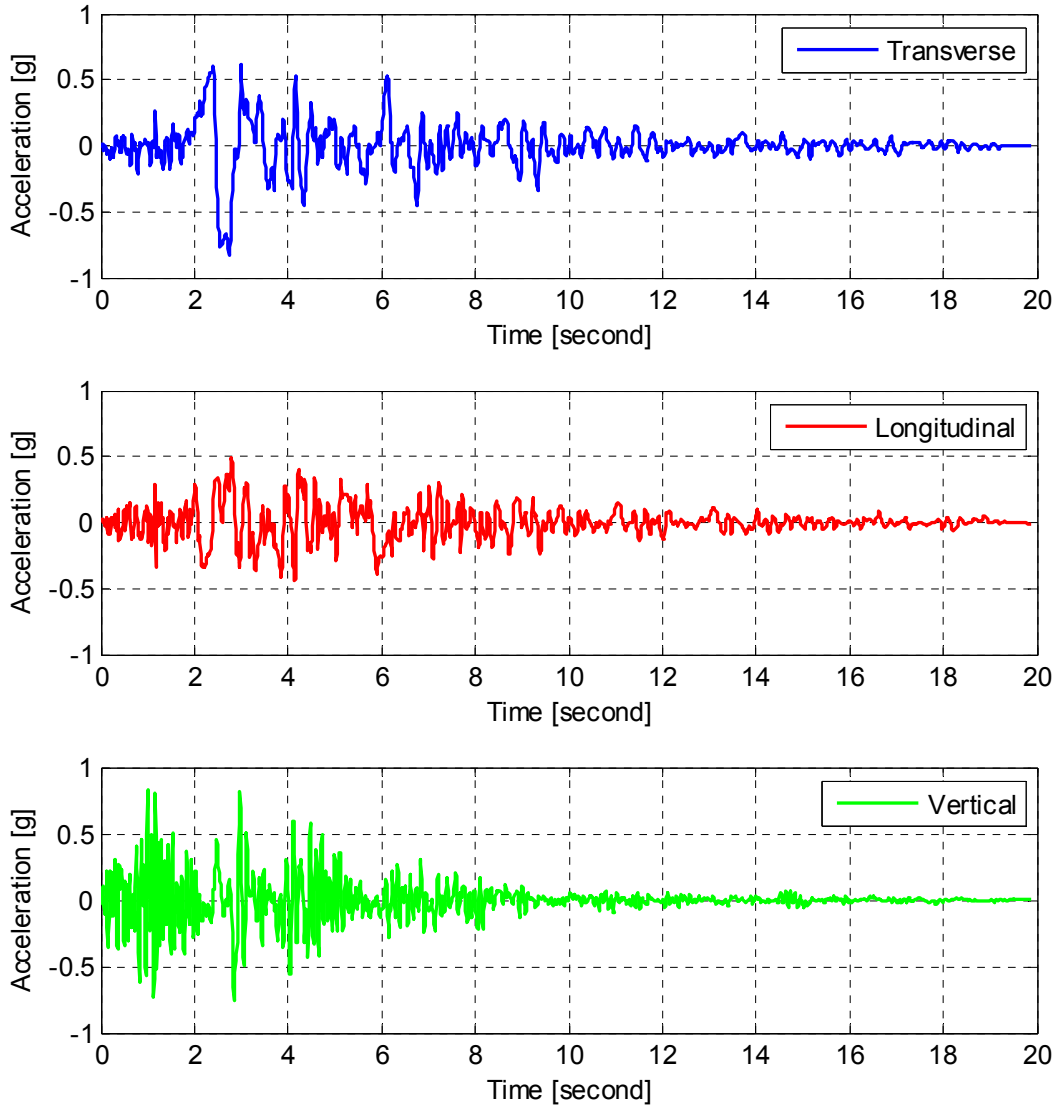
Figure 7.3 Three components of the Northridge earthquake recorded at Rinaldi Station

7.2.3 Physical Substructure

The hybrid nature of the tested model is attributed to the fact that part of the model is a computational analytical model, whereas the rest of the model is a physical experimental substructure. In the considered HS tests in this study, the physical specimen was the column-bent cap-box girder subassemblage, which was similar to the test specimen considered for the quasi-static cyclic loading tests. The computational model, as previously discussed, was a column model with lumped mass and damping. The input for the equation of motion was supplemented by the resisting force feedback, which reflects the lateral overall system behavior of the full column-bent cap-box girder subassemblage after the proper geometric transformations were applied. Figure 7.4 shows a view of the retrofitted SP2, before setting up the instrumentation and the test loading setup, which comprised the physical substructure of the HS tests.

Figure 7.4 Physical experimental substructure (retrofitted SP2) used in the HS tests

7.2.4   P-delta Correction

In structural analysis, P-delta refers to the abrupt changes in a sufficiently tall structural component base shear and bending moment when it is subjected to lateral displacement. The P-delta effect can be interpreted as a destabilizing secondary moment that results from a vertical gravity force multiplied by the lateral displacement as schematically represented in Figure 7.5. Accordingly, in case of progressing lateral displacements, the destabilizing secondary moment increases and can cause instability or complete collapse. The P-delta effect is more dramatic in buildings, especially tall buildings, more than bridges because of the elevated gravity load levels at the lower floors columns. The vertical ground excitations can additionally increase the axial load levels, which can accelerate the collapse. In bridges, the gravity loads are not typically high as in the case of buildings, yet at large lateral displacement, the P-delta effect might be pronounced.

In this study, an approximate method for accounting for the P-delta effect from both of the gravity load and the vertical excitations was devised for HS testing. That is through correcting the lateral force feedback before it is sent back to the computational model to solve for the next displacement input step. Given the known lateral displacement at a time step, the acting gravity load along with the additional axial load resulting from the solution of the computational model under the vertical excitation were utilized to calculate the P-delta secondary moment, and

255

accordingly, correct the lateral force feedback. Figure 7.5 shows schematically how the corrected force is achieved when the P-delta effect is incorporated. The simple arithmetic operation to correct the force feedback was performed using a Digital Signal Processor (DSP) subroutine. This split computations provided additional flexibility for future development where the conventional DAQ system can be used to accommodate a hybrid computational model, i.e. part of the computations are performed using the FE platform while another part is performed using a DSP subroutine, for instance.

The P-delta correction involved the applied gravity load during a HS test as well as the corresponding axial force resulting from the vertical excitation calculated using the model featured in Figure 7.6. Thus, a different P-delta correction force was calculated at each time step to accommodate the fluctuating total axial load from the gravity and the vertical excitation. The solution in the vertical direction assumed a bi-linear force-deformation of the interacting column-bent cap-box girder system as shown in Figure 7.6. This approximation aimed at capping the resulting vertical force at a certain limit that was dictated by the results of the vertical pushover and triaxial time history DIANA pre-test analysis. The capping value used for the vertical capacity of the system, $P_{capping}$, was ~350 kips as found from the DIANA results previously discussed in Chapter 3.

The P-delta correction was applied only in the HS tests up to 100% scale. Thus, the larger scale tests at 125%, 150%, 175%, and 200% ground motion scales, which were conducted only in the transverse direction due to the test setup limitations, did not include the P-delta correction. That is to avoid the resulting tension from the axial force fluctuation at larger scales of the vertical excitation during some time steps, i.e. P-delta correction was not applied for the runs when P_g + min (P_{ve}) < 0, i.e. tension. The developed tension axial force would reverse the correction component and cause a stiffening effect in the feedback. A future study that focuses more on identifying all the possible consequences of incorporating the P-delta effect might be useful. However, in this study, the main objective of the HS tests was the bent cap beam response and the box-girder contributions. Thus, the P-delta effect was not incorporated at the larger scale runs to avoid the influence of any factors that are not fully understood such as the effect of the column subjected to tension due to this effect.
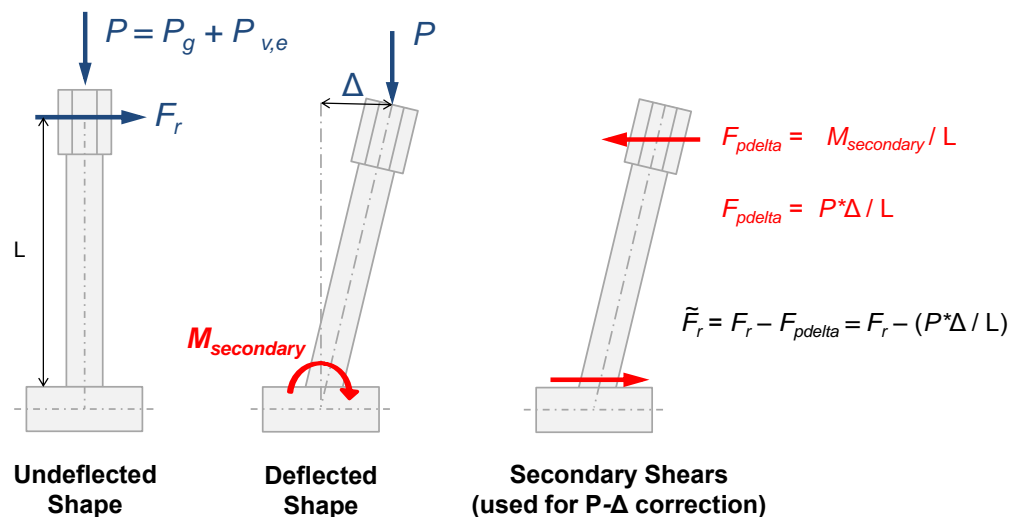
Figure 7.5 Schematic representation of the P-delta (P-Δ) correction

256
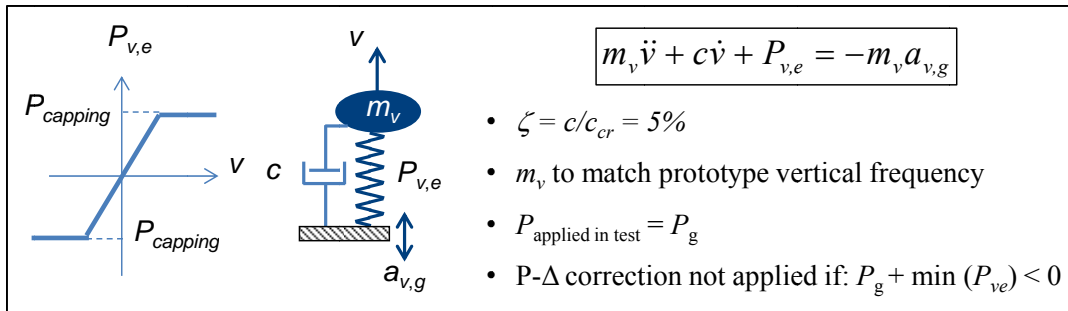
Figure 7.6 Computational model used for including vertical excitation in the P-Δ correction

7.3   HS NEW DEVELOPMENTS

To properly connect all the HSS components discussed in the previous section, a robust communication loop is indispensable. In a general sense, the readily available OpenFresco software comprised the biggest part of the necessary middleware needed for connecting the FEA software and the experimental control and DAQ systems as illustrated in Figure 7.7. On one hand, the OpenFresco lacked the needed experimental setup that performs the specific geometric transformations between the global DOF and the local DOF of the lateral actuators per the required setup in this study. Thus, implementing a new experimental setup object in OpenFresco was the first required development to achieve the sought HSS. On the other hand, to avoid using expensive shared-memory network cards, such as SCRAMNet, to communicate with the controllers, a practical way of utilizing inexpensive TCP/IP Ethernet connections was another objective sough in this HSS. A generic TCP control was already available in OpenFresco, However, a middleware that utilizes such TCP connection to communicate the commands to the controllers was required. The Pacific Instruments (PI) DAQ software was modified to encompass a new module that can integrate the networking capabilities of the DAQ console along with the programmable DSP card to achieve the desired middleware. The new PI interface was the second development achieved through this part of the study. The two developments are placed along the HSS flowchart shown in Figure 7.7, and more details about these two developments are presented in the following two subsections.
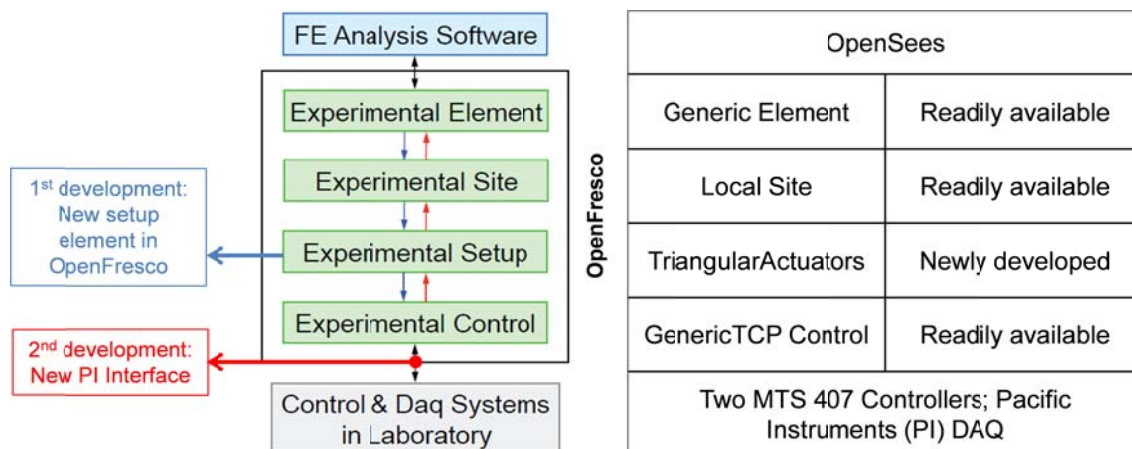
Figure 7.7 Overview of the HSS using OpenFresco and the new HSS developments

7.3.1 Development I: OpenFresco New Experimental Setup

The *ExperimentalSetup* is one of four main classes that compromise OpenFresco. The transformation of the prescribed boundary conditions from the local or basic element DOF of the experimental elements into the actuator DOF of the transfer system is the first core task of the *ExperimentalSetup* class. Similarly, the transformation of the work conjugates measured by transducers and load cells back to the experimental element DOF is the second core task of the *ExperimentalSetup* class (Schellenberg 2009). For the sake of the HS tests considered in this study, the two horizontal actuators used for applying the lateral load were arranged in a planer triangular configuration. A new *ExperimentalSetup* object was required in OpenFresco to perform the geometric transformation between the two model (global) DOFs, designated as x and y, and the two actuators (local) DOFs, designated as 1 and 2, as shown in Figure 7.8. The sough transformation is applied to the computed displacements such that displacement command readily in each actuator DOF is delivered to the corresponding controller. Similarly, the received force feedback in each actuator DOF is transformed to the x and y DOFs before passing it to the FE software to proceed with the next step calculations. The "TriangularActautors" object was successfully developed and implemented in an updated version of OpenFresco. The TCL syntax input for the new experimental setup is as follows:

expSetup TriangularActuators *$tag* -control *$ExpControltag $A1 $A2 $B1 $B2 $C1 $C2*

where *$ExpControltag* is the defined tag for the used experimental control object, which is the GenericTCP in this case, and *$A1, $A2, $B1, $B2, $C1,* and *$C2* are geometric input parameters that describe the relative locations of the two actuators as identified in Figure 7.8. The developed setup element was debugged and implemented in OpenFresco, which was compiled into an updated version that encompass the new setup. Further verification of the geometric transformation achieved through the newly implemented experimental setup element was conducted as discussed in the next section.
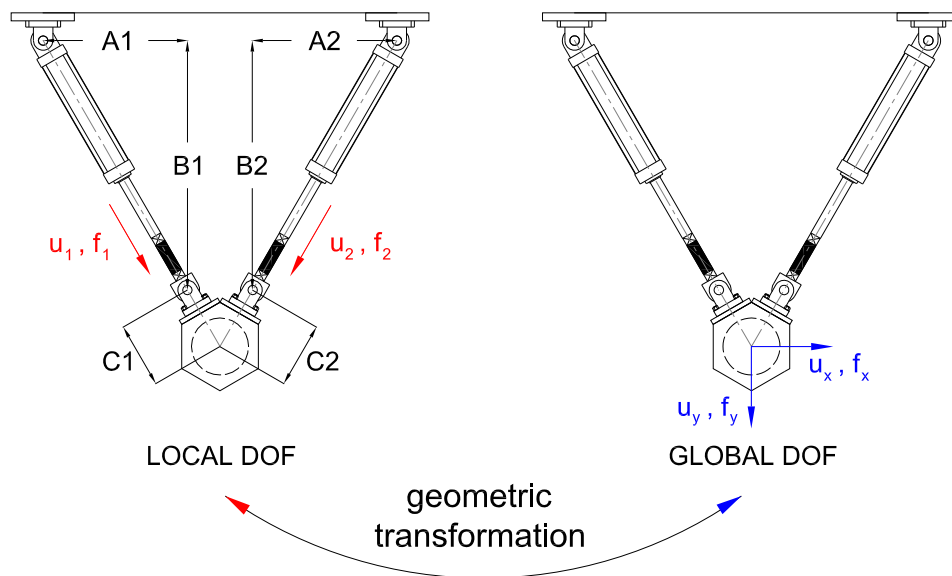
Figure 7.8 Input displacement and measured force feedback geometric transformation between the model global DOF and the actuators local DOF

258

7.3.2 Development II: New PI Interface

The central development achieved through this part of the study is a practical middleware between OpenFresco and the controllers. This interface is built into the PI DAQ system. The development was achieved through various collaborations with the staff at the Structures Laboratory at UC Berkeley. The final product consists of two related parts: (1) Microsoft Windows application customized from the PI DAQ software, and (2) PI test file containing specific PI6042 DSP routines. A more detailed description along with the main purpose of each of the two implemented interface pieces is presented here.

7.3.2.1 Microsoft Windows Custom Application

The Microsoft Windows application, namely PI660C UCB HybridSim interface, is a heavily modified version of the original PI660C DAQ program. The modifications include the addition of a TCP communications interface, an OpenFresco command interpreter, and a raw data format handler and translator. The main purpose of the developed new PI interface is to exchange displacement and force vectors, from 1 to 5 DOF, with OpenFresco over an Ethernet TCP/IP connection. Thus, this application is responsible of receiving the displacement vector from OpenFresco and passing it through the DSP routines to the controllers. In addition, it receives the force feedbacks from allocated memory locations and send them back to OpenFresco. All the operations performed through this part of the interface utilize data in the actuators DOF. The geometric transformation to the global DOF for solving the equations of motion under the responsibility of OpenFresco through the new *ExperimentalSetup* class, as previously discussed.

A screen shot of the PI660C UCB HybridSim Microsoft Windows application is shown in Figure 7.9. The figure shows the implemented module that handles the HS mode and sets its parameters. A set of the parameters that can be assigned beforehand are shown in Figure 7.10. All the parameters are considered input for the DSP routines that are called through the PI application. Because the interface can exchange data from up to 5 DOFs, a span definition is required for each of these 5 DOFs for control purposes. The rate of loading, defined in terms of the maximum velocity, is one of the parameters input shown in Figure 7.10. A maximum velocity is defined rather than a constant velocity because based on the number of controlled DOFs, one actuator might have to slow its velocity to match other actuators motion, which is discussed in more details in the section of the verification tests. Finally, two additional options that are still under development, but were not needed for the tests conducted in this study, are the super pipeline mode and the pipeline predict. These modes aim at minimizing the communication delays for the prospect of real-time HS application. However, this part of the ongoing development is out of the scope of this study and is not discussed further here.

7.3.2.2 PI6042 DSP routines

The DSP routines are responsible for the low-level, high-priority, and time-sensitive tasks. The main purpose of these routines is the motion interpolation and data generation tasks. Additionally, the DSP routines are responsible for data acquisition hardware handling, such as sending analog outputs or receiving analog inputs for reporting via the USB data link interface to the computer where the new PI interface is running. The DSP program code is uploaded via a USB link from the control computer to the PI6042 DSP cards residing in the PI6000 chassis,

shown in Figure 7.11, and executed once per data acquisition scan, which was set at 10 milliseconds intervals in this study.
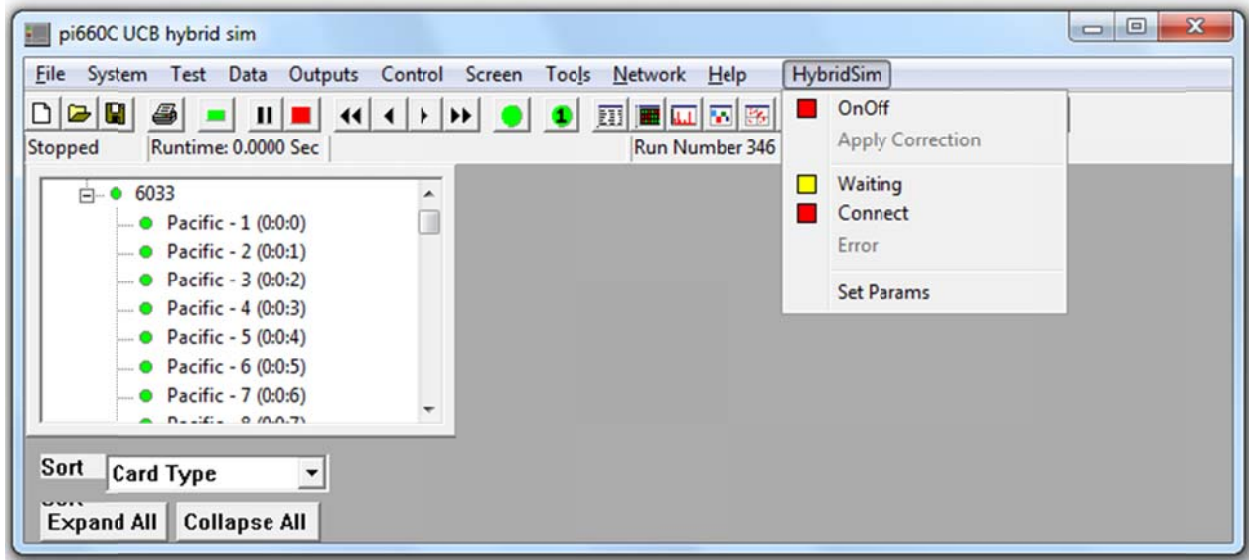
Figure 7.9 Screen shot of the developed new PI interface with the added HybridSim module and options
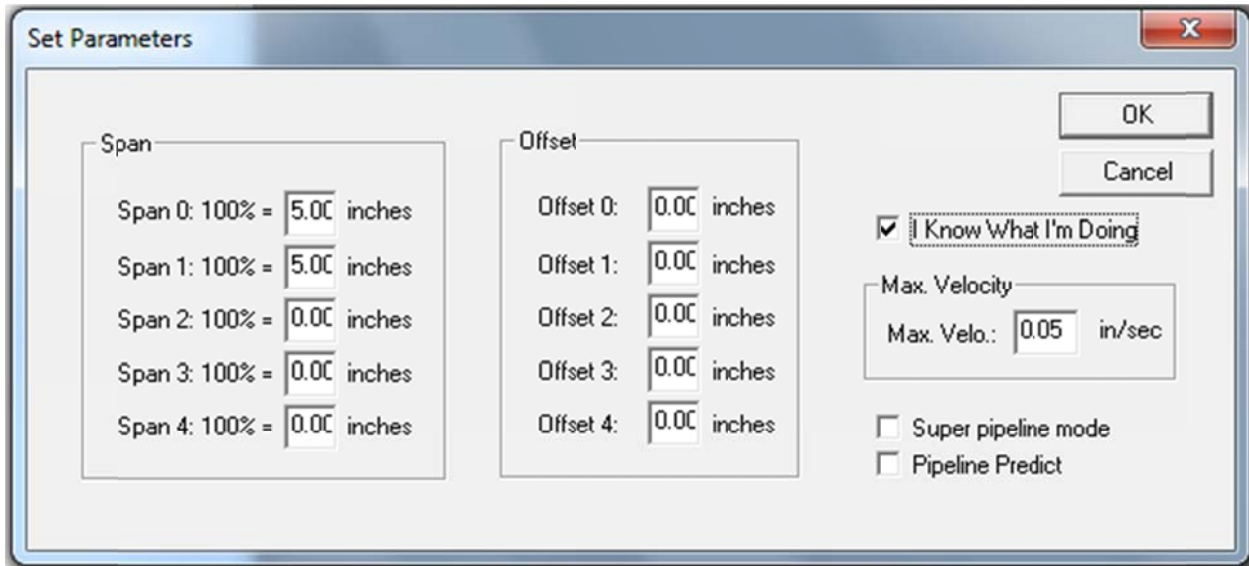
Figure 7.10 Screen shot of the HS parameters setting used in the new PI interface

The PI6042 DSP routines were written in a Reversed Polish Notation (RPN), which is a close variant to both Assembly language and the Hewlett-Packard calculator macro programming language. The RPN routines are executed once per data acquisition scan cycle at the requested sampling rate. For proper operation, the sampling rate required for defining the actuators path velocity was set to 10 milliseconds for the HS trials and tests conducted in this study. The RPN routines, called by the PI660C UCB HybridSim interface, are executed on the PI6042 DSP card sequentially at every data acquisition scan. One of the main functions of these routines is to interpolate the final end-displacement at a given time step, as received from

260

OpenFresco via the new PI interface, and deliver the interpolated calculated signal to the MTS 407 controllers. The physical connection for the interpolated signal transfer to the controllers is a standard BNC to BNC cable where one end is connected to the DSP card in the PI chassis, and the other end is connected to the controller as shown in Figure 7.12. It is worth noting that the capabilities of the PI6042 DSP card were utilized in a previous study to conduct real-time HS tests on a shaking table configuration for electrical disconnect switch single post insulators (Mosalam and Günay 2014). Specialized RPN routines that were programmed to solve the governing equation of motion in the study documented in (Mosalam and Günay 2014), were successfully executed at 1 millisecond intervals, which allowed the HS to take place in real-time.
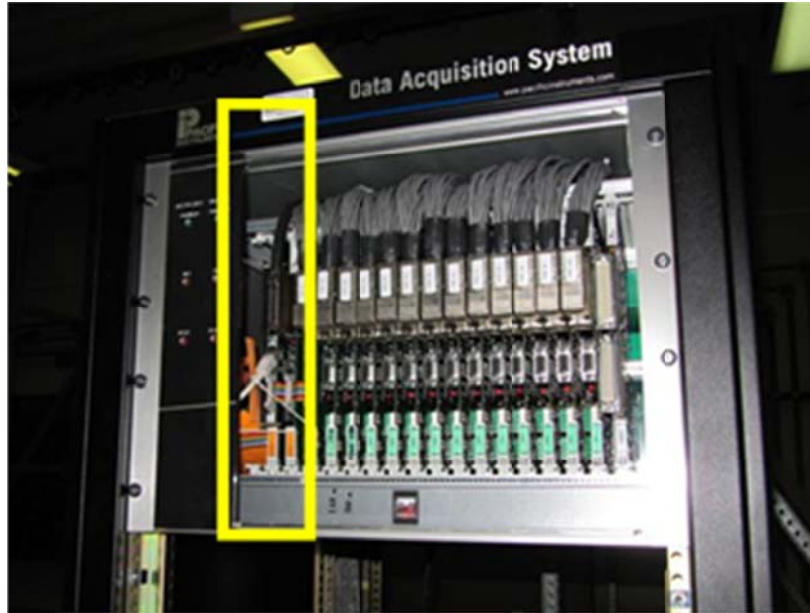
Figure 7.11 PI data acquisition system and DSP card (identified by the light rectangle box) used in the HSS
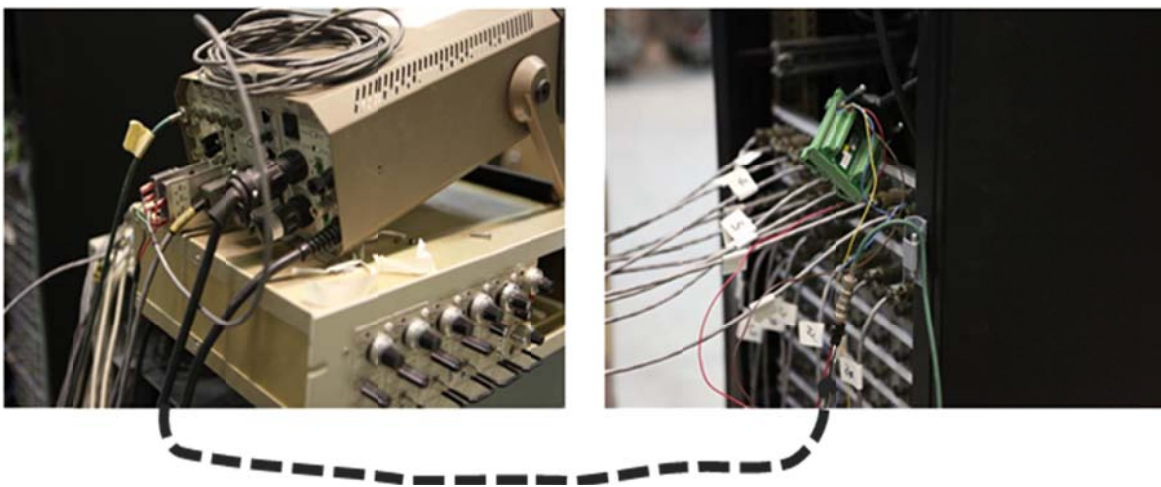
Figure 7.12 Physical connection for sending the interpolated calculated displacement input from the DSP to the MTS 407 controller

7.4 HSS VERIFICATIONS

The main components and developments used for conducting the HS tests in this study were identified and discussed in the previous sections. To confirm the performance of the implemented developments and validate the HSS for testing the retrofitted SP2, several trials and verification tests were conducted. The verification tests started with network protocol analysis, then utilized single and double free actuators, i.e. not attached to any physical specimens, as discussed in this section. Full HS tests that utilized the repaired SP1 to validate the whole HSS were finally conducted as discussed in the next section.

7.4.1 TCP/IP Network Stack

Numerous performance and characterization tests were performed on the TCP/IP performance between the OpenFresco/OpenSees platform and the new PI660C UCB HybridSim interface. These characterization tests were performed directly by using the Wireshark network protocol analyzer program. Wireshark attaches directly to the network software stack and records all the Ethernet packets traversing the Ethernet interface, which is commonly referred to as "sniffing". By looking at the timestamps and decoding the packet payloads, the traffic flow and timing were understood. A screenshot of the Wireshark sniffing of an established Ethernet TCP/IP connection in the developed HSS is shown in Figure 7.13.

The Ethernet TCP/IP network transactions flowing through a preliminary established connection between the OpenFresco platform and the new PI interface was analyzed. The timing data from the Ethernet transactions first indicated a latency of approximately 216 milliseconds. In order to reduce latency, the transmit buffer of OpenFresco was resized to be an integer multiple of the payload size of the Ethernet frame, i.e. the OpenFresco variable *OF_Network_dataSize* was modified from 256 to 365 such that on every network transaction, two totally filled Ethernet frames were utilized. Adjusting the OpenFresco packet size reduced the latency to 70 milliseconds. Due to the slow nature of the loading rate of the test in this study, the 70 milliseconds latency were found insignificant in altering the desired HS communication. For extension to real-time HS, this latency needs to be revisited.

262
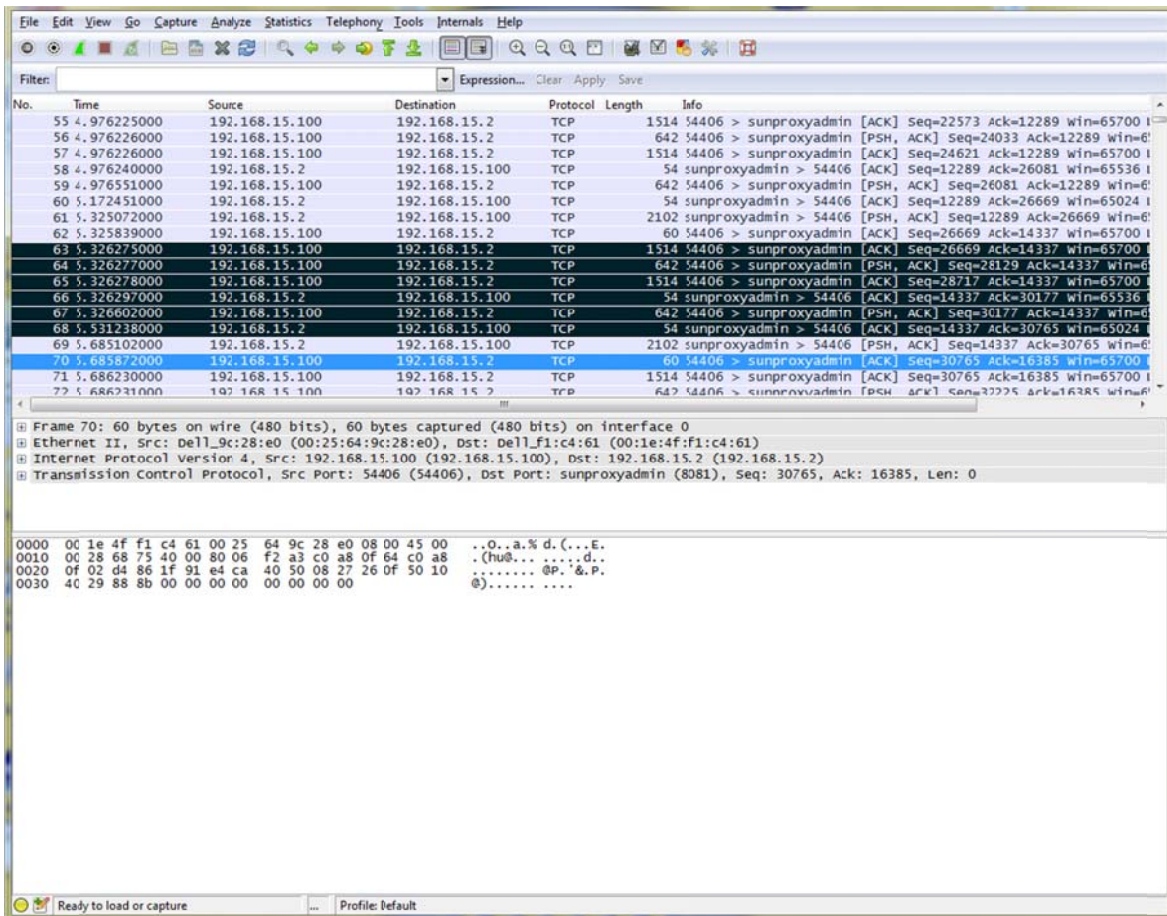
Figure 7.13 Screenshot of the Ethernet TCP/IP network packet analysis using Wireshark

7.4.2   Single Actuator Tests

To verify the robustness of the communication between OpenFesco and the controllers via the newly developed PI interface and DSP routines, HS trial tests were conducted on free actuators detached from the specimen. A single actuator was used first along with a large multi-DOF computational model to test the communication loop between all components of the HSS. The setup for the free actuators is shown in Figure 7.14. Two-way communication is necessary in HS; one way is for sending the displacement command and the other is for receiving the force feedback. A free actuator that is not attached to any specimen will report zero force feedback or only the load cell noise. Thus, for the free actuator trials, a multiplier (stiffness) of the displacement command was fedback to the DSP and DAQ as a virtual force feedback. The constant multiplier reflected the stiffness of a hypothetical linear force-displacement relationship. The advantage of this virtual feedback is the comparison with pure simulation results where an elastic element with a constant stiffness replaces the actuator displacement/force feedback virtual experimental element. The computational model used for the free actuator trial was a multi-story multi-bay frame, represented schematically in Figure 7.15, where one column in the first story is either modeled using a linear elastic element or replaced by a generic simulation experimental element in HS tests. El Centro ground motion record was used for these trials as it contained several cycles with various amplitudes rather than a single large pulse. A multiplier of 2 was

263

chosen for the displacement feedback to the DSP to reflect a hypothetical elastic element with 2 kip/inch stiffness, which was compatible with the other columns in the computational frame in the hybrid model, for comparison with the pure simulation case.

Figure 7.14 Actuators detached from the specimen for conducting trial HS tests
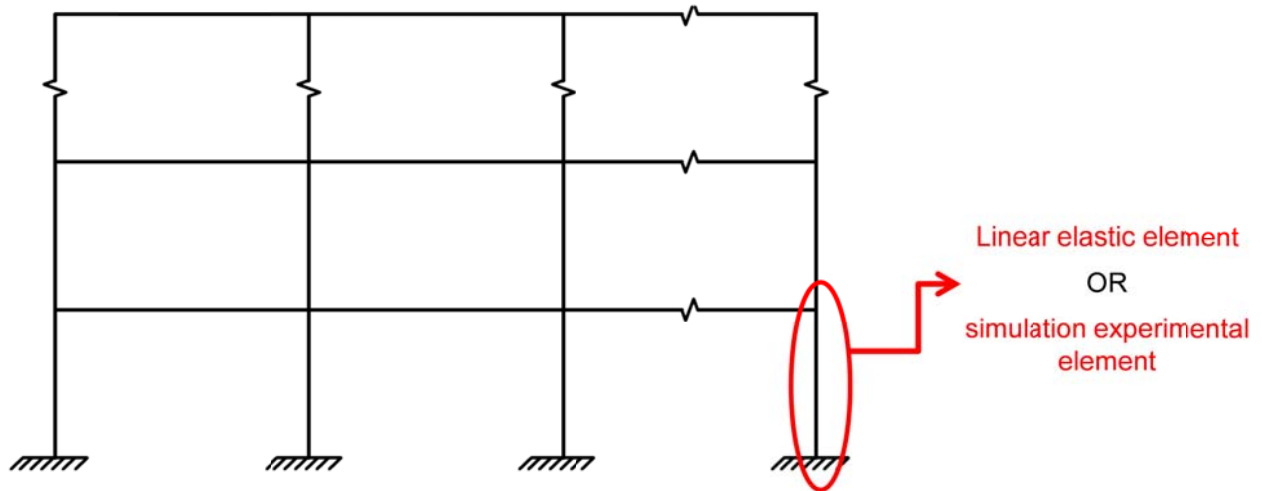
Figure 7.15 Schematic representation of multi DOF frame computational model used for HS actuators trial tests

The obtained displacement and force histories from the pure simulation were compared to those from the HS recorded data at both OpenSees and the PI DAQ in Figure 7.16 and Figure 7.17, respectively. OpenSees recorded the displacements obtained from the solution of the equation of motion at each time step along with the discrete force feedback at solution time steps only when received through the new PI interface. Meanwhile, the PI DAQ recorded the actual

command data, i.e. actuator motion, and its multiplier when received at the DSP card. In addition, the force-displacement relationships are plotted for all cases as shown in Figure 7.18 to demonstrate the constant stiffness used for the model and the case with the hypothetical feedback. The comparison shows the perfect match between the simulation and the HS tests.
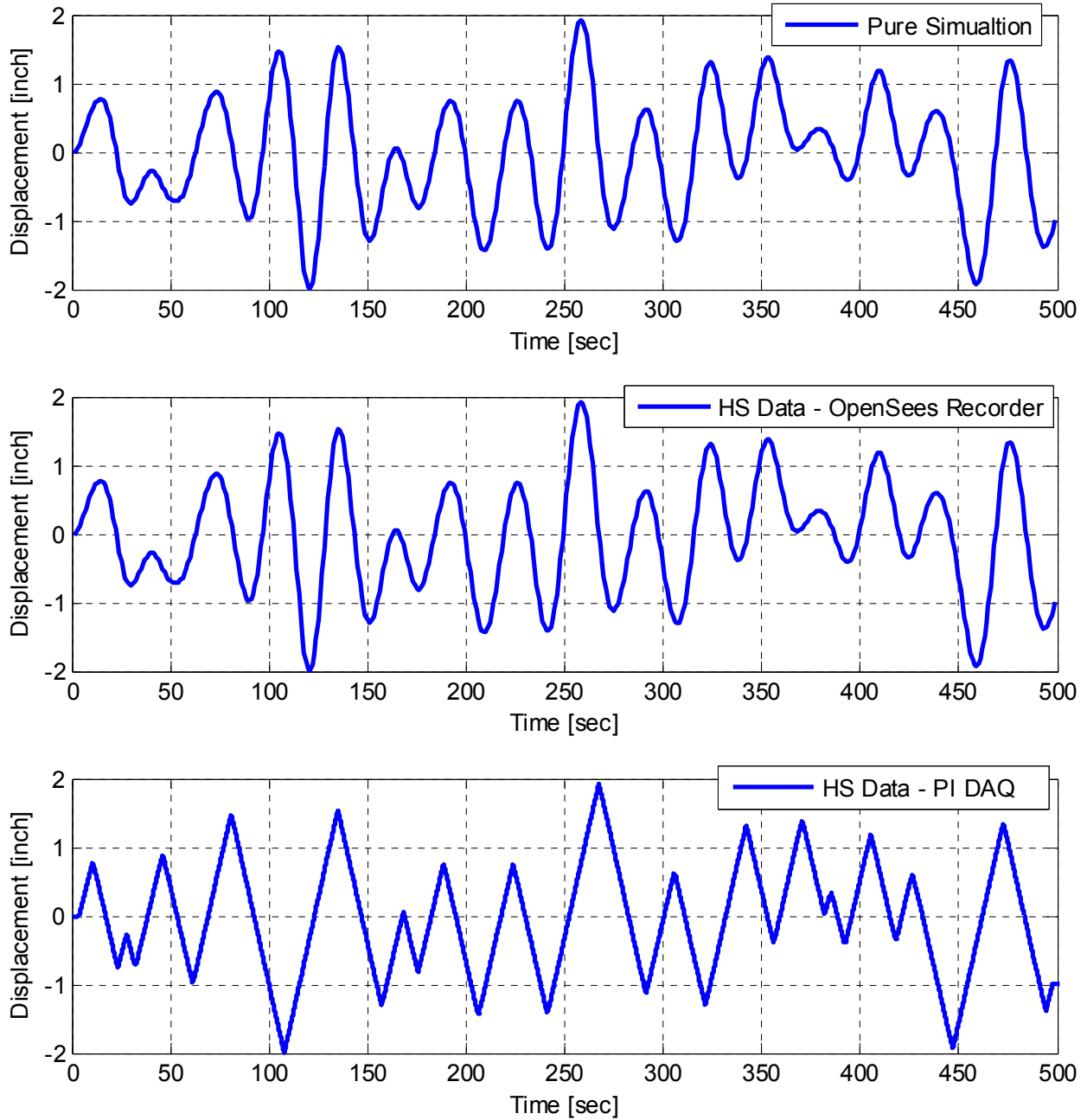
Figure 7.16 Comparison of the displacement history obtained from the pure simulation, the computed OpenSees command for HS, and the actual actuators motion obtained from HS tests using single free actuator
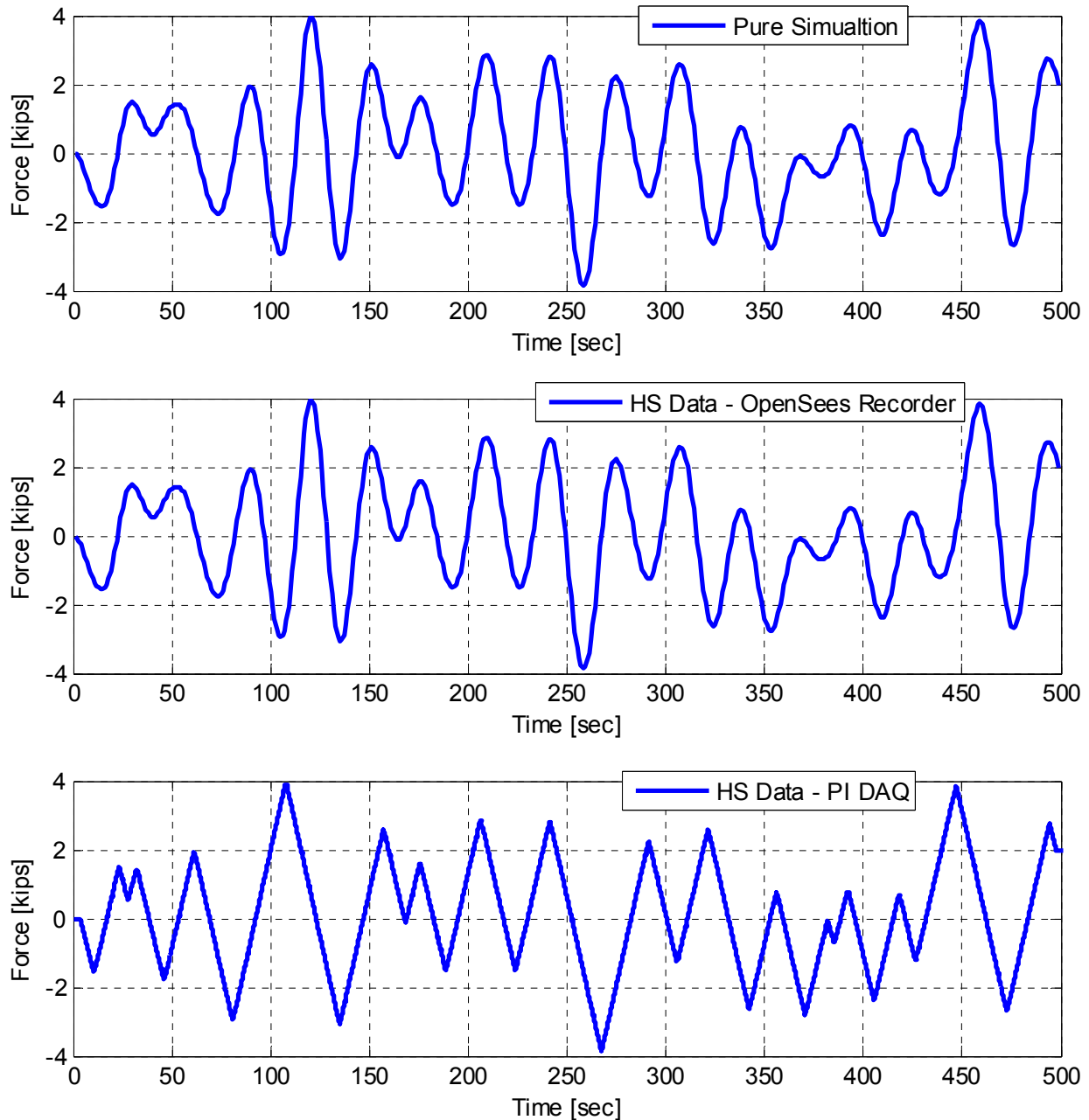
Figure 7.17 Comparison of the force history obtained from the pure simulation, the received feedback at OpenSees, and multiple of the actual actuator displacement feedback as force as obtained from HS tests using single free actuator

Despite the perfect match in the displacement amplitudes, the progression with time was different from the actual actuator motion and the OpenSees command, or pure simulation case. This is expected and attributed to the constant velocity or rate of loading used for commanding the actuator. The DSP routines were used to interpolate the received displacement command and apply it smoothly to the controller to pass it to the actuator. Thus, an obtained constant velocity would verify the communication loop and the DSP interpolation routines. Figure 7.19 shows the velocity history as calculated from the actual recorded interpolated commands. The constant

velocity at 0.05 inch/sec, which was the input rate through the PI660C UCB HybridSim parameters definition as shown previously in Figure 7.10, was successfully achieved as calculated from the actual recorded data. Therefore, the good comparison between the HS tests that used a hypothetical feedback of a constant multiplier applied to the actual command, and the pure simulation provided confidence on the accuracy of the communication loop among the different HSS components.
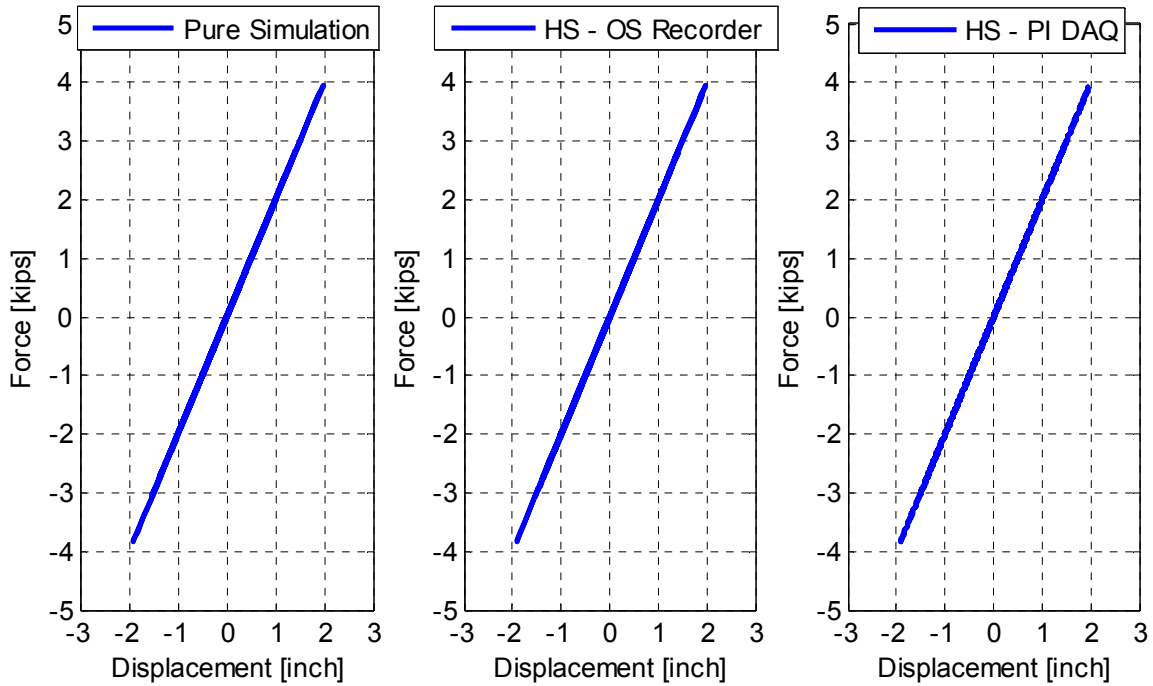
Figure 7.18 Force-displacement relationships from pure simulation and HS test data recorded at OpenSees (OS) and using the PI DAQ from HS tests using single free actuator
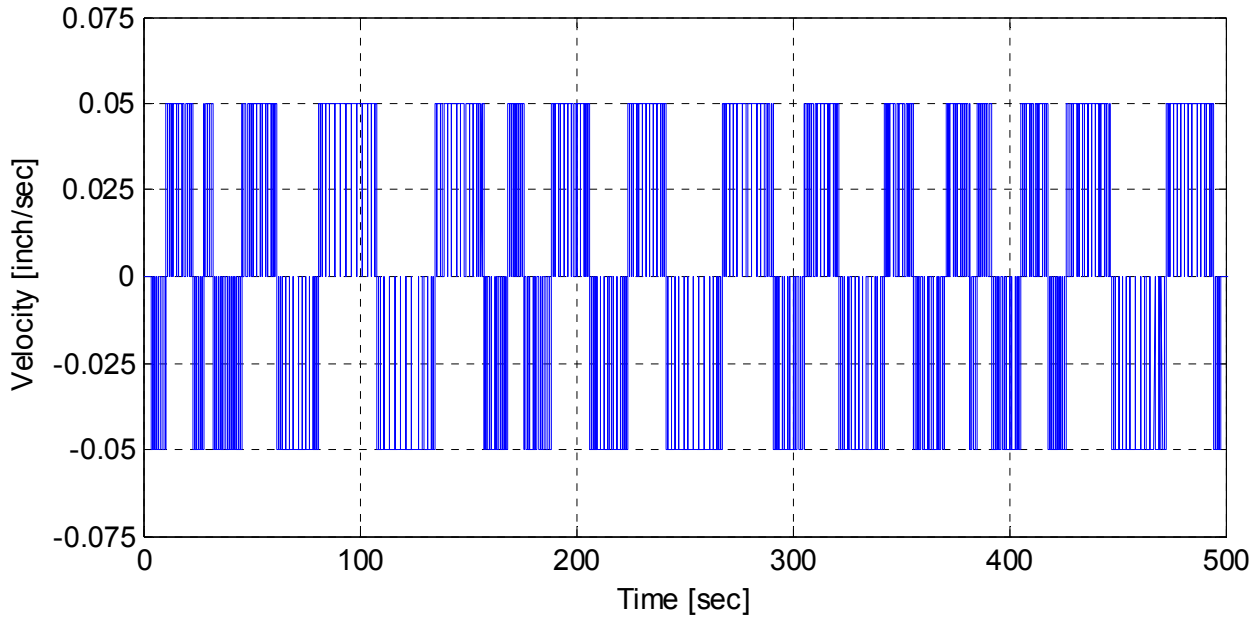
Figure 7.19 Velocity history of the actual actuator motion from single actuator HS tests

267

7.4.3 Double Actuators Tests

Similar trial tests were conducted using two free actuators setup with the actual computational model for the bridge subassemblage test specimen, i.e. utilizing the newly implemented geometric transformation setup (the TriangularActuators *ExperimentalSetup* class) in the OpenFresco/OpenSees input file. In addition, the Rinaldi ground motion considered in the actual HS tests in this study was used in these trials. The same concept of feeding back a hypothetical force that is 2 times the actual displacement command was used in these trials as well. These tests aimed at verifying the correctness of the newly implemented geometric transformation and the DSP routines in interpolating the displacement command for two actuators simultaneously. To verify the geometric transformation, the input of the OpenFresco "TriangularActuator" command was set up in a way that rendered each of the actuators inclined with a 45 degrees angle, e.g. *A1* and *B1* identified in Figure 7.8 were set to similar values. In this geometry, if a global transverse-only motion (u_x in Figure 7.8) is required, the two actuators should have identical input along the local DOFs. On the other hand, if a longitudinal-only motion (u_y in Figure 7.8) is required, the two actuators should have same magnitude but opposite direction local DOFs input. This anticipated geometric transformation was accurately verified as shown in Figure 7.20 through Figure 7.27. In subsection 7.4.3.1, the figures from the transverse-only case are shown. Figure 7.20 and Figure 7.21 compares the OpenSees displacement command and received force feedback for the two actuators with the actual PI DAQ recorded data, respectively. The force-displacement relationships are also compared in Figure 7.22 to demonstrate the communication effectiveness reflected into the shown linear relationship. To emphasis that the two actuators had identical motion as intended, the velocities for both actuators were calculated and plotted in Figure 7.23. Both actuators moved with the input constant velocity of 0.05 inch/sec, which verifies the capability of the DSP routines to interpolate the command for two actuators simultaneously.

Subsection 7.4.3.2 displays the plots for the longitudinal-only trial tests. The well-matching amplitudes from the OpenSees generated displacement command and the actual actuators motion is shown in Figure 7.24. Similarly, the hypothetical force feedbacks that were twice the actual displacements are similar to what OpenSees eventually received at each time step for solving for the new time step as illustrated in Figure 7.25. The force-displacement relationships are compared in Figure 7.26, and the calculated velocities for the two actuators are shown in Figure 7.27. The figures show that the two actuators had similar input along the local DOFs but with opposite direction (sign). This implies that the two components of the actuators motion in the transverse direction cancelled the effect of each other and hypothetically forced the actuators along a longitudinal path. Meanwhile, the velocities presented in Figure 7.27 show different signs but almost constant velocity for the two actuators as a similar magnitude of motion is commanded to each of them. While this preliminary tests verified the geometric transformation and DSP interpolation routines, a formal verification was obtained when a full HS test was conducted using the repaired SP1 specimen as discussed in the next section.

One final trial test that used the two free actuators was a generic bidirectional test. This generic case was useful in the final verification of the DSP interpolation routines rather than the geometric transformation as shown from the figures in subsection 7.4.3.3. Figure 7.28 and Figure 7.29 show the displacement command and force feedback comparison, respectively. Figure 7.30 shows the force-displacement relationship and Figure 7.31 shows the velocities of the actuators. The key observation from this test is how the actuators change their velocities

when one actuator has a longer displacement command to execute than the other. In this case, only the actuator with larger interpolated command moves at the maximum set velocity, while the other actuator slows its velocity to stay on the same spatial path of the anticipated column head where the actuators would be eventually connected. Figure 7.31 denotes when the two actuators had different command magnitude, actuator 2 moved at a slower velocity when actuator 1 was moving with the maximum 0.05 inch/sec and vice versa. This ultimately verified the DSP interpolation routines and the DSP/PI DAQ communication loop.

7.4.3.1 Transverse-only Ground Motion Input
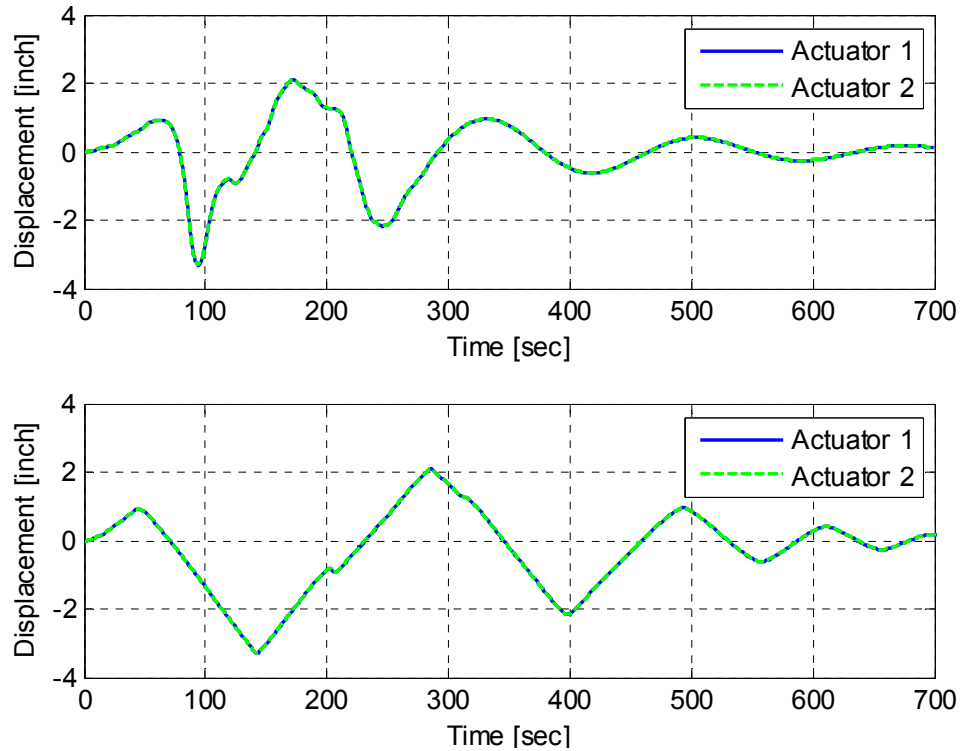
Figure 7.20 Actuators displacement history from the HS computed OpenSees signal (top) and actuators feedback from the DAQ (bottom) for transverse-only ground motion test
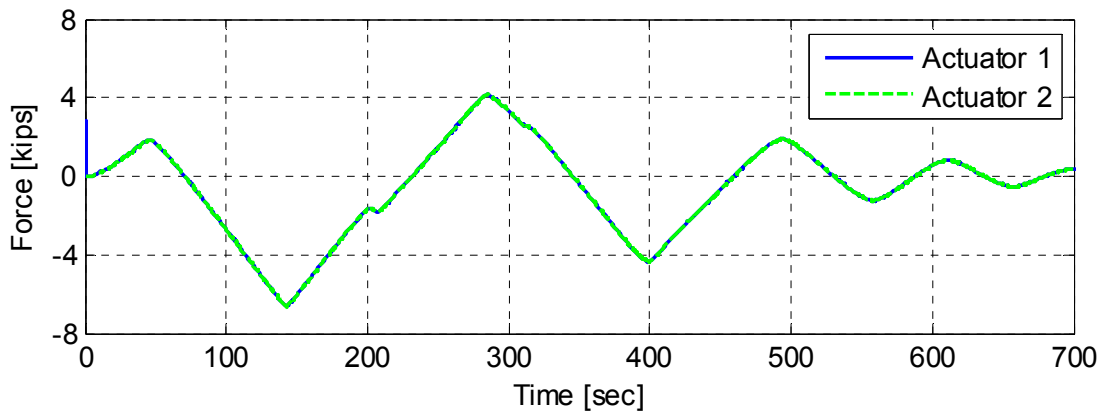
Figure 7.21 Actuators force history from load cell DAQ data for transverse-only ground motion test

269
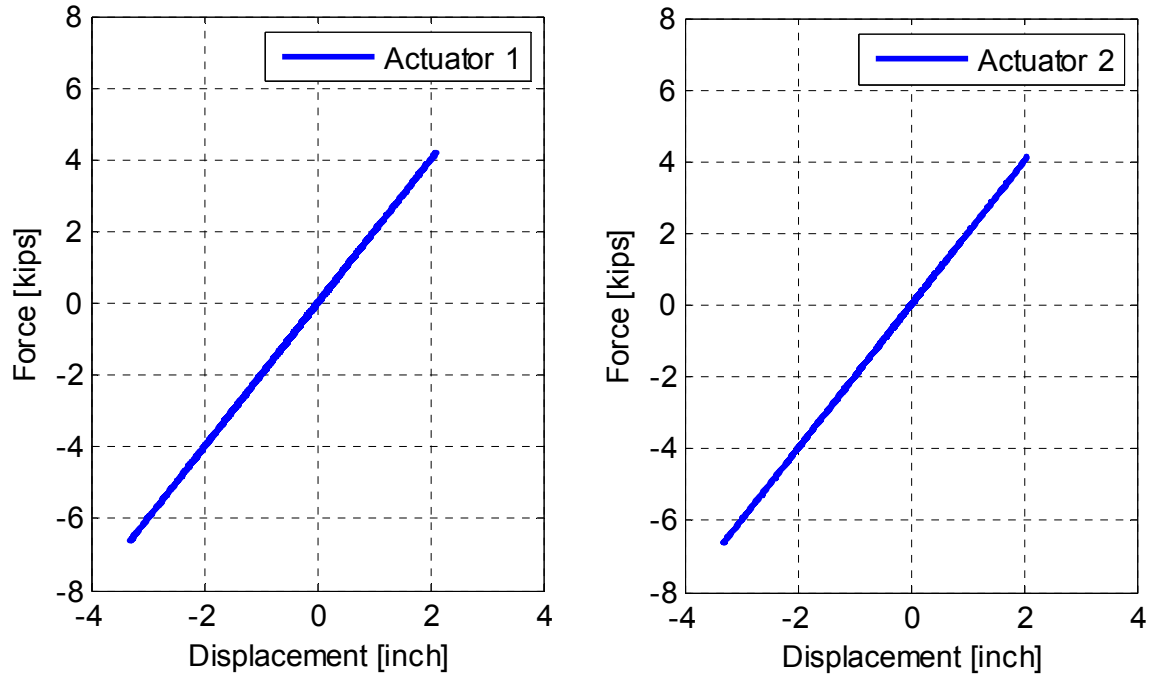
Figure 7.22 Actual force-displacement relationships obtained from the DAQ data for transverse-only ground motion test
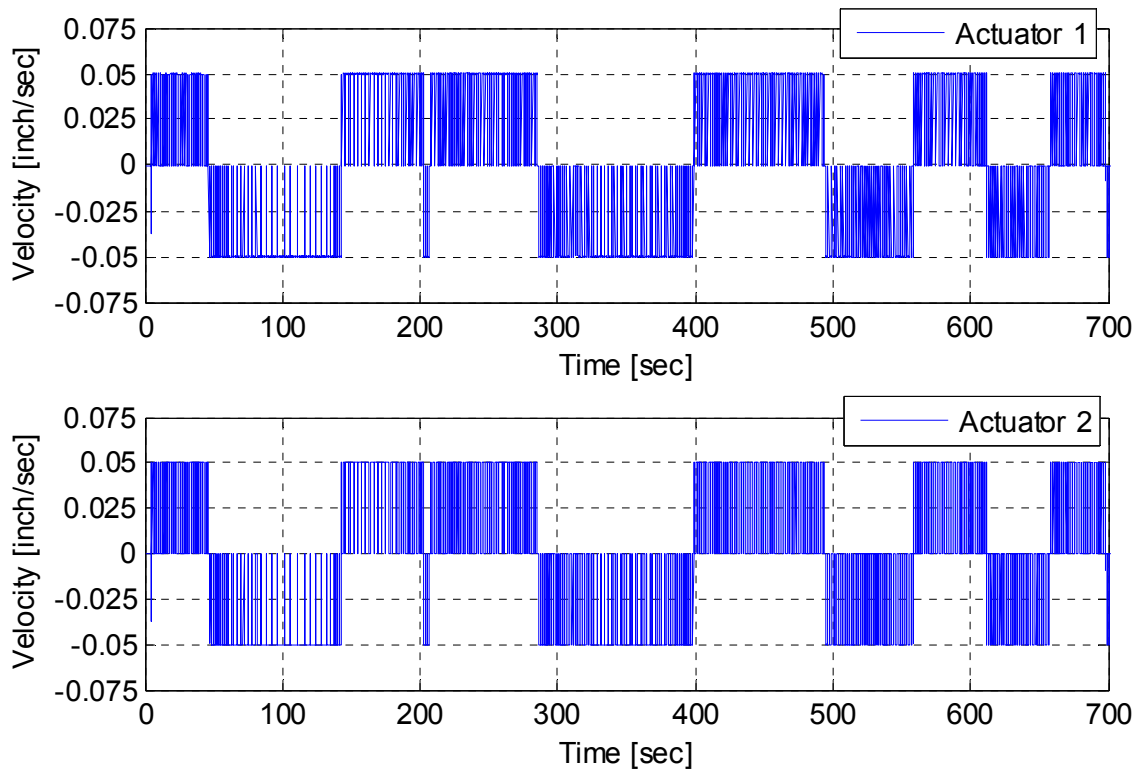
Figure 7.23 Actuators velocity as calculated from the obtained feedbacks from the DAQ data for transverse-only ground motion test

7.4.3.2 *Longitudinal-only Ground Motion Input*
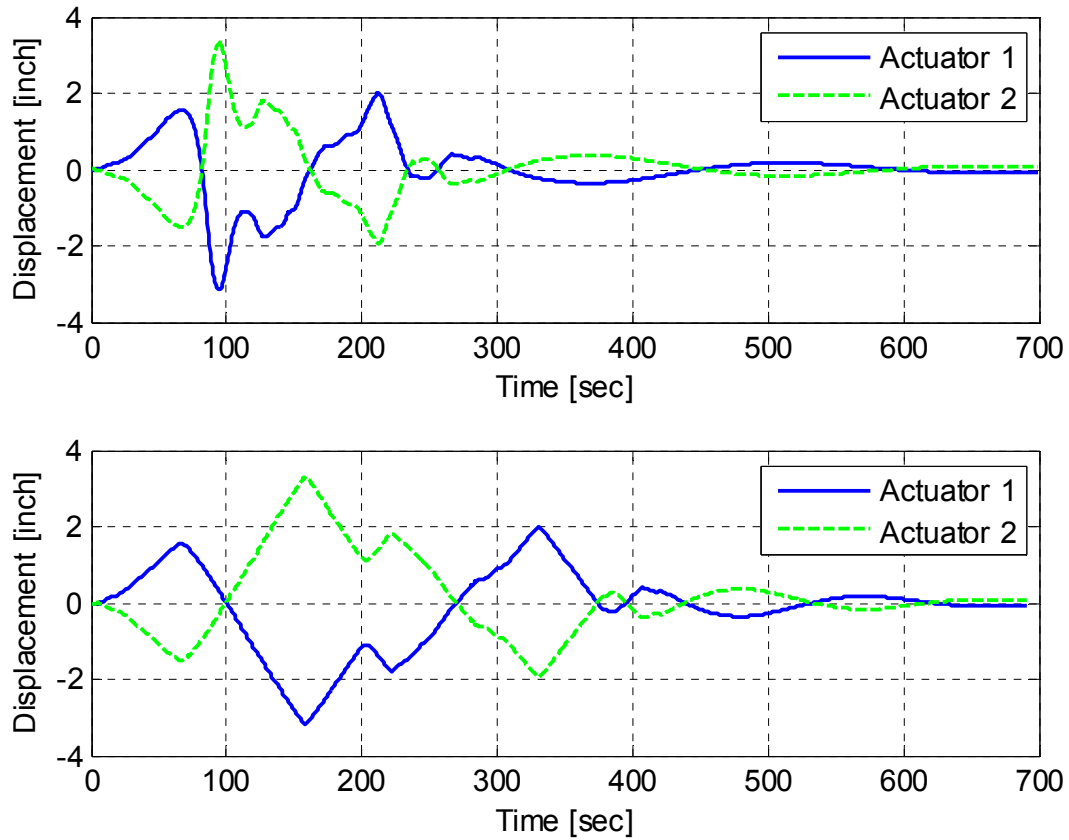
Figure 7.24 Actuators displacement history from the HS computed OpenSees signal (top) and actuators feedback from the DAQ (bottom) for longitudinal-only ground motion test
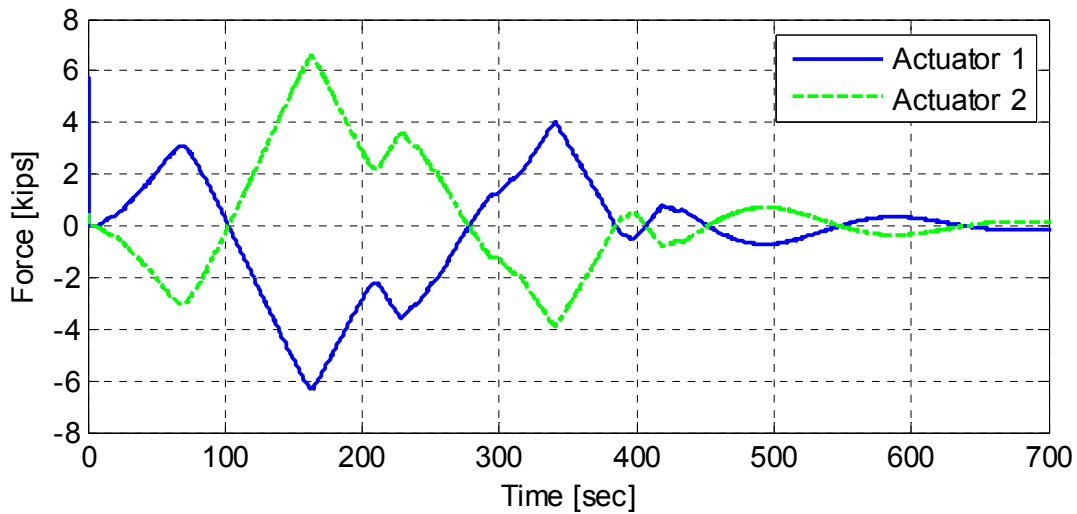
Figure 7.25 Actuators force history from load cell DAQ data for longitudinal-only ground motion test

271
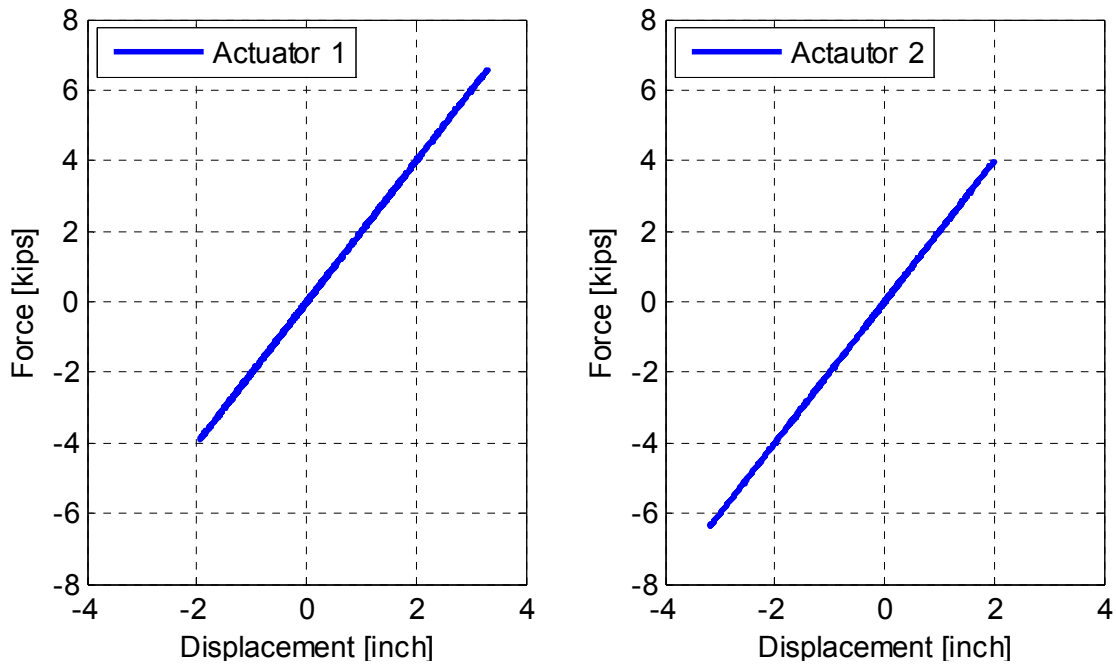
Figure 7.26 Actual force-displacement relationships obtained from the DAQ data for longitudinal-only ground motion test
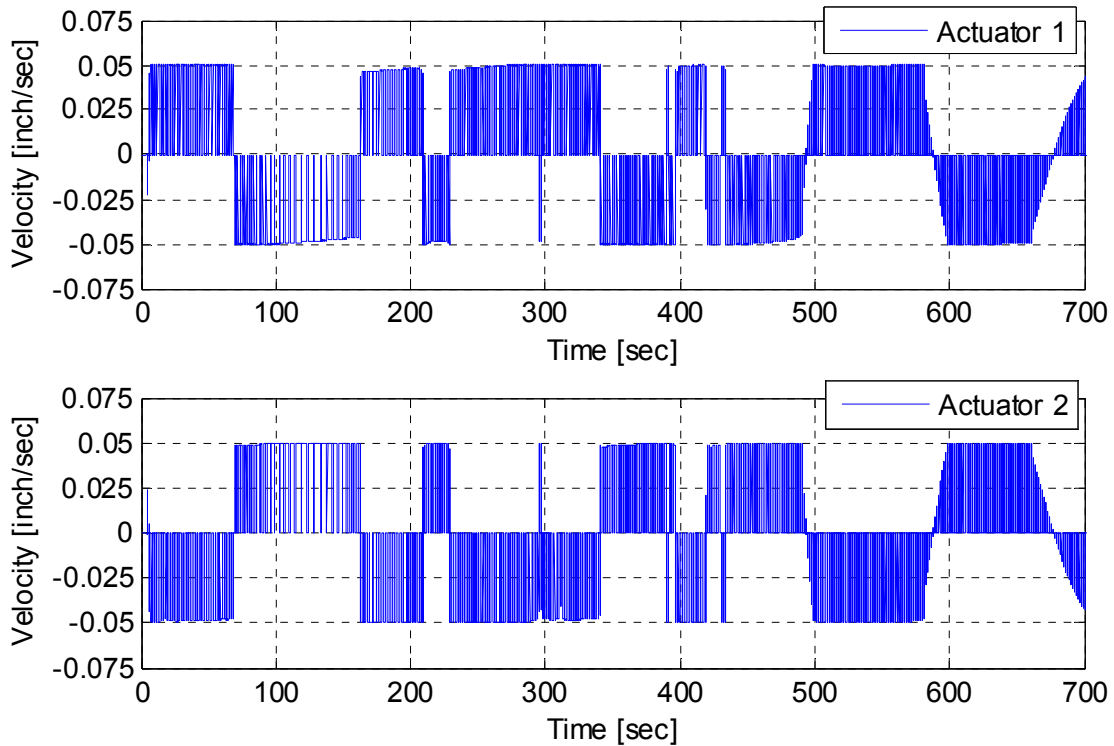
Figure 7.27 Actuators velocity as calculated from the obtained feedbacks from the DAQ data for longitudinal-only ground motion test

7.4.3.3   Bidirectional Ground Motion Input
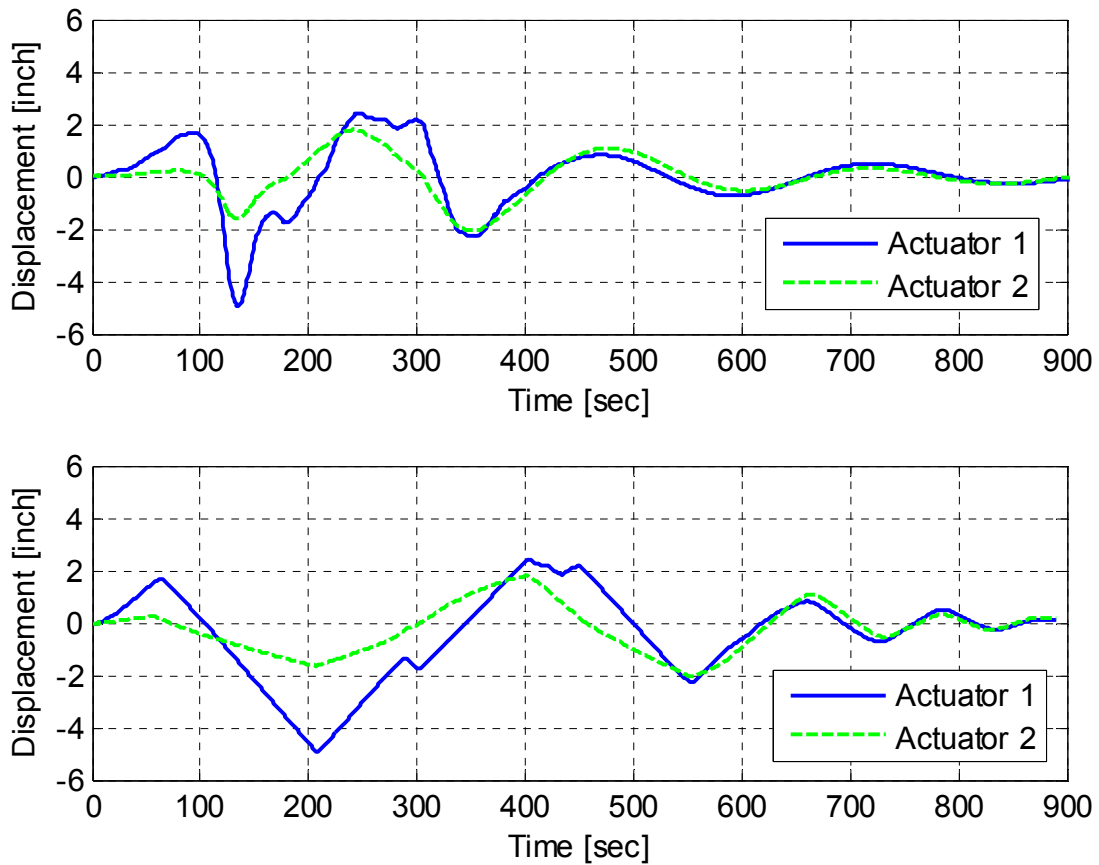
Figure 7.28 Actuators displacement history from the HS computed OpenSees signal (top) and actuators feedback from the DAQ (bottom) for bidirectional ground motion test
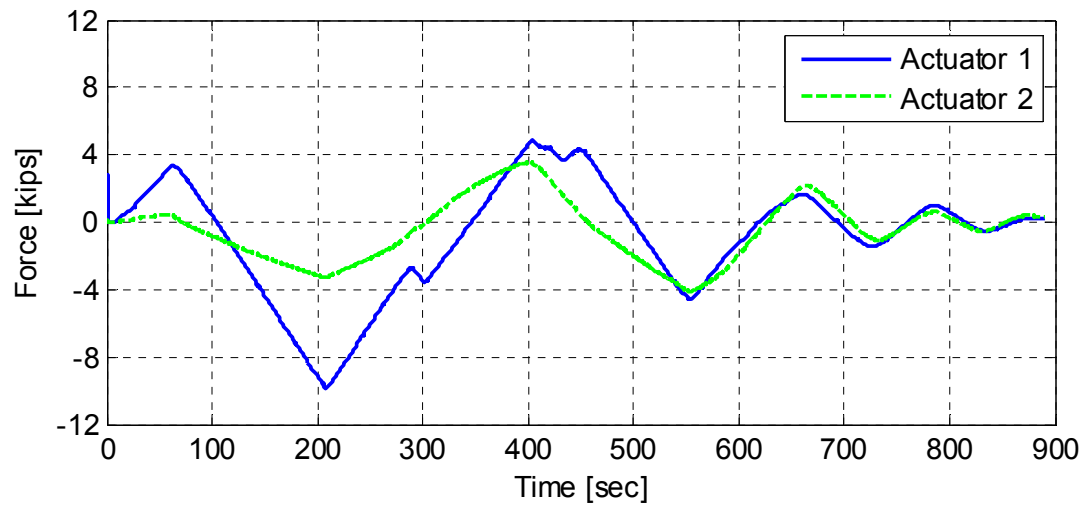
Figure 7.29 Actuators force history from load cell DAQ data for bidirectional ground motion test

273
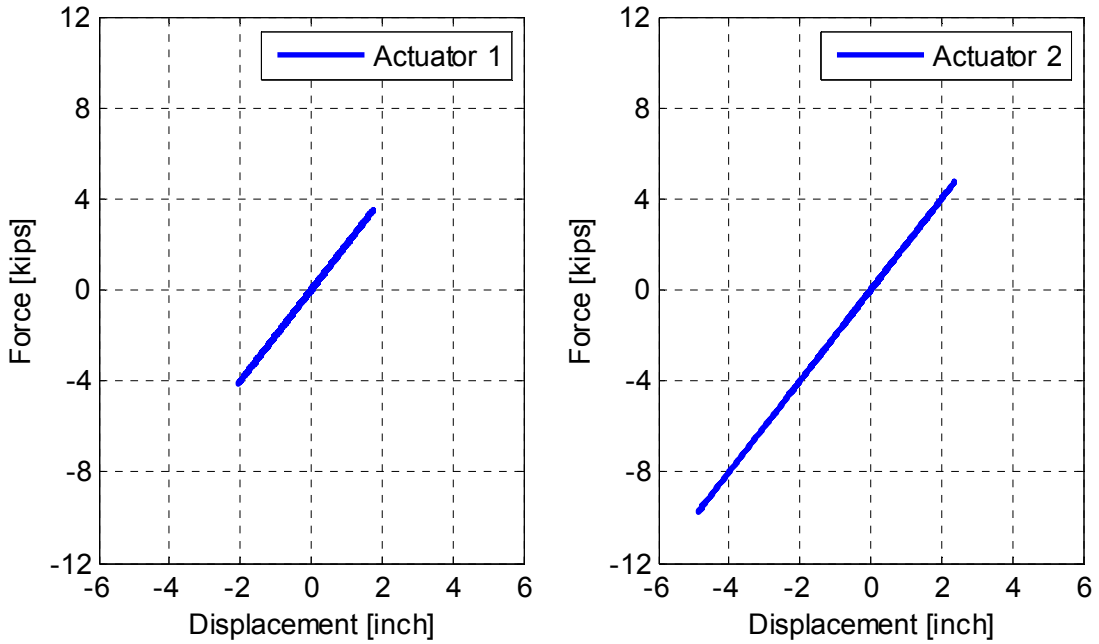
Figure 7.30 Actual force-displacement relationship obtained from the DAQ data for bidirectional ground motion test
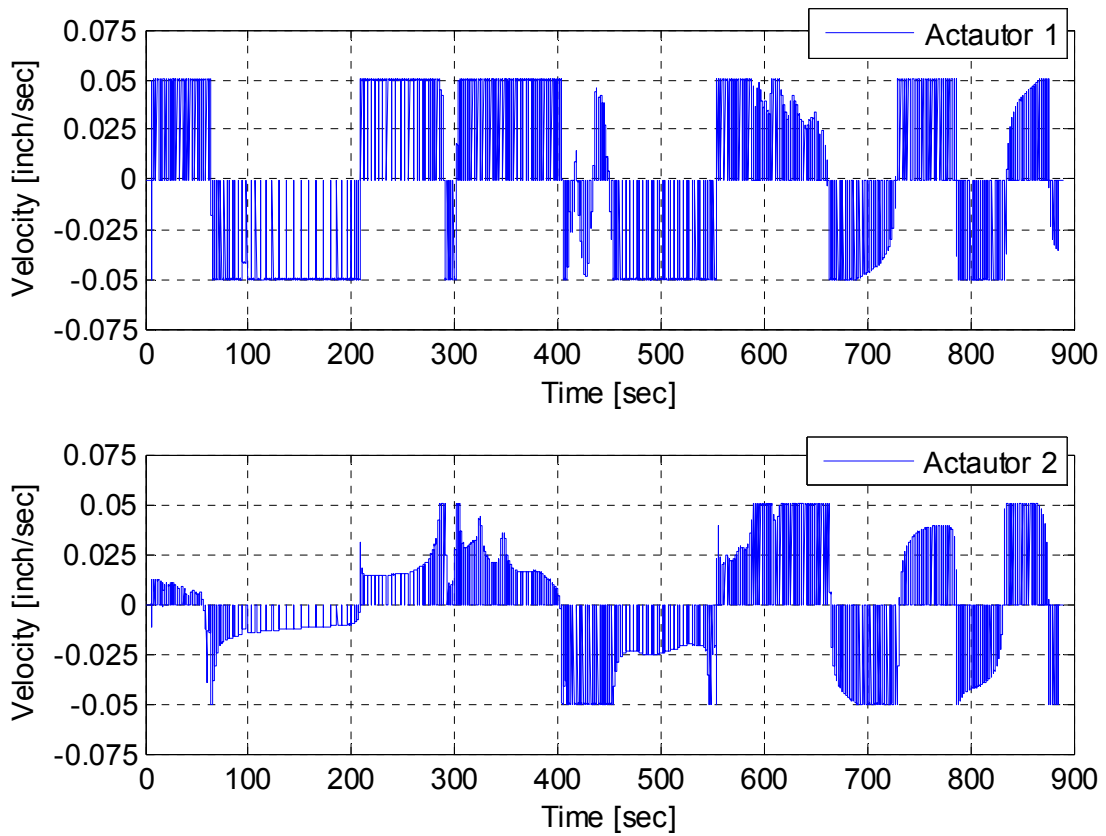
Figure 7.31 Actuators velocity as calculated from the obtained feedbacks from the DAQ data for bidirectional ground motion test

274

7.5   REPAIRED SPECIMEN SP1 HS TESTS

To complete the validation of the integrated HSS and its new developments at the Structures Laboratory at UC Berkeley, a full specimen HS test was conducted using the repaired SP1 as shown in Figure 7.32. Several HS trials with and without gravity load, and using different ground motion scales and components were conducted as summarized in Table 7-2. The main benefit of the full specimen HS tests was to validate the whole system using a true specimen with inelastic nonlinear behavior. Selected results from the SP1 HS trials that serve the purpose of the HSS validation are presented here.

Figure 7.32 Test setup used for conducting HS trial tests for the repaired SP1

Table 7-2 Summary of repaired SP1 HS tests

Test ID	Grvaity Load Level	Ground Motion	Ground Motion Scale	Components
1	0	Rinaldi	20%	Transverse only
2	0	Rinaldi	20%	Longitudinal only
3	0	Rinaldi	20%	Bidirectional
4	0	Rinaldi	50%	Bidirectional
5	10%	Rinaldi	50%	Bidirectional
6	10%	Rinaldi	80%	Transverse only
7	10%	Rinaldi	80%	Longitudinal only
8	10%	Rinaldi	80%	Bidirectional

7.5.1 50% Scale Bidirectional HS Tests

The first objective from the HS full specimen tests was to check the robustness of the developed HSS in different stability and loading conditions. For this purpose, a 50% Rinaldi bidirectional HS tests were conducted before (Test ID 4) and after (Test ID 5) applying the gravity load. The repaired SP1 was heavily tested under quasi-static cyclic loading in as-built and repaired conditions. Thus, the developed plastic hinge might provide instability if lateral loading is applied, which was checked from the HS tests comparison. Only the recorded data from OpenSees are presented in this comparison for brevity, whereas the next subsection presents the actual DAQ data for the 80% bidirectional tests.

The displacement and force responses from the 50% scale bidirectional HS tests with and without the applied gravity load are compared. Figure 7.33 shows the comparison of the computed displacement in both of the transverse (u_x) and longitudinal (u_y) directions with and without gravity load application. Additionally, the transverse (f_x) and longitudinal (f_y) force feedbacks received at the OpenSees side, after they went through the PI interface and the OpenFesco geometric transformation, are shown in Figure 7.34. The displacements history suggests that when the gravity load was not applied, the system oscillated around a shifted displacement due to the almost zero force feedback received. The HS computational model solution and load application from a full test gave confidence about the robustness of the HSS system even with almost zero feedback. Such zero force feedback can be seen in Figure 7.34, where the damaged column did not provide any resistance before the gravity load was applied.
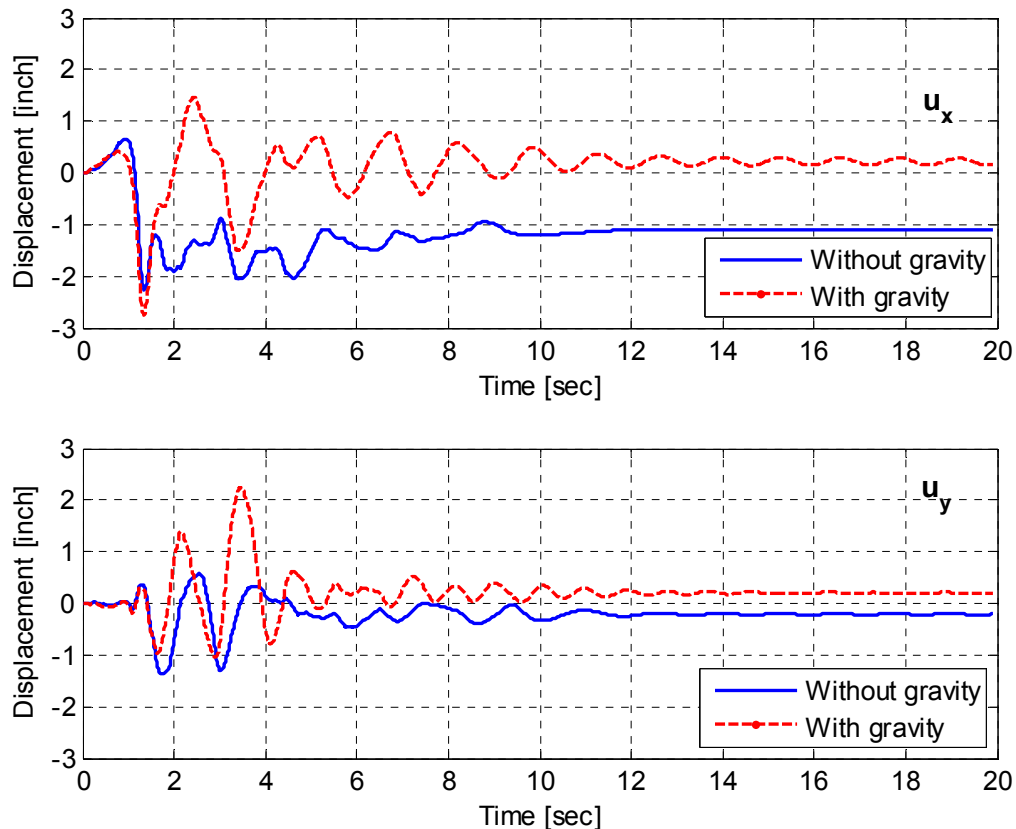
Figure 7.33 Comparison of the OpenSees computed displacements for SP1 HS subjected 50% Rinaldi bidirectional loading with and without the gravity load applied
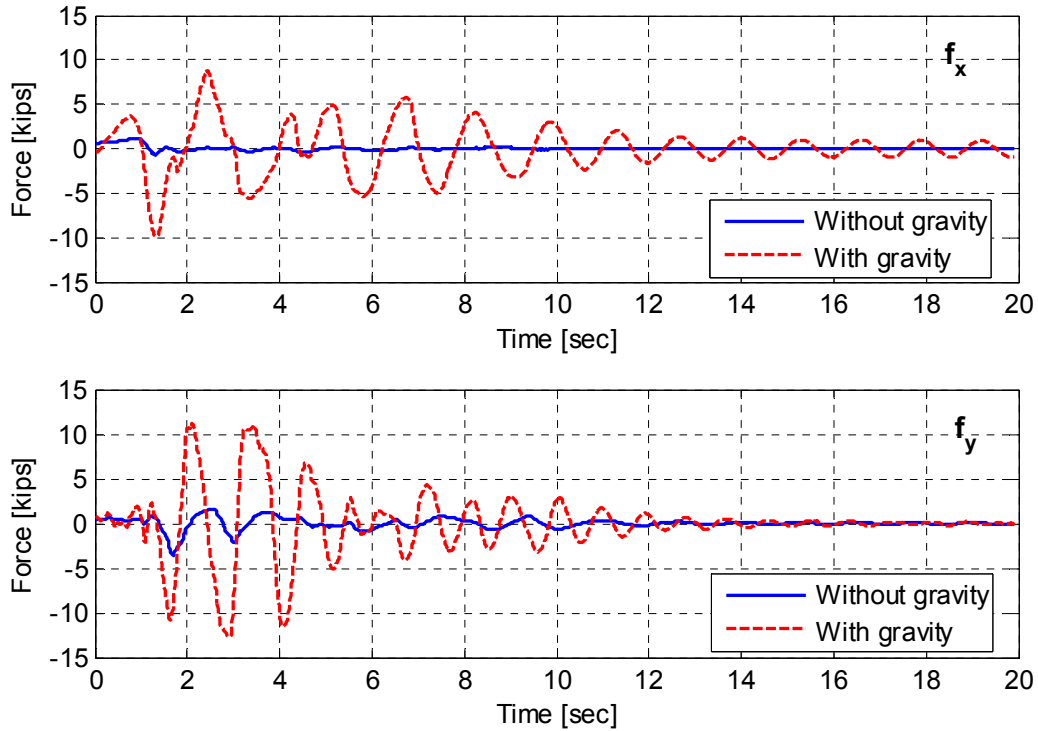
Figure 7.34 Comparison of the force feedbacks received at OpenSees for SP1 HS subjected to 50% Rinaldi bidirectional loading with and without the gravity load applied

As also illustrated in Figure 7.34, when the gravity load was applied, the increased compressive stresses in the column led to engaging partial lateral resistance from the column again. Reasonable maximum force feedbacks of about 10 kips in the transverse direction, and about 12 kips in the longitudinal direction, were measured when the gravity load was applied. These force feedback values are comparable with the residual forces after the repaired SP1 cyclic tests were completed (refer to Chapter 6).

7.5.2   80% Scale Bidirectional HS Tests

When a 10% gravity load was applied to the repaired SP1, the 50% scale HS tests demonstrated that the test specimen subassemblage preserved a reasonable force capacity. Thus, a larger 80% scale bidirectional test (Test ID 8) was conducted, and the data from the OpenSees side were compared to the actual recorded data at the PI DAQ. The directly measured responses in the global *x* and *y* directions were compared to the intended OpenSees commands to perform a final check of the geometric transformation. Moreover, the actuators performance was checked again to verify the DSP interpolation routines.

The actuators commands adopted from the OpenSees computations, but after applying the OpenFresco geometric transformation, were compared to the temposonic measurements of the actual actuators motion as previously conducted in the free actuators tests. Figure 7.35 and Figure 7.36 show such comparison for both the North and South actuators, respectively. These figures represent the transformed OpenSees commands, which were basically the commands sent to the DSP card to interpolate and send to the controllers versus the actual achieved commands, which progressed in time based on the set velocity and loading rate. Thus, only the amplitudes

are useful to compare in these plots as a final check of the HSS, which were found closely matching as labelled in the figures. The temposonic displacements also feature the constant slopes representing the velocities, which were computed and shown in Figure 7.37 for the two actuators. The velocity history demonstrates how each of the two connected actuators at the specimen's column head adjusted their speed to keep up with one another during bidirectional loading. The maximum velocity set as one of the PI660C UCB HybridSim interface parameters at 0.05 inch/sec was maintained during the HS tests, i.e. the actuator that received a smaller displacement command slowed its rate of loading according to the developed DSP routines. This observation is similar to what the two free actuators trial tests showed earlier. However, the full specimen actual HS test is more confirmative because the correct displacement orbit of the physical column head was verified, which in turn successfully verified the DSP interpolation routines.

A final check that concludes the discussion of the HSS verification is comparing the intended computed displacement commands and received force feedbacks in the global DOFs versus what was actually obtained from the tests, i.e. verifying the newly implemented OpenFresco geometric transformation. For this purpose, wirepots were set up to measure the global x and y displacements using proper triangulation relationships. Figure 7.38 and Figure 7.39 show the comparison of the command history in global DOFs, as directly calculated in OpenSees before any geometric transformation, and from the wirepots measurements. The amplitude closely matched with only less than 2.5% difference, which verified the geometric transformation in the displacement command. Furthermore, the backward transformation of the actuator load cell forces was also verified from comparing the overall force-displacement relationship (Figure 7.40) from OpenSees versus that where the global force calculated from the local load cell measurements along with the actual displacements from the wirepots.
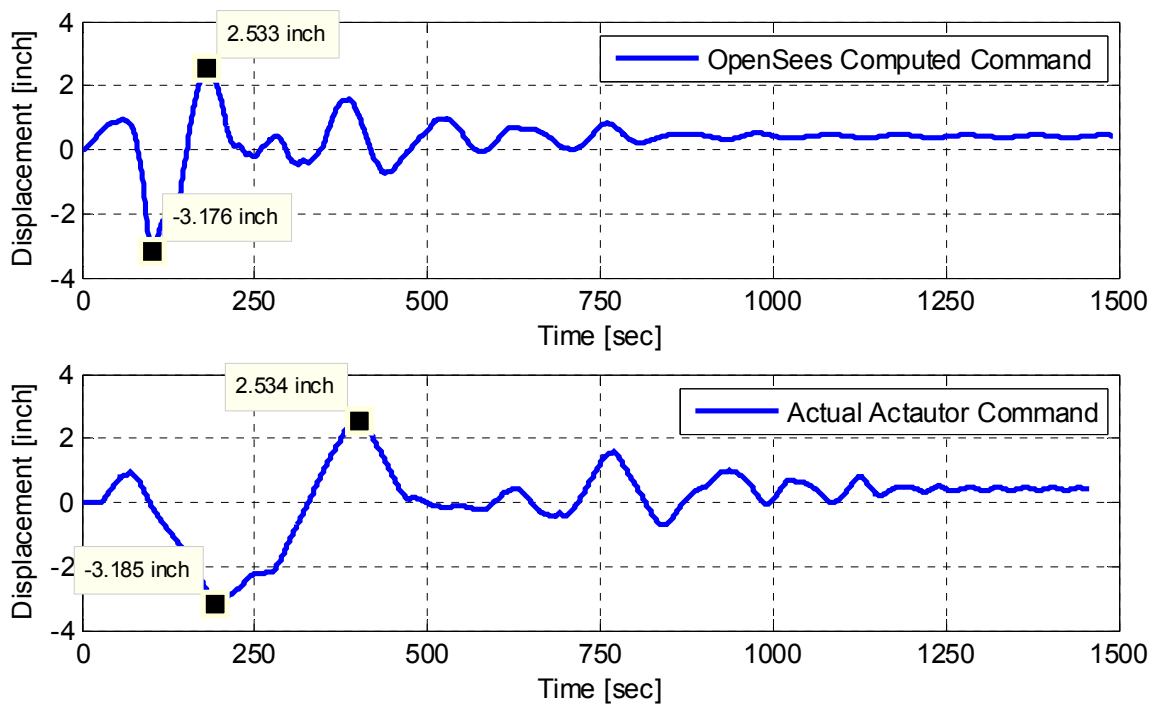
Figure 7.35 North actuator (u_1) generated command and actual motion history for the repaired SP1 80% Rinaldi bidirectional HS test

278
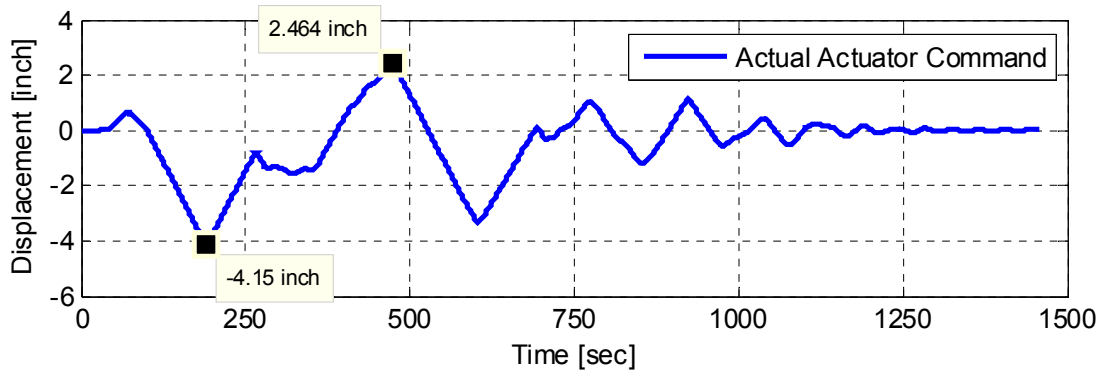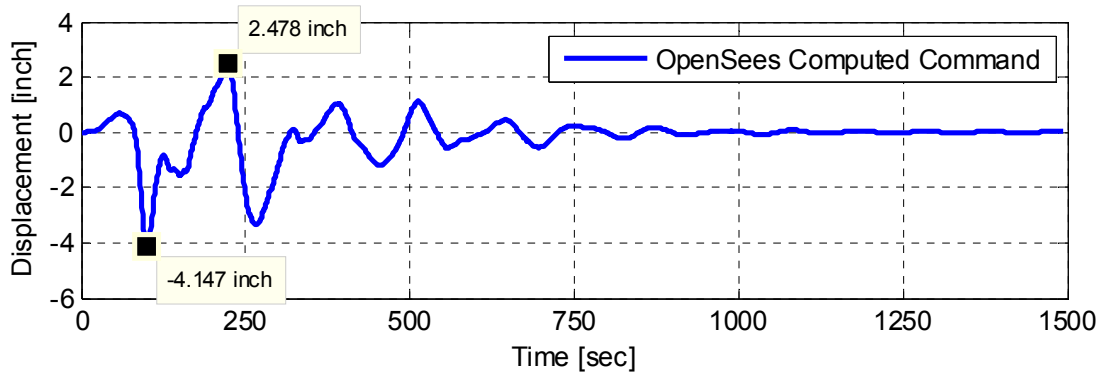
Figure 7.36 South actuator (u_2) generated command and actual motion history for the repaired SP1 80% Rinaldi bidirectional HS test
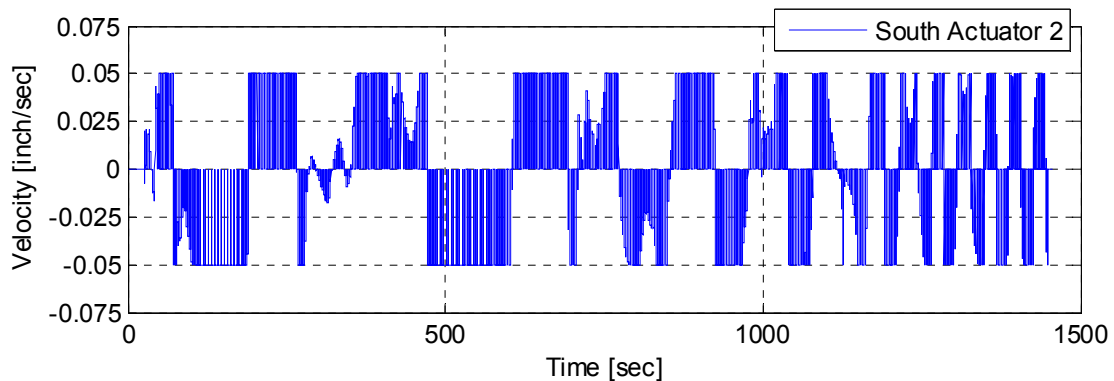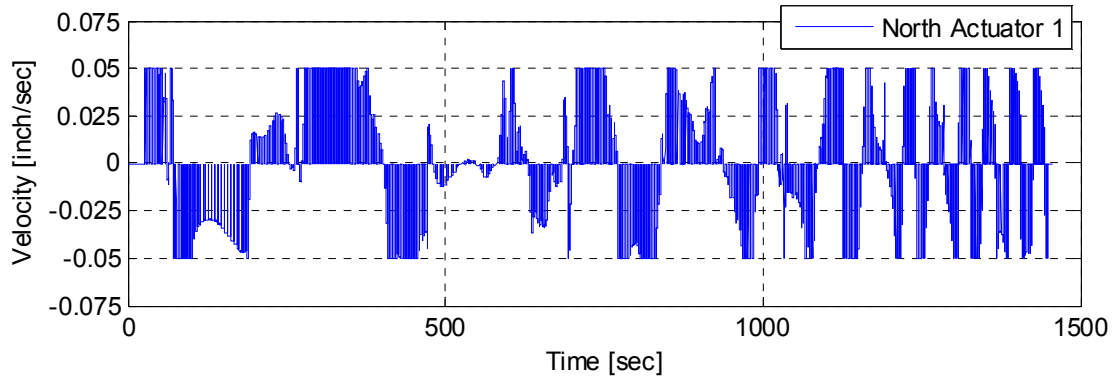
Figure 7.37 Actuators velocity as calculated from the obtained displacement measurements from the DAQ data for the repaired SP1 80% Rinaldi bidirectional HS test
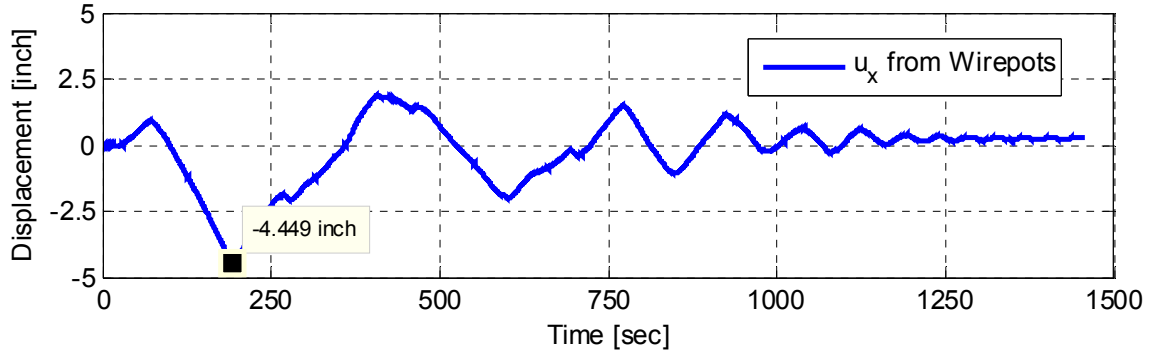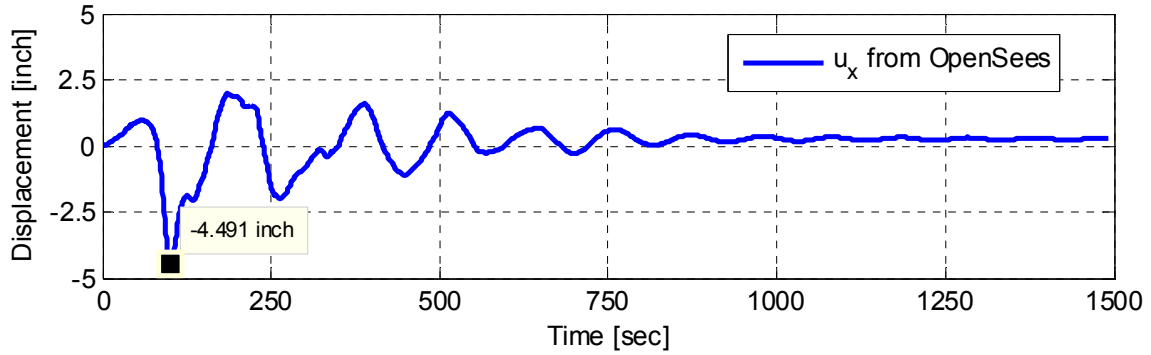
Figure 7.38 Global transverse displacement history (u_x) obtained from the OpenSees solution and that actually measured from wirepots for the repaired SP1 80% Rinaldi bidirectional HS test
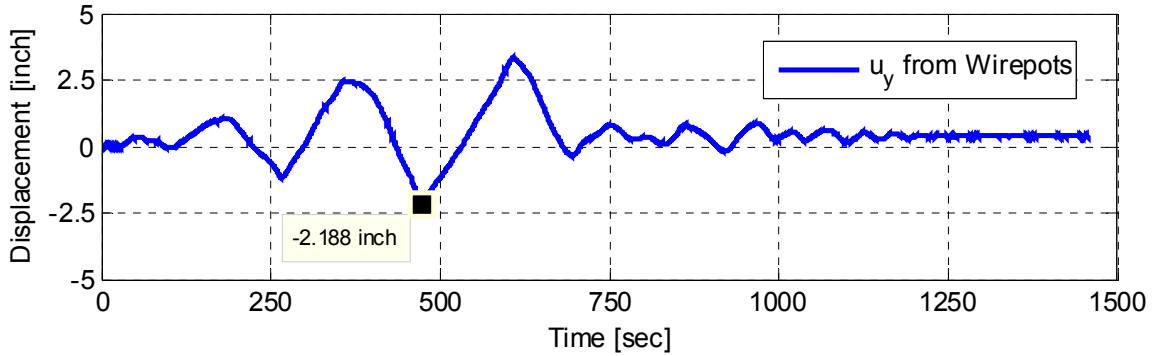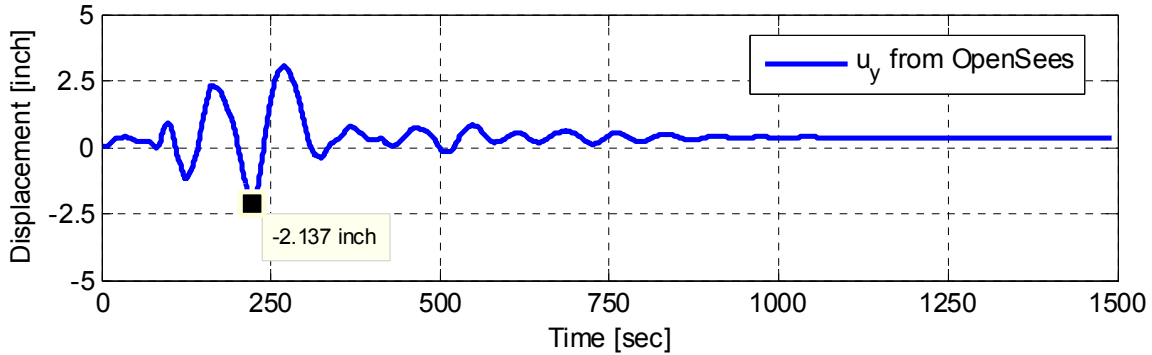
Figure 7.39 Global longitudinal displacement history (u_y) obtained from the OpenSees solution and that actually measured from wirepots for the repaired SP1 80% Rinaldi bidirectional HS test
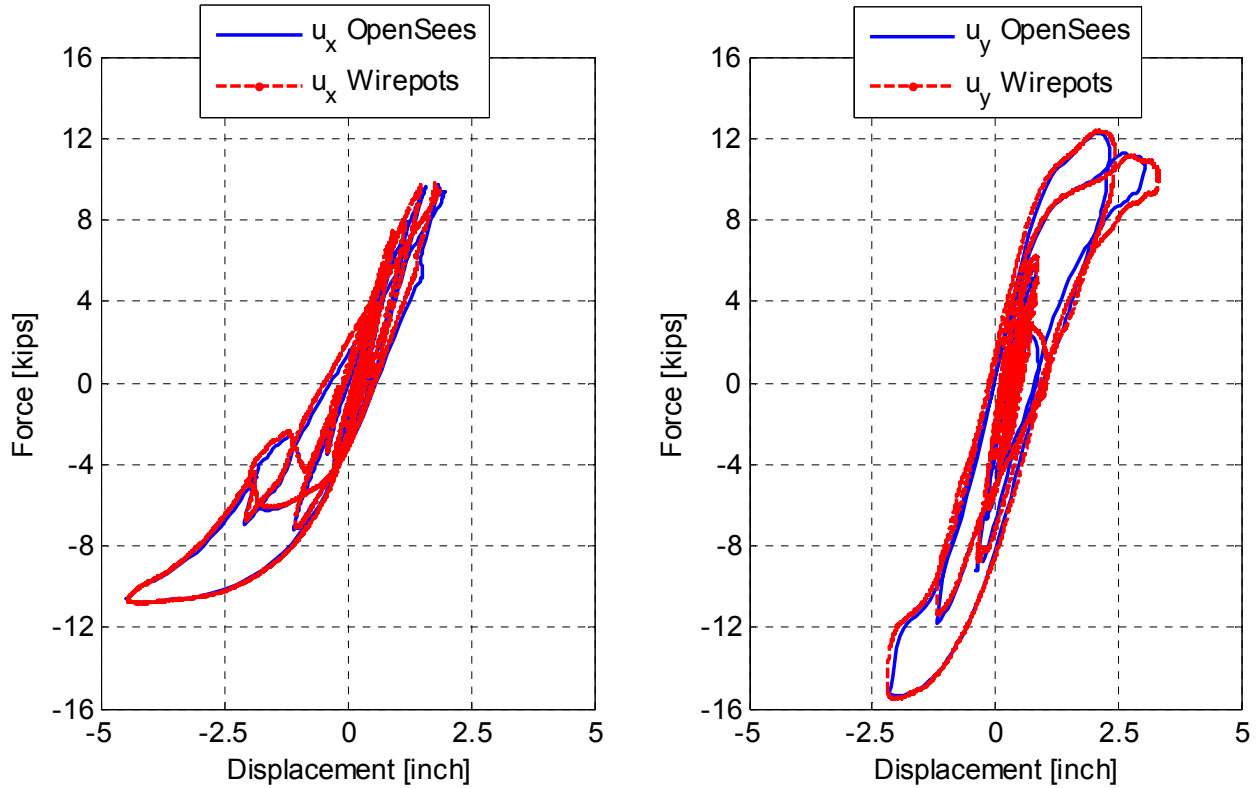
Figure 7.40 Comparison of force-displacement relationship in transverse (left) and longitudinal (right) directions from the recorded OpenSees data and actual load cells and wirepots DAQ data for the repaired SP1 80% Rinaldi bidirectional HS test

Based on all the verification tests from the free actuators and the repaired SP1 full specimen HS test, it was concluded that the sought HSS for testing is reliable and performs as expected. In particular, the new PI660C UCB HybridSim application (interface) successfully communicates the displacement and force feedback vectors between OpenFresco and the experimental hardware. The associated DSP routines developed within the PI660C UCB HybridSim successfully interpolated the commands for multi-actuators simultaneously, and communicated the DAQ actuators load cell measurements back to the PI interface. Finally, the newly implemented OpenFresco experimental setup object correctly performs displacement and force geometric transformation between the global DOFs and the two actuators in a triangular arrangement local DOFs. The HSS was then confidently used in the SP2 specimen HS tests as discussed in the next chapter.

8   Hybrid Simulation: Retrofitted Specimen Two Tests

The experimental program conducted in this study comprised mainly of two specimens that were tested using different loading protocols and in different conditions. The first specimen was tested as-built under cyclic loading as discussed in Chapter 5. The same specimen was repaired and retested under cyclic loading as discussed in Chapter 6. The repaired specimen one (SP1) was also utilized in HS test trials for HS system verification as presented in Chapter 7. The second specimen (SP2) was retrofitted before any testing and was only tested using HS. Discussions of specimen SP2 test results are the focus of this chapter. The chapter presents the retrofit procedure, the tests and damage progression, the global behavior, the column and bent cap beam local behavior, and effective width discussion. The chapter concludes with a brief discussion of the effectiveness of the retrofit through comparison of various behavior metrics against the corresponding quantities from the identical as-built SP1 Tests.

8.1   RETROFIT PROCEDURE

The objective of the retrofit considered in this part of the study was to increase the moment capacity of the column such that the bent cap beam could experience higher moment demands. For this purpose, three layers of CFRP were used to wrap the column to improve the confinement behavior and, in turn, increase its flexural capacity. Each of the three layers was 0.04 in. thick and the total thickness of the jacket was 0.12 in. A brief discussion of the material properties of the carbon sheets and the structural epoxy used for creating the jacket layers is included in Chapter 3. A similar procedure of wrapping the repaired column of SP1 with CFRP layers was followed for the untested column of SP2. A summary of the followed procedure is shown in Figure 8.1 through Figure 8.5.

The second specimen retrofit was carried out at a later stage after the construction of the specimen. A view of the as-built SP2 before the column retrofit is shown in Figure 8.1. The first step in preparation for the retrofit was cleaning and smoothing the concrete surface, Figure 8.1, for efficient wrapping. The surface was then wet with a layer of the primer epoxy and the carbon sheets were cut to the required length as shown in Figure 8.2. Each layer of the carbon sheets was generously coated from both sides with the primer epoxy as illustrated in Figure 8.3. All the wet carbon sheets were rolled and left for a short time to make sure the epoxy is well-immersed. The following stage was to apply the wet carbon sheets to the column in a circumferential manner to create the three-layer jacket one layer at a time. It is to be noted that the sought CFRP jacket extended to the mid height of the column. That is to guarantee that the moment demand in the unwrapped portion of the column did not exceed its capacity and not to migrate the plastic

hinge to an undesired upper location of the column in its inverted position, i.e. closer to the pin support. Thus, each layer of the jacket comprised two adjacent sheets provided in standard 24-inch wide rolls with no overlap. Figure 8.4 shows the application of the lower and upper parts of the first jacket's layer. The final retrofitted column is shown in Figure 8.5.
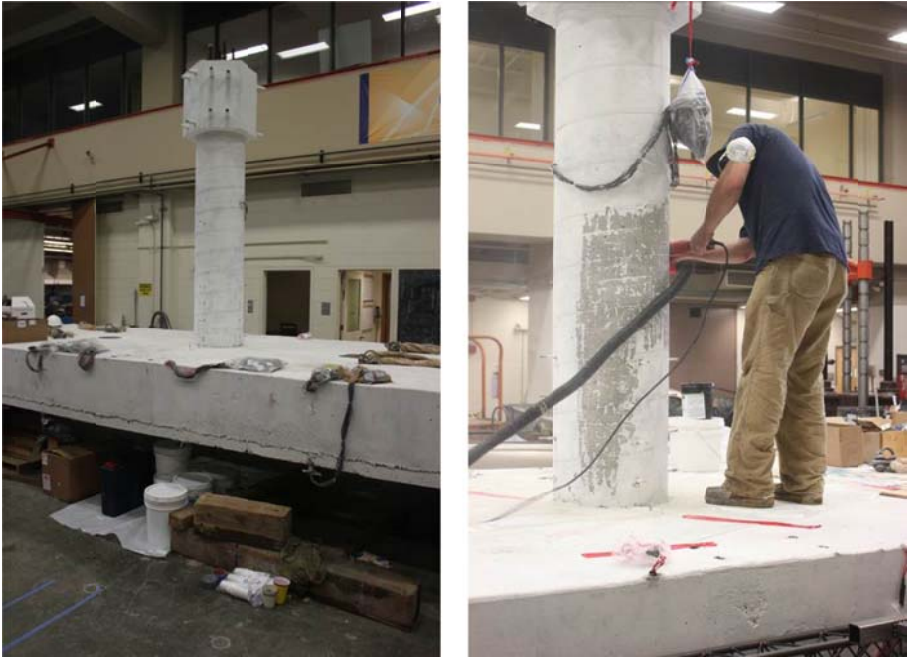
Figure 8.1 The as-built SP2 before retrofit (left); preparing the column surface for CFRP wrapping (right)
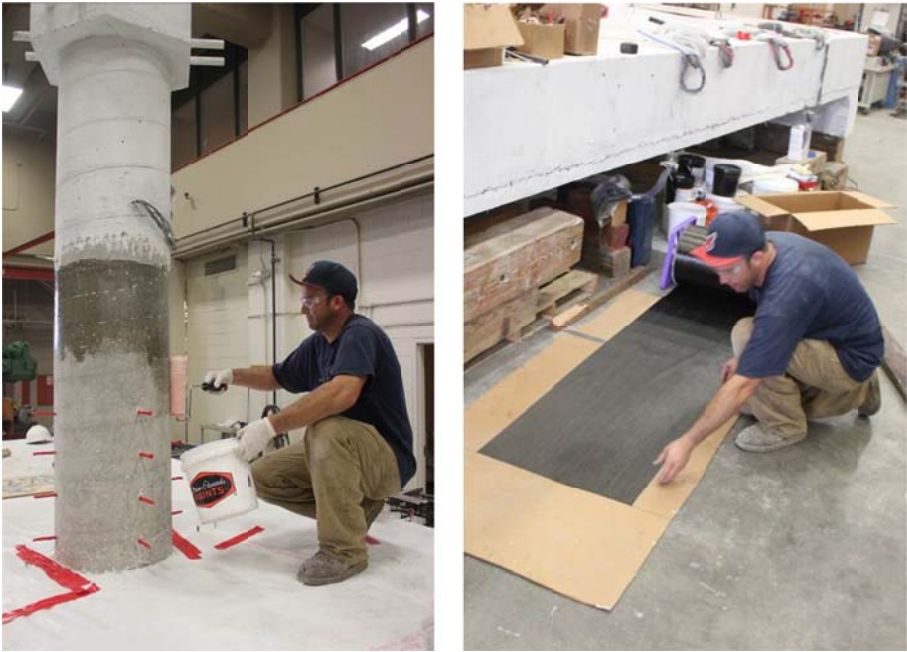
Figure 8.2 Applying a primer epoxy coat to the column surface before applying the CFRP layers (left); preparing a single layer of a carbon fibers sheet and cutting the sheet to the desired length (right)

283

Figure 8.3 Coating the carbon sheets with epoxy resin and rolling the wet sheets in preparation for wrapping

Figure 8.4 Applying the first CFRP layer of the lower part of the jacket (left) and of the upper part of the jacket (right) of the column using the ready CFRP wet rolls

Figure 8.5 An overview (left) and close-up view (right) of the final retrofitted column of SP2

8.2   PROGRESSION OF TESTING AND DAMAGE

A similar test setup to SP1 tests was used for conducting the SP2 HS tests as previously discussed. The main difference is that the displacement response of the column subjected to ground motion that is computed during the test using the forces feedback measured from the actuators were used for SP2 tests rather than using a prescribed cyclic loading pattern as used in SP1 quasi-static tests. In addition, the bidirectional loading was pursued in both of the transverse and longitudinal directions simultaneously in case of SP2 HS tests rather than separately as in the SP1 cross-orbit cyclic loading tests. An overview of the test setup and load progression during one of the HS tests is shown in Figure 8.6. Several HS tests were performed that varied in ground motion scale, components, and direction. Only the test runs that utilized the Rinaldi ground motion at 50% scale or higher are included in the test processing and discussion herein. Other smaller scale tests were mainly utilized to decide on a suitable loading rate with minimal error and are not included here for brevity. A summary of the 15 tests that are discussed in this chapter is listed in Table 8-1. The test runs of 100% scale or higher were conducted in two opposite directions of shaking, i.e. the ground motion direction in the HS input file was used twice: 1) positive (original) and 2) negative (inverted polarity). That is because of the pulse nature of the Rinaldi ground motion record that caused large inelastic deformations in one direction and did not have the same effect in the opposite direction because the pulse did have large enough reversal. More details are presented in the global behavior discussion in the next section.

Figure 8.6 Retrofitted SP2 HS test setup during a bidirectional run

Table 8-1 Summary of different SP2 HS runs discussed in this chapter

Test ID	Grvaity Load Level	Ground Motion Scale	Components	Direction	P-delta Correction
1	10%	50%	Bidirectional	Positive	Yes
2	10%	50%	Bidirectional	Positive	No
3	10%	50%	Transverse only	Positive	Yes
4	10%	50%	Longitudinal only	Positive	Yes
5	10%	75%	Bidirectional	Positive	Yes
6	10%	100%	Bidirectional	Positive	Yes
7	10%	-100%	Bidirectional	Negative	Yes
8	15%	125%	Transverse only	Positive	No
9	15%	-125%	Transverse only	Negative	No
10	15%	150%	Transverse only	Positive	No
11	15%	-150%	Transverse only	Negative	No
12	15%	175%	Transverse only	Positive	No
13	15%	-175%	Transverse only	Negative	No
14	15%	200%	Transverse only	Positive	No
15	15%	-200%	Transverse only	Negative	No

The observed global damage and overall mode of failure for the retrofitted SP2 was much different from that of the identical as-built SP1. The retrofitted column in SP2 did not experience extensive damage, i.e. no bar buckling or rupture because of the CFRP jacket confinement.

286

Instead, a slight damage was observed in the bent cap in the compression zone at one of the column sides as noticed from Figure 8.7. However, to better investigate the final damage state of the specimen, the CFRP jacket was carefully removed after all the test runs were concluded. Figure 8.8 shows the procedure for removing the jacket and an overview of the column and cap beam damage state. A uniform pattern of flexural cracks that were almost equally spaced within the anticipated plastic hinge zone was observed in the column after the jacket removal. All the loose concrete and dust were cleaned after the jacket removal to identify the final damage state. A close-up view of the column flexural circumferential cracks and bent cap beam concrete crushing is shown in Figure 8.9. The first column hoop inside the column-bent cap joint and the bent cap transverse stirrups were exposed (Figure 8.9). This indicates that the mode of failure is indeed cap beam compression crushing manifested by cover spalling rather than a column plastic hinging. This confirms the satisfaction of the intended estimation of the bent cap beam capacity experimentally by jacketing the column using CFRP to increase its capacity and accordingly the demand on the cap beam.
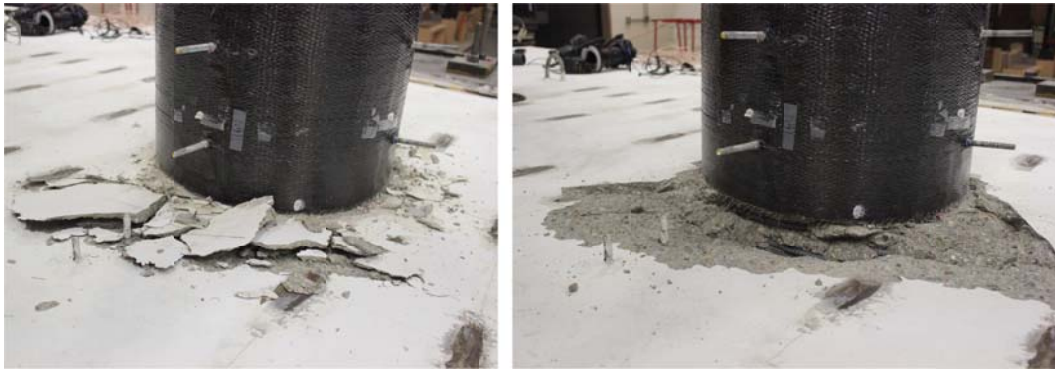
Figure 8.7 Damaged state of SP2 after all HS tests (left) and final view of this damage state after all loose concrete were removed (right)

Figure 8.8 Procedure of removing the CFRP jacket after the retrofitted SP2 tests were concluded (left) and final view of the column after the jacket removal (right)

287

Figure 8.9 A close-up view of SP2 column flexural cracks (CFRP jacket was removed) and bent cap beam concrete cover spalling after HS tests

8.3   GLOBAL BEHAVIOR

Post-processing and presenting the experimental test results of SP2 followed similar framework to that of SP1 quasi-static tests (Chapter 5). This includes a discussion of the global behavior, which is presented in this section, followed by a discussion of the column and bent cap beam local behaviors, then the effective width discussion. For the global behavior, the observed displacement and force histories, and force-displacement relationships are discussed.

8.3.1   Displacement History

Monitoring the displacements is central to HS tests because displacements are computed and updated online during the test based on the measured force feedback, i.e. applied displacements are not known beforehand. Similar to the quasi-static cyclic tests, displacements were measured using wire potentiometers to capture the global specimen displacements, and temposonics that were installed along the actuators axes to capture and control the actual input motion at each actuator. The actuators displacements were geometrically transformed to the global directions and compared to the wirepots measurements. The geometric transformation was reliable and was used to deduce the motion of the column head in the transverse and longitudinal directions. The entire displacement history that was computed and applied to the retrofitted SP2 during the 15 HS tests, summarized in Table 8-1, in the global transverse and longitudinal directions is shown in Figure 8.10. The transverse and longitudinal displacements are compared to the two actuator local displacements for the full history of the 15 HS tests in Figure 8.11. This figure gives an overview of the different components of the conducted tests and the sequence of the increased ground motion scales and reversed directions. Furthermore, zoomed-in views of the

288

displacement histories in the 50%-scale tests in bidirectional, transverse-only, and longitudinal-only tests are shown in Figure 8.12, Figure 8.13, and Figure 8.14, respectively.

Figure 8.12 shows that for the case of simultaneous bidirectional loading, one of the actuators consistently experienced much lower displacements which is attributed to the fact that the resultant of the nearly similar transverse and longitudinal components was almost aligned with the South inclined actuator direction. On the other hand, Figure 8.13 shows that both actuators had almost symmetric (same magnitude and direction) displacements when only transverse loading was applied. Figure 8.14 shows that both actuators had almost anti-symmetric (same magnitude but opposite directions) displacements when only a longitudinal loading was in progress. Moreover, Figure 8.12 to Figure 8.14 show constant slope lines (especially for large displacements) for all the global and local displacements. This is attributed to the conducted constant velocity slow rate HS tests. Obtaining this constant velocity for the displacement input was a fundamental criterion to verify the performance of the HSS and the communication between its components. More details were presented in Chapter 7 about the validation of the developed HSS. Another important observation from the displacement history figures, especially the full history demonstrated in Figure 8.10 and Figure 8.11, is the residual displacements at the end of each of the HS tests. For the small-scale tests, a small residual displacement was observed due to the minimal damage. However, much higher residual displacements were observed in the transverse-only large-scale tests that reached a final residual displacement of about 2 inch (drift ratio of 2.2%) after all the tests were concluded.
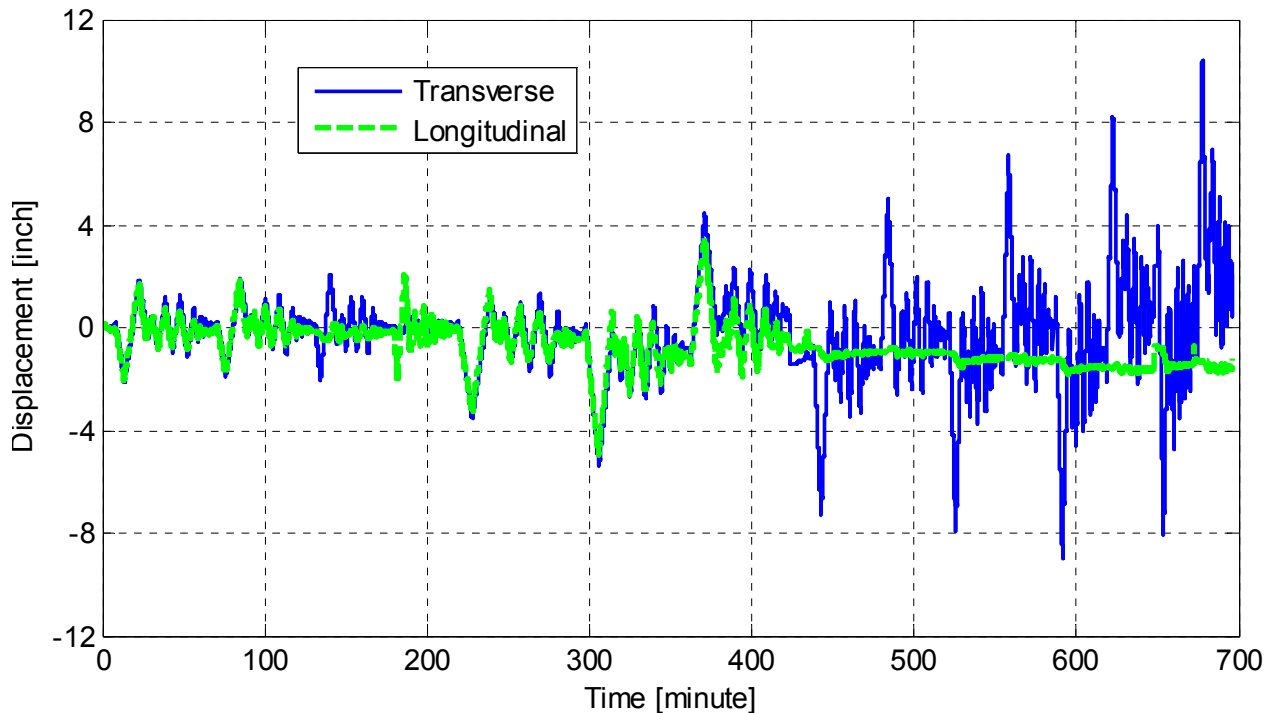
Figure 8.10 History of the online computed (and applied) displacements in the global transverse and longitudinal directions throughout all 15 HS test runs of the retrofitted specimen (SP2)

289
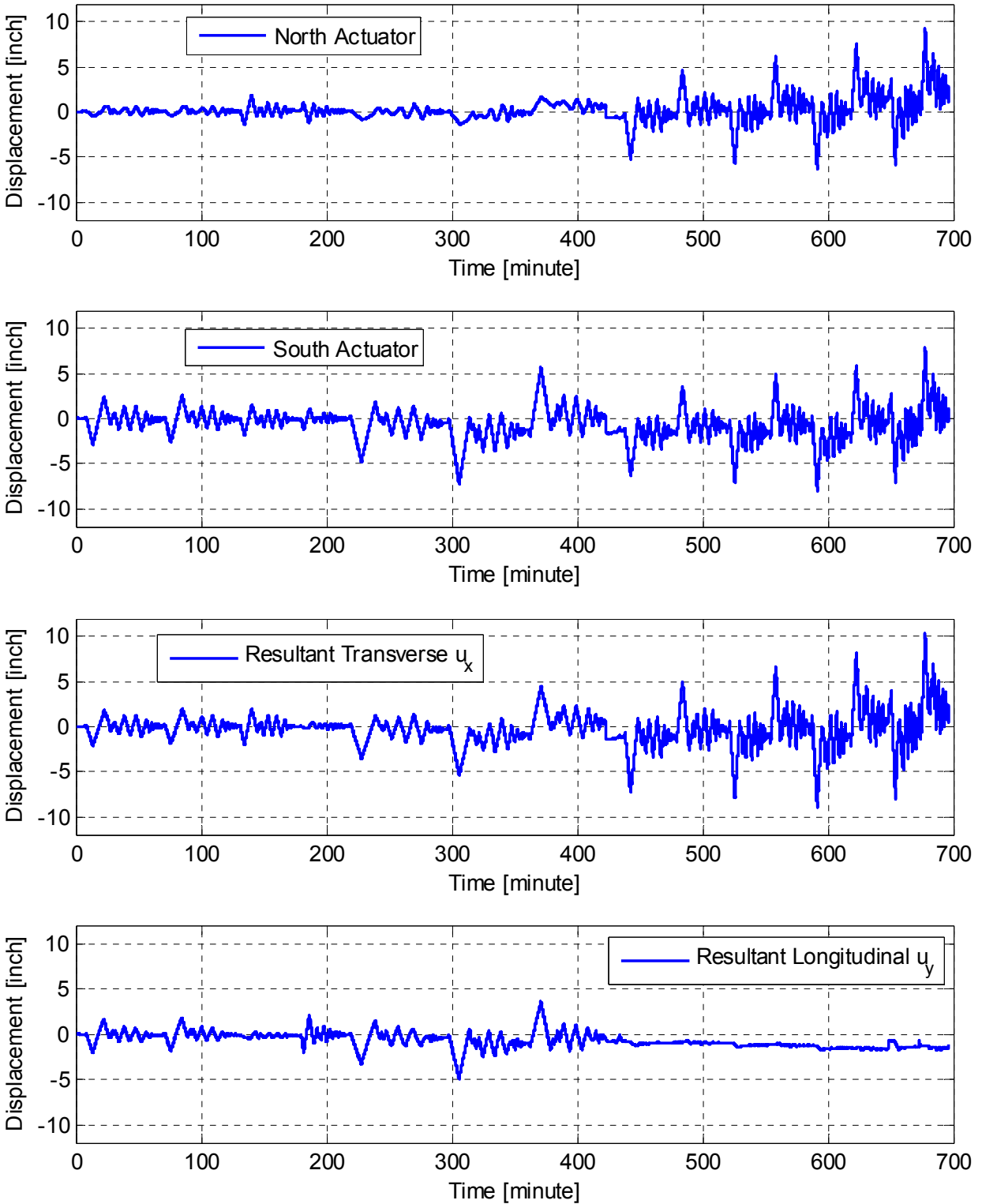
Figure 8.11 History of North and South lateral actuators temposonics measurements and the corresponding resultant displacements in transverse (u_x) and longitudinal (u_y) directions for all 15 HS test runs of SP2
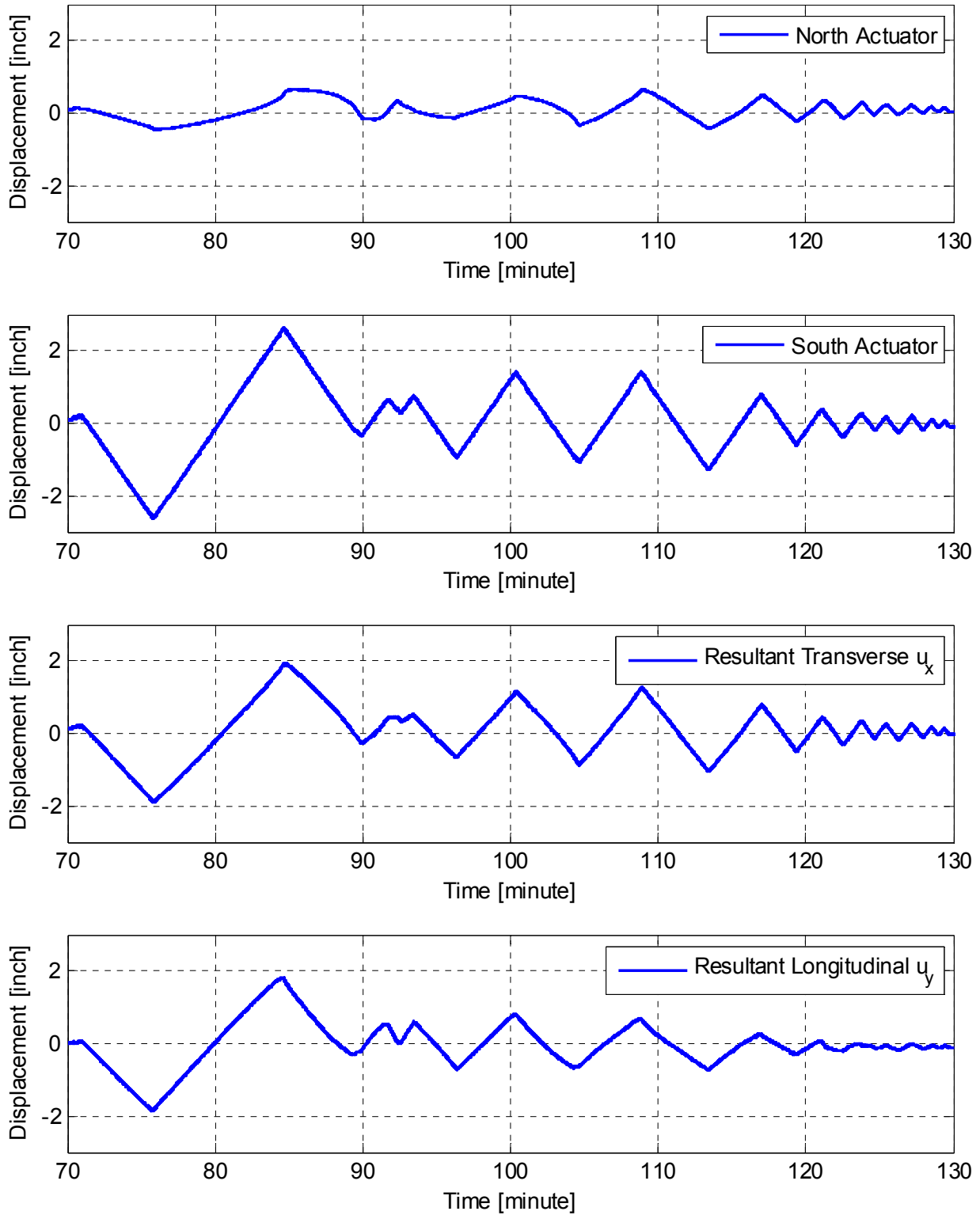
Figure 8.12 Zoomed-in view of the history of North and South lateral actuators temposonics measurements and the corresponding resultant displacements in transverse (u_x) and longitudinal (u_y) directions for the 50% scale bidirectional HS test

291
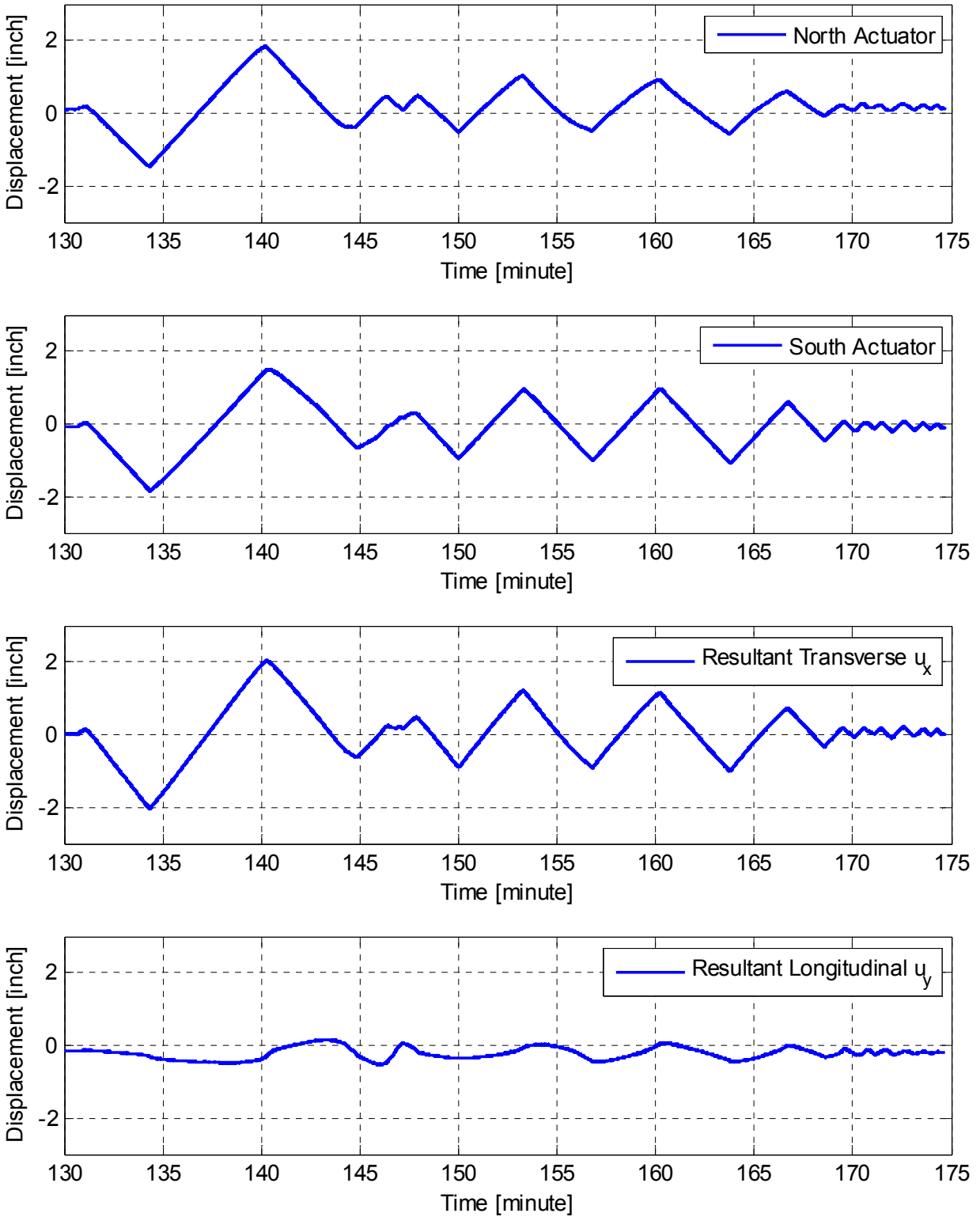
Figure 8.13 Zoomed-in view of the history of North and South lateral actuators temposonics measurements and the corresponding resultant displacements in transverse (u_x) and longitudinal (u_y) directions for the 50% scale transverse-only HS test
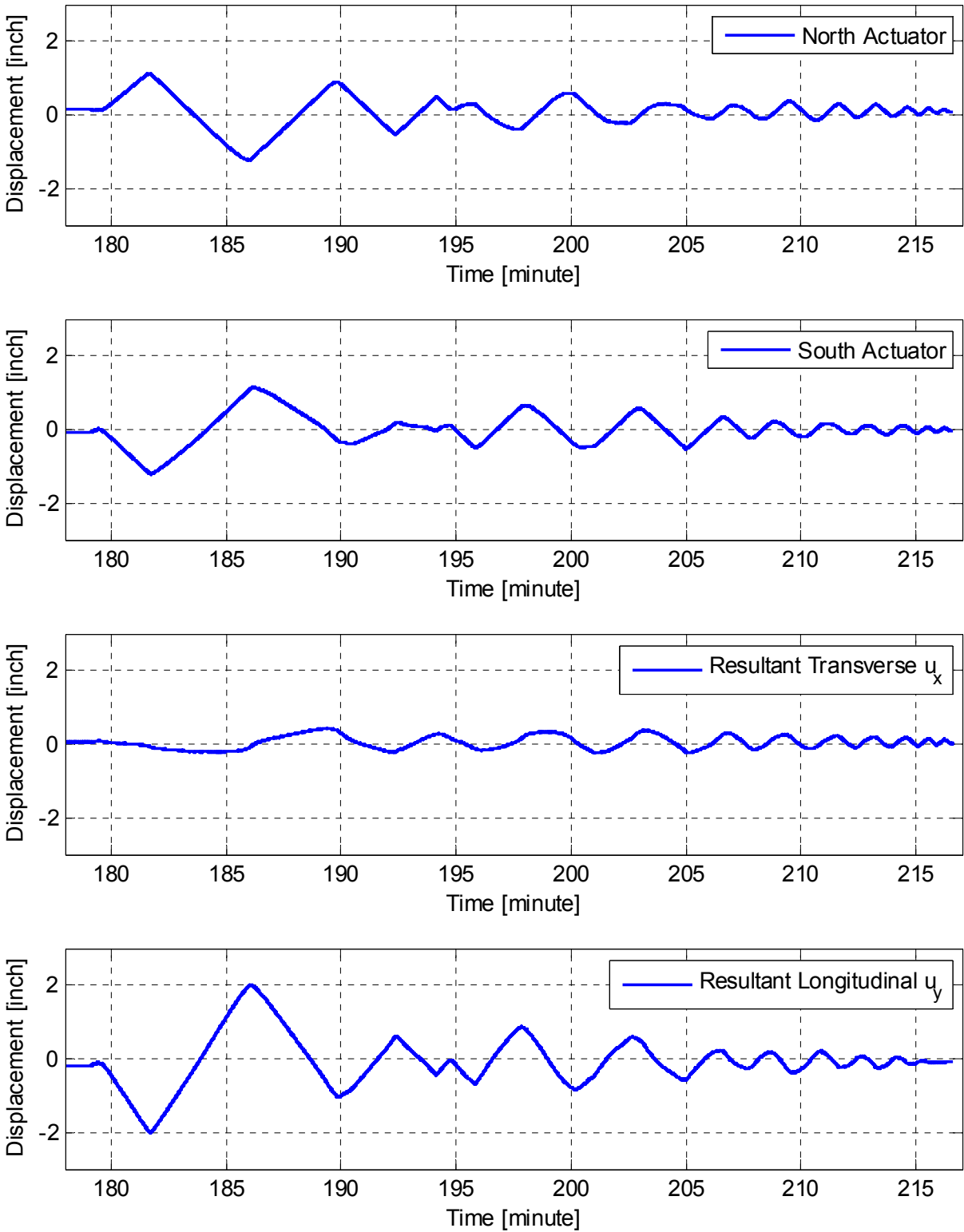
Figure 8.14 Zoomed-in view of the history of North and South lateral actuators temposonics measurements and the corresponding resultant displacements in transverse (u_x) and longitudinal (u_y) directions for the 50% scale longitudinal-only HS test

8.3.2   Force History

Displacements are crucial to monitor during displacement-controlled HS tests because that is the only way to know what deformations the specimen has gone through during HS testing. However, lateral forces are even more important to monitor because it is the force feedback that influences the next solution of the governing equations of motion, Equation (7-1) in Chapter 7, and in turn, the new displacement input. Meanwhile, a constant vertical gravity load was applied and maintained throughout the tests under force-control, which also needed to be monitored to make sure it remained constant during the test as intended. The gravity load history is shown in Figure 8.15 for all the 15 HS test runs. The total vertical reaction as the sum of the two strut forces is shown as well in Figure 8.15 to compare the total portion of the gravity load transmitted directly to the bent cap beam at its two supported ends by the two struts. The ratio between the total strut reactions and the gravity load was observed to be consistently around 70%, which agrees with the observation from SP1 cyclic tests as well. It is to be noted that the sudden drop and consequent increase at the beginning of the second gravity load level, which was 15% corresponding to ~240 kips, reflects the unloading and reloading again since testing was conducted during two separate days. The total gravity load values that was measured continuously was utilized along with the lateral displacement values and the prescribed numerical component of the vertical earthquake excitation by the computational model to estimate the equivalent lateral force considering the P-delta effect. Accordingly, the lateral force feedback was corrected before sending it to the computational model for the computation of the next displacement input, as discussed in Chapter 7. Only the bidirectional runs had the correction involving the P-delta effect considering both the time-varying vertical earthquake excitation and the applied constant gravity load. However, no such correction was applied during the large-scale transverse-only HS runs. That is because the corresponding axial load variation considering the large-scale runs with vertical excitation would experience tension at some time steps increasing the corrected lateral force value and affecting the computed displacement input in a somewhat unpredictable way because of possible column tension. Although this scheme might be realistic in some cases, it was decided to proceed with the transverse-only runs of scales 100% and higher 200% without accounting for the P-delta correction to limit the scope of the study to no-tension gravity load in combination with the applied lateral earthquake excitations.

The entire history of the measured force feedback in both transverse and longitudinal directions is shown in Figure 8.16. The force that was sent to the computational model for solving the equations of motion is slightly different as it incorporated the P-delta corrections for those runs that had that correction scheme applied. A more detailed discussion is presented in a following subsection. Similar to the displacements discussion, the local force measured at the actuators load cells was compared to the resulting force in the two intended transverse and longitudinal global directions. Figure 8.17 shows the full history of North and South actuator forces along with transverse and longitudinal force resultant for all the 15 HS test runs. Moreover, a zoomed-in view for the 50%-scale bidirectional, transverse-only, and longitudinal-only tests are shown in Figure 8.18, Figure 8.19, and Figure 8.20, respectively. The force residual at the end of each test was adjusted and reduced to zero before the start of a subsequent test to avoid any unrealistic force feedback at the start of the subsequent HS test. Zeroing the forces also allowed the determination of the corresponding residual displacements. However, due to the effect of the residual displacements, a minor force feedback was generated in the longitudinal direction when testing took place in the transverse direction only as seen from the

noise around the zero force value in the longitudinal force history in Figure 8.16. Another remark from the figure is that the constant slope mentioned above for the displacement histories could be observed only in the small runs where the behavior was still in the linear elastic range. However, for the large-scale tests, the constant slope in the force history plots was no longer observed because of the inelastic and hysteresis damage behavior.
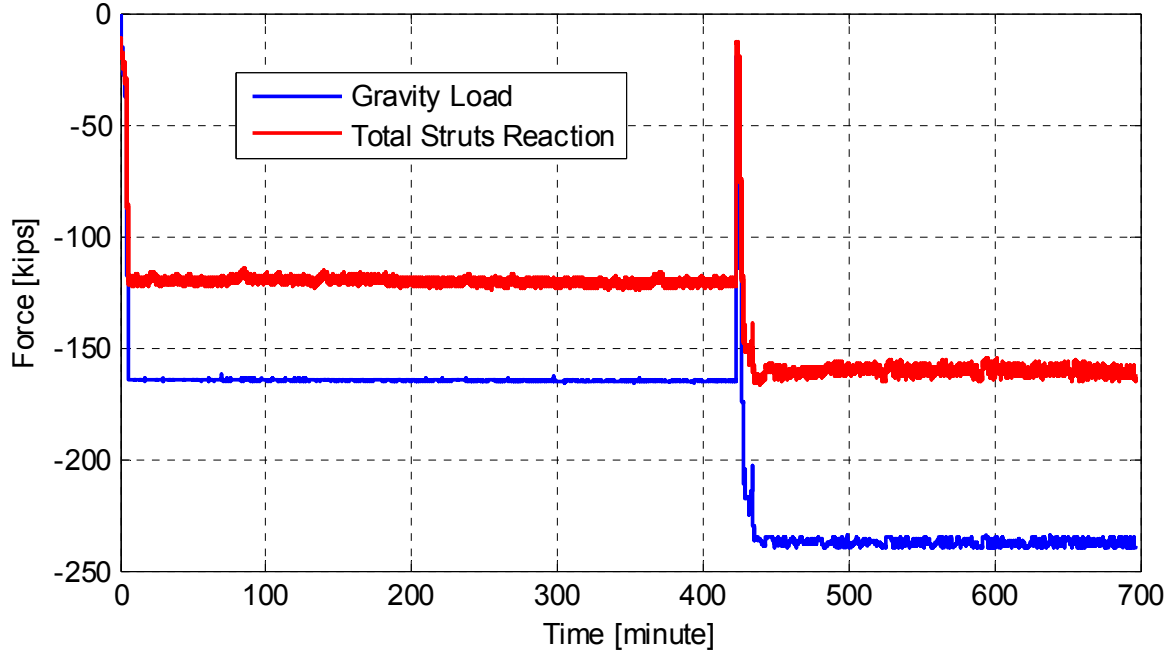
Figure 8.15 Gravity load history and corresponding two vertical strut reactions for all 15 HS test runs of SP2
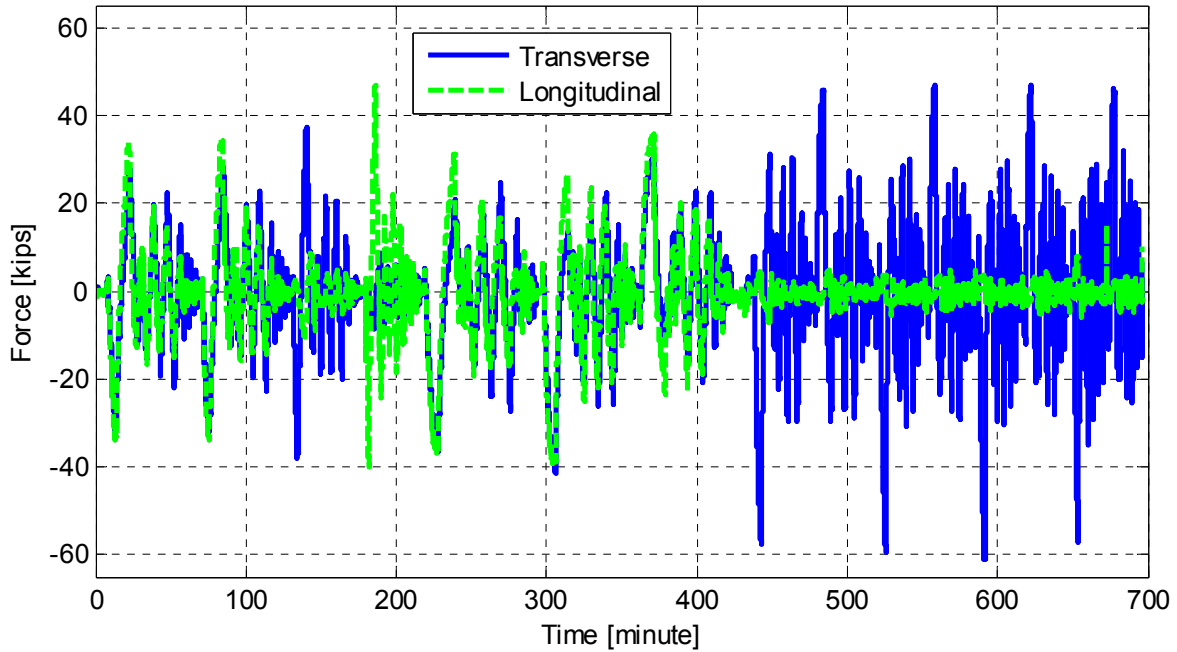
Figure 8.16 History of the force feedback in the transverse (f$_x$) and the longitudinal (f$_y$) directions for all 15 HS test runs of SP2
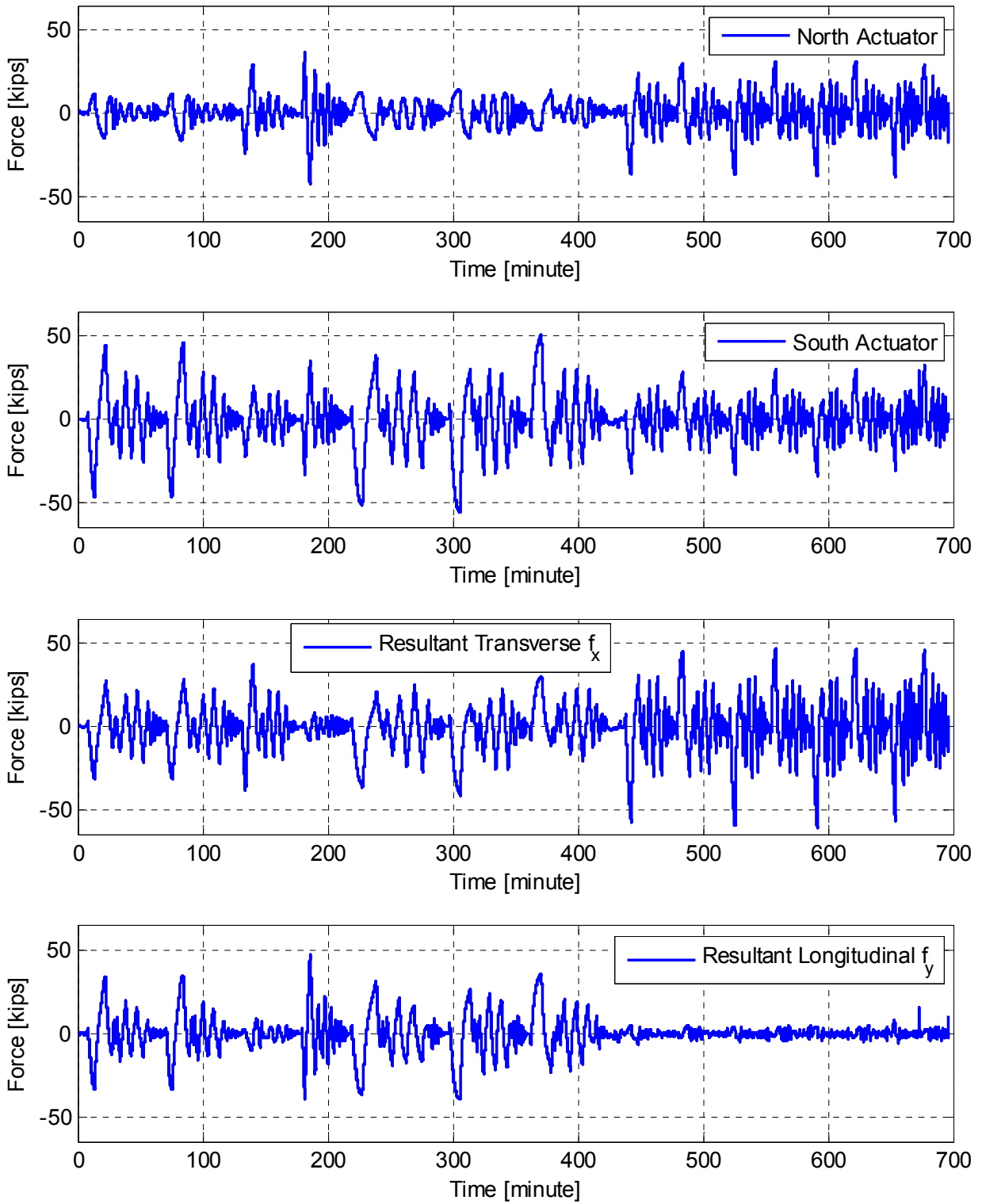
Figure 8.17 History of North and South lateral actuators load cells measurements and the corresponding resultant forces in the transverse (f_x) and the longitudinal (f_y) directions for all 15 HS test runs of SP2

296
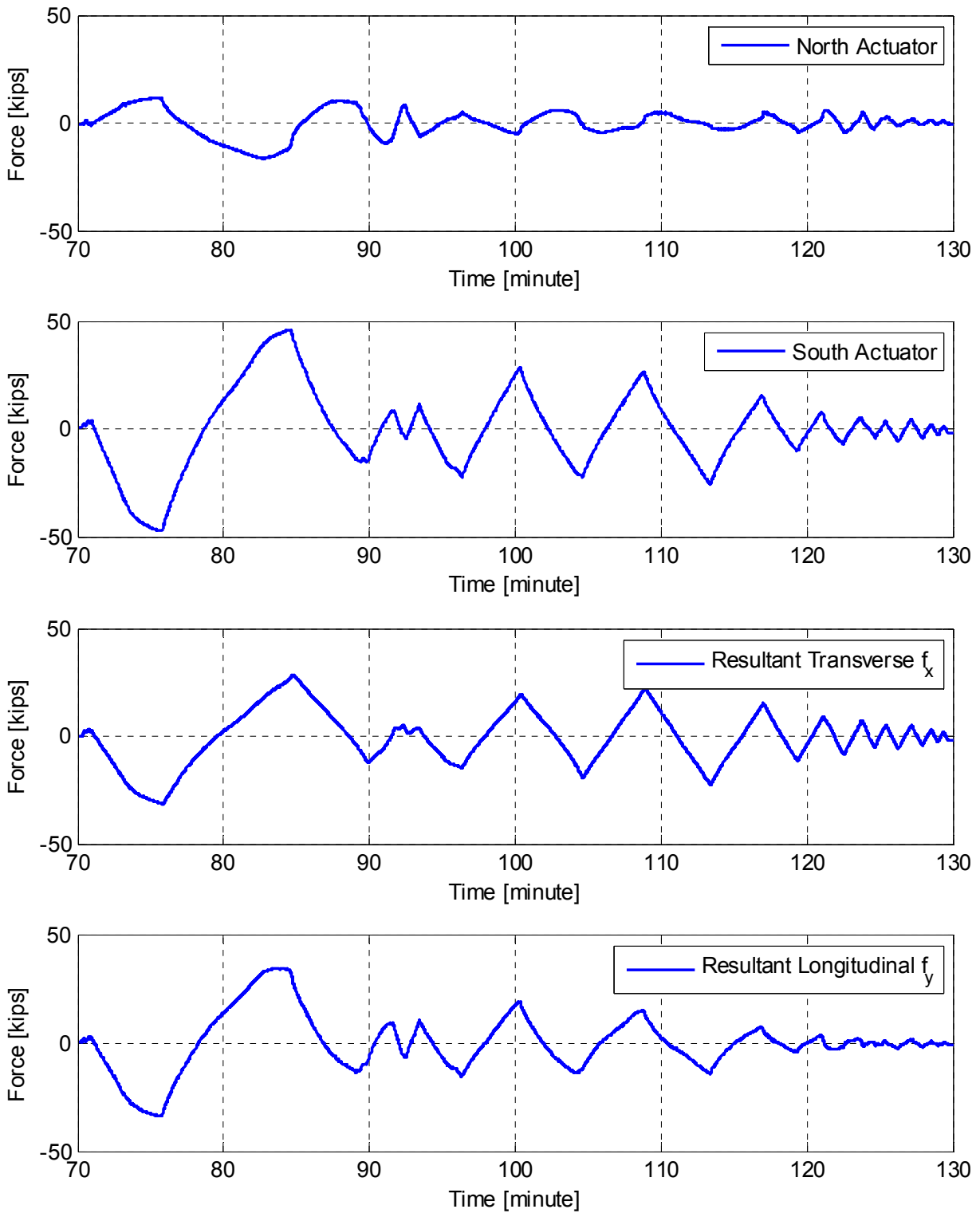
Figure 8.18 Zoomed-in view of the history of North and South lateral actuators load cells measurements and the corresponding resultant forces in the transverse (f$_x$) and the longitudinal (f$_y$) directions for the 50%-scale bidirectional HS test
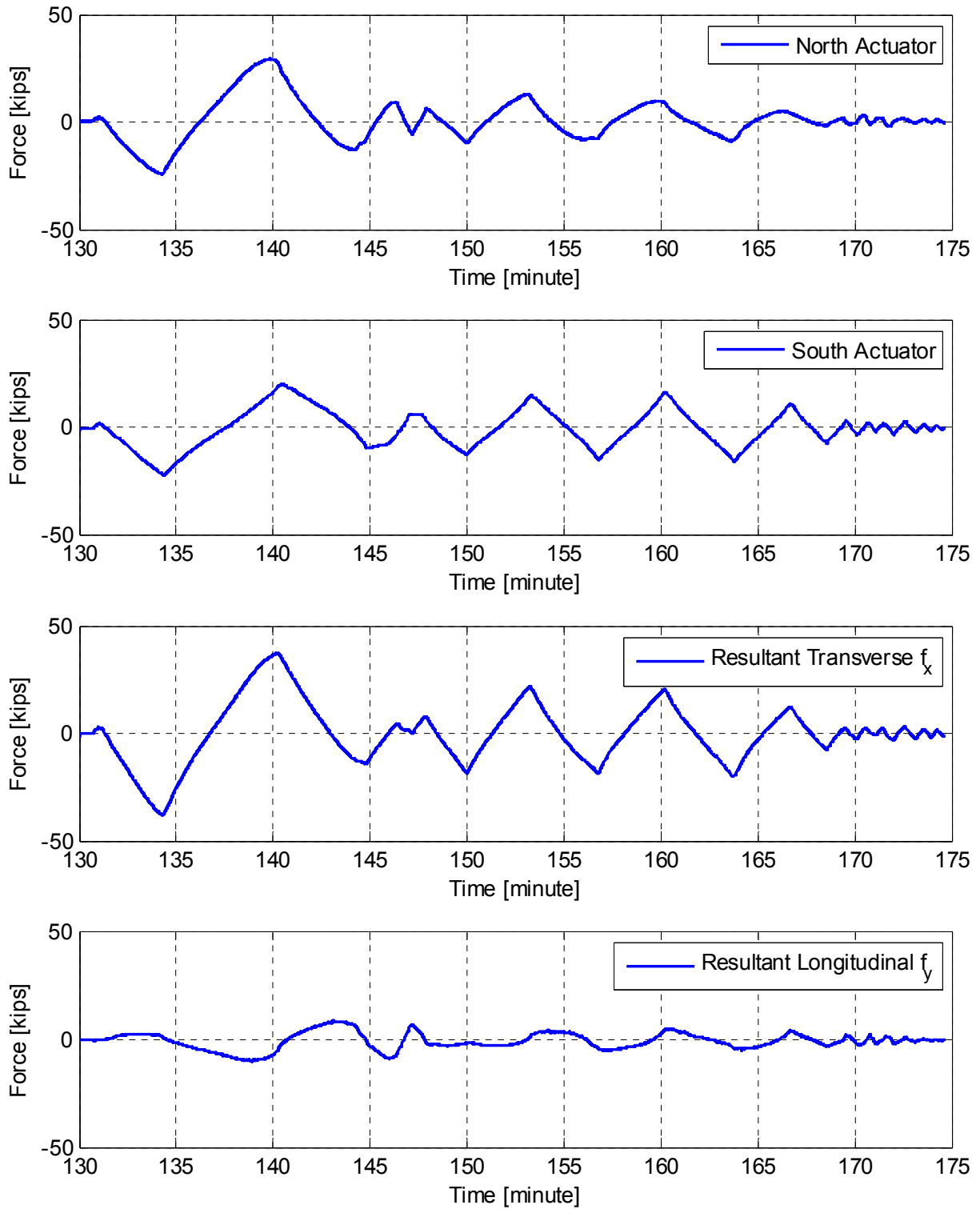
Figure 8.19 Zoomed-in view of the history of North and South lateral actuators load cells measurements and the corresponding resultant forces in the transverse (f_x) and the longitudinal (f_y) directions for the 50%-scale transverse-only HS test

298
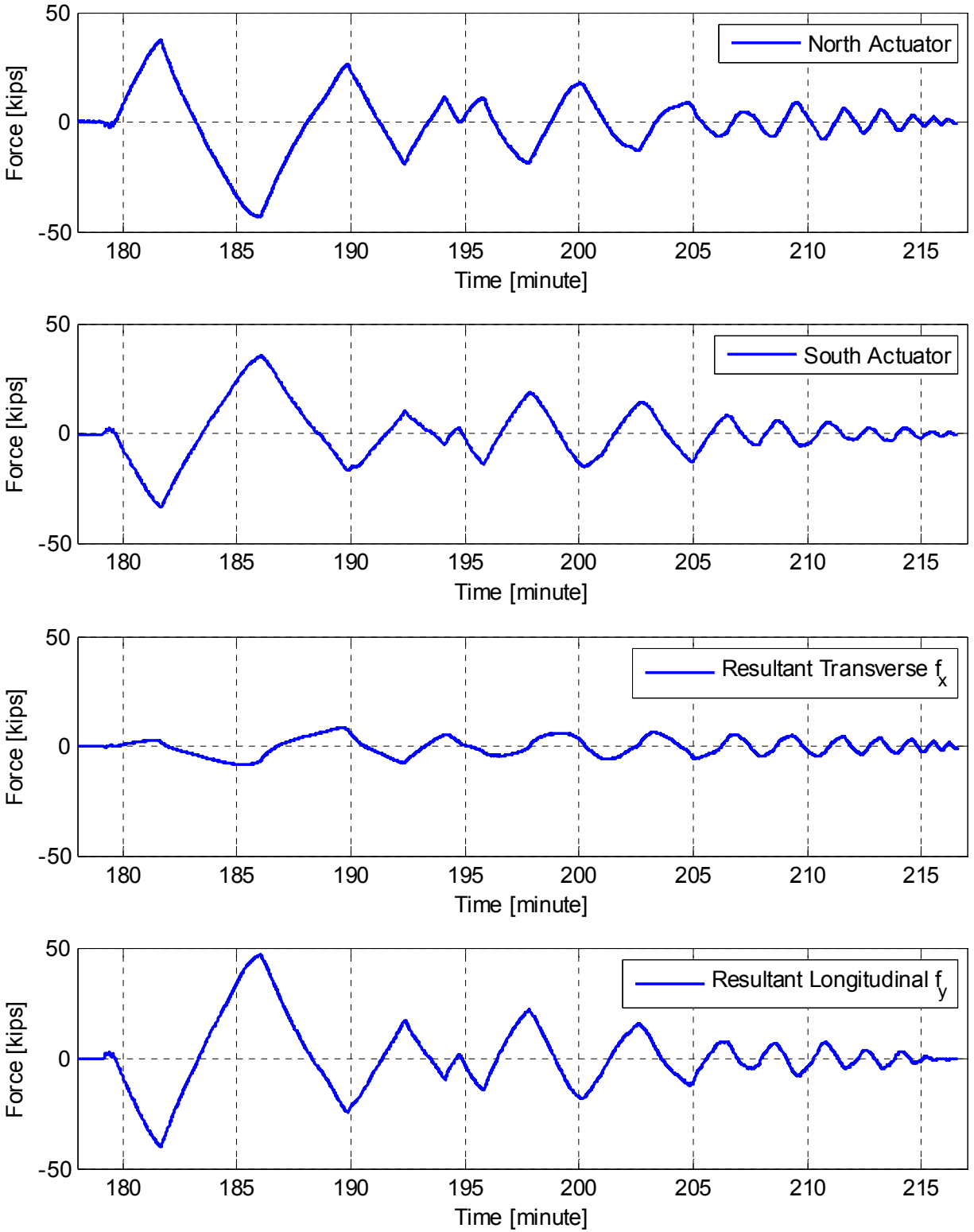
Figure 8.20 Zoomed-in view of the history of North and South lateral actuators load cells measurements and the corresponding resultant forces in the transverse (f$_x$) and the longitudinal (f$_y$) directions for the 50%-scale longitudinal-only HS test

8.3.3 Force-Displacement Relationship

The final global feedback forces and applied displacements in the specimen's transverse and longitudinal directions are plotted for the tested retrofitted bridge subassembly SP2. The force-displacement response is considered a whole system response rather than a single column response. That is because of the nature of the column-to-superstructure connection, especially where the contribution of the full superstructure to the column stiffness is engaged during bidirectional loading. The concatenated force-displacement relationships for all the 15 HS test runs in both transverse (f_x versus u_x) and longitudinal (f_y versus u_y) directions are shown in Figure 8.21 and Figure 8.22, respectively. It is observed from the figures that the force capacity was reached only in the transverse direction where the actuators stroke limitations did not allow reaching the specimen capacity while testing bidirectionally or in longitudinal direction only. For the large-scale transverse-only runs, the force capacity was reached as evidenced by the capped value of the force regardless of the increased input ground motion scale. However, the reached force capacity was higher in one direction than the other, which is attributed to the pulse nature of the ground motion that concentrated the initial damage in one side and the damage propagated according to this asymmetric behavior even when the input ground motion direction was reversed. As previously observed in the damage photographs in Figure 8.7 and Figure 8.9, the cap beam concrete crushing represented by cover spalling was the likely mode of failure that caused the bridge system force capacity to be reached as observed in the force-displacement relationship in the transverse direction. In addition, the revealed column surface underneath the CFRP jacked showed only flexural cracks without concrete crushing, which supports the argument that the force capacity was reached as the bent cap reached its capacity rather than the column reaching its capacity.
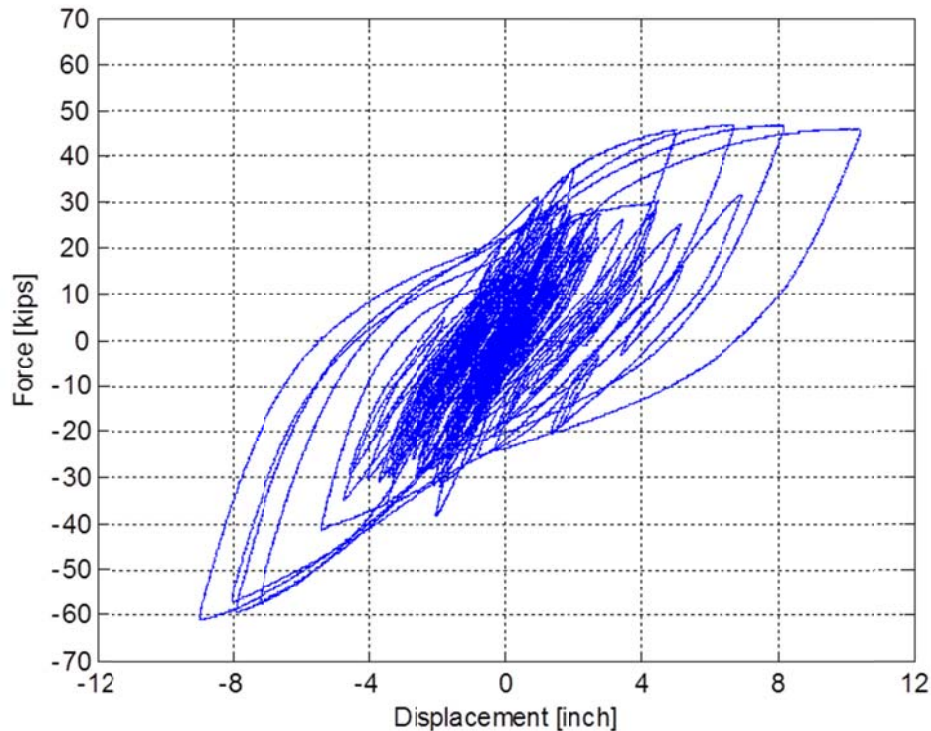
Figure 8.21 Force-displacement relationship in the transverse direction for all SP2 HS test runs

300
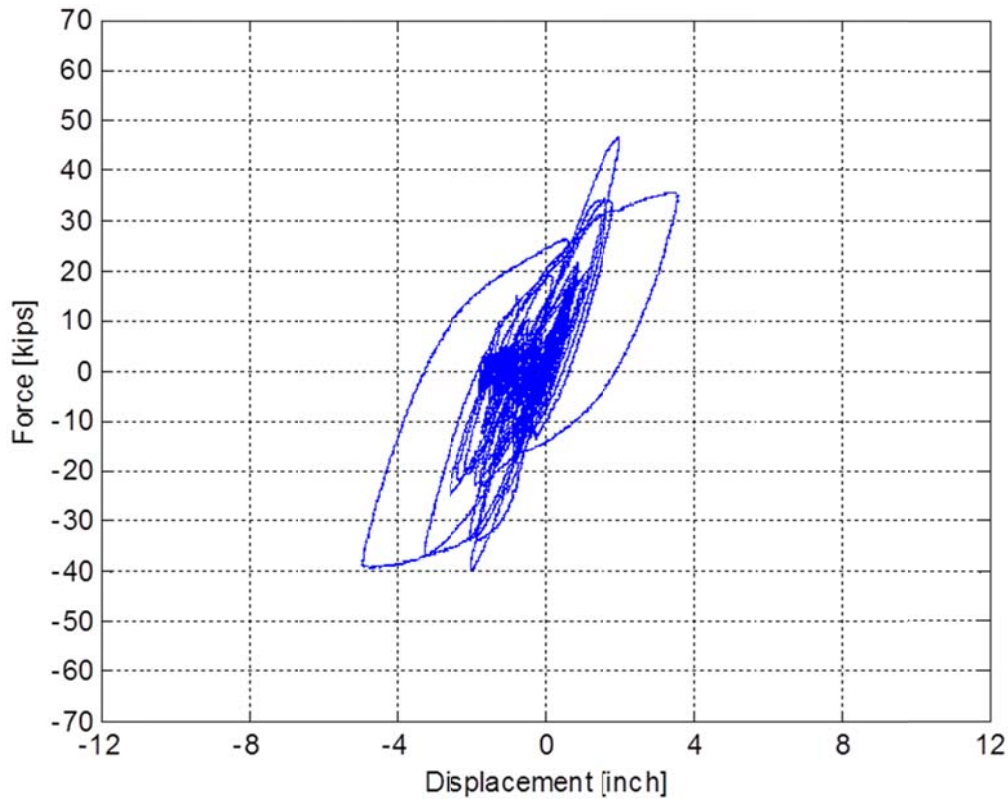
Figure 8.22 Force-displacement relationship in the longitudinal direction for all SP2 HS test runs

A closer look at the behavior during individual test runs is given in Figure 8.23 through Figure 8.25. The force-displacement relationship due to the 100% bidirectional tests only is shown in Figure 8.23 and Figure 8.24 when the ground motion was input in the positive direction and reversed in the negative direction, respectively, for both the transverse and longitudinal directions. These resolved force and displacement components revealed a slightly different response in each direction. Moreover, the initiation of damage and hysteretic inelastic behavior led to a different asymmetric response when the ground motion direction was reversed irrespective of the column symmetry and the similarity of the input motion. A maximum value of about 30 kips for the transverse force value was observed in one direction versus a maximum of almost 40 kips when loading was reversed in the other direction. The same observation was pronounced in Figure 8.25 where the force-displacement relationship obtained from the positive 175% transverse-only HS test is compared against the one obtained from the negative 175% test, i.e. reversed direction.
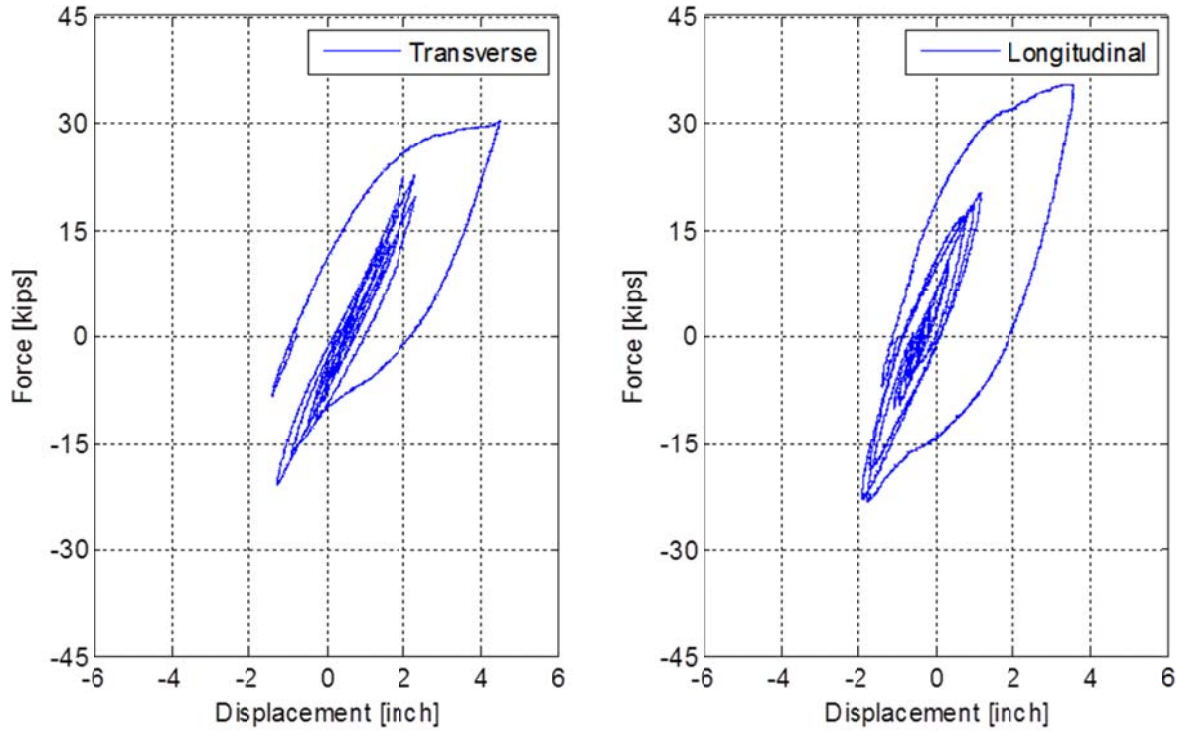
Figure 8.23 Force-displacement relationship in both transverse and longitudinal directions for the 100% bidirectional HS test with positive direction ground motion input
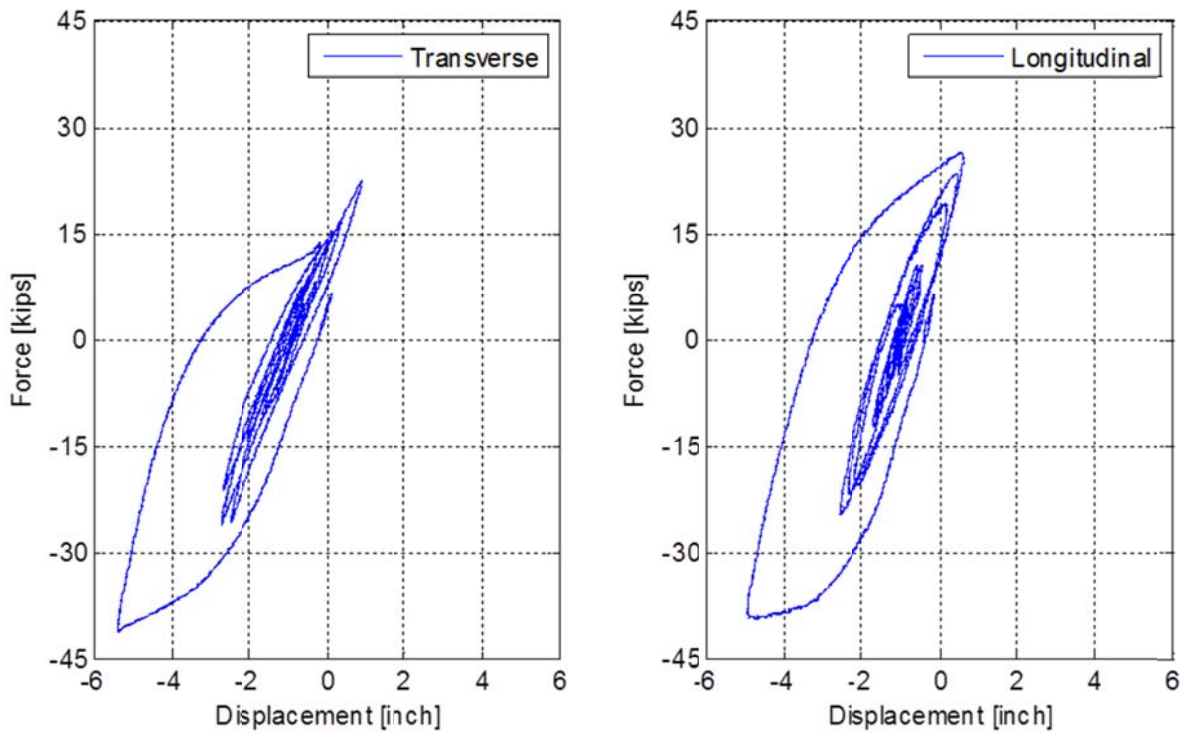
Figure 8.24 Force-displacement relationship in both transverse and longitudinal directions for the 100% bidirectional HS test with negative direction ground motion input
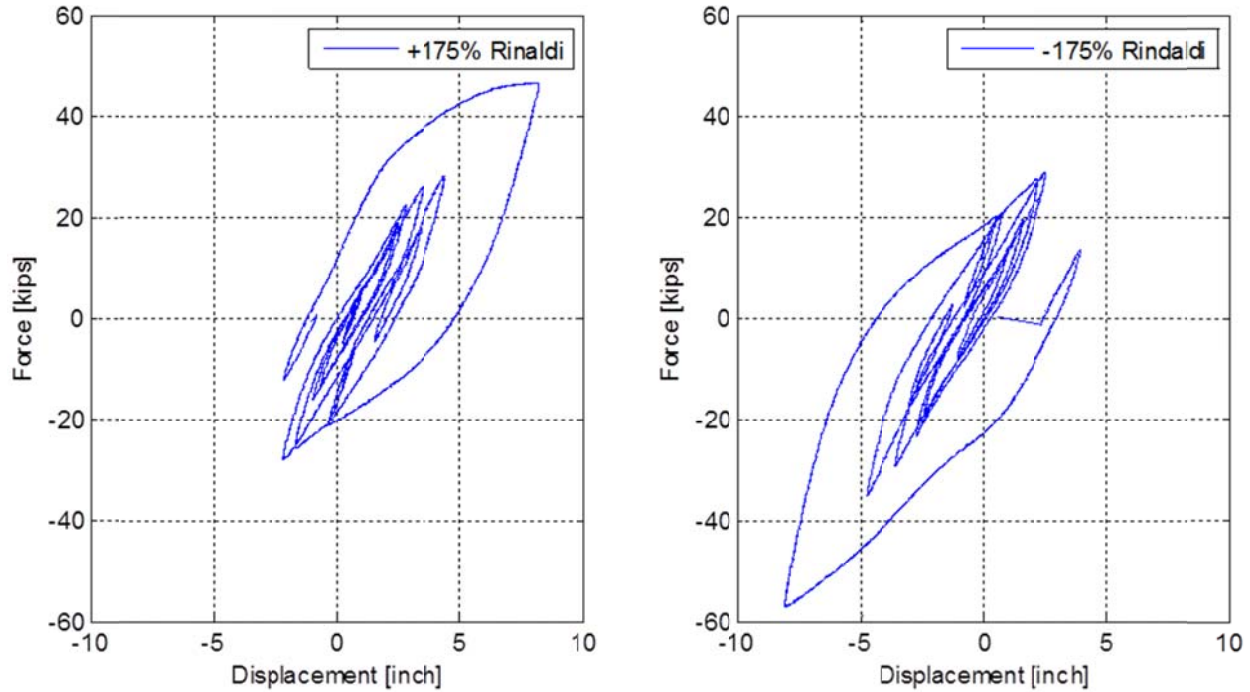
Figure 8.25 Force-displacement relationship in the transverse direction for the 175% transverse-only HS test with positive (left) and negative (right) ground motion inputs

8.3.4 Comparison with OpenSees data

One of the capabilities of utilizing OpenSees and OpenFresco for conducting the HS tests is recording the received force feedback and the computed displacements. Ideally, if the HSS does not have any delays or errors, the applied displacement should match perfectly the computed displacement at the computational platform end. Figure 8.26 and Figure 8.27 show the force-displacement relationships in the transverse and longitudinal directions, respectively, as comparisons between the measured test data and the OpenSees recorders for all 15 HS test runs. Although the effect of experimental errors and delays should be minimal as verified from the HSS development and validation trials discussed in Chapter 7, a large discrepancy, which was mainly because of displacements, can be observed from the comparisons. This is because the computed displacements in OpenSees started from zero each time a new test was conducted without recording the residual displacement from the previous test. Thus, a better comparison would be achieved if the residual displacement at the start of each test is added to the OpenSees data. However, this would not have add benefits as only the force comparison is more practical to assure that the measured load cells values where comparable to what OpenSees utilized in solving the equations of motion. To exclude the discrepancy in the displacements, only the force values in the transverse direction were plotted against the forces in the longitudinal direction and comparisons between the measured test data and the OpenSees recorders are shown in Figure 8.28. It is to be noted that although some runs incorporated P-delta corrections for the force feedbacks sent to OpenSees, the two plots compare reasonably well and give confidence that the correct measured forces were utilized in the displacement calculations. The difference due to the P-delta correction should be minimal as the largest correction force value did not exceed 10% of the actual measured value. Meanwhile, only the bidirectional runs included the P-

303

delta correction, while the transverse-only large-scale runs did not include the correction, as discussed above. Thus, for these large-scale runs, the measured force feedback was directly sent to the computational platform without any modifications.
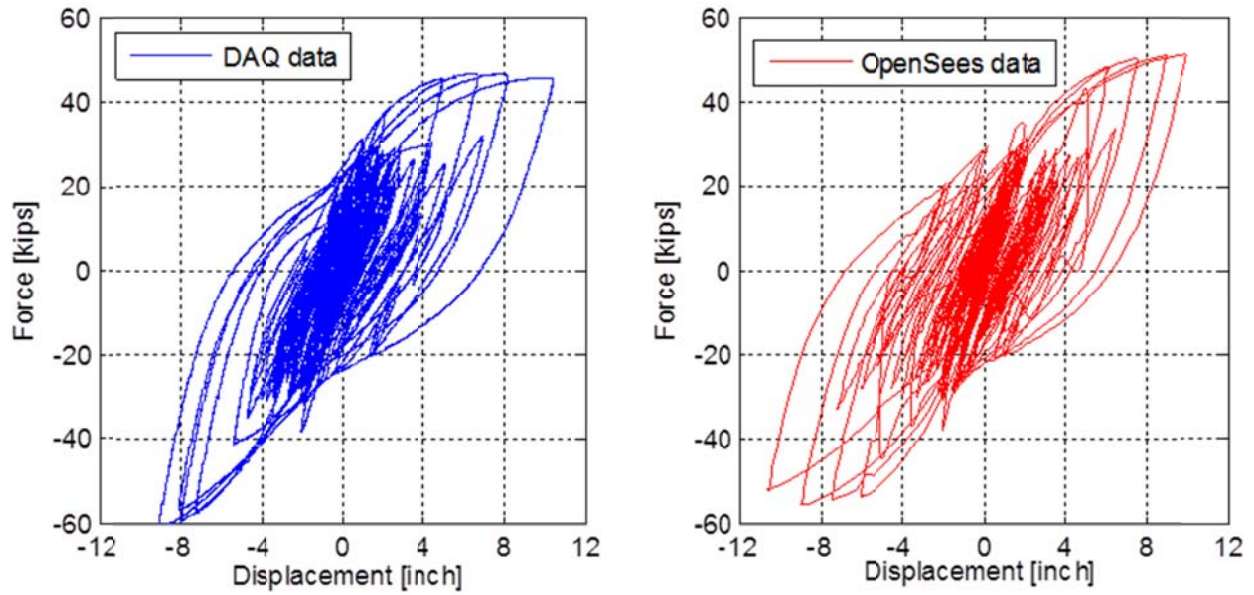
Figure 8.26 Comparison of force-displacement relationship for all HS test runs as obtained from the observed data acquisition (DAQ) experimental test data and the recorded OpenSees data in the transverse direction
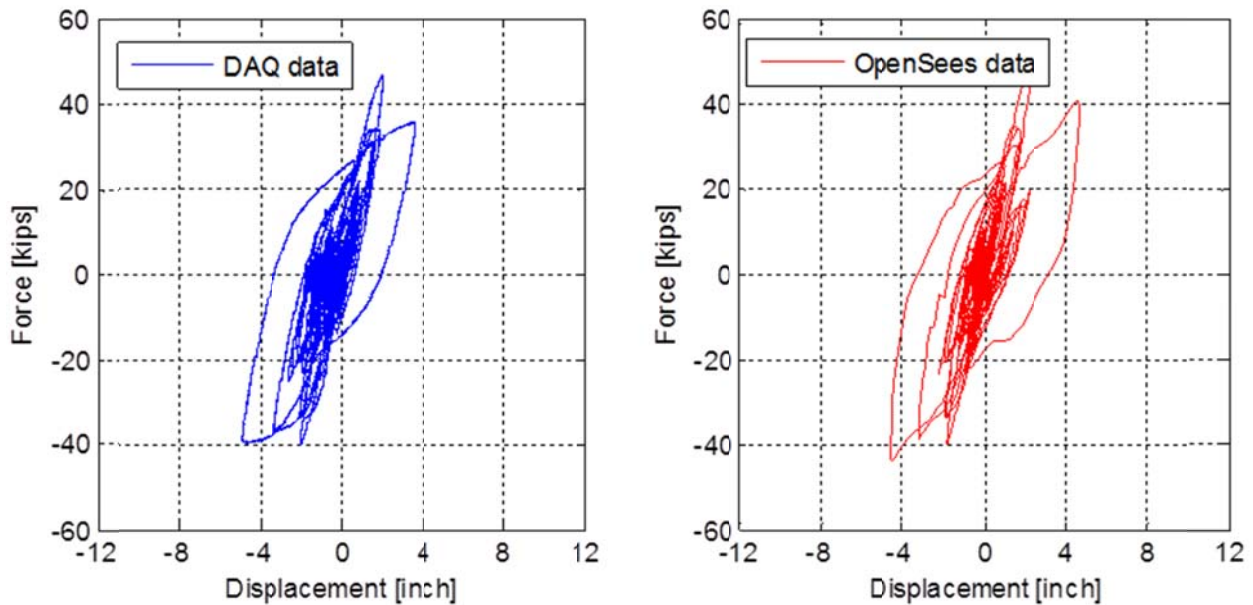
Figure 8.27 Comparison of force-displacement relationship for all HS test runs as obtained from the observed data acquisition (DAQ) experimental test data and the recorded OpenSees data in the longitudinal direction
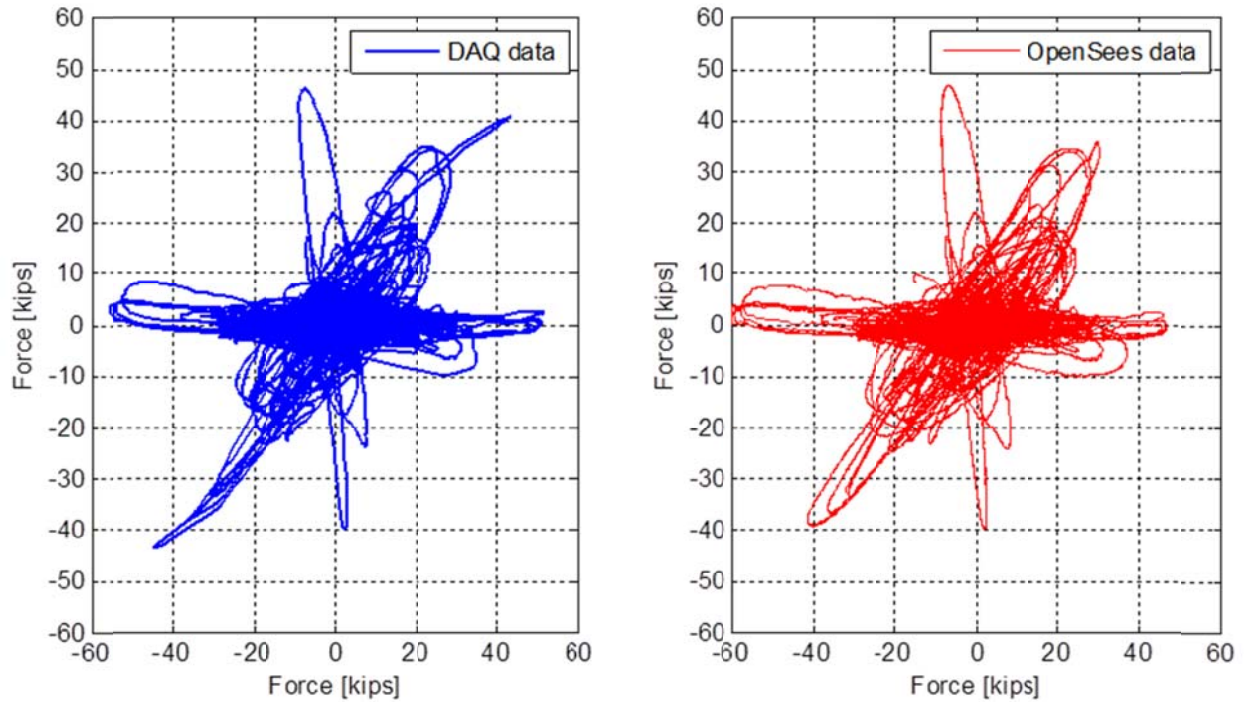
Figure 8.28 Comparison of the transverse-longitudinal force relationship for all HS test runs as obtained from the observed data acquisition (DAQ) experimental test data and the recorded OpenSees data

8.4   COLUMN LOCAL BEHAVIOR

The main objective of the experimental program is to evaluate the bent cap beam behavior and the effective slab width. However, the column local behavior from the as-built SP1 tests was extensively discussed in Chapter 5. Thus, only brief discussion of the column in the SP2 HS tests is presented here in relation to the column reinforcement strain history, section moments and curvatures, and the CFRP jacket strains. A complementary discussion is presented in the last subsection where a comparison is made between the as-built and retrofitted behavior to evaluate the effectiveness of the retrofitting technique.

8.4.1   Strain History

No bar buckling or rupture took place during the HS test runs due to the confinement provided by the CFRP jacket. However, extensive yielding was observed in the instrumented column longitudinal reinforcement within the plastic hinge zone. Before presenting the strain history at the maximum strain location, the four column instrumented bars as related to the loading direction is presented in Figure 8.29. Figure 8.30 shows the strain history in the two bars that experienced the highest strain for all the 15 SP2 HS tests in the North and South directions. Similarly, Figure 8.31 shows the strain history for the East and West sides. It is observed that the strain in the East and West sides of the column reached much higher strain levels because that was the direction where the transverse-only large-scale runs were applied. Meanwhile, to study the extent of extensive yielding in the column in the transverse direction, the strain history in the

305

East and West sides is plotted at two levels in addition to the level of maximum strain shown in Figure 8.31. One level is 18 in. from the face of the bent cap beam, which corresponds to the end of the anticipated plastic hinge zone in a conventional column without CFRP jacket, is shown in Figure 8.32. The second level is at the column mid-height, Figure 8.33. Extensive yielding was observed throughout the anticipated plastic hinge region, while the column mid-height remained elastic as expected.
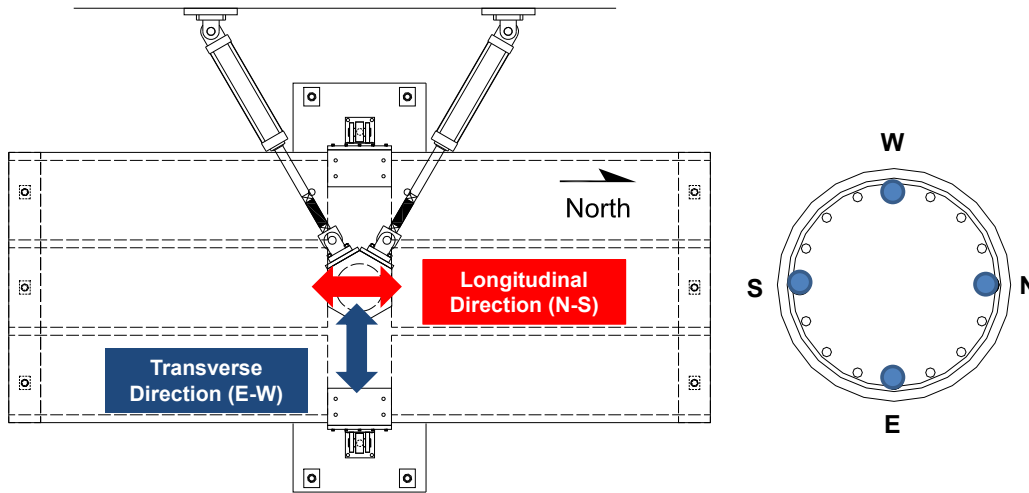
Figure 8.29 layout of the instrumented column rebars in SP2 as related to the loading directions
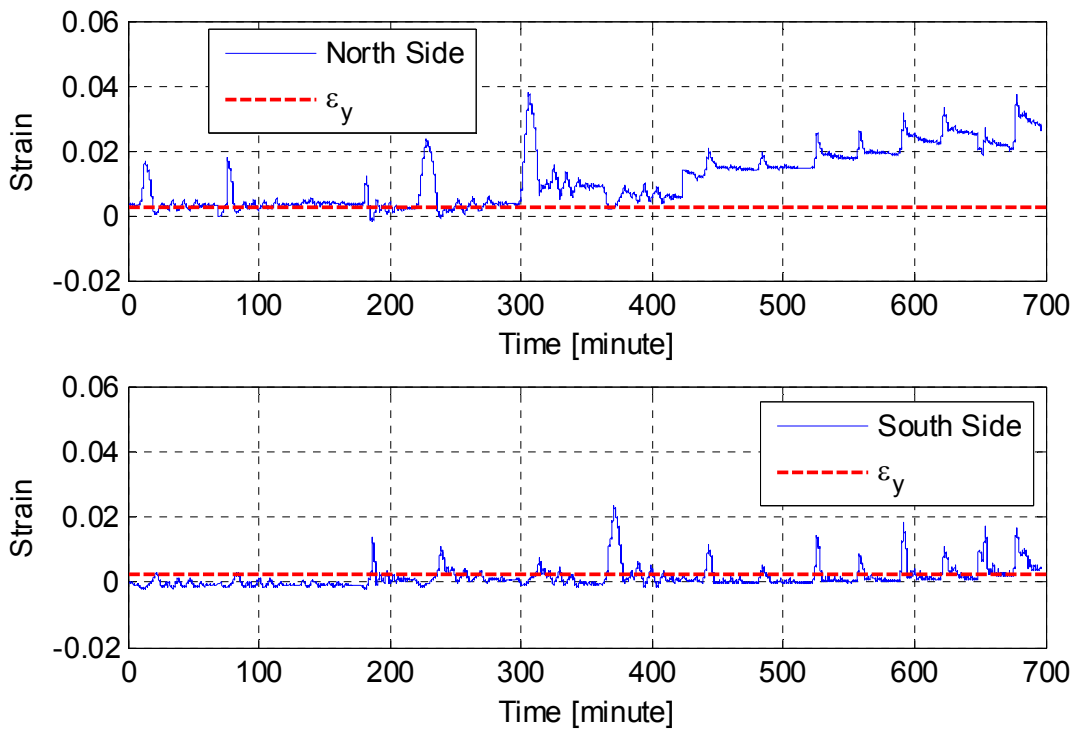
Figure 8.30 Strain history in North and South side column bars due to all HS tests at maximum strain location (close to the cap beam face
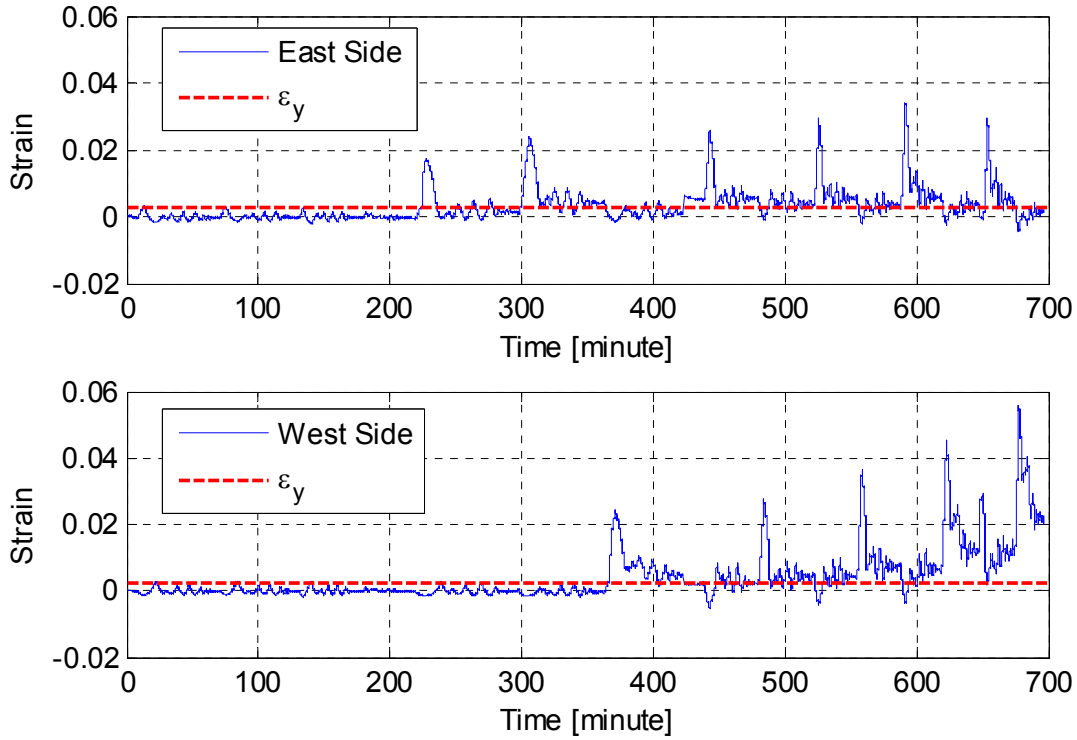
Figure 8.31 Strain history in the East and West side column bars due to all HS tests at maximum strain location (close to the cap beam face)
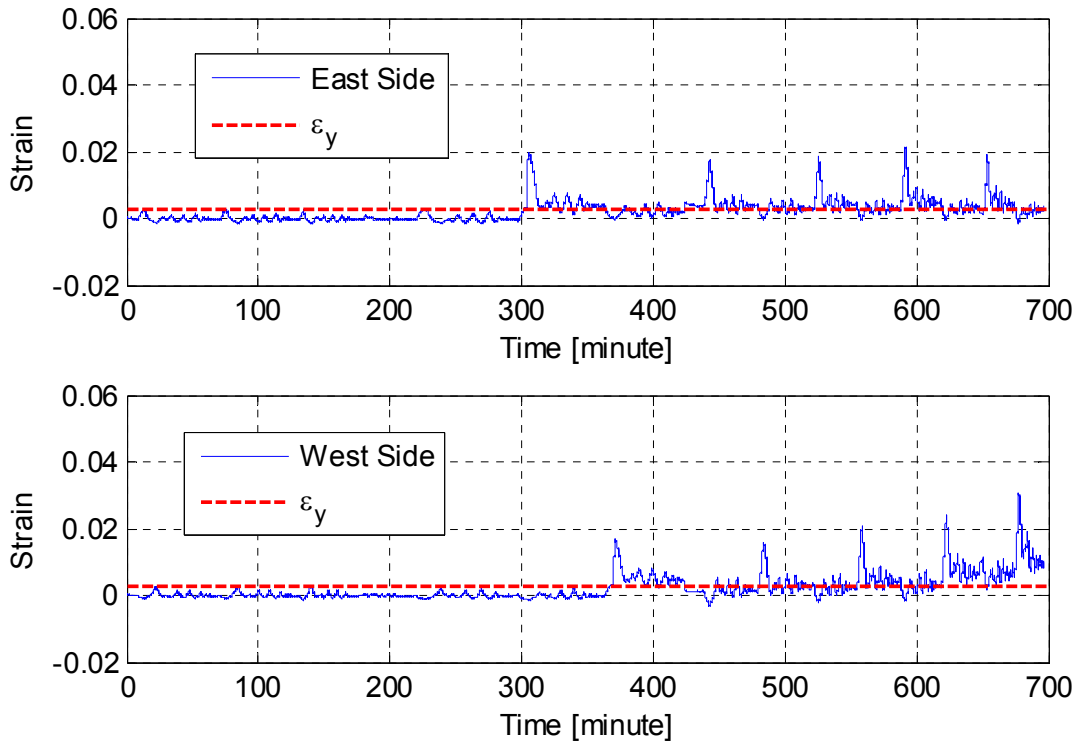
Figure 8.32 Strain history in the East and West side column bars due to all HS tests at height of 18 in. from the cap beam face

307
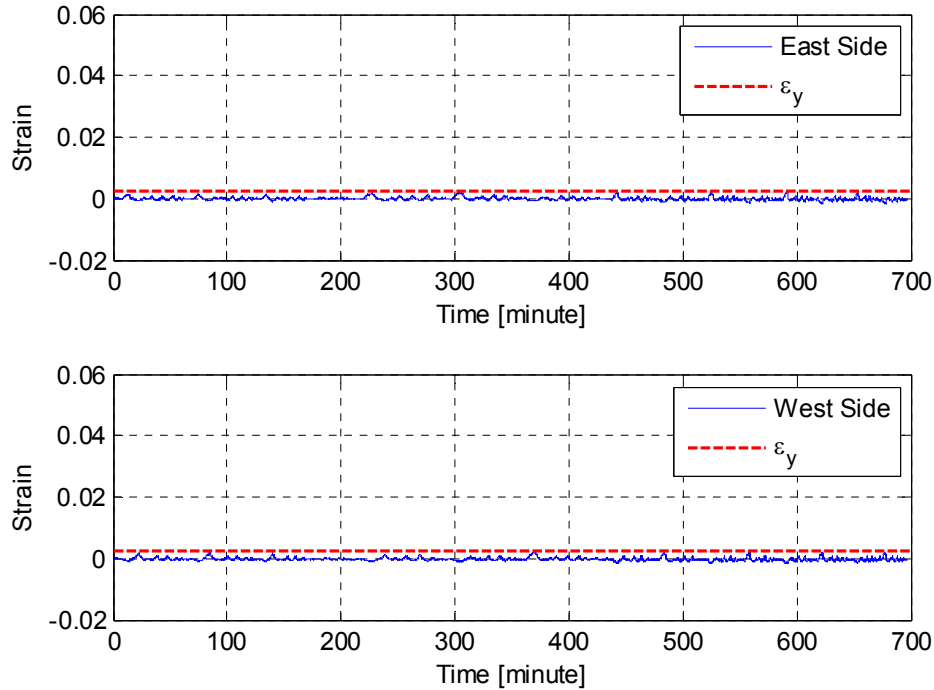
Figure 8.33 Strain history in the East and West side column bars due to all HS tests at the column mid-height (51 in. from the bent cap beam face)

8.4.2 Moment and Curvature History

The bending moment at the column-bent cap interface, where the maximum moment was expected, was estimated from the applied lateral force. Figure 8.34 shows the full history of the calculated column moment in both the transverse and longitudinal directions. A zoomed-in view of the column moment due to the large-scale transverse-only HS tests is shown in Figure 8.35. The maximum observed moment is compared to that of the as-built column in a later section. However, while that maximum moment can be considered larger than the yield moment, it cannot be claimed that this higher moment represented the retrofitted column moment capacity because the observed visual damage suggested that the system capacity was capped due to the bent cap beam concrete crushing manifested in the form of concrete cover spalling in the vicinity of the column.

The curvatures at various column sections were estimated during the HS test runs. A detailed discussion of the curvature distribution along the column height and a comparison between the strain-based versus the LVDT-based curvatures was previously presented in Chapter 5 for the as-built SP1 specimen. Thus, only the LVDT-based curvature history at the location of maximum expected curvature is shown in Figure 8.36 for all the 15 SP2 HS test runs in the transverse and longitudinal directions. Moreover, a zoomed-in view of the curvature history for the transverse-only large-scale runs is shown in Figure 8.37. It can be observed from Figure 8.37 that the column section was somewhat responding in the longitudinal direction although loading was only applied in the transverse direction. That is attributed to the residual displacements (discussed earlier) that led a portion of the transverse loading to actually be accompanied with some loading in the longitudinal direction. The obtained curvatures at other column-height levels are also presented through the moment-curvature relationships in the next subsection.

308
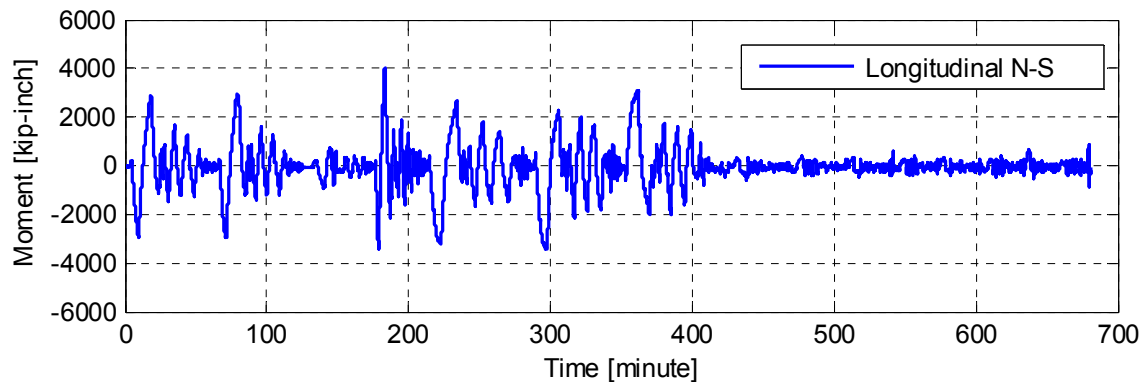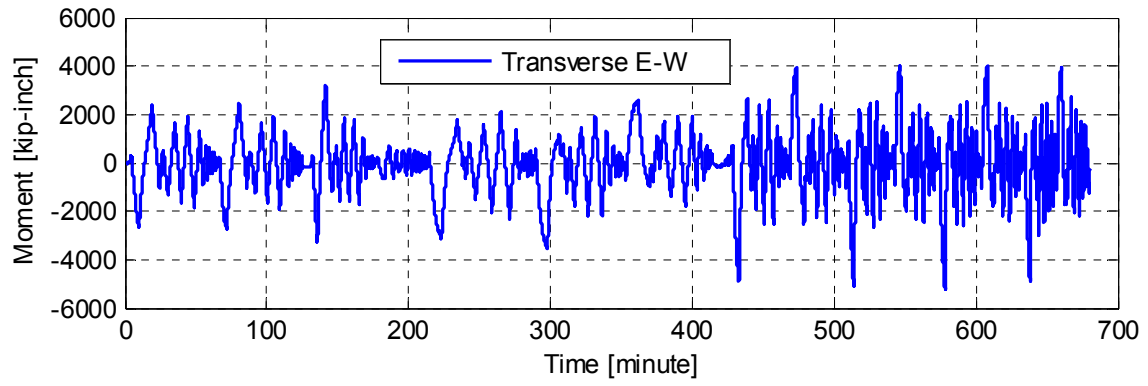
Figure 8.34 Column moment history at maximum location for all HS test runs
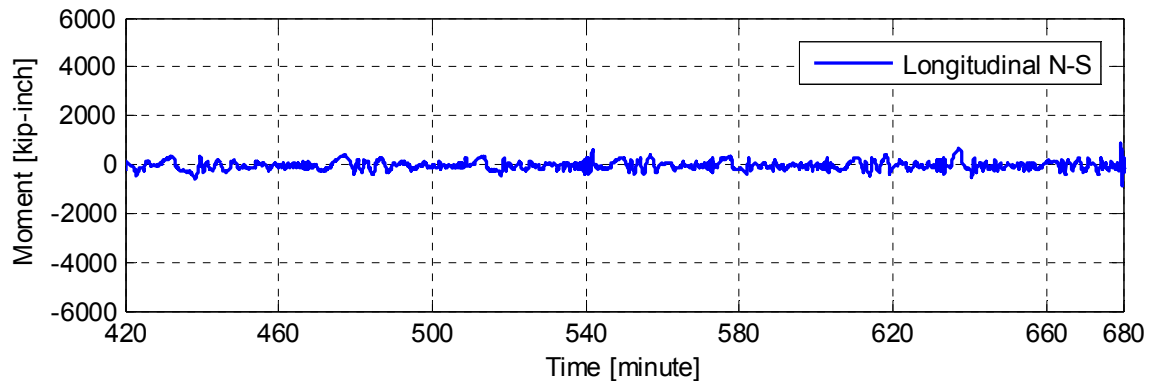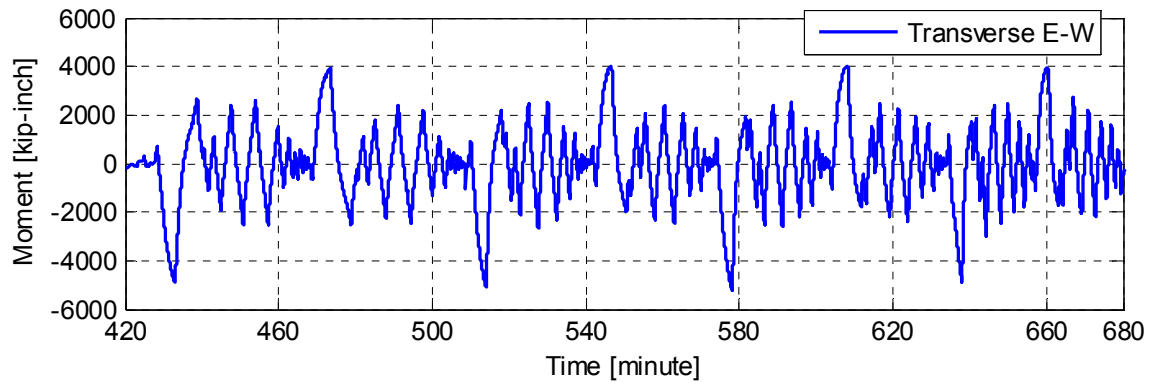
Figure 8.35 Zoomed-in view of the column moment history at maximum location for the large-scale transverse-only HS test runs

309
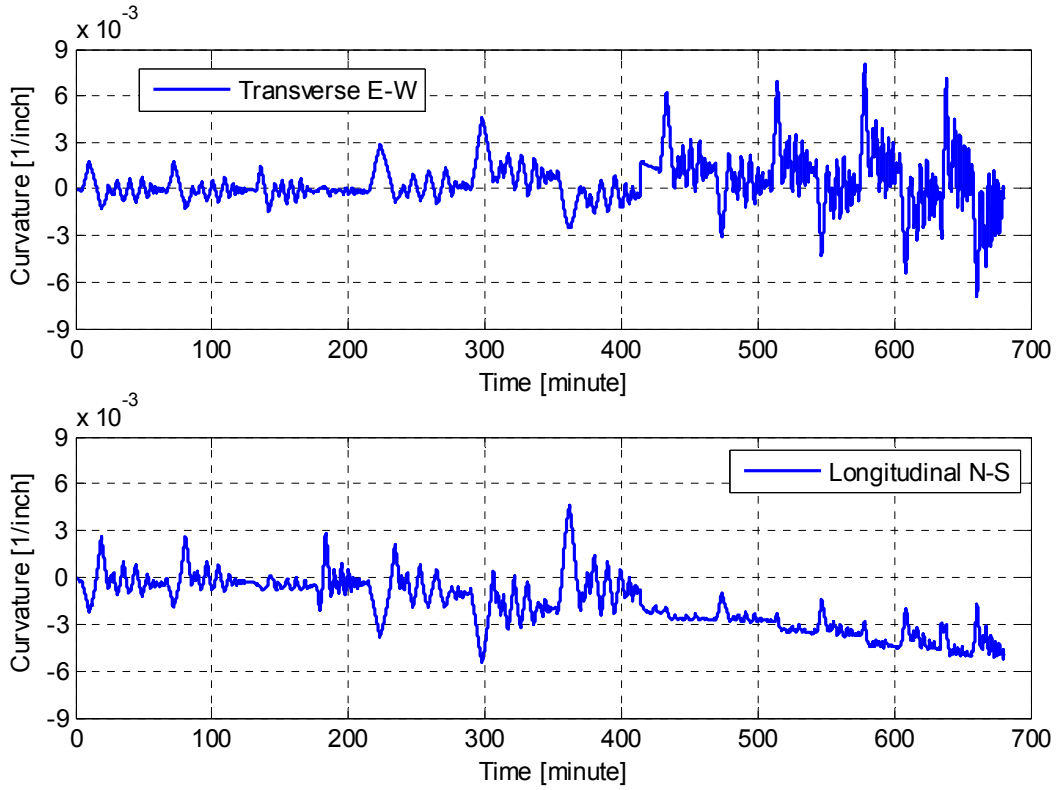
Figure 8.36 Column curvature history at maximum location for all HS test runs
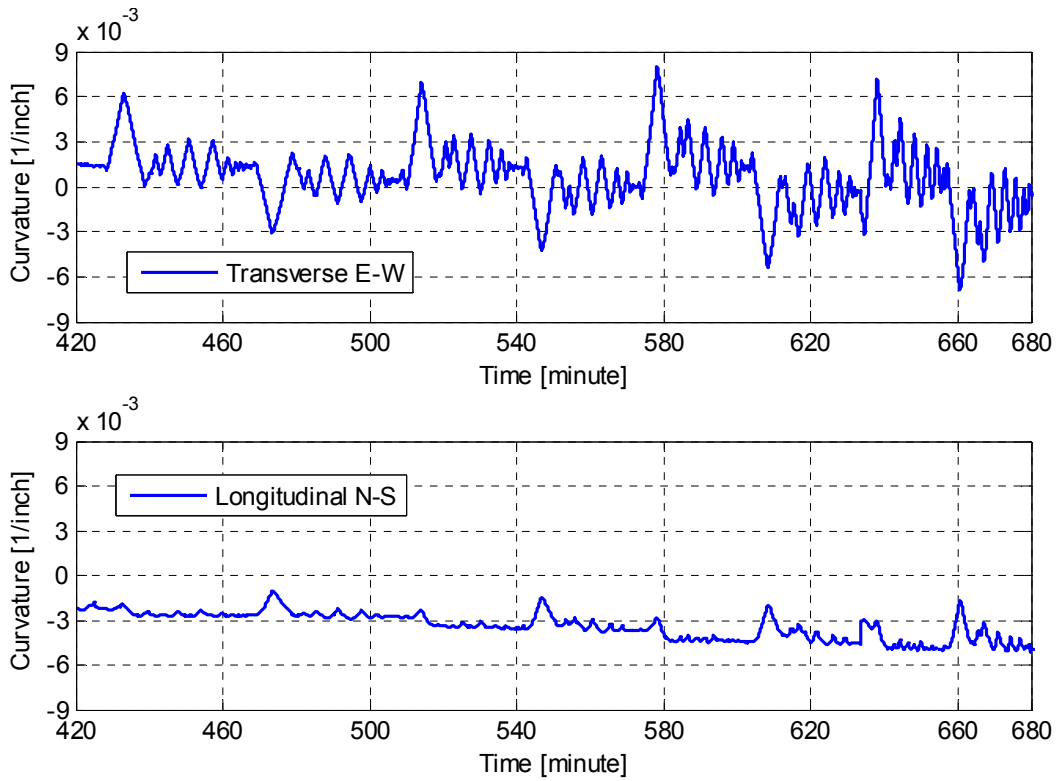
Figure 8.37 Zoomed-in view of the column curvature history at maximum location for the large-scale transverse-only HS test runs

310

8.4.3 Moment-Curvature Relationship

The moment and curvature histories were shown at few levels in both the transverse and longitudinal directions in the previous subsection. However, the moment-curvature relationship is shown here at all levels for completeness. As previously mentioned, all the presented curvature measurements for the HS tests are based on the LVDTs measurements rather than the strain measurements. That is because it was shown in Chapter 5 that the strain-based curvature calculations are not very reliable especially at higher deformation levels. The moment-curvature relationships from bidirectional HS tests are presented separately from the large-scale transverse-only runs to keep the plots simpler and more informative.

8.4.3.1 *Bidirectional Tests*

Bidirectional HS tests applied loading in both the transverse and longitudinal directions simultaneously as a result of solving the MDOF computational model under two-component horizontal excitation. The moment-curvature relationship is compared for all the bidirectional runs in the transverse and longitudinal directions at different levels along the column anticipated plastic hinge zone. Figure 8.38 shows the moment-curvature relationship at the section of expected largest moment and curvature, i.e. 4 in. from the cap beam face. Figure 8.39, Figure 8.40, and Figure 8.41 show the moment-curvature relationships at sections which were 10, 16, and 22 in. away from the bent cap beam face, respectively. It can be noticed that although the largest bidirectional HS test was conducted at 100%-scale, the column hysteresis was only pronounced within 10 inch from the cap beam face, i.e. no column damage extended through the whole conventional plastic hinge region up to the 100%-scale runs. It is shown in the following subsection that as larger ground motion scales were applied, the hysteretic damage extended to larger height of the column.
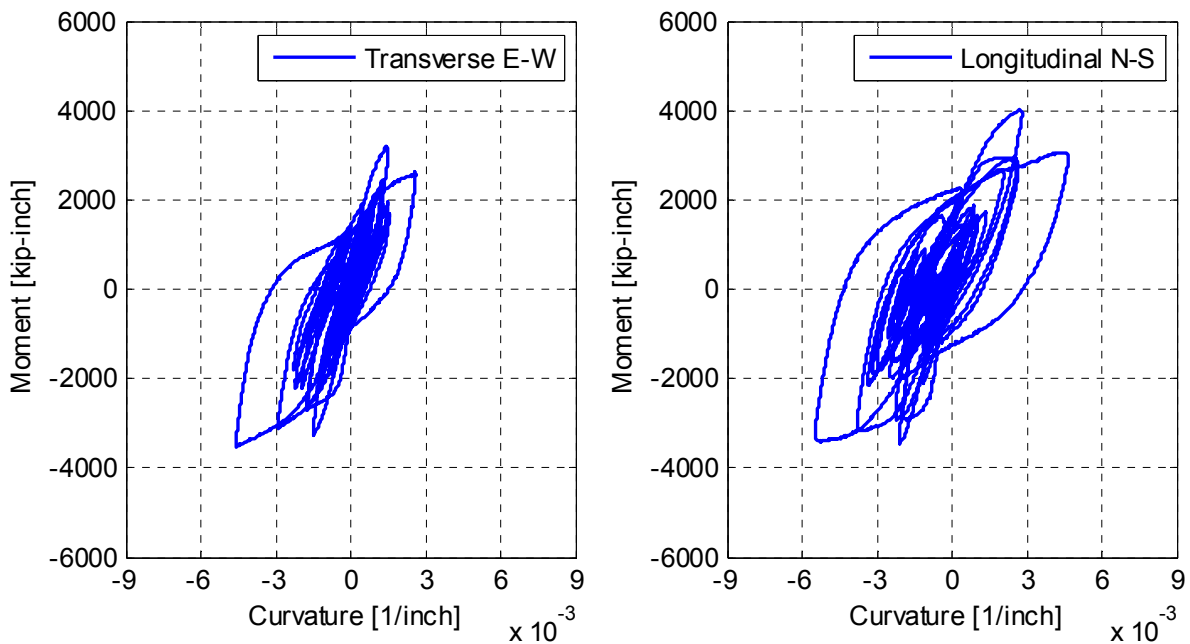
Figure 8.38 Column moment-curvature relationship in transverse and longitudinal directions at 4 inch from the cap beam face for all bidirectional HS test runs
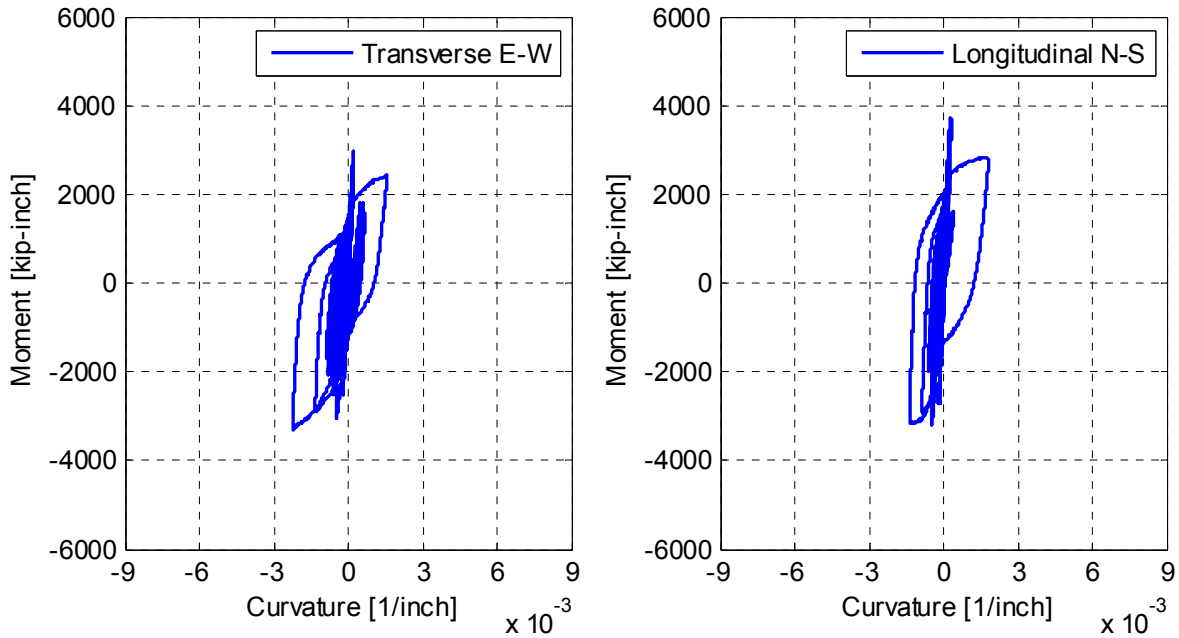
Figure 8.39 Column moment-curvature relationship in transverse and longitudinal directions at 10 inch from the cap beam face for all bidirectional HS test runs
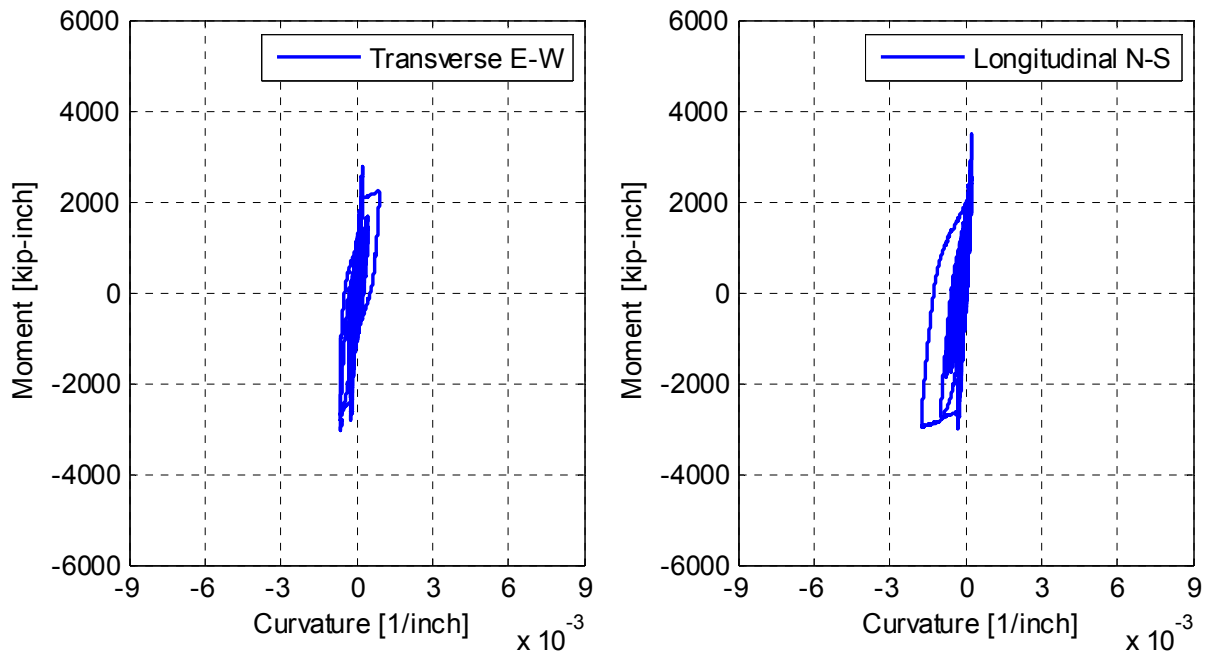
Figure 8.40 Column moment-curvature relationship in transverse and longitudinal directions at 16 inch from the cap beam face for all bidirectional HS test runs

It is also observed that the curvature values were slightly higher in the longitudinal direction than in the transverse direction for comparable moment demands. This led to wider hysteresis moment-curvature loops in the longitudinal direction and more energy dissipation than the transverse direction as obvious in Figure 8.38 where the largest moments and curvatures were measured.

312
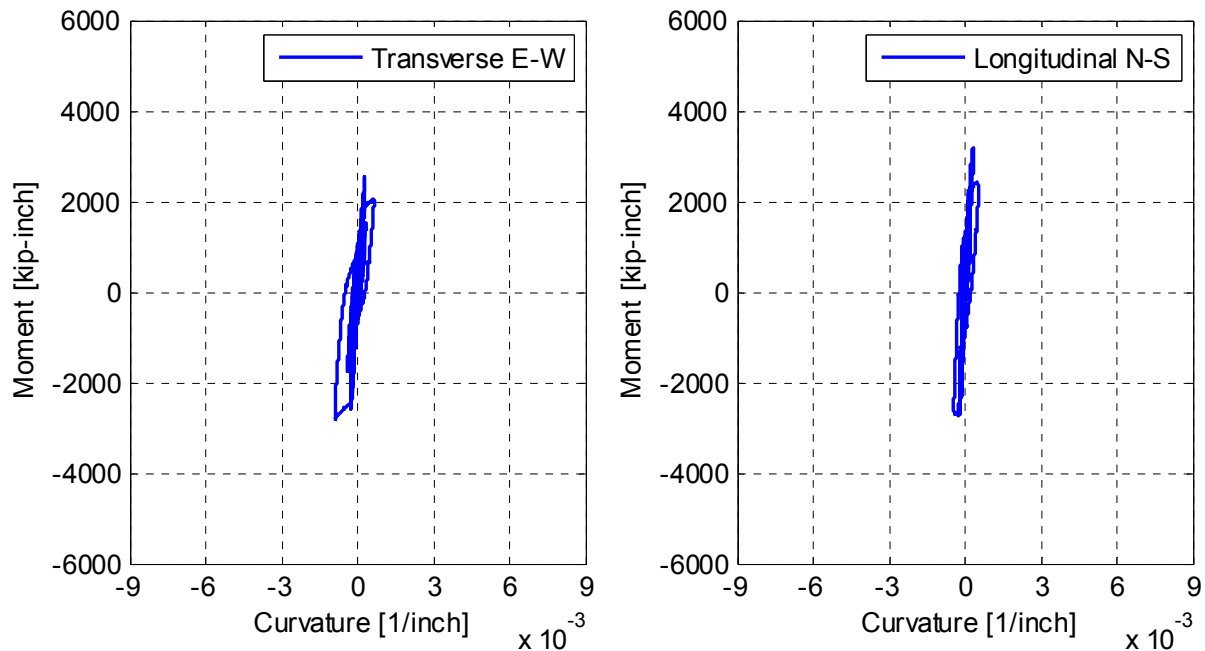
Figure 8.41 Column moment-curvature relationship in transverse and longitudinal directions at 22 inch from the cap beam face for all bidirectional HS test runs

8.4.3.2 *Transverse-Only Tests*

The moment-curvature relationships for the large-scale eight HS runs that applied the transverse-only Rinaldi ground motion scaled at 125% through 200% in positive and negative directions are shown here. Since the ground motion was applied only in the transverse direction, the moment-curvature in the transverse direction only is discussed. Similar to the above discussion, the moment-curvature relationship is plotted at various sections along the column height to explore the extent of the hysteresis damage in the column; especially that visual evidence was not possible because of the confining CFRP jacket. Five levels at 4, 10, 16, 22, and 51 inch away from the cap beam face were used to generate the moment-curvature relationship in the transverse direction as presented in Figure 8.42 to Figure 8.46, respectively.

It can be observed that the hysteresis damage was extensive at the largest measured moment and curvature location, i.e. 4 in. from the cap beam face. Figure 8.42 shows also that higher moments were reached in one side of the column than the other. That was attributed to the nature of the HS loading along with the accumulated residual displacement in a certain direction which generated displacement input loading of less value in one direction than the opposite one. It cannot be claimed from the observed moment values that the column reached its capacity as the visual evidence during the test suggested that the system force capacity was capped due to the onset of the concrete crushing in the compression zone of the bent cap beam, as previously stated. More details about the observed damage were presented earlier in Section 8.2. Moreover, when the CFRP jacket was removed, only a uniform pattern of flexural cracks were observed that extended to a region of almost 20 in., which roughly corresponded to the conventional plastic hinge length in columns without CFRP jackets. The moment-curvature relationships confirm that the hysteresis damage extended throughout the plastic hinge length as shown in

313

Figure 8.42 through Figure 8.45. On the other hand, Figure 8.46 shows that the column remained elastic at the mid-height as previously observed from the strain values.
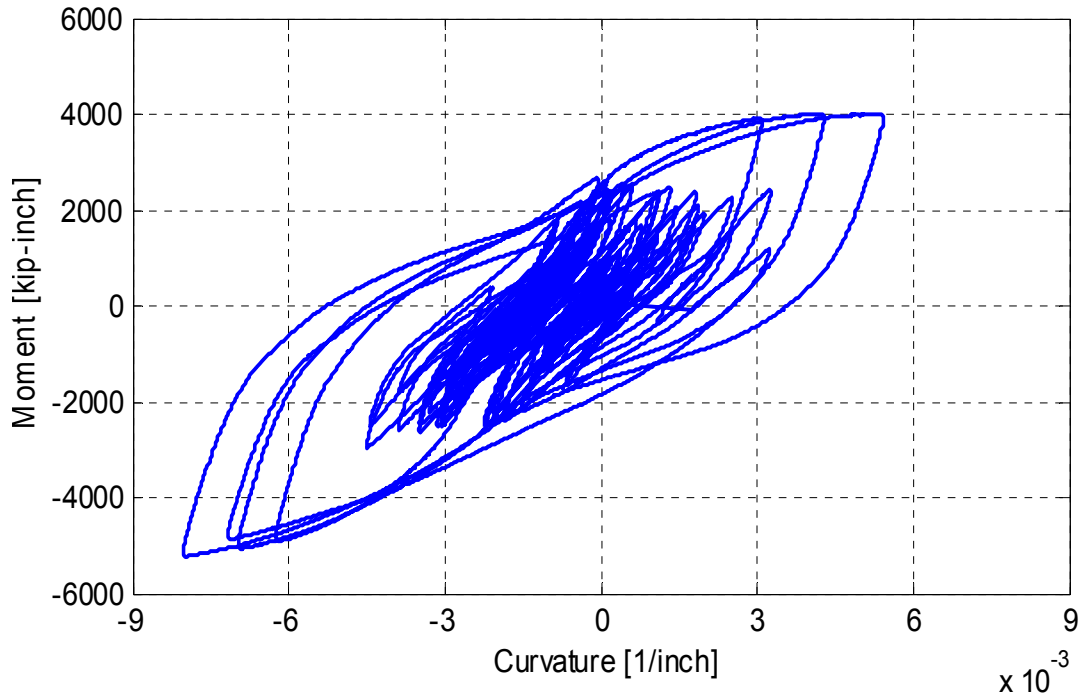
Figure 8.42 Column moment-curvature relationship in the transverse direction at 4 inch from the cap beam face for the large-scale transverse-only HS test runs
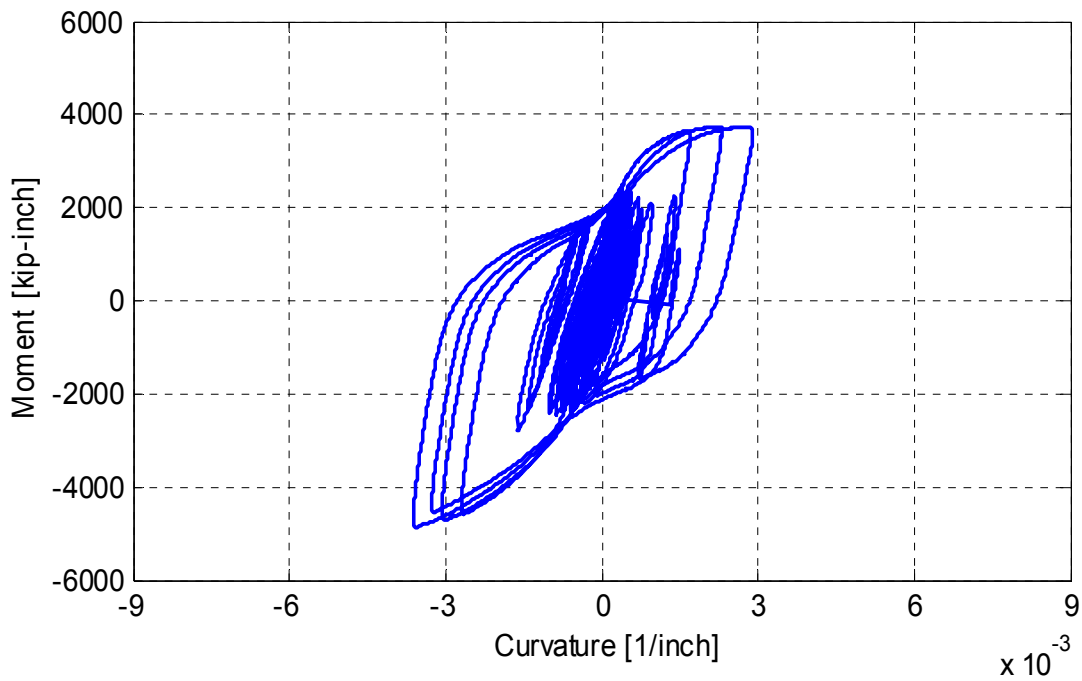
Figure 8.43 Column moment-curvature relationship in the transverse direction at 10 inch from the cap beam face for the large-scale transverse-only HS test runs
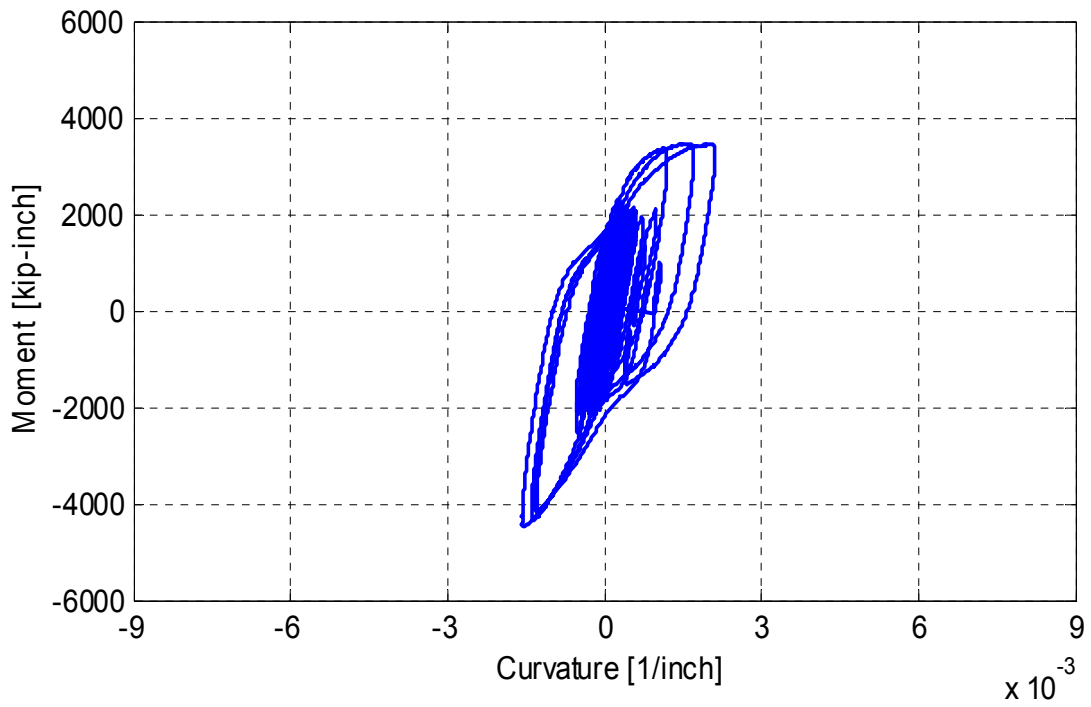
Figure 8.44 Column moment-curvature relationship in the transverse direction at 16 inch from the cap beam face for the large-scale transverse-only HS test runs
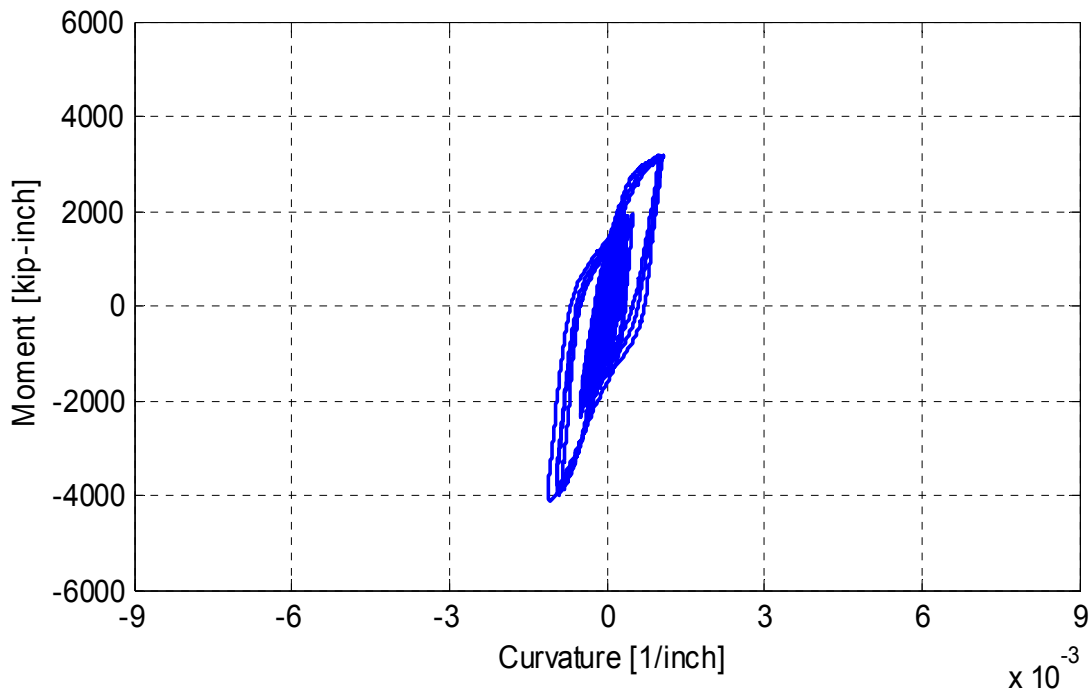
Figure 8.45 Column moment-curvature relationship in the transverse direction at 22 inch from the cap beam face for the large-scale transverse-only HS test runs
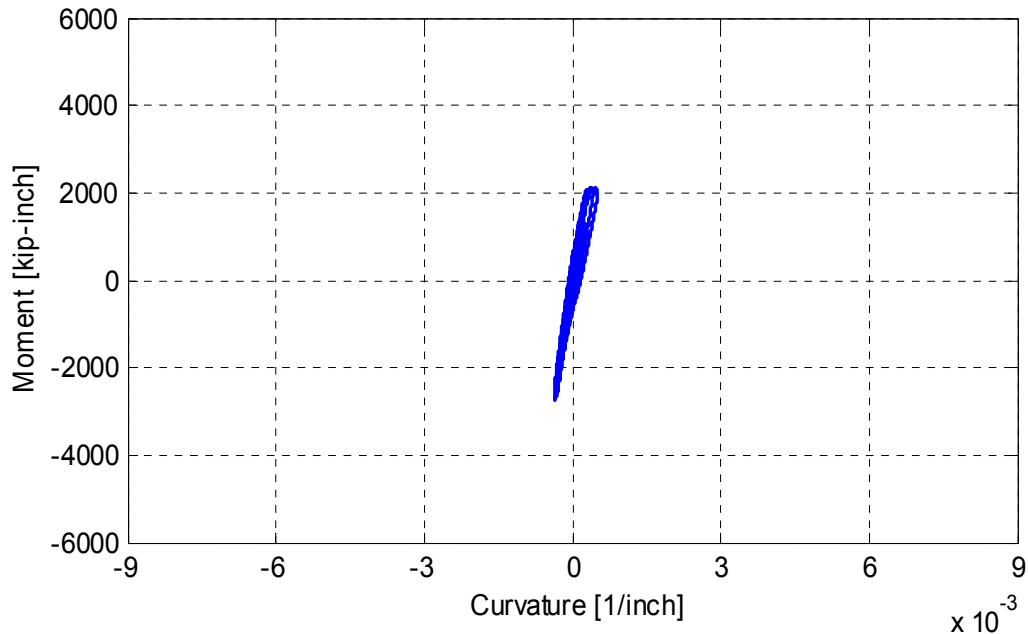
Figure 8.46 Column moment-curvature relationship in the transverse direction at the column mid-height for the large-scale transverse-only HS test runs

8.4.4 CFRP Jacket Strain

The second specimen differed from the originally identical first specimen because of the CFRP retrofit of the column. One central response quantity for column retrofitted using CFRP jacket is the confinement effectiveness due to the jacket. For this reason, several strain gages were installed around the circumference of the jacket at two levels 18 inch apart within the typical plastic hinge length. The first level was at 2 in. from the cap beam face. Each level was instrumented with 12 strain gages as shown in Figure 8.47.
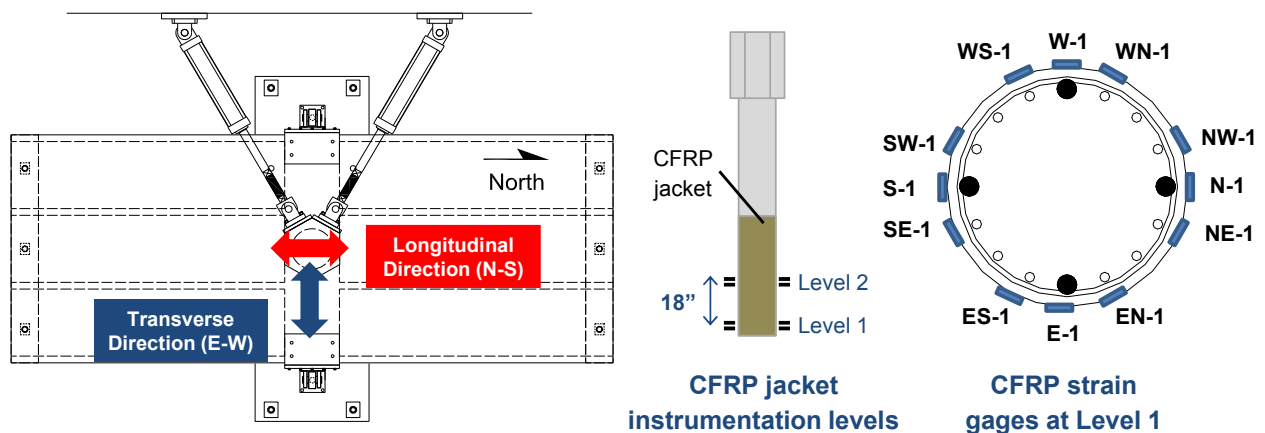
Figure 8.47 Layout of the CFRP jacket strain gages as related to the loading directions

The confining strain history at the outermost East and West sides of the first instrumentation level of the CFRP jacket, designated as E-1 and W-1 in Figure 8.47, is shown for

all the 15 HS test runs in Figure 8.48. Similarly, the strain history at the North and South strain gages N-1 and S-1 is shown in Figure 8.49 for all the HS test runs. The peaks observed in the confining strain history suggested that the jacket was effectively responding to the loading where a larger confining strain was developed at the compression side of the column relative to a certain loading direction. This is because as the increase in the compressive stress in one column side under combined axial and bending action might cause bar buckling, which was restrained by the concrete cover that in turn was well-confined by the CFRP jacket. Thus, any desired expansion in the concrete cover is outweighed by the confining CFRP jacket as long as the jacket remained intact and effective. A similar observation can be better demonstrated if the strain profile at a certain time instant at a given section in the CFRP jacket is graphically presented. Kumar et al. (2014) provided a novel approach to plot the recorded strain values at a given time instant for all strain gages in a given instrumentation level. The same approach is used to produce polar profiles of the confining strain around the entire jacket circumference as shown in Figure 8.50 to Figure 8.52. Figure 8.50 shows the confining strain profiles from each of the 12 installed strain gages at the two instrumentation levels when the displacement amplitude was reached during the negative 100% bidirectional test (ID 7). On the other hand, Figure 8.51 and Figure 8.52 show the strain profiles at the displacement amplitude of the positive 175% (ID 12) and 200% (ID 14) transverse-only HS tests, respectively. It can be observed that the confining strain was much less at the second instrumentation level, i.e. the confining strain decreased with the decrease pf the moment and stress demands, as expected. The profiles also point in a certain direction where the maximum compressive stress developed. In the bidirectional tests, it is implied that concrete expansion took place at both of the transverse and longitudinal directions, whereas the maximum strain at concrete expansion was aligned with the unidirectional transverse loading tests.
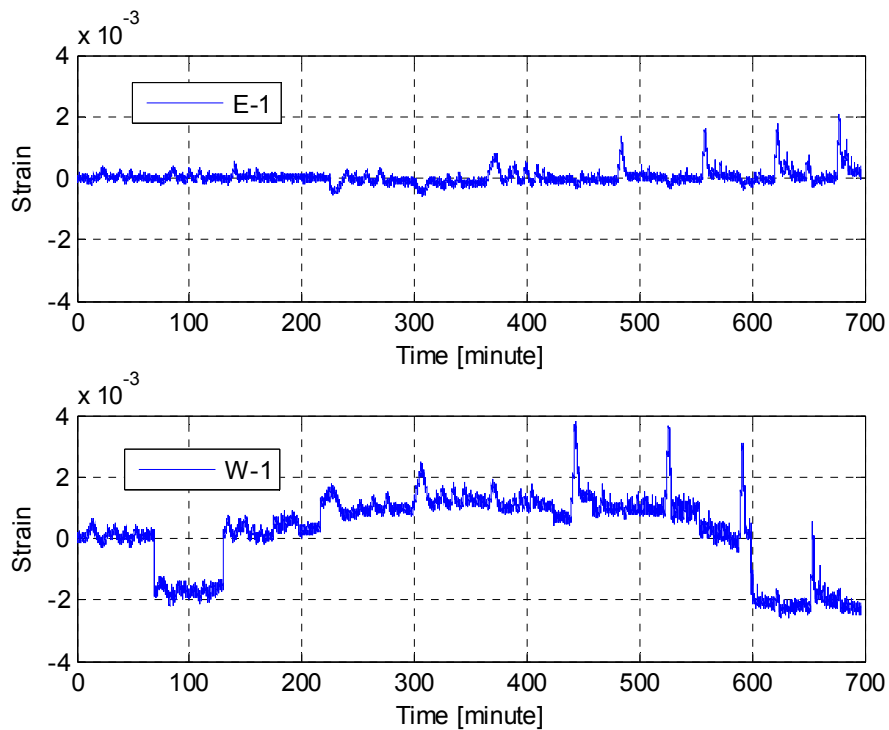
Figure 8.48 Confining strain history in the CFRP jacket East and West sides for all HS test runs
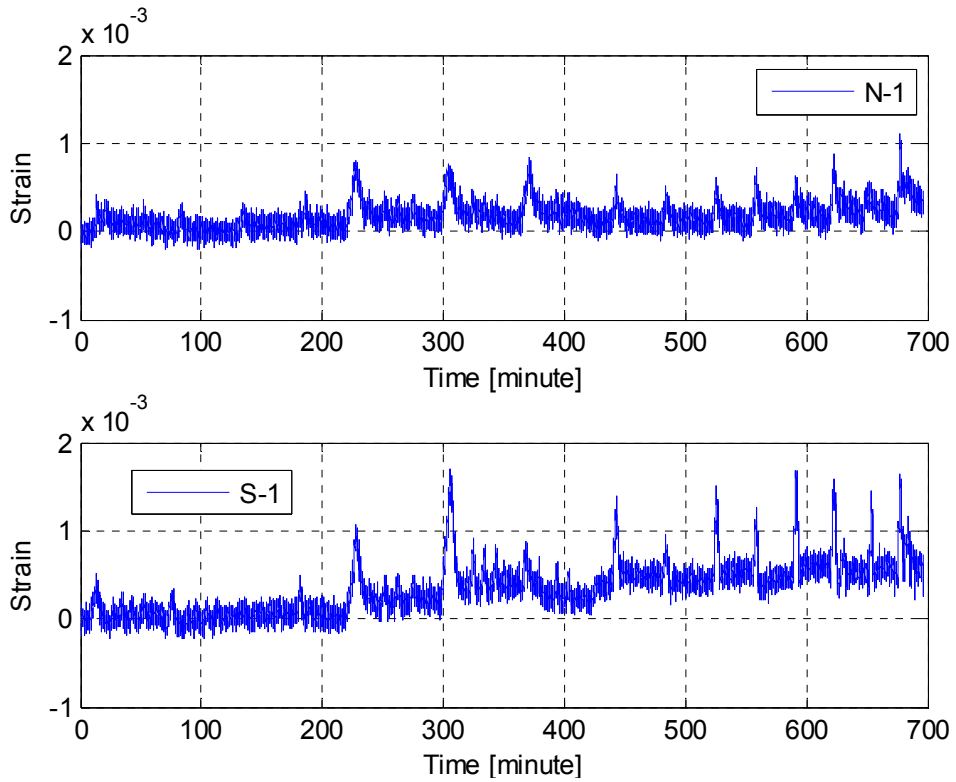
Figure 8.49 Confining strain history in the CFRP jacket North and South sides for HS test runs
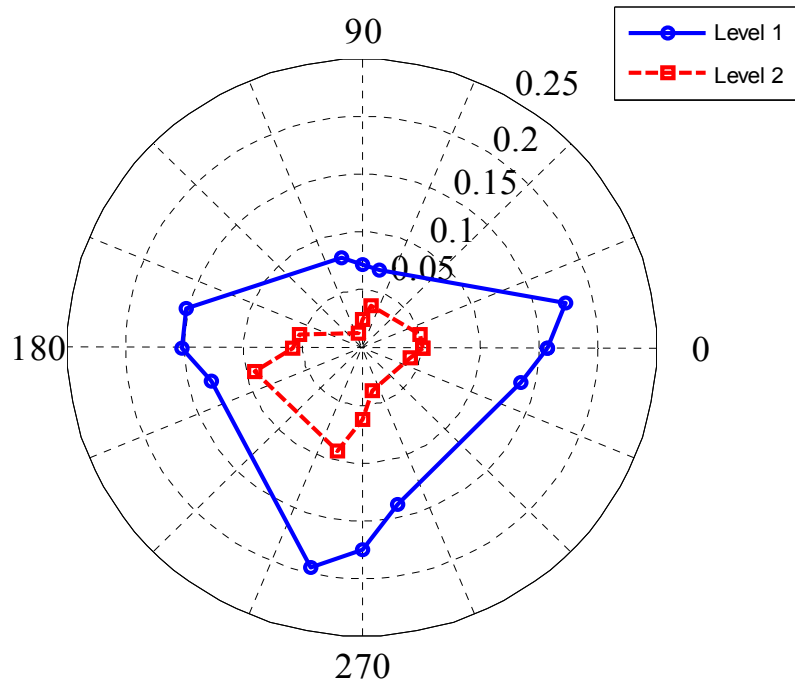
Figure 8.50 CFRP jacket confining strain profile [%] at the instant of displacement amplitude due to the 100%-scale bidirectional HS test (ID 7) for the two instrumented levels

318
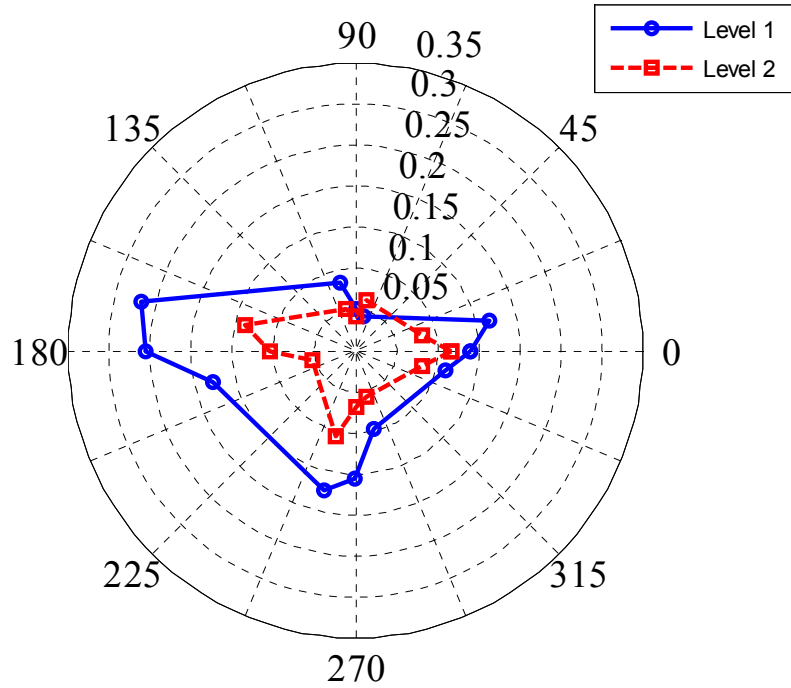
Figure 8.51 CFRP jacket confining strain profile [%] at the instant of displacement amplitude due to 175%-scale transverse-only HS test (ID 12) for the two instrumented levels
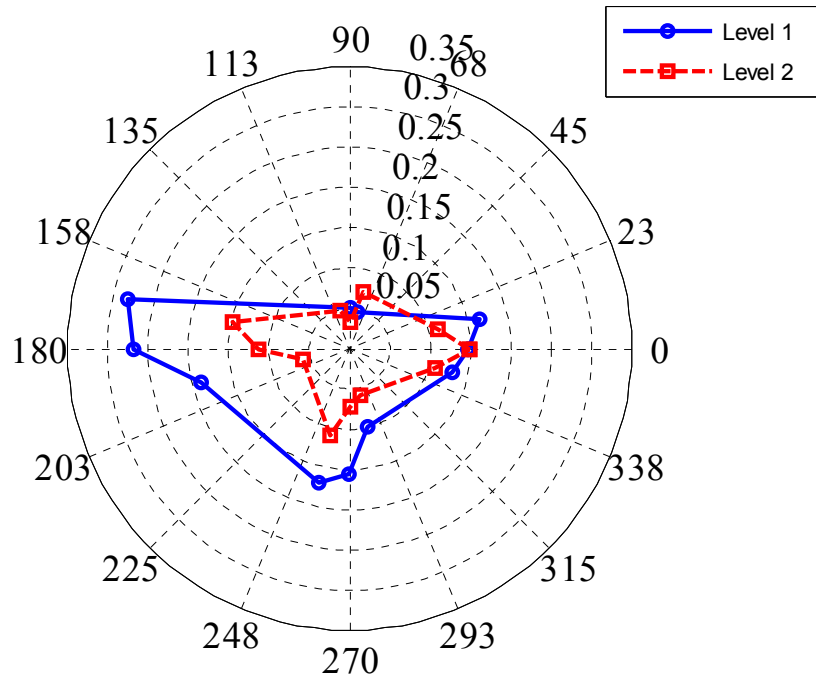
Figure 8.52 CFRP jacket confining strain profile [%] at the instant of displacement amplitude due to 200%-scale transverse-only HS test (ID 14) for the two instrumented levels

8.5   BENT CAP LOCAL BEHAVIOR

The structural behavior of the bent cap beam under combined gravity and lateral seismic loading is central to the undertaken experimental study. The main objective of this study is to evaluate the contribution of the box-girder slabs to the cap beam behavior and the capacity of the cap beam and its mode of failure. Thus, the strain, moment, and curvature histories at both sections B and D, which have been already used throughout the study to observe the bent cap beam behavior, are discussed in this section. In addition, the moment-curvature relationship is presented where the cap beam moment capacity is estimated.

8.5.1   Strain History

Extensive yielding was observed in the bent cap beam during the HS test runs. A sample of the strain history in one of the instrumented cap beam bottom rebars at sections B and D, where maximum strains along the beam length were recorded, is shown in Figure 8.53 and Figure 8.54, respectively, for all the 15 HS test runs. Figure 8.53 relates the strain evolution to the main phases of the bidirectional testing, increasing the gravity load to the 15% level, and the large-scale transverse-only HS testing. It is shown that the bidirectional tests led to the onset of the bent cap beam yielding, i.e. the observed strain values exceeded the 0.0026 yielding strain of the used reinforcing bars. An immediate significant increase in the strains at section B were observed as the 15% gravity load level was applied, whereas a more gradual increase was observed at section D. It is to be noted that testing was conducted in two days where the specimen was unloaded after the set of the bidirectional HS test runs was concluded in the first day of testing. For the second day of testing, the application of the 15% gravity load started from zero and was then followed by the eight large-scale transverse-only HS test runs. These runs increased the strain values more significantly at section D than section B as noticed from comparing Figure 8.54 to Figure 8.53. It is to be noted that up to 2% strain was observed in the bent cap reinforcement in the tension side during the retrofitted SP2 HS test runs, whereas only up to 1.3% strain was observed during the as-built SP1 cyclic tests. This reflected the higher moment demands in the case of the HS tests of SP2 compared to the cyclic tests of SP1, which was one of the objectives of the retrofit conducted for SP2 in this experimental program.

Another way of looking at the measured strains in the cap beam is plotting it against the progressing lateral load. The maximum strain measured at sections B and D is plotted against the lateral transverse force in Figure 8.55 and Figure 8.56, respectively. The strain evolving at zero lateral force corresponded to the strains resulting from the gravity load application as illustrated in Figure 8.55 and Figure 8.56. The figures present how the application of the 15% gravity load level on the already yielded cap beam increased the strains significantly. The reader is referred to the schematic representation of the moment distribution in the bent cap beam, shown in Chapter 5, for the complete picture of the moment due to the concentrated gravity load in the adopted inverted specimen and test setup. Figure 8.53 and Figure 8.54 also show that a jump in the strain took place at the start of each new HS test run. This was mainly attributed to the pulse-nature of the used Rinaldi ground motion where a large pulse was applied, causing the strain value to increase significantly, then followed by small cycles which followed an almost bilinear path according to Figure 8.55 and Figure 8.56 as the loading progressed and reversed.

320
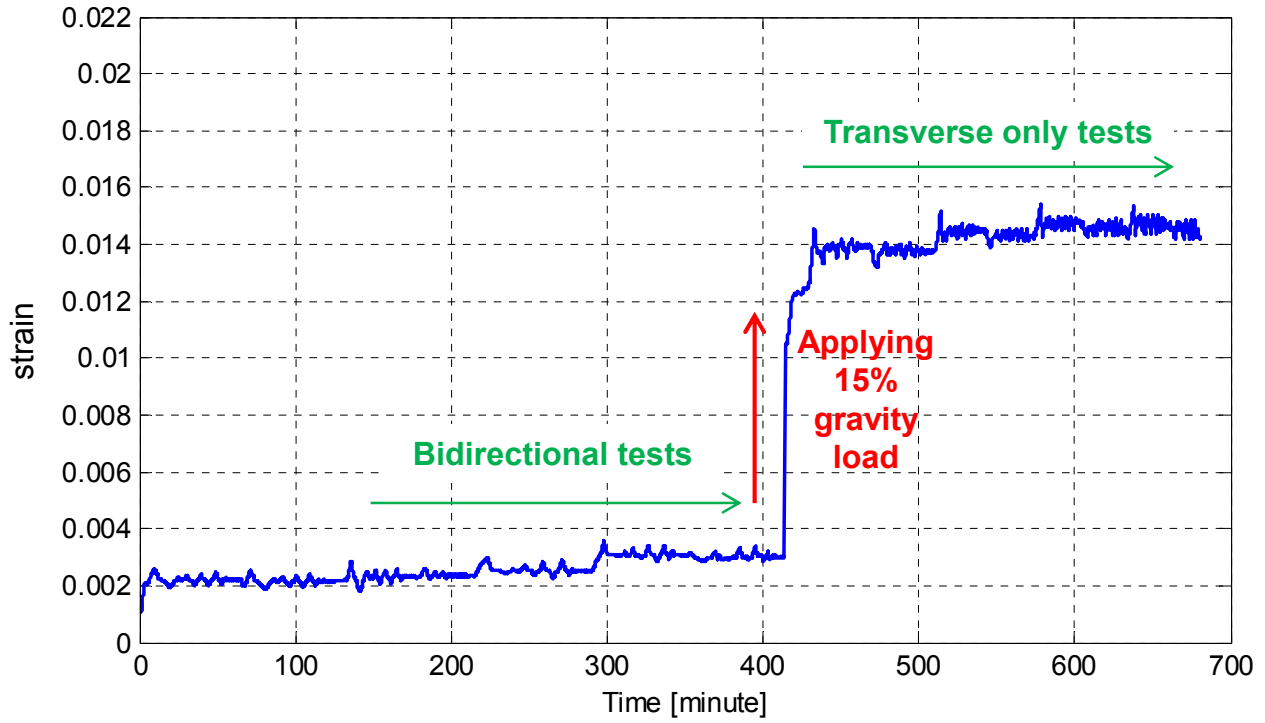
Figure 8.53 Bent cap beam strain history at section B due to all HS runs
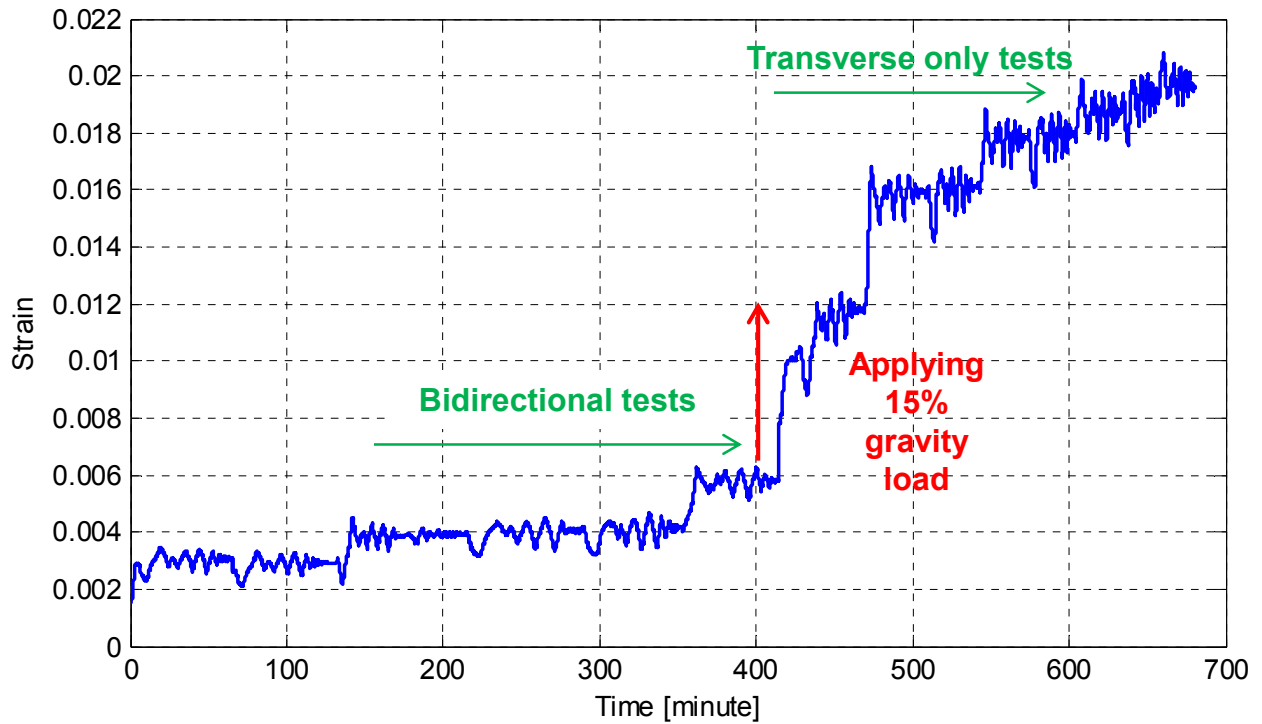
Figure 8.54 Bent cap beam strain history at section D due to all HS runs
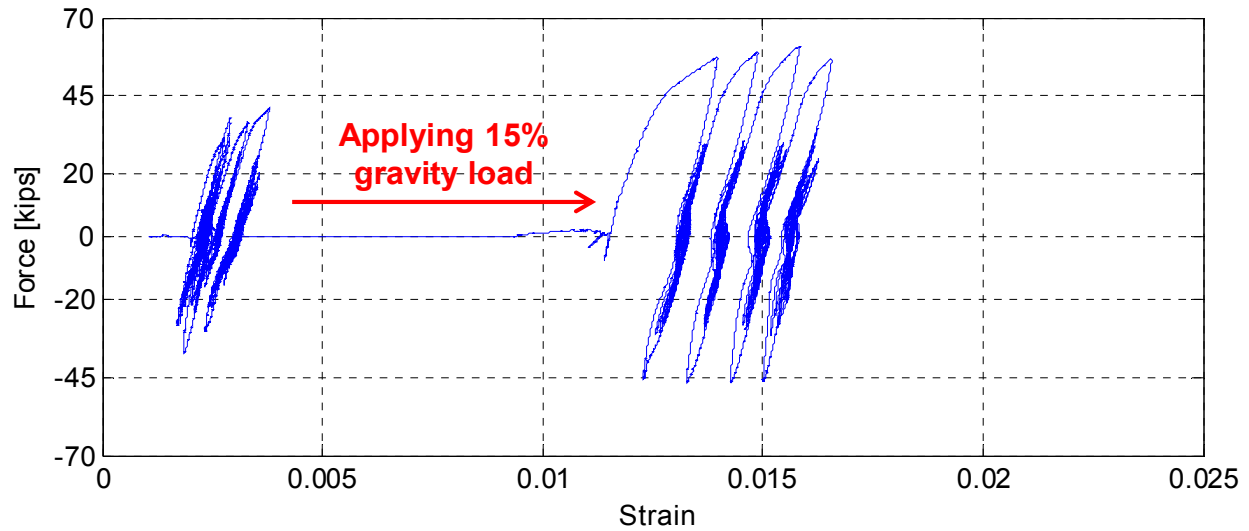
Figure 8.55 Global lateral force-strain relationship at section B of the bent cap beam due to all HS runs
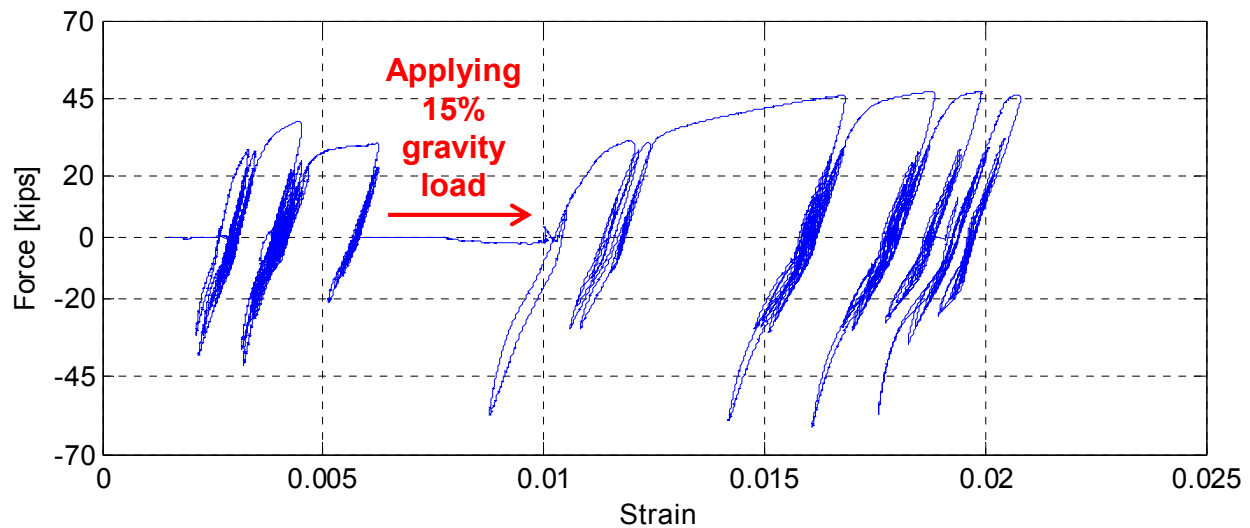
Figure 8.56 Global lateral force-strain relationship at section D of the bent cap beam due to all HS runs

8.5.2   Moment and Curvature History

While the strains are important to investigate partial section or localized behavior of the bent cap beam, the bending moments are more descriptive of the full bent cap section behavior. The bending moments in the bent cap beam were estimated using the calibrated end struts as previously discussed at various sections of this dissertation. The bent cap beam moment history at sections B and D for all the HS test runs is shown in Figure 8.57. Much higher moments were observed in the bent cap beam in the HS test runs compared to the case of the first specimen's cyclic tests. Higher bending moment demands in the bent cap were intended from the higher gravity load level and the undertaken retrofit scheme; which successfully increased the column

322

capacity and, in turn, the bent cap demands. The observed capped value of the bent cap moment of approximately 6500 kip-in., along with the compression zone concrete crushing, suggested that this moment value can be reasonably considered the overall bent cap beam capacity. The exact value of 6535 kip-in. was considered the experimentally-determined bent cap beam flexural capacity.

The total bent cap beam moment combined from sections B and D was compared to the column bending moment in Figure 8.58 as a typical practice throughout this study. This is to practically verify the bent cap beam bending moments based on the observation that the box-girder torsional stiffness in the cracked status after loading attracted small part of the moments applied to the superstructure through the column. In other words, almost the whole lateral transverse column moment was transferred as flexural moment to the bent cap beam only.
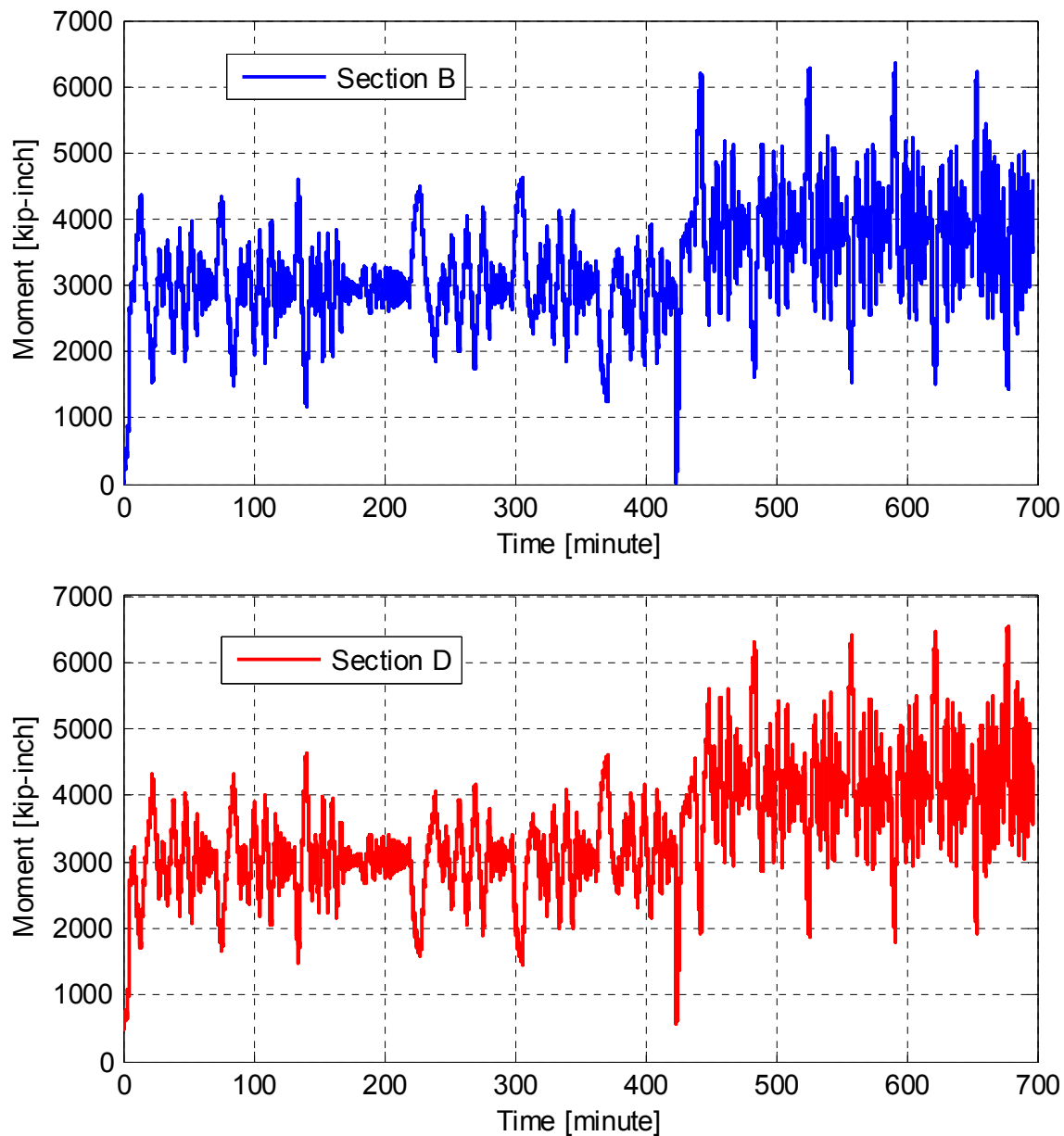
Figure 8.57 Bent cap beam moment history at sections B and D for all HS runs
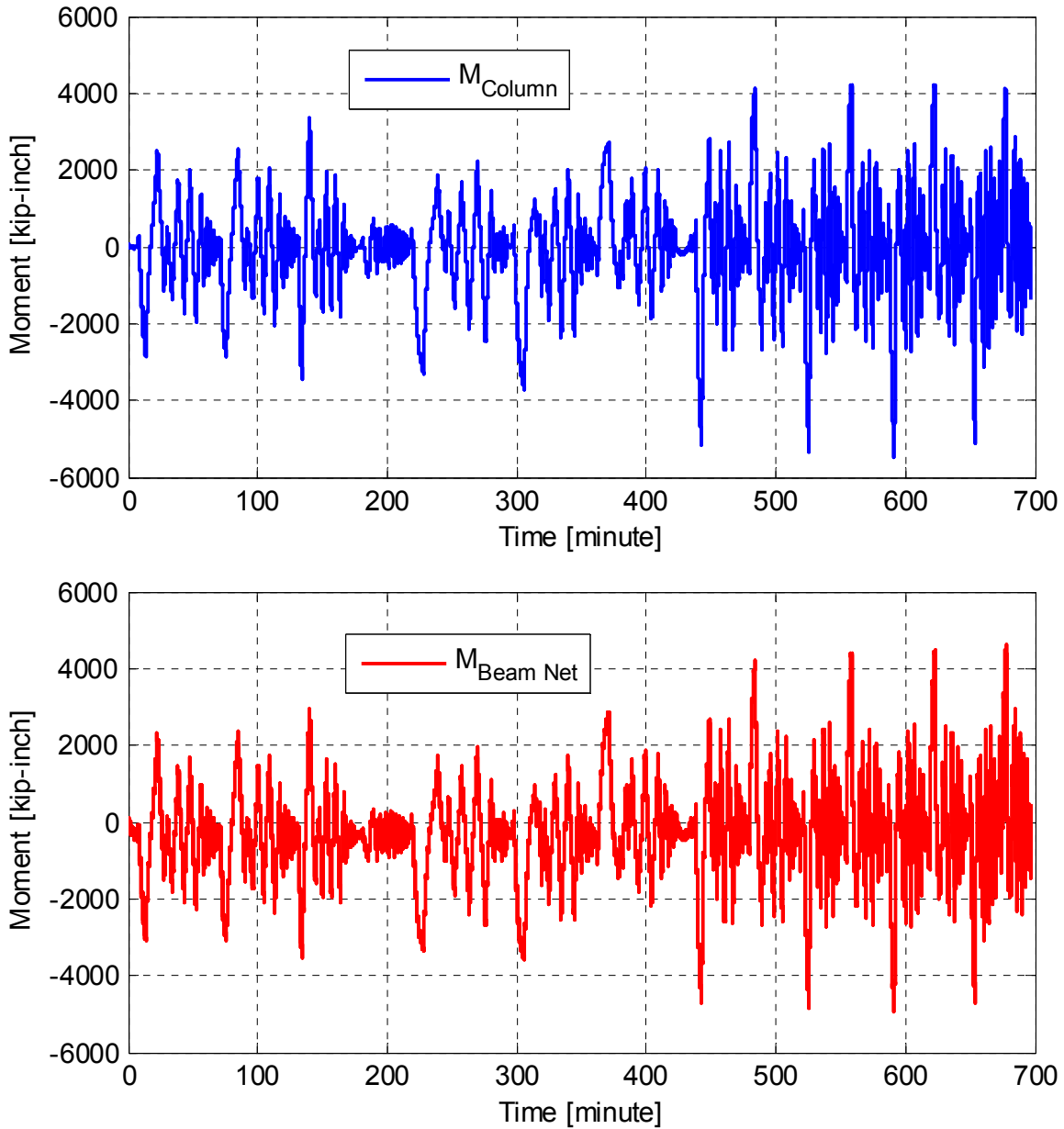
Figure 8.58 Comparison of the total bent cap beam moment at both sections B and D combined versus the column moment history

For a complete description of the bent cap section behavior, the curvature values were deduced from the observed strain in the bent cap top and bottom instrumented rebars. The procedure for estimating strain-based curvatures was previously discussed in Chapter 5. It is to be noted that the more accurate method of estimating a given section's curvature using LVDTs was not practical in the case of the bent cap. The history of the estimated curvatures from using one set of rebars at sections B and D is shown in Figure 8.59 and Figure 8.60, respectively. The estimated moments and curvatures were used to generate the moment-curvature relationships at both sections B and D as discussed next.
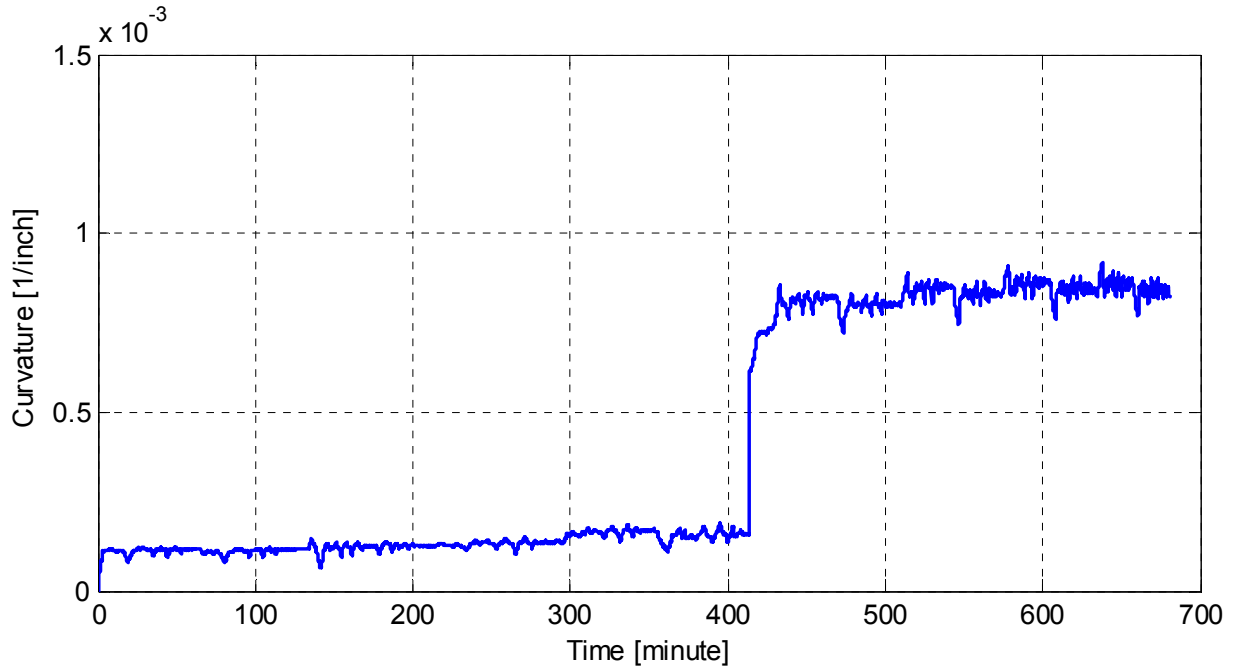
Figure 8.59 Bent cap beam curvature history at section B due to all HS runs
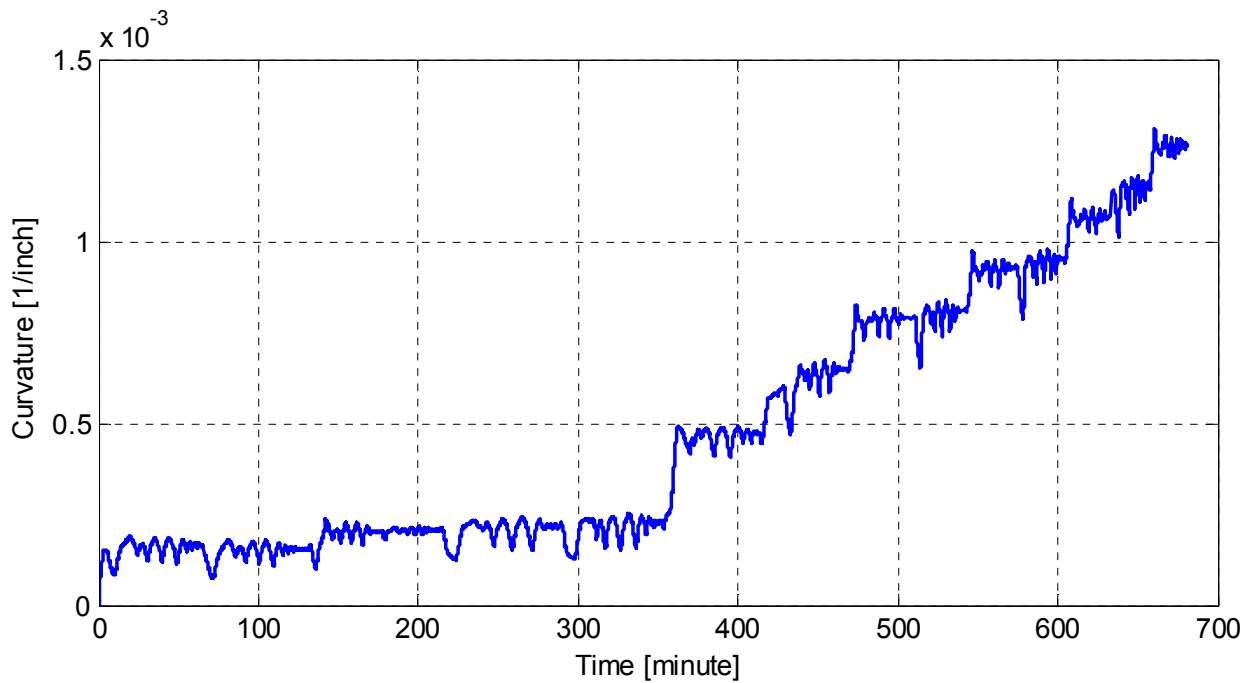
Figure 8.60 Bent cap beam curvature history at section D due to all HS runs

8.5.3 Moment-Curvature Relationship

The cap beam bending moments were discussed and verified in the previous subsection. A beneficial use of the bending moment to investigate the overall bent cap response is to plot it against the section curvatures, which were also estimated as discussed in an earlier subsection.

Figure 8.61 and Figure 8.62 show the moment-curvature relationship for the bent cap beam for all the 15 HS test runs at sections B and D, respectively. Similar to the moment history plot, the moment-curvature relationship plots show that the moment was capped at about 6500 kip-inch, which was claimed to be the bent cap capacity as previously discussed. The analytical nominal moment-curvature relationship obtained from a classical sectional analysis was previously shown together with the bent cap beam local behavior discussion in Chapter 5. It was shown from the sectional analysis performed based on the Caltrans SDC (2013) provisions that the bent cap beam capacity was 5024 kip-inch. The observed experimental value for the beam capacity of 6535 kip-inch demonstrated that the Caltrans provisions underestimated the bent cap capacity. This particular conclusion is an important outcome of this study. The design implications of the bent cap capacity underestimation are discussed along with the post-test analysis in Chapter 9. It is to be noted that the shown moment values in the moment-curvature relationships in Figure 8.61 and Figure 8.62 are slightly different from the moment history previously shown in Figure 8.57. This is because the moment values used in the moment-curvature relationships, unlike the exact moment values shown in the moment history plots, were approximately reproduced from the column moments. The reason is that the curvature data were collected at the NEFF data acquisition system while the strut forces used for moment calculations were collected at a totally different sampling rate at the PI. Only the global forces used in the column moment calculations were recorded at both data acquisition systems, and thus, enabling the approximate reproduction of the bent cap moments at the curvatures sampling rate to plot them together.
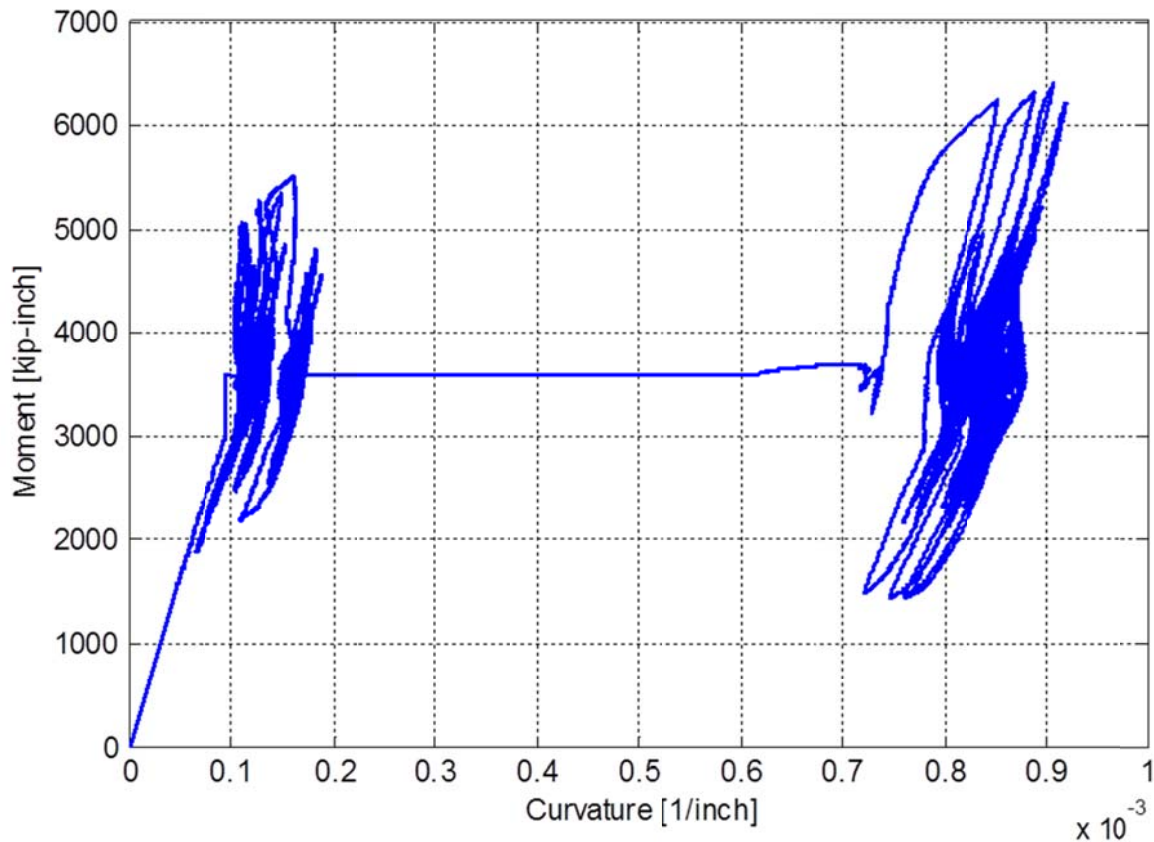
Figure 8.61 Moment-curvature relationship for the bent cap beam at section B for all the 15 HS bidirectional and transverse-only test runs

326
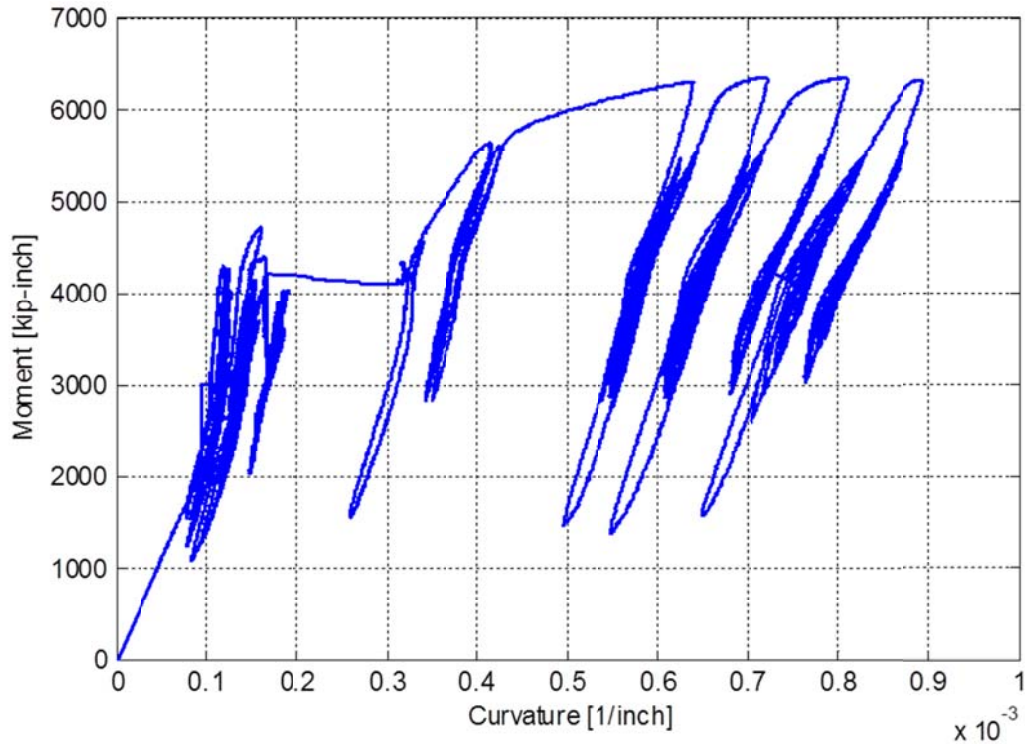
Figure 8.62 Moment-curvature relationship for the bent cap beam at section D for all the 15 HS bidirectional and transverse-only test runs

8.6   EFFECTIVE SLAB WIDTH

Besides the bent cap beam capacity estimation, understanding the box-girder slab contribution to the bent cap and accurately quantifying the effective slab width is another important outcome of this study. As mentioned before, the Caltrans SDC and AASHTO LRFD guidelines for seismic design require considering a flanged section with an effective slab width $12t_s$ for the integral RC bent cap beams balanced stiffness check and seismic capacity check. The effective slab width that is typically based on the equivalent strain block concept was revisited in this study. Similar to what was performed in the case of the as-built SP1 cyclic tests, the strain distribution in the bent cap beam reinforcement and the adjacent transverse slab reinforcement from both sides of the beam was determined for all the retrofitted SP2 HS test runs. Only the strain distribution in the tension side was found to be more reliable and therefore presented and utilized in this part of the study. It is noted that the compression side was found to be very sensitive to the concentrated gravity load applied through the column as previously shown in Chapter 5. The results from the tension side strain distribution and the revisited effective slab width from the HS tests are presented in this section. A brief discussion of the surface concrete strain gages is also included in this section.

The same procedure that was devised and used in Chapter 5 to find the equivalent strain block and effective width was used again in this part of the study. The reader is referred to Figure 5.22 in Chapter 5 for an overview of such procedure. To consider as many cases as possible from the full set of HS test runs, the strain distribution and effective width were investigated at both sections B and D and at nine positive and negative loading levels. The

327

chosen levels were the ascending sequence of the peak displacements in the positive and negative transverse loading directions as identified in Figure 8.63 in terms of the corresponding ductility levels. Moreover, Table 8-2 summaries those nine positive and negative loading levels, where all the effective slab width results were produced, along with the corresponding drift ratios and ductility levels.
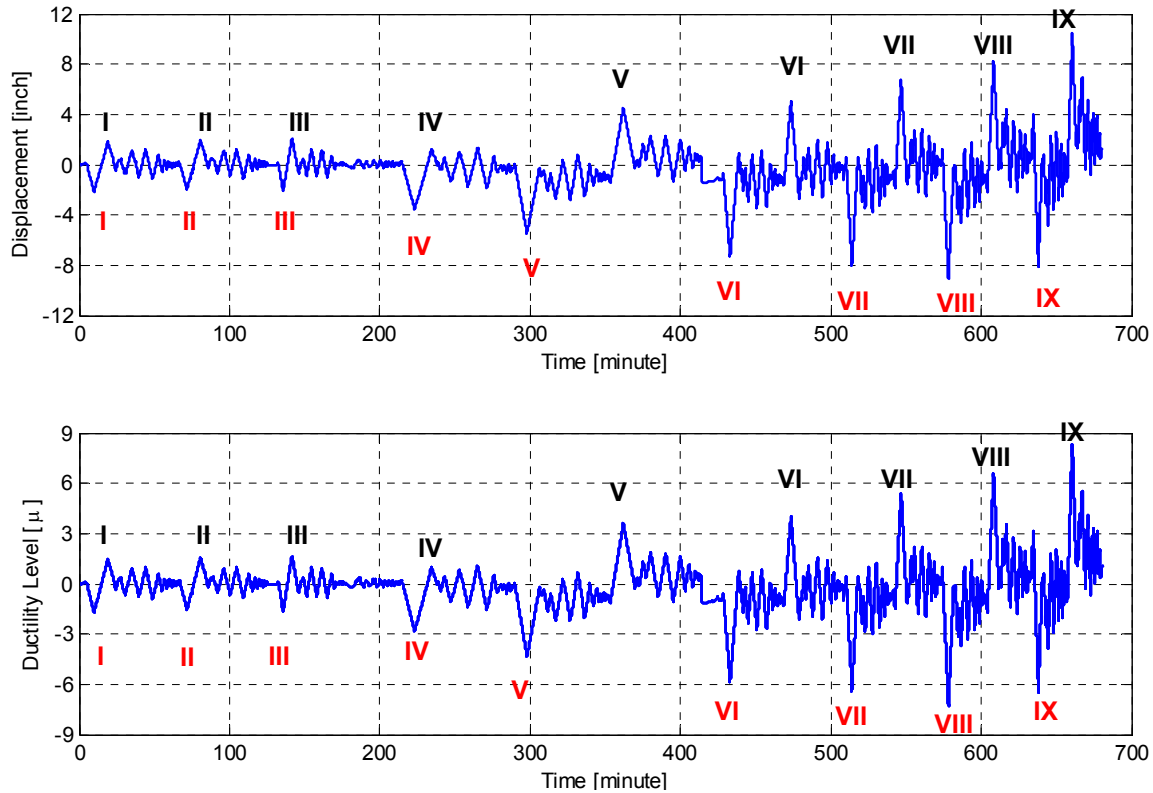
Figure 8.63 The main nine positive and negative displacement amplitudes (top) and the corresponding ductility levels (bottom) used for investigating the effective slab width for retrofitted SP2 tested using HS

Table 8-2 Summary of the peak displacements of the HS test runs in the transverse direction and their corresponding drift ratios and ductility levels

Positive Transverse Loading				Negative Transverse Loading			
Group ID	Displacement [inch]	Drift Ratio [%]	Ductility Level [μ]	Group ID	Displacement [inch]	Drift Ratio [%]	Ductility Level [μ]
I	1.83	2.0	1.47	I	-2.12	-2.4	-1.70
II	1.92	2.1	1.54	II	-1.92	-2.1	-1.54
III	1.99	2.2	1.59	III	-2.01	-2.2	-1.61
IV	1.22	1.4	0.98	IV	-3.53	-3.9	-2.82
V	4.49	5.0	3.59	V	-5.40	-6.0	-4.32
VI	5.01	5.6	4.00	VI	-7.28	-8.1	-5.82
VII	6.72	7.5	5.38	VII	-7.94	-8.8	-6.35
VIII	8.16	9.1	6.53	VIII	-8.98	-10.0	-7.19
IX	10.43	11.6	8.35	IX	-8.02	-8.9	-6.41

8.6.1 Strain Distribution

The strain distributions at different sections across the bent cap and transverse slab reinforcement based on different strain gages readings were recorded continuously throughout all the HS test runs. However, only strain values acquired at the loading peaks, previously identified in Figure 8.63 and summarized in Table 8-2, were considered. Similar to the discussion in Chapter 5, the strain distribution was compiled at sections B and D and was related to the drift ratio and ductility level (μ) in the figures presented in this subsection. It is worth noting that the distributions and the effective width were mainly considered under transverse loading in the cyclic tests. However, several cases of the strain distribution and effective width estimated from the HS test runs were determined from the more realistic concurrent bidirectional loading. Thus, the results are presented for the bidirectional tests separately from the large-scale HS transverse-only test runs.

Firstly, the strain distribution plots at section B from the bidirectional tests and the transverse-only tests are presented under subsections 8.6.1.1 and 8.6.1.2, respectively. Next, the results for section D are shown for bidirectional and transverse-only tests under subsections 8.6.1.3 and 8.6.1.4. Only the figures are categorized in those subsections but the discussion is presented here. Figure 8.64 and Figure 8.65 show the strain distribution in the tension side at section B for the five different loading levels that corresponded to the bidirectional tests at the positive and negative peaks, respectively. It is to be noted that the bidirectional tests at 50%-scale was repeated twice with and without the P-delta correction. In addition, a small transverse-only and longitudinal-only tests were conducted at 50%-scale and still included under the bidirectional tests discussion for simplicity. The results from the longitudinal-only test were shortened, however, due to some impractical strain distributions obtained during such test. Thus, the five loading levels in this case corresponded to drift ratios of 2.0%, 2.1%, 2.2%, 1.4%, and 50% at the positive peaks and 2.4%, 2.1%, 2.2%, 3.9%, and 6.0% at the negative peaks. The equivalent ductility levels can be read from Table 8-2.

As previously noted in the strain and curvature history of the bent cap beam discussion, a significant jump in the strain values at section B was observed when the 15% gravity load was applied to the already yielded cap beam. Figure 8.66 and Figure 8.68 capture the jump in the strain distribution at section B at the first big transverse-only run positive and negative peaks, respectively, when the 15% gravity load was applied. The immediate adjacent transverse bars in the North side of the bent cap beam experienced a similar behavior as the cap beam reinforcement. The distribution for the four large-scale transverse-only runs at the positive and negative amplitudes are shown in Figure 8.67 and Figure 8.69, respectively.

Similar to the strain distribution shown at section B, different loading levels and loading direction were considered to plot the strain distribution at section D. Figure 8.70 and Figure 8.71 show the distribution for the five bidirectional tests at the positive and negative peak, respectively. Moreover, Figure 8.72 and Figure 8.74, respectively, capture the change in the distribution as the first large-scale positive and negative transverse-only tests were conducted after the 15% gravity load was applied. The overall strain distribution for all of the four positive and negative large-scale transverse-only tests is shown in Figure 8.73 and Figure 8.75, respectively. It is to be noted that all plots in this subsection captured all the spatially extended distribution tails where the intercept at zero strain was determined as part of the effective slab width evaluation.

8.6.1.1 Section B – Bidirectional Runs
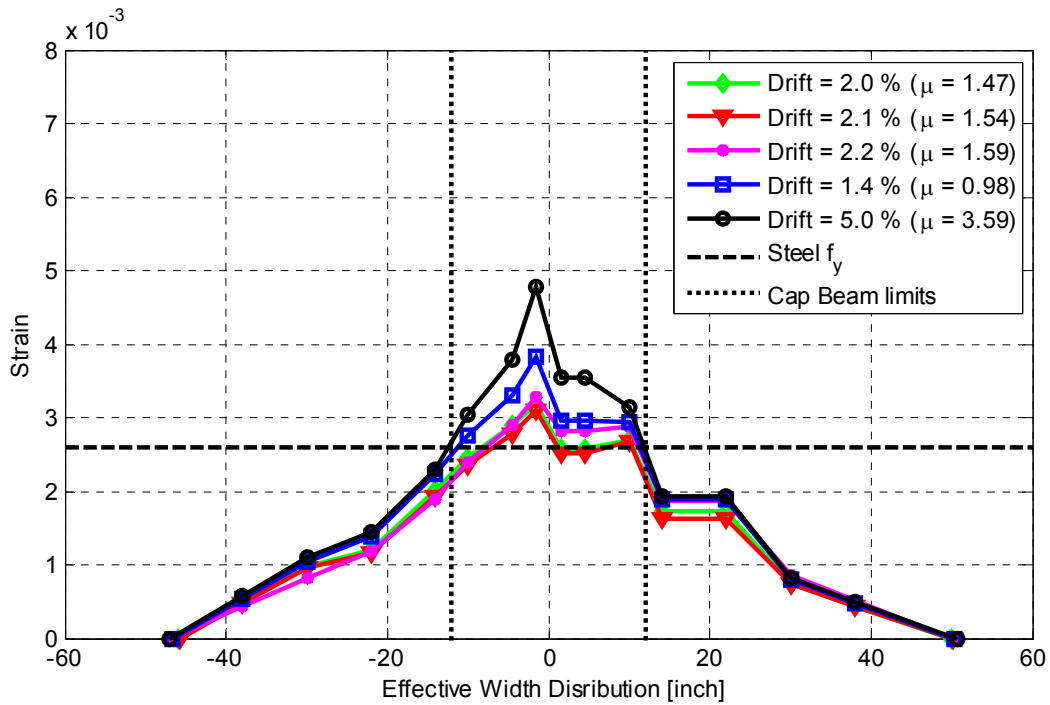
Figure 8.64 Strain distribution in the tension side at section B for all bidirectional HS test runs at the positive loading peak (expressed in terms of drift ratio and μ)
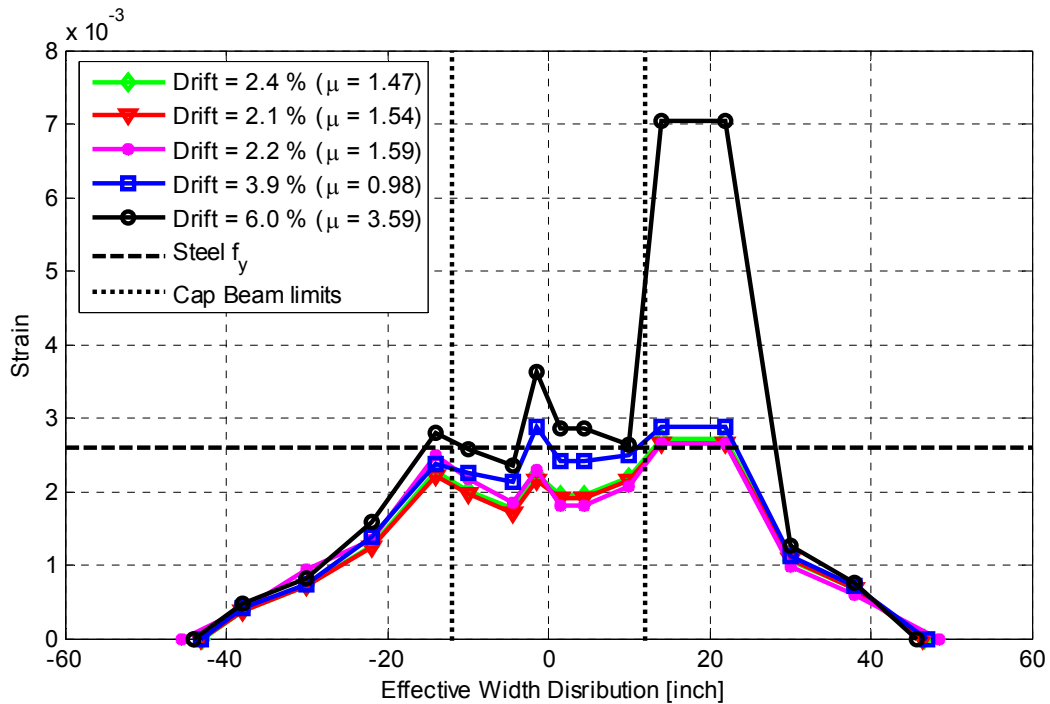
Figure 8.65 Strain distribution in the tension side at section B for all bidirectional HS test runs at the negative loading peak (expressed in terms of drift ratio and μ)

8.6.1.2 Section B – Transverse-Only Runs
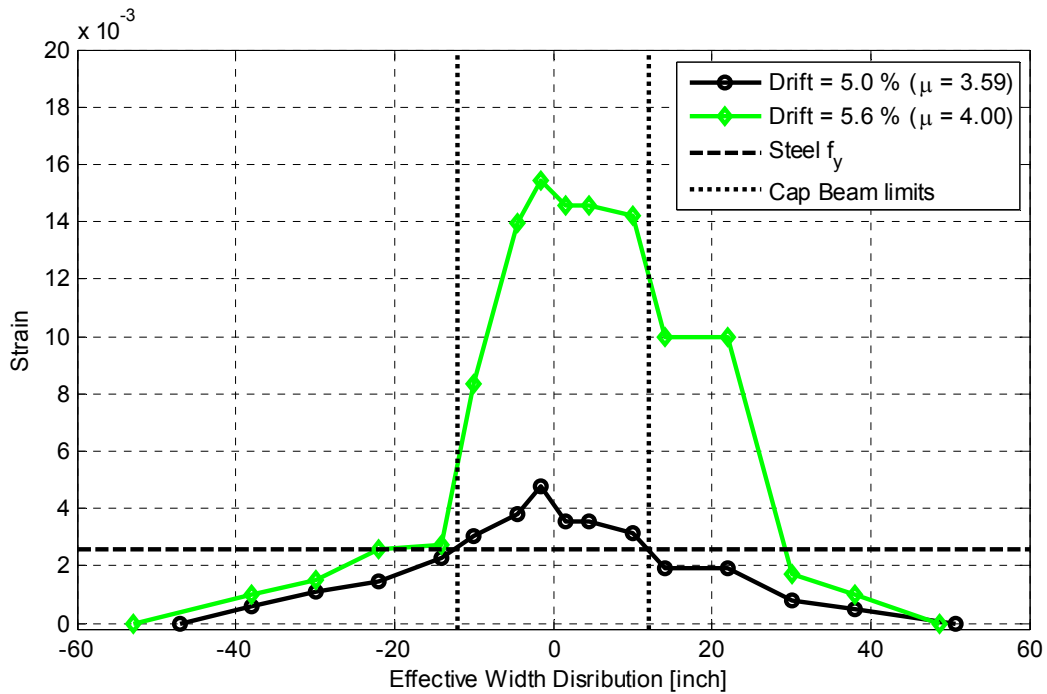
Figure 8.66 Strain distribution change at section B due to the increased gravity load and at the first large-scale transverse-only HS test run at positive loading peak
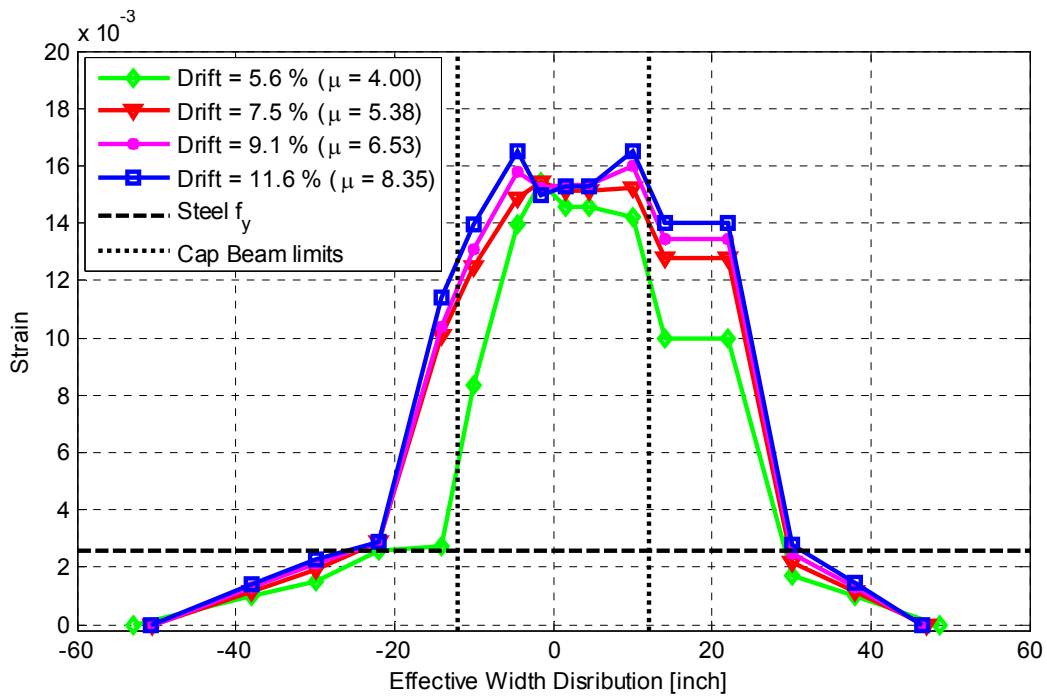
Figure 8.67 Strain distribution in the tension side at section B for the four large-scale transverse-only HS test runs at the positive loading peak (expressed in terms of drift ratio and μ)

331
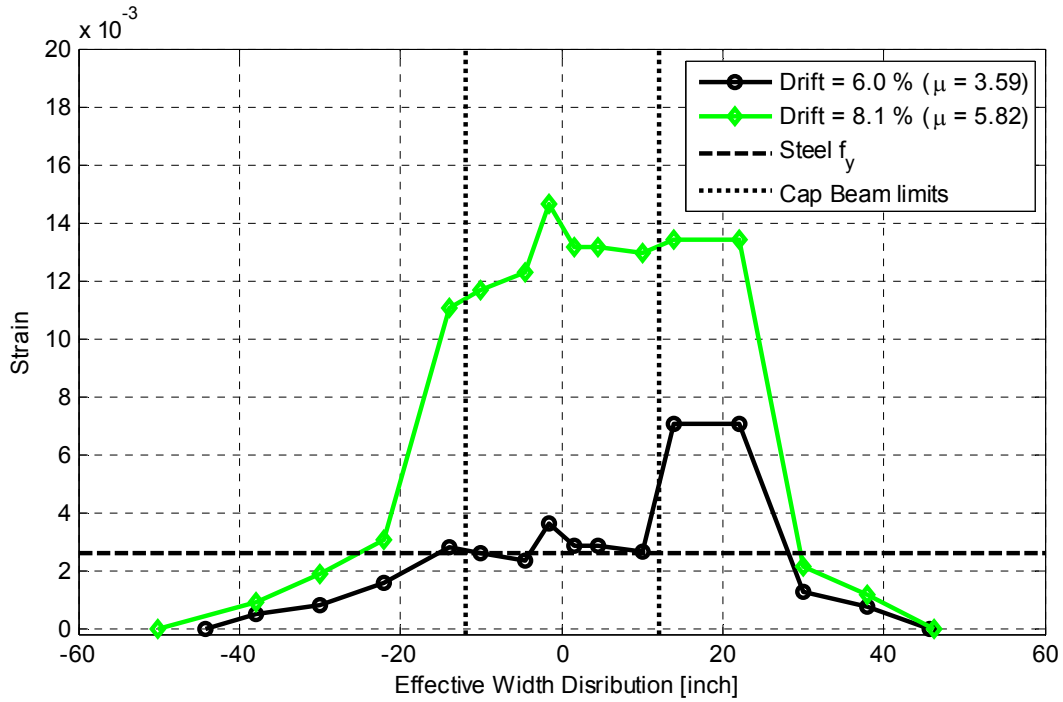
Figure 8.68 Strain distribution change at section B due to the increased gravity load and at the first large-scale transverse-only HS test run at negative loading peak
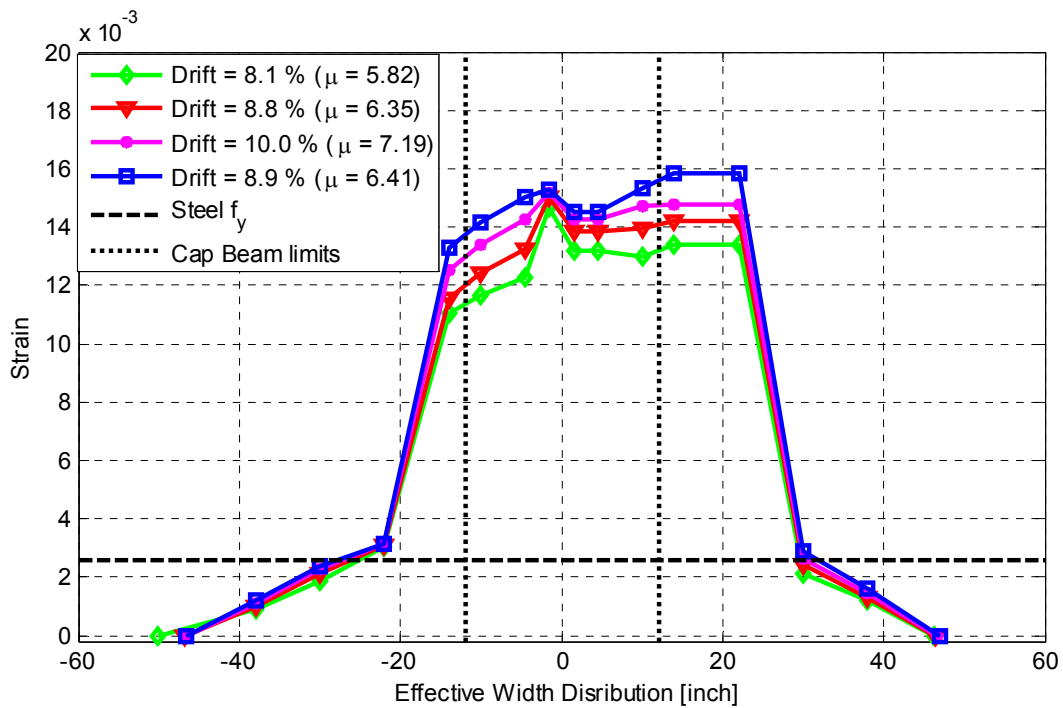
Figure 8.69 Strain distribution in the tension side at section B for the four large-scale transverse-only HS test runs at the negative loading peak (expressed in terms of drift ratio and μ)

332

8.6.1.3   Section D – Bidirectional Runs
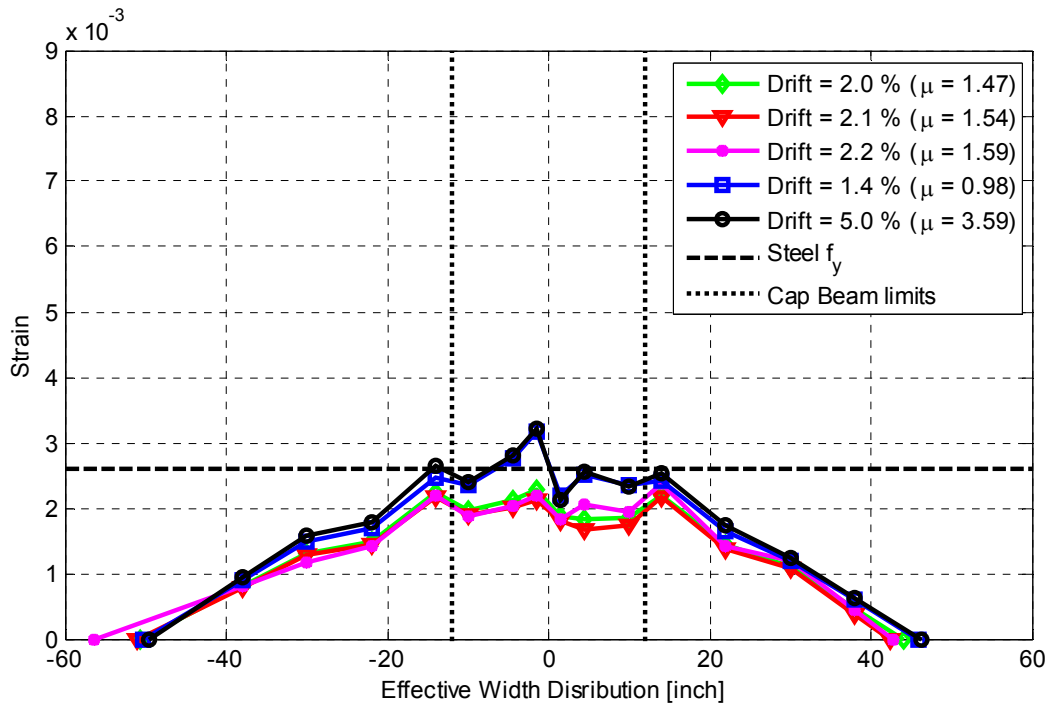
Figure 8.70 Strain distribution in the tension side at section D for all bidirectional HS test runs at the positive loading peak (expressed in terms of drift ratio and μ)
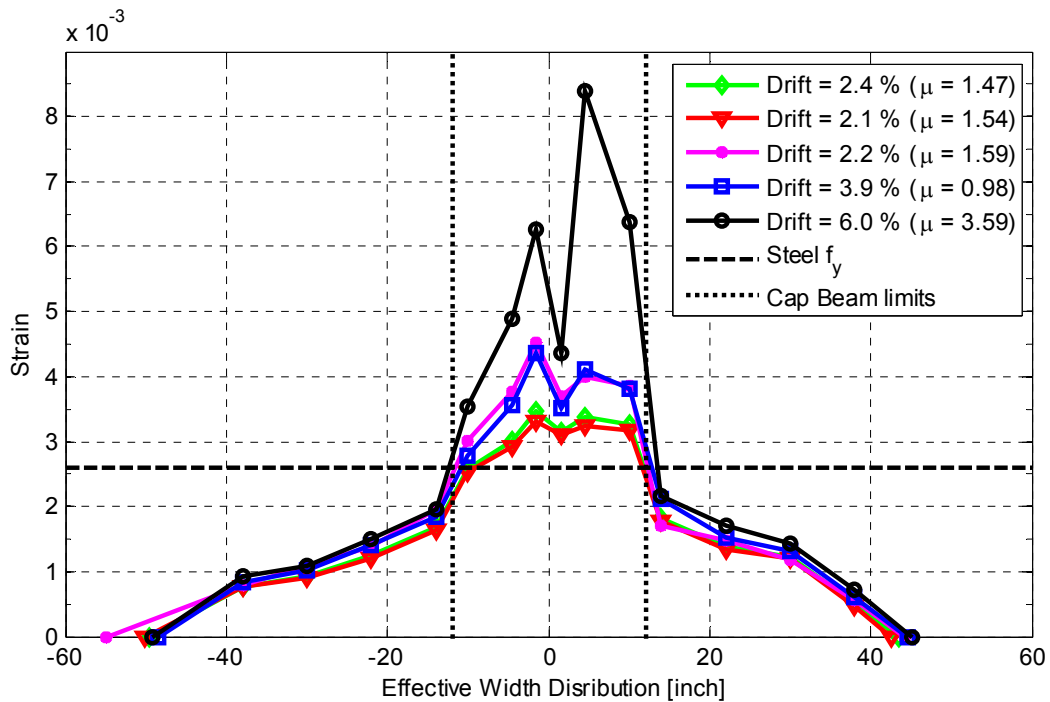
Figure 8.71 Strain distribution in the tension side at section D for all bidirectional HS test runs at the negative loading peak (expressed in terms of drift ratio and μ)

8.6.1.4 Section D – Transverse-Only Runs
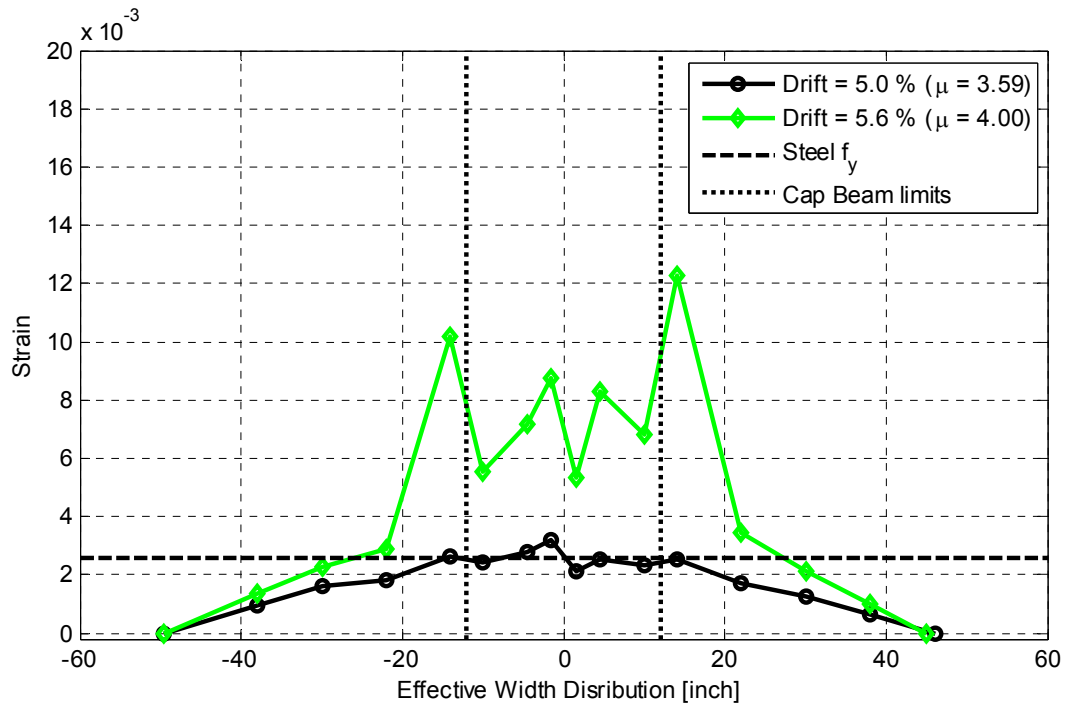
Figure 8.72 Strain distribution change at section D due to the increased gravity load and at the first large-scale transverse-only HS test run at positive loading peak
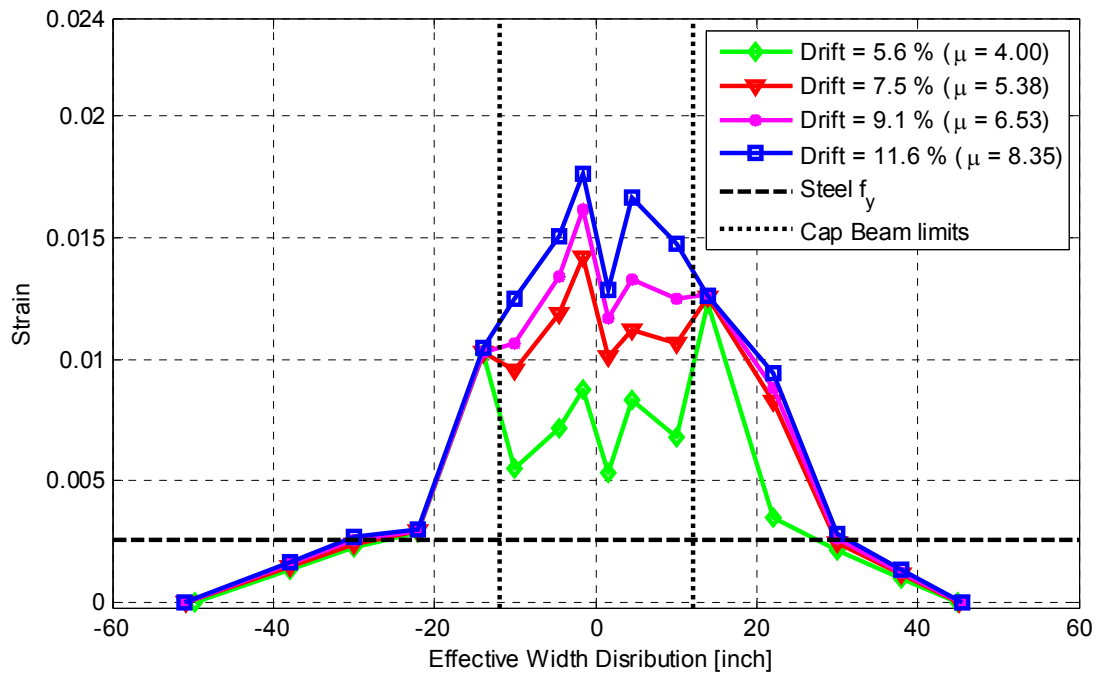
Figure 8.73 Strain distribution in the tension side at section D for the four large-scale transverse-only HS test runs at the positive loading peak (expressed in terms of drift ratio and μ)

334
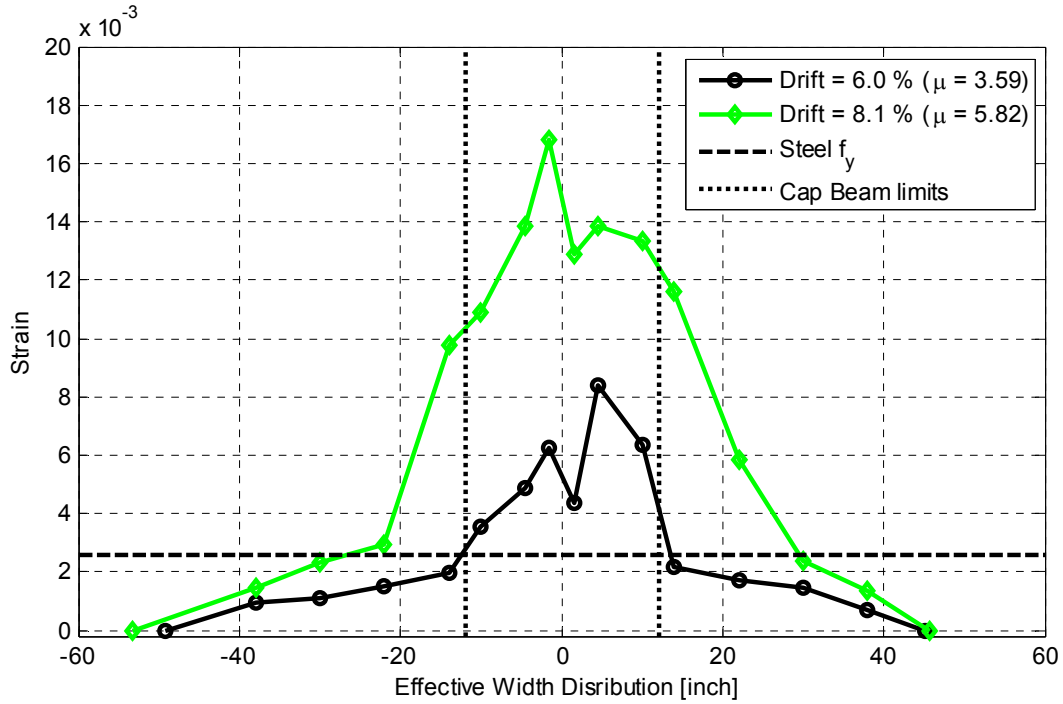
Figure 8.74 Strain distribution change at section D due to the increased gravity load and at the first large-scale transverse-only HS test run at negative loading peak
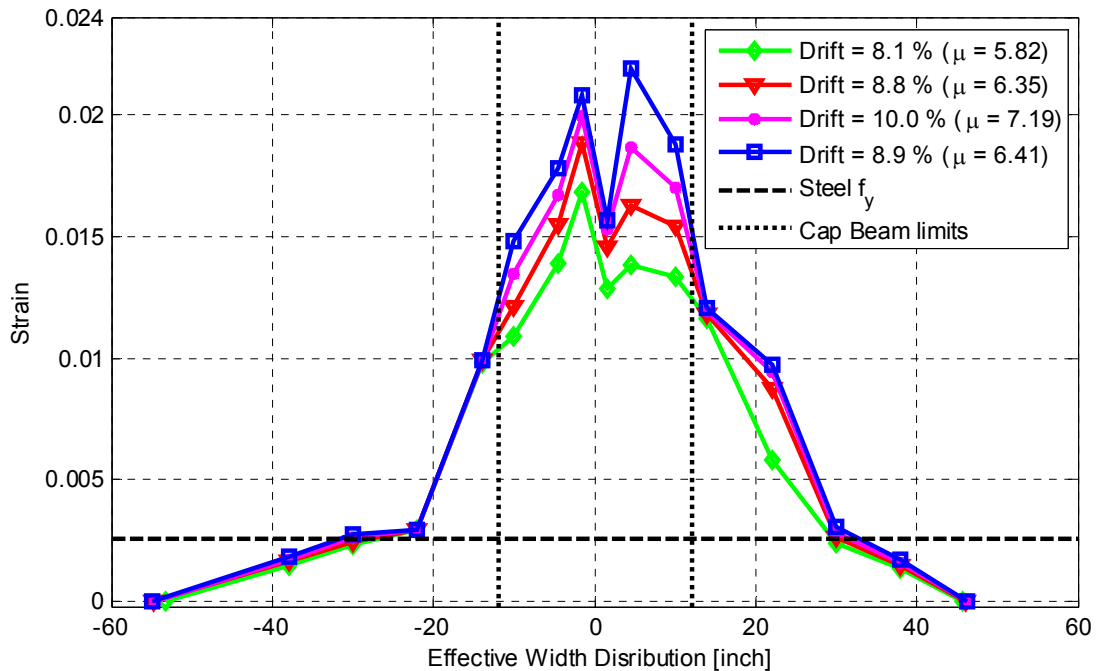
Figure 8.75 Strain distribution in the tension side at section B for the four large-scale transverse-only HS test runs at the negative loading peak (expressed in terms of drift ratio and μ)

335

8.6.2 Effective Slab Width Estimation

As previously mentioned, the effective slab width was determined using the equivalent strain block concept and the simple procedure devised in Chapter 5. The strain distributions presented in the previous subsection were utilized here to estimate the effective slab width at sections B and D at different loading levels and directions. Similar to the framework adopted in Chapter 5, two values for the bent cap beam strain value were used to define the equivalent strain block (B_{eff}). These are the minimum and the mean of the six instrumented rebars strain gage readings at a given cross-section in the cap beam.

8.6.2.1 Section B

An example of how the strain block was determined using the strain distribution at section B and using the minimum and mean cap beam strain values is shown in Figure 8.76. The total flange effective slab width, i.e. equivalent strain block width B_{eff}, was calculated for the different nine loading levels at the positive and negative amplitudes (Figure 8.63 and Table 8-2).
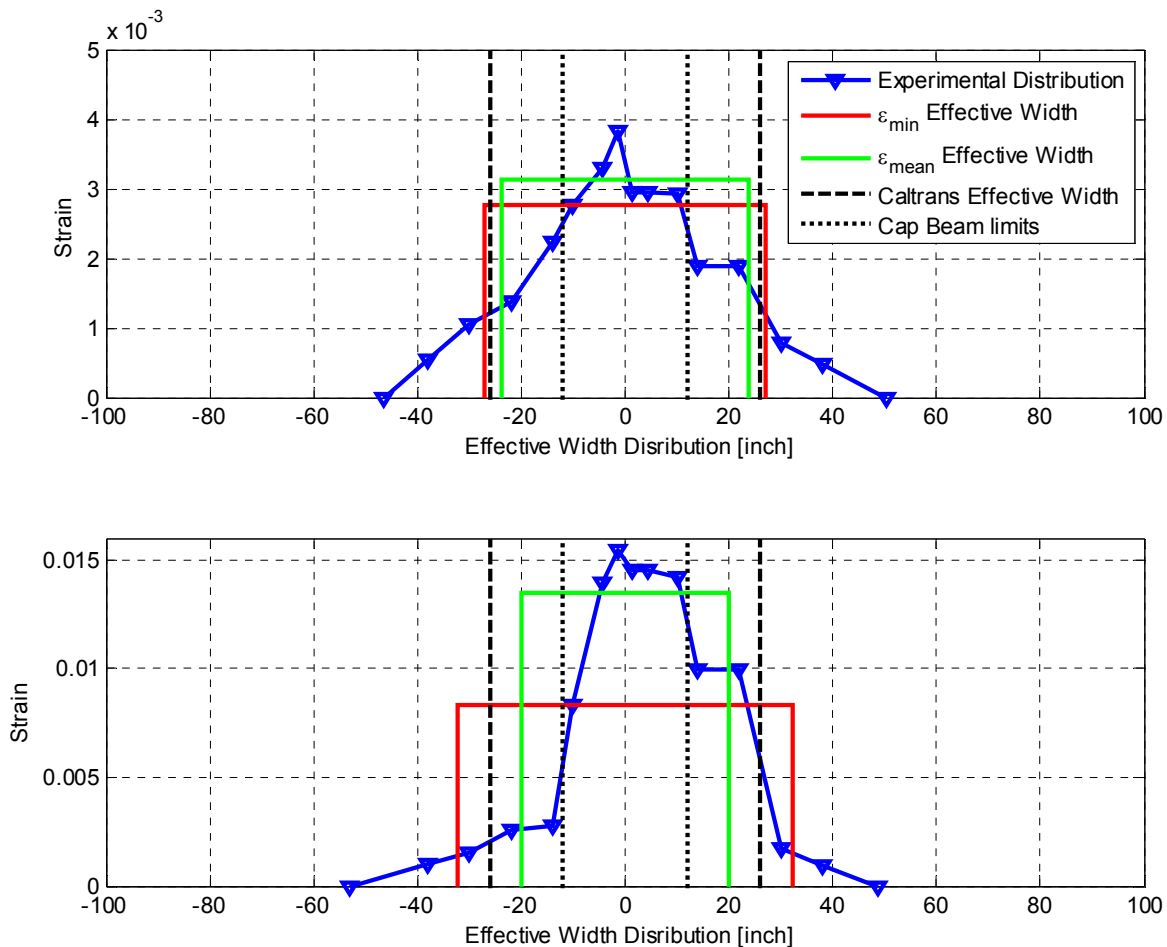
Figure 8.76 An example of the equivalent strain block at section B from a bidirectional (top) and a transverse-only (bottom) HS test runs

A summary of the calculated B_{eff}, as related to the drift ratios, at section B using both cap beam minimum (ε_{min}) and mean (ε_{mean}) strain values is shown in Figure 8.77 and Figure 8.78 for

the positive and negative amplitudes, respectively. The figures also show the B_{eff} that was estimated in light of the Caltrans SDC provisions for the integral bent cap beam flanged section, which is referred to as Caltrans value. The overall average of the nine positive and negative loading cases is summarized in Figure 8.79.
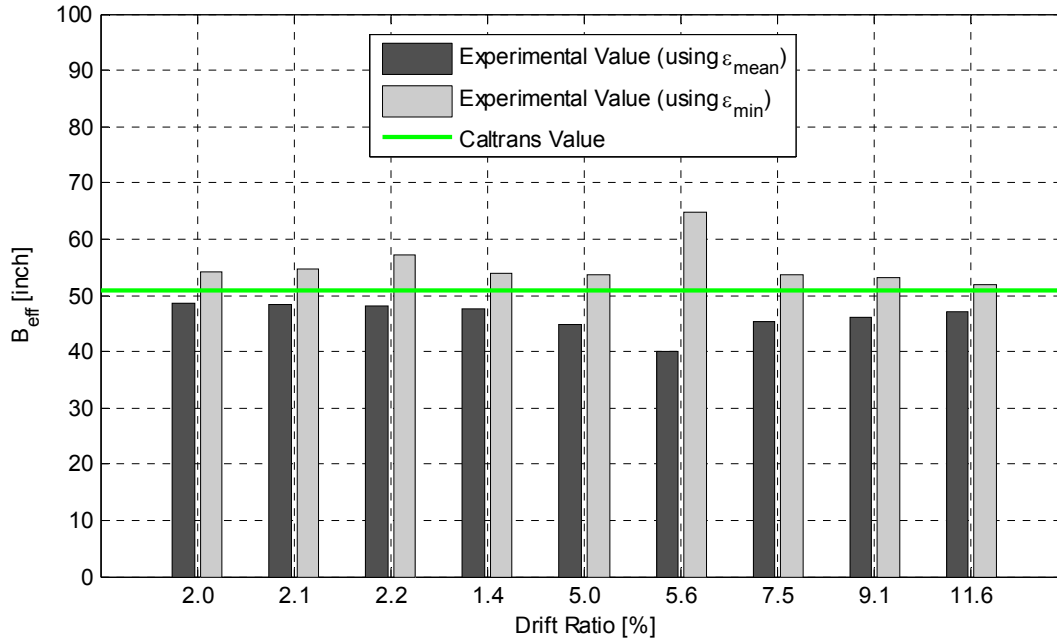
Figure 8.77 Summary of the estimated bent cap effective flange width at section B from all HS test runs at nine positive loading peaks
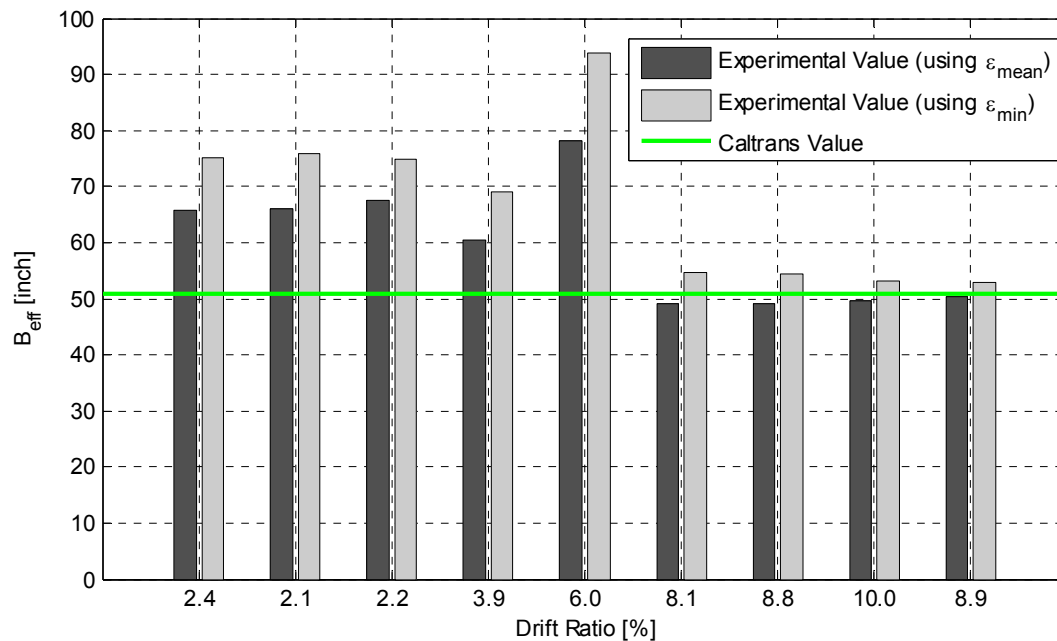
Figure 8.78 Summary of the estimated bent cap effective flange width at section B from all HS test runs at nine negative loading peaks
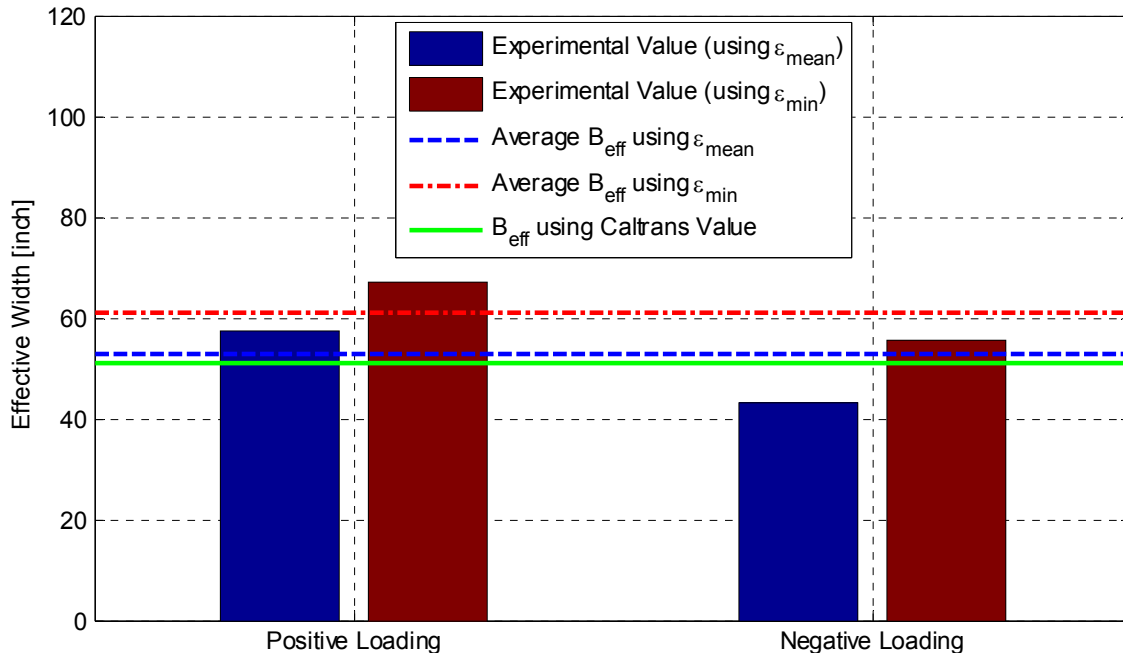
Figure 8.79 Mean effective width from HS test runs from positive and negative loading (bar chart) and overall average effective width from all HS test runs (dashed lines) at section B as compared to Caltrans SDC effective width value

Figure 8.79 shows that the effective width estimated at the negative loading amplitudes was less than that calculated at the positive loading amplitudes. It is noted that the overall average from all cases, shown as dashed lines in Figure 8.79, is higher than the Caltrans estimate. Moreover, the determined effective width could be related to the slab thickness (t_s) and bent cap beam width (b_{beam}) as previously conducted in Chapter 5 through a slab contribution constant (C) which quantifies the slab contribution as multiples of t_s. However, this step was skipped here for brevity and only the final overall mean value from all HS tests is related to t_s in the next section.

8.6.2.2 Section D

A similar framework as before is used to present the effective slab width results at section D. One example of how the strain block was determined using the strain distribution at section D using the minimum and mean cap beam strain values is shown in Figure 8.80 for a typical bidirectional and large-scale transverse-only HS test runs. A summary of the calculated B_{eff} at section D using both cap beam minimum and mean strain values is shown in Figure 8.81 and Figure 8.82 at all nine positive and negative amplitudes, respectively. Both figures express the loading level in terms of the drift ratios and the reader is referred to Table 8-2 for the corresponding displacement values or ductility levels. The Caltrans value for B_{eff} is also shown in Figure 8.81 and Figure 8.82 for comparison. Figure 8.83 summarizes the average value of each of the positive and negative loading sets and the overall average for all cases combined. A similar observation as discussed for section B is that the estimated effective flange width using the mean strain for section D was higher than the Caltrans value. It is also worth noting that on the contrary to the results at section B, the average effective width from the positive loading cases was less than that from the negative loading at section D.
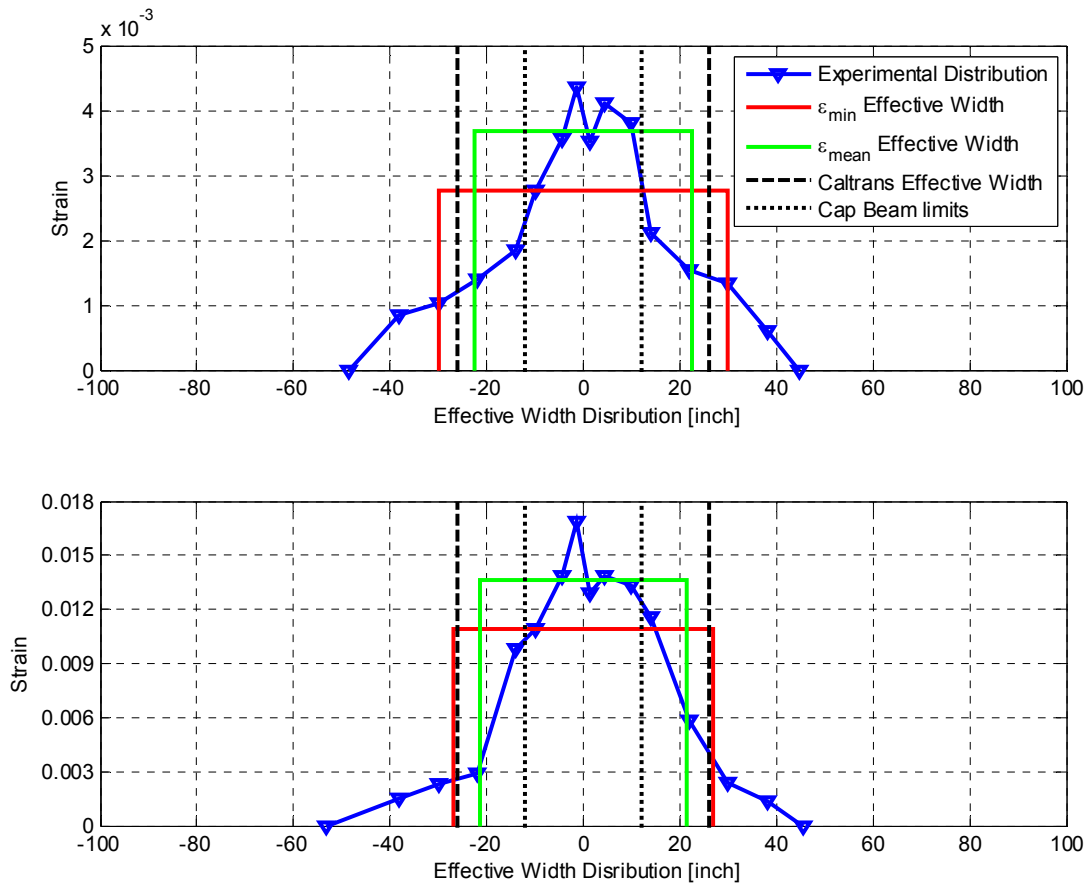
Figure 8.80 An example of the equivalent strain block at section D from a bidirectional (top) and a transverse-only (bottom) HS test runs
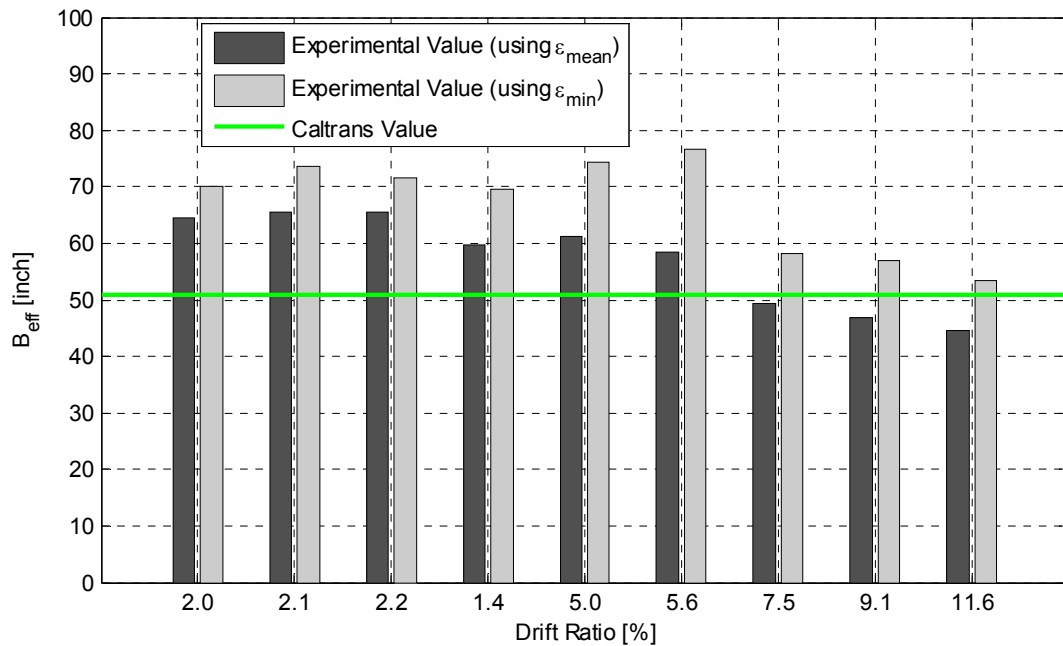
Figure 8.81 Summary of the estimated bent cap effective flange width at section D from all HS test runs at nine positive loading peaks
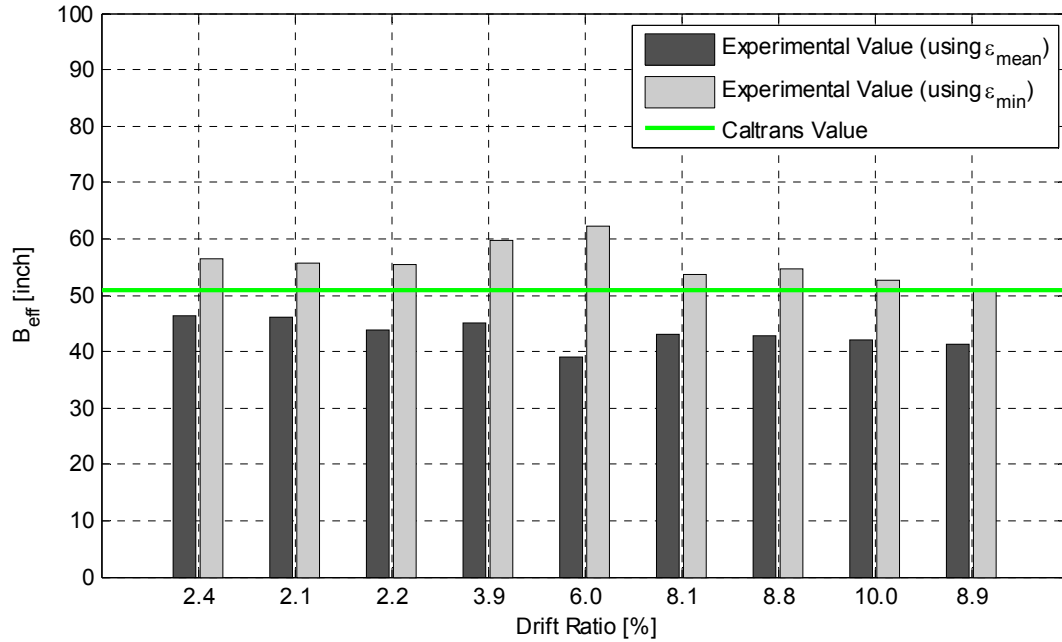
Figure 8.82 Summary of the estimated bent cap effective flange width at section D from all HS test runs at nine negative loading peaks
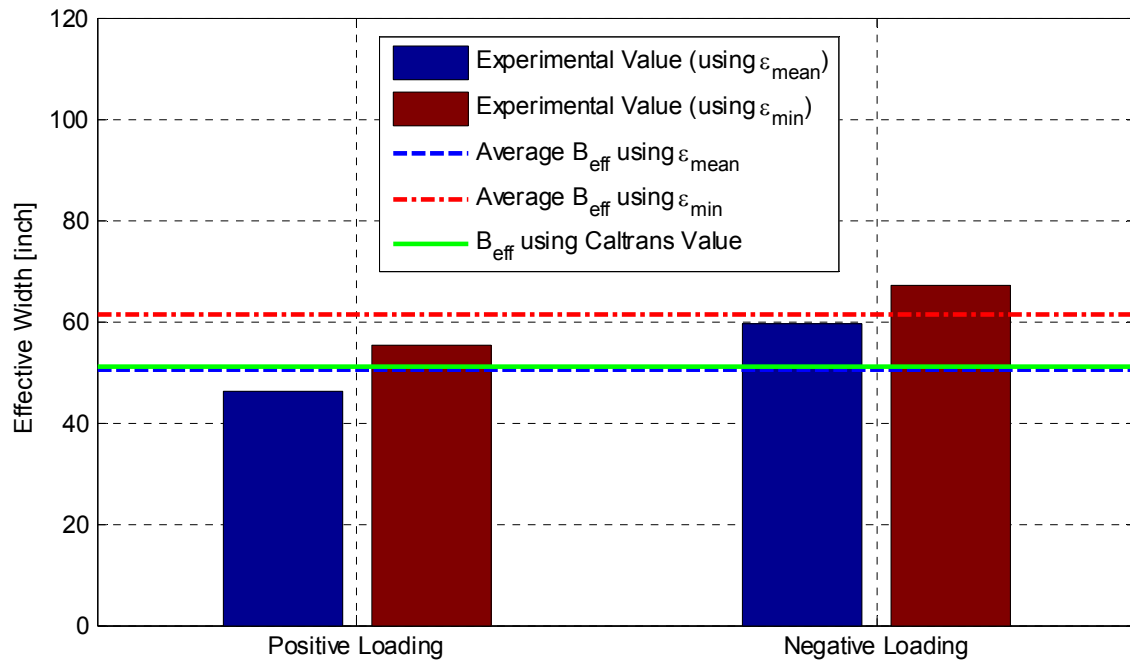
Figure 8.83 Mean effective width from HS test runs from positive and negative loading (bar chart) and overall average effective width from all HS test runs (dashed lines) at section D as compared to Caltrans SDC effective width value

8.6.3 Concrete Surface Strain Distribution

The strain distribution from the instrumented reinforcing steel bars in the bent cap beam tension side and its adjacent deck slab transverse reinforcement was found to be more accurate than the measurements in the compression side and those from the embedded and surface concrete gages. A sample of the embedded concrete gages in the compression soffit slab side was previously shown in Chapter 5. Here, a sample of the surface concrete strain gages is shown for completeness. Figure 8.84 shows the strain history obtained from six different surface concrete gages, which were located close to section B that has been used throughout this study, and distributed at the East and West sides of the column. The figure shows that surface concrete gages captured the overall trend of the effective width despite the noisy measurement. This is implied from the values at level W-1 (closest to column and bent cap) versus W-2 and W-3 levels (farther from the column and cap beam) in Figure 8.84, for instance.
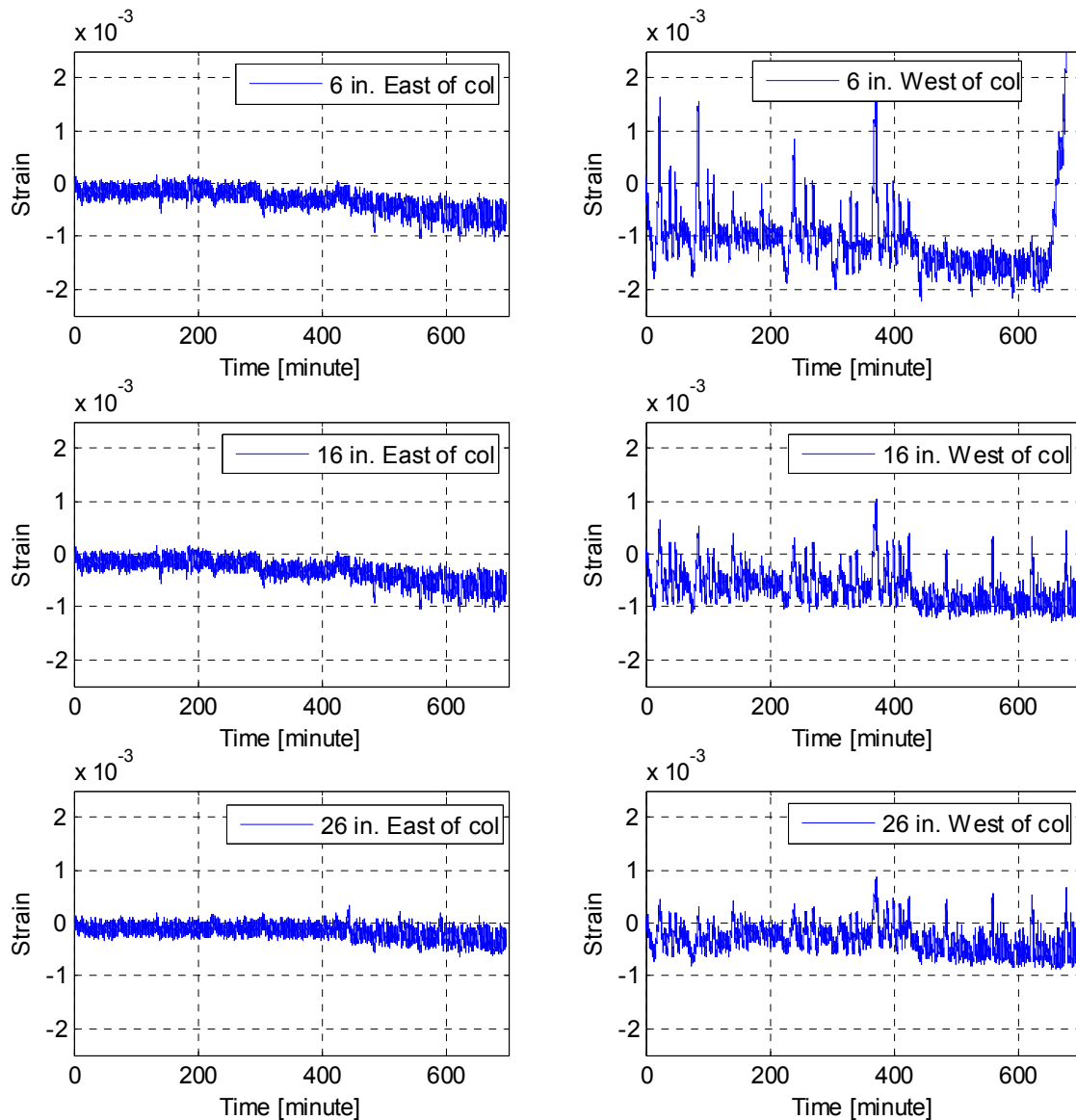
Figure 8.84 Strain history of six concrete surface gages at Section B for all HS test runs

8.7   EFFECTIVENESS OF THE RETROFITTING TECHNIQUE

The previous discussions in Chapter 5 and this chapter imply that the demands increased because of the undertaken retrofit. However, a formal comparison between the overall response of the as-built SP1 and the retrofitted SP2 was not carried out. Thus, this section briefly compares the global force-displacement, the column and bent cap beam moment-curvature, and the overall average value of the revisited effective flange width from the as-built SP1 cyclic tests and the retrofitted SP2 HS tests. This comparison aims at investigating the effectiveness of the retrofit and the CFRP jacket in amplifying the column capacity. Figure 8.85 and Figure 8.86 show such comparison for the global force-displacement and the column moment-curvature relationships in the transverse direction, respectively. The bent cap beam moment-curvature at section B is compared for SP1 and SP2 tests in Figure 8.87.

It is noted that the force capacity of the whole subassembly and the moment capacity of the column increased significantly in SP2 compared to SP1 by almost 25% because of the enhanced column confinement due to the CFRP jacket. On the other hand, the moment in the cap beam at section B of SP1 was capped at approximately 4500 kip-in in the cyclic test because the column reached its flexural capacity and no further demands were transferred to the cap beam. In the HS tests of SP2, the demands on the cap beam increased significantly due to the amplified moment from the column and the 15% gravity load used in these runs relative to the 10% in the cyclic tests of SP1. The moment in the cap beam was capped again but at about 6500 kip-in. This is attributed to reaching either the column or the cap beam capacity. However, the visual evidence of the cap beam concrete crushing in compression suggested that it was the cap beam that indeed reached its capacity. The observed damage at the end of SP1 and SP2 tests is shown side-by-side in Figure 8.88. Therefore, it is concluded that the CFRP jacket and retrofit effectively increased the column and the overall system capacity. However, the associated increase in the cap beam demands might not be favorable if its capacity is underestimated during the design because the failure can migrate to the bent cap.
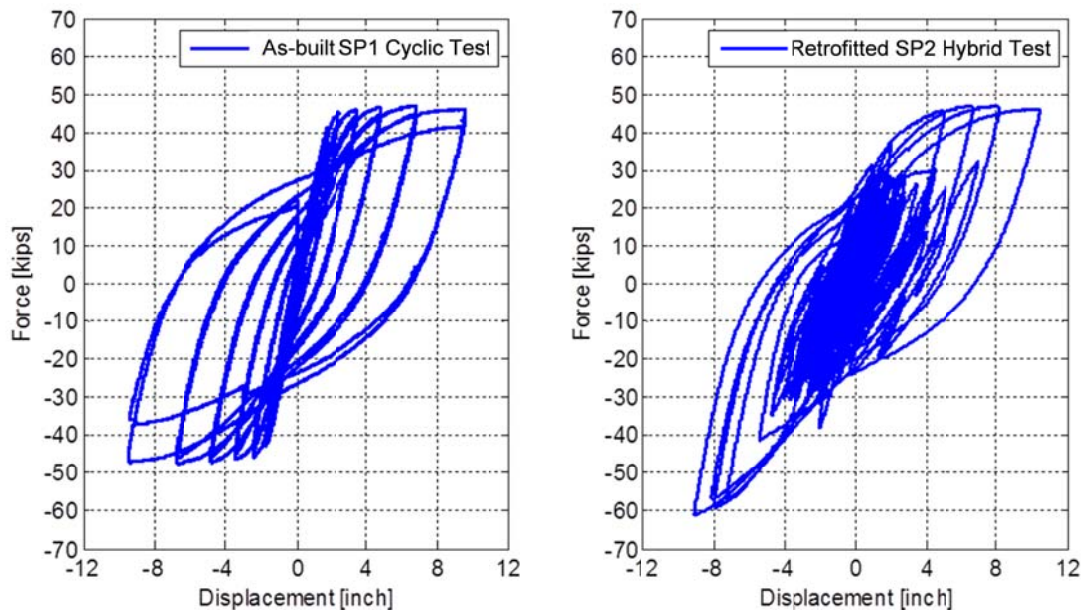
Figure 8.85 Comparison of the global force-displacement relationship in the transverse direction from the as-built SP1 cyclic tests and the retrofitted SP2 HS tests
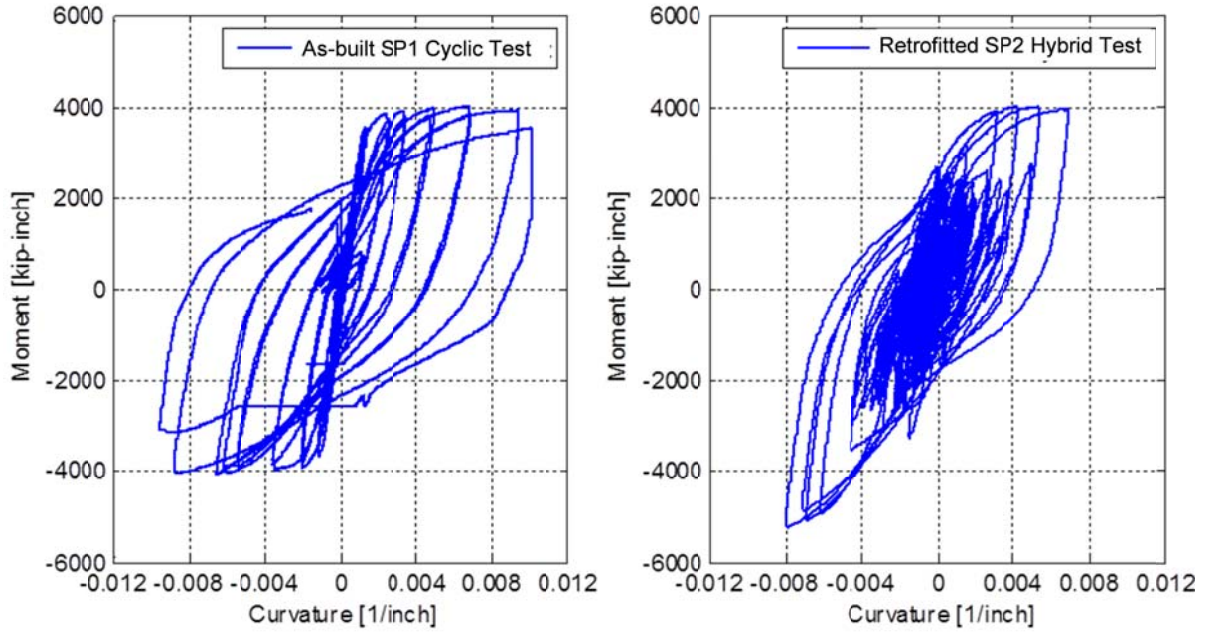
Figure 8.86 Comparison of the column moment-curvature relationship in the transverse direction from the as-built SP1 cyclic tests and the retrofitted SP2 HS tests
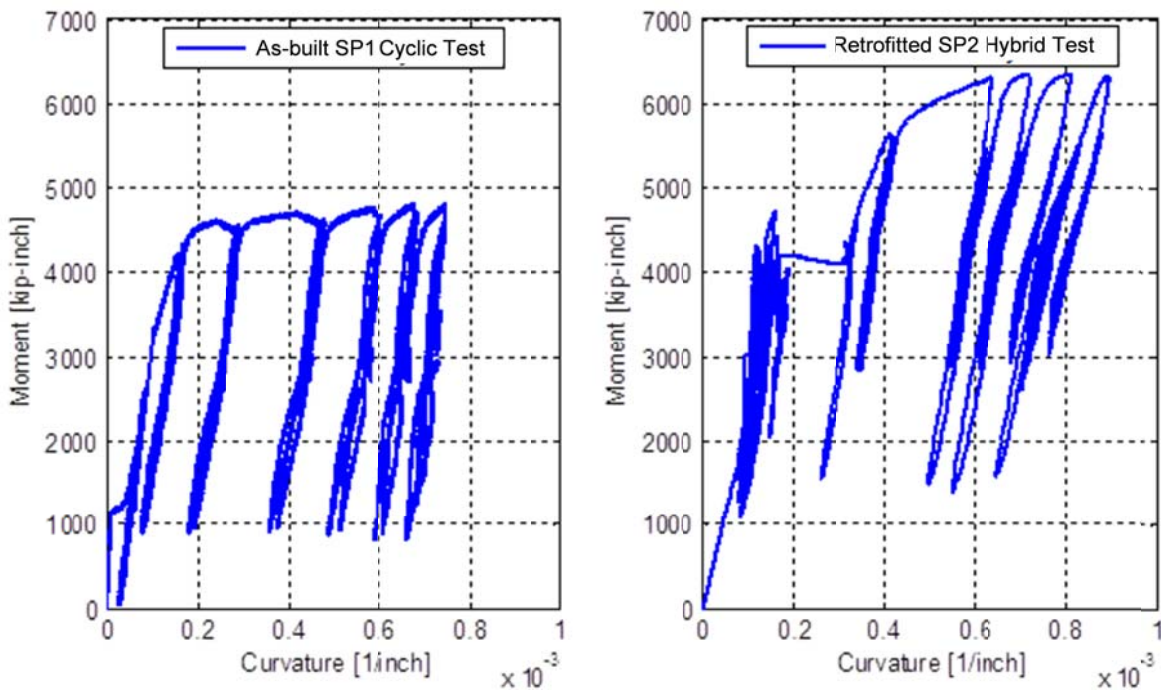
Figure 8.87 Comparison of the bent cap moment-curvature relationship at section B from the as-built SP1 cyclic tests and the retrofitted SP2 HS tests

For completeness, the effective slab width experimentally determined from both the as-built SP1 cyclic tests and the retrofitted SP2 HS tests is compared. As previously discussed, the area under the strain distribution was computed and transformed to an equivalent strain block with an effective width where two strain values were used, namely the minimum and the mean

343

strain among the used six gages at a given cross-section in the cap beam reinforcement. A summary of the mean effective flange width B_{eff}, which includes the cap beam width, from SP1 cyclic tests and SP2 HS tests along with the overall average value from all tests is shown in Figure 8.89 and compared to the Caltrans SDC (2013) value. It is noted that the estimated B_{eff} values from the experiments were significantly higher and slightly higher than the Caltrans SDC value when the minimum and the mean cap beam strain was used, respectively. In addition, it can be noticed that the effective width determined from the cyclic tests was relatively higher than that from the HS tests. When related to the slab thickness (t_s), the mean effective slab contribution (some of the slab potion to both sides of the cap beam width) from the tests ranged from approximately $13t_s$ to $19t_s$ compared to the $12t_s$ code value as shown in Figure 8.89. Accordingly, a recommended value of $18t_s$ is proposed to better reflect the box-girder slab contribution to the width of the integral bent cap beam. Sectional analysis and design implications based on the revisited effective slab width value are presented in details in the next chapter along with the post-test analysis.
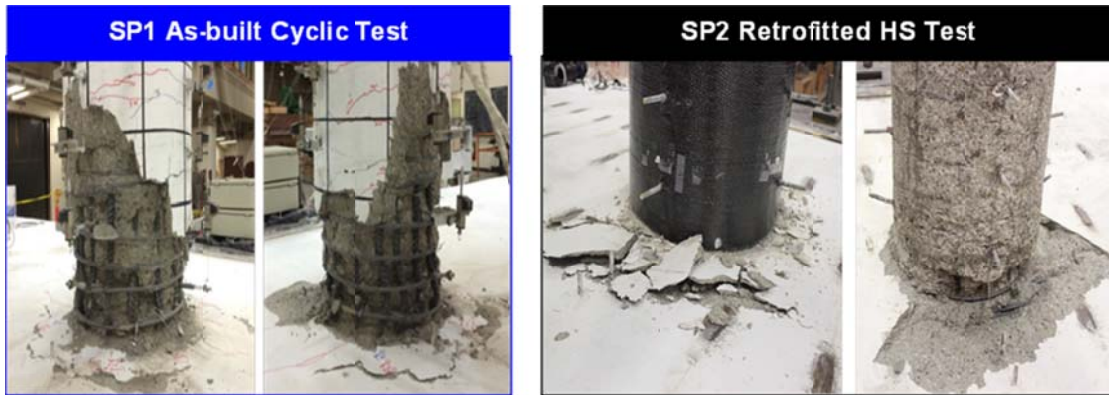
Figure 8.88 Column plastic hinge damage after SP1 cyclic tests and cap beam concrete crushing and column flexural cracks (observed after CFRP jacket removal) after SP2 HS tests
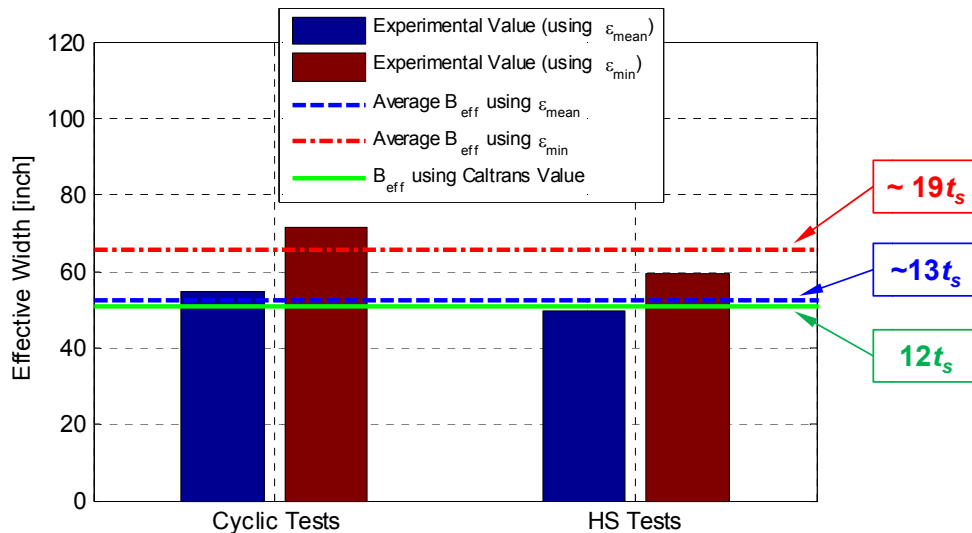
Figure 8.89 Average values for the effective flange width to be added to the cap beam width from the as-built SP1 cyclic tests and the retrofitted SP2 HS tests and overall mean value from all tests when the cap beam minimum and mean strain values were used

344

9   Post-Test Analysis

FE post-test analyses and conventional sectional analyses were conducted to further investigate the bent cap capacity with focus on design optimization. The FE model was first calibrated against SP1 cyclic test results. Next, the FE analysis was used to determine the cap beam capacity from two hypothetical designs having less reinforcement than what the original design required. On the other hand, the sectional analysis determined the nominal cap beam capacity using two values for the slab effective width with or without including the slab tensile reinforcement within that effective width. Moreover, for a comprehensive conclusion, the sectional analysis tool was used to investigate the design implications at the full prototype bridge level. The Caltrans Academy Bridge was utilized to check the design of the integral bent cap beam that corresponds to three different column designs to study the design implications of the revisited effective slab width value and the significance of including the slab transverse reinforcement. Four concise sections comprise this chapter and present (1) the DIANA test specimen model calibration, (2) hypothetical cap beam design FEA investigation, (3) test specimen cap beam sectional analysis, and (4) the design implications at the full-scale prototype bridge level.

9.1   DIANA MODEL CALIBRATION

The detailed 3D DIANA brick-element model of the test specimen previously used in the pre-test analysis was calibrated against the as-built SP1 cyclic tests. Various parameters were varied to understand the effect of each of these parameters on the specimen model response, and consequently, determine the best set of parameters for the most accurate match with the experimental test results. First, the effect of the components of the analysis input cyclic load pattern; the transverse-only versus the bidirectional loading schemes used in the experiments, was explored. Next, the effect of the gravity load was investigated. The effect of each of the concrete total strain-based crack model input parameters was briefly investigated as well. A different set of material model parameters for the column and the box-girder were used afterwards to recognize the actual difference in the concrete lifts used in the construction for better calibration.   Each of the above-mentioned four stages of the model calibration are presented in this section. The section concludes with a brief discussion of the final calibrated model results and comparisons with the experiments.

All the analyses conducted throughout this stage of the model calibration were nonlinear quasi-static analysis under prescribed cyclic loading patterns that mimic the experiments of the as-built SP1. Two cases for the prescribed displacement input were used in the analysis and adopted from SP1 cyclic loading patterns. The first is a bidirectional loading pattern that applied the prescribed displacement input at the column head in the transverse and the longitudinal

directions separately, i.e. in a cross orbit where loading is applied in one direction at a time. A shorter input signal was used as well which applied only the transverse component of the cyclic loading pattern. The bidirectional and transverse-only cyclic loading pattern used for the different DIANA post-test analyses are shown in Figure 9.1 and Figure 9.2, respectively.
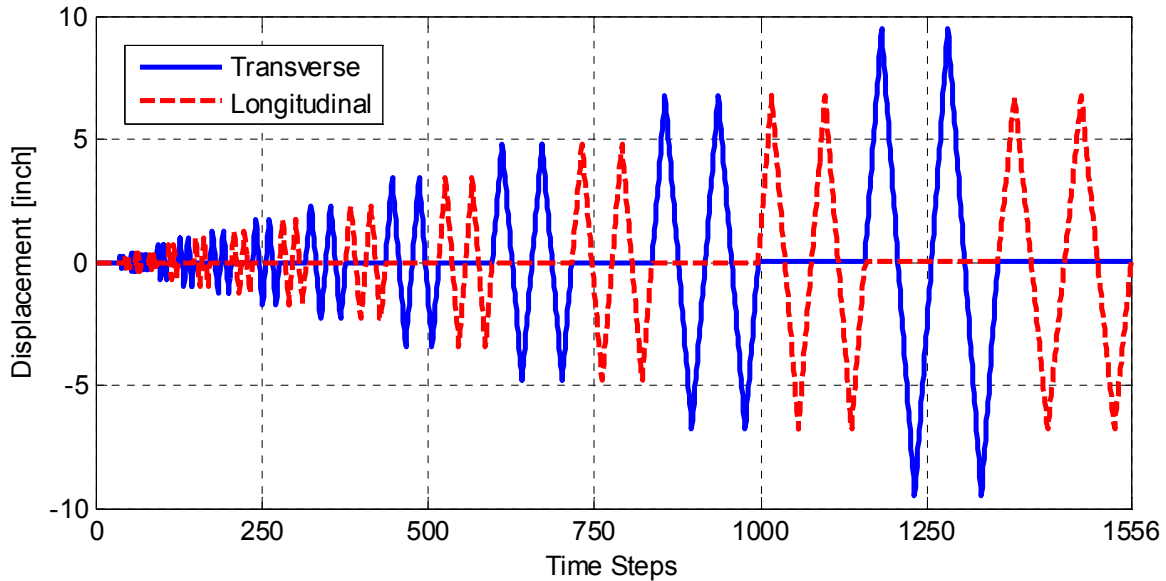
Figure 9.1 Bidirectional cyclic loading pattern adopted from SP1 experiments and used for part of the DIANA post-test analysis
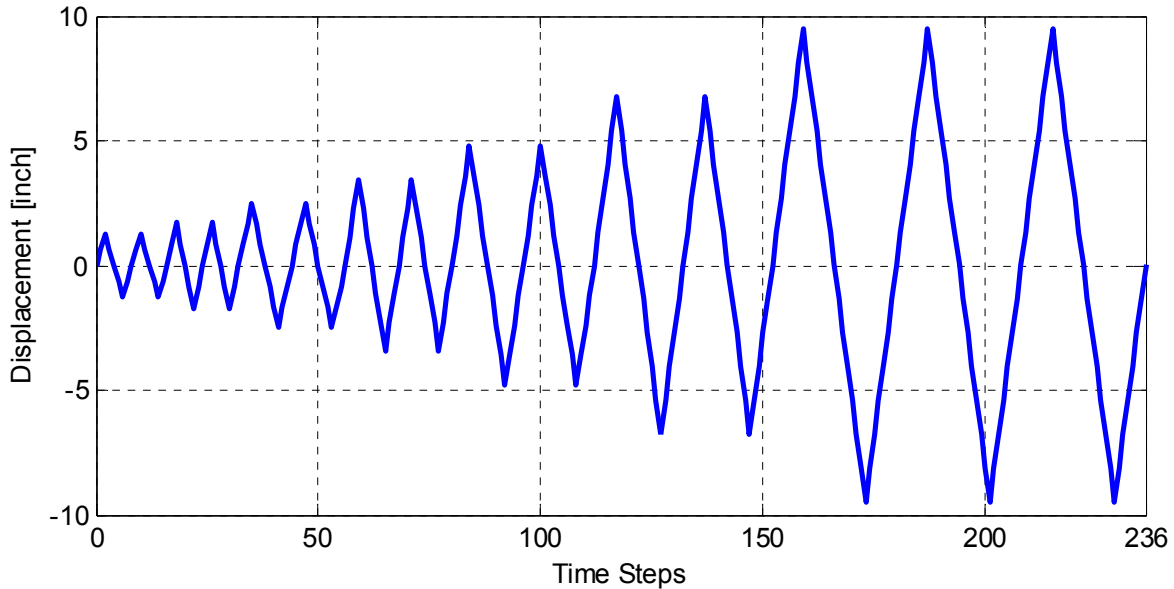
Figure 9.2 Transverse-only cyclic loading pattern adopted from SP1 experiments and used for part of the DIANA post-test analysis

The analysis results from two different cases conducted under the bidirectional and transverse-only cyclic load input are compared and presented in the next subsection. However, it is to be noted that the transverse-only input was the one used to study the effect of the material model parameters. That is because at least 16 analysis cases to be discussed in a later subsection

346

were performed for that task and using the more complex bidirectional input would have been computationally expensive with limited benefit to this particular parametric study.

9.1.1 Transverse vs. Bidirectional Input

A shorter input signal was adopted only in the transverse direction for computational efficiency in order to conduct larger number of parametric studies. Thus, it was desired to check first how much the overall response may differ if the loading and consequent damage in the longitudinal direction is not considered. The bidirectional and transverse-only input displacement patterns were applied to a preliminary model, which used one set of material model parameters for the FE model. This set was adopted from the mean material properties determined from the material tests. A constant gravity load that is equivalent to 10% of the column axial capacity was applied first in both cases. The obtained force-displacement relationships from the two cases are compared as shown in Figure 9.3.

It is observed from the figure that the hysteresis behavior is different. In addition, larger force values were observed when the transverse-only input was used. This is attributed to the effect of the inelastic behavior of the box-girder that introduced some damage when loading included application of cycles in the longitudinal direction in addition to the transverse direction. When only a transverse input was used, all the damage occurred in the column in the vertical plane that includes the longitudinal axis of the bent cap beam leading to higher transverse force capacity. It can be concluded that incorporating the longitudinal component of loading is necessary for accurate model calibration. However, using the transverse-only signal can be used only as a simplified approach to explore the sensitivity of the overall response to the material input parameters as discussed in a following subsection.
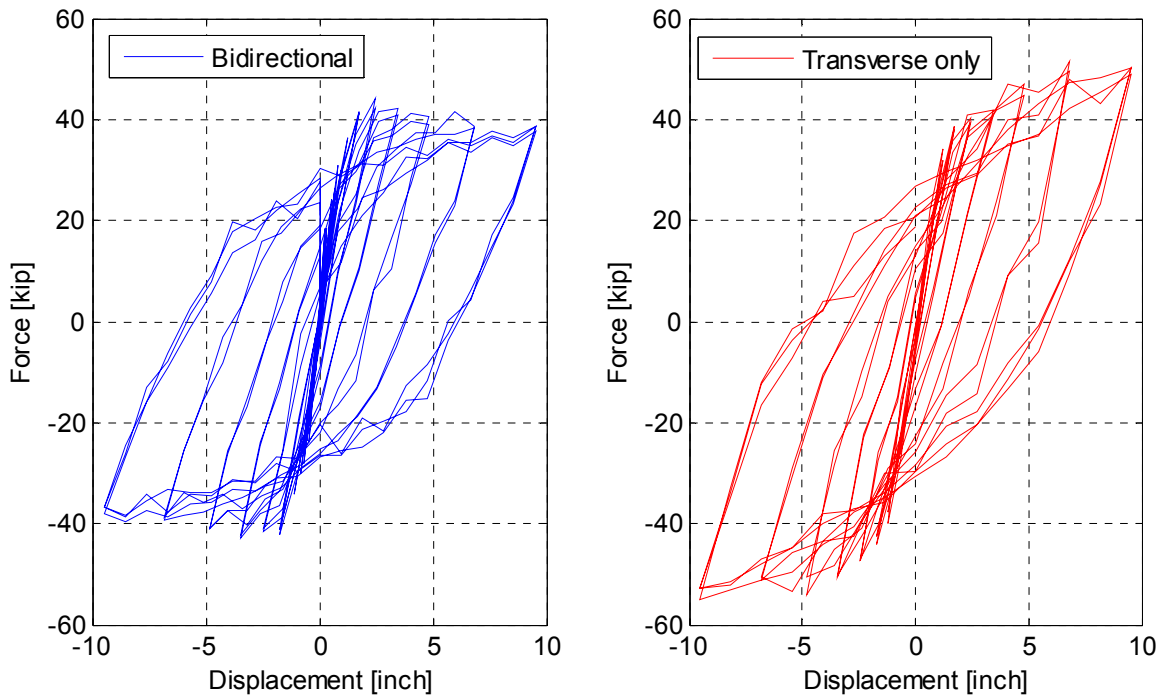
Figure 9.3 Force-displacement relationship in the transverse direction when a bidirectional (left) or transverse-only (right) cyclic loading pattern was used

347

9.1.2 Effect of Gravity

The total vertical reaction at the two roller supports at the ends of the bent cap beam in the DIANA model was compared to applied total gravity load. That is because the vertical reactions were central in estimating the cap beam moment capacity in further analyses. The ratio of the total reaction from the vertical roller supports to the applied gravity load was found to be about 80% from the DIANA analysis. However, the experimentally measured value for the total reaction from the calibrated struts to the applied gravity load was in the vicinity of 70% for both SP1 cyclic tests and SP2 HS tests. This implied that the FE solution distributed the gravity load based on a stiffer bent cap beam which is attributed to the full vertical restraints at its ends. A better method for modeling the end conditions of the bent cap beam is using vertical springs. For simplicity, instead of using springs, the gravity load was adjusted in the FE analysis such that the bending moments that were developed in the bent cap beam matched the values observed from the experiments.

A value of 8% gravity load produced comparable bending moments in the bent cap beam to those obtained under the 10% gravity load from the experiments. It is to be noted that applying the gravity before any lateral loading did not incorporate any inelastic behavior in the model and thus, the nonlinear material model parameters did not need to be calibrated for this part of the analysis. However, it was beneficial to check whether the slightly relieved axial load in the analysis would affect the column behavior. Accordingly, a nonlinear analysis using the bidirectional cyclic load input was conducted with the 10% gravity and without any gravity load. That is to explore the system behavior in the extreme case without any gravity load. Figure 9.4 and Figure 9.5 show the force-displacement relationship comparisons with and without including the gravity load in both the transverse and longitudinal directions, respectively. The figures show that the overall response and force capacity were comparable from both cases. The main difference, however, was only the response in the last group of cycles where a drop in the capacity is noticed because of the more damage in the bent cap as a result of the additional moment from the gravity load. Applying the 8% gravity load showed a similar response under the last group of cycles to the case of the 10% gravity as seen in the final calibrated model results later in this section. Thus, it was concluded that reducing the gravity load to 8% for the post-test analysis, to better match the bent cap beam moment demands, should not affect the overall behavior and is a reasonable approximation.
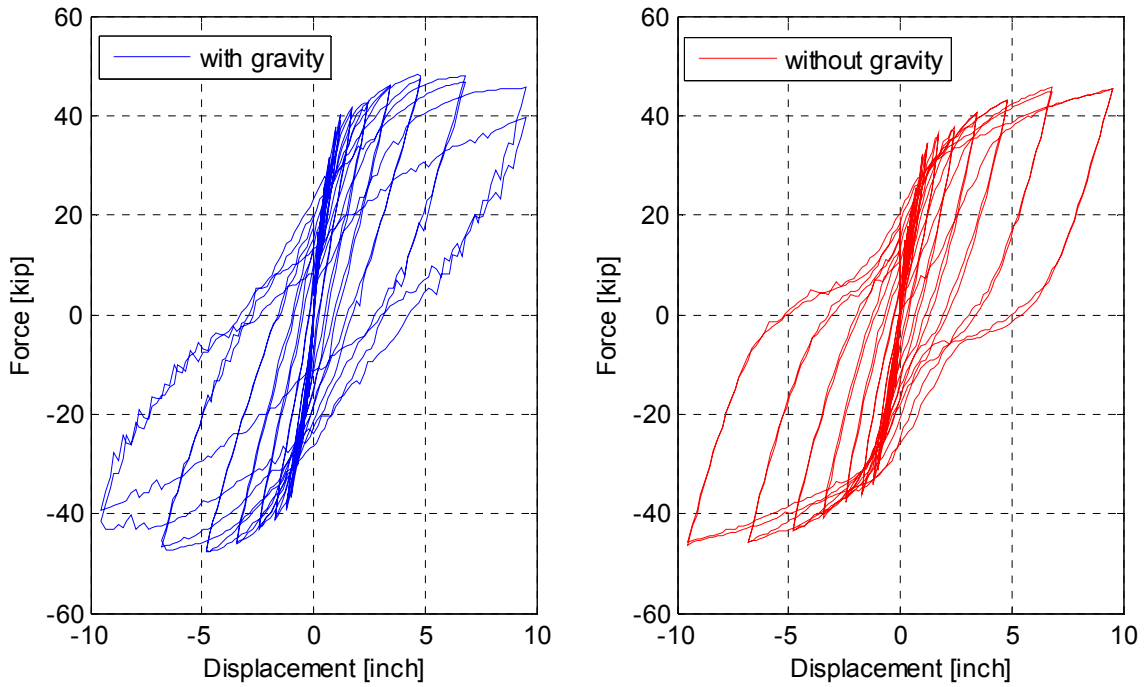
Figure 9.4 Force-displacement relationship in the transverse direction with and without the constant gravity load
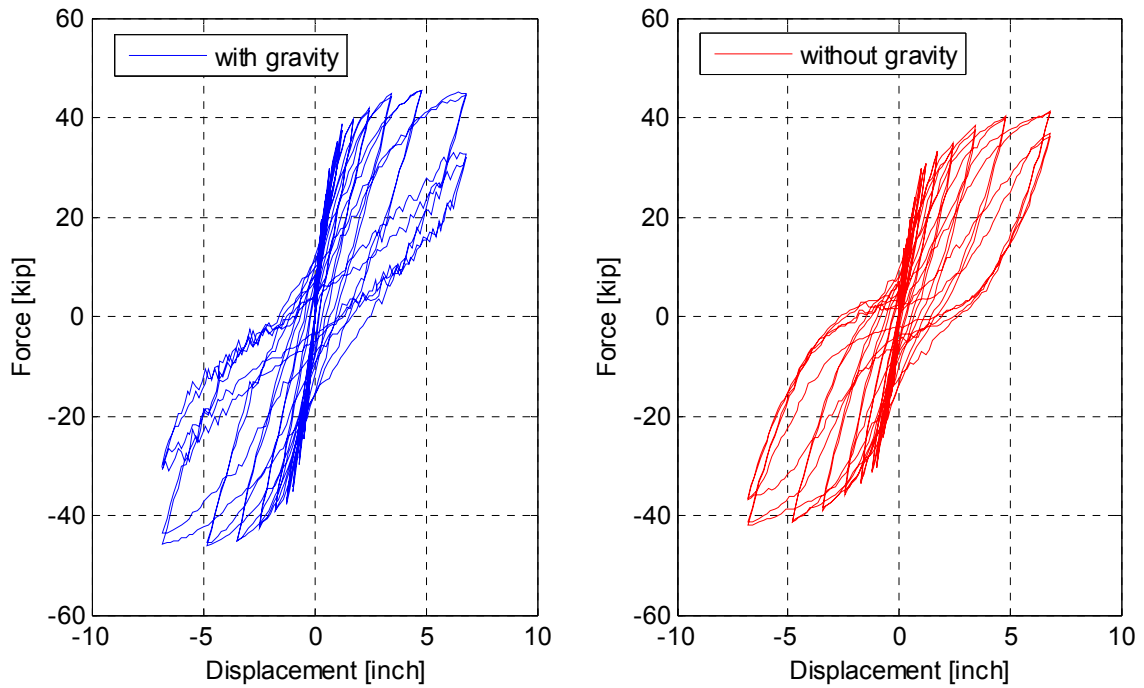
Figure 9.5 Force-displacement relationship in the longitudinal direction with and without the constant gravity load

349

9.1.3 Effect of Model Parameters

To facilitate deciding on the best set of material parameters, each of the concrete total crack strain model parameters: young's modulus (E), compressive strength (f_c), tensile strength (f_t), fracture energy (G_f), stress increase due to confinement, and reduction due to lateral cracking was varied one at a time using input from the material tests. The mean values from the material tests for all three concrete lifts were used for the total strain crack model parameters. Additionally, each parameter was varied one a time using the mean value, 50% less than the mean value, and 50% higher than the mean value. This variation used this range of the 50% difference only for investigating the relative effect of changing such material parameters on the overall response of the specimen model rather than for calibration purposes. Moreover, the transverse-only cyclic loading pattern was used for a computationally inexpensive study.

The force-displacement relationship due to the transverse-only cyclic loading was compared when each of the previously-mentioned parameters was varied. Figure 9.6 shows the effect on the global response due to varying the concrete Young's modulus (E_c) within 50% less or higher than the mean value. Similarly, the overall force-displacement response due to the compressive strength (f_c), tensile strength (f_t), and fracture energy (G_f) variation is shown in Figure 9.7 to Figure 9.9, respectively. Additionally, the total crack strain model in DIANA offers some other modifications to the constitutive model to account for phenomena such as compressive strength increase due to confinement and the Vecchio and Collins (1993) relationship for lateral crack reduction. The effect of these two modifications was investigated as well. Figure 9.10 and Figure 9.11, respectively, show the force-displacement relationships when the confinement and crack reduction modifications were either incorporated or not; one parameter at a time.
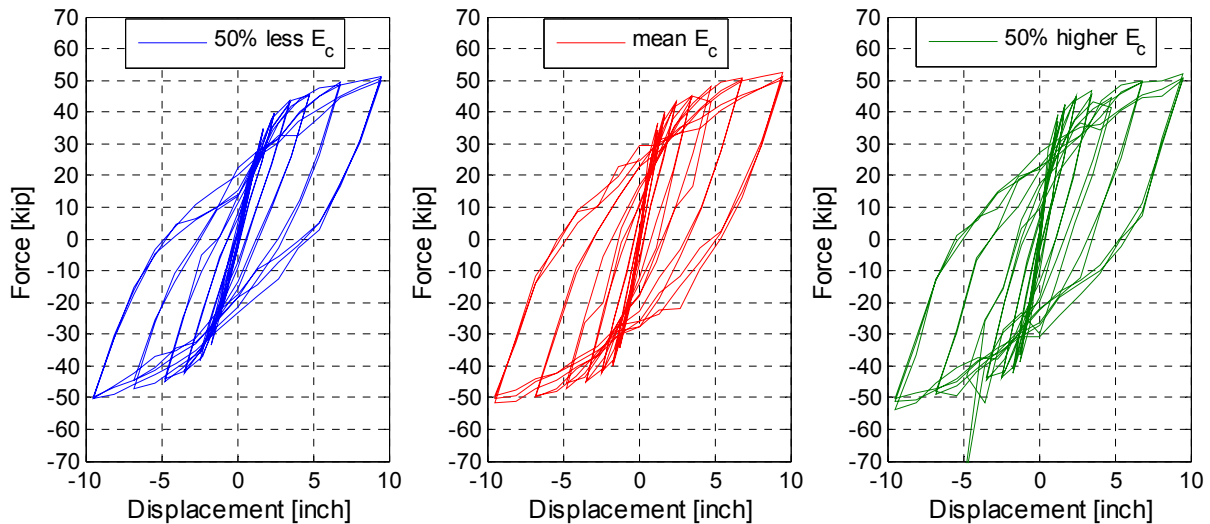
Figure 9.6 Force-displacement relationships for different Young's modulus (E_c) values
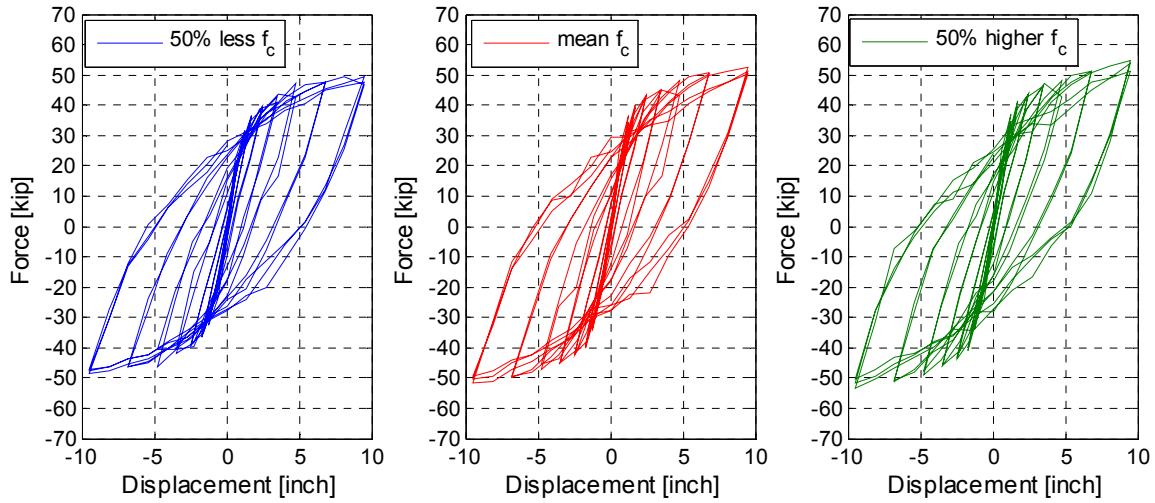
Figure 9.7 Force-displacement relationships for different compressive strength (*f$_c$*) values
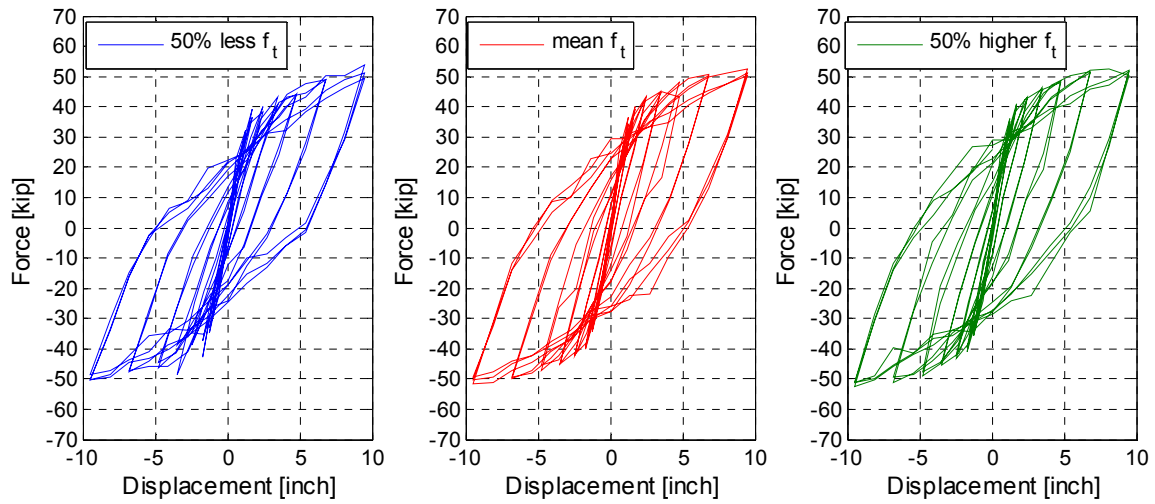
Figure 9.8 Force-displacement relationships for different tensile strength (*f$_t$*) values
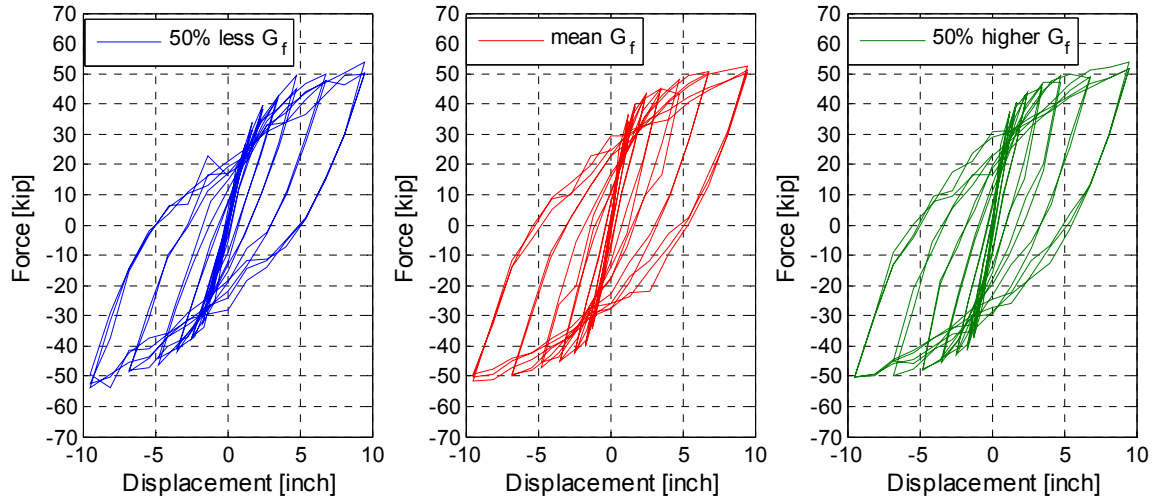
Figure 9.9 Force-displacement relationships for different fracture energy (G$_f$) values

351
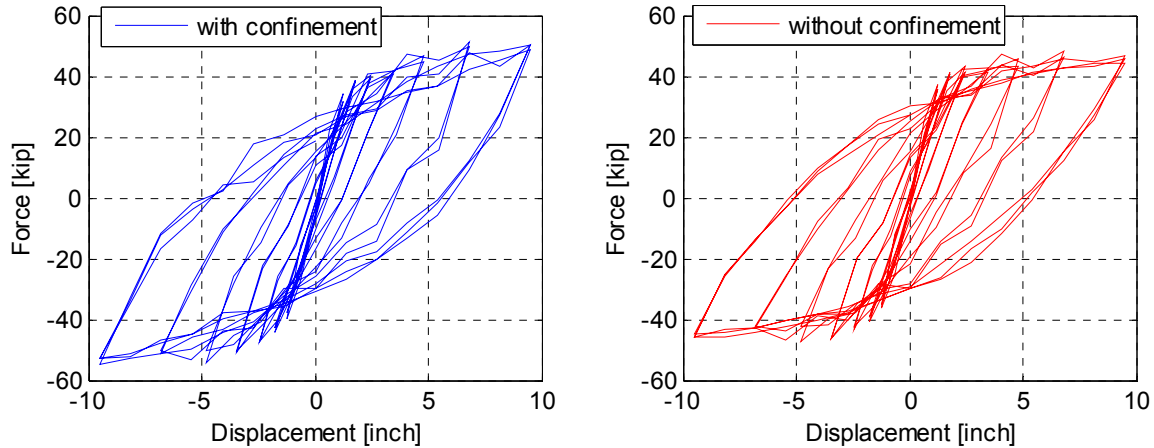
Figure 9.10 Force-displacement relationships when the stress increase due to the confinement option is either incorporated or not in the model
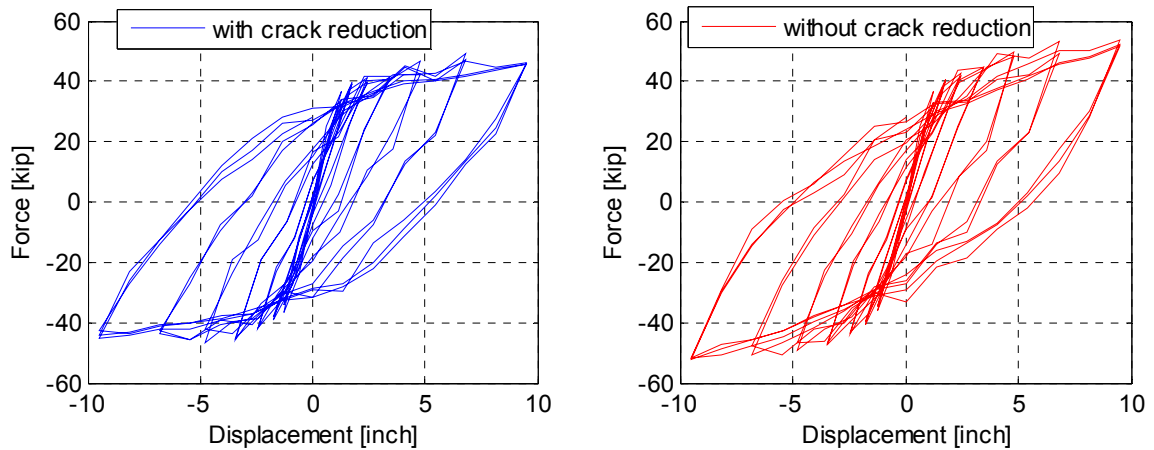
Figure 9.11 Force-displacement relationships when the reduction due to lateral cracking as defined by Vecchio and Collins (1993) is either incorporated or not in the model

In general, it can be observed from Figure 9.6 through Figure 9.11 that none of the material model parameters significantly change the response, the force capacity, or the mode of failure. The parameter that showed a relatively sizable change in the force capacity when it was not incorporated is the Vecchio and Collins (1993) crack reduction and to a lesser extent the confinement option. Thus, it was concluded that the crack reduction modification need to be always incorporated for a better capacity capping behavior that best match the experimental results. Moreover, it was shown that using only one set of material properties for the entire model, i.e. for the column, cap beam, and box-girder, did not reflect the natural difference in the concrete properties from the different lifts as varying the compressive strength, for instance, did not affect the response significantly, contradicting what was expected. Therefore, using two different sets of material parameters; one for the column and the other for the box-girder and cap beam were decided for the next phase of exploring the different ways of calibrating the model. The discussion from three different models that used different combinations of sets of material parameters is presented next.

352

9.1.4 Elastic Column vs. Elastic Superstructure

As mentioned in the previous subsection, it was recommended to investigate whether varying the set of material input parameters for the column from the superstructure would affect the response. This is mainly to recognize the natural difference in the concrete lifts used due to the different stages of construction. The first lift included only the specimen seat beams and the deck slab, while the second lift included the rest of the box-girder and bent cap beam. Thus, a set of material properties from the second lift was a better candidate for the superstructure concrete model. Finally, the third lift was only for the column, and accordingly, the material input for the column constitutive model should be based on the third lift material test results.

To study the effect of the variation in the column material model from the superstructure one, three different DIANA models were utilized. The first model used the mean values from the second concrete lift material tests for defining the superstructure model parameters, whereas the third lift tests were used for the column material input. The second and third models represented the two extreme cases if either the column or the superstructure is entirely linear elastic and damage and inelasticity are limited to the counterpart of the elastic one. Thus, the second model used an elastic concrete model for the superstructure, and the column concrete model properties were based on the third concrete lift material tests. On the other hand, the third model used the second concrete lift material tests to define the superstructure material input while an elastic model was used for the column. The described three different models in this subsection are designated as models A, B, and C, respectively. The force-displacement relationships in both the transverse and longitudinal directions for the three models are compared in Figure 9.12 and Figure 9.13, respectively. The elastic superstructure case, model B, is shown in the left side of the figures whereas the case of the elastic column, model C, is shown in the right side of the figures. The full inelastic model with different material properties for column and superstructure, model A, is shown in the middle part of the figures. Clearly, model A represents a transition between the other two extreme cases in terms of the mode of failure and overall system response.

A much wider hysteresis and energy dissipation occurred when all the damage was concentrated in the inelastic column of model B. On the contrary, a narrower hysteresis, less energy dissipation mechanism, and severe pinching around the zero force value during the unloading were observed when the damage was only concentrated in the superstructure of model C. The response of the full inelastic model with two different sets of material properties was somewhere in-between the two extreme cases of models B and C. This observation was valid for the behavior in both the transverse and longitudinal directions. Two main conclusions can be drawn accordingly. The column mode of failure is much more ductile than the superstructure mode of failure, which indeed, agrees with the seismic capacity design approach where the superstructure is capacity protected to remain essentially elastic. Moreover, the observed experimental response showed a ductile behavior that is, in a generic sense, more closer to model B behavior than model C. Therefore, an informed calibration procedure would to push the column properties to the lower bound of the material test values whereas, the superstructure material model is better to adopt the upper bound that approaches the elastic behavior. The two sets of material parameters were adjusted accordingly, and the results were found reasonably comparable to the experimental results as presented in the next subsection for the final calibrated model.
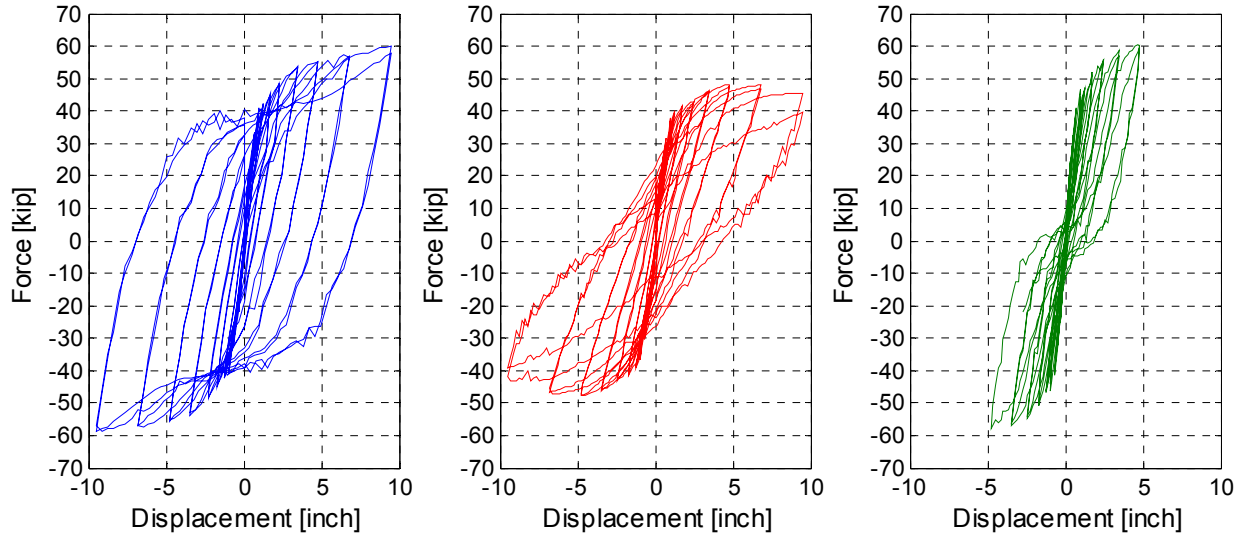
Figure 9.12 Force-displacement relationships in the transverse direction for the fully inelastic model A (middle), the elastic superstructure model B (left), and the elastic column model C (right)
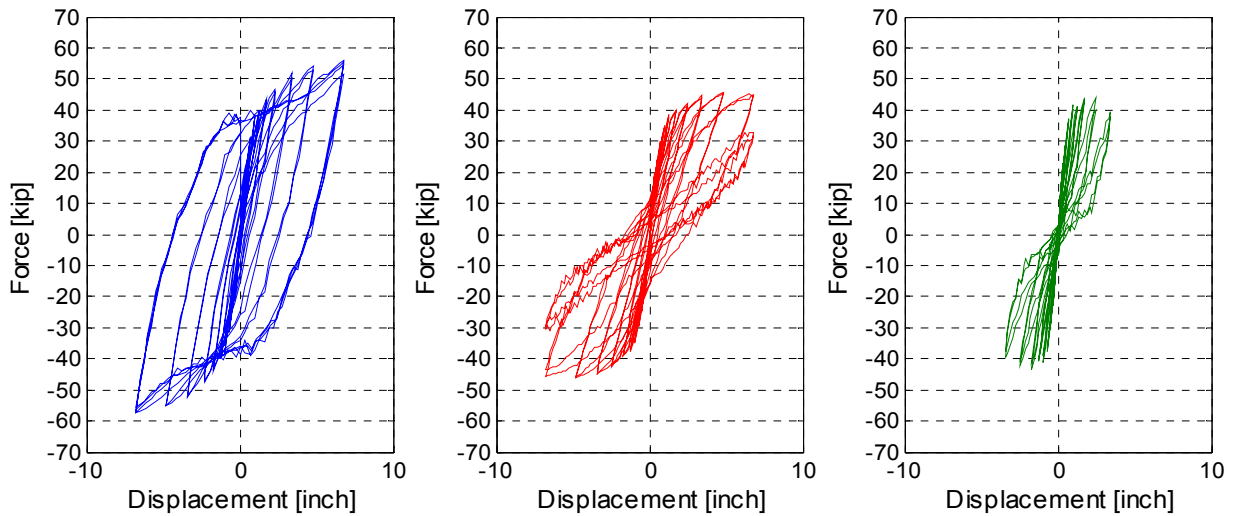
Figure 9.13 Force-displacement relationships in the longitudinal direction for the fully inelastic model A (middle), the elastic superstructure model B (left), and the elastic column model C (right)

9.1.5   Final Calibrated Model

The final calibrated model that was found to reasonably match the experimental results was based on using two different sets of parameters as previously mentioned; one for the column and the other for the bent cap beam and box-girder. This was intended to reflect the different concrete properties of the lifts used to construct the column and superstructure. Accordingly, and based on the observations from the previous subsection, the input for the column concrete was based on the lower bound values of the third concrete lift material tests. On the other hand, the superstructure, i.e. the bent cap beam and the box-girder, material input was based on the upper

bound of the second concrete lift material test results. Selected results for the global and local behavior from the final calibrated model and relevant comparisons with the experiment results are presented in this subsection.

9.1.5.1 *Global behavior*

The force-displacement relationships obtained from the final calibrated model in both the transverse and longitudinal directions are shown in Figure 9.14 and Figure 9.15, respectively. The response from the calibrated model is compared to the corresponding experimental response from SP1 cyclic loading tests in the same figures. Additionally, the bent cap beam moment history, recorded at section B, from the calibrated model analysis and the experiments were compared and shown in Figure 9.16. It is noted from the figures that the calibrated FE model reasonably captured the force capacity in both the transverse and longitudinal directions, and the maximum cap beam moment observed during the test with less than 5% difference. The calibrated model provided confidence to further use it to further investigate the cap beam capacity and other design implications.
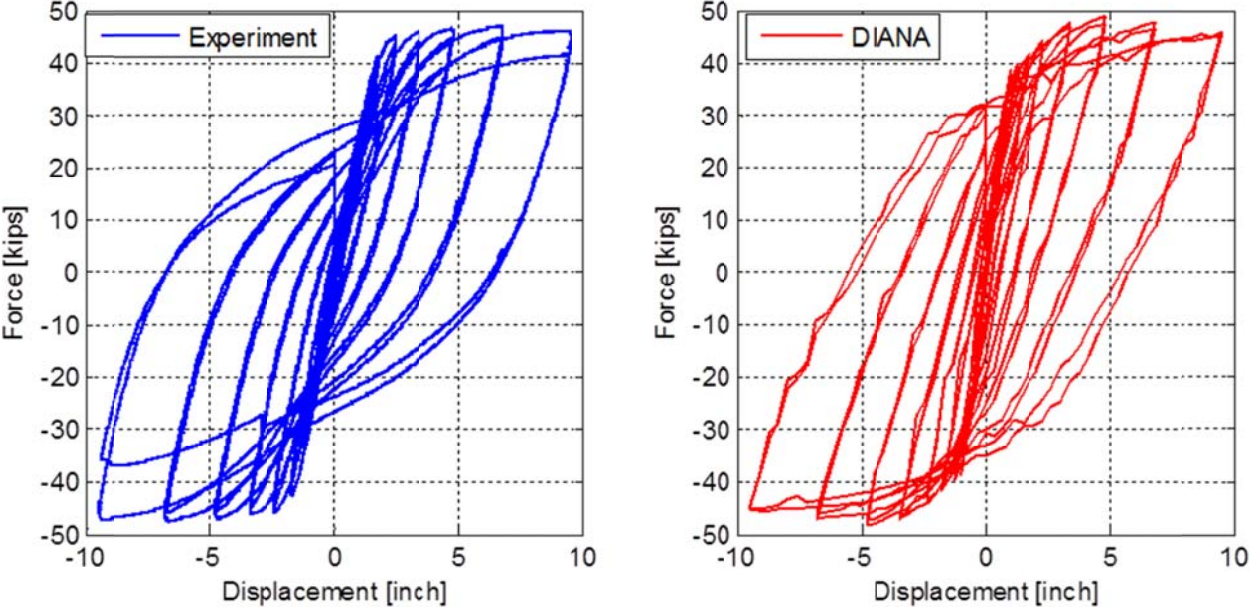
Figure 9.14 Force-displacement relationship in the transverse direction from SP1 cyclic tests and the final calibrated DIANA FE model
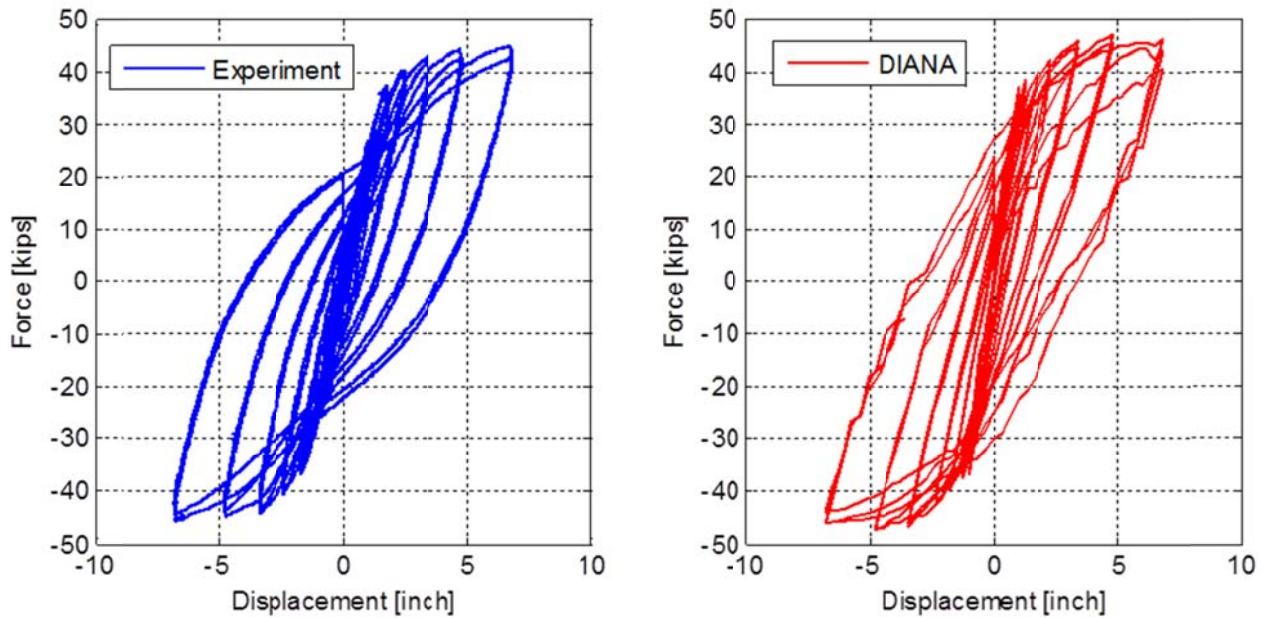
Figure 9.15 Force-displacement relationship in the longitudinal direction from SP1 cyclic tests and the final calibrated DIANA FE model
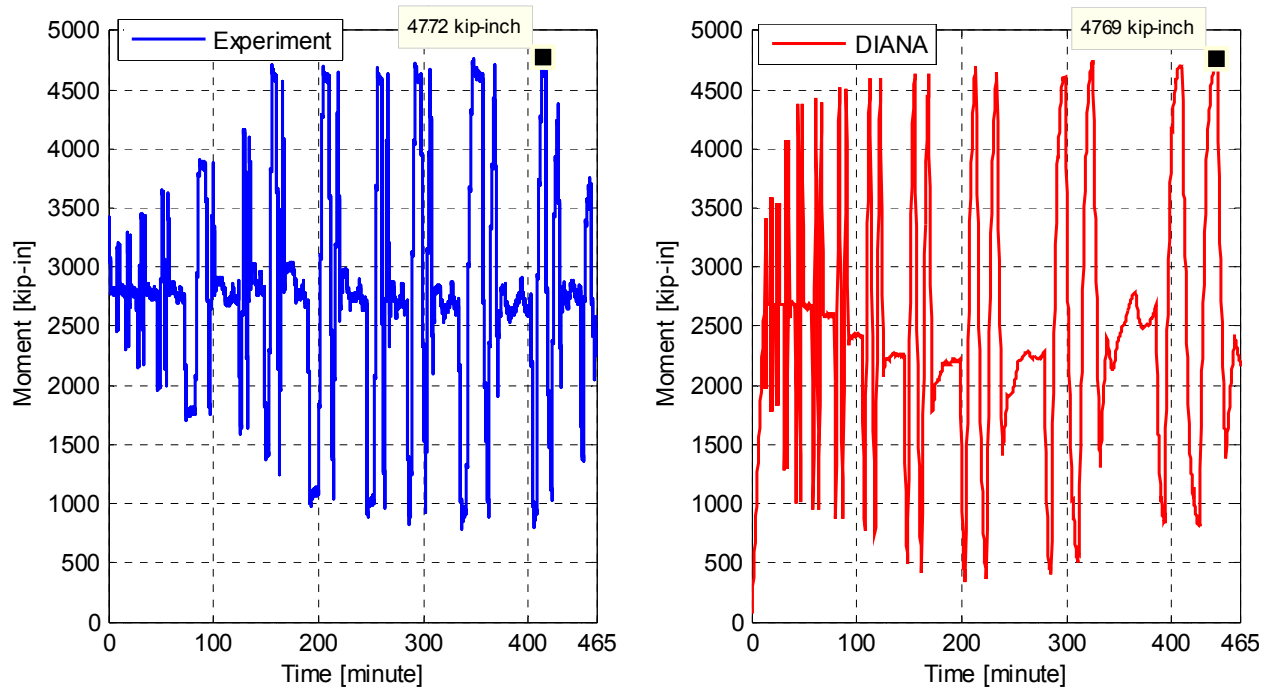
Figure 9.16 Bent cap beam moment history at section B from SP1 cyclic test and the final calibrated DIANA FE model

9.1.5.2 *Local behavior*

To complement the global behavior discussion, the calibrated model was used to investigate several local behavior response quantities as well. Figure 9.17 shows a view from FX+, the DIANA pre- and post-processor, for the crack pattern in the vicinity of the column and bent cap beam as the bidirectional loading progressed. The embedded reinforcement strains were recorded from the analysis and a sample of the strain history due to all the loading cycles at sections B and D of one of the bent cap embedded reinforcing bars is shown in Figure 9.18. The same strain history from the FE model at section B is compared to that from the experiments in Figure 9.19. Although the strain values are somewhat different, the model captured the strain evolution as loading progressed in a reasonable manner.

The strain values from the DIANA analysis, as any other local response quantity, are very sensitive to the nonlinear FE solution. Thus, no main conclusions are based on the FE local behavior, but only major observations or trends. Accordingly, the strain distribution was obtained from the analysis and was reordered at the peaks of the different loading cycles to check how accurate the model can capture the local behavior. The strain distribution at four small loading levels that corresponded to drift ratios of 0.4%, 0.8%, 1.4%, and 2.7% and equivalent to ductility levels 0.28μ, 0.56μ, 1.0μ, and 1.96μ, respectively is shown in Figure 9.20 and Figure 9.21 for sections B and D, respectively. In addition, Figure 9.22 and Figure 9.23 show the strain distribution for larger loading levels at drift ratios of 3.9%, 5.3%, 7.6%, and 10.5% at sections B and D, respectively. It is observed that while the bent cap beam and the box-girder remained elastic at the lower load levels, a uniform bell-shaped strain distribution was observed. At the higher load levels, a nonlinear non-uniform distribution was observed which was still reasonable enough when compared to one of the strain distributions obtained experimentally. The local strain distribution was obtained for completeness and to explore the capabilities and accuracy of the analysis rather than using it for arriving at any conclusion regarding the effective flange width. However, the results show great potential for further enhancements of the model to capture the local behavior even more accurately.
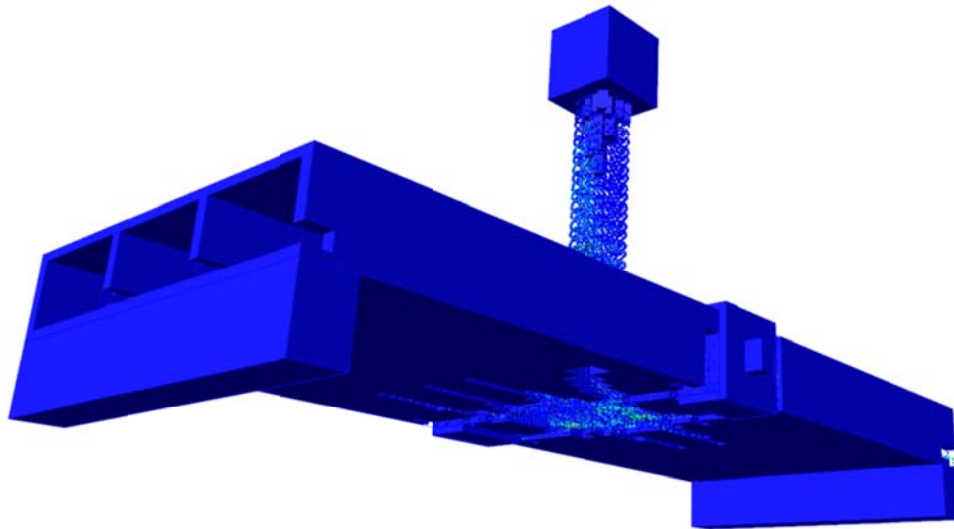
Figure 9.17 Overview of the crack pattern in the vicinity of the column and bent cap beam as observed from the DIANA calibrated model after the bidirectional cyclic load was applied
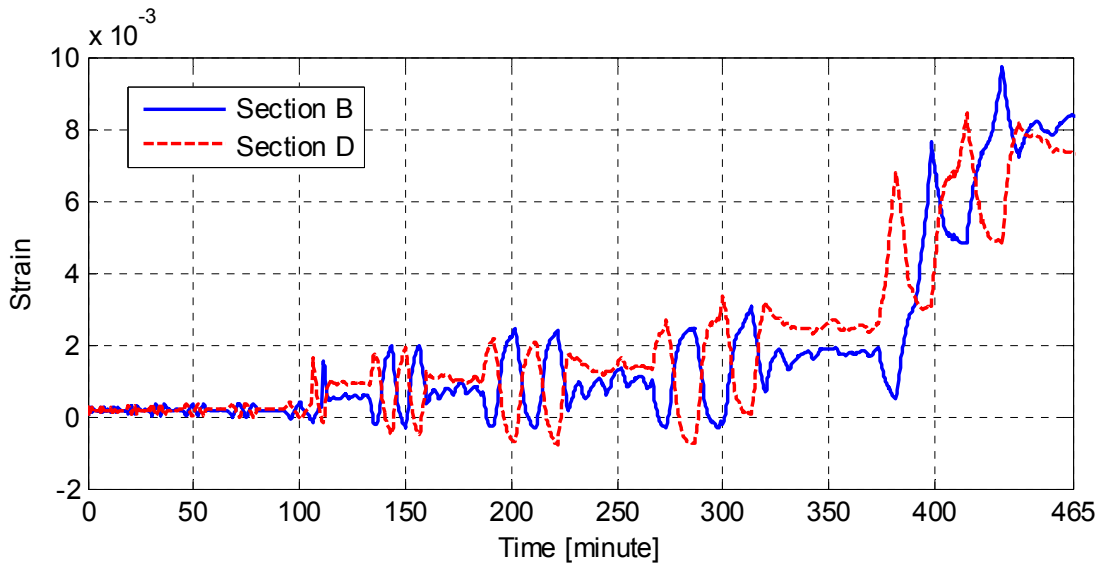
Figure 9.18 Strain history at one of the bent cap reinforcing bars at sections B and D obtained from the calibrated FE model for all the loading cycles
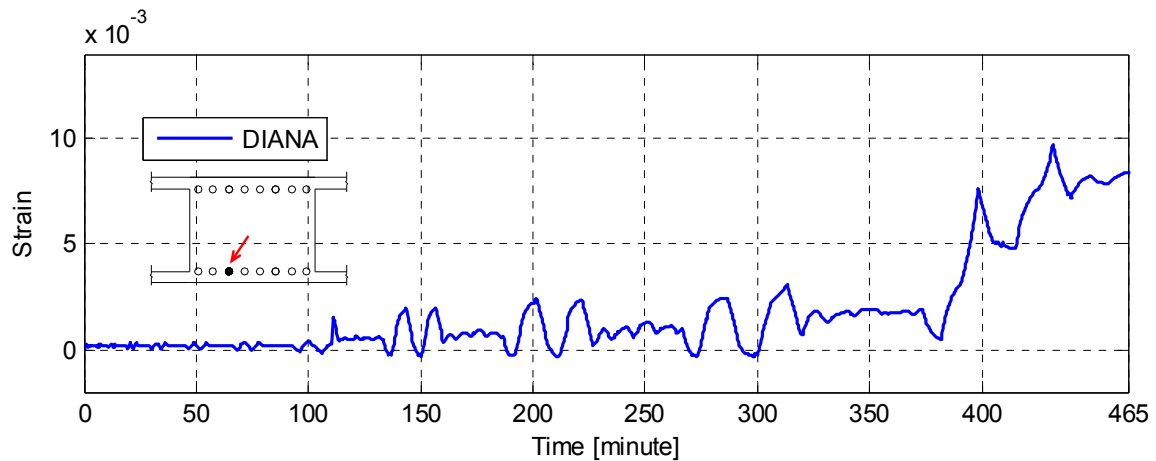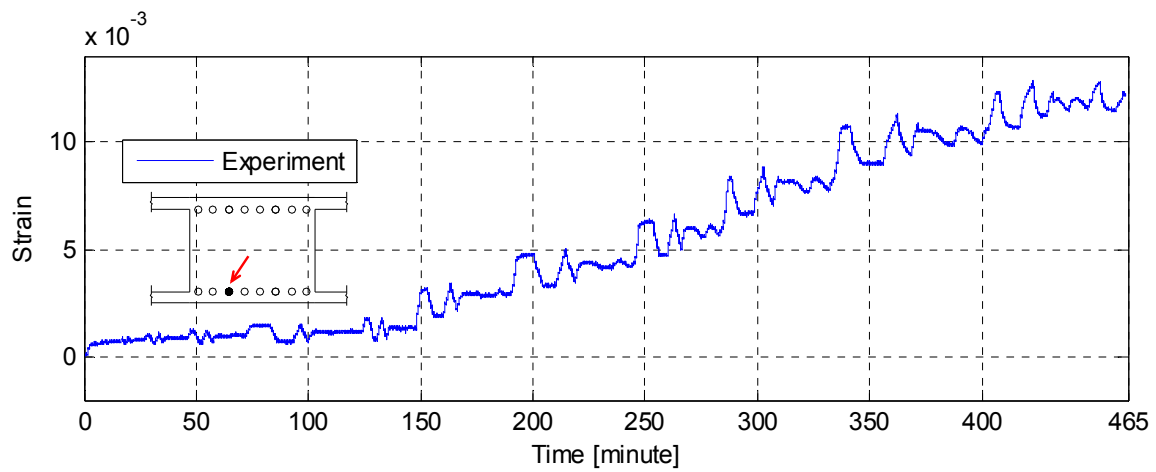
Figure 9.19 Comparison of the strain history at one of the bent cap reinforcing bars in the tension side at sections B from SP1 cyclic tests and the calibrated FE

358
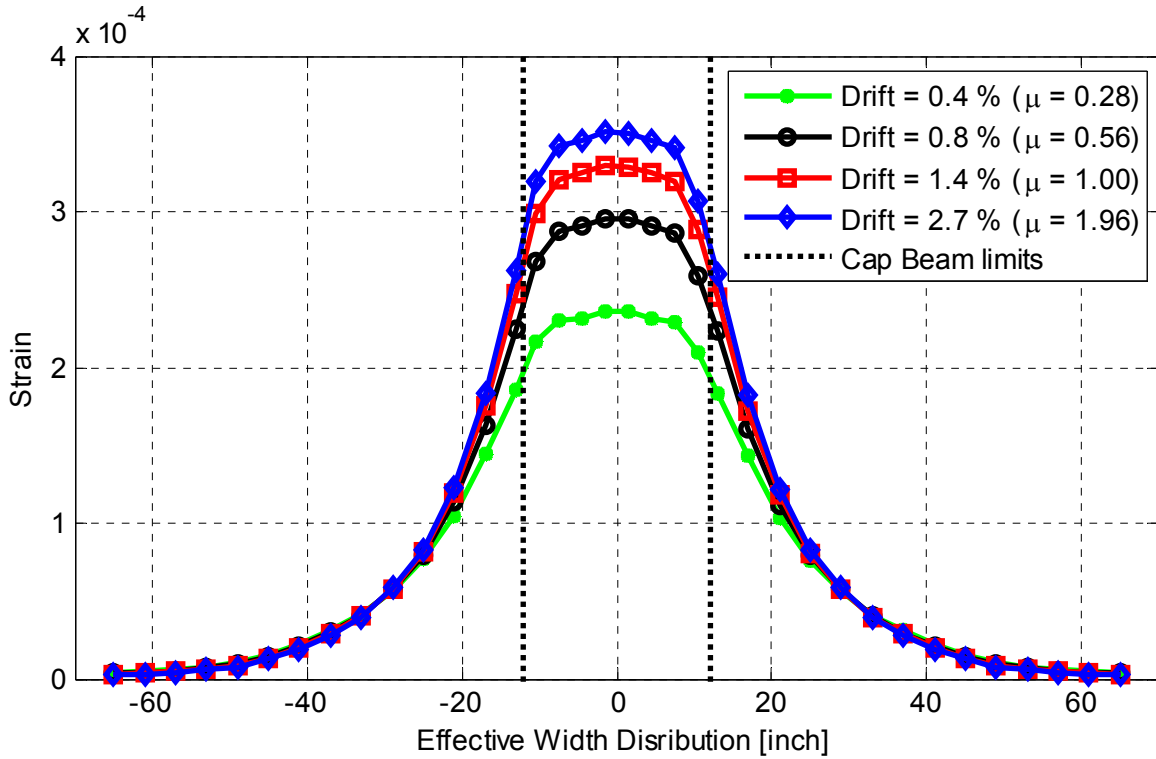
Figure 9.20 Strain distribution at section B for four different small loading levels as obtained from the calibrated FE model
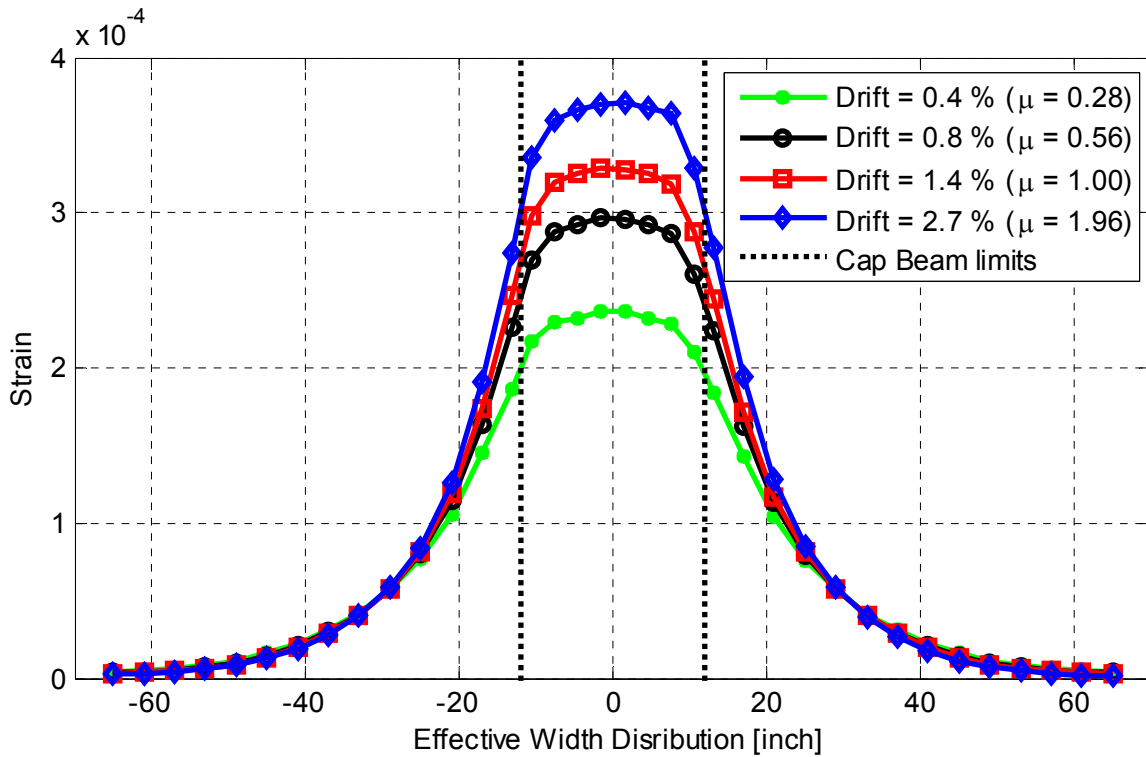
Figure 9.21 Strain distribution at section D for four different small loading levels as obtained from the calibrated FE model
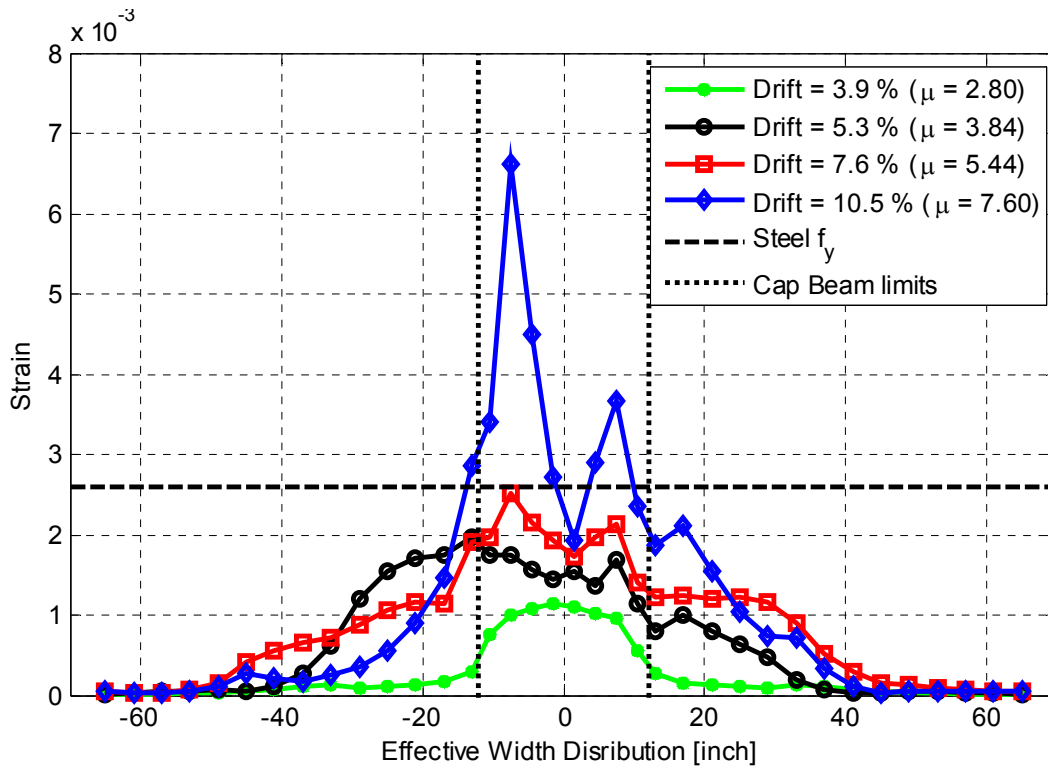
Figure 9.22 Strain distribution at section B for four different large loading levels as obtained from the calibrated FE model
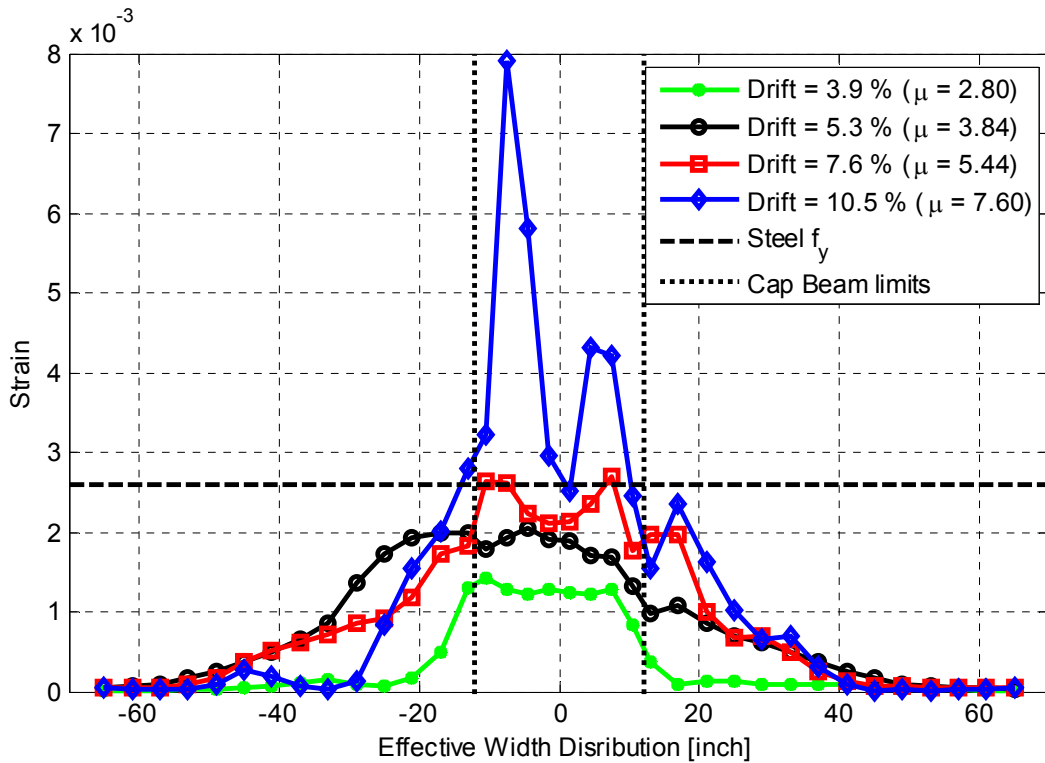
Figure 9.23 Strain distribution at section D for four different large loading levels as obtained from the calibrated FE model

9.2 FE ANALYSIS FOR DIFFERENT BENT CAP DESIGNS

The calibrated sets of material input parameters in the DIANA FE 3D model for the test specimen were used to investigate the bent cap capacity in case of the original specimen design and two other hypothetical designs. The main objective of this part of the study is to complement the experimental program through determining the bent cap beam capacity and the contribution of the box-girder to the overall system capacity in these three different cases of the bent cap designs. The goal was not to optimize the bent cap design, which is the considered in the design implication section of this chapter. However, less reinforcement in the bent cap was used to form two hypothetical cases of under reinforced bent cap beam to investigate whether the contribution from the box-girder to the system capacity is affected by the bent cap contribution or design. For this reason, the test specimen bent cap original 8 #5 top and bottom reinforcement were replaced with 8 #4 top and bottom reinforcement for the first hypothetical design, and 8 #3 top and bottom reinforcement for the second hypothetical design. For simplicity, the three designs are designated as original design (8 #5), design 1 (8 #4), and design 2 (8 #3).

The objective of this analysis, as mentioned above, is to determine the bent cap beam capacity rather than actual system response. Moreover, the exact system response has been already identified from the experimental part of the study, and was reasonably reproduced using the calibrated FE analysis as discussed in the previous section. Thus, it is desired to limit the mode of failure and concentrate the damage only in the bent cap beam. Accordingly, the calibrated set of material parameters for the superstructure, i.e. the bent cap and the box-girder, was used along with an elastic concrete model for the column. That is to amplify the demand on the bent cap beam until the capacity is reached. Three different types of analysis were used to determine the bent cap beam capacity. These are nonlinear quasi-static analysis using the bidirectional cyclic loading pattern, vertical pushover analysis, and lateral pushover analysis. Additionally, the full inelastic calibrated model was used to compare the system response from the three designs regardless of whether the cap beam reaches its capacity or not. Four subsections are presented next to discuss the response comparison of the three bent cap designs in case of the inelastic model subjected to cyclic loading, and the elastic column model under cyclic loading, vertical, and lateral pushover analyses. A final subsection is provided to summarize the bent cap capacity or response observed from all the analyses.

9.2.1 Inelastic Model: Cyclic Loading

The final calibrated inelastic DIANA FE model for the test specimen that used two sets of material parameters for the column and the superstructure was further utilized to investigate the overall response when the bent cap beam reinforcement is changed. The three different bent cap designs previously-mentioned were adopted in the inelastic FE model, which was analyzed in the three cases under constant gravity load and bidirectional cyclic loading. The obtained force-displacement relationships in the transverse and longitudinal directions from the three designs are compared in Figure 9.24 and Figure 9.25, respectively. The bent cap beam moment history at section B is compared for the different cases as well in Figure 9.26.

The overall response illustrated in the force-displacement relationships denotes that the system capacity did not almost change irrespective of the bent cap reinforcement. This is obviously attributed to the fact that the mode of failure and the system capacity is governed by the column rather than the bent cap or box-girder. This was already observed in SP1 cyclic tests

and confirms the observation that the bent cap beam remained essentially elastic as required by the adopted Caltrans and AASHTO capacity design provisions. The moment history shown in Figure 9.26 indicates that similar demand, dictated by the moment capacity, was transferred to the bent cap beam in the three reinforcement designs. These results show that in a successful capacity design approach, only the minimum amount of reinforcing steel is needed in the bent cap beam as long as it is guaranteed that only the column attracts all the damage in case of extreme events. In other words, if the bent cap capacity is accurately estimated, to perform the capacity check, unnecessary additional bent cap reinforcement can be avoided and the bent cap design can be optimized accordingly. More details are discussed in the design implications section.
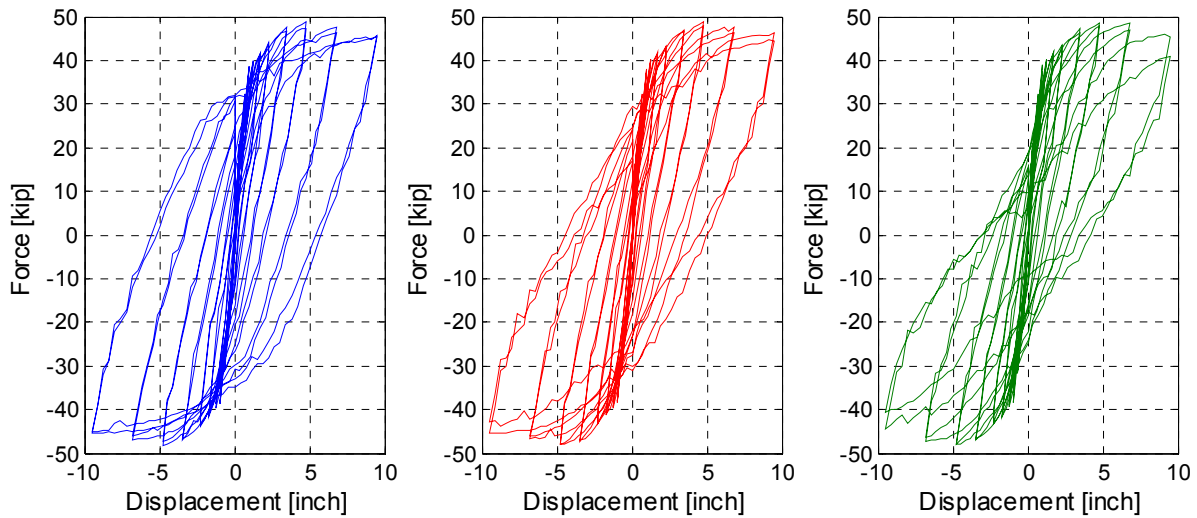
Figure 9.24 Force-displacement relationships in the transverse direction from the calibrated inelastic FE model for three bent cap cases: 8 #5 top and bottom of original design (left), 8 #4 top and bottom design 1 (middle), and 8 #3 top and bottom design 2 (right)
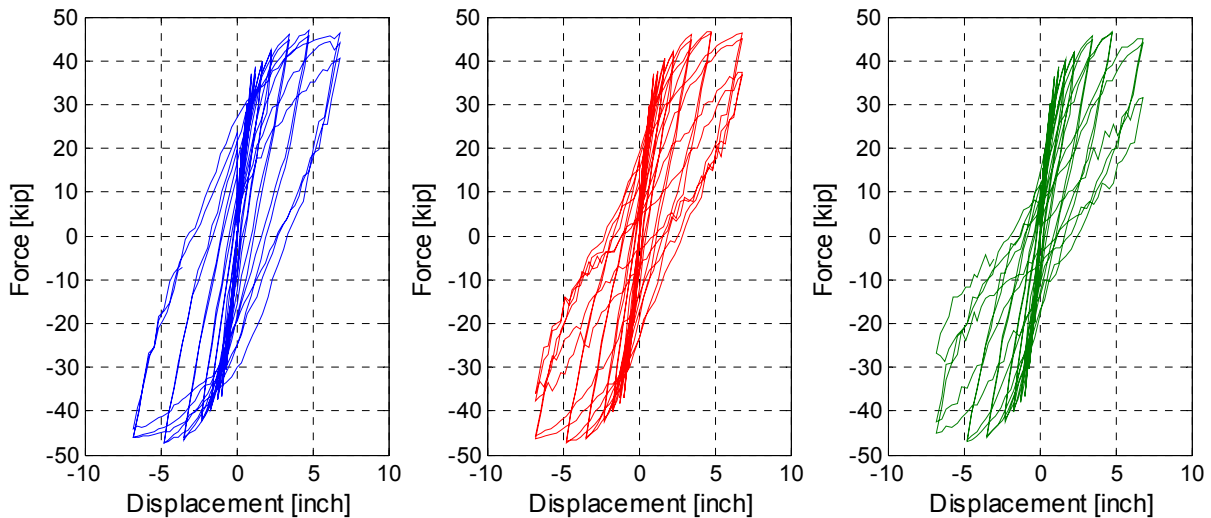
Figure 9.25 Force-displacement relationships in the longitudinal direction from the calibrated inelastic FE model for three bent cap cases: 8 #5 top and bottom original design (left), 8 #4 top and bottom design 1 (middle), and 8 #3 top and bottom design 2 (right)

362
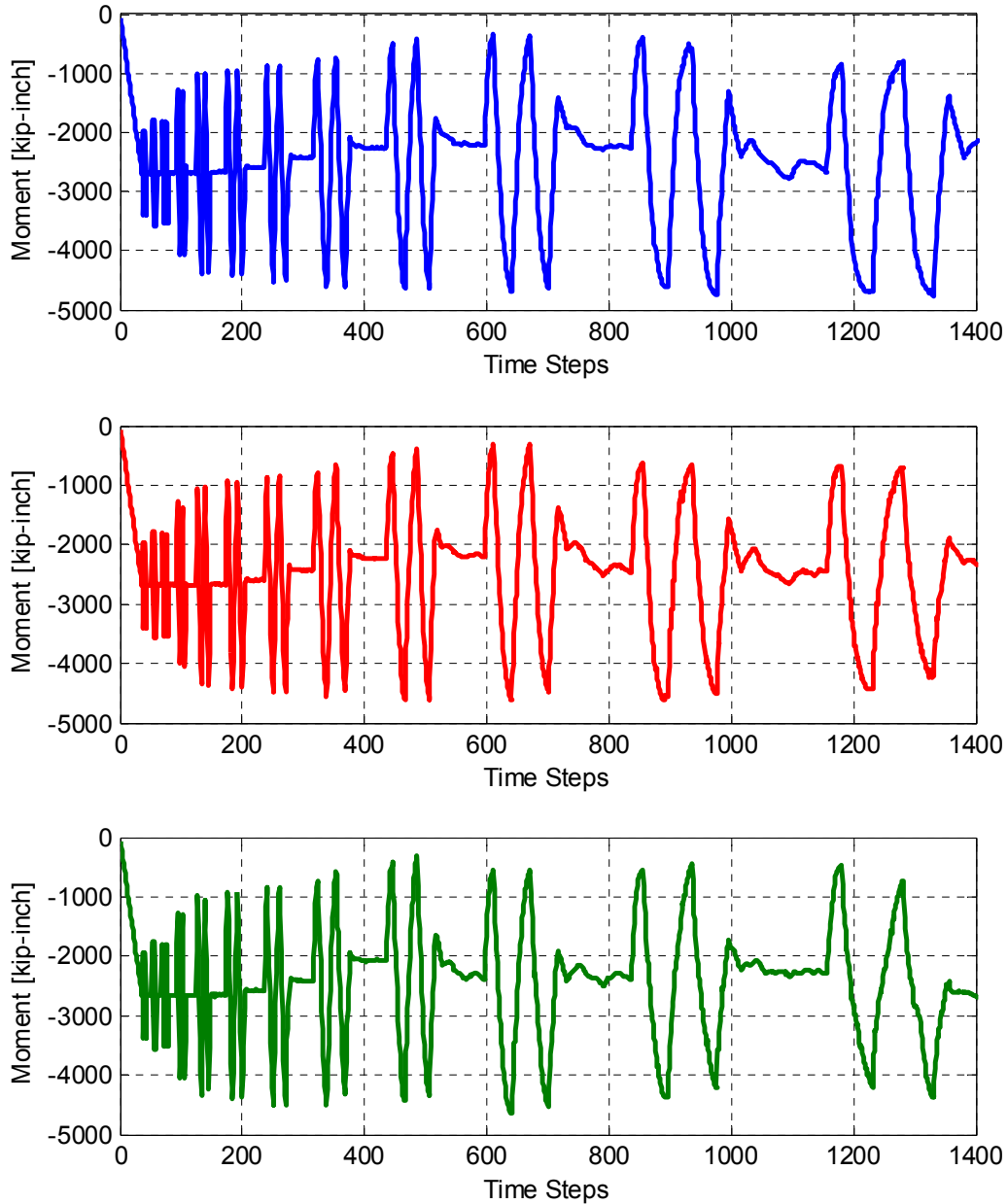
Figure 9.26 Bent cap beam moment history at section B from the calibrated inelastic FE model for three cases: 8 #5 top and bottom original design (top), 8 #4 top and bottom design 1 (middle), and 8 #3 top and bottom design 2 (bottom)

9.2.2 Elastic Column Model: Cyclic Loading

A completely different perspective of the bent cap beam capacity design check is tackled through the elastic column FE model. The inelastic behavior was limited to the bent cap beam and the box-girder, whereas the column concrete remained elastic to force the damage into the superstructure to analytically determine the bent cap beam and overall system capacity. This hypothetical case is not allowed by the design codes as discussed throughout this study. Only a similar case might be realized by an overdesign of a column retrofit to the extent it migrates all

363

the damage to the bent cap beam. Thus, providing an accurate way of estimating the bent cap beam capacity is very beneficial for the seismic capacity design check and for informed retrofit decisions as well.

In this subsection, the final calibrated FE model was modified such that the column used an elastic concrete material model but the reinforcing bars were still modeled using Von Mises plasticity along with the Voce hardening previously discussed in Chapter 4. A bidirectional cyclic loading under constant gravity was applied for the three cases of bent cap reinforcement. Figure 9.27 and Figure 9.28 compare the force-displacement relationships for those bent cap designs from the elastic column model in the transverse and longitudinal directions, respectively. Moreover, Figure 9.29 shows the bent cap moment history at section B for the different cases.
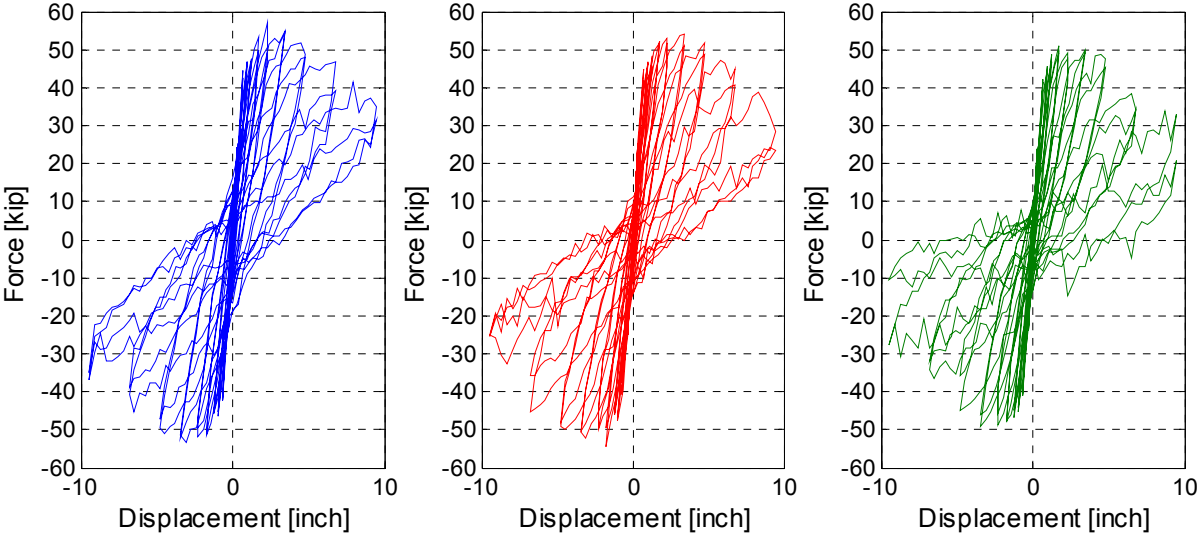
Figure 9.27 Force-displacement relationships in the transverse direction from the elastic column FE model for three bent cap cases: 8 #5 (left), 8 #4 (middle), and 8 #3 (right)
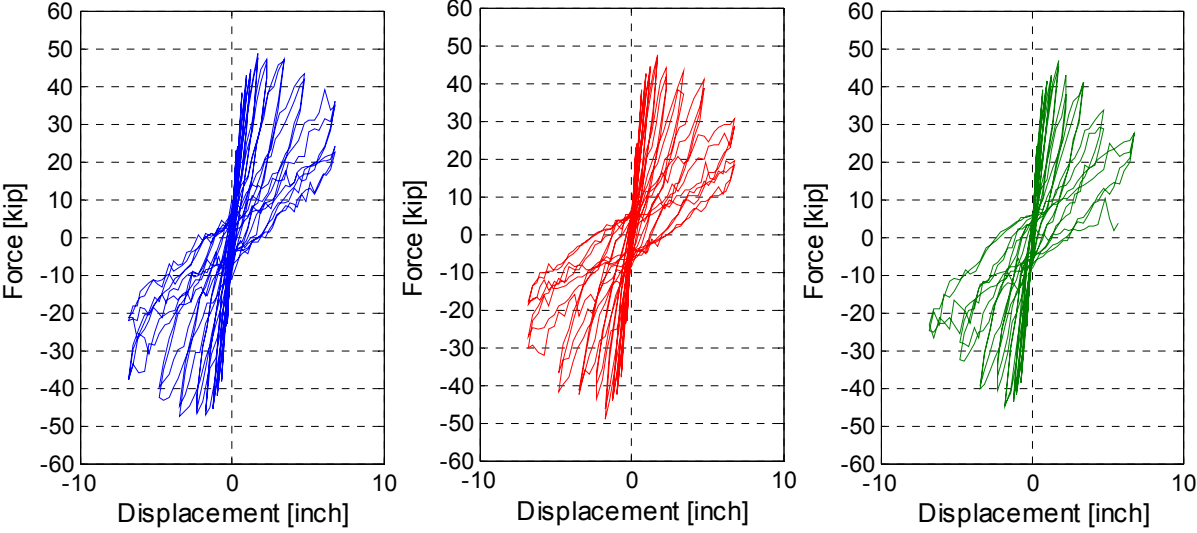
Figure 9.28 Force-displacement relationships in the longitudinal direction from the elastic column FE model for three bent cap cases: 8 #5 (left), 8 #4 (middle), and 8 #3 (right)
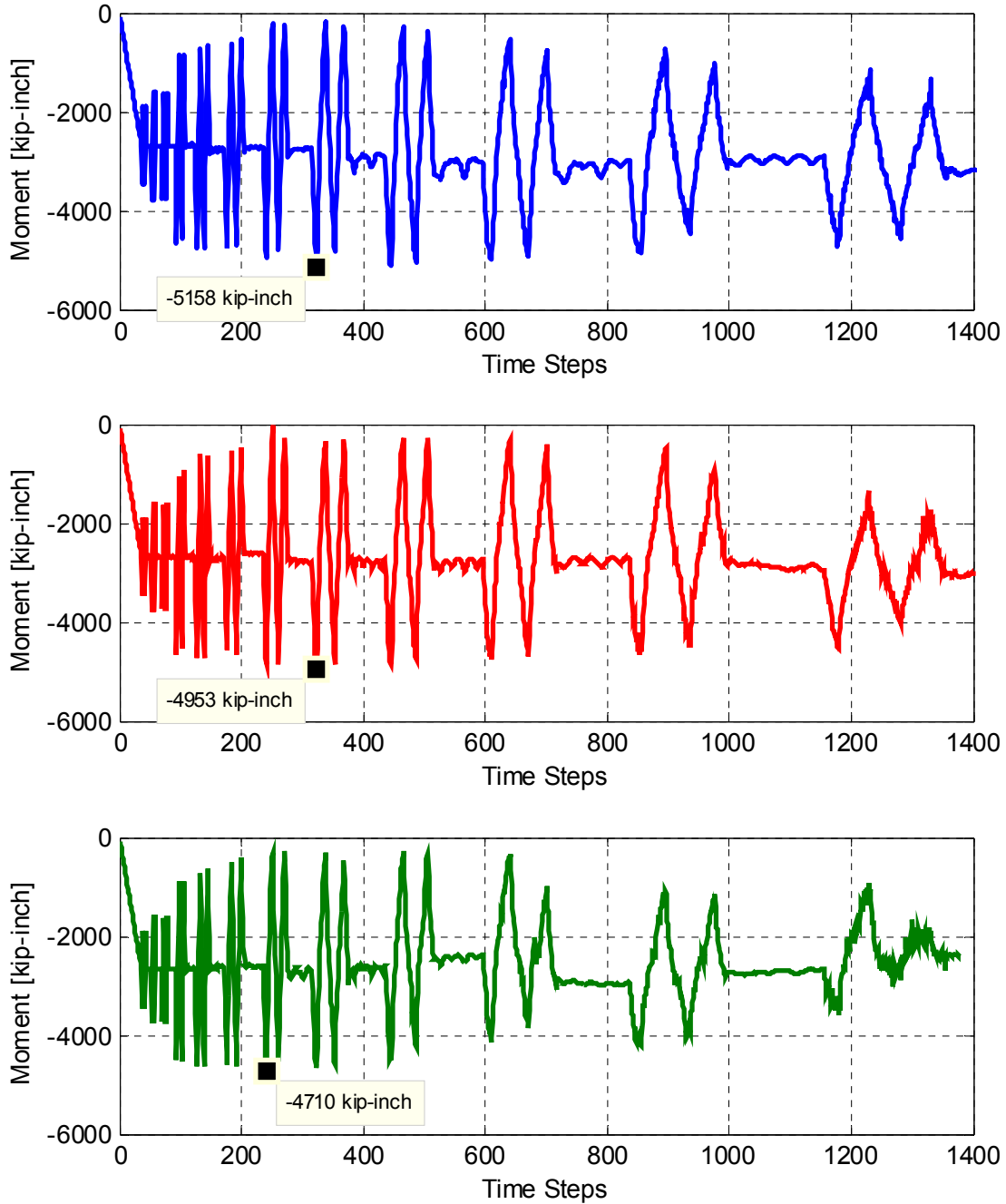
Figure 9.29 Bent cap beam moment history at section B from the elastic column FE model for three cases: 8 #5 top and bottom original design (top), 8 #4 top and bottom design 1 (middle), and 8 #3 top and bottom design 2 (bottom)

The figures show that the overall system capacity was slightly increased when the mode of failure is governed by the bent cap capacity rather than the column. The hysteresis behavior is also different from the ductile column hysteresis as previously discussed. The bent cap capacity, and the overall system capacity, in turn, was shown to vary as the cap beam design changed, which is expected. However, the surprising observation is that such variation in the capacity is considered minor with respect to the major change in the bent cap reinforcement. The cap beam

moment capacity, identified in Figure 9.29, was found to be 5158 kip-in., 4953 kip-in., and 4710 kip-in. for the case of 8 #5, 8 #4, and 8 #3 top and bottom bent cap reinforcement, respectively. These numbers indicate a maximum drop of 8.7% in the capacity versus an expected drop of almost 63% in the capacity if the standard Caltrans provisions are adopted for capacity estimation while excluding slab reinforcement. The details behind these numbers are discussed in the sectional analysis part in the next section. However, the main conclusion that can be drawn from this part of the FE analysis is that there is significant redundancy and force redistribution in the box-girder as the damage and failure of the bent cap progresses. Vertical and lateral pushover analyses were conducted as well to verify if the same conclusion still hold irrespective of the loading type.

9.2.3 Vertical Pushover Elastic Column

The model that used elastic concrete model for the column and the calibrated set of material properties for the superstructure inelastic constitutive total strain crack model was utilized with the three different bent cap designs to carry out a vertical pushover analysis. That is to determine the capacity of the bent cap beam and the whole bridge subassemblage. The vertical pushover in the given test specimen configuration acted upon both of the bent cap beam and the longitudinal box-girder. The vertical pushover curve for the three bent cap designs in addition to the developed bending moment at the bent cap at section B are shown in Figure 9.30 and Figure 9.31, respectively. The vertical force capacity of the whole system was determined in the three bent cap design cases. Only a slight difference in the capacity, which was reached as soon as the inelastic damage started, was observed at the beginning. However, as the pushover continued, the damage spread more and the less reinforcement in the bent cap, the more loss of capacity was observed. The moments in the cap beam in the three cases reached comparable peak value, which was again within 10% difference, before severe damage started.
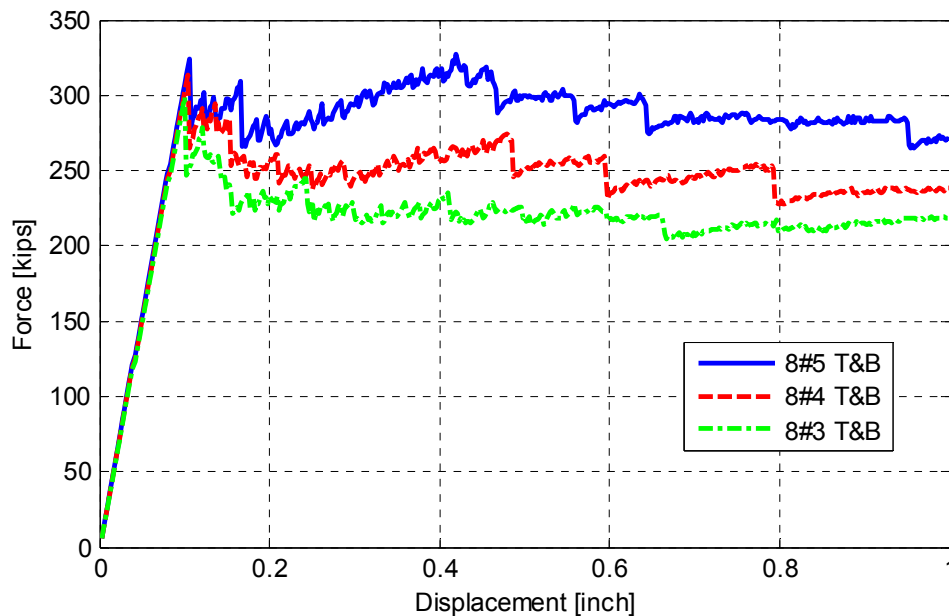
Figure 9.30 Vertical pushover force-displacement curve from the elastic column FE model for three bent cap cases: 8 #5, 8 #4, and 8 #3 top and bottom (T&B) reinforcement

366
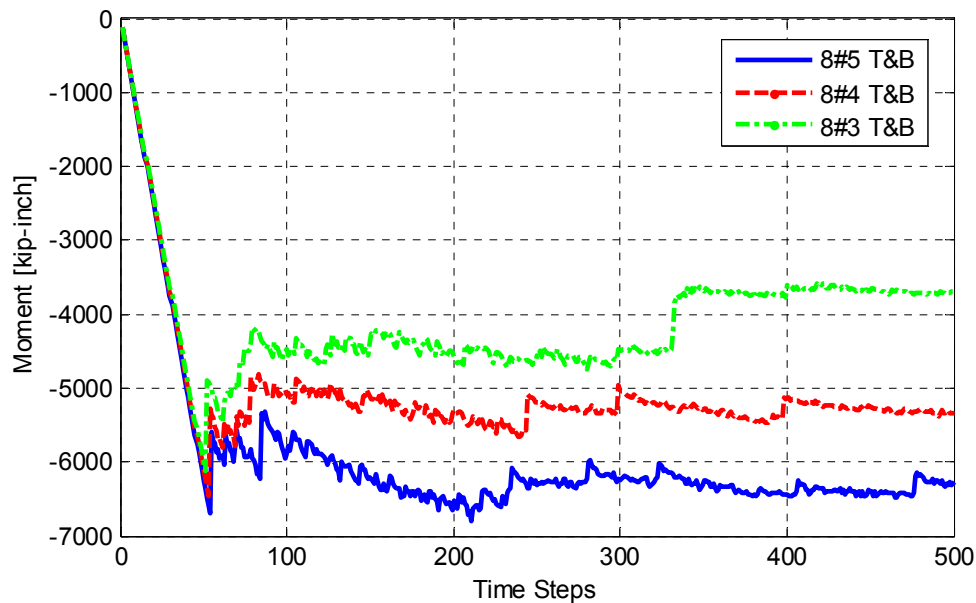
Figure 9.31 Bent cap beam moment history at section B due to vertical pushover for three bent cap cases: 8 #5, 8 #4, and 8 #3 top and bottom (T&B) reinforcement

The main conclusion from the vertical pushover analysis is the higher moment and system overall capacity that was observed relative to the cyclic loading case. For example, for the case of the original design of 8 #5 top and bottom reinforcement in the bent cap beam, a moment capacity of 5158 kip-inch was obtained from the cyclic loading versus a 6794 kip-inch from the vertical pushover. This can be explained in light of the resulting moment distribution along the bent cap due to the different cases of loading (Figure 5.52 in Chapter 5). In case of vertical pushover, the mode of failure is symmetric two plastic hinges in the two sections B and D simultaneously. However, the mode of failure due to lateral loading depends on the loading direction, and hence, only one plastic hinge at either section B or D is developed. The realistic moment distribution that considers the actual column and cap beam cross-sections suggests that the critical section where the plastic hinge develop is a larger cross-section, which involves partially the column contribution, when two plastic hinges are formed under vertical concentrated load. Therefore, a higher moment capacity was obtained from the vertical pushover. It is to be noted that the experimental value for the beam capacity from SP2 HS tests was reached as a result of the amplified moment demands from the column along with a 15% gravity load (240 kips). The high concentrated gravity load although was not enough to fail the bent cap, but suggests that the bent cap beam capacity and the box-girder contribution are significantly influenced by the gravity load.

9.2.4 Lateral Pushover Elastic Column

A lateral pushover analysis in the transverse direction only under constant gravity load was conducted for the three different bent cap designs using the same model previously utilized for the vertical pushover and cyclic loading. Figure 9.32 and Figure 9.33 show the lateral transverse pushover curves and the corresponding bent cap bending moments at section B, respectively. This analysis case emphasized the fact that although the column is elastic and the capacity is

dictated by the bent cap beam, yet close values for the moment capacity were obtained for the different bent cap designs. This implies again that there is a large force redistribution and redundancy because of the box-girder contribution.
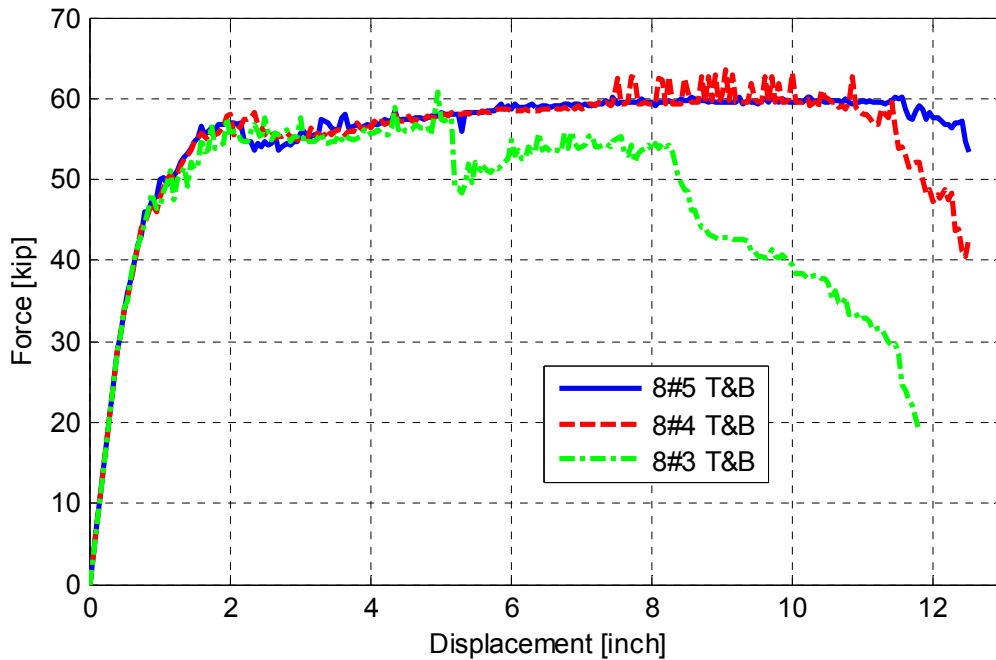
Figure 9.32 Lateral pushover force-displacement curve from the elastic column FE model for three bent cap cases: 8 #5, 8 #4, and 8 #3 top and bottom (T&B) reinforcement
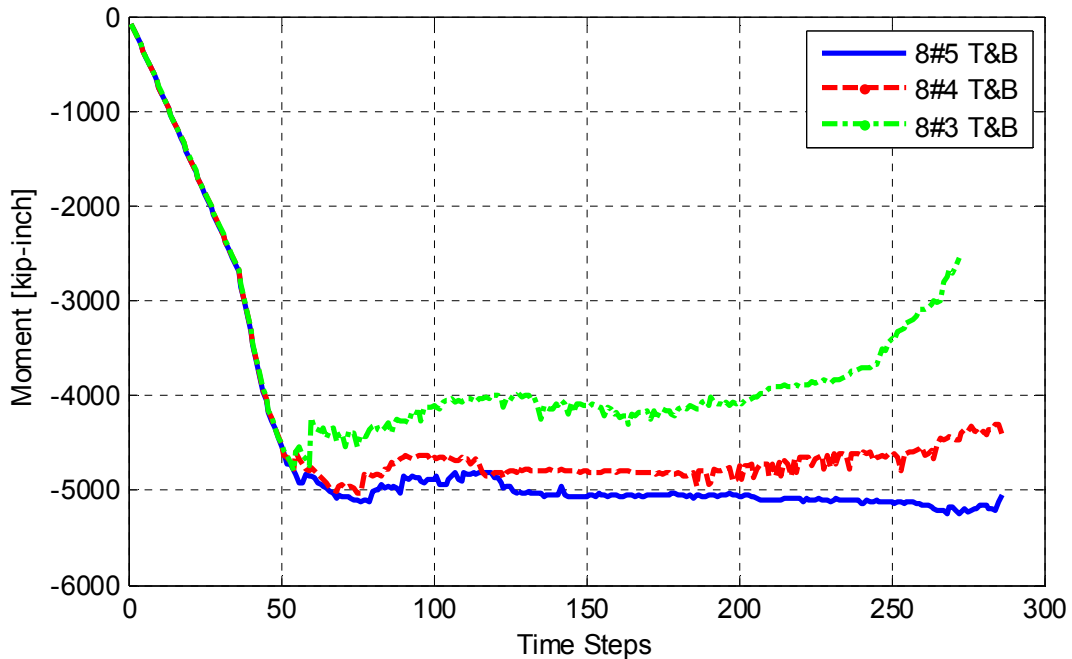
Figure 9.33 Bent cap beam moment history at section B due to lateral pushover for three bent cap cases: 8 #5, 8 #4, and 8 #3 top and bottom (T&B) reinforcement

9.2.5 Summary of Bent Cap Capacity

The previous subsections aimed at providing the overall system force-displacement relationships along with the developed moment in the bent cap beam. In this subsection, the cap beam moment capacity from the three designs for the different cases that involved elastic column along with the maximum observed moment from the fully nonlinear calibrated model are summarized and presented in Table 9-1. A better comparison of these numbers, i.e. the different values for the bent cap capacities, from different cases of loading can be achieved in light of the analytical estimation of the bent cap capacity using conventional sectional analysis. The next section focuses on such sectional analysis of the bent cap beam different designs.

Similar observations and conclusions as discussed in the previous subsections can be restated based on the values provided in Table 9-1. The maximum observed bent cap moments from both the as-built SP1 cyclic tests and the retrofitted SP2 HS tests are included in the table for comparison. It is to be noted that the moment values from the as-built SP1 were capped due to the reached column capacity, whereas the capped bent cap beam moments in the retrofitted SP2 were claimed to be the true bent cap capacity based on the observed damage. The capacity obtained from the FE analyses shows that the vertical pushover closely matched the experimental upper bound, which relates to the higher gravity load level (15%) used in the HS tests. It is noted from the table also that reducing the reinforcement from 8 #5 to 8 #4, i.e. 35% less reinforcement, was found to reduce the observed capacity by about 5% only for all cases of loading. Meanwhile, the reinforcement reduction from 8 #5 to 8 #3, i.e. 65% reduction, was accompanied by a reduction of only 10% in the observed capacity from the different loading cases. This indicates again that the box-girder contributes significantly to the overall system capacity and implies that large portion of the force and moment demand is redistributed to the box-girder even after cap beam extensive yielding or damage.

Table 9-1 Bent cap moment [kip-in] obtained from all cases of FE post-test analysis

Cap Beam Rft. (Top & Bottom)	Post-test FE Analysis				Experiments	
	Elastic Column			Calibrated Model	SP1 Cyclic Tests	SP2 HS Tests
	vertical pushover	lateral pushover	lateral cyclic			
8 #5	6794	5248	5158	4721	4770	6535
8 #4	6452	5031	4953	4720	-	-
8 #3	6120	4793	4710	4645	-	-

9.3 SECTIONAL ANALYSIS

Sectional analysis is instrumental for earthquake engineering, and particularly for capacity design or check of flexural members. A conventional sectional analysis for a beam in flexure aims at obtaining the moment-curvature relationship for the beam section to help identify key response metrics such as the yielding and the ultimate moment capacity. In bridge design, a moment-curvature analysis, or sectional analysis, is required for bent columns and cap beams for performing various design checks. The current Caltrans SDC (2013) and AASHTO guide specifications for LRFD seismic bridge design (2011) provisions require to calculate the integral bent cap beam capacity as part of the capacity check. This should be performed using the code-

defined expected material properties and considering an effective slab width of 12 times the slab thickness (t_s) for box-girder slab contribution without including any slab reinforcement.

The validity of using $12t_s$ for slab contribution without including the slab reinforcement has been challenged through this study. The experimental results suggest that $18t_s$ would better represent the equivalent strain block that reflects the slab contribution. Meanwhile, the experimental and FE post-test analysis results reflect that the Caltrans and AASHTO provisions underestimate the bent cap beam capacity. To investigate the accuracy of the effective slab width and the cap beam capacity, slab contributions of $12t_s$ and $18t_s$ with (w/) and without (w/o) slab tension reinforcement were used to determine the test specimen bent cap beam capacity. Figure 9.34 shows the integral bent cap beam cross-section used in the sectional analysis in three different cases of $12t_s$ w/ and w/o slab reinforcement and case of $18t_s$ w/ slab reinforcement. It is be noted that the sectional analysis should consider the expected material properties as defined by the Caltrans SDC. However, the actual determined material properties from the material tests, previously discussed in Chapter 3, have been used for better comparison with the experimentally determined capacity from SP2 HS tests.

$b_{beam} + 12t_s$ flange width (without slab reinforcement)

$b_{beam} + 12t_s$ flange width (with slab reinforcement)

$b_{beam} + 18t_s$ flange width (with slab reinforcement)
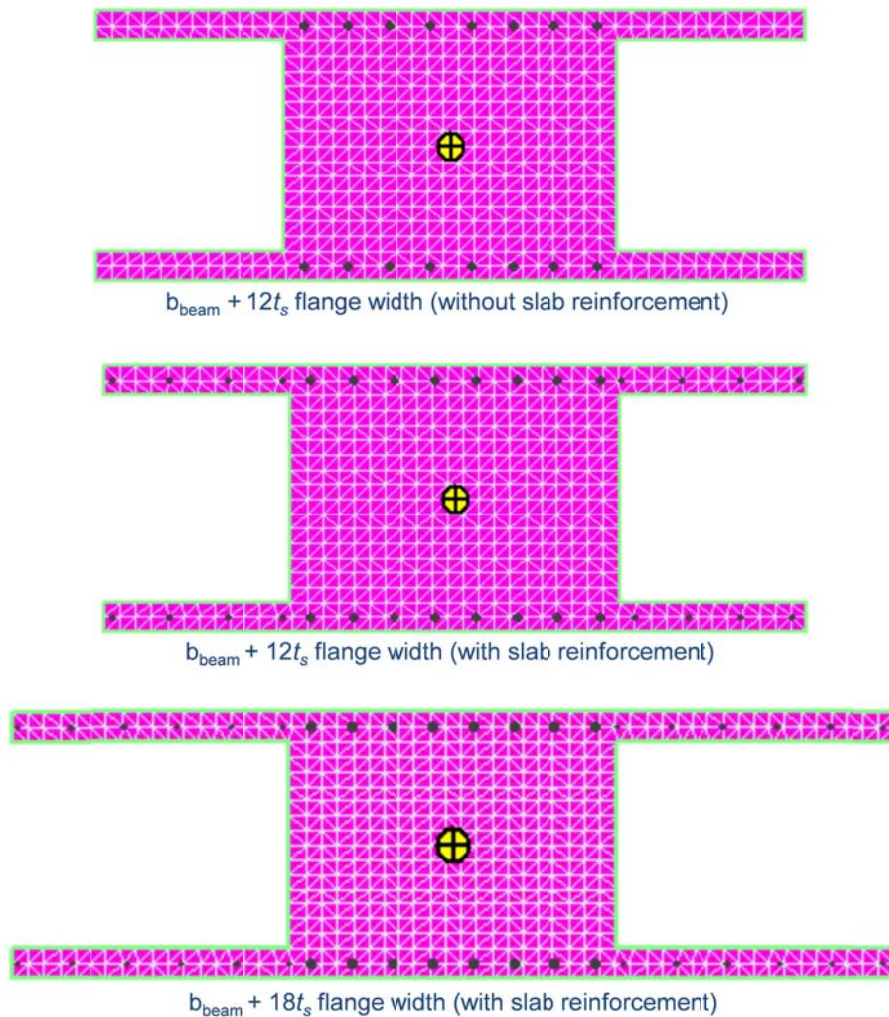
Figure 9.34 Schematic representation of three different cross-sections used to analyze the test specimen bent cap beam section

The computational program XTRACT (2002) was used for all the sectional analysis conducted in this study. Figure 9.35 shows a typical analysis results report along with the moment-curvature relationship (actual and idealized) for the case of the original bent cap design using the Caltrans provisions, i.e. $12t_s$ slab contribution without slab reinforcement. It is to be noted that the ultimate moment reported in the analysis is meant to be the moment value at the ultimate curvature reached. However, for the purpose of this study, the absolute ultimate moment was recorded for comparison reasons even if it was obtained before the ultimate curvature was reached. The moment-curvature relationship obtained for the three cross-sections defined in Figure 9.34 are shown in Figure 9.36. The figure shows that including the slab reinforcement within the defined effective slab width increases the capacity estimate significantly. To validate this observation at different reinforcement levels, the two hypothetical bent cap beam designs, previously used in the FE analyses and described in the previous section, were used to estimate their capacities using sectional analysis. Table 9-2 summarizes all the results of different designs and cases of slab contribution as obtained from the sectional analysis. The values from the experimental tests are included in this table for comparison. It should be noted the slab reinforcements in both compression and tension sides of the bent cap beam section were included in those cases of considering the slab reinforcement for simplicity, e.g. preserving symmetry. However, the effect of the compression steel, in general, whether from the cap beam itself or the adjacent slab reinforcement within the effective width, is minor on the capacity estimates. Thus, the notion of "slab reinforcement" in this discussion always implies the tension side reinforcement even when it is not mentioned explicitly.

Analysis Results:

Failing Material:	Steel1
Failure Strain:	.1000 Tension
Curvature at Initial Load:	0 1/in
Curvature at First Yield:	-.1424E-3 1/in
Ultimate Curvature:	-5.689E-3 1/in
Moment at First Yield:	-3008 kip-in
Ultimate Moment:	-4339 kip-in
Centroid Strain at Yield:	1.012E-3 Ten
Centroid Strain at Ultimate:	48.79E-3 Ten
N.A. at First Yield:	-7.108 in
N.A. at Ultimate:	-8.576 in
Energy per Length:	22.57 kips
Effective Yield Curvature:	.1765E-3 1/in
Effective Yield Moment:	3730 kip-in
Over Strength Factor:	-1.163
EI Effective:	2.11E+7 kip-in^2
Yield EI Effective:	110.6E+3 kip-in^2
Bilinear Harding Slope:	.5233 %
Curvature Ductility:	32.23
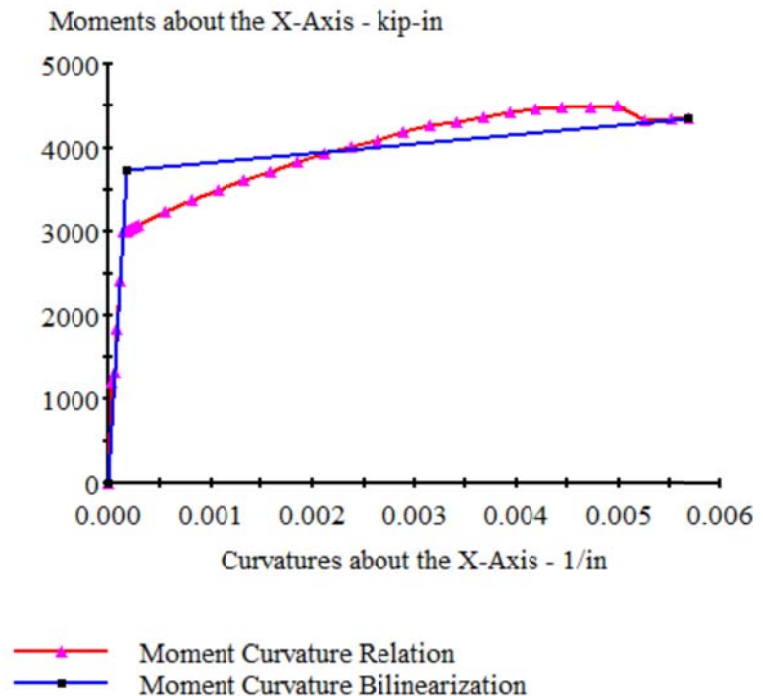
Figure 9.35 Typical moment-curvature analysis report obtained from XTRAXT for the test specimen bent cap using Caltrans provisions

371
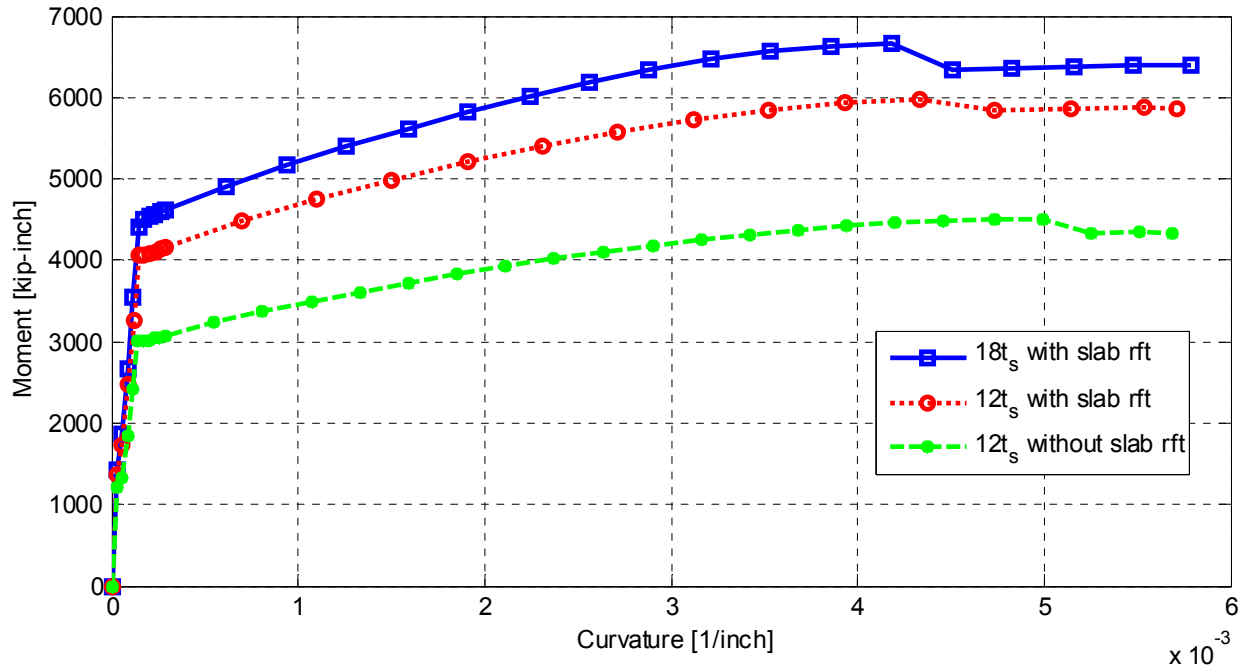
Figure 9.36 Moment-curvature relationships for postulated three different test specimen bent cap beam cross-sections as obtained from XTRACT sectional analysis results

Table 9-2 Summary of the bent cap moment capacity [kip-in] obtained from the sectional analysis

Cap beam top rft.	Cap beam bottom rft.	$12t_s$		$18t_s$		Experiments	
		w/o slab rft.	w/ slab rft.	w/o slab rft.	w/ slab rft.	SP1 Cyclic Tests	SP2 HS Tests
8 #5	8 #5	4504	5977	4566	6855	4770	6535
8 #4	8 #4	2945	4508	2965	5332	-	-
8 #3	8 #3	1667	3305	1676	4132	-	-

On one hand, it is noted that the observed reduction in the moment capacity from the FE analyses, as implied from Table 9-1, where the beam reinforcement was reduced is much less than that for the nominal flanged-section capacities from the section analyses (Table 9-2). For example, reducing the bent cap reinforcement from 8#5 to 8#3 led to approximately 9% reduction in the capacity from the FE analysis, whereas a 63% and 45% reduction was observed from the sectional analysis when a $12t_s$ slab contribution was used with and without slab reinforcement, respectively, compared to the case of $18t_s$ slab contribution with slab reinforcement. This better illustrates the previously drawn conclusion from the FE analyses that the box-girder contributes considerably to the system capacity and significant redundancy and force and moment demand redistributions take place as the cap beam yielding or damage progresses.

On the other hand, it is concluded from the sectional analysis results that neglecting the slab reinforcement underestimates the capacity. Meanwhile, considering $18t_s$ for the effective width led to the best match with the experimentally determined upper bound for the cap beam

moment from the HS tests. It is noted that the capacity reduction when using cap beam of 8 #3 instead of 8 #5 in this case becomes 40% compared to the 63% and 45% mentioned in the previous paragraph. A practical design problem is tackled next to investigate the design implications of considering the recommended $18t_s$ effective slab width along with including the slab reinforcement at a full-scale bridge level.

9.4   DESIGN IMPLICATIONS

The main objective of this study was to accurately quantify the box-girder slab contribution to the behavior of the integral bent cap beams in reinforced concrete box-girder bridges. That is to better estimate the cap beam strength and stiffness for seismic design and capacity checks purposes. The stiffness calculations of the bent cap rely primarily on what effective slab width to consider for the flanged I-section of the integral bent cap. However, the effective moment of inertia of the integral cap beam, and the corresponding initial stiffness estimate for the uncracked section, should not vary significantly if a $12t_s$ or $18t_s$ effective slab width is used. On the contrary, the strength calculations and capacity estimates were found to vary significantly based on two parameters: (1) the effective slab width and (2) the tension slab reinforcement inclusion within that effective slab width. Such conclusions were based on experimental and analytical evidences but only at the reduced-scale level of the tested column-supper structure subassembly as discussed throughout this entire study. Thus, it would be beneficial to extrapolate those conclusions to the full bridge scale to identify the design implications and potential design optimization of the integral bent cap beams.

The bent cap design of the original Caltrans Academy Bridge was revisited based on three different scenarios of the bent column design. For each scenario, the cap beam design, or more precisely the capacity check, was based on three cases. The first case is using the provisions of the current Caltrans SDC (2013) and AASHTO guide specifications for LRFD seismic design of bridges (2011), i.e. using an effective slab width of $12t_s$ without including the tension slab reinforcement. The second and third cases for the full scale bent cap design and capacity check are to include the tension slab reinforcement with $12t_s$ and $18t_s$ effective slab width, respectively. For all cases, the Caltrans SDC expected material properties for a 5000 psi characteristic concrete strength and Grade 60 reinforcing steel are used to resemble actual design conditions. The relevant design criteria and the different bent column design scenarios are presented in the first subsection. The bent cap beam capacity estimates in the three configurations described above is discussed in the second subsection. To conclude, the capacity check is performed and discussed in the third subsection,

9.4.1   Design Criteria

A typical bridge design would start with laying out the bridge spans to determine the bridge type and preliminary dimensions of different cross-sections. The next step is estimating the different loading actions primarily based on vertical gravity loads, i.e. dead loads and live traffic loads. Linear elastic analyses are then carried out to determine the different demands and finally perform LRFD design for the sections. Based on the bridge type, location, boundary and soil conditions, among other parameters, different design approaches might be undertaken to perform lateral design and checks. For the typical case considered in this study, which is a RC box-girder

bridge in California, performance-based approaches are typically used for seismic design and checks. In particular, for the case of the integral bent cap beam that is readily dimensioned and designed using LFRD, a capacity design check is required to guarantee that the bent cap beam remains essentially elastic during extreme seismic events. A weak column strong beam approach is used, which ties the cap beam capacity check directly to the bent column. The reader is referred to Chapter 3 for more details about the bridge seismic design philosophy. Moreover, the Academy Bridge design document (2006) provides supplementary details that are specific to the prototype used through this study.
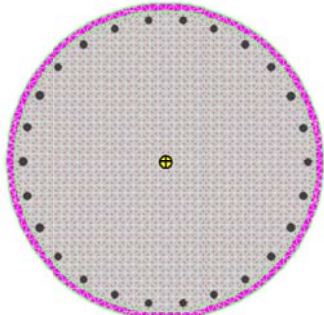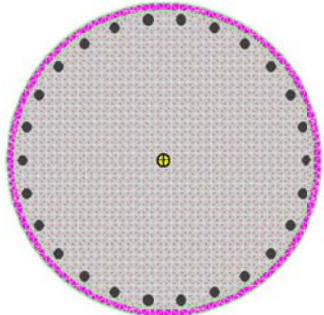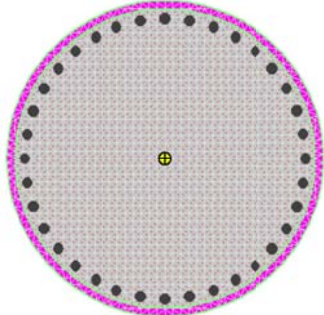
Three scenarios for the Academy Bridge column design are considered and the bent cap beam design is checked accordingly. All the necessary data has been adopted from the Academy Bridge design document (2008) and the relevant design information is briefly presented here for completeness. The typical practical method for designing the bent columns is to assume a longitudinal reinforcement ratio within the 1% to the 4% code limits, then perform all necessary design checks. The original Academy Bridge design involved a 6-ft diameter column with 1.44% reinforcement ratio, which satisfied all the design requirements and checks (design document 2006). To recognize possible scenarios that would require higher column reinforcement ratios, two additional designs that approximately used 2.6% and 3.5% column reinforcement ratios were used in this study. Sectional analyses were performed for all three column design scenarios and the column capacity was estimated based on the expected Caltrans material properties. A summary of the original column design and the two additional scenarios and relevant sectional analysis results are presented in Table 9-3.

Once the column design is completed and sectional analyses are used to compute the section capacity, the column overstrength is then estimated to use for the bent cap beam capacity check. The column overstrength is given as 1.2 times the ultimate plastic moment obtained from the sectional analysis. To calculate the moment demands in the bent cap beam based on the column overstrength moment, a nonlinear planer transverse pushover analysis is typically performed. The results from the 2D nonlinear model used for the bent frame as given by the Academy Bridge design document (2006) were used to estimate the bent cap beam moment demands. A schematic illustration of the model used for the transverse pushover analysis is shown in Figure 9.37. The estimated positive and negative bent cap beam moment demands are summarized in Table 9-3.

To perform the bent cap beam capacity check, the current Caltrans and AASHTO provisions, as mentioned before, require calculating the bent cap beam capacity based on a flanged section that includes a $12t_s$ effective slab width. The readily available design for the bent cap from the vertical load LRFD design is 24 #11 bottom reinforcement and 22 #11 top reinforcement, as given by the design document (2006). Additionally, the transverse slab reinforcement was required to calculate the bent cap capacity in the other two configurations, discussed before. The design document (2006) did not include any information on the transverse slab reinforcement since it is not involved in any seismic design checks. Therefore, the standard Caltrans design procedure for choosing the transverse slab reinforcement was adopted to determine the slab reinforcement. The current practice for deciding on RC box-girder soffit and deck slabs dimensions and reinforcement is using the design charts and tables provided by the Caltrans Memo to Designers 10-20 (2008). An excerpt for the relevant table required for determining the deck slab transverse reinforcement is shown in Figure 9.39 with the applicable data for the Academy Bridge identified. A similar procedure was followed to determine the soffit

slab reinforcement. The final Academy Bridge bent cap cross-section and slab reinforcement for the case of the $12t_s$ configuration is shown in Figure 9.38. Based on this complete data, the bent cap capacity was determined for the three selected configurations as discussed in the next subsection.

Table 9-3 Summary of the three column scenarios for Caltrans Academy Bridge

Column Cross Section			
Diameter	6 ft	6 ft	6 ft
Long. Rft.	26 #14	26 #18	36 #18
Rft. Ratio	1.44%	2.56%	3.53%
Hoops	#8 @ 5 in.	#8 @ 5 in.	#8 @ 5 in.
Ultimate Moment M_p [kip-ft]	14,510	21,140	26,200
Overstrength Moment M_o [kip-ft]	17,410	25,370	31,440
Cap Beam M_{+ve} Demand [kip-ft]	14,970	21,820	27,040
Cap Beam M_{-ve} Demand [kip-ft]	15,670	22,830	28,300

375
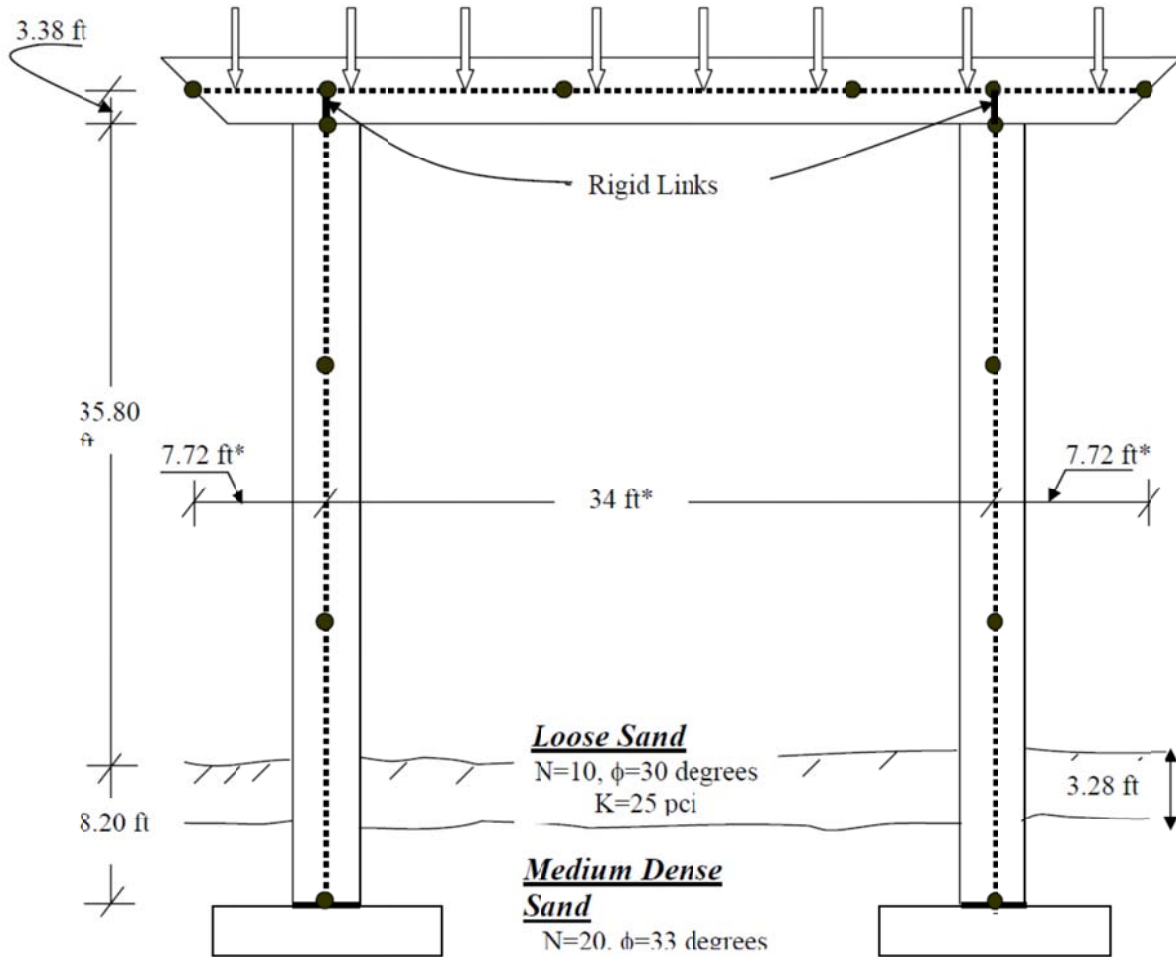
Figure 9.37 Transverse pushover analysis model for bent cap beam demand estimation for the capacity check (Academy Bridge LRFD design document, 2006
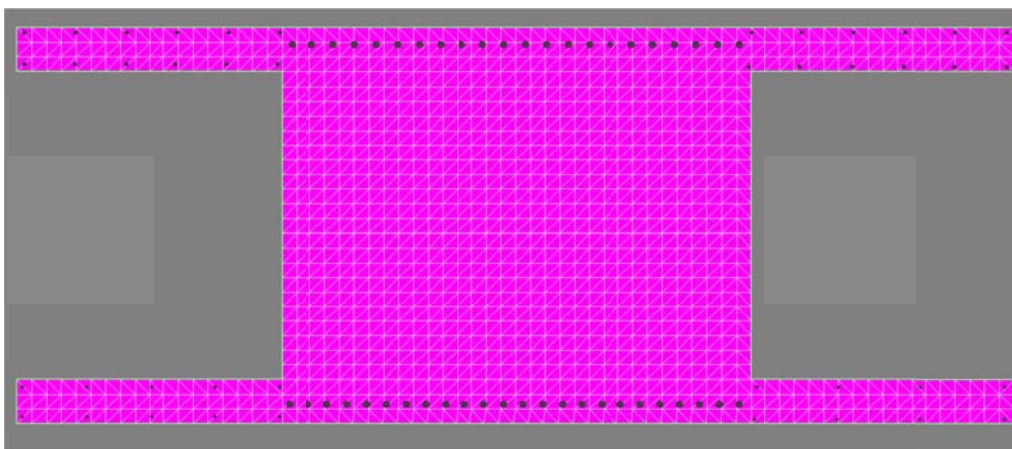
Figure 9.38 Typical bent cap cross-section of the full-scale Academy Bridge prototype for the case of $12t_s$ considered as the effective slab contribution and slab transverse reinforcement included in cap beam sectional analysis

Table 10-20.1(b) Deck Slab Thickness and Reinforcement Schedule

CIP PRESTRESSED BOX, PRECAST-I, & STEEL GIRDERS w/ flange width>=24"						
"S"	"t"	Dimension	Transverse Bars		"D" Bars	"G" Bars
Girder CL to CL Spacing	Top Slab Thickness	"F"	Size	Spacing [1]	#5 Bars	#4 Bars
4'- 0"	7"	5"	#5	12"	3	2
4'- 3"	7"	5"	#5	12"	3	2
4'- 6"	7"	6"	#5	12"	3	2
4'- 9"	7"	6"	#5	12"	3	2
5'- 0"	7"	6"	#5	12"	3	2
5'- 3"	7"	7"	#5	12"	3	2
5'- 6"	7"	7"	#5	12"	4	2
5'- 9"	7"	7"	#5	12"	4	3
6'- 0"	7"	8"	#5	12"	4	3
6'- 3"	7"	8"	#5	12"	4	3
6'- 6"	7 1/8"	9"	#5	12"	4	3
6'- 9"	7 1/8"	9"	#5	11"	5	3
7'- 0"	7 1/4"	9"	#5	11"	5	3
7'- 3"	7 3/8"	10"	#5	11"	5	3
7'- 6"	7 1/2"	10"	#5	11"	5	3
7'- 9"	7 1/2"	11"	#5	11"	5	3
8'- 0"	7 5/8"	11"	#5	11"	6	3
8'- 3"	7 3/4"	11"	#5	11"	6	3
8'- 6"	7 3/4"	1'- 0"	#5	11"	6	3
8'- 9"	7 7/8"	1'- 0"	#5	11"	6	4
9'- 0"	8"	1'- 1"	#5	11"	6	4
9'- 3"	8 1/8"	1'- 1"	#5	11"	7	4
9'- 6"	8 1/8"	1'- 1"	#5	11"	7	4
9'- 9"	8 1/4"	1'- 2"	#5	10"	8	4
10'- 0"	8 3/8"	1'- 2"	#5	10"	8	4
10'- 3"	8 3/8"	1'- 2"	#5	10"	8	4
10'- 6"	8 1/2"	1'- 3"	#5	10"	8	4
10'- 9"	8 5/8"	1'- 3"	#5	10"	8	4
11'- 0"	8 5/8"	1'- 4"	#6	11"	11	4
11'- 3"	8 3/4"	1'- 4"	#6	11"	11	4
11'- 6"	8 7/8"	1'- 4"	#6	11"	11	4
11'- 9"	8 7/8"	1'- 5"	#6	11"	12	5
12'- 0"	9"	1'- 5"	#6	11"	12	5
12'- 3"	9 1/8"	1'- 6"	#6	11"	12	5
12'- 6"	9 1/8"	1'- 6"	#6	11"	12	5
12'- 9"	9 1/4"	1'- 6"	#6	11"	12	5

Figure 9.39 Deck slab dimensioning and reinforcement design aid chart as excerpted from the Caltrans Memo to Designers 10-20 (2008)

9.4.2 Bent Cap Capacity

The necessary data to determine the bent cap capacity was properly acquired as discussed before. Three configurations or cross-sections were considered to investigate how the bent capacity can be accurately estimated and how the design can be optimized. The first configuration is using the provisions of Caltrans SDC, or similarly the AASHTO seismic LRFD specifications, i.e. using an effective slab width of $12t_s$ without including the tension slab reinforcement. The second and third configurations are considering the tension slab reinforcement within $12t_s$ and $18t_s$ effective

377

slab width, respectively. It should be noted that the double-column bent configuration of the Academy Bridge dictates positive and negative moment demands in the cap beam due to lateral loading. However, neither the top (22 #11) and bottom (24 #11) bent cap beam reinforcement nor the soffit (#5 @ 15 in.) and deck (#6 @ 11 in.) slab reinforcement are symmetric. Therefore, different capacities for positive and negative moments exist.

The conventional sectional analysis procedure using XTRAXT was adopted to determine the positive and negative bent cap beam capacities in the three different configurations previously mentioned. Figure 9.40 and Figure 9.41 show the moment-curvature relationships for different bent cap beam cross-sections (configurations) due to positive and negative moments, respectively. The positive and negative moment notion is defined here to avoid confusion. The negative moment is the moment that causes sagging in the cap beam and requires top reinforcement where tension is developed. On the contrary, the positive moment causes hogging in the cap beam and requires bottom reinforcement. Accordingly, the deck (top) slab reinforcement is the tension slab reinforcement for negative moment capacity, whereas the soffit (bottom) slab reinforcement is the tension reinforcement in case of positive moment capacity. Therefore, the positive moment capacity is slightly higher than the negative moment capacity when only the bent cap reinforcement is used in the capacity estimation (22 #11 for top versus 24 #11 for bottom), which can be observed from Figure 9.40 and Figure 9.41. However, the negative capacity exceeds the positive capacity when the slab reinforcement is included as observed from the same figures. The moment capacities determined from the section analyses were compared to the demands obtained from the transverse pushover analysis for the three column design scenarios to perform a capacity check as discussed next.
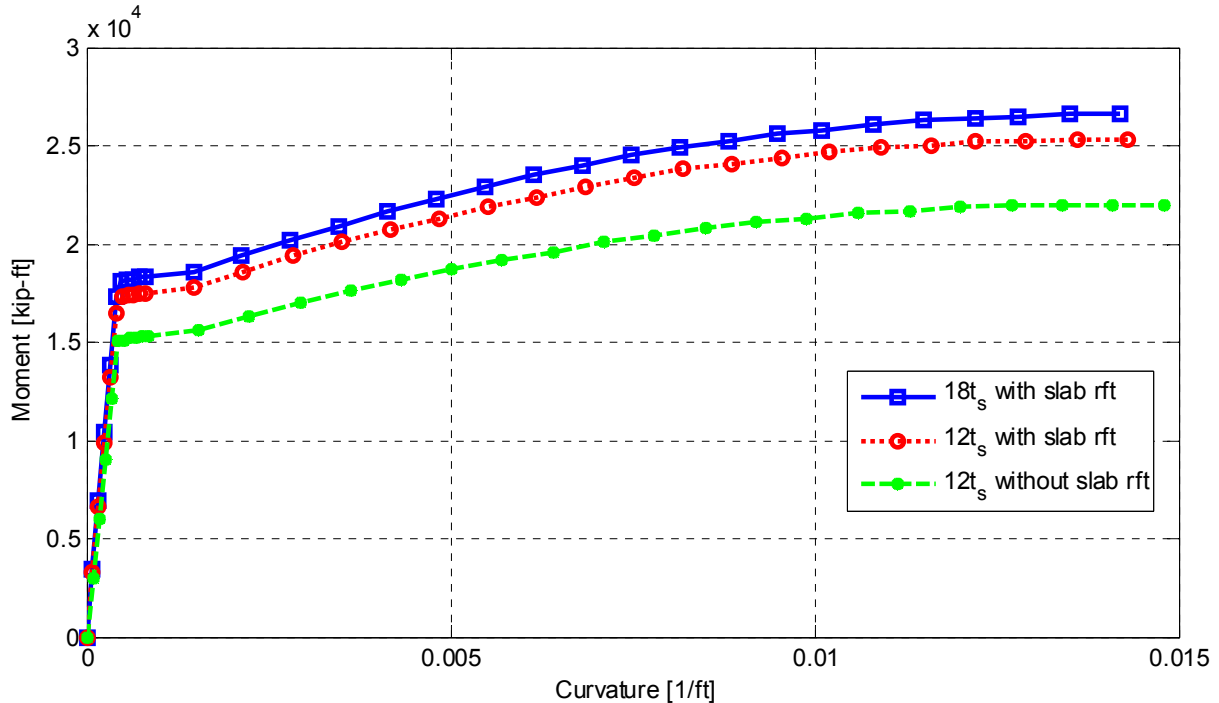
Figure 9.40 Moment-curvature relationships for positive moment demands for the full-scale Academy Bridge three different bent cap beam cross-sections as obtained from XTRACT sectional analysis results

378
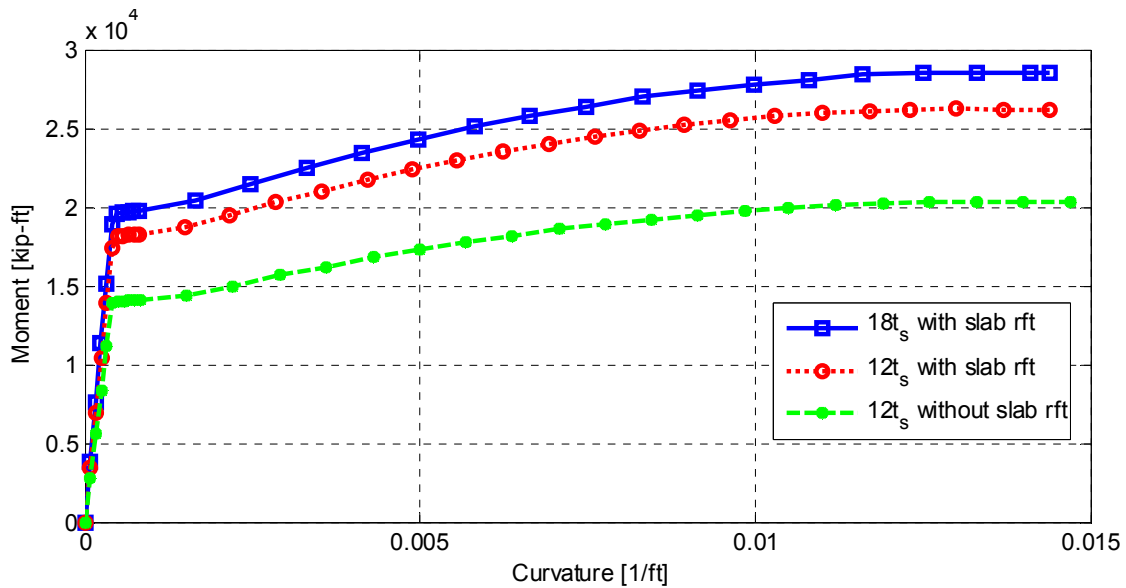
Figure 9.41 Moment-curvature relationships for negative moment demands for the full-scale Academy Bridge three different bent cap beam cross-sections as obtained from XTRACT sectional analysis results

9.4.3 Caltrans SDC Capacity Check

The seismic capacity check is required to avoid unfavorable mode of failure and guarantee that the superstructure, bent cap beam in this case, remains essentially elastic during extreme seismic events when the ductile bent columns reach their flexural capacities. The check is performed by comparing the demand, which is estimated from the pushover analysis based on columns overstrength moments rather than ultimate plastic moments, versus the capacity estimated for the given bent cap beam design. In this study, three different scenarios for the column design were pursued, whereas three different configurations for the capacity estimation were utilized. This resulted in a total of 18 combinations for the capacity check; nine for cases of positive demands and nine for cases of negative demands. The summary of the positive and negative demands in the three scenarios (column design cases) and the estimated capacities for the three different configurations along with the capacity check is shown in Table 9-4 and Table 9-5, respectively.

It is observed from the tables that there are cases where the seismic capacity check was not satisfied and a revised bent cap beam design was required. Accordingly, the bent cap beam reinforcement was increased until the obtained beam capacity satisfied the capacity check. The final revised design for the cases that required additional reinforcement along with the ratio of the needed increase in the reinforcement are summarized in Table 9-6 and Table 9-7 for cases of positive and negative demands, respectively. Additionally, Table 9-8 summarizes the overall increase in the reinforcement relative to the original design when positive and negative moment designs are combined. An assessment of the information in these tables reveals that neglecting the slab reinforcement did not require revised design only for the 1.5% column design scenario, but also required much higher reinforcement to satisfy the capacity checks for higher demands from 2.5% and 3.5% column design scenarios. Moreover, including the slab reinforcement, especially within the recommended $18t_s$ effective slab width from this study required the least design alteration and led to the most optimized bent cap beam design.

379

Table 9-4 Bent cap seismic capacity check for positive moment demands due to three design cases

Case	Column Design	Moment Demand [kip-ft]	12t_s no slab rft.		12t_s with slab rft.		18t_s with slab rft.	
			Capacity	Satisfy Capacity Check?	Capacity	Satisfy Capacity Check?	Capacity	Satisfy Capacity Check?
1	1.44%	14,970	21,990	YES	25,260	YES	26,590	YES
2	2.58%	21,820	21,990	YES	25,260	YES	26,590	YES
3	3.50%	27,040	21,990	NO	25,260	NO	26,590	NO

Table 9-5 Bent cap seismic capacity check for negative moment demands due to three design cases

Case	Column Design	Moment Demand [kip-ft]	12t_s no slab rft.		12t_s with slab rft.		18t_s with slab rft.	
			Capacity	Satisfy Capacity Check?	Capacity	Satisfy Capacity Check?	Capacity	Satisfy Capacity Check?
1	1.44%	15,670	20,270	YES	26,170	YES	28,460	YES
2	2.58%	22,830	20,270	NO	26,170	YES	28,460	YES
3	3.50%	28,300	20,270	NO	26,170	NO	28,460	YES

Table 9-6 Revised bent cap design and capacity check for positive moment demands resulting from the three different column design cases

Case		1	2	3
Column Design		1.44%	2.58%	3.50%
Moment Demand [kip-ft]		14,970	21,820	27,040
12t_s no slab rft.	Original Design	24 #11	24 #11	24 #11
	Original Capacity	21,990	21,990	21,990
	New Design	no change	no change	32#11
	New Capacity	no change	no change	28,790
	Increase in Rft. [%]	0	0	33.3
12t_s with slab rft.	Original Design	24 #11	24 #11	24 #11
	Original Capacity	25,260	25,260	25,260
	New Design	no change	no change	26 #11
	New Capacity	no change	no change	27,100
	Increase in Rft. [%]	0	0	8.3
18t_s with slab rft.	Original Design	24 #11	24 #11	24 #11
	Original Capacity	26,590	26,590	26,590
	New Design	no change	no change	26 #11
	New Capacity	no change	no change	28,680
	Increase in Rft. [%]	0	0	8.3

Table 9-7 Revised bent cap design and capacity check for negative moment demands resulting from the three different column design cases

Case		1	2	3
Column Design		1.44%	2.58%	3.50%
Moment Demand [kip-ft]		15,670	22,830	28,300
12t_s no slab rft.	**Original Design**	22 #11	22 #11	22 #11
	Original Capacity	20,270	20,270	20,270
	New Design	no change	24 #11	32 #11
	New Capacity	no change	22,050	28,790
	Increase in Rft. [%]	**0**	**9.1**	**45.5**
12t_s with slab rft.	**Original Design**	22 #11	22 #11	22 #11
	Original Capacity	26,170	26,170	26,170
	New Design	no change	no change	26 #11
	New Capacity	no change	no change	29,740
	Increase in Rft. [%]	**0**	**0**	**8.3**
18t_s with slab rft.	**Original Design**	22 #11	22 #11	22 #11
	Original Capacity	28,460	28,460	28,460
	New Design	no change	no change	no change
	New Capacity	no change	no change	no change
	Increase in Rft. [%]	**0**	**0**	**0**

Table 9-8 Summary of additional bent cap reinforcement required to satisfy the seismic capacity check for three different column design cases

Case		1	2	3
Column Design (long. rft. ratio) [%]		1.44	2.58	3.50
12t_s no slab rft.	Increase in Bottom rft. [%]	0.00	9.10	33.30
	Increase in Top rft. [%]	0.00	0.00	45.50
	Total Increase in rft. [%]	**0.00**	**4.55**	**39.40**
12t_s with slab rft.	Increase in Bottom rft. [%]	0.00	0.00	8.30
	Increase in Top rft. [%]	0.00	0.00	8.30
	Total Increase in rft. [%]	**0.00**	**0.00**	**8.30**
18t_s with slab rft.	Increase in Bottom rft. [%]	0.00	0.00	8.30
	Increase in Top rft. [%]	0.00	0.00	0.00
	Total Increase in rft. [%]	**0.00**	**0.00**	**4.15**

10 Conclusions and Future Extensions

10.1 SUMMARY

The study completed in this dissertation comprised computational and experimental frameworks to investigate the structural behavior and seismic response of bent cap beams in as-built and retrofitted RC box-girder bridges under the combined effect of vertical and lateral loading. In particular, the contribution of the box-girder slabs to the stiffness and strength of the integral bent caps was evaluated for optimized design and enhanced capacity estimation. Four main contributions are highlighted from this study: (a) Revisiting the effective slab width for integral bent caps in RC box-girder bridges; (b) Investigating the effectiveness of CFRP column retrofit in enhancing column capacity in light of the consequent amplified demands on bent cap and the resulting subassembly performance; (c) Developing and successfully conducting multi-DOF Hybrid Simulation (HS) test using a new practical approach for HS communication; and (d) Calibrating a detailed FE model and utilizing it for investigating the influence of box-girder contribution for several hypothetical cases of higher levels of bent cap damage when the bent cap beam reinforcement is reduced.

The computational part of the study consisted of two phases: pre-test and post-test analysis. On the other hand, the experimental program involved testing two 1/4 scale column-bent cap beam-box girder subassembly using quasi-static and HS testing methods. The test specimens were adopted from a prototype that was slightly modified from the Caltrans Academy Bridge, and were designed in light of the most recent AASHTO and Caltrans SDC provisions. An overview of the different parts of the study is summarized in the following paragraphs.

The problem of the effective slab width was tackled in many studies, mainly in buildings framing systems where flanged floor beams are very common. A survey of the available literature was pursued to better understand the research problem before embarking on the computational and experimental programs. The first phase of the computational framework, i.e. the pre-test analysis phase, utilized 1D, 2D, and 3D FE models, which were developed and used to carry out different types of analyses that varied from linear elastic static analysis to nonlinear time history analysis. Different models were developed for both of the full prototype bridge and the test specimen using OpenSees, SAP2000, and DIANA FE packages. The pre-test analysis successfully verified the expected subassembly behavior, provided the input for the final gravity load levels and lateral loading protocol, delivered the expected loads and straining actions for test setup design, and provided necessary information for instrumentation distribution.

The pre-test analysis was then followed by the experimental program that comprised the core of the study. The first stage of the experimental program involved quasi-static cyclic loading tests of the first specimen (SP1) in as-built and repaired conditions. Bidirectional cyclic

loading tests in both transverse and longitudinal directions were conducted under constant gravity load. A rapid repair scheme was adopted for the tested specimen using a three-layer CFRP column jacket. The partial repair aimed at providing at least minimal capacity for the specimen to be reused for the HS development and trial runs. However, a quasi-static cyclic test similar to the one applied to the as-built specimen was carried out for the repaired specimen for comparison purposes and to verify the essentially elastic status of the bent cap beam.

The second stage of the experimental program embraced the HS testing technique for providing realistic dynamic response input to the test specimens as the lateral loading. A new practical approach that utilized readily available laboratory data acquisition systems as a middleware for feasible HS communication was achieved. The proper communication among the HS components and the verification of the HS system were first performed using test runs conducted on standalone hydraulic actuators, i.e. they were not attached to any physical specimens. Next, the same first specimen SP1 that was tested as-built, then was repaired and retested in quasi-static cyclic tests, was utilized one last time to carry out actual HS trial tests. All the HS trials were successful, which verified the robustness of the developed HS system. The column of the second specimen SP2 was retrofitted using CFRP jacketing before any testing to increase the demands on the bent cap beam. The retrofitted SP2 was then tested using multi-degree of freedom HS under constant gravity load and using unidirectional and bidirectional near-fault ground motions in several intensity levels and polarity.

The post-test analysis was the final stage of the study. The results from the as-built first specimen cyclic tests were used to calibrate the most detailed 3D FE model, which was previously developed as part of the pre-test analysis stage. The calibrated model was used to explore the effect of reducing the bent cap reinforcement on the overall system behavior and to investigate how the box-girder contributes at higher levels of bent cap damage. The design implications of the main outcome from all of the different analyses and experiments concluded this study. A short illustrative design example was carried out to investigate the implications of the revisited effective slab width and bent cap capacity estimation on the optimization of the bent cap design for a full-scale bridge.

10.2 CONCLUSIONS

Several conclusions were drawn from this study as follows:

- The preliminary prototype bridge triaxial time history analysis showed that the inclusion of the vertical excitation component can lead to unfavorable damage or failure in the bent cap beams. A large number of near fault ground motions was used to run time history analysis on the modified Academy Bridge prototype with and without the vertical excitation component. Six out of 88 considered ground motions led to excessive curvature values, i.e. plastic hinge damage, at different locations of the bent cap beam only when the vertical excitation was included. These six ground motions were concluded to cause highest demands in the bent cap independently from the column capacity due to the vertical excitations. This observation violates the fundamental design principle of strong beam-weak column capacity design concept required by the Caltrans SDC and AASHTO seismic design guidelines and calls for further investigation.

- The most detailed and accurate 3D DIANA model for the test specimen successfully predicted the subassembly behavior and mode of failure. A lateral force capacity was determined from the DIANA nonlinear pushover analysis to be almost 45 kips, which is only within 5% difference from the 47.5 kips experimentally determined capacity. Different modes of failures were observed from the 3D DIANA model under different gravity load levels combined with the lateral pushover. At the 10% gravity load level, which was used in the large level cyclic loading tests, the predicted mode of failure from the analysis matched the experimentally observed failure mode of column plastic hinging. The detailed DIANA model was further calibrated and used in post-test analysis.

- The observed as-built SP1 behavior satisfied all the Caltrans SDC design objectives. The mode of failure was a fully developed plastic hinge in the subassembly column whereas the bent cap beam and superstructure remained essentially elastic. The bridge system performed well up to high performance levels that exceeded the minimum required performance levels set by Caltrans SDC. The bridge subassembly, and particularly its ductile column, successfully achieved a 7.6 ductility level, which corresponds to a 10.5% drift ratio, in the transverse direction. However, a 5.4 ductility level that corresponds to 7.5% drift ratio was achieved in the longitudinal direction. The buckled column rebars started to rupture at the 5.4 ductility level loading in the longitudinal direction leading to capacity loss. The 5.4 ductility level was still superior to the minimum displacement ductility of 4.0 required by Caltrans SDC.

- The bridge subassembly tests showed slightly different stiffness in the transverse and the longitudinal directions. This is attributed to the slightly more flexible column-box girder connection relative to the column-bent cap connection. The slightly higher transverse stiffness observation was more pronounced in the as-built SP1 tests in comparison with the retrofitted SP2 tests. The reason is that the stiffness in the longitudinal direction is sensitive to the soffit and deck slab thicknesses, which govern the box-girder overall stiffness. Therefore, due to construction imperfections, the stiffness can vary as observed from the two specimens. In addition, SP1 stiffness degradation in both transverse and longitudinal directions was monitored and related to the different ductility levels and drift ratios. Only SP1 was considered in that regard as it experienced the desired column mode of failure as required by code provisions. At 7.56 ductility level, the transverse stiffness was about 13% of its initial value, while a longitudinal stiffness of almost 10% of the initial value was observed at 5.40 ductility level, i.e. the specimen lost close to 90% of its initial stiffness at the final damaged state.

- The rapid CFRP repair technique successfully achieved its objective of partially restoring SP1 test subassembly capacity and significantly increased the stiffness in both transverse and longitudinal directions. To quantify the repair effectiveness, a maximum increase of 25% in the capacity was obtained due to the repair relative to the residual capacity after all column rebars buckled and six of them ruptured. Moreover, an increase of more than 300% was achieved in the stiffness from the final damaged state because of the repair. It is to be noted that regardless of the significant increase in the stiffness, yet the original initial stiffness and strength were not fully achieved. It is also noted that the injection of the cracks prior to the application of the CFRP was the main contributor to this increase of the stiffness, not the CFRP jacket itself.

384

- The retrofit CFRP technique was effective in increasing SP2 column capacity due to the enhanced confinement. It was observed that the force capacity of the whole subassembly and the moment capacity of the column increased significantly in SP2 compared to SP1 by almost 25%. The jacket confinement prevented any concrete spalling or bar buckling or rupture, which is important for post-earthquake bridge resiliency as it minimizes the down time for any column repairs. From a research perspective, the retrofit scheme also achieved its intended objective of increasing the demands on the bent cap beam and delaying, or preventing, the column failure to investigate bent cap beam mechanism in order to better estimate the bent cap capacity. Consequently, the amplified moment demands from the higher gravity level and retrofitted column led SP2 bent cap moment to cap at about 6500 kip-inch versus a maximum value of approximately 4500 kip-inch in SP1 cyclic tests.

- The bent cap beam experienced yielding through the as-built SP1 tests but remained essentially elastic. The essentially elastic state was confirmed by visual evidences that no extensive cracking took place at the tension side nor concrete crushing occurred in the compression side. In addition, the bent cap beam behaved linearly elastic when the subassembly was repaired and retested. A more accurate value for the yield moment of the bent cap beam was determined accordingly. The yield moment rendered the recommended Caltrans SDC and AASHTO bent cap beam flanged section conservative in terms of the effective slab width contribution.

- The onset of the bent cap beam damage and its moment capacity were captured through the retrofitted SP2 HS tests. The overall system force capacity and the bent cap beam moment were both capped and reached a steady state regardless of the amplified HS test scales. The visual evidence from SP2 observed damage, i.e. concrete crushing in the bent cap compression side and only uniform flexural crack pattern in the column underneath the CFRP jacket, suggested that the capacity reached was dictated by the bent cap capacity. The moment cap value of almost 6500 kip-inch was justified to be a reasonable experimental estimate of the bent cap beam capacity. On the other hand, it was shown from the sectional analysis that was based on the Caltrans SDC provisions and actual material properties that the bent cap beam capacity is only around 5000 kip-inch. Consequently, the Caltrans, and similarly the AASHTO, provisions were found to underestimate the bent cap capacity as was shown for the yield moment from SP1 as well.

- A simple procedure was devised to experimentally determine the bent cap beam effective slab width using the equivalent strain block concept from SP1 cyclic tests and SP2 HS tests. Two strain values from the different reinforcing steel bars in the bent cap were used for the equivalent strain block. These were the minimum and the mean of six instrumented bars at a given cross-section. Consequently, the effective slab width was evaluated for all SP1 and SP2 test runs and for different sections, mainly in the tension side. The results from the compression side were not conclusive because the strain measurements were sensitive to the concentrated gravity load. The results for the effective slab width, obtained from the tension side, rendered the $12t_s$ Caltrans SDC and AASHTO code value for effective slab width unnecessarily conservative. The overall mean value for the effective width as determined from all the as-built SP1 cyclic lading tests was $13.7t_s$ and $21.2t_s$ when the cap beam mean and minimum strain values were used, respectively. Smaller estimates for the effective slab width were obtained from SP2 HS tests. These were $11.5t_s$ and $15.8t_s$ when the cap beam mean and minimum strain values were used, respectively. Thus, the original $12t_s$ code value

was supplemented by a proposed revised value of $18t_s$ for investigating the bent cap beam capacity estimation and design implications. The basis for choosing the $18t_s$ value for the effective slab width is that it reasonably resembled the mean of the $21.2t_s$ and $15.8t_s$ upper bounds from the experiments, whereas the original $12t_s$ resembled the mean of the $13.7t_s$ and $11.5t_s$ lower bounds.

- A practical HS system that utilizes readily available laboratory data acquisition systems along with inexpensive TCP/IP-Ethernet connections to establish the communication between the physical and computational substructures was successfully developed, verified, and utilized in SP2 HS tests. The main development included augmenting the Pacific Instruments data acquisition with a new interface to communicate with OpenFresco from the computational side and the Digital Signal Processing (DSP) card from the experimental side. The new interface utilized an inexpensive Ethernet connection to replace expensive shared memory communication cards, such as SCRAMNet, for communicating with the computational side. Moreover, a DSP algorithm complemented the new interface to control the laboratory hardware and receive the physical substructure feedback. A new test setup component in OpenFresco was successfully developed as well to perform geometric transformations between the global DOF in the computational model and the actuators local DOF for command displacements and force feedback measurements. The HS test trials using the hydraulic actuators solely and the full repaired SP1 successfully validated the new communication interface and the OpenFresco geometric transformation new experimental setup object. Accordingly, the validation tests provided confidence on the robustness of the HS system to be used for SP2 tests.

- The most detailed DIANA 3D FE model for the test specimen was calibrated against the as-built SP1 cyclic test results. The calibrated model successfully captures the global behavior of the subassemblage and the bending moments that were developed in the bent cap beam within 5% difference. The sensitivity of the global behavior observed from the FE analysis was investigated under different model and constitutive material input parameters as part of the FE model calibration. It was concluded that using two different sets of material model parameters for the column and the superstructure, that reflect the natural material properties in the different concrete lifts used in construction, led to the best match with the experimental results. Thus, it is recommended for better analysis practices to use different material properties for the bridge bent component, if needed, to reflect actual conditions, especially for capacity checks and nonlinear analysis.

- FE analysis using the calibrated set of material parameters determined the cap beam capacity from the original test specimen design in addition to two hypothetical designs with less reinforcement than what the original design required. The capacity obtained from the vertical pushover closely matched the experimental upper bound, which is related in part to the higher gravity load level (15%) used in the HS tests where the cap beam reached its capacity. Moreover, the results from the hypothetically reduced-reinforcement bent cap designs revealed that only a slight reduction, which is not proportional to the reinforcement reduction, was observed in the system and the cap beam capacity. This indicates that the box-girder contributes significantly to the overall system capacity and implies that large portion of the force and moment demand is redistributed to the box-girder after the cap beam extensive yielding or damage.

386

- The underestimated yield moment and ultimate moment capacity from the code-based sectional analysis relative to the experimentally observed value was claimed to be a consequence of excluding the tension-side slab reinforcement, and conservatively using only a $12t_s$ effective slab width as well. Therefore, different configurations for the integral bent cap required for capacity estimation, that involved including or excluding the tension-side slab reinforcement within $12t_s$ or $18t_s$, were studied for different bent cap designs through sectional analysis. It was concluded that excluding the slab reinforcement underestimates the bent cap beam capacity significantly. Moreover, the best match with the experimentally observed value for the cap beam capacity from SP2 HS tests was achieved from the sectional analysis that considered flanged section with slab reinforcement and $18t_s$ effective slab contribution. Consequently, it is recommended to include the transverse deck and soffit slab tension reinforcement within a revised $18t_s$ effective slab width in the bent cap yield and capacity moment estimation.

- The design implications of the above recommendation of including the slab reinforcement within $18t_s$ effective slab width for capacity estimation of bent caps were explored at full bridge level. The design of the full-scale bent cap of the Caltrans Academy Bridge was checked in three different column design scenarios that corresponded to approximately 1.5%, 2.5%, and 3.5% longitudinal column reinforcement. A seismic capacity check was performed in light of Caltrans SDC provisions using different moment demands from the three scenarios and considering different bent cap beam configurations of a $12t_s$ and $18t_s$ effective slab width with and without slab reinforcement. It was concluded that neglecting the slab reinforcement did not require revised design only for the 1.5% column design scenario, but also required much higher reinforcement to satisfy the capacity checks for higher demands from 2.5% and 3.5% column design scenarios. Meanwhile, including the slab reinforcement within the revised $18t_s$ effective slab width proposed by this study, required the least design alteration and led to the most optimized bent cap beam design.

- The design implications previously shown are valid in all the cases where higher column demands require revising the bent cap design to satisfy the seismic capacity check. An important application of the recommended bent cap capacity estimation procedure is pronounced in undertaking older bridges retrofitting for resiliency. A typical retrofit scheme which aims at strengthening the column, as pursued in this study, amplifies the moment demands on the cap beam, i.e. the consequences of the 3.5% column design showed in the design implications can be reproduced from a less reinforced column that is efficiently retrofitted. Ignoring a check of the bent cap capacity against the new retrofitted column capacity could lead to an undesirable mode of failure that is migrated to the bent cap because of the amplified demands, especially in cases of overdesigned retrofit. Accurate estimation of bent cap capacity is necessary in this case to guarantee that it remains essentially elastic in case of extreme events. A different retrofit design might be needed as well if the accurately-estimated bent cap capacity falls short behind the retrofitted column overstrength moment. Therefore, it can be stated that the accuracy of the bent cap capacity estimation can lead to optimized reinforcement in case of new bridge designs, and informed retrofit decisions in case of older existing bridges.

- The main conclusions and design implications based on this study can be restated again in a form of design guidelines and possible code amendments as follows:

- The $12t_s$ code value for effective slab width is unnecessarily conservative. A revised value of $18t_s$ is recommended for accurate account of box-girder soffit and deck slab contributions to the integral bent cap stiffness and strength;

- Transverse deck and soffit slab tension reinforcement within an effective slab width, that is similar to the revised $18t_s$, should be included in the bent cap capacity estimation;

- The box-girder slab contribution should be carefully and accurately considered in the seismic design capacity check to avoid unnecessary use of bent cap reinforcement beyond what is required to satisfy the LRFD design for gravity loads;

- Accurate bent cap capacity estimate should be an integral part of the repair and retrofit designs for resilient infrastructure to avoid undesirable failure modes, leading to prolonged downtime, and uneconomical post-event repair in case of extreme events. This is particularly critical for older bridges that were not designed using the strong-beam weak-column capacity approach, i.e. the cap beam capacity is not necessarily higher than the column capacity. In such cases, an overdesigned column repair or retrofit might migrate the damage to the superstructure and a retrofit of the bent cap or superstructure might be required. Thus, the capacity design check is recommended for repair and retrofit decisions of older bridges as well as an existing condition assessment.

10.3 FUTURE WORK

Several research topics that are appropriate for future investigations can be extended from this the study. The following are relevant possible topics:

- Analytical investigation of the different parameters that could affect the bent cap beam behavior and the box-girder slab contribution at the full bridge level. The set of the calibrated nonlinear material model parameters can be further used in a full bridge model. Global bridge geometrical parameters, such as the bridge spans, superstructure depth, thicknesses of the soffit and deck slab, …etc., can be varied to investigate how these parameters affect the bent cap effective width and design. The current standards typically relate the effective slab width of the bent cap to the soffit and deck slab thicknesses. However, if other bridge geometric parameters are found to influence the effective slab width, then relating the effective width to such parameters via simple expressions should be beneficial.

- Comprehensive study can be pursued of the effect of the vertical excitation, especially in near fault regions, on the superstructure, bent caps, and outriggers of bridges. One part of the preliminary pre-test analysis conducted in this study rendered the bent cap beam vulnerable to excessive plastic damage due to vertical excitations. This was observed from the full prototype bridge OpenSees nonlinear dynamic analysis that used triaxial earthquake excitations, i.e. included the vertical excitation component, as discussed before. A 3D full bridge model should be considered for investigating any possible unfavorable modes of failure or damage due to the lack of proper account for the vertical excitations in bridge design. The 3D modeling is recommended because the vertical forces resulting from vertical excitations are sensitive to the mass distribution of the superstructure. Thus, approximate lumped mass at selected nodes of the bridge superstructure and bent cap model is not the most accurate method for tackling the issue of the vertical excitations.

- Investigate the behavior of bent caps in different bridge types beyond the RC box-girder bridges should be considered. Composite steel and RC bridge superstructure that still connects to a RC bent cap beam is another popular type of bridges where there is room for proper investigation of the bent cap behavior. The contribution from the RC box-girder slabs is natural in integral bent caps because of the monolithic connections. However, composite girders have stiffening and strengthening effect as well that might be required to be revisit for proper bent cap capacity estimation for seismic capacity design checks.

- Investigating the behavior of bent caps in different bridge geometries and configurations are needed. In particular, skew bridges with various skew angles might affect the overall box-girder soffit and deck slab contributions and, more critically, the bent cap beam capacity. Thus, a comprehensive study that relates the bent cap beam behavior, effective slab width, and capacity estimation to the skewness of the bridge should be useful. Currently, the Caltrans SDC and AASHTO recommend a similar $12t_s$ value for the effective width in a direction orthogonal to the bent cap axis. A revisited value might be strongly dependent on the skew angle and requires further investigations.

- Investigating the slab contribution to bridge girders in the longitudinal direction should be revised. Several studies have already studied the effective slab width and the slab contribution in composite bridge girders. The RC and PC box-girders need to be further investigated for a more accurate estimate of the slab contribution and the box-girder capacity, which is required for the bridge seismic capacity check in the longitudinal direction. Moreover, exploring the effect of post-tensioning on the effective slab width and including the prestressing and non-prestressing steel in the capacity estimation of the overall box-girder and the individual girders should be also useful.

REFERENCES

AASHTO (2007) LRFD Bridge Design Specification (2007). American Associate of State Highway and Transportation Officials." Washington, DC.

AASHTO (2009) AASHTO Guide Specifications for LRFD Seismic Bridge Design, 1st edition. American Associate of State Highway and Transportation Officials." Washington, DC.

AASHTO (2011) AASHTO Guide Specifications for LRFD Seismic Bridge Design, 2nd edition. American Associate of State Highway and Transportation Officials." Washington, DC.

ACI Committee 318 (2008) Building Code Requirements for Structural Concrete and Commentary, ACI 318-08. American Concrete Institute, Farmington Hills, MI.

ACI374.2R-13 (2013) Guide for Testing Reinforced Concrete Structural Elements under Slowly Applied Simulated Seismic Loads.

Alcocer, M. (1998). Investigación Acción Participativa. In Técnicas de investigación en sociedad, cultura y comunicación (pp. 433-464). Addison Wesley Longman.

ASCE-41-06 (2006) Seismic Rehabilitation of Existing Buildings. American Society of Civil Engineers

ASTM, (2005) Standard Test Method for Compressive Strength of Cylindrical Concrete Specimens: Designation C39/C39M -05. American Society for Testing Materials, West Conshohocken, Pa.

ASTM, (1997) Standard Specification for Welded Headed Bars for Concrete Reinforcement: Designation A970-97, American Society for Testing Materials, West Conshohocken, Pa.

ASTM, (2004)a Standard Test Method for Splitting Tensile Strength of Cylindrical Concrete Specimens: Designation C496/C496M-04. American Society for Testing Materials, West Conshohocken, Pa.

ASTM, (2004)b Standard Specification for Low-Alloy Steel Deformed and Plain Bars for Concrete Reinforcement: Designation A706-04. American Society for Testing Materials, West Conshohocken, Pa.

ASTM, (2004)c Standard Test Methods for Tension Testing of Metallic Materials: Designation E8-04. American Society of Testing Materials, West Conshohocken, Pa.

ASTM, (2007) Standard Test Method for Flexural Strength of Concrete (Using Simple Beam with Center-Point Loading: Designation C293-07. American Society for Testing Materials, West Conshohocken, Pa.

ATC-24, (1992) Guidelines for Cyclic Seismic Testing of Components of Steel Structures for Buildings, Report No. ATC-24, Applied Technology Council, Redwood City, CA.

Aviram, A., Mackie, K. & Stojadinovic, B. (2008) Guidelines for Nonlinear Analysis of Bridge Structures in California. University of California, Berkeley, Report PEER 2008/03.

Bayer V. Dorka U.E., Füllekrugc U., and Gschwilmd J. (2005) On Real-Time Pseudo-Dynamic Sub-Structure Testing: Algorithm, Numerical and Experimental Results. Aerospace Science and Technology 9(3): 223-232.

Berry, M. P. & Eberhard, M. O. (2007) Performance Modeling Strategies for Modern Reinforced Concrete Bridge Columns. University of California, Berkeley, Report PEER 2007/07.

Bas, A., (1990) Behavior of Reinforced Concrete Beam-Column Connections with Floor Slabs under Bi-Directional Loads, Master's thesis, Department of Civil Engineering, University of Toronto, Ontario, Canada.

Bonelli A. and Bursi O.S. (2004) Generalized- α Methods For Seismic Structural Testing. Earthquake Engineering and Structural Dynamics 33(10): 1067-1102.

Bozorgnia, Yousef, and Kenneth W. Campbell (2004) The Vertical-To-Horizontal Response Spectral Ratio and Tentative Procedures for Developing Simplified V/H and Vertical Design Spectra. Journal of Earthquake Engineering 8.2: 175-207.

Brendel, G. (1964) Strength of Compression Slab of T-Beams Subjected to Simple Bending. Journal of the American Concrete Institute, Proceedings No. 1, 61, pp. 57-75.

British Standards Institute (2008) BS-8110 Standard Use of Concrete

Brown, W. A., Lehman, D. E. & Stanton, J. F. (2007) Bar Buckling in Reinforced Concrete Bridge Columns. University of California, Berkeley, Report PEER 2007/11.

Bursi, O. S. & Shing, P. S. B. (1996) Evaluation of Some Implicit Time-Stepping Algorithms for Pseudodynamic Tests.

Calderone, A. J., Lehman, D. E. & Moehle, J. P. (2000) Behavior of Reinforced Concrete Bridge Columns Having Varying Aspect Ratios and Varying Lengths of Confinement. University of California, Berkeley, Report PEER 2000/08.

Caltrans, (2006) LRFD Design Example B: Bridge Design Academy Prototype Bridge, Sacramento, CA.

Caltrans, (2010) Seismic Design Criteria version 1.6. California Department of Transportation, Sacramento, CA.

Caltrans, (2013) Seismic Design Criteria version 1.7. California Department of Transportation, Sacramento, CA.

Campbell, Kenneth W., and Yousef Bozorgnia (2003) Updated Near-Source Ground-Motion (Attenuation) Relations for the Horizontal and Vertical Components of Peak Ground Acceleration and Acceleration Response Spectra. Bulletin of the Seismological Society of America 93.1: 314-331.

Campbell, S. & Stojadinovic, B. (1998) A System for Simultaneous Pseudodynamic Testing of Multiple Substructures. In 6th U.S. Nat. Conf. on Earth, Seattle, WA.

CEB-FIP Model Code 1990 (1993), Comité Euro-International du Béton

Chadwell, C. B., & Imbsen, R. A. (2002) XTRACT-Cross Section Analysis Software for Structural and Earthquake Engineering. TRC, Rancho Cordova, CA, http://www. imbsen. com/xtract. htm.

Chang S.-Y. (2002) Explicit Pseudodynamic Algorithm with Unconditional Stability. Journal of Engineering Mechanics, ASCE, 128(9):935-947.

Chang, S.-Y. (1997) Improved Numerical Dissipation for Explicit Methods in Pseudodynamic Tests. Earthquake Engineering and Structural Dynamics 26(9):917-929.

Chang S.-Y., Tsai K.-C. and Chen K.-C. (1998) Improved Time Integration for Pseudodynamic Tests. Earthquake Engineering and Structural Dynamics 27(7):711-730.

Chang, Y.-Y. (2008) Multi-Site Network Hybrid Testing of a Multi-Span Bridge System. Carleton University, Ottawa.

Chen C., and Ricles J. M. (2009) Improving the Inverse Compensation Method for Real-Time Hybrid Simulation through A Dual Compensation Scheme. Earthquake Engineering and Structural Dynamics 38(10), 1237–1255.

Cheung. Y. K. (1969) Folded Plate Structures by Finite Strip Method. ASCE Journal of the Structural Division, 95(ST12), pp. 2963-2979.

Cheung, M.S., & M.Y.T. Chan, (1978) Finite Strip Evaluation of Effective Flange Width of Bridge Girders. Canadian Journal of Civil Engineering, 5(2), 174-185.

Cheung, P. C., Paulay, T., & Park, R. (1991) New Zealand Tests on Full-Scale Reinforced Concrete Beam-Column-Slab Subassemblages Designed for Earthquake Resistance. ACI Special Publication, 123.

Chung J. and Hulbert G. M. (1993) A Time Integration Algorithm for Structural Dynamics with Improved Numerical Dissipation: the Generalized-Alpha Method. Journal of Applied Mechanics, ASME 60(2): 371-375.

Chwalla, E. (1936) Die Formeln zur Berechnung der "Voll Mittragenden Breite" diinner Gurt- und Rippenplatten. Stahlbau. No. 10, p. 73.

Computers and Structures Inc., (2012) SAP2000 V14: Integrated Finite Element Analysis and Design of Structures Basic Analysis Reference Manual, Berkeley, CA.

Darby A.P., Blakeborough A. and Williams M.S. (1999) Real-Time Substructure Test Using Hydraulic Actuator. Journal of Engineering Mechanics, ASCE, 125(10):1133-1139.

Darby A.P., Blakeborough A., and Williams. M.S. (2001) Improved Control Algorithm for Real-Time Substructure Testing. Earthquake Engineering and Structural Dynamics 30(3):431-448.

Dermitzakis, S. N. & Mahin, S. (1985) Development of Substructuring Techniques for On-Line Computer Controlled Seismic Performance Testing. Berkeley, California, Report UBC/EERC-85/04.

Dowell, R. K. (1998) Nonlinear Seismic Analysis and Design of Reinforced Concrete Bridge Structures.) University of California, San Diego.

Dryden, M. & Fenves, G. L. (2009) The Integration of Experimental and Simulation Data in the Study of Reinforced Concrete Bridge Systems Including Soil-Foundation-Structure Interaction. University of California, Berkeley, Report PEER 2009/03.

Durrani, A. J., & Wight, J. K. (1982) Experimental and Analytical Study of Internal Beam To Column Connections Subjected to Reversed Cyclic Loading.

DurraniI, A. J., & Wight, J. K. (1987) Earthquake Resistance of Reinforced Concrete Interior Connections Including A Floor Slab. ACI Structural Journal, 84(5).

Ehasani, M. R., and Wight, J. K. (1982) Behavior of External Reinforced Concrete Beam to Column Connections Subjected to Earthquake Type Loading. Report No. UMEE-82R5, Dept. of Civil Engineering, Univ. of Michigan, Ann Arbor, Mich.

Ehsani, M. R., & Wight, J. K. (1985) Effect of Transverse Beams and Slab on Behavior of Reinforced Concrete Beam-To-Column Connections. In ACI Journal Proceedings (Vol. 82, No. 2). ACI.

Elkhoraibi, T. & Mosalam, K. M. (2007) Generalized Hybrid Simulation Framework for Structural Systems Subjected to Seismic Loading. University of California, Berkeley, Report PEER 2007/101.

Esmaeily-Gh., A. & Xiao, Y. (2002) Seismic Behavior of Bridge Columns Subjected to Various Loading Patterns. University of California, Berkeley, Report PEER 2002/15.

European Standards (2009) Eurocode 2: Design of Concrete Structures

FEMA-416 (2007) InterimTesting Protocols for Determining the Seismic Performance Characteristics of Structural and Nonstructural Components.

Fenves, G. L. & Ellery, M. (1998) Behavior and Failure Analysis of a Multiple-Frame Highway Bridge in the 1994 Northridge Earthquake. University of California, Berkeley, Report PEER 98/08.

Frankie, T., Abdelnaby, A., Silva, P., Sanders, D., Elnashai, A., Spencer, B., Kuchma, D. & Chang, C.-M. (2013) Hybrid Simulation of Curved Four-Span Bridge, In Proceedings of Structures Congress.

French, C. W., & Boroojerdi, A. (1989) Contribution of R/C Floor Slabs in Resisting Lateral Loads. Journal of Structural Engineering, 115(1), 1-18.

French, C. W., & Moehle, J. P. (1991) Effect of Foor Slab on Behavior of Slab-Beam-Column Connections. ACI Special Publication, 123.

Gerolymos, N., Drosos, V. & Gazetas, G. (2009) Seismic Response of Single-Column Bent on Pile: Evidence of Beneficial Role of Pile And Soil Inelasticity. Bull Earthquake Eng(7).

Günay, S., & Mosalam, K. M. (2014) Seismic Performance Evaluation of High Voltage Disconnect Switches Using Real-Time Hybrid Simulation: II. Parametric Study. Earthquake Engineering & Structural Dynamics, 43(8), 1223-1237.

Hachem, M. M., & Mahin, S. A. (2000) Dynamic Response of Reinforced Concrete Columns to Multidirectional Excitations. In Proceedings of the 12th World Conference on Earthquake Engineering, New Zealand Society for Earthquake Engineering, Upper Hutt, New Zealand, Paper (No. 2446).

Harris, H. G. & Sabnis, G. M. (1999) Structural Modeling and Experimental Techniques. Second Edition edn.

Hassan, M., & S. El-Tawil, (2003) Tension Flange Effective Width in Reinforced Concrete Shear Walls. ACI Structural Journal, 100(3).

Hilber H., Hughes T. and Taylor R. (1977) Improved Numerical Dissipation for Time Integration Algorithms in Structural Dynamics. Earthquake Engineering and Structural Dynamics 5(3): 283-292.

Horiuchi T. and Konno T. (2001) A New Method For Compensating Delay in Time Hybrid Experiments, Philosophical Transactions of the Royal Society: Mathematical, Physical and Engineering Sciences 359, pp1893-1909.

Horiuchi T., Inoue M., Konno T. and Namita Y. (1999) Real-time Hybrid Experimental System With Actuator Delay Compensation and Its Application to a Piping System With Energy Absorber. Earthquake Engineering and Structural Dynamics 28(10):1121-1141.

Horiuchi, T. (1996) Development of A Real-Time Hybrid Experimental System With Actuator Delay Compensation. In 11th World Conference on Earthquake Engineering, Acapulco, México.

Horiuchi, T. (1999) Real-Time Hybrid Experimental System with Actuator Delay Compensation And Its Application To A Piping System With Energy Absorber.

Hose, Y. D. & Seible, F. (1999) Performance Evaluation Database for Concrete Bridge Components and Systems under Simulated Seismic Loads. University of California, Berkeley, Report PEER 1999/11.

Hube, M. A., & Mosalam, K. M. (2010) Experimental and Computational Evaluation of In-Span Hinges In Reinforced Concrete Box-Girder Bridges. Journal of Structural Engineering, 137(11), 1245-1253.

Hube, M. A., & Mosalam, K. M. (2011) Parametric Study and Design Recommendations for In-Span Hinges in Reinforced Concrete Box-Girder Bridges. Journal of Bridge Engineering, 17(2), 334-342.

Hughes T.J.R., Pister K.S. and Taylor R.L. (1979) Implicit-Explicit Finite Elements in Nonlinear Transient Analysis. Computer Methods in Applied Mechanics and Engineering, 17/18 (Part 1):159-182.

Ingham, J.M., Priestley, M.J.N, Seible, F., (1995) Bridge Knee Joint with Headed Reinforcement. Proceedings of Pacific Conference on Earthquake Engineering, Melbourne, Australia, Vol. 3, pp. 217-225, November 1995

ISO, (1998) Timber Structures – Joints Made with Mechanical Fasteners – Quasi-Static Reversed-Cyclic Test Method. ISO/TC 165 WD 16670. Secretariat, Standards Council of Canada.

Ketchum, M., Chang, V. & Shantz, T. (2004) Influence of Design Ground Motion Level on Highway Bridge Costs. University of California, Berkeley.

Kim, S. J. & Elnashai, A. S. (2008) Seismic Assessment of RC Structures Considering Vertical Ground Motion. Report 08-03.

Kramer, S. L., Arduino, P. & Shin, H. (2008) Using OpenSees for Performance-Based Evaluation of Bridges on Liquefiable Soils. University of California, Berkeley, Report PEER 2008/07.

394

Krawinkler, H. (1996) Cyclic Loading Histories for Seismic Experimentation on Structural Components. Earthquake Spectra, 12(1), 1-12.

Krawinkler, H. (2009). Loading Histories for Cyclic Tests in Support of Performance Assessment Of Structural Components. In The 3rd International Conference on Advances in Experimental Structural Engineering, San Francisco.

Krawinkler, H., Gupta, A., Medina, R., and Luco, N., (2000a) Development of Loading Histories for Testing of Steel Beam-to-Column Assemblies, SAC Background Report SAC/BD-00/10.

Krawinkler, H., Parisi, F., Ibarra, L., Ayoub, A., and Medina, R., (2000b) Development of a Testing Protocol for Woodframe Structures, CUREE Publication No. W-02.

Küçükarslan, S. (2010) A Finite Element Study on the Effective Width of Flanged Sections. Master's Thesis, Middle East Technical University, Ankara

Kumar, P., K. Mosalam, S. Abbasi, N. Abbasi and M. Kargahi, (2014) Reinforced Concrete Bridge Columns Repaired with Fiber Reinforced Polymer Jackets, ASCE Structures Congress 2014, Boston, MA, April 3-5, 2014, pp. 429-440

Kurose, Y., (1987) Recent Studies on Reinforced Concrete Beam-Column Joints in Japan, PMFSEL Report No. 87-8, Phil M. Ferguson Structural Engineering Laboratory, University of Texas, Austin, 164 pp.

Lee, H. & K.M. Mosalam (2014) Effect of Vertical Acceleration on Shear Strength of Reinforced Concrete Columns, PEER Technical Report 2014/04.

Lee, T.-H. & Mosalam, K. M. (2006) Probabilistic Seismic Evaluation of Reinforced Concrete Structural Components and Systems. University of California, Berkeley, Report PEER 2006/04.

Lehman, D. E. & Moehle, J. P. (1998) Seismic Performance of Well-Confined Concrete Bridge Columns. University of California, Berkeley, Report PEER 1998/01.

Leon, R. T., & Deierlein, G. G. (1996) Considerations for the Use of Quasi-Static Testing. Earthquake spectra, 12(1), 87-109.

Li, L., Mander, J. B. & Dhakal, R. P. (2008) Bidirectional Cyclic Loading Experiment on a 3D Beam–Column Joint Designed for Damage Avoidance. Journal of Structural Engineering.

Mackie, K. & Stojadinovic, B. (2003) Seismic Demands for Performance-Based Design of Bridges. University of California, Berkeley, Report PEER 2003/16.

MacRae, G.A., Priestley, M.J.N., Suible, F., (1994) Santa Monica Viaduct Retrofit – Large-Scale Column- Cap Beam Joint Transverse Test. Preliminary Report to the California Department of Transportation, August 1994

Magonette G. (2001) Development and Application of Large-Scale Continuous Pseudo-Dynamic Testing Techniques. Philosophical Transactions of the Royal Society: Mathematical, Physical and Engineering Sciences 359:1771-1799.

Mahin S.A. and Shing P.S.B. (1985) Pseudodynamic Method for Seismic Testing. Journal of Structural Engineering ASCE 111(7): 1482-1503.

Mahin, S. A. & Williams, M. E. (1980) Computer Controlled Seismic Performance Testing. Dynamic Response of Structures: Experimentation, Observation, Prediction and Control. New York, NY.

Mazzoni, S. (1997) Seismic Response of Beam-Column Joints in Double-Deck Reinforced Concrete Bridge Frames. PhD Disertation, University of California, Berkeley

McKenna, F., Fenves, G. L., Scott, M. H., and Jeremic, B., (2000) Open System for Earthquake Engineering Simulation (OpenSees). Pacific Earthquake Engineering Research Center, University of California, Berkeley, CA

Metzer. W. (1929) Die Mittmgende Breite. Luftfahrtforschung, P.

Miller, A. B. (1929) The Effective Width of A Plate Supported By A Beam. Institute Of Civil Engineers. Selected Engineering Papers, No. 83. 30 P.

Mitoulis, S. A. (2012) Seismic Design of Bridges with the Participation of Seat-Type Abutments. Engineering Structures(44).

Moehle, J.P. (2014) Seismic Design of Reinforced Concrete Buildings. McGraw-Hill Professional; 1 edition

Mosalam K.M., White R.N. and Ayala G. (1998) Response of Infilled Frames Using Pseudodynamic Experimentation. Earthquake Engineering and Structural Dynamics 27(6): 589-608.

Mosalam, K. M. & Günay, S. (2014) Seismic Performance Evaluation of High Voltage Disconnect Switches Using Real-Time Hybrid Simulation: I. System Development and Validation. Earthquake Engineering & Structural Dynamics. Vol. 43, No. 8, pp. 1205-1222.

Mosalam, K. M., C.J. Naito, & S. Khaykina, (2002) Bidirectional Cyclic Performance of Reinforced Concrete Bridge Column-Superstructure Subassemblies. Earthquake spectra, 18(4), 663-687.

Mosalam, K. M., Talaat, M. & Binici, B. (2006) A Computational Model for Reinforced Concrete Members Confined with Fiber Reinforced Polymer Lamina: Implementation and Experimental Validation. Elsevier.

Mosqueda G. (2003) Continuous Hybrid Simulation with Geographically Distributed Substructures, University of California, Berkeley. PhD. Dissertation: 232 pages.

Mosqueda, G., Stojadinovic, B. & Mahin, S. (2005) Implementation and Accuracy of Continuous Hybrid Simulation with Geographically Distributed Substructures. Berkeley, California, Report UCB/EERC 2005-02.

Mosqueda, G., Stojadinovic, B., Hanley, J., Sivaselvan, M., & Reinhorn, A. M. (2008) Hybrid Seismic Response Simulation on A Geographically Distributed Bridge Model. Journal of structural engineering, 134(4), 535-543.

Naito, C. J., Moehle, J. P. & Mosalam, K. M. (2001) Experimental and Computational Evaluation of Reinforced Concrete Bridge Beam-Column Connections for Seismic Performance. University of California, Berkeley, Report PEER 2001/08.

Nakashima M. and Masaoka N. (1999) Real-Time On-Line Test for MDOF Systems. Earthquake Engineering & Structural Dynamics 28(4): 393-420.

Nakashima M., Ishii. K., Kamagata S., Tsutsumi H. and Ando K. (1988) Feasibility of Pseudo Dynamic Test Using Substructuring Techniques. Proceedings of the Ninth World Conference on Earthquake Engineering. Tokyo, Japan.

Nakashima M., Kaminosono T., Ishida I. and Ando K. (1990) Integration Techniques for Substructure Pseudo Dynamic Test. Proceedings of the Fourth U.S. National Conference on Earthquake Engineering, EERI.

Nakashima M., Kato M. and Takaoka E. (1992) Development of Real-Time Pseudo-Dynamic Testing. Earthquake Engineering and Structural Dynamics 21(1):79-92.

Nakashima, M., Kaminosono, T., Ishida, M. & Ando, K. (1990) Integration Techniques for Substructure Pseudodynamic Testing. In 4th U.S. National Conference on Earthquake Engineering.), Palm Springs, California.

Newmark, N.M., (1959) A Method of Computation for Structural Dynamics. Journal of Engineering Mechanics, ASCE, 85 (EM3) 67-94.

Nguyen N.V. and Dorka U. (2009) Adaptive Error Compensation Based On Online System Identification For Real-Time Substructure Testing. Proceedings of the 3rd International Conference on Advances in Experimental Structural Engineering San Francisco, CA.

Pantazopoulou, S. J., & Bas, A. (1994) Participation of Floor Slabs in the Mechanisms of Resistance of Beam-Column Connections. In Proceedings (pp. 119-128).

Pantazopoulou, S. J., Moehle, J. P., & Shahrooz, B. M. (1988) Simple Analytical Model for T-Beams In Flexure. Journal of Structural Engineering,114(7), 1507-1523.

Pantazopoulou, S.J., and C.W. French, (2001) Slab Participation In Practical Earthquake Design Of Reinforced Concrete Frames. ACI Structural Journal, 98(4).

Park, R., and Pauley, T. (1975) Reinforced Concrete Structures, John Wiley and Sons, New York, N.Y

Pecknold, D. A. (1975) Slab Effective Width for Equivalent Frame Analysis. In ACI Journal Proceedings (Vol. 72, No. 4), ACI.

Porter KA, Beck JL, Shaikhutdinov RV. (2002) Sensitivity of Building Loss Estimates to Major Uncertain Variables. Earthquake Spectra; 18(4):719–743.

Porter, D. M., & Cherif, Z. E. (1987) Ultimate Shear Strength of Thin Webbed Steel and Concrete Composite Girders. Elsevier Applied Science Publishers, 55-64.

Proveti, J.R.C. and Michot G. (2006) The Brazilian Test: A Tool For Measuring the Toughness of A Material and Its Brittle to Ductile Transition. International Journal of Fracture, Vol. 139, No. 3-4, pp. 455-460.

Qi, X., & Pantazopoulou, S. J. (1991) Response of RC Frame under Lateral Loads. Journal of Structural Engineering, 117(4), 1167-1188.

RILEM Draft (1985) Determination of the Fracture Energy of Mortar and Concrete by Means of Three-Point Bend Tests on Notched Beames. Materials and Structures 18, no. 106 (1985): 285-290.

Sarrazin, J. (2004) Advanced Composite Materials Systems Comparative Analysis o f Reinforced Concrete Columns Seismic Retrofit Schemes.) University of Ottawa, Ottawa, pp. 66 -76.

Schellenberg, A. H., Mahin, S. A. & Fenves, G. L. (2009) Advanced Implementation of Hybrid Simulation. University of California, Berkeley, Report PEER 2009/104.

Shahrooz, B. M., Pantazopoulou, S. J., & Chern, S. P. (1992) Modeling Slab Contribution in Frame Connections. Journal of Structural Engineering, 118(9), 2475-2494.

Seible, F., Priestley, M.J.N., Latham, C.T., Terayama, T., (1993) Full- Scale Test on the Flexural Integrity of Cap/Column Connections with #18 Column Bars. Preliminary Report to the California Department of Transportation, January 1993.

Seible, F., Priestley, M.J.N., Silva, P., Gee, D., (1994) Full- Scale Bridge Column Test of Redesigned Cap/Column Connection with #18 Column Bars. Preliminary Report to the California Department of Transportation, January 1994

Shelman, A. T. (2013) Advancing the Seismic Design of Reinforced Concrete Bridge Columns by Aaron Trask Shelman.) Iowa State University, Ames, Iowa.

Shing P.B. and Mahin S.A. (1987) Cumulative Experimental Errors in Pseudodynamic Tests. Earthquake Engineering & Structural Dynamics 15(4): 409-424.

Shing P.B., Bursi O.S. and Vannan M.T. (1994) Pseudodynamic Tests of A Concentrically Braced Frame using Substructuring Techniques. Journal of Construction Steel Research 29(1-3):121-148.

Shing P.B., Vannan M.T. and Cater E. (1991) Implicit Time Integration for Pseudodynamic Tests. Earthquake Engineering and Structural Dynamics 20(6):551-576.

Shing, P. B. & Mahin, S. A. (1985) Experimental error propagation in pseudodynamic testing. Berkeley, California, Report UBC/EERC-85/04, pp. 175.

Suzuki, N.; Otani, S.; and Kobayashi, Y., (1984) Three-Dimensional Beam-Column Subassemblages under Bidirectional Earthquake Loadings, Proceedings, Eighth World Conference on Earthquake Engineering, V. 6, San Francisco, Prentice-Hall, Inc., 453 pp.

Takahashi, Y., Iemura, H., Mahin, S. A. & Fenves, G. L. (2008) International Distributed Hybrid Simulation of 2-Span Continuous Bridge In Proceedings of 14th World Conference on Earthquake Engineering.

Takanashi K., Udagawa K., Seki M., Okada T., and Tanaka H. (1975) Non-linear Earthquake Response Analysis of Structures By A Computer-Actuator On-Line System (Details Of The System). Trans. of the Architectural Institute of Japan, 229, 77-83.

Takanashi, K. & Nakashima, M. (1987) Japanese Activities on On-Line Testing. Journal of Engineering Mechanics 113(7):1014-1032.

Takanashi, K., Udagawa, K., Seki, M., Okada, T. & Tanaka, H. (1975) Non-Linear Earthquake Response Analysis of Structures by A Computer-Actuator Online System--Part 1: Detail Of The System. Transactions of the Architectural Institute of Japan (229).

Terzic, V. & Stojadinovic, B. (2010) Post-Earthquake Traffic Capacity of Modern Bridges in California. University of California, Berkeley, Report PEER 2010/103.

Timoshenko, S., & Goodier, J. N. (1970) Theory of Elasticity. Engineering societies monographs. International Student Edition. New York, Tokyo.

Thewalt C.R. and Mahin S.A. (1987) Hybrid Solution Technique for Generalized Pseudodynamic Testing. EERC-87/09, Earthquake Engineering Research Center, University of California, Berkeley.

Thewalt C.R. and Roman M. (1994) Performance Parameters for Pseudodynamic Tests. Journal of Structural Engineering 120(9): 2768-2781.

Thewalt, C.R. and Stojadinovic, B., (1995) Behavior of Bridge Outrigger Knee Joint Systems. Earthquake Spectra, Volume 11, No. 3, August 1995.

Thomsen, J. H., & Wallace, J. W. (1995) Displacement-Based Design of RC Structural Walls: An Experimental Investigation of Walls With Rectangular And T-Shaped Cross-Sections. Clarkson University, Department of Civil Engineering.

Thomsen IV, J. H., & Wallace, J. W. (2004) Displacement-Based Design of Slender Reinforced Concrete Structural Walls-Experimental Verification. Journal of Structural Engineering, 130(4), 618-630.

TNO Diana, (2014) User's Manual - Release 9.5, Delft, Netherlands

Trono, W., Jen, G., Panagiotou, M., Schoettler, M., & Ostertag, C. P. (2014) Seismic Response of a Damage-Resistant Recentering Posttensioned-HYFRC Bridge Column. Journal of Bridge Engineering. in-press

Uniform Building Code, (1994) International Conference of Building Officials, Whittier, CA

Velez, O., and French, C. W., (1989) R/C Beam-Column-Slab Subassemblages Subjected to Lateral Loads, Journal of Structural Engineering, ASCE, V. 115, No. 6, pp. 1289-1308

Wallace, J. W. (1996) Evaluation of UBC-94 Provisions for Seismic Design of RC Structural Walls. Earthquake Spectra, 12(2), 327-348.

Wang, K. J., Tsai, K. C., Wang, S. J., Cheng, W. C., & Yang, Y. S. (2007) ISEE: Internet-based Simulation for Earthquake Engineering—Part II: The application protocol approach. Earthquake engineering & structural dynamics,36(15), 2307-2323.

Watanabe, E., Sugiura, K., Nagata, K. & Suzuka, Y. (1998) Development of Parallel Pseudo-Dynamic Test System. In 10th Japan Earth. Engineering Symposium.

Wight, J. K., and Sozen, M. A., (1975) Shear Strength Decay of RC Columns under Shear Reversals, Proceedings, ASCE, V. 101, No. ST5, May 1975, pp. 1053-1065.

Wolfgram, C. E. (1984) Experimental Modelling and Analysis of Three One-Tenth Scale Reinforced Concrete Frame-Wall Structures, thesis presented to the Graduate College,

University of Illinois, at Urbana, 111., in partial fulfillment of the requirements for the degree of Doctor of Philosophy.

Xin-jiang, C. & Shi-zhu, T. (2009) Seismic Hybrid Simulation of a Multi-Span Bridge. In ICCTP.

Yang, Y. S., Hsieh, S. H., Tsai, K. C., Wang, S. J., Wang, K. J., Cheng, W. C., & Hsu, C. W. (2007) ISEE: Internet-based Simulation for Earthquake Engineering—Part I: Database approach. Earthquake Engineering & Structural Dynamics, 36(15), 2291-2306.

Yamazaki Y., Nakashima M. and Kaminosono T. (1989) Reliability of Pseudodynamic Test In Earthquake Response Simulation. Journal of Structural Engineering, ASCE 115(8): 2098-2112.

Zerbe, H. E., & Durrani, A. J. (1985) Effect of A Slab on The Behavior of Exterior Beam To Column Connections. Report, Department of Civil Engineering, Rice University.

Appendix A: Specimen Design

A.1 DESIGN LOADS

For the design of the subassembly reduced-scale specimen, a full scale model for the modified prototype was used first to compute the loads and straining actions, basically due to dead and live loads, at each relevant structural element. The computed straining actions were then scaled down using the proper similitude relationships and used to design the different specimen sections. Moreover, the seismic design loads and criteria were considered according to the Caltrans Seismic Design Criteria (SDC) and AASHTO LRFD Bridge Design Specifications. Three-dimensional elastic models were developed for the modified prototype using SAP2000 to compute the straining actions under different vertical loads.

Box-Girder Straining Actions:

For the full scale box-girder having entire bridge width, the bending moments and shear forces are:

Dead Load (self-weight): $M_{DL(-ve)} =$ -54,016 kip-ft. ; $M_{DL(+ve)} =$ 31,738 kip-ft.

Additional Dead Load (wearing surface): $M_{ADL\,(-ve)} =$ -8,822 kip-ft. ; $M_{ADL\,(+ve)} =$ 5,183 kip-ft.

Live Load (design vehicle – truck load): $M_{LDT\,(-ve)} =$ -2,290 kip-ft; $M_{LDT\,(+ve)} =$ 1,327 kip-ft.

Live Load (design vehicle – lane load): $M_{LDL\,(-ve)} =$ -1,673 kip-ft. $M_{LDL\,(+ve)} =$ 983 kip-ft.

The ultimate (factored) moments for the full-scale box-girder can be computed according to the AASHTO load combinations as follows:

$$M_{ult} = \sum_i \eta_i \times \gamma_i \times M_i \quad (AASHTO\,3.3.1-1)$$

$$M_{ult} = 1.0 \times [1.25 \times M_{DL} + 1.75 \times M_{LL-design}(1+IM)]$$

$$M_{ult(-ve)} = -1.0 \times [1.25 \times (54016 + 8822) + (1.75 \times 1.33 \times (2290 + 1673))] = -87,771 \text{ kip-ft.}$$

$$M_{ult(+ve)} = 1.0 \times [1.25 \times (31738 + 5183) + (1.75 \times 1.33 \times (1327 + 983))] = 51,528 \text{ kip-ft.}$$

Similarly, the factored shear force for the full-scale box-girder can be computed as follows:

$$V_{ult} = \sum_i \eta_i \times \gamma_i \times V_i \quad (AASHTO\,3.3.1-1)$$

$$V_{ult} = 1.0 \times [1.25 \times V_{DL} + 1.75 \times V_{LL-design}(1+IM)]$$

$$V_{ult} = 1.0 \times [1.25 \times (1960 + 320) + (1.75 \times 1.33 \times (51.6 + 38.2))] = 3059 \text{ kips}$$

Next, the shear and moment for the specimen design can be calculated using the proper similitude and scale factors from "Structural Modeling and Experimental Techniques, Harris and Sabnis, 1999". Since the specimen will have the same materials as the prototype but with reduced geometric scale (S = 4), the bending moments are reduced by $1/S^3 = 1/64$ and the Forces are reduced by $1/S^2 = 1/16$. Also the subassembly specimen consists of only 4 webs and 3 cells, while the full prototype box-girder consists of 8 webs and 7 cells. So the straining actions are reduced accordingly. Therefore, the specimen straining actions are calculated as follows:

$$M_{ult(-ve)} = -87771 \times (3/7) \times (1/64) = -587.76 \text{ kip-ft}$$

$$M_{ult(+ve)} = 51528 \times (3/7) \times (1/64) = 345.10 \text{ kip-ft}$$

$$V_{ult/web} = 3059 \times (1/8) \times (1/16) = 23.90 \text{ kips}$$

Bent Cap Beam and Column Straining Actions:

A planer two-dimensional elastic SAP2000 model was developed for the three-column and integral cap beam bent. The loads applied to the bent model were adopted from the full bridge model and the components self-weights were also applied. Only factored design straining actions from vertical loads are shown here and the seismic forces considerations are presented in the next section.

- The factored moment for the full-scale cap beam is calculated as follows:

$$M_{ult} = 1.0 \times [1.25 \times M_{DL} + 1.75 \times M_{LL-design}(1 + IM)]$$

$$M_{ult(-ve)} = -1.0 \times [1.25 \times (5174 + 751.5) + (1.75 \times 1.33 \times 1631.4)] = -11,204 kip - ft.$$

$$M_{ult(+ve)} = 1.0 \times [1.25 \times (3505 + 518) + (1.75 \times 1.33 \times 1883.4)] = 9,412 kip - ft.$$

- The factored shear for the full-scale cap beam is calculated as follows:

$$V_{ult} = 1.0 \times [1.25 \times V_{DL} + 1.75 \times V_{LL-design}(1 + IM)]$$

$$V_{ult} = 1.0 \times [1.25 \times (907 + 131) + (1.75 \times 1.33 \times 156.3)] = 1661.3 kips$$

- The factored axial force for the full-scale middle column is calculated as follows:

$$P_{ult} = 1.0 \times [1.25 \times P_{DL} + 1.75 \times P_{LL-design}(1 + IM)]$$

$$P_{ult} = 1.0 \times [1.25 \times (1814.1 + 261.6) + (1.75 \times 1.33 \times 171.7)] = 2994 kips$$

- Thus, the specimen column and beam straining actions are calculated as follows:

$$M_{Bult(-ve)} = -11204 \times (1/64) = -175 kip - ft$$

$$M_{Bult(+ve)} = 9412 \times (1/64) = 147.1 kip - ft$$

$$V_{Bult} = 1661.3 \times (1/16) = 103.8 kips$$

$$P_{Colult} = 2994 \times (1/16) = 187.2 kips$$

Specimen Lateral (Seismic) Design Loads:

The seismic loads are designed to be carried by the bent columns and beams framing action. According to the SDC (Section 3.4), the bent cap beam and box-girder superstructure are capacity protected components that shall be designed flexurally to remain elastic when the column reaches its overstrength capacity. Consequently, the cap bam and box-girder will be designed under vertical loads only, then the designed cross-sections' capacity will be computed and checked to make sure the beam and box-girder remain elastic when column reaches its capacity. The specimen column design is presented first and then followed by the cap beam and box-girder designs and checks.

A.2   DESIGN OF SPECIMEN CROSS-SEECTIONS

The design of the specimen includes flexural and shear design for the following components:

- Column
- Cap beam
- Column and cap beam joint
- Box girder deck and soffit slabs
- Box girder webs
- Concrete beams (seats) for specimen attachment to lab rigid floor

The design is made according to the following Codes and Standards:

- AASHTO LRFD Bridge Design Specifications, 2007.
- Caltrans Seismic Design Criteria (SDC), 2010.
- ACI Building Committee 318, 2008.

A.2.1 Column Design

Geometry :

Scaling Factor, $S = 4.0$

Diameter of column, $D_{col} = 18 in.$

Height of column, $H_{col} = 90 in.$

Gross cross-section area of column $= A_g = \dfrac{\pi}{4}\left(D_{col}\right)^2 = \dfrac{\pi}{4} \times 18^2 \approx 254.5 in^2.$

Material :

The nominal material properties to be used in the specimen construction are :

Concrete Compressive Strength, $f_c' = 5 ksi.$

Yield strength of steel, $f_y = 60 ksi.$

Ultimate strength of steel, $f_u = 80 ksi.$

The expected material properties are determined from nominal properties according to Caltrans SDC Section 3.2,

$$f_{ce}' = the\ greater\ of : \begin{cases} 1.3 \times f_c' = 1.3 \times 5000 = 6500\ psi = 6.5 ksi \\ 5000\ psi = 5.0 ksi \end{cases}$$

Expected concrete comp. strength, $f_{ce}' = 6500\ psi.$

Expected yield strength of Steel, $f_{ye} = 68\ ksi.$

Expected Ulitmate strength of steel, $f_{ue} = 95 ksi.$

Column Axial Load :

Due to the nature of the test setup that the specimen is inverted upside down, the gravity load will be applied at the column top during the test. The value of the test's gravity load is chosen such that the moments in the specimen column and cap beam joint region are the same as produced by distributed gravity loads in the scaled prototype bridge.

Thus, from an elastic SAP2000 model for the specimen where the moment in the cap beam is:

$M_{DL-service} = (5085 + 738.4) \times (1/64) = 91 kip\text{-}ft. = 1092 kip - in.$

The column axial load was found to be: $P_{col} = 72 kips.$

This corresponds to axial load ratio $= \dfrac{P_{col}}{A_c \times f_c'} = \dfrac{72}{254 \times 5} = 5.66\%$

Longitudinal Steel Reinforcement Requirement:

According to SDC, the minimum and maximum column reinforcement ratios are:
1.0% and 4.0%, respectively

For the sake of the test aiming at achieving failure in both the cap beam and column,
a longitudinal reinforcment ratio $\rho_l = 2.5\%$ is chosen to start with.

Required $A_{s,col} = 0.025 \times A_g = 0.025 \times 254.5 = 6.36\,in^2$.

If using longitudinal rebars #6,

$A_{\#6} = 0.44\,in^2$. $\quad and \quad \phi_{\#6} = 0.75\,in$.

$number\ of\ bars = 6.36 \div 0.44 = 14.5 \rightarrow use\ 16\#6,\ \rho_l = \dfrac{16 \times 0.44}{254.5} = 2.77\%$

Check spacing requirements between bars,

Define D_o as the distance from center of long. rebar to the outer edge of column.

$D_o = D_{col} - 2\left(Clear\ Cover + \phi_{\#3} + \dfrac{\phi_{\#6}}{2}\right)$

For clear cover $= 1.0\,in$. and hoop #3 ($\phi_{\#3} = 0.375\,in$.),

$D_o = 18 - 2\left(1.0 + 0.375 + \dfrac{0.75}{2}\right) = 14.5\,in$.

$Then,\ spacing\ between\ long.\ bars,\ \delta_l = \dfrac{\pi D_o}{number\ of\ bars - 1} = \dfrac{\pi \times 14.5}{15} = 3.04\,in. < 8\,in.\ OK$

Plastic Hinge Length (Equivalent):

$L_p = 0.08L + 0.15f_{ye}\phi_{\#6} = 0.08 \times 90 + 0.15 \times 68 \times 0.75 = 14.85\,in$.

$L_p \geq 0.3f_{ye}\phi_{\#6} = 0.3 \times 68 \times 0.75 = 15.3\,in. \rightarrow consider\ L_p = 15.3\,in$

Plastic Region Extent:

$L_{pr} \geq 1.5D_{col} = 1.5 \times 18 = 27\,in.$

$L_{pr} \geq 0.25H_{col} = 0.25 \times 90 = 22.5\,in.$

$L_{pr} \geq \left(length\ where\ M > 0.75M_p\right) = 0.25H_{col} = 22.5\,in.$

$\left. \right\} \quad L_{pr} = 27\,in.$

Transverse Steel Reinforcement Requirement:

- Determine minimum transverse steel according to AASHTO:

$$\frac{A_v}{s} \geq 0.0316 \times \sqrt{f_c'} \times \frac{b_v}{f_y} \quad (AASHTO, 5.8.2.5-1)$$

$$\frac{A_v}{s} \geq 0.0316 \times \sqrt{5} \times \frac{18}{60}$$

$$\frac{A_v}{s} \geq 0.021 in^2 / in$$

If using #3 hoops, $s_{required} \leq \dfrac{0.11}{0.021} \approx 5.2 in.$

- Minimum spacing of transverse steel in compression members:

According to Section 5.10.6.3, The spacing of ties along the longitudinal axis of the compression member shall not exceed the least dimension of the compression member or 12.0 in.

Then, for the scaled specimen,

minimum spacing outside plastic hinge zone $= 12 \times (1/4) = 3.0 in.$

- Minimum transverse steel in plastic hinge zone for seismic design:

$$\rho_s \geq 0.12 \times \frac{f_c'}{f_y} \quad (AASHTO, 5.10.11.4.1d-1)$$

$$\rho_s \geq 0.12 \times \frac{5}{60} \geq 0.01$$

$$\rho_s = \frac{4 A_{sh,required}}{D' s_h} \geq 0.01$$

If using #3 hoops, $s_{h,required} \leq \dfrac{4 \times 0.11}{0.01 \times 15.25} \approx 2.8 in.$

Then, minimum stirrups to use: #3 hoop at 2.5 in. center-to-center spacing

The above column design is used to run a moment-curvature analysis using the software XTRACT to calculate the section capacity. The column section capacity will be used consequently to design the specimen cap beam and box-girder cross sections. The confined concrete model parameters can be calculated automatically in XTRACT for the moment-curvature analysis. However, those parameters are calculated manually here to check if different from program values.

Column M - ϕ Analysis and Results (Based on Caltrans SDC):

Diameter $D_{col} = 18\,in., length\ of\ the\ column = 90\,in., 16\#6\ longitudinal\ rebars, P_{axial} = 72\,kips.$

$f_{ye,\#6} = 68\ ksi,\ E_s = 29,000\,ksi,\ Clear\ cover = 1.0\,in.,\ hoop\#3@2.5\,in., f_{ye,\#3} = 68\ ksi,$

$f_{ce}' = 6.5\ ksi,\ unconfined\ concrete\ ultimate\,(spalling)\,strain\ \varepsilon_{sp} = 0.0050,$

Confined Conrete:

1. *Confinement effectiveness,* $k_e = 1 - \dfrac{S_h}{D'} = 1 - \dfrac{2.5}{15.25} \approx 0.84$

2. *Maximum stress capacity of confining renforcement*

$$f_s = E_s \left(0.0025 + 0.21\sqrt[3]{\dfrac{k_e \rho_s}{f_c'}} \right) \le f_{yt} = 60,000$$

$$f_s = 29,000,000 \left(0.0025 + 0.21\sqrt[3]{\dfrac{0.84 \times 0.014}{5000}} \right) = 154,406\ psi$$

Then, use $f_s = 60,000\ psi.$

3. *Effective confinement stress,* $f_{1e} = k_e \dfrac{\rho_s f_s}{2} = 0.84 \times \dfrac{0.0144 \times 60000}{2} \approx 361.2\ psi$

4. *Confined concrete strength* (*using Mander et.al. curves*):

$$\dfrac{f_{1e}}{Cf_c'} = \dfrac{361.2}{0.85 \times 5000} = 0.085 \xrightarrow{from\ curves\ with\ f_{1e}=f_{2e},} \dfrac{f_{cc}}{Cf_c'} \approx 1.50$$

$$f_{cc} = 1.50 \times Cf_c' = 1.50 \times 0.85 \times 5000 = 6375\ psi \approx 6.38\ ksi$$

5. *Strain at peak stress,* $\varepsilon_{cc} = \varepsilon_0 \left(1 + 5\left(\dfrac{f_{cc}}{Cf_c'} - 1 \right) \right)$

ε_0 =strain at peak stress in unconfined concrete = 0.003, $\varepsilon_{cc} = 0.003\left(1 + 5\left(1.50 - 1\right)\right) = 0.0105$

6. *Ultimate strain in confined concrete,* $\varepsilon_{cu} = 0.004 + 0.25\dfrac{f_{e\min}}{f_c'} = 0.004 + 0.25\dfrac{0.365}{5} \approx 0.0222$

7. *Using Mander Model,* $E_c = 57,000\sqrt{f_c'} = 57,000\sqrt{5000} = 4030\ ksi$

$$r = \dfrac{E_c}{E_c - \dfrac{f_{cc}}{\varepsilon_{cc}}} = \dfrac{4030}{4030 - \dfrac{6.38}{0.0105}} = 1.086, \quad x = \dfrac{\varepsilon_c}{\varepsilon_{cc}} = \dfrac{0.0222}{0.0105} \approx 2.11$$

$$f_c = \dfrac{f_{cc} x r}{r - 1 + x^r} = \dfrac{6.38 \times 2.11 \times 1.086}{1.086 - 1 + 2.11^{1.086}} = 6.26\,ksi$$

Results of $M - \phi$ Analysis:

Moment at first yield (XTRACT): $M_y = 2246\,kips\text{-}in$ and curvature: $\phi_y = 0.00022\,rad\,/\,in.$

Effective yield moment (XTRACT): $M_y' = 3244\,kips\text{-}in$ and curvature: $\phi_y' = 0.00031\,rad\,/\,in.$

Ultimate yield moment (XTRACT): $M_u = 3667\,kips\text{-}in$ and curvature: $\phi_u = 0.0045\,rad\,/\,in$

Idealized Caltrans SDC Plastic Moment, $M_p \approx \dfrac{M_y' + M_u}{2} \approx \dfrac{3244 + 3667}{2} = 3456\,kips\text{-}in$

$\phi_Y = \dfrac{M_p \phi_y}{M_y} = \dfrac{3456 \times 0.00022}{2246} = 0.000338\ rad\,/\,in$

Curvature ductility, $\mu_{\phi,c} = \dfrac{\phi_u}{\phi_Y} = \dfrac{0.0045}{0.000338} = 13.29$

Calculate and check the displacement ductility capacity:

$\Delta_Y = \phi_Y \dfrac{L^2}{3} = 0.000338 \times \dfrac{90^2}{3} = 0.912\,in$

$\phi_p = \phi_u - \phi_Y = 0.0045 - 0.000338 = 0.00416\,rad\,/\,in$

$\theta_p = \phi_p L_p = 0.00416 \times 15.3 = 0.0637\,rad$

$\Delta_p = \theta_p \left(L - \dfrac{L_p}{2} \right) = 0.0637 \left(90 - \dfrac{15.3}{2} \right) = 5.244\,in$

$\Delta_u = \Delta_Y + \Delta_p = 0.912 + 5.244 = 6.16\,in$

Displacement ductilituy, $\mu_{\Delta,c} = \dfrac{\Delta_u}{\Delta_Y} = \dfrac{6.16}{0.91} = 6.75 \geq 4.0\,OK$

The SDC also defines overstrength moment M_o to be used at different design aspects.
According to SDC Equation (4.4), $M_o = 1.2 \times M_p = 1.2 \times 3456 = 4147\,kips - in$

Column Shear Design (SDC Section 3.6):

As per the SDC requirements, the shear capacity for ductile concrete members is given by:
$Capacity\,(\phi_v V_n) \geq Demand\,(V_o)$

It shall also be conservatively based on the nominal material strengths.

$Overstrength\ shear,\ V_o = \dfrac{1.2 M_p}{L} = \dfrac{1.2 \times 3456}{90} = 46.08\,kips$

$Nominal\ shear\ capacity,\ V_n = \phi_v \left(V_c + V_s \right)$

A.2.2 Cap Beam Design

According to the SDC, the cap beam is considered a capacity protected member. Thus, it is required that the cap beam remains elastic when the column reaches its plastic moment capacity taking into consideration the overstrength factor (=1.2). The specimen cap beam will be designed first using the factored moments and shear, then a moment-curvature analysis will be carried out for the designed section using XTRACT to check that beam remains elastic as the column reaches its overstrength moment.

Beam factored design straining actions:

$$M_{Bult(-ve)} = -175kip - ft = -2100\,kip - in$$

$$M_{Bult(+ve)} = 147.1kip - ft = 1765.2\,kip - in$$

$$V_{Bult} = 103.8\,kips$$

Geometry and Material Properties:

$beam\,width, b = 24\,in\;$ and $\;beam\,height, h = 20.375\,in$

$clear\,cover = 0.75\,in$

$use\;\#5\,bars\;for\,longitudenal\;reinforcement\;(\phi_{\#5} = 0.625\,in\,,A_{s,\#5} = 0.31\,in^2\,)$

$use\;\#3\,bars\;for\,transverse\;reinforcement\;(\phi_{\#3} = 0.375\,in\,,A_{s,\#5} = 0.11\,in^2\,)$

$define\,distance\,between\,upper\,most\,compression\,fiber\,and\,tension\,reinforcement\,c.g.\,as\,"d",$

$$d = h\,\text{-}\,(clear\,cover + stirrup\,bar\,diameter + \frac{1}{2} \times long.bar\,diameter)$$

$$d = 20.375 - (0.75 + 0.375 + \frac{1}{2} \times 0.625) \approx 18.94\,in$$

Same materials properties used in column design are also used in beam and other elements design.

Flexural Design:

$$\phi_f M_n \geq M_u$$

Start the first beam design trial by neglecting compression steel and assuming a moment arm of "0.90×d" between the tension steel reinforcement c.g. and the compression stress block c.g.

For negative moment :

$$M_{u,-ve} = 2100 \, kip - in$$

$$\phi_f = 0.9 \, (according \, to \, AASHTO, Section \, 5.5.4.2)$$

$$M_n = Tension \, force \, in \, steel \times moment \, arm = A_s \times f_{sy} \times 0.90 \times d$$

then, required reinforcement :

$$A_{s,required} \geq \frac{M_{u,-ve}}{\phi_f \times f_{sy} \times 0.9 \times d} = \frac{2100}{0.9 \times 60 \times 0.90 \times 18.94} = 2.28 \, in^2$$

$$number \, of \, \#5 \, bars \, required = \frac{A_{s,required}}{A_{s,\#5}} = \frac{2.28}{0.31} = 7.36 \rightarrow use \, 8 \, \#5 \, bars \, for \, negative \, moment$$

$$C = T = A_s \times f_{sy} = 8 \times 0.31 \times 60 = 148.8 \, kips$$

$$C = c \times b \times \beta_1 \times f_c', \beta_1 = 0.85 - \frac{0.05}{1000}(f_c' - 4000) = 0.80 \, (AASHTO, Section \, 5.7.2.2)$$

$$then, \, c = \frac{C}{b \times \beta_1 \times f_c'} = \frac{148.8}{24 \times 0.80 \times 5} = 1.55 \, in$$

$$M_n = T \times (d - \frac{a}{2}) = 148.8 \times (18.94 - 0.775) = 2702.9 \, kip - in > \frac{M_u}{\phi_f} = \frac{2100}{0.9} = 2333.3 \, kip - in \, OK$$

check minimum reinforcement according to AASHTO :

According to AASHTO, Section 5.7.3.3.3, a minimum reinforcement to develop at least 1.2 times the cracking moment of the cross-section is needed.

The cracking moment can be given as $M_{cr} = \frac{f_r \times I_g}{y_t}$

$$f_r = 0.24 \times \sqrt{f_c'} = 0.24 \times \sqrt{5} = 0.537 \, ksi$$

I_g and y_t are calculated from section properties , $y_t = 10.42 \, in \, \& \, I_g = 18101.9 \, in^4$

$$then, \, M_{cr} = \frac{0.537 \times 18102}{10.42} = 932.9 \, kip - in$$

The required steel to develop such moment can be approximately calculated as follows :

$$A_{s,min} = \frac{1.2 \times M_{cr}}{\phi \times f_{sy} \times 0.9 \times d} = \frac{1.2 \times 932.9}{0.9 \times 60 \times 0.9 \times 18.94} = 1.22 \, in^2 \ll 8 \times 0.31 = 2.48 \, in^2 \, OK$$

For positive moment :

$M_{u,+ve} = 1765.2\,kip - in$

$\phi_f = 0.9\,(according\ to\ AASHTO, Section\,5.5.4.2)$

$M_n = Tension\ force\ in\ steel \times moment\ arm = A_s \times f_{sy} \times 0.9 \times d$

$then, required\ reinforcement :$

$$A_{s,required} \geq \frac{M_{u,+ve}}{\phi_f \times f_{sy} \times 0.9 \times d} = \frac{1765.2}{0.9 \times 60 \times 0.9 \times 18.94} = 1.92\,in^2$$

$$number\ of\ \#5\ bars\ required = \frac{A_{s,required}}{A_{s,\#5}} = \frac{1.92}{0.31} = 6.2$$

However, use 8 #5 bars for symmetric section capacity under cyclic and earthquake load reversals.

check bars' center – to – center spacing :

$$s_b = \frac{b - 2 \times (cover + \phi_{\#3} + \frac{\phi_{\#5}}{2})}{number\ of\ bars - 1} = \frac{24 - 2 \times (0.75 + 0.375 + \frac{0.625}{2})}{8 - 1} \approx 3\,in \begin{cases} < 8\,in\ OK \\ > 1.5\,in\ OK \end{cases}$$

Shear Design:

According to AASHTO (Section 5.8.2.1), $V_u \leq \phi_s \times V_n$

$\phi_s = 0.90\,(AASHTO, Section\,5.5.4.2.1)$

$V_u = 103.8\,kips$

$V_n = lesser\ of\ (V_c + V_s)\ and\ (0.25 \times f_c' \times b \times d)$

$V_c = 0.0316 \times \beta \times \sqrt{f_c'} \times b \times d\ \ (AASHTO, 5.8.3.3 - 3),\ \beta = 2.0\,(Section\,5.8.3.4.1)$

$V_c = 0.0316 \times 2 \times \sqrt{5} \times 24 \times 18.94 = 64.24\,kips$

$then, required\ V_s \geq \dfrac{V_u}{\phi_s} - V_c = \dfrac{103.8}{0.90} - 64.24 = 51.1\,kips$

$V_s = \dfrac{A_v \times f_{sy} \times d}{s_h},$

$if\ using\ \#3\ stirrups\ with\ 4\ branches \rightarrow A_v = 4 \times A_{s,\#3} = 4 \times 0.11 = 0.44\,in^2$

$then\ required\ spacing\ s_{h,required} = \dfrac{A_v \times f_{sy} \times d}{V_s} = \dfrac{0.44 \times 60 \times 18.94}{51.1} = 9.78\,in$

Check minimum shear reinforcement:

max stirrups spacing $(AASHTO\ Section\ 5.8.2.7) = 0.8 \times d = 0.8 \times 18.94 = 15.1 in \leq \dfrac{24}{4} = 6 in$

use 4 branch #3 stirrups at 5 inch spacing

$$A_v \geq 0.0316 \times \sqrt{f_c'} \times \dfrac{b \times s}{f_y} = 0.0316 \times \sqrt{5} \times \dfrac{24 \times 5}{60} = 0.141 in^2 < 0.44 in^2\ OK$$

Check Cap Beam Design According to SDC:

The SDC requires that the cap beam remains elastic when column reaches its overstrength moment. For the considered specimen, a middle bent column is connected to the cap beam forming a T-shape connection. Accordingly, the column overstrength moment is likely splitted equally between the two beam sections at the column right and left sides.

Thus, the cap beam is expected to remain elastic up to $\dfrac{M_o}{2} = \dfrac{1.2 \times 3456}{2} = 2073.6\ kip - in$

From the moment-curvature analysis using XTRACT,
Moment at first yield $= 3002\ kip - in \gg 2073.6\ kip - in\ OK$

Check Beam Torsion Design:

One way to check if additional torsion reinforcement is needed is using the ACI-318,
"The design criteria for combined torsion and shear"
The speciemn cap beam will be exposed to torsion if the column is pushed in the longitudinal direction, thus, the maximum expected torsion (T_u) on cap beam when elastic column moment is equivalent to its capacity was found approximately from SAP2000 model to be 105.4 $kips - in$

Permitted factored Torque to neglect torsion effects $T_p = \phi \times \sqrt{f_c'} \times \dfrac{A_{cp}^2}{P_{cp}}$ (ACI-318, Section 11.5.1)

$A_{cp} =$ *area enclosed by beam perimeter* $= 24 \times 20.375 = 489 in^2$, *neglect slab contribution*
$P_{co} =$ *beam perimeter* $= 2 \times (24 + 20.375) = 88.75 in$

$$T_p = 0.75 \times \sqrt{5000} \times \dfrac{489^2}{88.75} = 142888\ lb - in = 142.9\ kip - in$$

Since $T_u < T_p$, *the torsion effects can be neglected on beam*

A.2.3 Column-Cap Beam Joint Design

The specimen column-beam joint is considered a T-joint and designed according to Section 7.4 in Caltrans SDC. The joint dimensions and proportionality are checked first, then the required reinforcement is calculated.

Check Joint Propotioning:

The principal stresses in the joint should not eexceed certain limits.

$$A_{jh} = (D_c + D_s) B_{cap} = (18 + 20.375) \times 24 = 921 \, in^2$$

$$f_v = \frac{P_c}{A_{jh}} = \frac{72}{921} = 0.0782 \, ksi = 78.2 \, psi$$

$$A_{jv} = l_{ac} \times B_{cap} = 18 \times 24 = 432 \, in^2$$

$$T_c = \frac{M_o^{col}}{h} = \frac{4147.2}{0.75 \times 18} = 307.2 \, kips$$

$$v_{jv} = \frac{T_c}{A_{jv}} = \frac{307.2}{432} = 0.711 \, ksi = 711 \, psi$$

$$f_h = \frac{P_f}{B_f \times D_f} = 0 \; as \, beam \, axial \, force \, P_f \, is \, 0$$

$$then, \; p_t = \frac{f_v + f_h}{2} - \sqrt{\left(\frac{f_v + f_h}{2}\right)^2 + v_{jv}^2} = \frac{78.2 + 0}{2} - \sqrt{\left(\frac{78.2 + 0}{2}\right)^2 + 720^2} = 39.1 - 721.1 = -681.96 \, psi$$

Check $p_t < 12\sqrt{f_c'} = 12\sqrt{5000} = 848.5 \, psi$, *So* $p_t < 848 \, psi$ *OK*

$$p_c = \frac{f_v + f_h}{2} + \sqrt{\left(\frac{f_v + f_h}{2}\right)^2 + v_{jv}^2} = \frac{78.2 + 0}{2} - \sqrt{\left(\frac{78.2 + 0}{2}\right)^2 + 720^2} = 39.1 + 721.1 = 760.2 \, psi$$

Check $p_c < 0.25 f_c' = 0.25 \times 5000 = 1250 \, psi$, *Also* $p_c < 1250 \, psi$ *OK*

So joint proportioning is OK

Joint Shear Reinforcement:

Check the principle tensile stress for minimum reinforcement

$If\ p_t < 3.5\sqrt{f_c'} \rightarrow minimum\ joint\ shear\ reinforcement\ is\ needed$

$but\ p_t = 681.96\ psi >> 3.5\sqrt{5000} = 247.5\ psi$

$then,\ Shear\ reinforcement\ is\ needed!$

Vertical Stirrups :

$percentage\ of\ column\ reinforcement,\ A_s^{jv} = 0.2 \times A_{st} = 0.2 \times 16 \times 0.44 = 1.41 in^2$

$if\ using\ \#3\ stirrups\ with\ 2\ legs,\ number\ of\ stirrups\ needed = \dfrac{1.41}{2 \times 0.11} = 6.4$

$use\ \#3\ stirrups\ at\ 4\ inch\ spacing\ and\ distrbuited\ in\ a\ distance = 2 \times D_c = 36 in$

Horizontal Stirrups :

$percentage\ of\ column\ reinforcement,\ A_s^{jh} = 0.1 \times A_{st} = 0.1 \times 16 \times 0.44 = 0.704 in^2$

$if\ using\ \#3\ cross\ ties,\ number\ of\ ties\ needed = \dfrac{0.704}{0.11} = 6.4$

$and\ maximum\ vertical\ spacing\ in\ the\ scaled\ speciemn\ is\ 18 \times \dfrac{1}{4} = 4.5 in,$

$then\ use\ total\ of\ 9\ \#3\ cross\ ties\ at\ 3\ layers$

Horizontal Side Reinforcement :

$A_s^{sf} = greater\ of\ 0.1 \times A_{cap}^{top}\ and\ 0.1 \times A_{cap}^{bot} = 0.1 \times 8 \times 0.31 = 0.248 in^2$

$if\ using\ \#3\ side\ bars,\ number\ of\ bars\ needed = \dfrac{0.248}{0.11} = 2.25$

$but\ maximum\ spacing\ in\ the\ scaled\ speciemn\ is\ 12 \times \dfrac{1}{4} = 3 in,\ then\ use\ 4\ \#3\ equally\ spaced\ at\ each\ side$

Minimum Continuing Column hoops :

$\rho_s = 0.4 \times \dfrac{A_{st}}{l_{ac}^2} = 0.4 \times \dfrac{18 \times 0.44}{18^2} = 0.0098 < \rho_s\ from\ design\ (0.014)$

$then,\ the\ column\ hoops\ \#3\ at\ 2.0\ in.\ spacing\ continue\ into\ the\ joint$

A.2.4 Box-girder Slabs Design

The scaled design bending moments of the prototype box-girder slabs can be used to design the specimen slabs, but typically, the gravity loads and bridges spans are large enough to be resisted by ordinary reinforced concrete sections. Consequently, box-girder bridges are pre-stressed (post-tensioned) to reduce cross-sections dimensions and required ordinary reinforcement, which is the case in the used Academy bridge prototype.

However, due to the nature of the test and specimen orientation, the specimen box-girder slabs will not be carrying any direct gravity loads during the test. Thus, for practical reasons, no pre-stressing is needed to be applied to the specimen. Instead, enough ordinary reinforcement can be used to satisfy the SDC and AASHTO requirements. That is to keep the box-girder section elastic when the column reaches its overstrength moment since the bridge superstructure, similar to the cap beam, is a capacity protected member.

Longitudinal Steel :

According to AASHTO, Section 5.7.3.3.3,, a minimum reinforcement to develop at least 1.2 times the cracking moment of the cross-section is needed. Only the longitudinal bars in the soffit and deck slabs are assumed to provide all the required tensile reinforcement and no contribution is considered from the box-girder web longitudenal reinforcement.

The cracking moment for the specimen box-girder is: $M_{cr} = \dfrac{f_r \times I_g}{y_t}$

$f_r = 0.24 \times \sqrt{f_c'} = 0.24 \times \sqrt{5} = 0.537\, ksi$

I_g and y_t are calculated from section properties, $y_t = 10.47\, in\ \&\ I_g = 41104.2\, in^4$

then, $M_{cr} = \dfrac{0.537 \times 41104}{10.47} = 2106.9\, kip-in$

The required steel to develop such moment can be approximately calculated as follows :

$A_{s,long,\min} = \dfrac{1.2 \times M_{cr}}{\phi \times f_{sy} \times 0.9 \times d} = \dfrac{1.2 \times 2107}{0.9 \times 60 \times 0.9 \times 18.94} = 2.75\, in^2$

Because of the slab thickness limitations in the scaled speciemn, use only a single #3 layer,

and to guarantee the capacity of box-girder is higher than overstrength of moment of column,

try #3 bars at 2.5 inch spacing and check the section capacity

$$number\ of\ bars = \frac{102-2}{2.5} + 1 = 41\ bars$$

$$A_{s,long} = 41 \times 0.11 = 4.51\ in^2 > A_{s,long,min} = 2.72\ in^2 \quad OK$$

$$\rho_{deck} = \frac{A_{s,long}}{A_{deck\ slab}} = \frac{4.51}{102 \times 2.25} = 1.97\% \ , \rho_{soffit} = \frac{A_{s,long}}{A_{soffit\ slab}} = \frac{4.51}{102 \times 2.125} = 2.08\% > \rho_{min} = 0.4\%\ OK$$

$$also\ maximum\ spacing\ between\ bars\ for\ scaled\ specimen = 18 \times \frac{1}{4} = 4.5\ in > 2\ in\ OK$$

The SDC also requires that box-girder remains elastic when column reaches its overstrength capacity. Thus, moment-curvature analysis was carried out for the specimen box-girder section using XTTRACT.

The moment at first yield, $M_y^{box} = 5554\ kip-in > \dfrac{M_o^{col}}{2} = \dfrac{4156}{2} = 2078\ kip-in\ \ OK$

Transverse Steel :

Similar to longitudinal direction, the minimum reinforcement to develop at least 1.2 times the cracking moment of the cross-section is calculated first. The cracking moment for a 1-foot slice of the specimen

box-girder in the transverse direction can be caluculated from $M_{cr} = \dfrac{f_r \times I_g}{y_t}$

$$f_r = 0.24 \times \sqrt{f_c'} = 0.24 \times \sqrt{5} = 0.537\ ksi$$

I_g and y_t are calculated from slice section properties , $y_t = 10.645\ in\ \&\ I_{g,1\text{-}ft\ slice} = 4348.5\ in^4$

$then,\ M_{cr} = \dfrac{0.537 \times 4348.5}{10.645} = 219.4\ kip-in\ /\ ft$

The calculated M_{cr} per foot length was found larger than the scaled design transverse bending moments from prototype SAP2000 model, and thus the minimum reinforcement from M_{cr} governs the design.

The required steel to develop such moment can be approximately calculated as follows :

$$A_{s,long} = \frac{1.2 \times M_{cr}}{\phi \times f_{sy} \times 0.9 \times d} = \frac{1.2 \times 219.4}{0.9 \times 60 \times 0.9 \times 18.94} = 0.286\ in^2\ /\ ft$$

Because of the slab thickness limitations in the scaled speciemn, use only a single #3 layer,

$required\ number\ of\ bars = \dfrac{0.286}{0.11} = 2.59\ i.e. 3\#3\ /\ ft\ or 1\#3\ at\ 4\ inch\ spacing$

then, use 1#3 *at* 4 *inch spacing in each of the soffit and deck slabs*

A.2.5 Box-girder Webs Shear Design

The scaled design shear force of the prototype box-girder slabs can be used to design the specimen webs. The factored shear force for the entire prototype box-girder section and each web share was found from SAP2000 model as:

$$V_{u,box-girder} = 3059\,kips \quad and \quad V_{u,web} = 437\,kips$$

Accordingly, the factored shear/web for specimen design:

$$V_{u,web}^{spec.} = V_{u,web}^{proto} \times \frac{1}{S_l^2} = 437 \times \frac{1}{4^2} = 27.31\,kips$$

According to AASHTO (Section 5.8.2.1), $V_u \le \phi_s \times (V_c + V_s)$

$$\phi_s = 0.90\,(AASHTO, Section\,5.5.4.2.1)$$

$$V_c = 0.0316 \times \beta \times \sqrt{f_c'} \times b \times d \quad (AASHTO, 5.8.3.3-3),\ \beta = 2.0\,(Section\,5.8.3.4.1)$$

$$V_c = 0.0316 \times 2 \times \sqrt{5} \times 3 \times 18.94 = 8.03\,kips$$

$$then, required\ V_s \ge \frac{V_u}{\phi_s} - V_c = \frac{27.31}{0.90} - 8.03 = 22.3\,kips$$

$$V_s = \frac{A_v \times f_{sy} \times d}{s_h},$$

$Due\ to\ the\ limited\ web\ thickness, try\ \#3\ tie\ with\ single\ leg \to A_v = 1 \times A_{s,\#3} = 0.11\,in^2$

$$then\ required\ spacing\ s_{h,required} = \frac{A_v \times f_{sy} \times d}{V_s} = \frac{0.11 \times 60 \times 18.94}{22.3} = 5.6\,in$$

$\to use\ \#3\ tie\ at\ 5\ inch\ spacing$

$Check\ minimum\ shear\ reinforcement:$

$max\ stirrups\ spacing\ (AASHTO\ Section\ 5.8.2.7) = 0.8 \times d = 0.8 \times 18.94 = 15.1in \le \dfrac{24}{4} = 6\,in > 5\,in\ OK$

$use\ 4\ branch\ \#3\ stirrups\ at\ 5\ inch\ spacing$

$$A_v \ge 0.0316 \times \sqrt{f_c'} \times \frac{b \times s}{f_y} = 0.0316 \times \sqrt{5} \times \frac{3 \times 5}{60} = 0.018\,in^2 < 0.11\,in^2\ OK$$

A.2.6 Specimen RC Seat Beam Design

<u>Geometery:</u>

Start with a seat beam with width, $b=12\,in$ and height, $h=19\,in$

The materials are the same as the speciemn since the seat beams will be casted inplace with the specimen

<u>Flexural Design:</u>

$\phi_f M_n \geq M_u$

From the preliminary analysis of the speciemn in addition to considereing the three prestressing forces per seat to attach the specimen to the laboratory rigid floor, $M_u = 640\,kip - in$

Start the first beam design trial by neglecting compression steel and assuming a moment arm of "$0.9 \times d$" between the tension steel reinforcement c.g. and the compression stress block c.g.

$$d = h - cover - \phi_{stirrup} - \frac{\phi_{long.bar}}{2} = 19 - 0.75 - 0.375 - \frac{0.625}{2} = 17.56\,in$$

$\phi_f = 0.9$

$M_n = Tension\,force\,in\,steel \times moment\,arm = A_s \times f_{sy} \times 0.9 \times d$

$then, required\,reinforcement :$

$$A_{s,required} \geq \frac{M_u}{\phi_f \times f_{sy} \times 0.9 \times d} = \frac{640}{0.9 \times 60 \times 0.9 \times 17.56} = 0.75\,in^2$$

$$number\,of\,\#5\,bars\,required = \frac{A_{s,required}}{A_{s,\#5}} = \frac{0.75}{0.31} = 2.4 \rightarrow use\,4\,\#5\,bars\,for\,bottom\,reinforcement$$

$C = T = A_s \times f_{sy} = 4 \times 0.31 \times 60 = 74.4\,kips$

$C = c \times b \times \beta_1 \times f_c'., \beta_1 = 0.85 - \frac{0.05}{1000}(f_c' - 4000) = 0.80\ (AASHTO, Section 5.7.2.2)$

$$then,\,c = \frac{C}{b \times \beta_1 \times f_c'} = \frac{74.4}{12 \times 0.80 \times 5} = 1.55\,in$$

$$M_n = T \times (d - \frac{a}{2}) = 74.4 \times (17.56 - 0.775) = 1248.2\,kip - in > \frac{M_u}{\phi_f} = \frac{640}{0.9} = 711.11\,kip - in\ OK$$

$check\,bars'\,center - to - center\,spacing :$

$$s_b = \frac{b - 2 \times (cover + \phi_{\#3} + \frac{\phi_{\#5}}{2})}{number\,of\,bars - 1} = \frac{12 - 2 \times (0.75 + 0.375 + \frac{0.625}{2})}{4 - 1} \approx 3\,in \begin{cases} <8\,in\ OK \\ >1.5\,in\ OK \end{cases}$$

Shear Design:

$V_u \le \phi_s \times (V_c + V_s)$

From analysis, $V_u = 84\,kips,\ \phi_s = 0.90,$

$V_c = 0.0316 \times \beta \times \sqrt{f_c'} \times b \times d$ (*AASHTO*, 5.8.3.3 − 3), $\beta = 2.0$ (*Section* 5.8.3.4.1)

$V_c = 0.0316 \times 2 \times \sqrt{5} \times 12 \times 17.56 = 29.78\,kips$

then, required $V_s \ge \dfrac{V_u}{\phi_s} - V_c = \dfrac{84}{0.90} - 29.8 = 63.5\,kips$

$V_s = \dfrac{A_v \times f_{sy} \times d}{s_h},$

if using #3 stirrups with 2 legs $\rightarrow A_v = 2 \times A_{s,\#3} = 2 \times 0.11 = 0.22\,in^2$

then required spacing $s_{h,required} = \dfrac{A_v \times f_{sy} \times d}{V_s} = \dfrac{0.22 \times 60 \times 17.56}{63.5} = 3.65\,in$

if using 2 #3 stirrups with 2 legs each $\rightarrow A_v = 4 \times A_{s,\#3} = 4 \times 0.11 = 0.44\,in^2$

then required spacing $s_{h,required} = \dfrac{A_v \times f_{sy} \times d}{V_s} = \dfrac{0.44 \times 60 \times 17.56}{63.5} = 7.30\,in$

Check minimum shear reinforcement:

$A_v \ge 0.0316 \times \sqrt{f_c'} \times \dfrac{b \times s}{f_y} = 0.0316 \times \sqrt{5} \times \dfrac{12 \times 5}{60} = 0.07\,in^2 < 0.22\,in^2\ OK$

$\rightarrow use\ 2\,\#3\ stirrups\ with\ 2\ legs\ each\ at\ 5.0\,inch\ center - to - center\ spacing$

Appendix B: Structural and Shop Drawings

The final bidding document (Figure B.1 through Figure B.9, and Table B-1 through Table B-3) that was provided for the steel fabricators and the construction contractor for building the test specimens is attached in this appendix.

University of California, Berkeley
Structures Laboratory

Box-Girder and Column Subassembly Test Specimens – Final Bidding Document

Final Test Setup, Specimen Drawings and
Reinforcement Tables

March 2013

NOTES:

Concrete:
- f'c = 5000 psi at 28th day.
- Maximum aggregate size = 3/8 inch.

Reinforcing steel:
- All ASTM A706 Grade 60 except for stirrups.
- Stirrups can be either A706 Grade 60 or A615 Grade 60.
- Supply all reinforcements made from the same batch such that they have consistent material properties.

A minimum concrete cover of 3/8" is required for stirrups and ties.

A minimum concrete cover of 3/4" is required for main longitudinal reinforcement.

3D Schematic
Representation
of test Setup
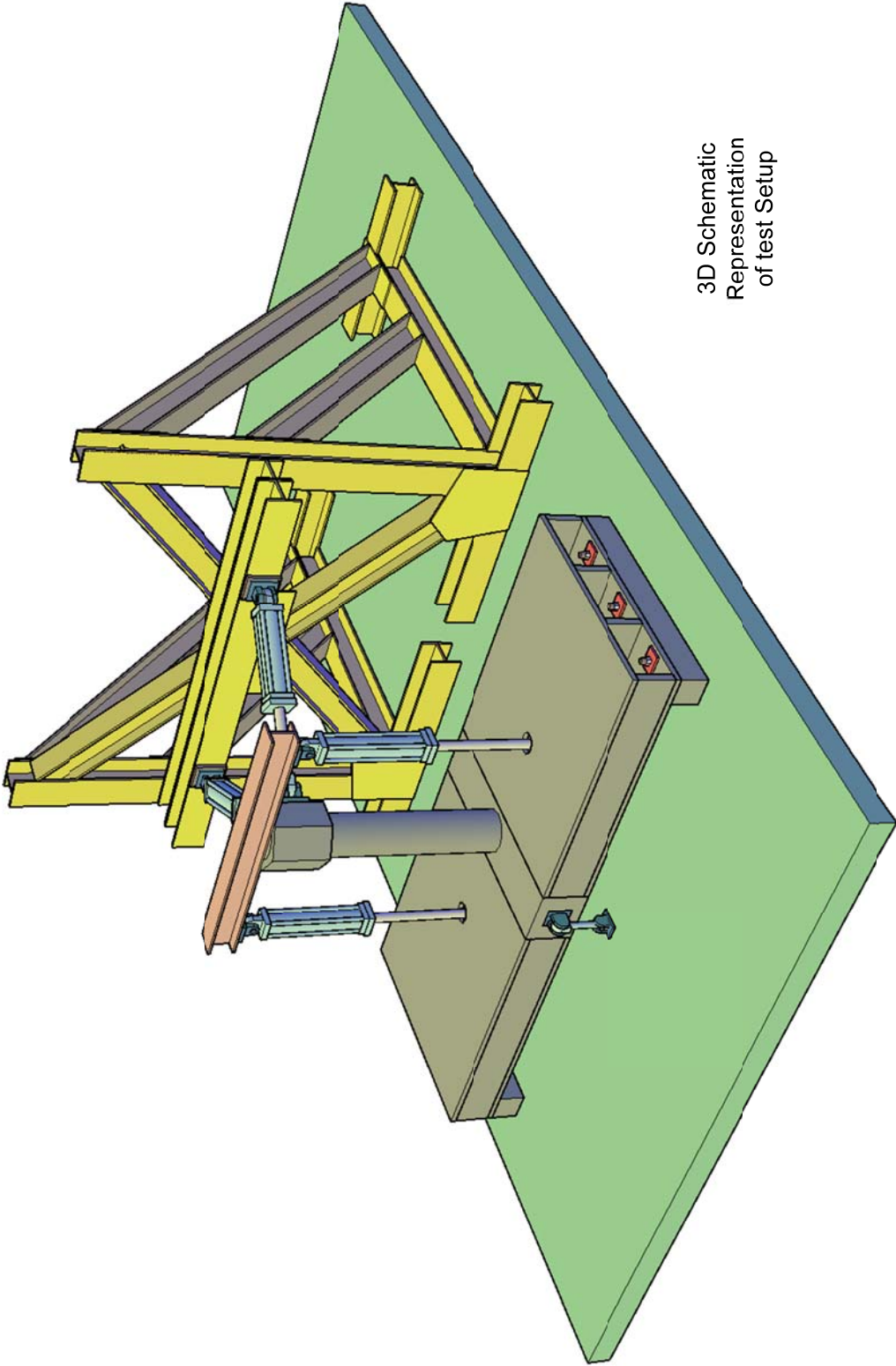
Figure B. 1 Three-dimensional schematic representation of the test setup at the Structures Laboratory at University of California, Berkeley

SIDE VIEW

Lateral Loading System

ELEVATION

Vertical Loading System

Lateral Loading System

North

PLAN

Vertical Loading System
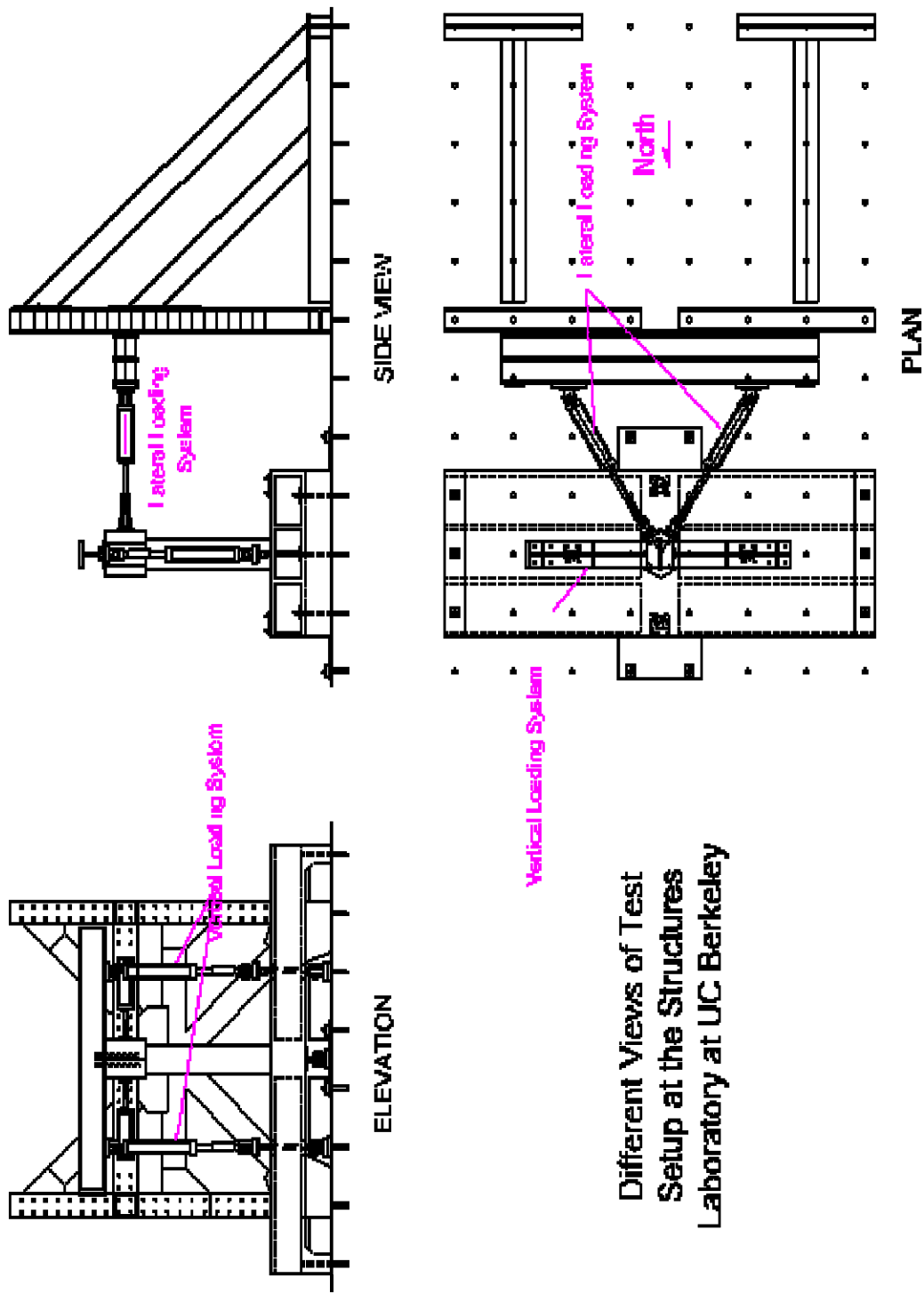
Different Views of Test Setup at the Structures Laboratory at UC Berkeley

423

Figure B. 2 Different views of the test setup at the Structures Laboratory at University of California, Berkeley
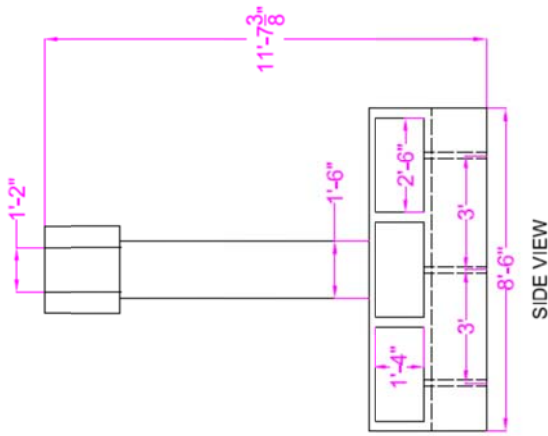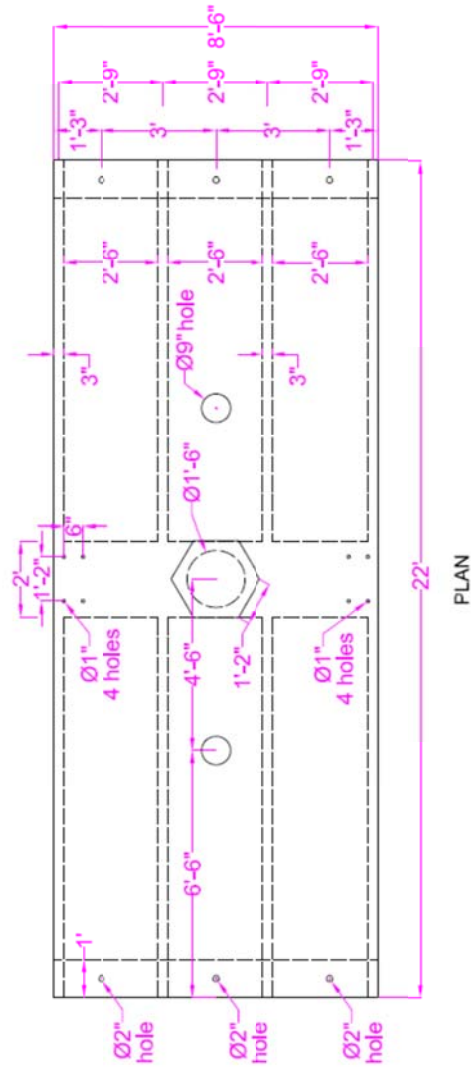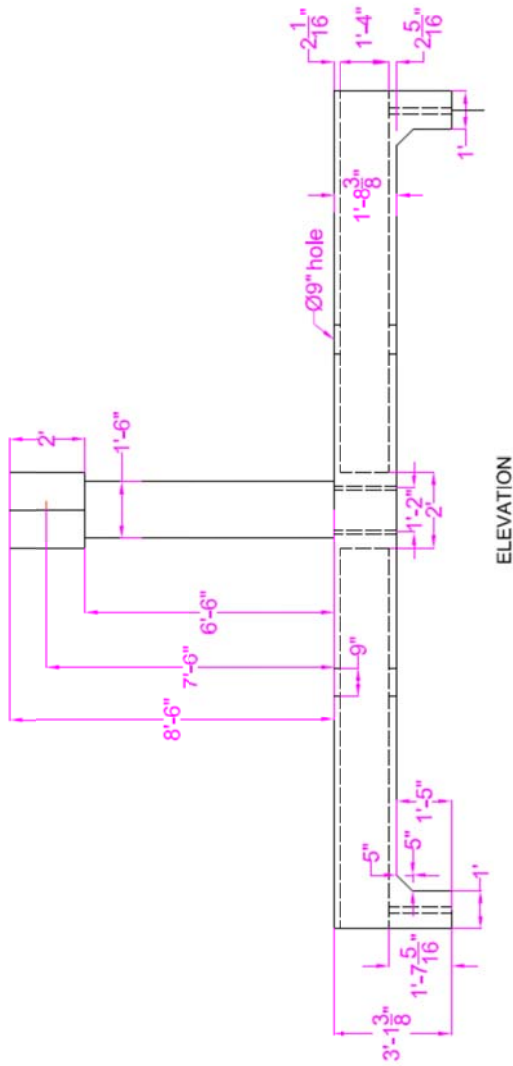
Figure B. 3 Different views of the test specimen dimensions

424

Construction Stages:

- Concrete quantities shown are for one specimen only.
- For two specimens built concurrently, double the shown concrete quantities will be needed for each pour.

Stage Three:
0.7 yard^3 (19 ft^3)

Stage Two:
3.1 yard^3 (82 ft^3)

Stage One:
2.3 yard^3 (62 ft^3)
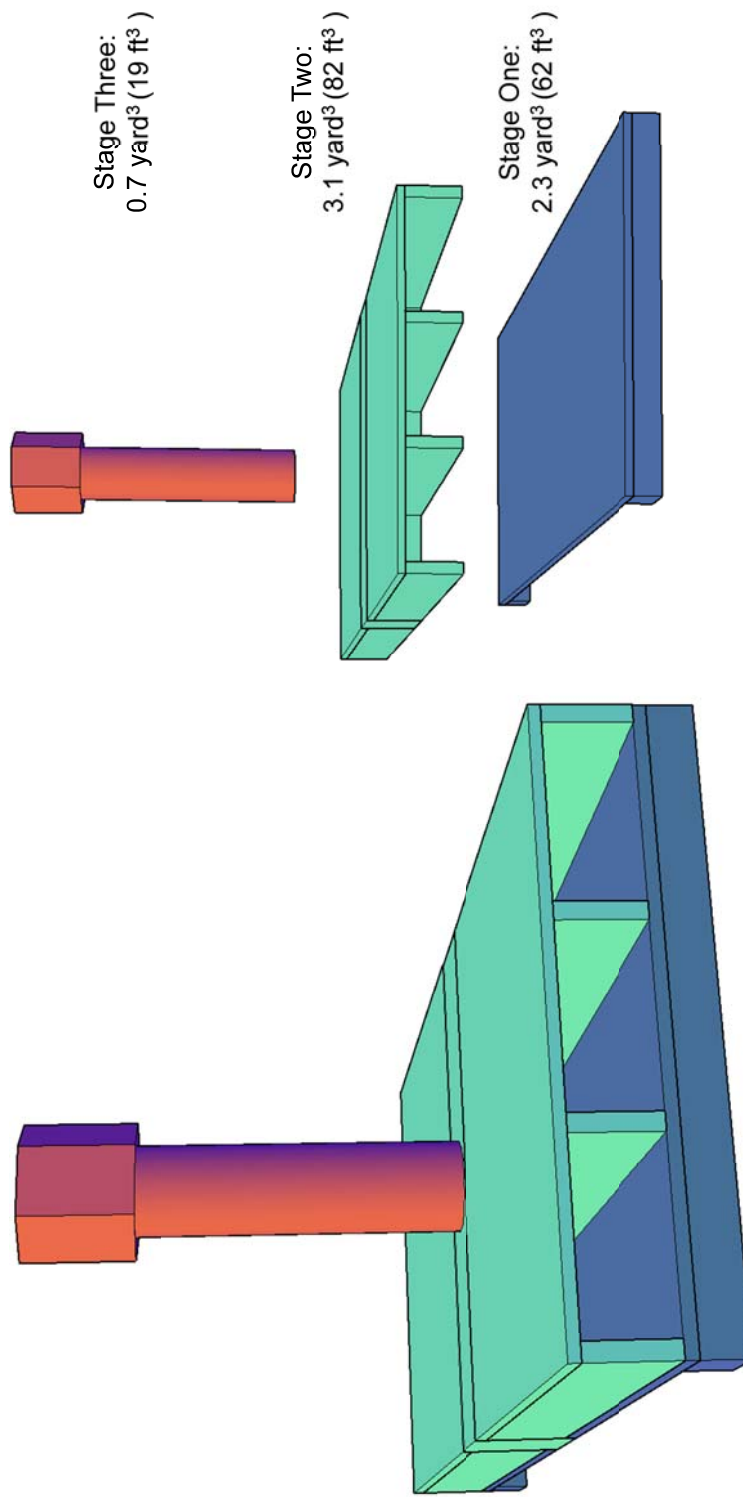
Figure B. 4 Three phases and concrete lifts sought for the specimens construction

425

Six embedded 1-inch rods locations

Column Head pipes locations
"Total of 8 1-inch through pipes"

Cross-Section A-A

Cross-Section B-B

Column Elevation
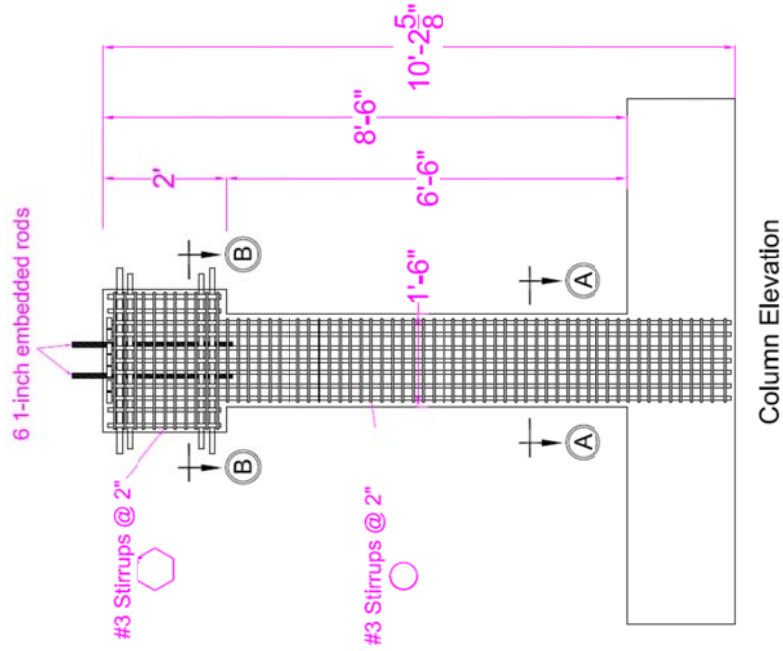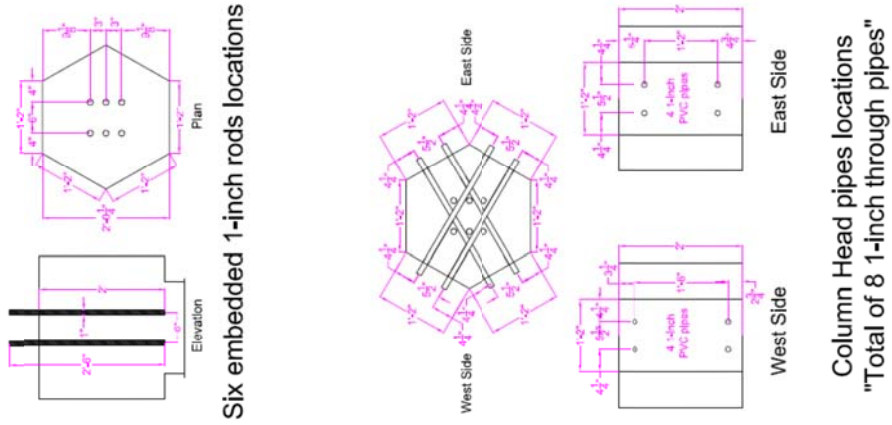
Figure B. 5 Different views and cross-sections of the column reinforcement and location of construction pipes

426
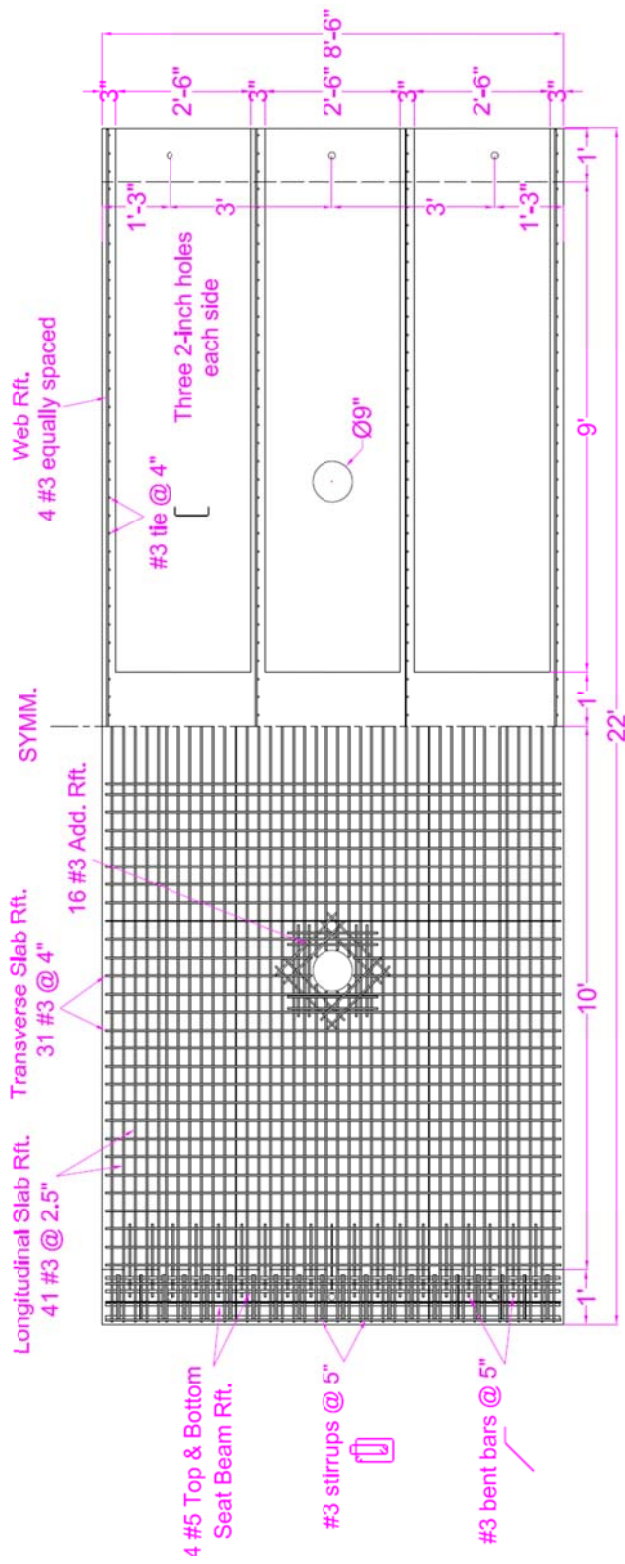
Figure B. 6 Deck slab reinforcement and details
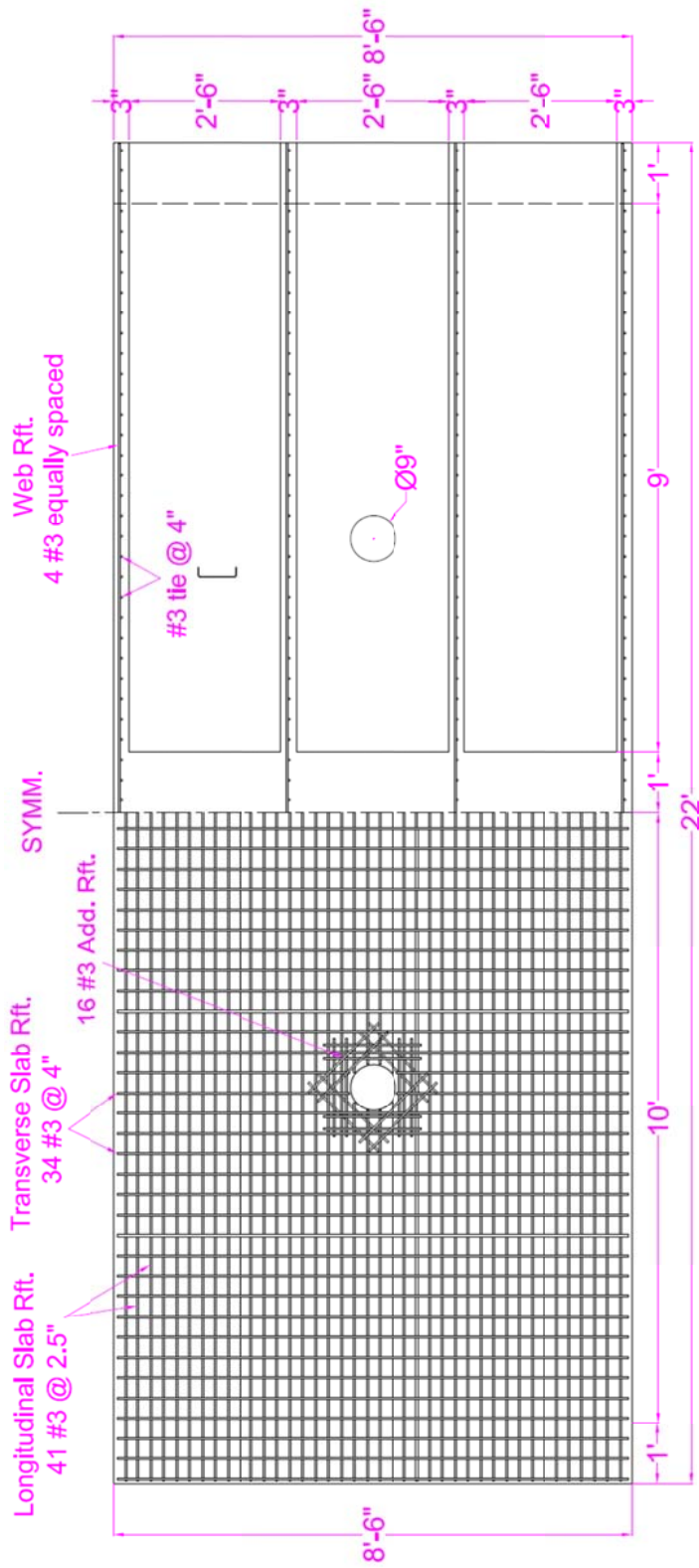
Figure B. 7 Soffit slab reinforcement and details

18 # 6

#3 Stirrups

#3 Spiral Stirrups

16 # 6

Column Head Cross-Section

1'-2"

Ø1'-6"

#3 Stirrups @ 2"

3/4"

16 # 6

Column Cross-Section

#3 Stirrups @ 2"

1'-8"

1'-4"

#3 Stirrups @ 5"

Box Girder Rft.

Cap Beam Cross-Section

Positive Rft.
8#5

4#3 Each Face
equally spaced

Negative Rft.
8#5

2

2 1/16"

2 5/16"
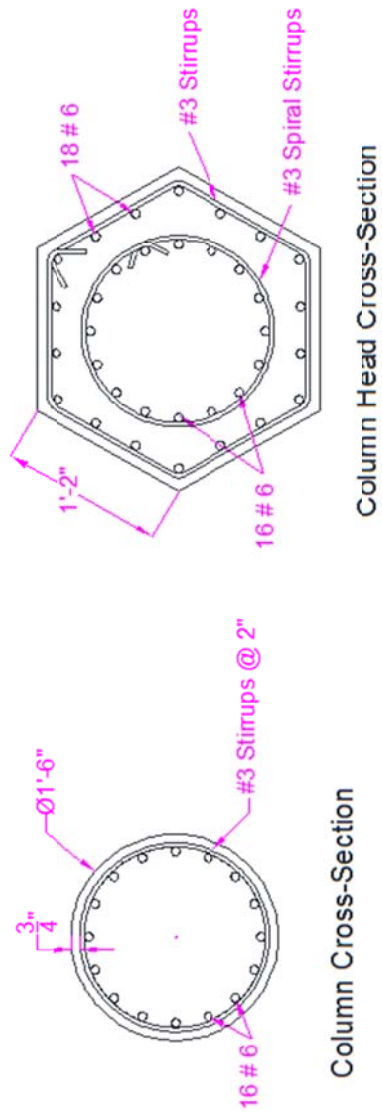
Figure B. 8 Details of longitudinal and transverse reinforcement for the specimens column and cap beam sections

429
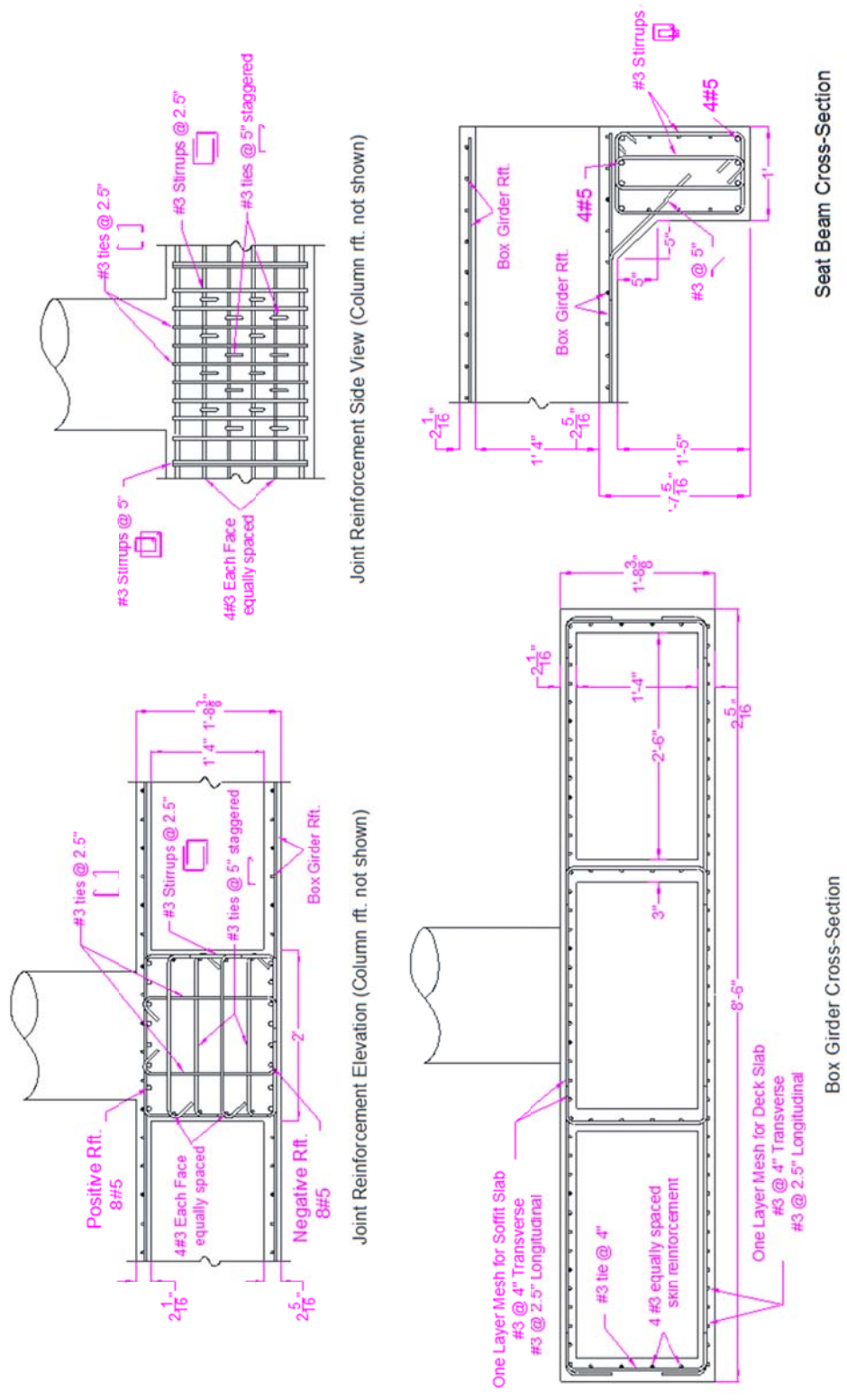
Figure B. 9 Details of longitudinal and transverse reinforcement for the specimens' joint, box-girder , and seat beams sections

430

Table B- 1 Longitudinal reinforcement shop drawing for one specimen (Quantity)

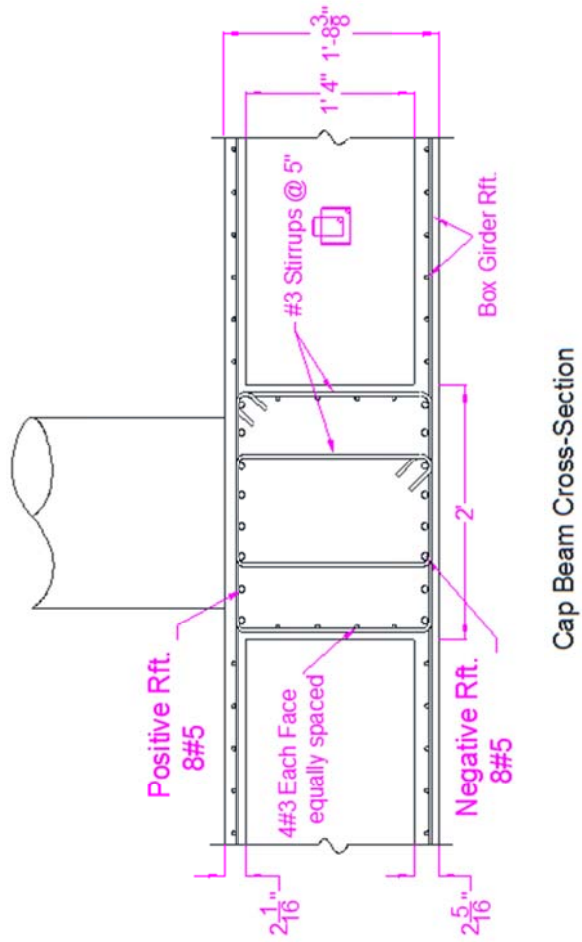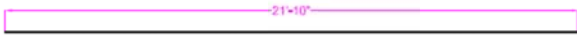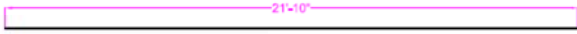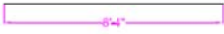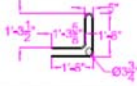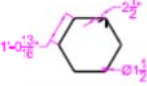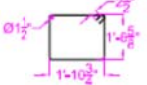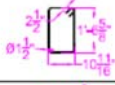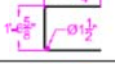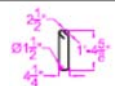| Item Discription		Bar Length	Diameter	Total bar length	Quantity
Soffit & Deck Slabs	Long. Slab Rft.		#3	21' 10"	82
	Transverse Slab Rft.		#3	9' 4.5"	136
	Trans. Rft. @ hole		#3	4' 3.5"	16
	Long. Rft. @ hole (two ends)		#3	6' 0.5"	16
	Long. Rft. @ hole (middle)		#3	8' 2.5"	8
	Rft. around hole		#3	1' 8"	68
Box girder Web Long. Rft.			#3	21' 10"	16
Column Long. Rft. (Headed Rebars)		Rebar Head Dimensions	#6	10' 0.5"	19
Column Head Rft.			#6	2' 11"	18
Cap Beam	Negative & Positive Rft.		#5	10' 4"	18
	Skin Rft.		#3	8' 4"	8
Seat Beams	Negative & Positive Rft.		#5	10' 4"	16
	Skin Rft.		#3	8' 4"	12
Lifting Hook			#5	6' 5"	6

431

Table B- 2Transverse reinforcement shop drawing for one specimen (Quantity and total weights and length)

Item No.	Discription	Bar Length	Diameter	Quantity	Bar weight (lb.)	Total weight (lb.)	Total length (ft.)
1	Long. Slab and web Rft.		#3	98	8.21	673.2	1791
2	Transverse Slab Rft.		#3	136	3.53	479.4	1275
3	Trans. Rft. @ hole		#3	16	1.61	25.8	69
4	Long. Rft. @ hole (two ends)		#3	16	2.27	36.4	97
5	Long. Rft. @ hole (middle)		#3	8	3.09	24.7	66
6	Add. Slab Rft. around hole		#3	68	0.63	42.6	114
7	Column Long. Rft. (headed bars)	Rebar Head Dimensions	#6	19	15.08	286.6	191
8	Column head Long. Rft.		#6	18	4.38	78.9	53
9	Cap and Seat Beams Long. Rft.		#5	34	10.78	366.5	352
10	Cap and Seat Beams Skin Rft.		#3	20	3.13	25.1	67
11	Lifting Hook		#5	6	6.69	40.2	39

Total weight of #3 rebars ~ 1476 lb	Total length of #3 rebars ~ 3926 ft
Total weight of #5 rebars ~ 407 lb	Total length of #5 rebars ~ 390 ft
Total weight of #6 rebars ~ 365 lb	Total length of #6 rebars ~ 244 ft

432

Table B- 3 Longitudinal reinforcement shop drawing for one specimen (Total weight and length)

Item No.	Dimensions	Length (in.)	Diameter	Quantity	Unit weight (lb.)	Total weight (lb.)	Total length (ft.)
1		57	#3	60	1.79	107.2	285
2		85	#3	11	2.66	29.3	78
3		91	#3	32	2.85	91.2	243
4		67	#3	24	2.10	50.4	134
5		65	#3	18	2.04	36.66	98
6		29	#3	264	0.91	239.9	638
7		28.5	#3	20	0.89	17.9	48
8		32.75	#3	16	1.03	16.4	44
9		62.5	#3	42	1.96	82.3	220
10		50	#3	42	1.57	65.8	175
11		21	#3	42	0.66	27.6	74

All dimensions are outer dimensions, and a minimum 1.5"-diameter bend to be used for hooks and corners

Total weight of #3 stirrups and ties ~ 737 lb	Total length of #3 stirrups and ties ~ 2034 ft

433

Appendix C: Specimens Construction

This appendix illustrates in Figure C.2 through Figure C.17 the different stages and phases for constructing the two test specimens formwork, fabricating the reinforcement cages, casting the concrete in three different lifts, then all formwork removal. All the construction work took place inside the Structures laboratory at University of California, Berkeley where the specimens were set up and tested.
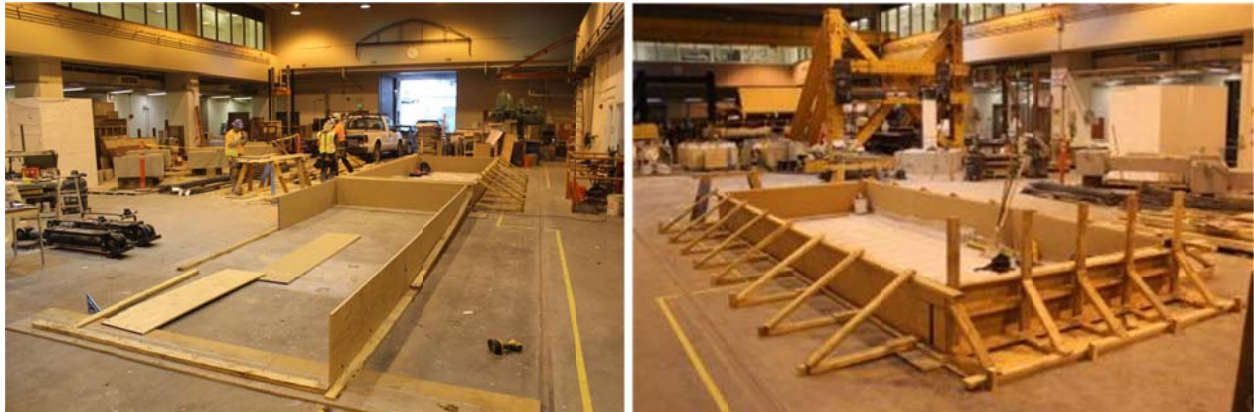
Figure C.1 Laying out the construction space and setting up the formwork for specimen's seat beams
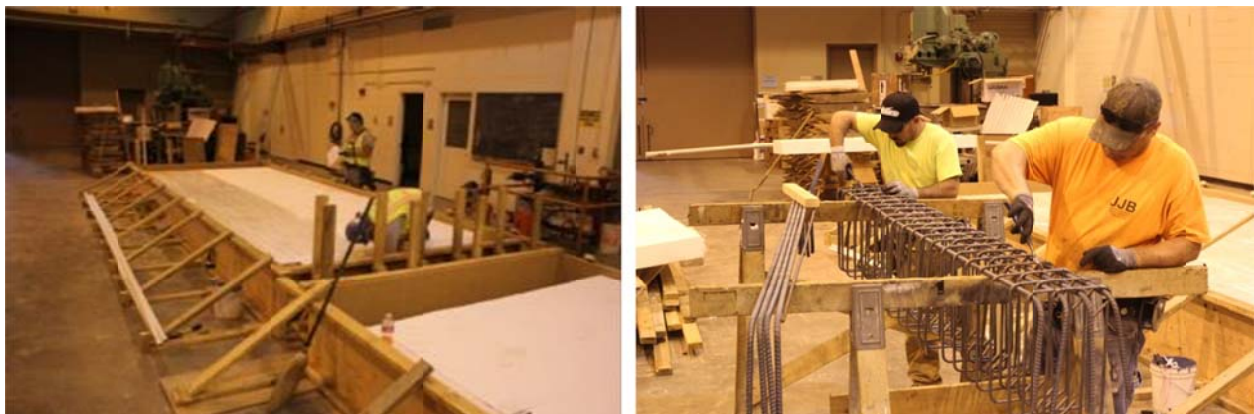
Figure C.2 Preparing styrofoam blocks used to fill the void between seat beams then covering it with plastic surface (left); fabricating the reinforcement cage of the seat beams (right)

Figure C.3 laying out the deck slab longitudinal and transverse reinforcement and installing two styrofoam cylinders to construct the 9-inch holes for actuator rods to pass through (left); final completed deck slab reinforcement mesh (right)

Figure C.4 Fabrication of the bent cap beam (left) and columns (right) cages

Figure C.5 Different stages of assembling the bent cap beam and column cages then installing the assembly in place using the overhead crane

435
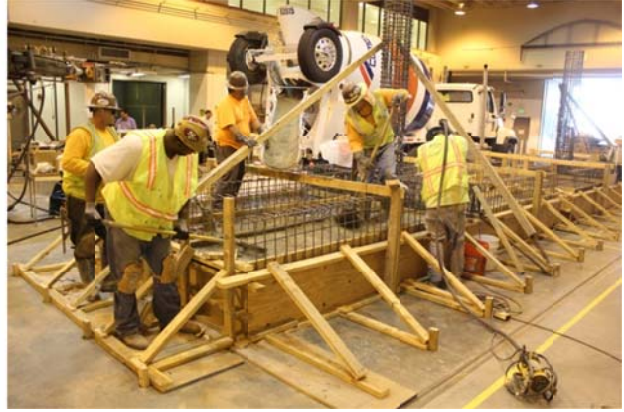
Figure C.6 A view of the complete reinforcement installation for the first construction phase including the box-girder webs reinforcement (left); and casting the seat beams and box-girder deck slab concrete first lift (right)

Figure C.7 Finishing the concrete surface after first lift (left); and covering the deck slab fresh concrete with curing blankets to avoid shrinkage cracks (right)

Figure C.8 Setting up the side formwork for the second construction phase to build the box-girder (left); and installing special custom-made cardboard boxes for the box-section cells (right)

436

Figure C.9 Laying out the soffit slab reinforcement mesh (left); and casting the box-girder soffit slab and cap beam concrete second lift (right)

Figure C.10 Finishing the surface of the second concrete lift (left); and using curing blankets in addition to the E-CURE to avoid any shrinkage cracks in the soffit slab (right)

Figure C.11 Installing the column sonotube (left); building the column head scaffolding (middle); and inserting instrumentation rods into the column formwork (right)
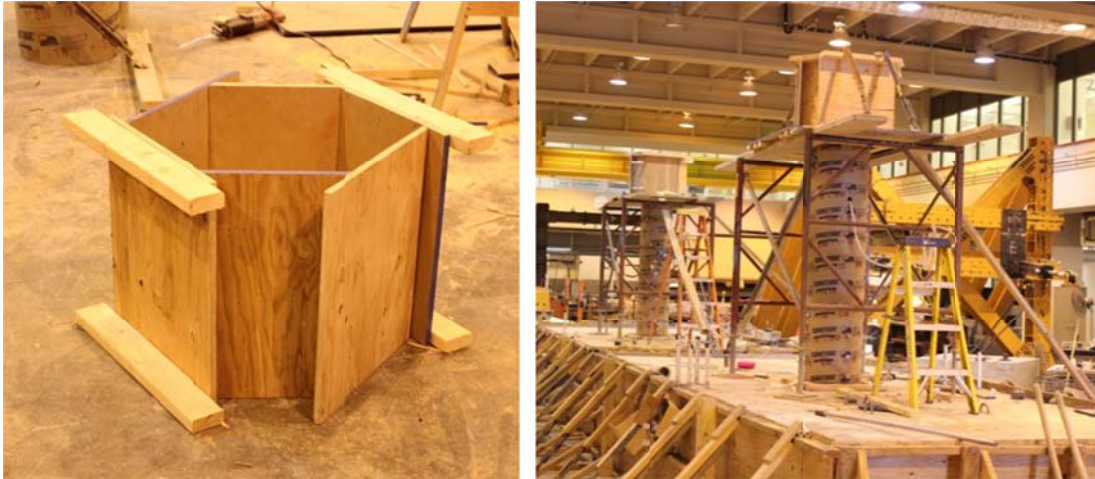
Figure C.12 Special hexagonal formwork for the column head (left); and overview of the complete formwork and scaffolding for the columns and column heads (right)

Figure C.13 Placing concrete into an overhead hopper for the concrete third lift (left); moving the hopper using the overhead crane (middle); and placing and vibrating the concrete of the column and column head (right)

Figure C.14 The two specimens' construction after it was completed in 3 stages and left to cure for 21 days before removing the formwork

Figure C.15 Removal of column scaffolding (left), side formwork (middle), and inside cardboard boxes (right)

Figure C.16 Ripping all the cardboard boxes from inside the box-girder cells (left); and grinding any styrofoam or plastic wrap stuck to the concrete surface (right)
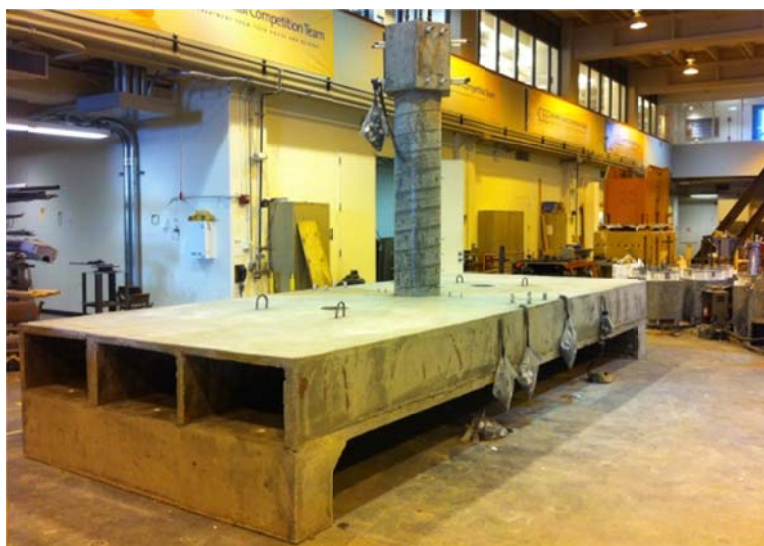
Figure C.17 A view of one of the two constructed box-girder subassembly specimens after all formwork removal

439

Appendix D: Test Setup Procedure

This appendix illustrates in Figure D.1 through Figure D.14 the different stages and phases for setting up and testing the bridge column-bent cap beam-box girder subassembly specimens at the Structures laboratory at University of California, Berkeley.
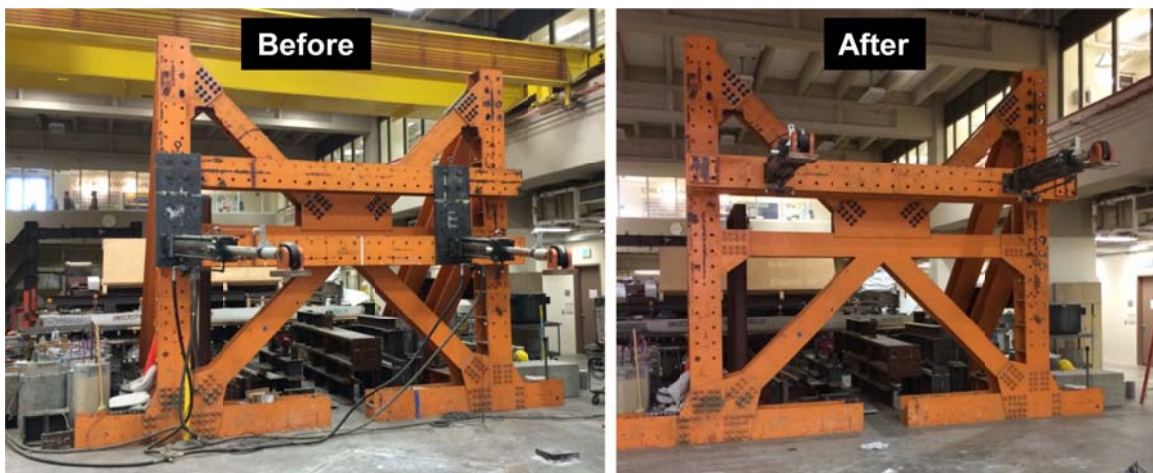
Figure D.1 Reconfiguring the reaction frame and horizontal actuators at the Structures laboratory at University of California, Berkeley to match the test specimens' height
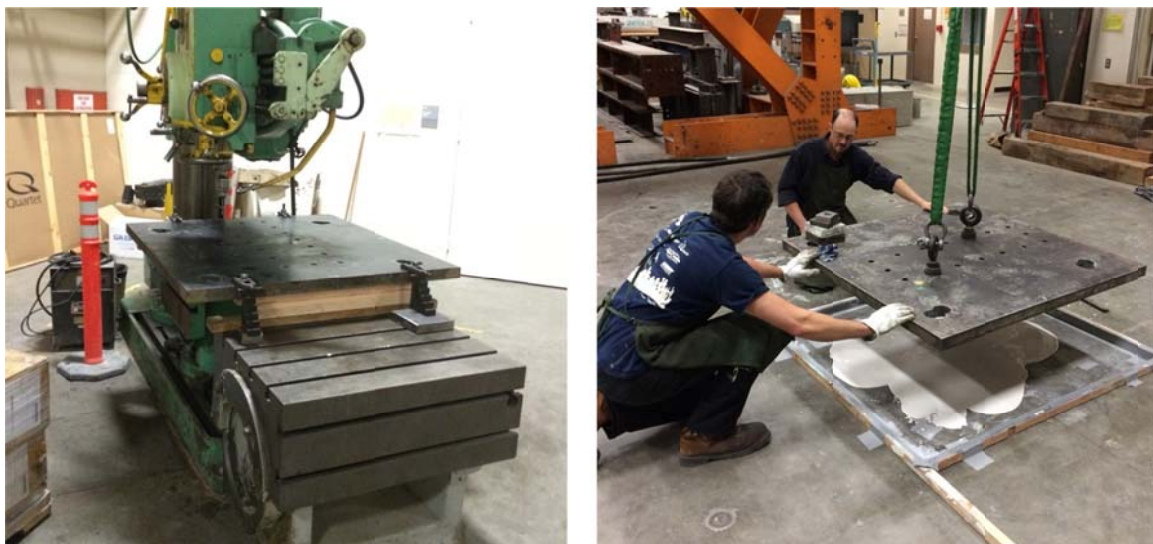
Figure D.2 Preparing the transfer plates where the vertical struts were attached by drilling matching set of holes (right) then hydrostoning it to the laboratory floor (right)
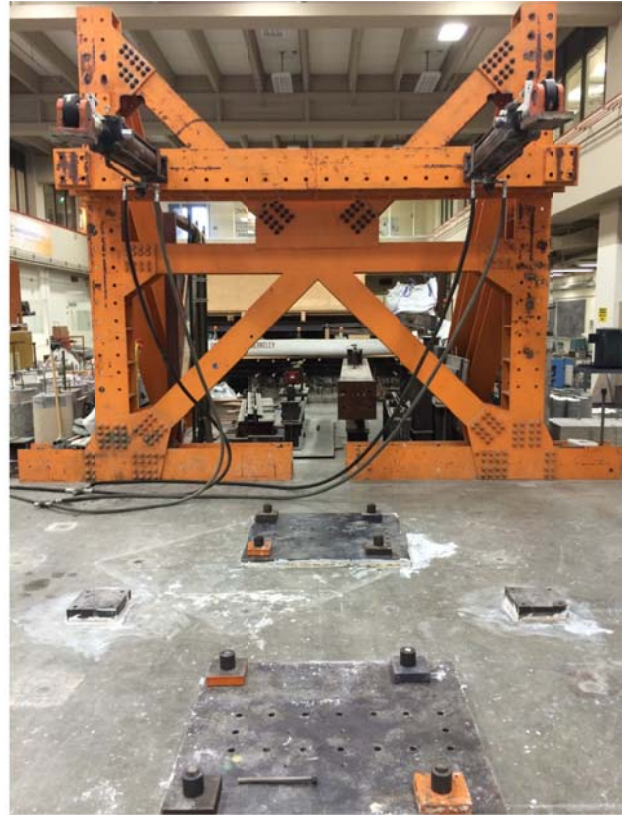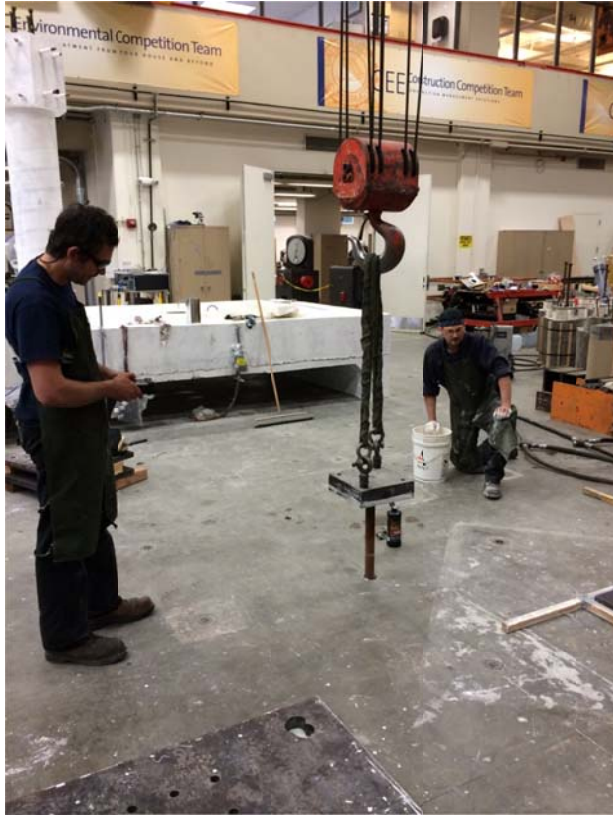
Figure D.3 Installing the vertical actuators base plates (left); and an overview of the vertical struts transfer plates and vertical actuators base plates after hydrostoning and prestressing to the rigid floor (right)

Figure D.4 Moving the first specimen from where it was constructed to where it was tested using the laboratory overhead 10-ton crane

441
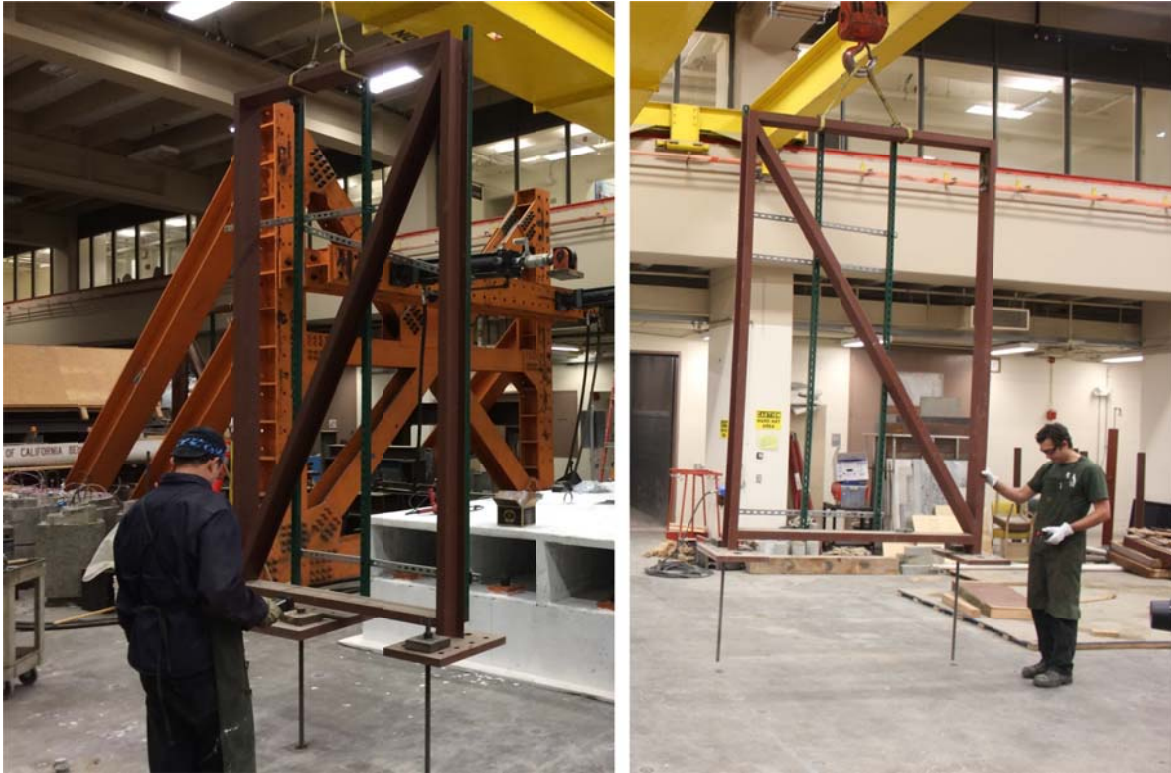
Figure D.5 Installing the South (left) and East (right) auxiliary instrumentation frames
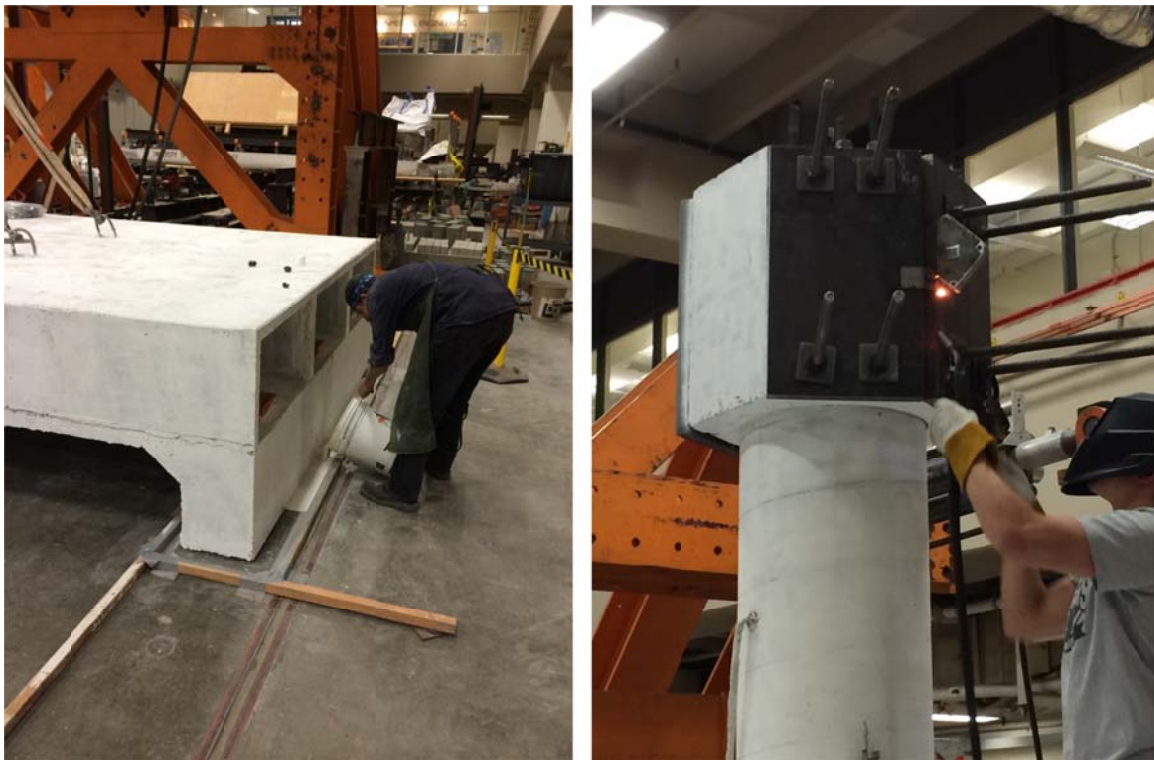
Figure D.6 Hydrostoning the specimens' seat beams to the rigid floor (left); and installing the column head plates and instrumentation target eyebolt (right)

442
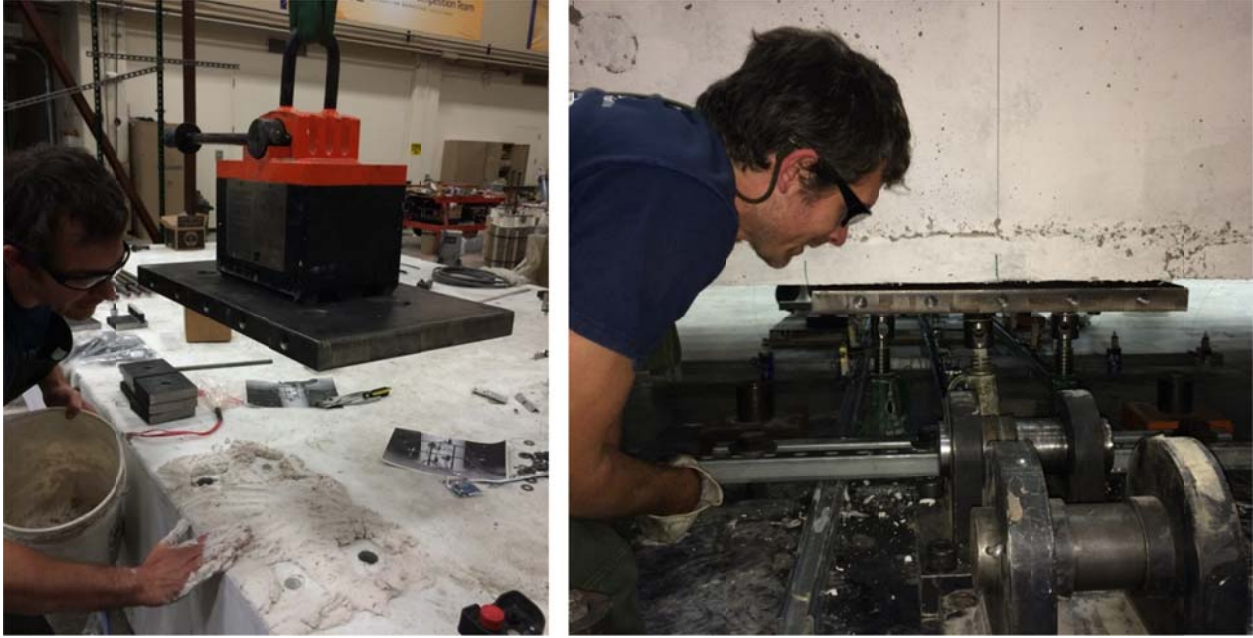
Figure D.7 Installing the top (left) and bottom (right) plates used as part of the vertical strut connection at one of the bent cap beam ends

Figure D.8 Assembling one of the vertical struts using the instrumented load cell and two clevises (left); aligning and attaching the side plate used as part of the vertical strut connection (middle); final vertical strut connection at one of the bent cap beam ends

Figure D.9 Different stages of assembling the vertical gravity loading system by assembling the actuators extensions (top left) then attaching the actuators to the spreader beam (top right and bottom left); then moving the whole gravity loading system by the overhead crane to install it on top of the column (bottom right)

Figure D.10 Different stages of instrumenting the test specimen with LVDTs at the column expected plastic hinge zone (top left), and under the specimen (bottom left); extending instrumentation cables (middle); and preparing the specimen for digital image correlation advanced monitoring technique (right)
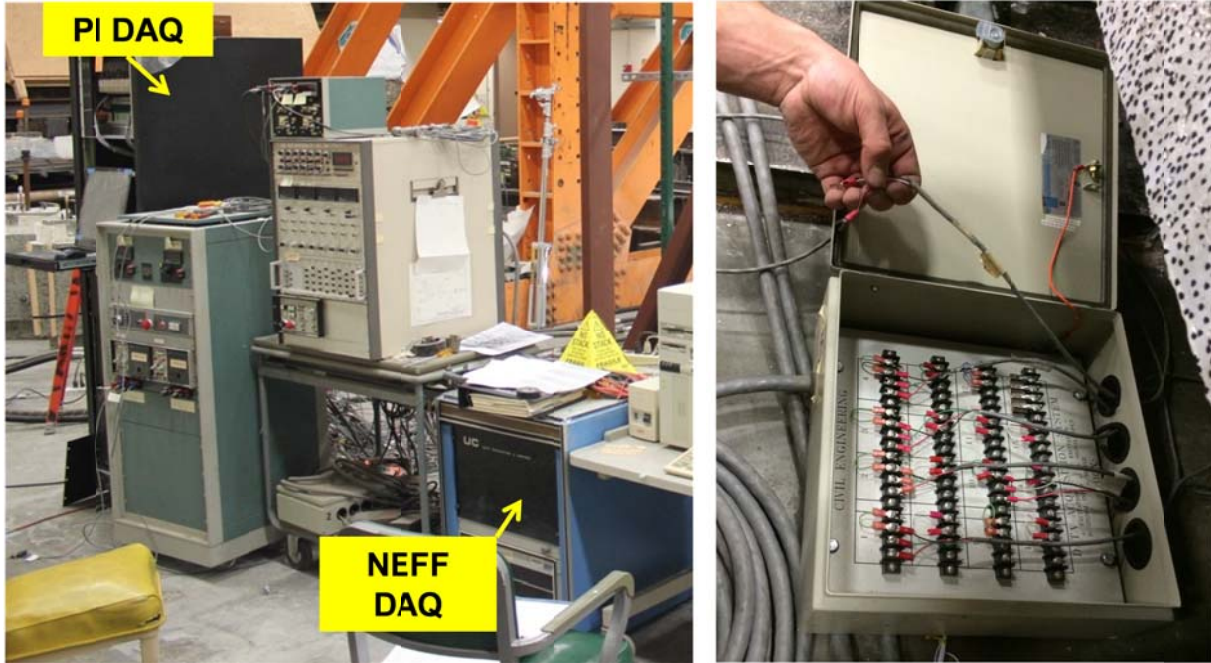
Figure D.11 Two different types of data acquisition system (DAQ) used for collecting over 250 instruments data (left); and example of connecting instruments cables to one of the NEFF DAQ special connection boxes (right)

Figure D.12 Attaching the two horizontal actuators to the column head to complete the last step of the test setup procedure

445

Figure D.13 Overview of the test setup and final cameras and flash light installations

Figure D.14 Close-up view of the test setup while one of SP1 tests is in progress

Appendix E: Instrumentations List

More than 250 instruments were used during the course of the experimental program conducted in this study. The instruments were split between two data acquisition systems: Pacific instruments (PI) and NEFF. The list of channels acquired from the PI and NEFF data acquisition systems is shown in Table E-1 and Table E2, respectively.

Table E-1 List of instrumentation channels connected to the PI data acquisition

Channel #	Name	Type of Instrument	Unit
1	Time	n/a	microsecond
2	Run	n/a	n/a
3	Pacific - 129 (0:2:0) N lat tem	Tempasonic	inch
4	Pacific - 130 (0:2:1) s lat tem	Tempasonic	inch
5	Pacific - 135 (0:2:6) n grav te	Tempasonic	inch
6	Pacific - 136 (0:2:7) s grav te	Tempasonic	inch
7	Pacific - 131 (0:2:2) n gravity	Load cell	kips
8	Pacific - 132 (0:2:3) s grav lo	Load cell	kips
9	Pacific - 133 (0:2:4) n lat loa	Load cell	kips
10	Pacific - 134 (0:2:5) s lat loa	Load cell	kips
11	Pacific - 137 (0:3:0) bs-out-e1	Strain gage	microstrain
12	Pacific - 139 (0:3:2) bs-out-e3	Strain gage	microstrain
13	Pacific - 141 (0:3:4) bs-out-w2	Strain gage	microstrain
14	Pacific - 142 (0:3:5) bs-out-w3	Strain gage	microstrain
15	Pacific - 143 (0:3:6) bs-in-e1	Strain gage	microstrain
16	Pacific - 144 (0:3:7) bs-in-e2	Strain gage	microstrain
17	Pacific - 145 (0:4:0) bs-in-e3	Strain gage	microstrain
18	Pacific - 146 (0:4:1) bs-in-w1	Strain gage	microstrain
19	Pacific - 147 (0:4:2) bs-in-w2	Strain gage	microstrain
20	Pacific - 148 (0:4:3) bs-in-w3	Strain gage	microstrain
21	Pacific - 149 (0:4:4) js-out-w1	Strain gage	microstrain
22	Pacific - 151 (0:4:6) jv-e1	Strain gage	microstrain
23	Pacific - 152 (0:4:7) jv-e2	Strain gage	microstrain
24	Pacific - 153 (0:5:0) jv-w2	Strain gage	microstrain
25	Pacific - 155 (0:5:2) jh-e2	Strain gage	microstrain
26	Pacific - 156 (0:5:3) jh-w1	Strain gage	microstrain
27	Pacific - 157 (0:5:4) jh-w2	Strain gage	microstrain
28	Pacific - 158 (0:5:5) cbt-n1-a	Strain gage	microstrain
29	Pacific - 159 (0:5:6) cbt-n1-b	Strain gage	microstrain
30	Pacific - 160 (0:5:7) cbt-n1-d	Strain gage	microstrain
31	Pacific - 161 (0:6:0) cbt-n1-a	Strain gage	microstrain
32	Pacific - 162 (0:6:1) cbt-n2-b	Strain gage	microstrain

Table E-1(continued) List of instrumentation channels connected to the PI data acquisition

Channel #	Name	Type of Instrument	Unit
33	Pacific - 163 (0:6:2) cbt-n2-c	Strain gage	microstrain
34	Pacific - 164 (0:6:3) cbt-n2-d	Strain gage	microstrain
35	Pacific - 165 (0:6:4) cbt-n2-e	Strain gage	microstrain
36	Pacific - 166 (0:6:5) cbt-s1-b	Strain gage	microstrain
37	Pacific - 167 (0:6:6) cbt-s1-d	Strain gage	microstrain
38	Pacific - 168 (0:6:7) cbt-s1-e	Strain gage	microstrain
39	Pacific - 169 (0:7:0) cbt-s2-a	Strain gage	microstrain
40	Pacific - 170 (0:7:1) cbt-s2-b	Strain gage	microstrain
41	Pacific - 171 (0:7:2) cbt-s2-c	Strain gage	microstrain
42	Pacific - 172 (0:7:3) cbt-s2-d	Strain gage	microstrain
43	Pacific - 173 (0:7:4) cbt-s2-e	Strain gage	microstrain
44	Pacific - 174 (0:7:5) cbb-n1-a	Strain gage	microstrain
45	Pacific - 175 (0:7:6) cbb-n1-b	Strain gage	microstrain
46	Pacific - 176 (0:7:7) cbb-n1-c	Strain gage	microstrain
47	Pacific - 177 (0:8:0) cbb-n1-d	Strain gage	microstrain
48	Pacific - 178 (0:8:1) cbb-n2-a	Strain gage	microstrain
49	Pacific - 179 (0:8:2) cbb-n2-b	Strain gage	microstrain
50	Pacific - 181 (0:8:4) cbb-n2-d	Strain gage	microstrain
51	Pacific - 182 (0:8:5) cbb-n2-e	Strain gage	microstrain
52	Pacific - 183 (0:8:6) cbb-s1-b	Strain gage	microstrain
53	Pacific - 184 (0:8:7) cbb-s1-c	Strain gage	microstrain
54	Pacific - 130 (0:9:1) cbb-s1-e	Strain gage	microstrain
55	Pacific - 131 (0:9:2) cbb-s2-a	Strain gage	microstrain
56	Pacific - 132 (0:9:3) cbb-s2-b	Strain gage	microstrain
57	Pacific - 133 (0:9:4) cbb-s2-c	Strain gage	microstrain
58	Pacific - 134 (0:9:5) cbb-s2-d	Strain gage	microstrain
59	Pacific - 135 (0:9:6) cbb-s2-e	Strain gage	microstrain
60	Pacific - 136 (0:9:7) cbb-s0-b	Strain gage	microstrain
61	Pacific - 137 (0:10:0) cbb-n0-b	Strain gage	microstrain
62	Pacific - 138 (0:10:1) cbb-s0-d	Strain gage	microstrain
63	Pacific - 139 (0:10:2) cbb-n0-d	Strain gage	microstrain
64	Pacific - 140 (0:10:3) cg-n1-b	Strain gage	microstrain
65	Pacific - 141 (0:10:4) cg-n2-b	Strain gage	microstrain
66	Pacific - 142 (0:10:5) cg-n3-b	Strain gage	microstrain
67	Pacific - 143 (0:10:6) cg-s1-b	Strain gage	microstrain
68	Pacific - 144 (0:10:7) cg-s2-b	Strain gage	microstrain
69	Pacific - 145 (0:11:0) cg-s3-b	Strain gage	microstrain
70	Pacific - 146 (0:11:1) cg-n1s1-	Strain gage	microstrain
71	Pacific - 147 (0:11:2) col-n1-a	Strain gage	microstrain
72	Pacific - 148 (0:11:3) col-s1-a	Strain gage	microstrain
73	Pacific - 149 (0:11:4) col-s1-b	Strain gage	microstrain
74	Pacific - 150 (0:11:5) col-e1-a	Strain gage	microstrain
75	Pacific - 151 (0:11:6) col-e1-b	Strain gage	microstrain
76	Pacific - 152 (0:11:7) col-w1-a	Strain gage	microstrain
77	Pacific - 153 (0:12:0) col-w1-b	Strain gage	microstrain
78	Pacific - 154 (0:12:1) hoop-3-a	Strain gage	microstrain
79	Pacific - 155 (0:12:2) LCl East	Strain gage	microstrain
80	Pacific - 156 (0:12:3) Loadcell	Strain gage	microstrain
81	Pacific - 157 (0:12:4) Loadcell	Strain gage	microstrain

Table E-1(continued) List of instrumentation channels connected to the PI data acquisition

Channel #	Name	Type of Instrument	Unit
82	Pacific - 158 (0:12:5) LC West	Strain gage	microstrain
83	Pacific - 159 (0:12:6) Loadcell	Strain gage	microstrain
84	Pacific - 160 (0:12:7) Loacell2	Strain gage	microstrain
85	Pacific - 161 (0:13:0) Col-N-1	LVDT	inch
86	Pacific - 162 (0:13:1) Col-N-2	LVDT	inch
87	Pacific - 163 (0:13:2) Col-N-3	LVDT	inch
88	Pacific - 164 (0:13:3) Col-N-4	LVDT	inch
89	Pacific - 165 (0:13:4) Col-S-1	LVDT	inch
90	Pacific - 166 (0:13:5) Col-S-2	LVDT	inch
91	Pacific - 167 (0:13:6) Col-S-3	LVDT	inch
92	Pacific - 168 (0:13:7) Col-S-4	LVDT	inch
93	Pacific - 169 (0:14:0) Col-E-1	LVDT	inch
94	Pacific - 170 (0:14:1) Col-E-2	LVDT	inch
95	Pacific - 171 (0:14:2) Col-E-3	LVDT	inch
96	Pacific - 172 (0:14:3) Col-E-4	LVDT	inch
97	Pacific - 173 (0:14:4) Col-E-5	LVDT	inch
98	Pacific - 174 (0:14:5) Col-W-1	LVDT	inch
99	Pacific - 175 (0:14:6) Col-W-2	LVDT	inch
100	Pacific - 176 (0:14:7) Col-W-3	LVDT	inch
101	Pacific - 65 (0:15:0) Col-W-4	LVDT	inch
102	Pacific - 66 (0:15:1) Col-W-5	LVDT	inch
103	Pacific - 67 (0:1:2) WP-FH-H-E	Wire pot	inch
104	Pacific - 68 (0:1:3) WP-FH-A-E	Wire pot	inch
105	Pacific - 69 (0:1:4) WP-FH-H-S	Wire pot	inch
106	Pacific - 70 (0:1:5) WP-FH-A-S	Wire pot	inch
107	Pacific - 71 (0:1:6) WP-MH-A-E	Wire pot	inch
108	Pacific - 72 (0:1:7) WP-MH-H-E	Wire pot	inch
109	Pacific - 177 (0:16:0)WP-MH-S	Wire pot	inch
110	Pacific - 178 (0:16:1)WP-MH-S	Wire pot	inch
111	Pacific - 179 (0:16:2)WP-BH	Wire pot	inch
112	Pacific - 180 (0:16:3)WP-BA	Wire pot	inch
113	Pacific - 181 (0:16:4)WP-fh-AL	Wire pot	inch
114	Pacific - 182 (0:16:5)WP-fh-AS	Wire pot	inch
115	Pacific - 184 (0:16:7) Pulse	electric pulse	volt

Table E-2 List of instrumentation channels connected to the NEFF data acquisition

Channel #	Name	Type of Instrument	Unit
1	DATE		
2	TIME		
3	CLOCK		millisecond
4	LOG		
5	Top North actuator load	laod cell	kip
6	Top South actuator load	laod cell	kip
7	Gravity North actuator load	laod cell	kip
8	Gravity South actuator load	laod cell	kip
9	Top North actuator tempo disp	temposonic	inch
10	Top South actuator tempo disp	temposonic	inch
11	Gravity North actuator disp	temposonic	inch
12	Gravity South actuator disp	temposonic	inch
13	disp slab a-5	LVDT	inch
14	disp slab c-3	LVDT	inch
15	disp slab c-2	LVDT	inch
16	disp slab b-5	LVDT	inch
17	disp slab b-4	LVDT	inch
18	disp slab c-4	LVDT	inch
19	disp slab d-4	LVDT	inch
20	disp slab c-5	LVDT	inch
21	disp slab e-5	LVDT	inch
22	disp slab d-5	LVDT	inch
23	disp slab c-7	LVDT	inch
24	disp slab c-8	LVDT	inch
25	disp slab d-6	LVDT	inch
26	disp slab c-6	LVDT	inch
27	disp slab b-6	LVDT	inch
28	disp wp-twist	wire pot	inch
29	disp wp-mh-h-e	wire pot	inch
30	disp wp-fh-ael	wire pot	inch
31	disp wp-mh-a-e	wire pot	inch
32	disp wp-fh-aer	wire pot	inch
33	disp wp-fh-h-e	wire pot	inch
34	disp wp-fh-a-e	wire pot	inch
35	disp wp-mh-a-s	wire pot	inch
36	disp wp-mh-h-s	wire pot	inch
37	disp wp-fh-a-s	wire pot	inch
38	disp wp-fh-h-s	wire pot	inch
39	disp wp-beamh	wire pot	inch
40	disp wp-beama	wire pot	inch
41	tds-s1-b	strain gage	microstrain
42	tds-s3-c	strain gage	microstrain
43	tds-s1-a	strain gage	microstrain
44	lds-s1-a	strain gage	microstrain
45	lds-s2-b	strain gage	microstrain
46	tds-s2-a	strain gage	microstrain
47	tds-s3-b	strain gage	microstrain
48	tds-s4-b	strain gage	microstrain
49	tds-s4-c	strain gage	microstrain
50	cg-s3-a	strain gage	microstrain

Table E-2(continued) List of instrumentation channels connected to the NEFF data acquisition

Channel #	Name	Type of Instrument	Unit
51	cg-s2-a	strain gage	microstrain
52	cg-s1-a	strain gage	microstrain
53	col-w1-h	strain gage	microstrain
54	col-n1-g	strain gage	microstrain
55	col-n1-e	strain gage	microstrain
56	col-n1-d	strain gage	microstrain
57	col-w1-g	strain gage	microstrain
58	col-n1-c	strain gage	microstrain
59	hoop-2-c	strain gage	microstrain
60	hoop-1-c	strain gage	microstrain
61	col-w1-f	strain gage	microstrain
62	col-w1-e	strain gage	microstrain
63	hoop-1-b	strain gage	microstrain
64	hoop-2-a	strain gage	microstrain
65	col-w1-d	strain gage	microstrain
66	col-w1-c	strain gage	microstrain
67	ws-e1-north	strain gage	microstrain
68	tds-n3-d	strain gage	microstrain
69	tds-n1-e	strain gage	microstrain
70	tds-n2-a	strain gage	microstrain
71	lds-n2-b	strain gage	microstrain
72	lds-n4-b	strain gage	microstrain
73	ws-w1-north	strain gage	microstrain
74	tds-n1-d	strain gage	microstrain
75	tds-n2-e	strain gage	microstrain
76	lds-n1s1-b	strain gage	microstrain
77	tds-n2-c	strain gage	microstrain
78	tds-n3-b	strain gage	microstrain
79	lds-n1-c	strain gage	microstrain
80	tds-n1-a	strain gage	microstrain
81	col-s1-g	strain gage	microstrain
82	hoop-3-c	strain gage	microstrain
83	col-e1-g	strain gage	microstrain
84	col-e1-h	strain gage	microstrain
85	col-s1-e	strain gage	microstrain
86	hoop-3-b	strain gage	microstrain
87	col-s1-c	strain gage	microstrain
88	col-e1-f	strain gage	microstrain
89	col-e1-d	strain gage	microstrain
90	col-s1-d	strain gage	microstrain
91	col-e1-e	strain gage	microstrain
92	hoop-1-a	strain gage	microstrain
93	hoop-2-b	strain gage	microstrain
94	col-e1-c	strain gage	microstrain
95	tds-n2-d	strain gage	microstrain
96	tds-n2-b	strain gage	microstrain
97	tds-n4-c	strain gage	microstrain
98	tds-n4-d	strain gage	microstrain
99	tds-n1-c	strain gage	microstrain
100	tds-n3-c	strain gage	microstrain

Table E-2(continued) List of instrumentation channels connected to the NEFF data acquisition

Channel #	Name	Type of Instrument	Unit
101	lds-n1-b	strain gage	microstrain
102	tds-n1-b	strain gage	microstrain
103	lds-n1-a	strain gage	microstrain
104	cg-n1s1-a	strain gage	microstrain
105	cg-n3-a	strain gage	microstrain
106	cg-n2-a	strain gage	microstrain
107	cg-n1-a	strain gage	microstrain
108	tss-n3-d	strain gage	microstrain
109	tss-n1-b	strain gage	microstrain
110	lss-n1-a	strain gage	microstrain
111	tss-n2-c	strain gage	microstrain
112	lss-n1-b	strain gage	microstrain
113	lss-n2-b	strain gage	microstrain
114	lss-n1-c	strain gage	microstrain
115	tss-n1-a	strain gage	microstrain
116	tss-n3-c	strain gage	microstrain
117	tss-n2-b	strain gage	microstrain
118	tss-n2-d	strain gage	microstrain
119	tss-n1-c	strain gage	microstrain
120	tss-n1-e	strain gage	microstrain
121	tss-n3-b	strain gage	microstrain
122	tss-n1-d	strain gage	microstrain
123	tss-s1-c	strain gage	microstrain
124	lss-s2-b	strain gage	microstrain
125	tss-s1-a	strain gage	microstrain
126	tss-s1-d	strain gage	microstrain
127	tss-s3-b	strain gage	microstrain
128	tss-s3-d	strain gage	microstrain
129	tss-s3-c	strain gage	microstrain
130	lss-s1-a	strain gage	microstrain
131	lss-s1-c	strain gage	microstrain
132	tss-s1-b	strain gage	microstrain
133	lss-s1-b	strain gage	microstrain
134	tss-s2-d	strain gage	microstrain
135	tss-s1-e	strain gage	microstrain
136	tss-s2-c	strain gage	microstrain
137	tss-s2-b	strain gage	microstrain
138	lds-n1s1-c	strain gage	microstrain
139	tds-s1-e	strain gage	microstrain
140	ws-w1-south	strain gage	microstrain
141	tds-s2-e	strain gage	microstrain
142	tds-s1-d	strain gage	microstrain
143	tds-s2-d	strain gage	microstrain
144	lds-s1-c	strain gage	microstrain
145	ws-e1-south	strain gage	microstrain
146	tds-s2-c	strain gage	microstrain
147	lds-s1-b	strain gage	microstrain
148	tds-s1-c	strain gage	microstrain
149	tds-s4-a	strain gage	microstrain
150	lds-n1s1-a	strain gage	microstrain

Appendix F: Struts Fabrication and Calibration

This appendix describes the characteristics of the two vertical struts fabricated and instrumented specifically for this study. These struts were fabricated with a target capacity of 250 kip each and were made of AISI 4140 steel. More details about the fabrication, instrumentation and calibration of the two instrumented strut load cells are presented.

F.1   FABRICATION AND INSTRUMENTAION

The two struts were meant to provide vertical roller supports at the two ends of the bent cap beam in the test specimen. Two special rods were fabricated with female threaded ends such that two clevises can be attached from the two sides of each of the two rods. Longitudinal and cross-sections showing the geometry and dimensions of the typical strut rod is shown in Figure E.1. The rods were fabricated from a hollow AISI 4140 steel cylinder as shown in Figure E.2. One of the two final fabricated rods and typical strain gage instrumentation is shown in Figure E.3. For the importance of determining the bent cap beam moments in this study, the two vertical struts were instrumented and calibrated to relate the strain readings to the axial force in the strut. Each of the two struts was instrumented with two rosettes and two linear strain ages. Each rosette comprised two strain gages that were attached to the strut that that one gage is aligned with the centerline of the strut, while the other is aligned with the circumference. Meanwhile, the linear strain gages were aligned with the rod centerline. All the strain gages had 120 Ω resistance and a gage length of 0.062 in. The gages were glued to the struts and were covered with three protective coating layers. For each strut, the 4 gages in the 2 rosettes were connected using a full Wheatstone bridge circuit, while the two linear gages were connected separately each through a quarter bridge circuit. The layout of the linear and rosettes strain gages and the Wheatstone bridge connections are schematically shown in Figure E.4. The final instrumented strut attached to the two clevises from the two ends is shown in Figure E.5.
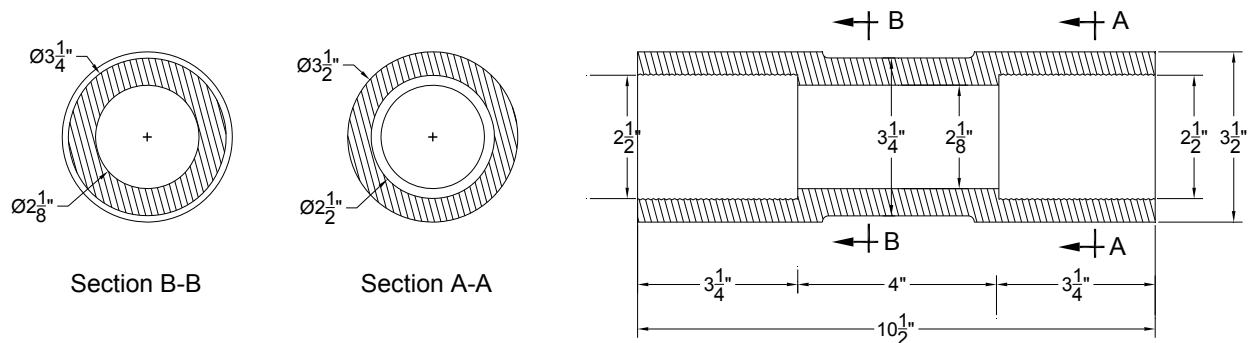

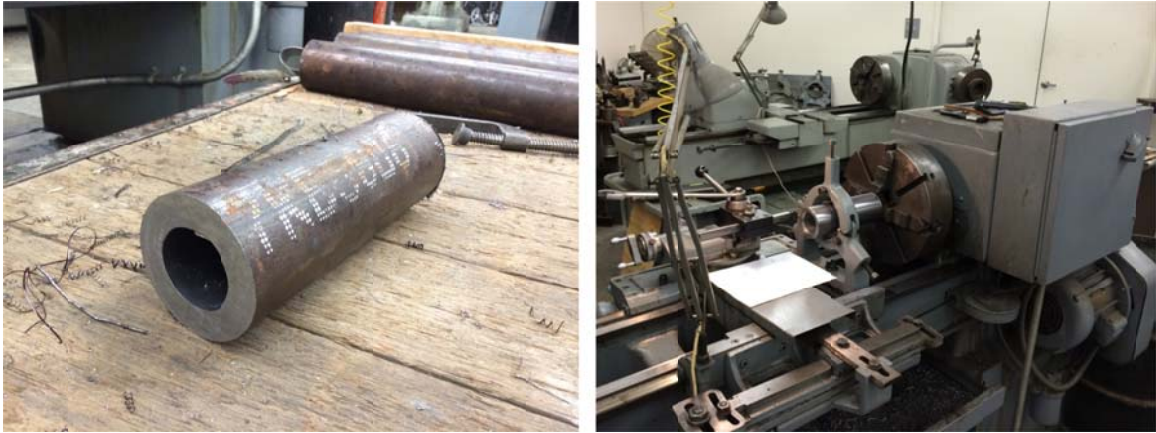**Figure E.1 Longitudinal and cross sections of the fabricated vertical struts**

Figure E.2 Fabrication of the struts from raw 4140 steel cylinders using the milling machine at the machine shop at University of California, Berkeley

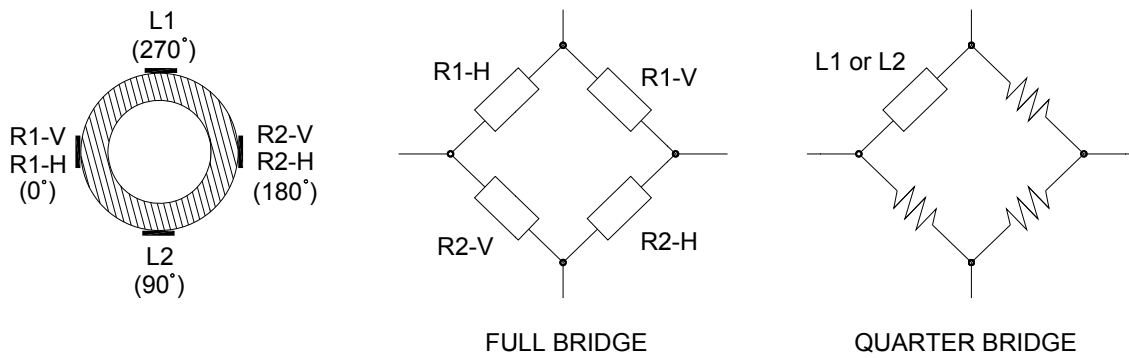**Figure E.3 Final fabricated vertical strut (left) and installing a rosette strain gage (right)**

Figure E.4 Lay out of the strut strain gages and bridge connections for rosettes and linear gages
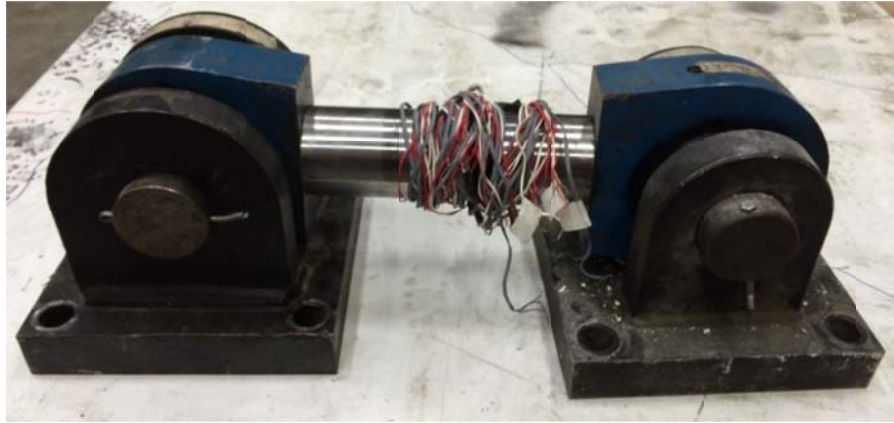
454

Figure E.5 A fully assembled vertical strut with two clevises at the two ends

F.2 LOAD CELLS CALIBRATION

The two instrumented load cell struts were calibrated using a Universal Testing Machine with a capacity of 140 kip as shown in Figure E.6. To perform the calibration, the two struts were loaded up to 120 kips and unloaded several times. The force and different strain gages reading were acquired continuously through the PI data acquisition system. Meanwhile, the force and the full bridge strain reading were manually recorded at 10-kips increments. The force-strain relationships were plotted using the rosettes full bridge strain and the linear gages strain as well. The data from the full bridge strain were found more accurate and less noisy than the linear gages. A linear slope was best fit to the force-full bridge strain data for each of the two struts and the calibration factor was estimated accordingly. Figure E.7 shows the calibration data for one of the struts which was acquired manually at 10 kips increments. Moreover, the calibration data from the PI for both struts are shown in Figure E.8. The calibration revealed excellent linearity of the load cells during loading and unloading.
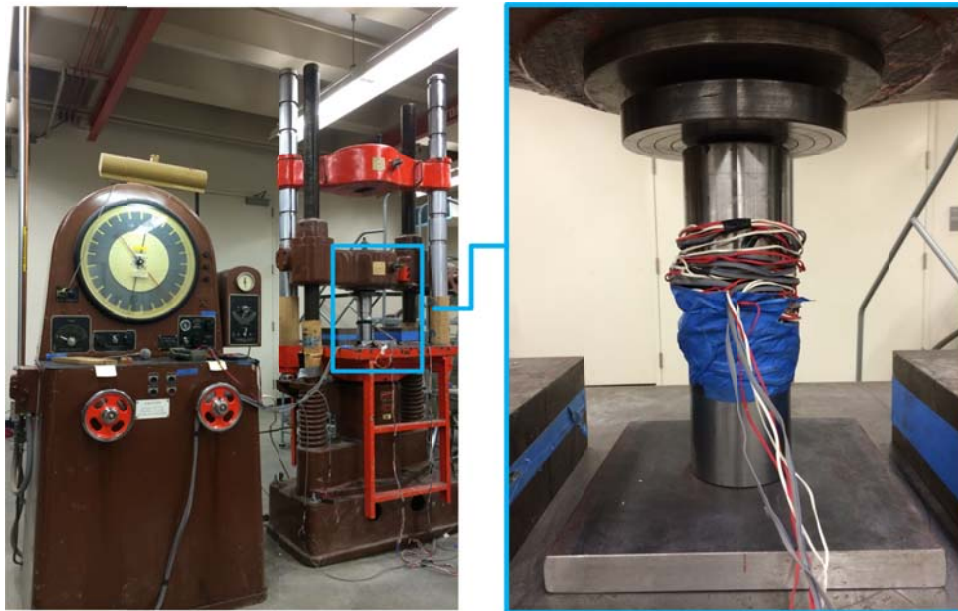

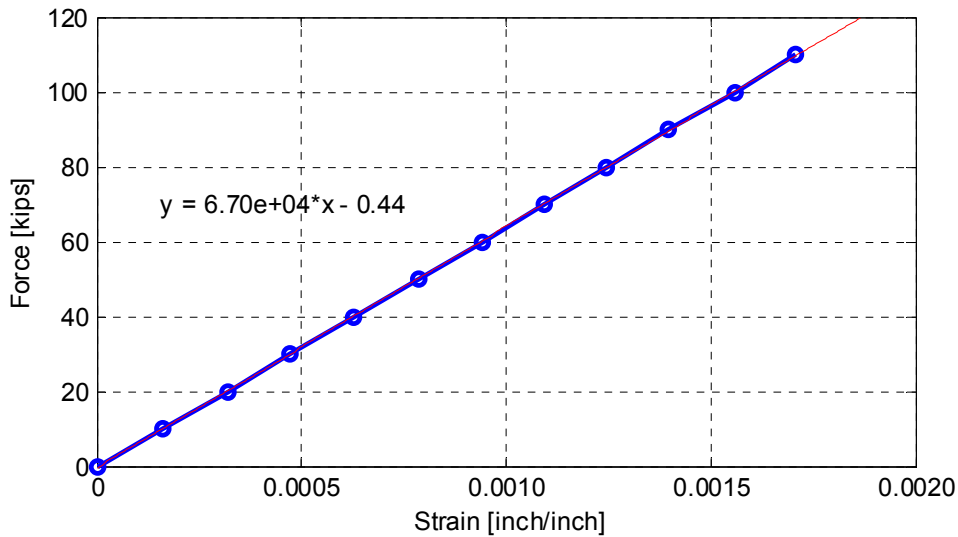**Figure E.6 Vertical struts load cell calibration using Universal Testing Machine**

455

Figure E.7 Force-strain relationship for the first load cell using manually acquired data
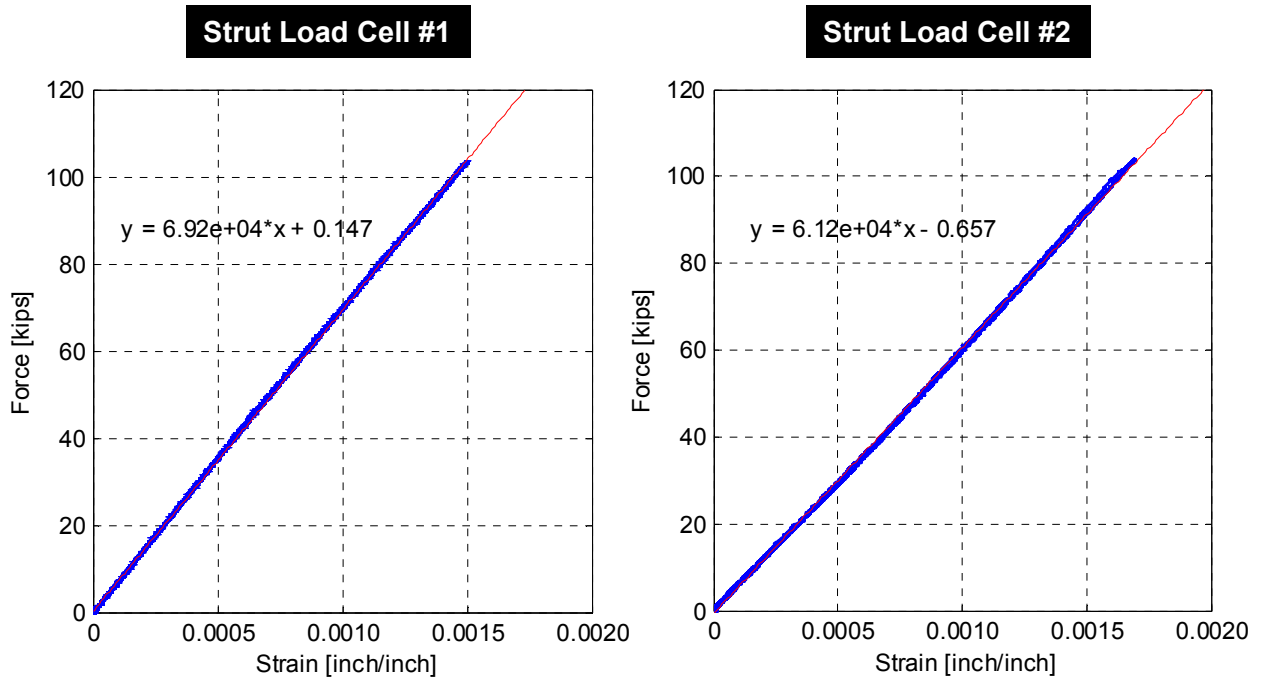

Figure E.8 Force-strain relationship for both load cells using the PI acquired data for the rosettes full bridge strain (the best fit slope resembles the calibration factor and identified on the plots)

The calibration factor is considered the slope of the best fitted linear function. It is noted that for the same load cell, the slope obtained from the manually collected data is little lower than the more accurate value obtained from the continuously recorded PI data. Meanwhile, the calibration factor for the two load cells is little different, 0.0069 for the first strut load cell versus 0.0061 for the second strut load cell. This could be attributed to possible slight differences in fabrication, but mainly because of the variation of the strain gages location and orientation from the two struts.